Jerzy Leszczynski · Manoj K. Shukla

Editors

European Academy of Sciences

Practical Aspects of Computational Chemistry II

An Overview of the Last Two Decades and Current Trends

Springer

Practical Aspects of Computational Chemistry II

Jerzy Leszczynski • Manoj K. Shukla
Editors

Practical Aspects of Computational Chemistry II

An Overview of the Last Two Decades and Current Trends

Springer

Editors
Prof. Jerzy Leszczynski
Department of Chemistry
Jackson State University
P.O. Box 17910
1400 Lynch Street
Jackson, MS 39217
USA

Prof. Manoj K. Shukla
Department of Chemistry
Jackson State University
P.O. Box 17910
1400 Lynch Street
Jackson, MS 39217
USA

Present affiliation:
Environmental Laboratory
US Army Engineer Research
    and Development Center
3909 Halls Ferry Road
Vicksburg, MS 39180
USA

Preface

It is a rare event that the impressive group of leading experts is willing to share their views and reflections on development of their research areas in the last few decades. The editors of this book have been very fortunate to attract such contributions, and as an effect two volumes of "Practical Aspects of Computational Chemistry: Overview of the Last Two Decades and Current Trends" are being published. Astonishingly, we found that this task was not so difficult since the pool of authors was derived from a large gathering of speakers who during the last 20 years have participated in the series of meetings "Conferences on Current Trends in Computational Chemistry" (CCTCC) organized by us in Jackson, Mississippi. We asked this group to prepare for the 20th CCTCC, organized in October 2011; the reviews of the last 20 years of the progress in their disciplines and their response to our request were overwhelming. This initiative was conveyed to Springer who, in collaboration with the European Academy of Sciences (EAS), invited us to edit such a book. We are now pleased to present a second volume (the first one has been published in January 2012) of this publication.

The current volume presents the compilation of splendid contributions distributed over 14 chapters. The very first chapter contributed by R. Cammi discusses the important aspects of recent development of the Polarizable Continuum Model (PCM) at the coupled cluster level. The effects of extreme pressure on the molecular properties within the PCM framework are also discussed. M.V. Basilevsky, A.V. Odinokov, and N. Kh. Petrov have used Bjerrum-Fuoss-Kraus approach to describe the theory of association/dissociation of ion pairs in binary solvent mixtures in the next chapter. The third chapter describes the application of graph theory to determine all the possible structures and temperature-dependent distribution of water cluster, and this has been contributed by M. Aida et al. In the following chapter, H. Okumura, S.G. Itoh, and Y. Okamoto discuss generalized-ensemble algorithms for the complex molecular simulation. Such an approach has advantage over the conventional Monte Carlo and molecular dynamics simulations since the problem of trapping of simulation in the energy local minima does not arise.

Next three contributions are devoted to nano-science. In the fifth chapter S. Irle et al. present results of QM-/MD-based investigation of formation of different

nanostructures such as fullerene, carbon nanotube, and graphene under nonequilibrium conditions. And this chapter is followed by a contribution on quantum mechanical study of chemical reactivity of carbon nanotube in which T. Yumura and M. Kertesz have reviewed recent progress made on covalent functionalization of single-walled carbon nanotube. Chapter 7, contributed by J. Huang et al., discusses the designing of functional materials using theoretical methods. The importance of long-range dispersion interaction to study nanomaterials is also described.

In the next chapter, L.N. Ognichenko et al. present recent advances in QSPR/QSAR analysis of nitrocompounds where solubility, lipophilicity, and toxicity are adequately discussed. In Chapter 9, L. Gorb et al. discuss the application of quantum chemical calculations for the prediction of physicochemical properties of energetic materials. Chapter 10, written by I. Kaplan and U. Miranda, encompasses the state-of-the-art calculations on electronic structure and properties of 3d transition metal dimmers, namely, the dimers of Mn and Sc. On the other hand, S. Sakaki presents the results of the σ-bond activation reactions by transition metal complexes in the next chapter. Chapter 12 deals with the theoretical modeling of environmental mercury depletion reaction and is contributed by D. Majumdar, S. Roszak, and J. Leszczynski. In the next chapter, B.R. Ramachandran and L.M. Pratt describe organolithium chemistry using quantum mechanical methods. The last chapter of the current volume is presented by J. Gu, J. Wang, and J. Leszczynski. It presents review of the computational modeling of low-energy electron-induced DNA damage.

With great pleasure, we take this opportunity to thank all authors for devoting their time and hard work, enabling us to complete the current volume "Practical Aspects of Computational Chemistry II: Overview of the Last Two Decades and Current Trends." We are grateful for the excellent support from the President of the EAS as well as to the editors of Springer. Many thanks go to our families and friends without whom the realization of the book was not possible.

Jackson, Mississippi, USA   Jerzy Leszczynski
                                                                        Manoj K. Shukla

Contents

Contributors

Misako Aida Center for Quantum Life Sciences, and Department of Chemistry, Graduate School of Science, Hiroshima University, Hiroshima, Japan

Dai Akase Center for Quantum Life Sciences, and Department of Chemistry, Graduate School of Science, Hiroshima University, Hiroshima, Japan

A.G. Artemenko Laboratory of Theoretical Chemistry, Department of Molecular Structure, A.V. Bogatsky Physical-Chemical Institute National Academy of Sciences of Ukraine, Odessa, Ukraine

M.V. Basilevsky Photochemistry Center RAS, Moscow, Russia

Ariana Beste Oak Ridge National Laboratory, Oak Ridge, TN, USA

Roberto Cammi Dipartimento di Chimica G.I.A.F, Università di Parma, Parma, Italy

K.R.S. Chandrakumar Fukui Institute for Fundamental Chemistry, Kyoto University, Kyoto, Japan

Edurado Cruz-Silva Rensselaer Polytechnic Institute, Troy, NY, USA

Hideo Doi Center for Quantum Life Sciences, and Department of Chemistry, Graduate School of Science, Hiroshima University, Hiroshima, Japan

Miguel Fuentes-Cabrera Oak Ridge National Laboratory, Oak Ridge, TN, USA

Leonid Gorb SpecPro, Inc, Vicksburg, MS, USA

Badger Technical Services, LLC, Vicksburg, MS, USA

Jiande Gu Drug Design & Discovery Center, State Key Laboratory of Drug Research, Shanghai Institute of Materia Medica, Shanghai Institutes for Biological Sciences, CAS, Shanghai, China

Interdisciplinary Nanotoxicity Center, Department of Chemistry and Biochemistry, Jackson State University, Jackson, MS, USA

Frances C. Hill US Army ERDC, Vicksburg, MS, USA

Jingsong Huang Oak Ridge National Laboratory, Oak Ridge, TN, USA

Stephan Irle Institute for Advanced Research and Department of Chemistry, Nagoya University, Nagoya, Japan

Satoru G. Itoh Department of Theoretical and Computational Molecular Science, Institute for Molecular Science, Okazaki, Aichi, Japan

Research Center for Computational Science, Okazaki, Aichi, Japan

Department of Structural Molecular Science, The Graduate University for Advanced Study, Okazaki, Aichi, Japan

Jacek Jakowski Oak Ridge National Laboratory, Oak Ridge, TN, USA

Ilya G. Kaplan Instituto de Investigaciones en Materiales, Universidad Nacional Autónoma de México, México D.F, Mexico

Miklos Kertesz Department of Chemistry, Georgetown University, Washington, DC, USA

Yana Kholod Badger Technical Services, LLC, Vicksburg, MS, USA

Interdisciplinary Center for Nanotoxicity, Department of Chemistry, Jackson State University, Jackson, MS, USA

N.A. Kovdienko Laboratory of Theoretical Chemistry, Department of Molecular Structure, A.V. Bogatsky Physical-Chemical Institute National Academy of Sciences of Ukraine, Odessa, Ukraine

Victor E. Kuz'min Laboratory of Theoretical Chemistry, Department of Molecular Structure, A.V. Bogatsky Physical-Chemical Institute National Academy of Sciences of Ukraine, Odessa, Ukraine

Jerzy Leszczynski Interdisciplinary Center for Nanotoxicity, Department of Chemistry, Jackson State University, Jackson, MS, USA

US Army ERDC, Vicksburg, MS, USA

Department of Chemistry and Biochemistry, Jackson State University, Jackson MS, USA

Alejandro Lopez-Bezanilla Oak Ridge National Laboratory, Oak Ridge, TN, USA

Devashis Majumdar Department of Chemistry and Biochemistry, Jackson State University, Jackson, MS, USA

Vincent Meunier Rensselaer Polytechnic Institute, Troy, NY, USA

Ulises Miranda Instituto de Investigaciones en Materiales, Universidad Nacional Autónoma de México, México D.F, Mexico

Keiji Morokuma Cherry L. Emerson Center for Scientific Computation and Department of Chemistry, Emory University, Atlanta, GA, USA

Fukui Institute for Fundamental Chemistry, Kyoto University, Kyoto, Japan

Eugeniy N. Muratov Laboratory of Theoretical Chemistry, Department of Molecular Structure, A.V. Bogatsky Physical-Chemical Institute National Academy of Sciences of Ukraine, Odessa, Ukraine

Yoshio Nishimoto Institute for Advanced Research and Department of Chemistry, Nagoya University, Nagoya, Japan

A.V. Odinokov Photochemistry Center RAS, Moscow, Russia

L.N. Ognichenko Laboratory of Theoretical Chemistry, Department of Molecular Structure, A.V. Bogatsky Physical-Chemical Institute National Academy of Sciences of Ukraine, Odessa, Ukraine

Yuko Okamoto Department of Physics, Graduate School of Science, Nagoya University, Nagoya, Aichi, Japan

Structural Biology Research Center, Graduate School of Science, Nagoya University, Nagoya, Aichi, Japan

Center for Computational Science, Graduate School of Engineering, Nagoya University, Nagoya, Aichi, Japan

Hisashi Okumura Department of Theoretical and Computational Molecular Science, Institute for Molecular Science, Okazaki, Aichi, Japan

Research Center for Computational Science, Okazaki, Aichi, Japan

Department of Structural Molecular Science, The Graduate University for Advanced Study, Okazaki, Aichi, Japan

Alister J. Page Fukui Institute for Fundamental Chemistry, Kyoto University, Kyoto, Japan

N.Kh. Petrov Photochemistry Center RAS, Moscow, Russia

P.G. Polishchuk Laboratory of Theoretical Chemistry, Department of Molecular Structure, A.V. Bogatsky Physical-Chemical Institute National Academy of Sciences of Ukraine, Odessa, Ukraine

Lawrence M. Pratt Department of Chemistry, Fisk University, Nashville, TN, USA

Hu-Jun Qian Institute for Advanced Research and Department of Chemistry, Nagoya University, Nagoya, Japan

B. Ramu Ramachandran College of Engineering & Science, Louisiana Tech University, Ruston, LA, USA

Szczepan Roszak Institute of Physical and Theoretical Chemistry, Wroclaw University of Technology, Wroclaw, Poland

Biswajit Saha Fukui Institute for Fundamental Chemistry, Kyoto University, Kyoto, Japan

Shigeyoshi Sakaki Fukui Institute for Fundamental Chemistry, Kyoto University, Kyoto, Japan

Bobby G. Sumpter Oak Ridge National Laboratory, Oak Ridge, TN, USA

Alvaro Vazquez-Mayagoitia Argonne National Laboratory, Argonne, IL, USA

Ying Wang Institute for Advanced Research and Department of Chemistry, Nagoya University, Nagoya, Japan

Tomoki Yoshida Center for Quantum Life Sciences, and Department of Chemistry, Graduate School of Science, Hiroshima University, Hiroshima, Japan

Jarod Younker Oak Ridge National Laboratory, Oak Ridge, TN, USA

National Institute for Computational Science, Oak Ridge, TN, USA

Takashi Yumura Department of Chemistry and Materials Technology, Kyoto Institute of Technology, Kyoto, Japan

Chapter 1
On Two Recent Developments in the Description of Molecular Properties in Solution by Using the Polarizable Continuum Model (PCM): The Coupled-Cluster Theory and the Molecules at Extreme Pressures

R. Cammi

Abstract A summary of the key aspects of polarizable continuum model (PCM) for the calculations of molecular properties in solution is accompanied with the description of some new computational features recently introduced within the PCM framework. These features regard the extension of the quantum-mechanical description of the solute to the coupled-cluster level and the description of the effects of the extreme pressure on the molecular properties.

1.1 Introduction

A major concern of the modern quantum chemistry is the prediction of molecular properties and processes in solution [1–3]. There are two main approaches for the description of solvation effects, making use the first of a discrete representation of the solvent, and the second of a continuous responsive distribution. For a systematic exploration of a wide range of molecular properties and processes, the continuum methods are by far preferable. The justification of this statement is easily done. The discrete models are forcibly based on a computer simulation, in which all the numerous degrees of freedom of the solvent molecules have to be explicitly considered, with numerous repeated calculations of the interactions among the molecular partners of the system, required to reach convergence in the thermal average given by the simulation procedure MD or MC, with millions of steps or moves. The continuum solvation methods have a by far simpler computational structure. Considering an ab initio QM description of the solute, the procedure is based on the definition of an effective Hamiltonian accompanied by a solute-solvent integral interactions operators with a two body kernel, in which no

R. Cammi (✉)

Dipartimento di Chimica G.I.A.F, Università di Parma, I-43100 Parma, Italy
e-mail: roberto.cammi@unipr.it

degrees of freedom of the solvent molecules enter explicitly. The solution of this effective Schrödinger equation is obtained with the standard procedure of ab initio calculations in gas phase. With this standard iterative process, the complete effect of the solvent on the solute is obtained.

In this contribution, we review on prediction of molecular properties within polarizable continuum model (PCM), which well represents one of the several versions of the continuum methods [1–3]. The review presents an overview of key aspects of the PCM modeling as well as of the two recent developments in title.

1.2   The Basic and the Standard PCM

The PCM was originally formulated as an ab initio quantum-mechanical (QM) methods to describe the solvent effects over molecules [4]. It uses an effective molecular Hamiltonian for the solute, given by adding to the Hamiltonian of the isolated molecule (H^0) a term describing the interaction with the external medium, which is represented as a homogeneous and infinite dielectric medium having the same dielectric permittivity of the pure solvent:

$$H_\Psi = H^0 + V^{MS}(\Psi). \tag{1.1}$$

The solute-solvent interaction operator $V^{MS}(\Psi)$ describes the electrostatic interaction of the solute M with the dielectric medium, and its argument denotes that it depends on the wavefunction (Ψ) of the solute itself. PCM has been the prototype of the continuum methods based on the apparent surface charge (ASC) approach, characterized by a continuous charge distribution σ spread on the boundary of the cavity in the continuum medium containing the solute M. The cavity in PCM is accurately modeled on the shape of M starting from a set of interlocking spheres centered on the nuclei of the atoms of M and with radii related to the corresponding atomic van der Waals radii.

The surface charges are obtained by solving the boundary conditions at the cavity surface which determine a jump into the directional derivative of the total electrostatic potential $V = V_M + V_\sigma$ (V_M is the electrostatic potential produced by the electronic and nuclear charge distribution of the solute). The apparent surface charges are source of the electrostatic potential V_σ which interact with the electrons and nuclei of the molecule. V_σ is called the solvent reaction potential and completely determines the solute-solvent iteration operator $V^{MS}(\Psi)$.

The basic energy quantity of the PCM model has the thermodynamical status of a free energy of the whole solute-solvent systems and is given by the following functional:

$$G_{el} = < \Psi | H^0 + \frac{1}{2} V^{MS}(\Psi) | \Psi >, \tag{1.2}$$

where the factor one-half in front of the solute-solvent interaction operator $V_{MS}(\Psi)$ is a consequence of its dependence of the solute wavefunction. The free-energy functional (1.2) assumes a reference state given by the noninteracting electron and nuclei, at rest, and by the unperturbed, pure solvent at the standard thermodynamic conditions of temperature and pressure. G_{el} acts as potential energy surface (PES) for the nuclei of the molecular solute.

1.2.1 The Standard PCM

The standard PCM [5] maintains the essential aspect of the basic version, with some changes and numerous additions.

PCM has been extended to almost all the levels of the QM theory, with inclusions of analytical expressions of the first and second derivatives of the energy. Nonelectrostatic solute-solvent interaction terms have been added; all the energy terms have the status of a free energy, and the total free-energy, G, of the solute-solvent system is written as

$$G = G_{el} + G_{rep} + G_{dis} + G_{cav} + G_{th}, \qquad (1.3)$$

where G_{rep} and G_{dis} represent, respectively, the contribution to the solute-solvent interaction due the Pauli repulsion and to the dispersion mechanisms; G_{cav} represent the work need to build up the void solute cavity within the pure solvent; and finally, G_{th} represent the contribution to the free energy due to the thermal motions of the nuclei of the solute [3].

For the definition of the apparent charge distribution new algorithms have been added in the standard PCM, called IEF-PCM [6], D-PCM (the original version) and C-PCM, a version which introduces a simplification [7].

1.3 The PCM Modeling of Molecular Properties

In this section, we describe some of key extensions of the standard PCM model for the calculation of molecular properties in the ground and excited states [8, 9].

Several properties regard excited states. The passage to excited states, which are not considered in the standard model, introduced new features of the theory.

Nonequilibrium effects due to the dynamical nature of the solvation have to be considered in the description of dynamical properties of the molecular solutes.

Several molecular response properties are determined in terms of higher-order derivatives of the PCM free-energy functional (1.2). The analytical evaluation of these derivatives introduces additional extensions to the standard model.

The description of the molecular response properties in solution also requires extensions able to connect the properties at the microscopic quantum level with the corresponding macroscopic responsive properties.

1.3.1 Electronic Excited States

1.3.1.1 Electronic Vertical Excitation: Nonequilibrium Effects

The QM approach to the excitation of a molecular system in solution by a vertical transition must take into account of the characteristic times of the solvent degrees of freedom. The information on these characteristic times is embodied in the spectrum of the dielectric permittivity of the solvent as a function of the frequency $\epsilon(\omega)$ of the perturbing electric field. A vertical transition excitation has very short relaxation times ($CT = 10^{-16}$ s), and the only active portion of dielectric permittivity is that associated with the electronic degrees of the solvent.

The solution of the electrostatic problem for the vertical excitation of a chromophore exploits a partition of the solvent polarization into two components: the first related to the fast motion (i.e., electron motion) and the second to all the remaining relaxation modes, related to the nuclei motion of the solvent molecules. This extension of the theory was first elaborated for the basic model [10] and then revised in the standard PCM [11–13].

1.3.1.2 Electronic Excited States: State-Specific vs. Linear Response Methods

The standard method in quantum mechanics to define excited states is based on the use of a CI expansion, with all the electronic states orthogonal each other. This property is modified in calculations in solution because each of the different electronic states is subjected to a different reaction potential.

Another aspect of this dependence of the reaction potential on the excited state is that it is not possible to get in a single run the energies for all the states. This picture of the excited states is called state specific (SS) because for each state, a specific computational procedure has to be used.

The state-specific approach (SS) has been implemented at different QM levels: MCSCF [11, 13–16] CISD [11]. The PCM-MCSCF is provided of algorithms with analytical gradients for geometry optimization [16].

There is another approach based on the theory of the linear response (LR). Its simpler formulation, called time-dependent Hartree-Fock (TD-HF) or random-phase approximation (RPA), gives a description of excited state energies comparable to that given by the standard approach in the absence of solvent effects. This equivalence is not preserved in the continuum solvation picture. An accurate analysis [17, 18] has revealed that the origin of the lack of this equivalence is due to a problem of the LR formulation in describing the solvent response associated

to the excited states. Corrections to the LR description (which is computationally faster than SS) are now in use. [19, 20]

The formulations of the linear response (LR) methods have been implemented at different QM levels of accuracy: ZINDO [21], CIS, TD-HF, and TD-DFT all provided of algorithms with analytical gradients for geometry optimization [22, 23].

The QM levels of the state-specific (SS) methods and of the linear response (LR) methods have been recently increased to include the coupled-cluster (CC) theory (see Sect. 1.4.1 for the basic CC theory of the PCM model).

1.3.2   Electric and Magnetic Properties

1.3.2.1   The Local Field Effect

Response properties of molecules in a condensed phase are related to the actual intensity of the perturbing field experienced by the molecules, which differs from the field intensity measured experimentally. The solution of this problem for the PCM model is more general with respect to the corrections due to Lorentz (1909) and Onsager (1936) [24], which are limited to spherical or ellipsoidal cavities.

The formulation [25] introduces an additional electrostatic PCM calculation, with the empty cavity in the presence of an external field, to determine the additional set of apparent charges induced by the field at the boundary of cavity. This set of charges is then included as an additional perturbation in the QM calculation on the molecule for to the determination of the electric response functions. This procedure can be applied to a static as well to an oscillating (i.e., time dependent) electromagnetic field.

1.3.2.2   Electric Response

The electric response functions of the molecular solutes are defined in terms of the derivatives of the PCM free-energy functional with respect to the macroscopic field in the bulk solvent (i.e., the Maxwell field). The first derivative gives the dipole moment μ, the second, third, and fourth derivatives give the polarizability α, and the first and second hyperpolarizabilities β and γ. These quantities are defined for static as well for time-dependent electromagnetic fields. For each hyperpolarizbilities, there are several time-dependent response properties depending on the combination of field of different frequencies and describing different nonlinear optical phenomena.

The calculation of these response functions has been given at HF, DFT, and MC-SCF QM level using a time-dependent coupled-perturbation approach [12, 26–29].

1.3.2.3 Magnetic Responses

Magnetizability, nuclear shielding tensor, and spin-spin coupling of molecules in solution are examples of linear magnetic response properties that can be expressed as suitable second derivative of the PCM free-energy functional with respect to a suitable combination of the two magnetic fields present in the systems: the external magnetic field **B** and the field due to the collection of nuclear magnetic moments **m**. The calculation of these quantities with approximate QM methods suffers of the dependence of the magnetic response functions on the origin of the molecular reference frame. Different methods have been introduced to avoid the gauge dependence, and a PCM version has been elaborated for the GIAO, LORG, IGLO, and CSGT methods [30–35]. Nonequilibrium and local field effects are of marginal relevance.

1.3.3 Properties Related to Nuclear Motions

1.3.3.1 Molecular Vibrations: Harmonic Frequencies and IR/Raman Intensities

Calculations of the vibrational frequencies of solvated molecules involve the second derivative of the PCM freeenergy of the systems with respect to the nuclei [36–41]. They require a preliminary geometry optimization of the solute to locate the local minima of the PES. Some further refinements include the corrections due to the effects of the nonequilibrium solvation and the mechanical anharmonicities. The effect of the nonequilibrium corrections to the different timescale between the vibrations and the inertial degrees of freedom of the solvent molecules is numerically negligible save for fast vibrations [42–46].

The IR absorption intensity requires the evaluation of a mixed second derivative of the PCM freeenergy with respect to the position and to the external field. The external field is modified by the boundary of the cavity hosting the solute: this is the local field modification we have already discussed for the polarizability. Nonequilibrium effects are of sizable entity on the IR intensities [44, 47].

Raman spectra involve the derivatives of the polarizability with respect to the normal coordinates. There are two sources of nonequilibrium effect: the incomplete solvent response to the external field oscillation in the solute electronic density and to the molecular vibrations; the two effects are active in different ranges of frequencies and must be treated differently [48, 49].

1.3.4 Dichroic Phenomena: Optical Activity Phenomena

The modeling of solvent effects has been historically a key ingredient of the quantum-mechanical (QM) theories of chiro-optical properties circular dichroism (CD) and optical rotation (OR). This is due to the fact that the chiro-optic phenomena, since their discovery in the nineteenth century, are observed in condensed phases (mostly in solutions) and that the measured quantities depend on the nature of the phase (the solvent). The PCM computational procedures have been elaborated for the electronic CD/OR (ECD/OR) and for the vibrational IR/Raman CD (VCD/VROA) dichroic phenomena. The procedures contain the whole set of features introduced in the elaborations for the preceding properties (local field, non-equilibrium effects, geometry optimization) to which we have to add an efficient code to get the free-energy weights of the molecular conformations contributing to the spectroscopic signal [50–56].

1.4 New Features of the PCM

In this section, we review two new features of the PCM model for the descriptions of the properties of molecular solutes: the extension to the analytical gradients at the QM coupled-cluster level and the extension toward the study of the properties of molecular systems at the extreme pressure regime.

1.4.1 The Coupled-Cluster Theory for the Polarizable Continuum Model: Analytical Gradients

The study of several molecular processes (response functions and electronic excitations) may require a higher level of the QM theory. This has motivated recent efforts for a systematic extension of the PCM to various coupled-cluster methods for the descriptions of the ground and excited state properties [57–64]. We report here on the PCM coupled-cluster analytical derivatives theory.

1.4.1.1 The PCM Coupled-Cluster Energy Functional and Equations

The coupled-cluster theory for molecular solute exploits a coupled-cluster energy functional (PCM-CC) having the expected thermodynamics status of free energy of the whole solute-solvent system. The properties of the molecular solutes are expressed in terms of derivate of the PCM-CC functional. These derivatives satisfy a generalized Wigner "2n + 1" perturbation rules [57].

We start by considering the coupled-cluster wavefunction defined by the usual exponential ansatz [65]

$$|CC> = e^T |HF>, \tag{1.4}$$

where $|HF>$ is the single determinant Hartree-Fock state of the molecular solute and the cluster operator T is given as a sum of all possible excitation operators over the N electrons

$$T = T_1 + T_2 + \cdots + T_N; \qquad T_n = \frac{1}{(n!)^2} \sum_{aibj\dots} t_{ij\dots}^{ab\dots} a_a^\dagger a_i a_b^\dagger a_j \dots \tag{1.5}$$

being $t_{ij\dots}^{ab\dots}$, the coupled-cluster amplitudes. The excitation operators are here represented as products of second quantization electron creation $(a_i^\dagger, a_b^\dagger)$ and annihilation operators (a_i, a_b). As usual, indexes $(i, j, k, \dots)$ and $(a, b, c, \dots)$ denote, respectively, occupied and vacant spin orbitals MO, while $(p, q, r, \dots)$ denote general spin orbitals.

The PCM coupled-cluster functional $\Delta G_{CC}(\Lambda, T)$ is defined as

$$\Delta G_{CC} = < HF|(1 + \Lambda)e^{-T}[H(0)_N + \frac{1}{2}\bar{\mathbf{Q}}_N(T, \Lambda) \cdot \mathbf{V}_N]e^T|HF>, \tag{1.6}$$

where Λ is a de-excitation operator,

$$\Lambda = \Lambda_1 + \Lambda_2 + \cdots; \qquad \Lambda_n = \frac{1}{(n!)^2} \sum_{ijkabc\dots} \lambda_{abc\dots}^{ijk\dots} a_i^\dagger a_a a_j^\dagger a_b a_k^\dagger a_c \dots \tag{1.7}$$

$H(0)_N$ is the normal-ordered form of Hamiltonian of the solute in presence of the frozen Hartree-Fock reaction field[1]; $\mathbf{V}_N$ is a vector collecting the electrostatic potential operator of the solute at the surface of cavity (enclosing it within a medium of dielectric permittivity ϵ_0) (see Chap. I (Appendix) an operative definition) and $\bar{\mathbf{Q}}_N$ is the coupled-cluster expectation values

$$\bar{\mathbf{Q}}_N = < HF|(1 + \Lambda)e^{-T}\mathbf{Q}_N e^T|HF> \tag{1.8}$$

for the apparent charge operator $\mathbf{Q}_N$ [3]. There are several versions of the PCM methods which differ for the definition of the operator $\mathbf{Q}_N$. Here, we refer to the integral equation formalism version (PCM-IEF) in which $\mathbf{Q}_N$ is related by a linear transformation to the operator $\mathbf{V}_N$ introduced above. The linear transformation is

---

[1] More specifically, $H(0)_N$ is defined as

$$H(0)_N = H_N^o + \bar{\mathbf{Q}}_{HF}\mathbf{V}_N,$$

where H_N^o is the normal-ordered Hamiltonian of the isolated molecule, and $\bar{\mathbf{Q}}_{HF}$ collects the Hartree-Fock polarization charges.

acted by a matrix $\mathbf{T}_\Sigma(\epsilon)$ representing the polarization response of the solvent and depending on its dielectric permittivity ϵ_0 and on the geometry Σ of the cavity hosting the solute, $\mathbf{Q}_N = \mathbf{T}_\Sigma(\epsilon)\mathbf{V}_N$.

The coupled-cluster amplitudes of the T and Λ operators are determined by the stationary conditions of the free-energy functional $\Delta G_{CC}(\Lambda, T)$. The stationarity with respect to the Λ amplitudes, $\frac{\partial \Delta G_{CC}}{\partial \lambda_{ab..}^{ij..}} = 0$, gives the equations for the T amplitudes

$$< HF|\tau_p^\dagger e^{-T} H_N e^T |HF >= 0, \tag{1.9}$$

where $\tau_p^\dagger$ is the adjoint of an elementary excitation operator $\tau_p = a_a^\dagger a_i a_b^\dagger a_j \ldots$, and H_N is the Hamiltonian of the molecular solute:

$$H_N = H(0)_N + \bar{\mathbf{Q}}_N(\Lambda, T) \cdot \mathbf{V}_N \tag{1.10}$$

sum of the normal-ordered form of Hamiltonian of the solute in the presence of the frozen HF reaction field, $H(0)_N$, and of the coupled-cluster component of the solvent reaction potential, $\bar{\mathbf{Q}}_N(\Lambda, T) \cdot \mathbf{V}_N$. The T amplitudes of Eq. 1.9 correspond to projection in the manifold spanned by all the orthogonal excitations to $|HF >$ of the coupled-cluster Schrodinger equation for the molecular solute.

The stationarity with respect to the T amplitudes, $\frac{\partial \Delta G_{CC}}{\partial t_{ij..}^{ab..}} = 0$, gives the equations for the Λ amplitudes:

$$< HF|(1 + \Lambda)e^{-T}[H_N, \tau_p]e^T |HF >= 0, \tag{1.11}$$

where the square brackets denote the commutator of their arguments.

Being the Hamiltonian H_N dependent on both T and Λ parameters, the equations for the T amplitudes (1.9) and for the Λ amplitudes (1.11) are coupled, and they must be solved in an iterative and self-consistent way.

1.4.1.2 Analytical Derivatives Theory of the Molecular Properties

The analytical derivatives of the PCM-CC free-energy functional have presented up to the third order of differentiation [57, 64]. As in the case of isolated molecules [65], the coupled-cluster analytical derivatives can be performed with or without considering the relaxation of the molecular orbital (MO) under the effect of the perturbation. We limit here to consider differentiation with respect to perturbations $(\alpha, \beta, \ldots)$ given by time-independent electric or magnetic fields for which we can consider the unrelaxed MO orbital approach. For sake of simplicity, explicit expressions will be given up to the second analytical derivatives.

When the stationary conditions for the coupled-cluster parameters T and Λ are satisfied, the first derivative (i.e., the gradients) of the free-energy functional, $\partial \Delta G_{CC}/\partial \alpha = \Delta G_{CC}^\alpha$, can be expressed in the following form:

$$\Delta G^{\alpha}_{CC} = <HF|(1+\Lambda)e^{-T}X_N e^T|HF>, \tag{1.12}$$

where X_N denotes the normal-ordered operator ($X_N = X - <HF|X|HF>$) representing the external perturbation having amplitude α. The analytical derivative ΔG^{α}_{CC} satisfies a generalized Hellmann-Feynman theorem in the framework of the PCM solvation model [12] and does not require the first derivatives of the coupled-cluster parameters, in agreement with the perturbative "2n + 1" rule.

The second derivative of the PCM-CC energy is obtained by differentiation with respect to a second perturbation β of the analytical gradients of Eq. 1.16, and it may be written as

$$\Delta G^{\beta\alpha}_{CC} = <HF|\frac{\partial \Lambda}{\partial \beta}e^{-T}Xe^T|HF> + <HF|(1+\Lambda)[e^{-T}Xe^T, \frac{\partial T}{\partial \beta}]|HF>. \tag{1.13}$$

To evaluate the analytics second derivative $\Delta G^{\alpha\beta}_{CC}$, we need to determine the first derivative of the Λ amplitude and of the T amplitudes. These derivatives are obtained by solving at first order the T and Λ. The first-order equations for the amplitudes T are given by

$$0 = <HF|\tau_p e^{-T}Ye^T|HF> + <HF|\tau_p[e^{-T}H_N e^T, \frac{\partial T}{\partial \beta}]|HF>$$
$$\bar{\mathbf{Q}}^{\beta}_N \times <HF|\tau_p e^{-T}\mathbf{V}_N e^T|HF>, \tag{1.14}$$

where Y denotes the operator representing the external perturbation having amplitude β and where $\bar{\mathbf{Q}}^{\beta}_N$ is defined as

$$\bar{\mathbf{Q}}^{\beta}_N = <HF|(1+\Lambda)e^{-T}[\mathbf{Q}^{|\omega|}_N, \frac{\partial T}{\partial \beta}]e^T|HF> + <HF|\frac{\partial \Lambda}{\partial \beta}e^{-T}\mathbf{Q}^{|\omega|}_N e^T|HF>. \tag{1.15}$$

The first-order equations for the amplitudes T are given by

$$0 = <HF|\tau_p e^{-T}\tilde{Y}e^T|HF> + <HF|\tau_p[e^{-T}H_N e^T, \frac{\partial T}{\partial \beta}]|HF>, \tag{1.16}$$

where $\tilde{Y}$ is an effective perturbing operator defined as

$$\tilde{Y} = Y + \bar{\mathbf{Q}}^{\beta}_N \mathbf{V}_N, \tag{1.17}$$

where Y denotes the operator representing the external perturbation having amplitude β and $\bar{\mathbf{Q}}^{\beta}_N$ is given by

$$\bar{\mathbf{Q}}^{\beta}_N = <HF|(1+\Lambda)e^{-T}[\mathbf{Q}^{|\omega|}_N, \frac{\partial T}{\partial \beta}]e^T|HF> + <HF|\frac{\partial \Lambda}{\partial \beta}e^{-T}\mathbf{Q}^{|\omega|}_N e^T|HF>. \tag{1.18}$$

The effective perturbing operator $\tilde{Y}$ is due to the coupling between the external field and the solute-solvent interaction, as perturbing agents acting on the molecular solute.

The corresponding first-order Λ equations are given by

$$
\begin{aligned}
0 = \ & <HF|(1+\Lambda)[e^{-T}Ye^{T}, \tau_p]|HF> + \\
& + <HF|(1+\Lambda)[[e^{-T}H_N e^{T}, \frac{\partial T}{\partial \beta}], \tau_p]|HF> \\
& + <HF|\frac{\partial \Lambda}{\partial \beta}[e^{-T}H_N e^{T}, \tau_p]|HF> \\
& + \bar{\mathbf{Q}}_N^{\beta} \times <HF|(1+\Lambda)[e^{-T}\mathbf{V}_N e^{T}, \tau_p]|HF> .
\end{aligned}
\tag{1.19}
$$

We finally note that by exploiting the perturbative "2n + 1" rule, also the third derivative of the free energy functional, $\Delta G_{CC}^{\alpha,\beta\delta}$, can be expressed in terms of the first derivatives of the coupled-cluster parameters. This allows to obtain coupled-cluster static response functions up to third order for molecular solutes perturbed by static external fields.

1.4.2   Effects of High Pressures on the Molecular Properties

As described in Sect. 1.2, continuum solvation methods have gained a wide popularity in the description of solvent effects on the electronic structure, geometry, and properties of molecules in solution. The continuum approach has also been extended to other media, as polymers and crystals. There are, however, fields for which this approach has not yet been applied. Among them, there is solvation at high pressure. In the last years, important progresses have been made in the experimental studies on molecular systems subjected to very high pressures [66–73]. Ab initio Carr-Parrinello simulations of systems at high pressure have appeared, [74, 75] with interesting results but at a considerable computational cost. What it lacks is an accurate computational methods of cost comparable with that of isolated molecules to support, confirm, and also predict the outcome of experimental studies.

We have presented a new computational method based on the polarizable continuum model (PCM) [76]. The method has two key items: the definition of the pressure (p) in such extreme conditions and the elaboration of an analytical codes for the calculation of molecular energy gradients for the present applications to the regime of high pressures.

1.4.2.1 Pressure and Quantum Repulsion Energy

The pressure is a macroscopic thermodynamic property not immediately transferable into QM methods addressing the detailed description of a single molecule. We have proposed a possible solution for this problem resorting an analytical formulation based on the energy derivatives with respect to volume of the cavity hosting the solute in a quantum-mechanical (QM) confining (i.e., repulsive) environment.

The quantum-mechanical description of confined systems dates back to the early days of quantum chemistry [77]. The pressure for a molecular system confined within a cavity of Volume (V) is defined as energy derivatives with respect to volume of the cavity [78]. The pressure is called kinetic pressure, and it has been demonstrated that it is equivalent to the pressure derived from the quantum statistical mechanics, i.e., the thermodynamics pressure [79]. The applications were limited so far to simple confining volumes of spherical or ellipsoidal shape only and for atoms or very simple molecules [80–82].

The extension of this definition of the pressure into PCM permits to remove the limitations as the PCM cavity is accurately modeled on the shape of the molecular solute. In passing to the PCM, the pressure of the external medium acting on the molecule is defined as

$$p = -\left(\frac{\partial G_{el-rep}}{\partial V} \right), \tag{1.20}$$

where G_{el-rep} denotes the PCM free-energy functional including the solute-solvent interaction energies corresponding to the electrostatic and to the repulsion interactions. The free-energy G_{el-rep} is then defined as sum of 2 terms:

$$G_{el-rep} = G_{el} + G_{rep}, \tag{1.21}$$

where G_{el} denotes the free energy of the solute-solvent systems in presence of the solute-solvent electrostatic interaction and G_{rep} represents the contribution due to the solute-solvent Pauli repulsion interaction. A quantum version of the repulsion term G_{rep} is here compulsory.

The QM Pauli repulsion contribution G_{rep} is given by the functional form [83]

$$G_{rep} = \alpha \int_{r \notin C} \rho_M(\mathbf{r}) d^3 r \tag{1.22}$$

with

$$\alpha = \frac{4\pi}{0.7} \rho_S n_{val}^S,$$

where the integral in Eq. 1.22 denotes the electronic charge density lying outside the cavity, 0.7 is a numerical parameter (in a.u.) obtained from super-molecule

calculations, ρ_S is the numeral density of the solvent, and n_{val}^S is the number of its valence electrons.

With respect to the other simple confining models, based on impenetrable potential wall, the nature of QM Pauli repulsion contribution to the PCM free-energy functional G_{rep} allows a confining of the electronic charge distribution of the solute in a smooth way, according to the term used by Le Sar and Herschbach in the concluding remarks of Ref. [81].

To compute $G_{\mathrm{el-rep}}$ and its derivatives, we need to redefine for the appropriate pressure some of the physical parameters used in PCM, namely, the dielectric permittivity of the medium and its numeral density, and the size of the molecular cavity.

1.4.2.2 Effect of the Pressure on the Equilibrium Geometries and on the Vibrational Frequencies of Conjugated Polyenes

In this subsection, we present an illustrative calculation of the effect of the pressure on the equilibrium geometries and vibrational frequencies of the conjugated polyenes trans-polyenes 1,3-butadiene (butadiene), 1,3,5-hexatriene (hexatriene), and 1,3,5,7-octatetraene (octatetraene), a class of systems of interest in the field of high-pressure chemistry. [73]

The analytical first and second derivatives of $G_{\mathrm{el-rep}}$ have been implemented into a local version of the Gaussian 09 [84] computational code and allow to determine equilibrium geometries and vibrational frequencies of molecular systems as a function of the pressure. The pressure of the environment is determined by a proper reduction of the size of the molecular cavities hosting the molecular solute. In the PCM procedure, the cavity is defined in terms of interlocking spheres centered on the atoms' nuclei and with radii equal to the corresponding vdW radius multiplied a scaling factor, f, which can be varied to obtain the desired reduction of the cavity, being $f = 1.2$ the value used in standard PCM calculations [3]. Numerical test shows that a variation of f within the range (1.2–0.8) allows to span a range of pressure up to 16 GPa. All the calculations have been performed at the DFT/B3LYP [85] level using the 6–31g** basis set [86].

Table 1.1 reports the equilibrium bond lengths for the single (C–C) and double (C=C) carbon–carbon bond length of butadiene, hexatriene, and octatetraene as a function of the pressure. The data show a shortening of all the bond lengths, with a slightly greater compressibility of the single C–C bonds with respect to the double C=C bonds. The mean compressibilities of the C–C and C=C bonds are 0.00066 Å/GPa and 0.00053 Å/GPa, respectively.

Table 1.2 reports the vibrational frequencies of selected Raman active C=C stretching modes for the same systems. The vibrational frequencies increase with the increase of the pressure. The mean pressure coefficient of vibrational frequencies is of $1.9 \, \mathrm{cm}^{-1}/\mathrm{GPa}$. There are no experimental data to compare with

Table 1.1 Carbon-carbon bond lengths (Å) of *trans* 1,3-butadiene, 1,3,5-hexatriene, and 1,3,5,7-octatetraene as a function of the pressure p(GPa). Results refer to the PCM/DFT/B3LYP/ 6-31G(d,p) level. Data at 0.0 GPa refer to the gas phase; f is the scaling factor applied to the atomic van der Waals sphere used for the PCM cavity

	f	$p(GPa)$	$r(C_1{=}C_2)$	$r(C_2{-}C_3)$	$r(C_3{=}C_4)$	$r(C_4{-}C_5)$
1,3-Butadiene	–	0.00	1.3409	1.4576		
	1.2	0.11	1.3411	1.4579		
	0.8	9.2	1.3371	1.4517		
1,3,5-Hexatriene	–	0.00	1.3424	1.4494	1.3517	
	1.2	0.41	1.3424	1.4494	1.3517	
	0.8	12.4	1.3351	1.4401	1.3441	
1,3,5-Octatetraene	–	0.00	1.3434	1.4471	1.3551	1.4402
	1.2	0.44	1.3434	1.4471	1.3551	1.4402
	0.8	15.7	1.3361	1.4379	1.3475	1.4311

Table 1.2 Vibrational frequencies cm^{-1} involving Raman active C=C stretchings of 1,3-butadiene, 1,3,5-hexatriene, and 1,3,5,7-octatetraene as a function of the pressure, p(GPa). Results refer to the PCM/DFT/B3LYP/ 6-31G(d,p) level. Data at 0.0 GPa refer to the gas phase; f is the scaling factor applied to the atomic van der Waals sphere used to define the PCM cavity

	f	$p(GPa)$	ν'	ν''
1,3-Butadiene	–	0.00	1,673.0	–
	1.2	0.11	1,673.0	–
	0.8	9.16	1,690.8	–
1,3,5-Hexatriene	–	0.00	1,710.3	1,654.3
	1.2	0.41	1,710.3	1,654.3
	0.8	12.4	1,737.93	1,677.9
1,3,5-Octatetraene	–	0.00	1,687.4	1,687.4
	1.2	0.44	1,687.4	1,687.4
	0.8	15.7	1,713.1	1,713.1

directly for butadiene, hexatriene, and octatetraene. The pressure coefficient of the vibrational frequencies of the Raman active C=C stretching modes has been measured for the all-trans-polyene retinal (ATR). The corresponding experimental value is $3.5\,cm^{-1}$/GPa [87].

These preliminary results for the effects on the pressure on the vibrational frequencies in all trans-polyenes, indicate the potentialities of the PCM approach to study high-pressure effects on molecular properties.

1.5 Conclusions

In this contribution, we have presented a brief overview of the PCM approach of Tomasi and coworker for the study of the properties of molecular systems in solution

and other more complex environments. We have focused on the PCM general features included to systematically describe a wide range of molecular properties and on two recent developments. The general features regard the description on the excited state properties of molecular solute, the nonequlibrium solvation effects, and the accurate description of the perturbing field acting locally on the solutes. The two new developments presented are (i) the accurate QM coupled-cluster level of description of the response properties and (ii) the description of the properties of molecules in the presence of an extreme pressure (i.e., in the presence of a strong repulsive environment). These recent developments give a further example of the flexibility of the PCM method, able self-consistently to adapt both the QM level of the molecular solutes to the needed accuracy, and the description of the solute-solvent interaction to the essential physics of the target system.

References

1. Tomasi J, Persico M (1994) Chem Rev 94:2027
2. Cramer CJ, Truhlar DG (1999) Chem Rev 99:2161
3. Tomasi J, Mennucci B, Cammi R (2005) Chem Rev 105:2999
4. Miertuš S, Scrocco E, Tomasi J (1981) Chem Phys 55:117
5. Tomasi J (2011) Wired: computational molecular science. Wiley, Hoboken
6. Cancès, MB, Tomasi J (1997) J Chem Phys 107:3032
7. Barone V, Cossi M (1998) J Phys Chem A 102:1995
8. Tomasi J, Cammi R, Mennucci B, Cappelli C, Corni S (2002) Phys Chem Chem Phys 4:5697
9. Tomasi J (2007) In: Mennucci M, Cammi R (eds) Continuum solvation models in chemical physics. Wiley, New York, pp 1–28
10. Bonaccorsi R, Ghio C, Tomasi J (1982) In: Carb R (ed) Current aspects of quantum chemistry 1981. Elsevier, Amsterdam, pp 407–425
11. Aguilar MA, Olivares del Valle FJ, Tomasi J (1993) J Chem Phys 98:7375
12. Cammi R, Tomasi J (1995) Int J Quantum Chem Quantum Chem Symp 29:465
13. Mennucci B, Cammi R, Tomasi J (1998) J Chem Phys 109:2798
14. Amovilli C, Mennucci B, Floris FM (1998) J Phys Chem B 102:3023
15. Cossi M, Barone V, Robb MA (1999) J Chem Phys 111:5295
16. Cammi R, Frediani L, Mennucci B, Tomasi J, Ruud K, Mikkelsen KV (2002) J Chem Phys 117:13
17. Cammi R, Corni S, Mennucci B, Tomasi J (2005) J Chem Phys 122:104513
18. Corni S, Cammi R, Mennucci B, Tomasi J (2005) J Chem Phys 123:134512
19. Caricato M, Mennucci B, Tomasi J, Ingrosso F, Cammi R, Corni S, Scalmani G (2006) J Chem Phys 124:124520
20. Improta R, Barone V, Scalmani G, Frisch MJ (2006) J Chem Phys 125:054103
21. Caricato M, Mennucci B, Tomasi J (2004) J Phys Chem A 108:6248
22. Cammi R, Mennucci B, Tomasi J (2000) J Phys Chem A 104:5631

23. Scalmani G, Frisch MJ, Mennucci B, Tomasi J, Cammi R, Barone V (2006) J Chem Phys 124:094107
24. Böttcher CJF (1973) Theory of electric polarization, vol 1. Elsevier, Amsterdam
25. Cammi R, Mennucci B, Tomasi J (1998) J Phys Chem A 102:870
26. Cammi R, Cossi M, Tomasi J (1996) J Chem Phys 104:4611
27. Cammi R, Cossi M, Mennucci B, Tomasi J (1996) J Chem Phys 105:10556
28. Cammi R, Mennucci B (1999) J Chem Phys 110:9877
29. Cammi R, Frediani L, Mennucci B, Ruud K (2003) J Chem Phys 119:5818
30. Cammi R (1998) J Chem Phys 109:3185
31. Cammi R, Mennucci B, Tomasi J (1999) J Chem Phys 110:7627
32. Mennucci B, Cammi R, Tomasi J (1999) Int J Quantum Chem 75:767
33. Mennucci B, Martinez JM, Tomasi J (2001) J Phys Chem A 105:7287
34. Mennucci B, Cammi R (2003) Int J Quantum Chem 93:121
35. Ruud K, Frediani L, Cammi R, Mennucci B (2003) Int J Mol Sci 4:119
36. Cammi R, Tomasi J (1994) J Chem Phys 101:3888
37. Cammi R, Mennucci B, Tomasi J (1999) J Phys Chem A 103:9100
38. Mennucci B, Cammi R, Tomasi J (1999) J Chem Phys 110:7627
39. Cossi M, Scalmani G, Rega N, Barone V (2002) J Chem Phys 117:43
40. Cammi R, Mennucci B, Pomelli C, Cappelli C, Corni S, Frediani L, Trucks GW, Frisch MJ (2004) Theor Chem Acc 111:66
41. Scalmani G, Barone V, Kudin KN, Pomelli C, Scuseria GE, Frisch MJ (2004) Theor Chem Acc 111:90
42. Olivares del Valle FJ, Tomasi J (1987) Chem Phys 114:231
43. Olivares del Valle FJ, Aguilar M, Tolosa S, Contador JC, Tomasi J (1990) Chem Phys 143:371
44. Cammi R, Cappelli C, Corni S, Tomasi J (2000) J Phys Chem A 104:9874
45. Cappelli C, da Silva CO, Tomasi J (2001) J Mol Struct (Theochem) 544:191
46. Cappelli C (2007) In: Mennucci M, Cammi R (eds) Continuum solvation models in chemical physics. Wiley, New York, pp 167–179
47. Cappelli C, Corni S, Cammi R, Mennucci B, Tomasi J (2000) J Chem Phys 113:11270
48. Cappelli C, Corni S, Tomasi J (2001) J Chem Phys 115:5531
49. Corni S, Cappelli C, Cammi R, Tomasi J (2001) J Phys Chem A 105:8319
50. Gontrani L, Mennucci B, Tomasi J (2000) J Mol Struct (THEOCHEM) 500:113
51. Cappelli C, Corni S, Mennucci B, Cammi R, Tomasi J (2000) J Phys Chem A 106:12331
52. Stephens PJ, Devlin FJ, Cheeseman JR, Frisch MJ, Mennucci B, Tomasi J (2000) Tetrahedron Asymmetry 11:2437
53. Mennucci B, Tomasi J, Cammi R, Cheeseman JR, Frisch MJ, Devlin FJ, Gabriel S, Stephens PJ (2002) J Phys Chem A 106:6102
54. da Silva CO, Mennucci B, Vreven T (2004) J Org Chem 69:8161
55. Pecul M, Lamparska E, Cappelli C, Frediani L, Ruud K (2006) J Phys Chem A 110:2807
56. Mennucci B, Cappelli C, Cammi R, Tomasi J (2011) Chirality 23:717–729
57. Cammi R (2009) J Chem Phys 131:164104
58. Cammi R (2010) Int J Quantum Chem 110:3040
59. Cammi R, Fukuda R, Ehara M, Nakatsuji H (2010) J Chem Phys 133:024104
60. Caricato M, Scalmani G, Trucks GW, Frisch MJ (2010) J Phys Chem Lett 1:2369
61. Caricato M, Scalmani G, Frisch MJ (2011) J Chem Phys 134:244113
62. Caricato M (2011) J Chem Phys 135:074113
63. Fukuda R, Cammi R, Ehara M, Nakatsuji H (2011) J Chem Phys 134:104109
64. Cammi R (2012) Int J Quantum Chem 112:2547–2560
65. (a) Bartlett RJ (1995) In: Yarkony D (ed) Modern electronic structure theory, vol 2. World Scientific, Singapore, pp 1047–1131; (b) Gauss J (1999) Coupled-cluster theory. In: Schleyer PvR (ed) Encyclopedia of computational chemistry, vol I. Wiley, New York, pp 617–636 (d) Bartlett RJ, Musiał M (2007) Rev Mod Phys 79:291
66. Hemsley RJ (2000) Ann Rev Phys Chem 51:763
67. Ceppatelli M, Santoro M, Bini R, Schettino V (2000) J Chem Phys 113:5991

68. Citroni M, Ceppatelli M, Bini R, Schettino V (2002) Science 295:2058
69. McMillan PF (2002) Nat Mater 1:18
70. Schettino V, Bini R (2003) Phys Chem Chem Phys 5:1951
71. Schettino V, Bini R, Ceppatelli M, Ciabini L, Citroni M (2005) Adv Chem Phys 131:105
72. Mao HK, Herschbach DR (2005) In: Manaa R (ed) Chemistry under extreme conditions. Elsevier, Amsterdam, p 189
73. Schettino V, Bini R (2007) Chem Soc Rev 36:869
74. Mugnai M, Cardini G, Schettino V (2004) Phys Rev B 70:020101(R)
75. Mugnai M, Pagliai M, Cardini G, Schettino V (2008) J Chem Theo Comp 4:646
76. Cammi R, Verdolino V, Mennucci B, Tomasi J (2008) Chem Phys 344:135
77. Wigner EP, Huntington H (1935) J Chem Phys 3:764
78. Byers Brown W (1958) J Chem Phys 28:522
79. Marc G, McMillan WG (1985) Adv Chem Phys 58:209
80. Ludeña EV (1978) J Chem Phys 69:1770
81. LeSar R, Herschbach DR (1981) J Phys Chem 85:2798
82. Cruz SA, Soullard J (2004) Chem Phys Lett 391:138
83. Amovilli C, Mennucci B (1997) J Phys Chem B 101:1051
84. Frisch MJ et al (2009) Gaussian 09. Pitsburgh, Gaussian Inc
85. Becke AD (1993) J Chem Phys 98:5648
86. Hehre WJ, Ditchfield R, Pople JA (1972) J Chem Phys 56:2257
87. Moroni L, Ceppatelli M, Gellini C, Salvi PR, Bini R (2002) Phys Chem Chem Phys 4:5761

Chapter 2
The Distribution of Internal Distances for Ionic Pairs in Solvents of Various Polarity

M.V. Basilevsky, A.V. Odinokov, and N.Kh. Petrov

Abstract The theory of association/dissociation of ion pairs in binary solvent mixtures is presented and analyzed based on the classical Bjerrum-Fuoss-Kraus approach. The probability distribution of interionic separation distances serves as the basic quantity underlying the thermodynamics of the ion pair equilibrium in solution. Its dependence on the binary solvent composition can be measured in electrochemical and spectroscopic experiments, and it provides the unique and essential information on the microscopic structure, stability, and kinetic behavior of ion/solvent associates which are formed in such systems. The perspective of their computer simulation by applying advanced technologies of recent computational chemistry is illustrated by our studies and interpretation of the counterion effect in the deactivation kinetics, which had been observed for the excited singlet state of the cyanine dye in the toluene/dimethylsulfoxide mixture.

2.1 Introduction

The concept of electrolytic dissociation in solution is an essential element of the chemical theory. In the aqueous solution, strong electrolytes dissociate almost completely. The properties of such systems are well established and fully understood. On the other hand, the theory of electrolyte solutions, where the dissociation is incomplete and the solute molecules are associated in a large extent, is more sophisticated and requires further elaboration. In the present work, we consider the background of this theory, discuss its present status, and illustrate the material by some recent computations.

M.V. Basilevsky (✉) • A.V. Odinokov • N.Kh. Petrov
Photochemistry Center RAS, Novatorov Str., 7a, Moscow, Russia, 119421
e-mail: basil@photonics.ru; ale.odinokov@gmail.com; npetrov@photonics.ru

Let us consider the dissociation equilibrium for the ion pair AB:

$$AB \rightleftarrows A + B. \tag{2.1}$$

Here A and B are ions (say, cation A and anion B) having opposite charges $\pm Q$ of the same magnitude Q. The consideration of more complicated systems makes both the presentation and notation more complicated but no enrichment in the basic ideas is gained. As usually, the association constant is defined via concentrations of the reactant and product ingredients (they are denoted as [...]):

$$K_{\text{ass}} = \frac{[AB]}{[A][B]}. \tag{2.2}$$

It is closely related to the degree of association, defined as

$$\alpha = \frac{[A]}{c} = \frac{[B]}{c},$$
$$c = [A] + [AB] = [B] + [AB]. \tag{2.3}$$

The total concentration of pairs AB, both associated and dissociated, is denoted as c.

Although the majority of applications are addressed to aqueous solutions, the studies of the equilibrated system (2.1) in nonaqueous media are of great interest. A binary mixture of polar and nonpolar solvents conventionally serves as an instrument for fine-tuning the solvent polarity (i.e., its dielectric permittivity ε) in wide extent by gradually varying the mixture composition. In such systems, the degree of dissociation α can be varied in its entire range $0 < \alpha < 1$. The corresponding association constants K_{ass} may vary within 1–15 orders of magnitude. The pairs AB, with large degree of association, exist in weakly polar and nonpolar solvents even at the concentrations c which are rather weak. Strong interionic interactions are responsible for the unusual properties which appear in such systems but are not fully understood at the present time.

Theoretical investigations of electrolyte solutions, in which the degree of dissociation varies within a wide range, were initiated and promoted by the classical papers of Bjerrum [1] and Fuoss and Kraus [2] (BFK). This BFK theory, developed from the thermodynamic approach, introduces as a basic quantity the effective intrapair potential (i.e., the potential of mean force, PMF) $W(R)$, where R denotes the inter-ionic separation within the pair ($R = R_{AB}$). Another essential element of this theory is the distribution function $\exp(-W(R)/kT)$ (where kT means the Boltzmann factor), in terms of which the main thermodynamic properties of the equilibrium (2.1) are formulated.

It should be noted at this point that the alternative theory of the association/dissociation system (2.1) has been developed. It is based on the concepts, which are, at the first glance, very different from those underlying the BFK theory.

The associated state of the AB pair can be imagined as a collection of localized chemical structures, including one or more solvent molecules as ingredients. The sophisticated set of local equilibria mutually connects these local states. It is also involved in the global equilibrium between all of the local states and the dissociated pairs $A + B$. The kinetics of transitions between each pair of states is treated in terms of the diffusion equations specially elaborated for treating ionic species [3–7]. The interrelation between this kinetic treatment and the thermodynamic BFK approach can be established. From the point of practical interest, the thermodynamic methodology, based on the Boltzmann distribution with the PMF $W(R)$, is most straightforward and advantageous. It is specially adapted for treating those systems in which the ionic association effects dominate in the equilibrium (2.1). Henceforth, we deliberately restrain the presentation by this method.

2.2 The Definitions and Notation for Basic Quantities

For the simplest case of structureless spherical ions, the isotropic PMF $W(R)$ is defined as a function of interionic distance R:

$$W(R) = G(R) - G(\infty), \tag{2.4}$$

where $G(R)$ is the Gibbs free energy of system AB immersed in the medium. It is convenient to be expressed as

$$G(R) = G_{\text{gas}}(R) + G_{\text{solv}}(R). \tag{2.5}$$

This is a sum of gas-phase and solvation components. The gas-phase part represents a wide and deep potential well. Its attractive branch is mainly determined by the Coulomb interaction, whereas the repulsive branch represents the van der Waals interaction which will be assumed as a combination of two Lennard-Jones (LJ) terms:

$$G_{\text{gas}} = -\frac{Q^2}{R} + \frac{C_{12}}{R^{12}} - \frac{C_6}{R^6}. \tag{2.6}$$

Here C_{12} and C_6 are the conventional LJ coefficients, and Q is the absolute value of the ion charge. The first repulsive LJ term is slightly screened by its second attractive dispersion counterpart. The quantum-mechanical charge transfer effect is neglected in this model.

The most simple representation of the solvation component reads

$$G_{\text{solv}} = \left(1 - \frac{1}{\varepsilon}\right)\left(\text{const} + \frac{Q^2}{R}\right), \tag{2.7}$$

where ε denotes the dielectric permittivity. The const is R-independent; it therefore disappears when the difference (2.4) is considered. The simplest version of the PMF then becomes

$$W(R) = -\frac{Q^2}{\varepsilon R} + \frac{C_{12}}{R^{12}} - \frac{C_6}{R^6}. \tag{2.8}$$

Its long-range asymptotic behavior is determined by the first screened Coulomb term.

In the general anisotropic situation, when $\mathbf{r} = \mathbf{r_B} - \mathbf{r_A}$ means the relative position vector and the PMF is denoted as $W(\mathbf{r})$, the distribution function $F(\mathbf{r})$ is proportional to the nonnormalized Boltzmann probability function, i.e.,

$$F(\mathbf{r}) = \frac{1}{Z} \exp\left(-\frac{W(\mathbf{r})}{kT}\right). \tag{2.9}$$

It is convenient to retain the one-dimensional representation by introducing spherical coordinates $\mathbf{r} : (R, \theta, \varphi)$. In terms of the interionic distance R, the probability density function is expressed as

$$F(R) = \frac{1}{Z} P(R); \qquad P(R) = R^2 \left\langle \exp\left(-\frac{W(R)}{kT}\right)\right\rangle_{\theta,\varphi}, \tag{2.10}$$

where $\langle \ldots \rangle_{\theta,\varphi}$ means the integration over angular variables. The partition function Z is defined as the integral

$$Z = \int\limits_V \exp\left(-\frac{W(\mathbf{r})}{kT}\right) d^3\mathbf{r} = \int\limits_0^{R_{\max}} P(R)dR. \tag{2.11}$$

The total volume $V = 4\pi R_{\max}^3/3$ contains both associated and dissociated pairs AB. In a macroscopic system containing N pairs, it is spatially restrained because the distributions under consideration are attributed to a single ion pair. In the isotropic limit

$$P(R) = 4\pi R^2 \exp\left(-\frac{W(R)}{kT}\right). \tag{2.12}$$

Function $P(R)$ is shown schematically in Fig. 2.1. Its first peak, generated by the PMF well, is located in the same space region, whereas the second peak is determined by the asymptotic square R-dependence. The minimum point R_B, which conditionally separates these peaks, will be termed as Bjerrum radius. The corresponding Bjerrum volume is $V_1 = 4\pi R_B^3/3$. In the original work [1], the expression $R_B = Q^2/2\varepsilon kT$ was assumed based on the model (2.8)–(2.12). Alternative estimates were discussed and tested in subsequent publications [8–16] because the underlying continuum solvation model was oversimplified. Typically, the two peaks of the probability function are separated by a flat and long interval in which $W(R)/kT \ll 1$. The explicit location of R_B within this region has no real significance.

Fig. 2.1 Schematic representation of the $P(R)$ function. The peak distribution area is denoted as Z_1 and Z_2. The radius R_{max} bounds the region where the second peak is defined
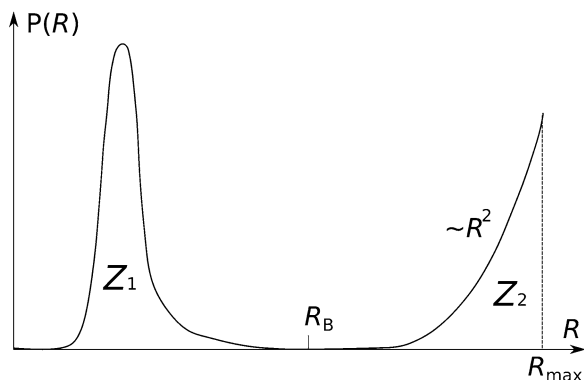
Following the BFK theory, the association constant (2.2) is expressed as the integral over the space surrounding the first peak of function $P(R)$:

$$K_{ass} = Z_1 = \int\limits_{V_1} P(R)dR = \int\limits_{a}^{R_B} R^2 \left\langle \exp\left(-\frac{W(\mathbf{r})}{kT}\right)\right\rangle_{\theta,\varphi} dR. \qquad (2.13)$$

The final detailed expression contains the single-dimensional BFK quadrature and is adapted for treating angle-averaged Boltzmann distributions. The appearance of the lower integration boundary $R = a$ follows the original BFK prescription. In advanced treatments, when the PMF is properly defined, the integrand is suppressed automatically for $R < a$, and accepting $R = 0$ for the lower boundary is equally well relevant.

2.3 The Low Concentration Regime

The definition (2.3) for the ion pair concentration includes both associated and dissociated pairs:

$$[AB] = c(1-\alpha),$$
$$[A] = [B] = c\alpha. \qquad (2.14)$$

The equation for α which follows from (2.3) reads

$$K_{ass} = \frac{1-\alpha}{\alpha^2 c}. \qquad (2.15)$$

Its solution is

$$\alpha = \frac{1}{2K_{\text{ass}}c}\left[\sqrt{1 + 4K_{\text{ass}}c} - 1\right]. \tag{2.16}$$

The limit of infinite dilution is formulated by means of the relations

$$c \to 0, \quad \alpha \to 1, \quad 1 - \alpha \ll 1,$$
$$Z = \frac{1}{c}. \tag{2.17}$$

The expression for Z appears under conditions listed in the first line of (2.17). This is derived below. The basic relation (2.13) becomes an immediate consequence of (2.15) under conditions (2.17).

The extension of these asymptotic trends for the case of finite (but small) concentrations is possible because, owing to the mass action law, the K_{ass} is a concentration-independent quantity. This conjecture works until the interpair interactions remain so weak that the concept of concentration is valid and can be applied without invoking the absolute activity $a = \gamma c$. In other words, the assumption $\gamma = 1$ for the activity coefficient remains an acceptable approximation. We call such situation "the low concentration regime" and consider it in more detail. Within this regime, the product $Z_1 c$ may not at all be small, although the concentration is small by the definition. This corresponds to the case of strong association with deep PMF wells. The partition function Z then becomes a complicated function of c which can be derived from identities (2.14) as

$$Z = \frac{[AB] + [A]}{[AB]}Z_1 = \frac{Z_1}{1 - \alpha}. \tag{2.18}$$

Here α is extracted from (2.16) with $K_{\text{ass}} = Z_1$. The asymptotic result (2.17) for Z appears when $c \to 0$. In this way, the problem of finding the upper limit R_{max}, when Z is evaluated as the one-dimensional integral (2.11) (see Fig. 2.1), is avoided. If desired, R_{max} may be found as a root of the equation $Z - Z_1 = \int_{R_B}^{R_{\text{max}}} P(R)R^2 dR$, where Z is given by (2.18). Because $P(R) \approx R^2$ for $R > R_B$, the integral can be approximated as $4\pi(R_{\text{max}}^3 - R_B^3)/3$. In accord with (2.18), the integral Z_1 can (depending on the α value) contribute to the partition function in a larger or lesser extent. The absolute values of the probability density $F(R)$ become available by this means.

It is seen from (2.18) that Z decreases when α falls down within its total range $0 < \alpha < 1$. The maximum radius R_{max} also decreases. If we denote as $V_0 = 4\pi R_0^3/3$ the volume per a single ion pair, i.e., $V_0 = 1/c$, then

$$R_{\text{max}} = R_0 = \frac{3}{4\pi}c^{-\frac{1}{3}}. \tag{2.19}$$

2.4   The Formal Background for the BFK Approach

In the most general formulation, the ion pair AB is a compound composed of individual particles, i.e., ions A and B. The equilibrated many-particle system (2.1) ($2N$ ionic particles in volume V) is entirely determined by the configuration integral

$$L_N = \int \exp\left[-\frac{U_N\left(\mathbf{r}_{a1},\ldots \mathbf{r}_{aN}; \mathbf{r}_{b1},\ldots \mathbf{r}_{bN}\right)}{kT}\right] \times \prod_{ai=1}^{N} d^3\mathbf{r}_{ai} \prod_{bj=1}^{N} d^3\mathbf{r}_{bj}. \quad (2.20)$$

The subscripts ai and bj label the coordinates $\mathbf{r}$ of ions A_i and B_j, respectively. The notation can be simplified without damaging the essential conclusions by introducing two extra conditions:

(a) Only two-particle interactions between different sorts of particles (A and B) are included in U_N. The pairs $A_i A_j$ and $B_i B_j$ with repulsive Coulomb interactions are withdrawn. This allows for contracting the notation. The subscripts i, j can now be dropped, whereas the meaning of remaining subscripts a, b is extended: they serve for direct numbering of the particles A, B with the count $a, b = 1, 2, \ldots N$.

(b) The elementary two-particle interactions are isotropic, i.e., U_N is composed of pair potentials $W(R_{ab})$ where $R_{ab} = |\mathbf{r}_a - \mathbf{r}_b|$.

By this means, the many-particle potential U_N reduces to

$$U_N(R_{ab}) = \sum_{a,b=1}^{N} W(R_{ab}), \quad (2.21)$$

where $W(R)$ represents the PMF (2.8). The nonseparable potential (2.21) still represents the multiparticle combination of interactions. Its further simplified separable counterpart reads

$$U_N(R_{ab}) = \sum_{a=1,\quad b=a}^{N} W(R_{ab}). \quad (2.22)$$

The indices a and b are rigidly correlated in (2.22) which results in the separation of the remaining variables. It is the approximation which underlies the BFK approach. The counterion B_b with $b = a$ remains as a single partner for the ion A_a. Only isolated pairs $A_a B_b$ ($b = a$) with intrapair interactions $W(R_{ab})$ are counted. The interaction between these pairs is neglected, and the pairs themselves are non-correlated. The difference between potentials (2.21) and (2.22) determines the interpair correlations which comprise the essentially multiparticle effects. It can be said that Eq. 2.22 represents the ideal gas of ion pairs AB with an internal degree

of freedom R_{ab} characterized by the interaction $W(R_{ab})$. The internal partition function for a single pair, defined by (2.11), is related in this approximation to the configuration integral (2.20) as

$$\ln Z = \frac{1}{N} \ln L_N. \tag{2.23}$$

Additional comments both in favor of approximation (2.22) [17, 18] and against it [15, 16] can be considered:

(a1) This is indeed a reasonable approach for the short-range association region ($R < R_B$). Once a pair AB is formed and its Helmholtz free energy is $A = -kT \ln Z$, its association with another pair would gain the free energy excess that is much smaller in magnitude than A. Although the interpair and intrapair van der Waals repulsion effects are similar, the intrapair attraction effects are much stronger than the interpair ones. Firstly, the intrapair electrostatic interaction is Coulomb-like, with distance dependence $\sim 1/R_{ab}$, but the total distance dependence for the dipole-dipole interpair interaction decays as $\sim 1/R_{ab}^3$. Therefore, at interpair distances R_{ab}, exceeding the sum of van der Waals radii of A and B, which are only significant, the relative interpair electrostatic contribution to the total stabilization effect is not large for a double-pair aggregate. Secondly, the intrapair covalent binding, appearing at short separations, additionally stabilizes individual pairs, but it is suppressed at the level of the interpair interaction.

(b1) The argument of comment (a1) becomes doubtful as applied to the dissociation region ($R > R_B$) where all short-range effects, both stabilizing and destabilizing, are exhausted. The existence of separated ions, rather than individual ion pairs, is implied for the pertaining ensemble with the accompanying condition $W(R_{ab})/kT \ll 1$. The potential (2.21), symmetric relative to the interchange of pair interactions, appears to be the most relevant for this case.

Returning now to the BFK approach, we note that the comment (a1), which is reliable, is accepted as its background, whereas the unfavorable comment (b1) is safely avoided owing to the relation (2.18). This argument, based on the mass action law, i.e., on the solid thermodynamic platform, covers implicitly all necessary multiparticle effects and rigorously allows for eliminating their explicit consideration in the dissociation region. The most essential statistical distinction, which discriminates the identification and count of particles for the two regions, is taken into account by applying Eqs. 2.15 and 2.16. The idea of independent noninteracting ion pairs in the association region (the geminate pairs [19]) is complemented by the concept of uncorrelated independent ions (i.e., of the ideal gas of ions) in the dissociation region. Neglecting the interion interactions remains the weakest point of the original BFK model.

2.5   The Interaction Between Ions in the Dissociation Region

2.5.1   Cluster Expansions

The outlined above status of the BFK approach poses it as a model which combines the ideal gas approximation for pairs AB, with the internal degree of freedom R_{ab} (in the association region), and the same approximation for isolated ions A and B (in the dissociation region). By this means, its identity with the standard thermodynamic treatment of dissociation processes is revealed [18]. As applied to the ionic dissociation, the only doubt which remains concerns the long-range Coulomb interactions. The peculiarity of ionic ensembles cannot indeed be ignored because of the divergence problem which we discuss briefly below.

The multiparticle extension of the BFK approach has been developed [1, 13–16, 20–25] mainly in the context of the Debye-Hückel (DH) theory. As a rule, it is applied only to the dissociation region, where such correction is especially desirable, whereas the application of the DH method is straightforward. The single pair probability $\exp\left(-W(\mathbf{r})/kT\right)$ is substituted by the generalized pair distribution function

$$g(\mathbf{r}) = \exp\left(-\frac{\overline{W}(\mathbf{r})}{kT}\right) \tag{2.24}$$

with the standard asymptotic condition $\lim_{R \to \infty} g(\mathbf{r}) = 1$. The methodology for a consistent treatment of $g(\mathbf{r})$ and the corresponding effective PMF $\overline{W}(\mathbf{r})$ for the general many-particle potential U_N that appears in (2.20) is formulated in the statistical theory. For the isotropic case, when $g(\mathbf{r})$ and $W(\mathbf{r})$ become functions of the interionic distance R, we can proceed further with a contracted notation as accepted below.

The ensemble of ions A and B with charges $\pm Q$ and ionic concentrations $[A] = [B] = \alpha c = c_{ion}$ are considered with $0 < \alpha < 1$. The interactions between similar ions are disregarded. We introduce these simplifications in order to adjust for the model pairwise potential U_N (2.21). The following expansions in powers of the ionic concentration are established [26, 27]:

$$g(R) = \exp\left(-\frac{\overline{W}(R)}{kT}\left[1 + O\left(R|c_{ion}\right)\right]\right),$$

$$-\frac{\overline{W}(R)}{kT} = -\frac{W(R)}{kT} + O\left(R|c_{ion}\right). \tag{2.25}$$

The Helmholtz free energy $\overline{A} = -\frac{1}{N}kT \ln L$, where L is the configuration integral (2.20), has the expansion (written again for the isotropic case)

$$-\frac{\Delta A}{kT} = \frac{c_{\text{ion}}}{2} \int\limits_{0}^{\infty} 4\pi R^2 \left\{ \exp\left[\left(-\frac{W(R)}{kT}\right) - 1\right] \right\} dR + O\left(c^2\right),$$

$$\overline{A} = A + \Delta A. \tag{2.26}$$

Here the zero-order free energy A represents the ideal gas (i.e., ions without interaction) approximation. The correction terms $O(R|c_{\text{ion}})$ in (2.25) and $O(c^2)$ in (2.26) represent further expansions in powers of c_{ion}:

$$O\left(R|c_{\text{ion}}\right) = \sum_{n \geq 1} c_{\text{ion}}^n \Theta_n\left(R\right); \qquad O\left(c^2\right) = \sum_{n \geq 2} c_{\text{ion}}^n \delta_n. \tag{2.27}$$

The explicit algorithms for finding the multiparticle coefficients $\Theta_n\left(R\right)$ and δ_n (the cluster graph techniques) are formulated [26–28]. Equations 2.25 and 2.26 reveal and verify the important conclusion that in the infinite dilution limit $c \to 0$, the multiparticle effects disappear and the simple description in terms of functions $W(R)$ and $\exp\left(-W(R)/kT\right)$, as accepted in Sects. 2.2–2.4, is legitimate.

A comment is required regarding the Helmholtz free energy A, which has appeared here instead of the Gibbs free energy G, as used conventionally in other places of this chapter (see Sect. 2.2). From the point of the rigorous derivation [26–28], invoking A is most relevant in the context of relations (2.25) and (2.26). In applications, which are addressed here, the slight distinction between A and G can be ignored, and we retain the same notation $W(R)$ for the PMF appearing in (2.25) and (2.26) and for its counterpart defined via Eqs. 2.4 and 2.7. The small discrepancy may be included in the correction $O(c^2)$ in (2.26).

2.5.2   The Debye-Hückel Theory

The problem of systems with long-range Coulomb potentials stems from the divergence of expansions (2.26) and (2.27). This can be immediately demonstrated by considering the integral in (2.26) as an example. When R is large ($R \gg R_B$), the PMF $W(R)$, defined as (2.8), provides the integrand which is proportional to $1/\varepsilon R$. Therefore, the integral diverges at its upper limit. The similar breakdown appears with terms $\Theta_n\left(R\right)$ and δ_n in (2.27). They represent complicated sums of multiparticle integrals containing as integrands the product of functions $(\exp\left[-\overline{W}\left(R_{ab}\right)/kT\right] - 1)$, with $a, b = 1, \ldots N$, arranged in different compositions (the cluster integrals). These integrals diverge at the upper limit. However, all divergences would mutually cancel and ultimately disappear provided the total amount of expansion terms with different powers c_{ion}^n could be accurately collected.

The DH theory performs this collection idea at the approximate level. The initial PMF $W(R)$ (2.8) is reformulated as [20]

$$W(R) = \frac{C_{12}}{R^{12}} - \frac{C_6}{R^6} + W_{DH}(R) + \xi(R), \tag{2.28}$$

where

$$W_{DH}(R) = -\frac{Q^2}{\varepsilon R}\exp\left(-\frac{R}{R_D}\right). \tag{2.29}$$

The modified Coulomb term $W_{DH}(R)$ now contains the exponential screening factor which is tuned by the parameter R_D (the Debye radius). The last term $\xi(R)$ in (2.28) represents extra multiparticle (cluster) potentials which cannot be captured in terms of the DH approximation. Only numerical solutions for $g(R)$, provided they are available [20], can serve for their explicit estimation. It is now readily seen that the screened DH potential (2.29) produces no divergences. The same can be verified for $\xi(R)$, but this term is neglected in the majority of applications. Altogether, the main outcome of the modification (2.28) (restrained by dropping the term $\xi(R)$) is the convergent expansion (2.26), which can be evaluated explicitly. The readily accessible result with the closed expression for the first order term is [16, 20, 26, 27]

$$-\frac{\Delta A}{kT} = \frac{1}{12\pi}\frac{V_0}{R_D^3} + O\left(\eta^2\right) = \frac{1}{9}\left(\frac{R_0}{R_D}\right)^3 + O\left(\eta^2\right),$$

$$\eta = \left(\frac{R_0}{R_D}\right)^3. \tag{2.30}$$

Here η is the DH smallness parameter with $R_0 = (3/4\pi c_{\mathrm{ion}})^{1/3}$ that represents the effective radius attributed to the unit volume $V_0 = 1/c_{\mathrm{ion}}$. The expression for the Debye radius R_D reads [26, 27]

$$R_D = \left(\frac{\varepsilon kT}{4\pi Q^2 c_{\mathrm{ion}}}\right)^{\frac{1}{2}}. \tag{2.31}$$

The essential note is required about the choice of the effective concentration: $c_{\mathrm{ion}} = \alpha c$ where α is the degree of dissociation and c is the total concentration of ion pairs (see Eq. 2.19). This detail distinguishes V_0 in (2.30) from the standard unit volume, the inverse of the concentration c. According to Fig. 2.1, $V_0(\mathrm{ion}) = V_2$. Returning to the conventional notation yields

$$\eta = 6Q^3\sqrt{\frac{\pi c\alpha}{(\varepsilon kT)^3}}. \tag{2.32}$$

The square root dependence on $c\alpha$ is the typical feature of the DH theory.

The correction introduced by $O\left(\eta^2\right)$ originates from the extra term $\xi(R)$, which is neglected in (2.28), as well as from the linearization $\exp\left(-W(R)/kT\right) \approx 1 - (W(R)/kT)$, which is inherent to the DH approximation. Provided this correction is disregarded, the expression for the ionic activity coefficient γ immediately follows from (2.15) and (2.30):

$$\ln\gamma^2 = -\frac{1}{9}\eta. \tag{2.33}$$

It grows up as $(c\alpha)^{1/2}$.

Fig. 2.2 Activity coefficient γ as a function of ionic strength I for 1:1 electrolyte in water solution. Various curves were obtained by different versions of the integral equation theory. Reprinted from Ref. [20] with kind permission of © The American Institute of Physics (1968)
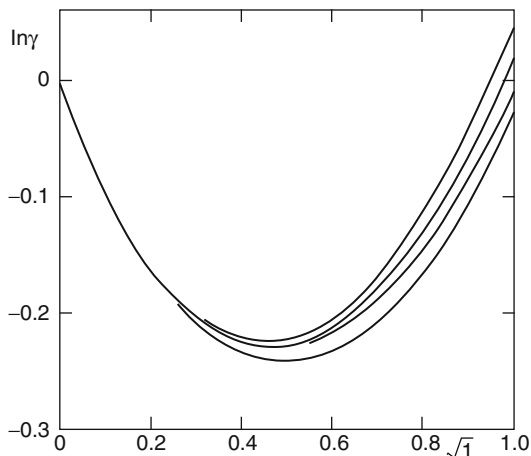
2.5.3   When the Interaction Is Important?

We can test how the DH methodology works in real systems. For typical spectro-scopic experiments, with $c_{ion} = c\alpha$ and $c = 10^{-4}$ M, we obtain $R_0 = 160\alpha^{1/3}$ Å and $R_D = 35\varepsilon^{1/2}$ Å. The smallness parameter η is of order of 1 when $\alpha \approx 1$ and $\varepsilon > 30$, whereas for $c = 10^{-5}$ M the solid estimate $\eta \ll 1$ is expectable. This tentative example establishes the range of validity of the DH approach. However, the DH correction in (2.30) is $-\Delta A/kT \approx 10^{-1}$ even for $c = 10^{-4}$ M, which is negligible in practice. Therefore, the "low concentration regime" (Sect. 2.3) is most typical in spectroscopic applications, and c serves as a quantity which is quite legitimate. The situation may appear different for electrochemical applications with $c \approx 10^{-1}–10^{-2}$ M, although even in this regime the concentration variable remains to be not without utility. As an example, Fig. 2.2 shows the results of several computations, performed beyond the DH approximation, of the activity coefficients in water solvent for the 1:1 electrolyte [20]. The dependence on $\sqrt{I}$ (where the ion strength $I = c$ for the system under consideration) reveals that γ value is reasonably close to 1 for $I < 0.5$ M.

We conclude that significant deviations from the ideal behavior are expected only for electrolyte solution systems where $\eta \geq 1$, i.e., for those systems with high concentrations of ions and low dielectric permittivity. Under so specified conditions, the association of ions and ion pairs in more complex aggregates was predicted [29]. Ionic triplets ABA or BAB and pair dimers ABBA are observed experimentally (see extensive reviews in Refs. [15] and [16]). In this way, the higher cluster terms appearing in virial expansions (2.25)–(2.27) find their material incarnation.

## 2.6   The Structure of Ion Pairs in the Associated Region

The definition of the boundary distance R_B, separating the association and dissociation regions (Fig. 2.1), was originally formulated by Bjerrum [1] based on the most primitive continuum solvation model. Alternative algorithms invoking microscopic models of the solvent were considered by many authors [8, 10–16, 30, 31]. The ion pair AB can combine with one or more solvent particles to form the so-called "contact," "solvent-shared," "solvent separated" pairs, etc. [32, 33]. Molecular level simulations in support of this idea have been reported [34–37]. Each of such aggregates is characterized by its own chemical structure, geometric parameters, and other properties. In terms of them, the range of ionic separations bounded within the association region may be specified. The contact distance (denoted as a) between A and B and the cutoff distance (denoted as R_B in the preceding text) serve as the lower and upper integration limits in the BFK formula (2.13). By considering these values as empirical parameters, a satisfactory fit of experimental association energies can be gained in the frame of the BFK approach [12–16, 38–40] within the wide range of solvent polarity (see Refs. [15, 16] as the key reviews).

The original work by Fuoss and Kraus [2] may serve as a proper illustration. Association constants for tetraisoamyl ammonium nitrate in dioxane/water mixtures were measured and calculated in terms of Eq. 2.13 which was reduced to the one-dimensional integral similar to Eqs. 2.11 and 2.12. The PMF (2.8) was reduced to the single-screened Coulomb term $-1/\varepsilon R$ bounded from below by the infinitely high potential wall placed at $R = a$. The experimental values of K_{ass} are listed in Table 2.1, borrowed from this pioneering work, together with other relevant information. Parameter a, i.e., the lower integration limit in (2.13), was selected so as to reproduce the experiment. It remains constant for the whole range of the solvent composition, which verifies the validity of the BFK approach. We have added to this table the computed values of the degree of dissociation α (corresponding to the solute concentration $c = 10^{-4}$ M). It is seen that the whole association/dissociation range is covered both by the experiment and the theory.

Table 2.1 Association constants for tetraisoamyl ammonium nitrate in dioxane/water mixtures [2]

% Water	ε	K_{ass}, M^{-1}	a, Å	$\alpha(c = 10^{-4}\,\mathrm{M})$
0.60	2.38	2.0×10^{-16}	6.01	1.4×10^{-6}
1.24	2.56	1.0×10^{-14}	6.23	1.0×10^{-5}
2.35	2.90	1.0×10^{-12}	6.36	1.0×10^{-4}
4.01	3.48	2.5×10^{-10}	6.57	1.5×10^{-3}
6.37	4.42	3.0×10^{-8}	6.65	1.7×10^{-2}
9.50	5.84	1.65×10^{-6}	6.45	1.2×10^{-1}
14.95	8.5	1.0×10^{-4}	6.50	6.8×10^{-1}
20.2	11.9	9.0×10^{-4}	6.70	0.9
53.60	38.0	0.25	6.15	1

Fig. 2.3 PMF profile for
aqueous Na$^+$Cl$^-$ system.
Reprinted from Ref. [43] with
kind permission of © The
American Chemical Society
(1999)
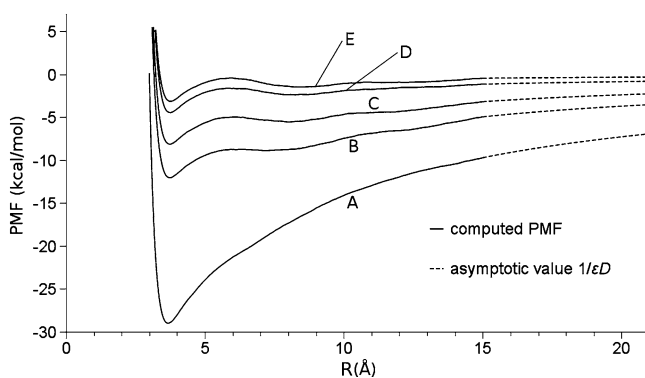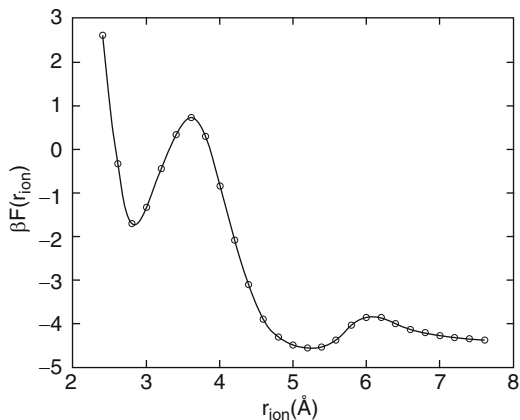
Fig. 2.4 The PMF profiles for benzene/DMSO mixtures. A–E label the solvent contents as the
DMSO molar fraction x: $x = 0$ (A); $x = 0.1$ (B); $x = 0.2$ (C); $x = 0.5$ (D); $x = 1$ (E). Reprinted
from Ref. [44] with kind permission of © Taylor & Francis Ltd (2011)

The refined empirical theory of this sort covers solution systems with higher
electrolyte concentrations c and lower dielectric permittivities ε, i.e., with higher
value of parameter η in (2.30). As described in Sect. 2.5, such systems are expected
to involve ionic clusters [13–16, 29, 41, 42], whose appearance accompanies the
formation of isolated associated ion pairs AB. Altogether, the association region
represents a collection of diverse ion/solvent structures, more or less complicated,
which coexist within a sophisticated and mobile equilibrium.

Recent molecular simulations provide new and valuable information on this
issue. A shallow local minimum with the barrier height of $1–2\,kT$ appears on the
PMF profile calculated by a number of authors for the NaCl pair in water solvent.
Figure 2.3 [43] demonstrates a typical example of such computation. Figure 2.4 [44]
is another example which extends the study for a number of solvent mixtures

with varying polarity. The system considered is Cl^+Cl^- pair dissolved in the benzene/dimethylsulfoxide (DMSO) mixture. The solvent composition, measured as a molar fraction of DMSO, is denoted as x, which changes in a wide range. The virtual particle Cl^+ in this model computation has the same LJ parameters as Cl^-, for which the coefficients C_{12} and C_6 in Eq. 2.8 are well defined. Several conclusions can be inferred from this computation

(a) Broad and extremely deep PMF wells appear in solvents with low ε values. The minimum depth value is ca. 30 kcal/mol for pure benzene ($x = 0$) with $\varepsilon = 2.2$.

(b) A molecular simulation, based on a reliable force field, reveals uniquely the lower integration limit for Eq. 2.11, i.e., the contact distance a.

(c) Being inserted in the BFK Eq. 2.11, the distribution function $P(R)$ (Eq. 2.10) establishes the total size of the association region in the case when the depth of the PMF well is sufficiently large (say, > 10 kT). For such wells, when they are broad and deep (say, for $x < 0.5$), the peak of $P(R)$ is extremely high and narrow. The integration around its maximum position in many cases defines the values of association constants, whereas the contribution coming from the wings of $P(R)$ is negligible. This is why the explicit choice of the integration limits a and R_B does not matter much.

(d) The wavy PMF profiles visualize the molecular structure of solvation shells in the vicinity of AB pairs. They transform into small local wells, separated by low barriers from the external (dissociation) region (see Fig. 2.3 and the profile for $x = 1$ in Fig. 2.4), which is typical for highly polar solvents ($x > 0.2$). No real energy barriers occur on the steep background attractive slopes of broad and deep Coulomb-like wells, appearing at lower DMSO concentrations ($x < 0.1$). Computations show that the remainder of smeared wavy structure makes little impact during the computation of the association constant.

(e) For the case of local PMF wells surviving in the hight-polarity solvents ($x > 0.2$), and displaying a pair of clearly distinguishable minima and the barrier between them, the idea of the underlying individual chemical structures makes sense. This, however, has no serious consequences because the dissociation of AB pair is almost complete ($\alpha \rightarrow 1$) in such situation even for the pair concentrations c of order of 1 M. This signals that the depopulation of associated states is almost complete.

It follows from the present discussion that the theoretical treatment of the association region in terms of the PMF and the pertaining single peak distribution function $P(R)$, which is actually available via an advanced continuum-level computation of the solvation free energy, may be often acceptable for a practical application. The multitude of mobile and vague local molecular structures can often be captured by means of such treatment. This one-peak description will be used henceforth in the remainder text of the present article.

The statement (e) should, however, be formulated with more caution. It assumes that the consideration of the single main distribution peak, associated here with contact ion pairs, is always sufficient in practice. An opposite opinion may arise

when one compares the two alternative theories of the ion pair dissociation, namely, the present thermodynamic BFK approach and the alternative kinetic approach, based on the diffusion theory [3–7]. The so called cage effect [19], implying the complicated diffusion kinetics in the association region, is an essential element of the diffusive treatment [45, 46]. This phenomenon, observed experimentally as the influence of the magnetic field on the recombination kinetics of radical and ion-radical pairs, could be as well included in the thermodynamic approach by the assumption that the presence of the second (i.e., the solvent-separated) PMF well serves as its natural origin. Provided this is so, the presence of the second distribution peak in the association region is definitely observable, at least via the studies of the diffusion kinetics [47–49]. Probably, it could also be revealed by precise studies of how dissociation degree varies between its limit values $\alpha = 1$ and $\alpha = 0$. Fine-tuning of α in its transition region can be provided by a smooth variation of the binary solvent composition (see Table 2.1). The transition interval of α variation is especially sensitive to the presence of the second peak, which is expected to disappear rapidly but steadily in this region. Unfortunately, a quite reliable computational studies of this fine effect are not available at present because they require a complicated combination of the quantum-chemical and MD simulation techniques during the 3D integration procedure (2.11), which is obligatory for the computation of α as a function of the solvent composition. In our computations reported below, a continuum solvent treatment was applied for this purpose, and the second peak effect is certainly missing in such procedure.

2.7 Advanced Computations for Real Systems

A lot of computations of association constants (2.13) are reported in the literature. Many of them are mentioned in Sect. 2.6. Additional references [50–52] deal with the solute ion pairs which represent really complicated chemical systems. The common feature of all these theoretical studies is the oversimplified electrostatic PMF (2.8) in which the short-range (LJ) part is reduced to a Heaviside step function with the step boundary $R = a$ determining the lower integration limit in the BFK integral (2.13).

Recent computational technologies allow for essentially improving the treatment of $W(\mathbf{r})$. The following refinement elements are available at the present time:

(a) The quantum-mechanical short-range interaction effect (the interionic charge transfer) is explicitly included in terms of a quantum-chemical calculation. It involves partial covalent binding between ions A and B.

(b) The solvent-modulated Coulomb interactions, treated by means of the combined MD/continuum approach, take into account the nonuniform medium effects, which always appear in binary solvent mixtures. The origin of such phenomenon is the strong electric field created by the solute particle, provided
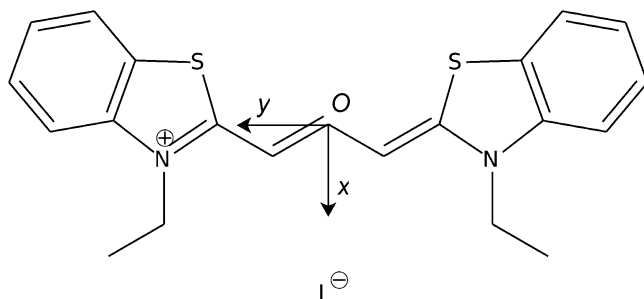
Fig. 2.5 Structure of the TCCI ion pair. Ethyl fragments (C_2H_5—) denoted as broken lines are attached to the nitrogen atoms. The positive charge is distributed symmetrically over the cation

it is charged or polarized. As a response, the polar component of a binary solvent accumulates in the vicinity of the ion pair or its ionic fragments, which results in the position dependence of the solvent composition and the dielectric permittivity $\varepsilon = \varepsilon(\mathbf{r})$. This changes significantly the simple Coulomb potential in (2.8) screened by the constant dielectric permittivity ε. The advanced continuum methodology properly treating such effects is described [53–55].

(c) Typical organic ion pair solutes appearing in applications loose the double-spherical symmetry inherent to inorganic salts AB where A and B are either monoatomic ions or can be treated as spherical particles at least approximately. The immediate result appears as an anisotropy of the interaction coordinate $\mathbf{r}$ in Eq. 2.9, which requires the explicit three-dimensional (3D) computation of the integral (2.13).

All such complications, which are technical but important, are illustrated below using the organic dye molecule thiacarbocyanine iodide (TCCI) as an example. The advanced computation performed for this molecule [56, 57] was required in order to rationalize the measurements of its fluorescent decay kinetics in the mixed toluene/DMSO solvent [58]. This explains why the excited S_1 state of the TCCI is the main object considered below. The resulting interpretation is described in Sect. 2.9.

Figure 2.5 here illustrates the structure accepted for the first excited singlet state of this molecule. It is composed of the two planar heterocyclic fragments connected by the three-center polymethine bridge. The origin of the coordinate frame (point O) is located at the central carbon atom of this bridge. Axes Ox and Oy define the plane of the Fig. 2.5 in which the aromatic cycles are disposed. The rigorously symmetric configuration with the symmetry plane xOz is postulated below. The geometry of its excited state was optimized, based on the TDDFT computation [59], under this symmetry condition. As follows from the analysis of quantum-chemical and solvation studies, the Ox axis represents the direction of the energetically most favorable approach for the ions.

2.8 The Thiacarbocyanine Iodide (TCCI) in Its Excited S_1 State: The Overview of PMF Computations

2.8.1 The Computational Scheme

The computation of association constants for the cyanine dye system Cy^+I^- (thiacarbocyanine iodide, TCCI) was performed for the series of mixtures toluene/DMSO [56]. The excited S_1 state of this chromophore molecule was considered.

For its PMF computation, the usually applied classical force field (2.8) proved to be inefficient. This is illustrated by Fig. 2.6, where three gas-phase PMF profiles drawn along the Ox axis are shown.

Profile A was found by means of a high-level quantum-chemical computation (CC2 [60]). It is considered as a benchmark for other more simplistic approaches. Profile B represents the polyatomic molecular-mechanical potential, the counterpart of the approximation (2.6):

$$W_{\text{gas}}(\mathbf{r}) = \sum_i -\frac{q_i |q_0|}{R_{i0}} + \frac{C_{12}^{i0}}{R_{i0}^{12}} - \frac{C_6^{i0}}{R_{i0}^6}, \tag{2.34}$$

with indices "i" labeling atomic sites of the cation Cy^+ and index "0" belonging to the iodine anion. Partial electrostatic charges q_i, q_0, the interatomic distances R_{i0}, and the corresponding LJ coefficients C_{12} and C_6 are involved in this primitive computation. The charges q_i were found in a gas-phase CC2 computation for the isolated Cy^+, whereas $q_0 = -1$.

The so computed PMF is indeed a poor approximation. The important quantum-mechanical charge transfer effect observed in the CC2 computation at short interionic distances (the contact pair) is totally missing in (2.34). The result of this drawback appears as a large error in the depth of the PMF minimum (ca 10 kcal/mol)
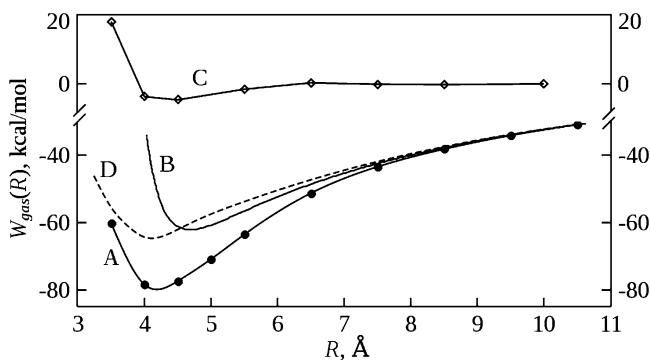
Fig. 2.6 PMF profiles for the TCCI along the Ox axis. Reprinted from Ref. [56] with kind permission of © The American Institute of Physics (2011)

and its position (the global minimum is located outside the Ox axis in the xOz plane, i.e., the true profile B in Fig. 2.6 goes beyond the global classical minimum, as predicted by (2.34) [56]).

Profile C provides a preliminary illustration of the strong solvation effect. It was calculated by CC2 with the implicit account for the solvent reaction field (DMSO, dielectric permittivity $\varepsilon = 46.8$) within the COSMO dielectric continuum approximation [61]. Owing to the intensive dielectric screening, the free energy minimum point has raised by 75 kcal/mol. The depth of the remaining potential well does not exceed 5 kcal/mol.

It is impossible to perform the 3D integral (2.13) based on the CC2 approach even for the gas-phase component of the PMF. This is why we invoked the semiempirical RM1 quantum-chemical computation [62] as an available alternative for capturing the charge transfer effect. The RM1 was selected among other semiempirical procedures after several trial tests. In the vicinity of the PMF minimum, the position of the RM1 potential and its shape reproduce tentatively their CC2 benchmark counterparts. This is seen from Fig. 2.6. Based on such preliminary consideration, we formulated the most realistic strategy for 3D PMF computations as the following prescription:

$$W(\mathbf{r}) = \left[W_{\mathrm{gas}}(\mathbf{r} \mid RM1) - W_{\mathrm{gas}}(\mathbf{r_0} \mid RM1) + W_{\mathrm{gas}}(\mathbf{r_0} \mid CC2) \right] + W_{\mathrm{solv}}(\mathbf{r}).$$
(2.35)

It shifts down the RM1 gas-phase potential in order to combine as closely as possible its minimum with the CC2 benchmark. Here $\mathbf{r_0}$ means the gas-phase CC2 minimum position, shown in Fig. 2.6, which corresponds also to the global 3D minimum as found in numerical tests. This PMF is certainly too flat, but the wrong asymptotic behavior at the wings of this profile is neutralized, at least partially, by the cutoff at $R = R_B$, which is imposed by the upper bound of the integral (2.13). The solvation term in (2.35) was computed in terms of the advanced continuum model [44, 54, 55].

2.8.2   The Resulting PMF Profiles

More refined solvation curves were also constructed in one dimension along the Ox axis. Here the CC2 gas-phase profile A can be used instead of the first term of (2.35), contained in square brackets:

$$W(\mathbf{r}) = W_{\mathrm{gas}}(\mathbf{r} \mid CC2) + W_{\mathrm{solv}}(\mathbf{r}).$$
(2.36)

The so obtained PMF profiles are displayed in Fig. 2.7 for a variety of toluene/DMSO solvent mixtures. The range of solvent composition $0.03 < x < 1$ (i.e., the molar percentage of DMSO varying from 100% to 3%) is established by the conditions of the experiment considered for the interpretation in the following Sect. 2.9. The remarkable comment, which is important, is the notion that the spatial positions of the PMF minima remain practically constant over the whole range of the changing DMSO contents.
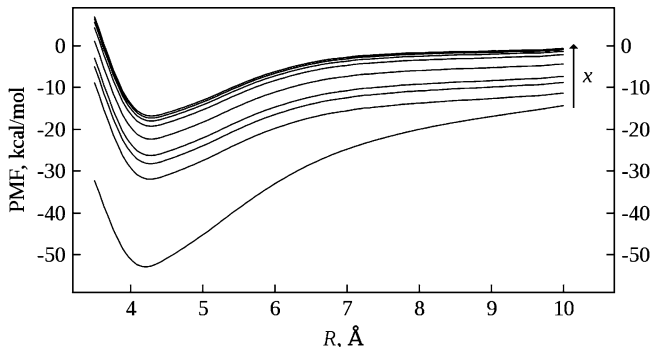
Fig. 2.7 One-dimensional PMFs along the Ox axis for different DMSO concentrations x. Eq. 2.36 is applied; x varies upwards from 0 to 1 as $x = 0$, 0.03, 0.07, 0.1, 0.2, 0.4, 0.6, 0.8, 1.0. Reprinted from Ref. [56] with kind pemission of © The American Institute of Physics (2011)

The computations of association constants K_{ass} were done by performing the 3D integral (2.13). The PMF function $W(\mathbf{r})$ was found in terms of the algorithm (2.35). The results are listed in Table 2.2. It contains the values K_{ass} so determined and the related quantities, which are useful for the analysis of these results. The percentage of the DMSO given in the first line is denoted as x below. In the association free energies, defined as usually

$$\Delta G_{\mathrm{ass}}^0 = -kT \ln\left[K_{\mathrm{ass}} \cdot C_0\right], \tag{2.37}$$

the standard concentration $C_0 = 1\,\mathrm{M}$ is applied in order to cancel the dimensionality of the association constant.

The results of the straightforward 3D integration of the first peak of the distribution function $P(\mathbf{r})$ can now be extended in order to investigate its shape characteristics. The corresponding PMFs $W(\mathbf{r})$ are examined in Fig. 2.7 in detail in a single dimension directed along the Ox axis. Their minima are located on this line within a small interval (less than 0.1 Å) around $R_0 = 4.25\,\text{Å}$. This means that the impact of the medium variation on the value of the minimum position R_0 can be considered as negligibly small. The average shift relative to the gas-phase PMF minimum ($R_0 = 4.2\,\text{Å}$, see Fig. 2.6) is also quite small. We assume now that the first peak components of the 3D probability distributions (see Fig. 2.1) can be approximated as isotropic sharp and narrow Gaussian peaks, denoted as $P_1(R)$

$$P_1(R) = Z_1 b(R); \qquad b(R) = \frac{1}{\sigma\sqrt{2\pi}} \exp\left[-\frac{1}{2}\left(\frac{R - R_0}{\sigma}\right)^2\right]. \tag{2.38}$$

Here $b(R)$ are normalized Gaussian functions. The normalizing factor Z_1 is visualized in Fig. 2.1. The positions R_0 and half-widths σ can be found as the pertaining moments:

Table 2.2 Association constants K_{ass} and related parameters computed for the TCCI

x	0.0	0.03	0.07	0.1	0.2	0.4	0.6	0.8	1.0
R_0, Å	4.361	4.565	4.566	4.567	4.568	4.569	4.570	4.570	4.571
σ, Å	0.1045	0.1344	0.1353	0.1357	0.1364	0.1371	0.1375	0.1378	0.1379
K_{ass}, M^{-1}	$1.8 \cdot 10^{20}$	$1.2 \cdot 10^{14}$	$5.3 \cdot 10^{10}$	$1.0 \cdot 10^{9}$	$1.9 \cdot 10^{7}$	$3.2 \cdot 10^{5}$	$4.6 \cdot 10^{4}$	$1.4 \cdot 10^{4}$	$6.3 \cdot 10^{3}$
ΔG_{ass}^0, $\frac{\text{kcal}}{\text{mol}}$	-27.62	-19.20	-14.62	-12.93	-9.93	-7.50	-6.35	-5.66	-5.18

$$R_0 = \frac{1}{Z_1} \int\limits_{V_1} R \exp\left(-\frac{W(\mathbf{r})}{kT}\right) d^3\mathbf{r},$$

$$\sigma^2 = \frac{1}{Z_1} \int\limits_{V_1} (R - R_0)^2 \exp\left(-\frac{W(\mathbf{r})}{kT}\right) d^3\mathbf{r}. \tag{2.39}$$

The results of the integration are also listed in Table 2.2.

The basic observation is that 3D peaks are slightly shifted, relative to the one-dimensional (1D) R_0 values, along the Ox axis. The variation of R_0 as a response to the medium composition x remains again negligibly small. The half-width σ values can be also considered as constant ones within the whole x range.

It can be concluded that the shapes of averaged distributions $P_1(R)$ are quite insensitive to the variation of the medium composition. Intuitively, this observation can be understood in terms of the concept of the "dielectric enrichment" [63], which suggests that the local solvent environment in the close vicinity of a solute mainly consists of the polar solvent component. For the case of spherical ions, that effect was verified by direct MD simulations [53,54] which have demonstrated that the first solvation shell of a ionic solute in benzene/DMSO mixtures included exclusively DMSO molecules within a wide range of the solvent composition x down to quite low percentage of the DMSO. The deviation of R_0 and σ values, observed for pure toluene ($x = 0$ in Table 2.2), from those found for other solvent compositions ($x > 0$), becomes understandable under this notion.

2.9   The Decay Kinetics of the TCCI in the First Excited State

2.9.1   The Kinetic Scheme

This investigation has been performed [57] for the purpose of interpretation of spectroscopic experiments in which the quantum yields for several decay channels were measured for the singlet S_1 states of the two dyes: trans TCCX (or Cy$^+$X$^-$) with counterions X$^-$ = I$^-$ or Cl$^-$ [58].

For the case X$^-$ = I$^-$, the kinetic scheme to be considered is shown in Fig. 2.8. The four arrows denote four decay processes, namely, the fluorescence, the inter-combination ST conversion, the trans-cis isomerization, and some other undetected processes (most possibly, the radiationless internal conversion). The pertaining rate
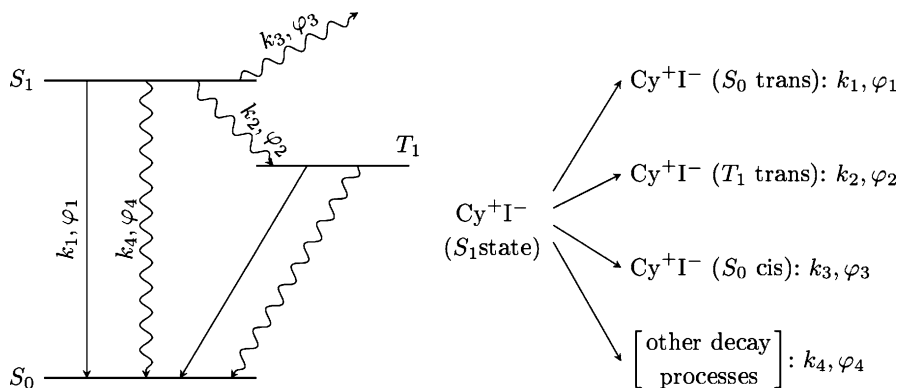
Fig. 2.8 Scheme of degradation channels for the TCCI (its first singlet state) in the toluene/DMSO mixtures

constants and quantum yields are denoted as k_i and φ_i, $i = 1 - 4$. For this combination of photophysical and photochemical transformations, the kinetics has been studied in the mixture toluene/DMSO with the solvent composition x varied between $x = 1$ down to $x = 0.03$ [58]. Figure 2.9a, b illustrates the results found for the TCCX cases with counterions I^- and Cl^-, respectively. Note that process 2 (the ST transition) is practically absent in the second case of the chlorine anion.

In Fig. 2.9a, b, the experimental values of quantum yields φ_i [58] appear as dots corresponding to different values of the solvent composition x. For the chlorine counterion in the solvent of weak polarity ($x \ll 1$), the yield φ_1 (the fluorescence) increases weakly while x falls down. In the case of the iodine counterion, the same process is strongly suppressed in the medium of low polarity. The isomerization quantum yield φ_3 demonstrates the similar trends. For Cy^+I^-, the decrease in φ_1 and φ_3 is balanced by the strong increase of φ_2 (the ST transition, i.e., this process is absent in the Cy^+Cl^-).

The natural guess on the origin of this effect involves the idea of the relativistic heavy atom effect as promoted by the iodine ion, which generates ST transitions facilitated by the spin-orbital interaction. However, the understanding of how and why the quantum yields depend on the solvent composition is a more delicate matter. The work described here [57] is addressed for clarifying this issue. It applies the microscopic computation considered in Sect. 2.8. The calculated there function $F(R)$ [56] serves as an efficient tool for reaching the desired objective.

2.9.2 The Distribution Function

The distribution function $F(R)$ exists under the condition that the total solution system is equilibrated. The equilibrium is perturbed by the decay reactions which proceed according to the scheme shown in Fig. 2.8, but it is regenerated owing to the
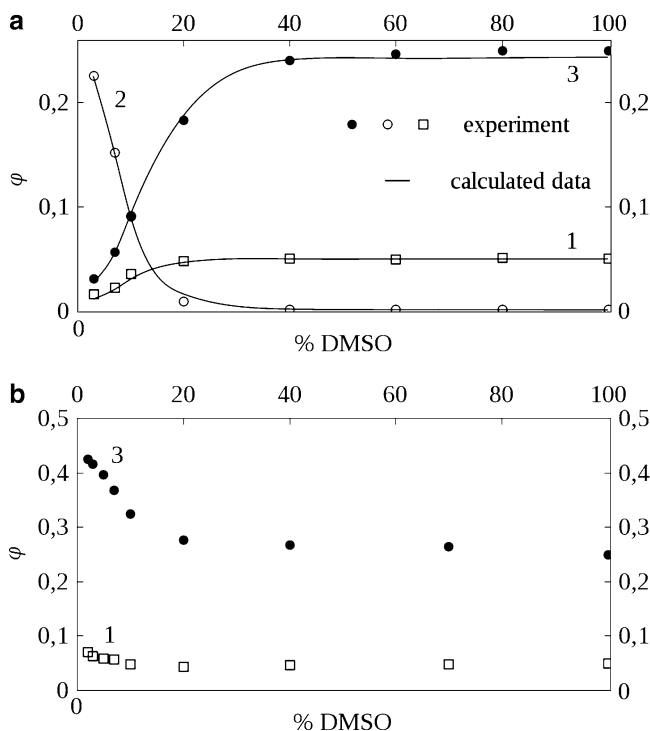
Fig. 2.9 Quantum yields for different decay channels of TCCX as functions of the solvent composition x. (**a**) The experimental (*dots* [58]) and computed (*full lines* [57]) results for Cy^+I^-. (**b**) The experimental results for Cy^+Cl^-. Reprinted from Ref. [57] with kind permission of © The American Institute of Physics (2011)

relaxation processes via the spatial diffusion of the counterions and the orientational reorganization of their solvation shells. The basic assumption, which underlies the present approach, postulates that the relaxation processes are much faster than the decay ones. Under this condition, the local values of rate constants $k_i(R)$ and quantum yields $\varphi_i(R)$ (see Fig. 2.8) can be introduced as functions of the interionic separation R. The possible anisotropic nature of the decay processes is neglected.

Then the average (i.e., observed) quantum yields for different decay channels can be expressed as

$$\langle \varphi_i \rangle = \int_0^\infty \frac{k_i(R)}{\sum_{j=1}^{4} k_j(R)} F(R)dR; \qquad i = 1-3. \tag{2.40}$$

Actually, only three first channels are involved because the last one ($i = 4$) is fixed by the condition $\sum_{j=1}^{4} \varphi_j(R) = 1$.

At this point, a reasonable but simple assumption on the R-dependence of kinetic constants in (2.40) is in order [57]. According to this prescription, the rate constant k_2 (the ST transition) decreases with the increase of R and vanishes at large separations. The rate constants k_1 and k_3 increase and reach their asymptotic values k_{01} and k_{03} when R is large. Their profiles along R were represented by Morse curves. By this means, the width of the limited region, where the variations of $k_i(R)$ are significant, is governed by the exponent parameters γ_i ($i = 1 - 3$). Only dependencies of such kind proved to be successful for the interpretation of the experimental data. They are as well understandable from the physical argumentation stating that the exponential changes at short separations can be naturally attributed to the effects of overlap between the wave functions of the partner ions.

The asymptotic values k_{0i} were assumed to be equal to the same constants observed in pure DMSO:

$$k_i = k_{0i} = k_{0i}(\text{DMSO}), \qquad i = 1, 3, 4. \tag{2.41}$$

A special structure of the distribution $F(R)$ is now utilized:

$$F(R) = (1 - \alpha)b(R) + \alpha f(R). \tag{2.42}$$

Here $b(R)$ and $f(R)$ represent normalized to unity probability distributions for the first and second peaks appearing in Fig. 2.1. The representation (2.42) follows from (2.18). The parameters for $b(R)$ are listed in Table 2.2. No such specification is required for $f(R)$ (except for the normalizing condition $\int f(R)dR = 1$) because the asymptotic values (2.41) are R-independent. Thereby, the final result for quantum yields is obtained as

$$\langle \varphi_i \rangle = (1 - \alpha) \int_0^\infty b_i(R)\varphi_i(R)dR + \alpha\varphi_{0i},$$

$$\varphi_i(R) = \frac{k_i(R)}{\sum\limits_{j=1}^{4} k_j(R)}, \qquad i = 1 - 3,$$

$$\varphi_{0i} = \frac{k_{0i}}{\sum\limits_{j=1}^{4} k_{0j}}, \qquad i = 1, 3, 4; \qquad \varphi_{02} = 0. \tag{2.43}$$

The suggested computational scheme leaves undetermined four kinetic parameters, namely, k_2/k_4, γ_1, γ_2, γ_3. The values k_2 and k_4 are defined at $R = 0$. It was shown [57] that only ratios of kinetic coefficients are involved in the computation, so we can select k_4 as a rate unit.

Table 2.3 The dependence of the fitted peak parameters on the solvent composition x

x	0.03	0.07	0.1	0.2	0.4	0.6	0.8	1.0
R_0, Å	4.565	4.679	4.799	5.189	5.189	5.189	5.189	5.189
α	2.8×10^{-5}	1.4×10^{-3}	0.01	0.07	0.42	0.74	0.89	0.94

2.9.3 The Fitting Results

The parameter optimization results in the data listed in Table 2.3. The Gaussian approximation (2.38) and (2.39) accepted for the normalized distribution $b(R)$ characterize, according to (2.42), the first peak of the total distribution function $F(R)$. As already noted, the direct evaluation of the Gaussian parameters R_0 and σ [56] has revealed their insensitivity upon the variation of the solvent composition. For all experimental points specified in Fig. 2.9a, they proved to be practically identical. With this unexpected outcome, the available derivation of the dependence of quantum yields $\langle \varphi_i \rangle$ on the solvent composition becomes entirely controlled by the changes in dissociation degree α. Such straightforward procedure is not sufficiently flexible for a properly smooth description of the experimental data in the transition region. The result of the computation appears as a sharp stepwise change. The desired smooth variation of α could only be gained under the condition that the positions $R_0(x)$ of the Gaussian peaks are allowed to vary as fitting parameters. The directly calculated value $R_0 = 4.57$ Å [56] can be, without any inconsistency, attributed to $x = 0.03$ (point 1 in Fig. 2.9a), but for the other x values, the R_0 positions must be detected via empirical fitting. In such a way, the R_0 values listed in Table 2.3 were obtained. Their fitting is actually required for three next points 2–4, corresponding to $x = 0.07$, 0.1 and 0.2. For the larger values of x, the same upper limit $R_0(0.2) = 5.19$ Å can serve without problems. Here the α values are close to 1 and the fitting results are insensitive to a variation of R_0 in a wide range. Note that the calculated from the PMFs constant value $\sigma = 0.136$ Å [56] was throughout used in the fitting computations.

Thereby, the result of satisfactory reproducing the experimental quantum yields could be obtained [57] at the expense of treating three extra values ($R_0(0.07)$, $R_0(0.1)$ and $R_0(0.2)$) as adjustable parameters. Simultaneously, the fitting procedure provided four regular kinetic parameters, specified after Eq. 2.43, as

$$k_2/k_4 = 1.3 \cdot 10^3, \quad \gamma_1 = 0.90 \, \text{Å}^{-1}, \quad \gamma_2 = 5.73 \, \text{Å}^{-1}, \quad \gamma_3 = 0.48 \, \text{Å}^{-1}. \quad (2.44)$$

2.9.4 Discussion

The algorithm for computing the spatial distribution function $F(R)$ (Eq. 2.42) has been elaborated for ion pairs dissolved in mixed solvents. It requires a preliminary preparation of the PMF $W(\mathbf{r})$ based on the quantum-chemical computation

combined with the advanced dielectric continuum theory [56]. For an organic ion pair of complicated structure (the TCCI dye) in the binary toluene/DMSO mixture, the 3D distribution $\exp(-W(\mathbf{r})/kT)$ was computed and averaged to give $F(R)$. On this basis, the rational interpretation of the nontrivial counterion effect observed experimentally in photochemical kinetics of the TCCI (in the S_1 state) decay is formulated.

The results cannot be qualified as totally successful. The methodology we have applied seems to be insufficiently flexible and sensitive for completely revealing the impact of the solvent composition on the distribution function. This seeming deficiency contaminated its computation by extra fitting parameters reducing the reliability of the interpretation. Several reasons for such failure can be considered. Firstly, we cannot, indeed, eliminate the methodological drawbacks, which possibly appear in the dielectric continuum treatment of the observed fine solvation effects. For instance, the alternative molecular simulation predicts the oscillating behavior of the PMF profiles in the close vicinity of a solute particle, which is smeared and cannot be reproduced via the continuum treatment. On the other hand, the parameters of $F(R)$ (i.e., the peak position R_0 and its variance σ^2), found within the continuum approach, were qualitatively confirmed in the specially arranged MD simulation. This is why the different explanation, which is not addressed to the methodology of the $F(R)$ computation, may be as well legitimate. The guess is prompted by the simplifying assumption inherent to the kinetic model suggested by the parametrization of rate coefficients $k_i(R)$. It discards totally their orientational specificity involved in the decay kinetics. For an intricate organic structure, like the TCCI (in the S_1 state), the expectable anisotropy of ion pair configurations, provided it is neglected, can result as spurious solvent dependencies of $F(R)$, i.e., those effects observed in our calculations.

Given this latter comment, which is obvious, let us return to the problems specific for the continuum-level computation of the solvation free energy [44, 54, 55]. Based on Eq. 2.35, the total PMF was specially fitted in order to reproduce the benchmark MD profile of the same PMF. The total shape was reliable, whereas the position and the depth of the global potential minimum were always determined quite accurately. However, the wavy structure of the PMF profiles (see Figs. 2.3 and 2.4) was inevitably lost in continuum computations (see Fig. 2.7).

As discussed in Sect. 2.6, the small second peak always appears in MD profiles specific for polar solvents (water and DMSO). It fully dissipates in the nonpolar solvents (benzene and toluene), but its disappearance proceeds steadily when the proportion of the polar component decreases gradually in the solvent mixture. Following the terminology of local solvent structures (Sect. 2.6), we can consider the main (permanent) PMF peak and the accompanying (gradually disappearing) peak as a contact and a solvent-separated ion pairs, respectively. Taking into account such fine structure, inherent to the association region of ion pair configurations, could be an extra factor to increase the flexibility of computations implemented in treating the probability distribution $F(R)$ (2.42). The general comment on this point is given at the end of Sect. 2.6. With such a refinement, function $b(R)$ would appear, depending on the solvent composition, as a variable combination of two peak components,

with the second one gradually disappearing. Unfortunately, the straightforward MD simulation is too laborious for being included in the 3D integration procedure, while the present version of the continuum approximation cannot allow for detecting this effect.

2.10   Conclusion

In the present work, the ionic equilibrium (2.1) was analyzed in terms of the interionic PMF $W(\mathbf{r})$ and the corresponding probability density $F(R) = \frac{R^2}{Z} \left\langle \exp\left(-\frac{W(\mathbf{r})}{kT}\right)\right\rangle_{\theta,\varphi}$ which represents the distribution of interionic distances R. This general approach is expected to be reliable for a practical implementation provided the PMF is calculated with due precision. In applications, it may be more convenient and universal than the alternative treatment of ion pairs in solution in terms of equations of the diffusion theory [3–7].

The details of the PMF structure are especially important for treating the short-range association region $R < R_B$. The customarily applied primitive molecular-mechanical potential (2.8) should be refined by considering several more sophisticated effects.

(a) Partial covalent binding (the interionic charge transfer)
(b) The nonuniformity of solvent composition and its dielectric properties arising in binary mixtures of polar/nonpolar solvents in the vicinity of an ion pair solute (the so-called dielectric enrichment effect [63])
(c) The PMF anisotropy which must be taken into account for the majority of real solute systems composed of nonspherical organic cations and/or anions

Inclusion of these effects in the treatment of the PMF requires an extra computational effort, which is significant. So, item (a) implies performing a lot of quantum-chemical computations at a reliable level. For treating item (b), the molecular simulation is the most solid but costly approach. The advanced dielectric continuum solvent model [53–55] can be also applied. It is specially adapted for treating the pertaining anisotropy effects, being much more appropriate computationally than the alternative molecular level (say, MD) calculation. Item (c) implies performing straightforward 3D integration according to Eq. 2.11, which is not an ordinary task under the condition that items (a) and (b) are incorporated. Such advanced program was tentatively covered using the TCCI as a representative example [56], which is briefly described in Sect. 2.8.

With the details extracted at the stage of items (a) and (b), the PMF usually acquires fine structure appearing as a set of shallow local minima which accompany the main global minimum created by a competition of Coulomb and LJ forces inherent to the primary potential (2.8). Such a complication, specific for the associated region of ion separation ($R < R_B$) in a polar solvent, finds its counterpart in the diffusion theories, which reveals in this context as the kinetic cage effect

[47–49]. The so arising wavy structure of PMF profiles reproduces itself as several peaks in the 1D distribution function $F(R)$. As discussed in the concluding remarks of Sects. 2.6 and 2.9, the effect of accompanying secondary peaks, which is suppressed steadily when the polarity of a solvent is gradually decreasing, may be discovered by studying the composition dependence of several experimental observations performed in binary solvent mixtures.

For the long-range dissociation region $R > R_B$, the screened Coulomb interaction $-Q^2/\varepsilon R$ remains as a single essential PMF component. This allows one to treat successfully the dissociated ion pairs as an ideal gas of separate ions (no interaction), provided the concentration c of pairs is sufficiently low. Such an approximation is legitimate in spectroscopic experiments ($c < 10^{-2}$ M). For higher concentrations ($c > 10^{-2}$ M) of ion pair solutions, no other methodology than the DH theory is available at present for treating the ionic interaction within a practically available implementation.

It is important to emphasize that even in dilute solutions, typical for spectroscopic applications, nontrivial effects may become quite visible when the association constants become large ($K_{ass}c \gg 1$). This condition implies a small dissociation degree ($\alpha \ll 1$). It is typical for solvent mixtures of low polarity ($\varepsilon < 10 - 15$), containing a small proportion ($< 20\%$) of the polar component.

Up to this point, the probability function $F(R)$ was exclusively considered as a source for a computation of association constants K_{ass}. However, the scope of its application is more rich. Section 2.9 gives an example of how it can be extended. When $K_{ass}c \gg 1$, the degree of dissociation α provides, according to Eq. 2.18, an important extra information required for a proper normalization of $F(R)$. The absolute values of this function in the association region become available by this means which may found numerous applications. The competition of different decay channels contributing to the deactivation kinetics of the excited state of an organic dye, and its dependence on the composition of the solvent mixture, is the single particular example existing at the present time. Its extension in various research directions can be anticipated. This promising combined branch of experimental and computational chemistry deserves a further elaboration.

References

1. Bjerrum N (1926) Kongelige Danske Videnskabernes Selskab 7:1
2. Fuoss RM, Kraus C (1933) J Am Chem Soc 55:1019
3. Onsager L (1938) Phys Rev 54:554
4. Eigen M (1954) Z Phys Chem Neue Folge 1:179
5. Sano H, Tachiya M (1979) J Chem Phys 71:1276
6. Mauzerall D, Ballard SG (1982) Ann Rev Phys Chem 33:377
7. Wojcik M, Tachiya M (2009) J Chem Phys 130:104107
8. Denison JT, Ramsey JB (1955) J Am Chem Soc 77:2615
9. Gilkerson WR (1956) J Chem Phys 25:1199
10. Mattina CF, Fuoss RM (1975) J Phys Chem B 79:1604
11. Buchner R, Cheng T, Hefter G (2004) J Phys Chem B 108:2365

12. Bester-Rogac M, Hauptman N, Barthel J (2007) J Mol Liq 29:131
13. Fuoss RM (1958) J Am Chem Soc 80:5059
14. Fuoss RM (1978) J Phys Chem 82:2427
15. Barthel JMG, Krienke H, Kunz W (1998) Physical chemistry of electrolyte solutions, modern aspects. Stienkopf, Darmshtadt/Springer, New York
16. Marcus Y, Hefter G (2006) Chem Rev 106:4585
17. Andersen HC (1973) J Chem Phys 59:4714
18. Mihailescu M, Gilson MK (2004) Biophys J 87:23
19. Noyes RM (1961) Prog React Kinet 1:129
20. Rasaiah JC, Friedman HL (1968) J Chem Phys 48:2742
21. Justice MC, Justice JC (1976) J Solut Chem 5:543
22. Justice MC, Justice JC (1977) J Solut Chem 6:819
23. Justice JC (1991) J Solut Chem 20:1017
24. Simonin JP, Bernard O, Blum L (1998) J Phys Chem B 102:4411
25. Krienke H, Bartel JZ (1998) Z Phys Chem 204:713
26. Balescu R (1975) Equilibrium and non-equilibrium statistical mechanics. Wiley, New York
27. Friedman HL (1985) A course in statistical mechanics. Prentice Hall College Division, Englewood Cliffs
28. McMillan WGJ, Mayer JE (1944) J Chem Phys 13:276
29. Fuoss RM, Kraus CA (1933) J Am Chem Soc 55:2387
30. Barthel J (1979) J Ber Bunsen-ges Phys Chem 83:252
31. Bester-Rogac M, Babic V, Perger TM, Neueder R, Barthel J (2005) J Mol Liq 118:11
32. Eigen M, Tamm K (1962) Z Electrochem 66:93
33. Eigen M, Tamm K (1962) Z Electrochem 66:107
34. Hirata F, Levy RM (1987) J Phys Chem 91:4788
35. Rashin AA (1989) J Phys Chem 93:4664
36. Buckner JK, Jorgensen WL (1989) J Am Chem Soc 111:2507
37. Dang LX, Pettitt BM (1990) J Phys Chem 94:4309
38. Rousset E, Barthel J, Justice JC (1993) J Solut Chem 22:571
39. Hsia KL, Fuoss RM (1968) J Am Chem Soc 90:3055
40. Sinha A, Roy MN (2007) Phys Chem Liq 45:67
41. Fuoss RM, Hsia KL (1967) Proc Natl Acad Sci USA 57:1550
42. Barthel J, Krienke H, Holovko MF, Kapko VI, Protsykevich IA (2000) Condens Matter Phys 3:657
43. Geissler PL, Dellago C, Chandler D (1999) J Phys Chem B 103:3706
44. Odinokov AV, Leontyev IV, Basilevsky MV, Petrov NK (2011) Mol Phys 109:277
45. Salikhov KM, Molin YN, Sagdeev RZ, Buchachenko AL (1984) Spin polarization and magnetic effects in radical reactions. Elsevier, New York
46. Harris AL, Brown JK, Harris CB (1988) Annu Rev Phys Chem 39:341
47. Petrov NK, Borisenko VN, Starostin AV, Alfimov MV (1992) J Phys Chem 96:2901
48. Shushin AI (1986) Mol Phys 58:1101
49. Savitsky AN, Paul H, Shushin AI (2006) Helv Chimica Acta 89:2533
50. Zagrebin PA, Nazmutdinov RR, Spector MI, Borzenko EA, Tsirlina GA, Mikhelson KN (2010) Electrochimica Acta 55:6065
51. Leroy F, Miró P, Poblet JM, Bo C, Bonet AJ (2008) J Phys Chem B 112:8591
52. Chaumont A, Wipff G (2008) Phys Chem Chem Phys 10:6940
53. Basilevsky M, Odinokov A, Nikitina E, Grigoriev F, Petrov N, Alfimov M (2009) J Chem Phys 130:024504
54. Basilevsky M, Odinokov A, Nikitina E, Grigoriev F, Petrov N, Alfimov M (2009) J Chem Phys 130:024505
55. Basilevsky MV, Odinokov AV, Nikitina EA, Petrov NK (2011) J Electroanal Chem 660:339
56. Odinokov AV, Basilevsky MV, Nikitina EA (2011) J Chem Phys 135:144503
57. Odinokov AV, Basilevsky MV, Petrov NK (2011) J Chem Phys 135:144504
58. Chibisov AK, Voznyak DA, Petrov NK, Alfimov MV (2009) High Energy Chem 43:38

59. Laikov DN, Ustynyuk YA (2005) Russian Chem Bull Int Edit 54:820
60. Hättig C, Köhn A (2002) J Chem Phys 117:6939
61. Klamt A, Schüürmann G (1993) J Chem Soc Perkin Trans 2 5:799
62. Rocha GB, Freire RO, Simas AM, Stewart JJP (2006) J Comput Chem 27:1101
63. Suppan P (1990) J Photochem Photobiol A 50:293

Chapter 3
Digraphs in Chemistry: All Possible Structures and Temperature-Dependent Distribution of Water Clusters

Misako Aida, Dai Akase, Hideo Doi, and Tomoki Yoshida

Abstract Graphs, digraphs, and rooted digraphs play important roles in chemistry. We present a graph-theoretical procedure to generate all the topology-distinct structures for water clusters. The NVT ensemble of water clusters is divided into the configurational subsets, which correspond to the topology-distinct hydrogen-bonding patterns, and the relative molar Helmholtz energies of the hydrogen-bonding patterns are evaluated. The method is based on the combination of standard Monte Carlo techniques with defined hydrogen-bonding patterns. The structure distributions of water clusters at finite temperatures are presented on the basis of the hydrogen-bonding patterns instead of the inherent structures. The thermodynamically favored structures of water clusters are presented. A list of new potential energy functions for water is given. An assessment of potential energy functions for water is also presented. A rooted digraph is used to represent the features of protonated water clusters. From detailed investigation of the structural patterns obtained, several restrictions which should be satisfied in the stable structures of protonated water clusters are found. The generated hydrogen-bonding matrices of the restrictive rooted digraph are used as the theoretical framework to obtain all the local minima on the potential energy surfaces of those protonated water clusters using ab initio molecular orbital and density functional theory methods.

3.1   Introduction: A Historical View of Graphs in Chemistry

When and how did the connection begin between chemistry and graph theory? In the 1870s, the mathematician Cayley [1] used graph theory to solve a problem concerning the number of isomers of chemical compounds. He investigated $C_nH_{2n+1}OH$ in

M. Aida (✉) • D. Akase • H. Doi • T. Yoshida
Center for Quantum Life Sciences, and Department of Chemistry, Graduate School of Science, Hiroshima University, 1-3-1 Kagamiyama, Higashi-Hiroshima, Hiroshima 739-8526, Japan
e-mail: maida@hiroshima-u.ac.jp; dai-akase@hiroshima-u.ac.jp; hideo-doi@hiroshima-u.ac.jp; tyoshida@hiroshima-u.ac.jp

the cases where *n* was from 1 to 6. He compared the numbers of known isomers and the numbers of the possible isomers. He noticed that there were some isomers which had not been found. This was the first encounter of chemistry with graph theory. If he had not realized that, we would not have been able to understand how many isomers may exist in chemical compounds. The number of isomers that has been observed does not tell us the number of possible isomers. Experimental methods may not be available by which all isomers can be observed. By means of graph theory, we can obtain the maximal number of isomers. To clarify the limits of possibility is very important in chemistry.

Chemists have used graph theory as criteria to determine the properties of chemical compounds, but this is not recognized by most chemists. In 1947, Wiener [2] investigated the relationship of boiling points with structures for paraffin. In 1971, Hosoya [3, 4] investigated the relationship of boiling points with structures for octane. Although their investigations were not such that they could explain the origin of the phenomenon, they were epoch-making works. This is because they were aiming at property prediction. They pointed out that once we know the structure of a chemical compound, we can predict the property. This means that we do not need to synthesize a molecule or observe a molecule to know its properties. This concept is especially useful in procedures used in drug development and drug discovery. The properties of an enormous number of drug candidates can be evaluated without molecular syntheses. This is a success of chemists.

Another important concept in chemistry is how to name a molecule. A nomenclature must meet the following conditions. First, a specific chemical name must be given to a molecule. Second, a chemical name must correspond to a chemical structure, one to one. You may think that you can give any individual name to any molecule. However, this approach will fail. Suppose there are 1,000 compounds, then you must make individual 1,000 names and memorize those 1,000 names. This is why a nomenclature must exist. Even though the rules of a nomenclature that you must memorize might be difficult to learn, you can produce names that can explain the structures of chemical compounds. Here you must be aware that a nomenclature is not always complete: namely, a chemical structure may have several different names.

The evolution of computers has made this incompleteness a problem. Nowadays, people tend to search for a chemical compound by a keyword or by a name, not by a structure. This is a troublesome issue. Searching with a different keyword gives a different result. In fact, the IUPAC nomenclature allows some different names to be given to a molecule. This is because the IUPAC nomenclature includes some ambiguity so that the naming rules are simple. On the other hand, the Chemical Abstracts index name and Chemical Abstracts Service (CAS) registry number have a different concept from that of IUPAC. The Chemical Abstracts index name does not give the same name to a different molecule. The CAS registry number is the molecular discrimination number. Thus, by using these, we can search for a molecule. If we use these, however, it is difficult to search for other molecules which are "analogous" to a given molecule.

Then, how can we search for "analogous" molecules of a given molecule? Here, "analogous" may mean that we can convert a molecule to other molecules by changing one functional group. This is the subgraph isomorphism problem. There are many computer programs which can search for "similar" compounds. These programs probably do not solve the subgraph isomorphism problem, but they calculate an indicative value of a structure and use that to find "similar" compounds.

Graph theory is thus a powerful tool in chemistry. It is noteworthy that the information only exists in the connections. In other words, if a connection exists, we can extract a property. From now on, graph theory will play a more important role in chemistry [5–7].

In this chapter, we concentrate on the hydrogen bonding in a water cluster, i.e., the connection between water molecules. We introduce how graph theory is used to extract the properties of water clusters and how it works hand in hand with current computational chemistry.

3.2 Graphs and Digraphs

3.2.1 Graphs, Digraphs, and the Adjacency Matrix

First, we give a brief introduction to graphs. We refer only to some basic terms of graphs which are used later, and we attempt to express the terms schematically with less mathematical expressions.

A graph is a set of vertices and edges. Vertices are often called nodes or points, and edges are also called lines. The edge donates the connectivity between two vertices. Vertices and edges may be distinguishable by labels. Graphs are widely used for schematic representations (Fig. 3.1). In chemistry, a chemical formula is described as a graph whose vertices represent atoms and whose edges represent chemical bonds, in which the labels for vertices are element symbols and the labels for edges mean the kind of bonds, such as single bonds, double bonds, and aromatic bonds (Fig. 3.2).

A digraph (or directed graph) is a graph whose edges are directed. The digraph contains more information about the relation between two vertices, i.e., the direction from a vertex toward another vertex. A directed edge is also called an arc. In contrast to a digraph, a graph where the edges are not directed is called an undirected graph.
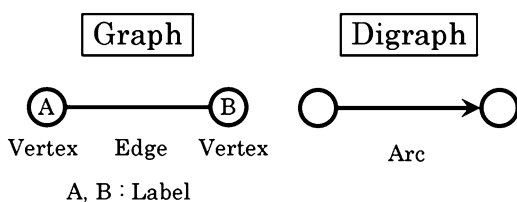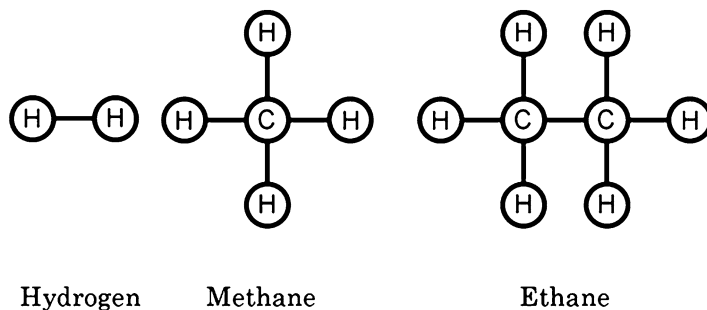

Fig. 3.1 A graph and a digraph

Hydrogen   Methane   Ethane

Fig. 3.2 Molecular structures and graph representations

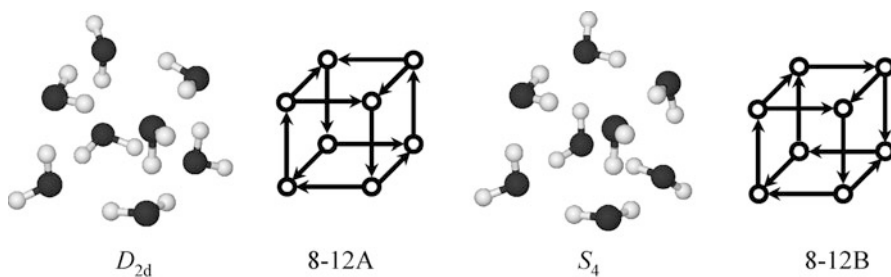D_{2d} 8-12A S_4 8-12B

Fig. 3.3 Water cluster and digraph representation

There are different ways of representing graphs. One easy way is to use an adjacency matrix. The adjacency matrix of an undirected graph with n vertices is the nth-order square matrix, whose element a_{ij} is equal to 1 if there is an edge between vertex i and vertex j, and 0 otherwise, hence the matrix is symmetric. For a digraph, the element a_{ij} of the adjacency matrix is 1 if and only if an arc from vertex i toward vertex j exists.

A graph invariant is a property of graphs. The number of vertices and the number of edges are two simple graph invariants. The Hosoya index [3] is also a kind of graph invariant. If two graphs are equivalent, the graphs are called isomorphic. Of course, isomorphic graphs have the same graph invariants.

3.2.2 Hydrogen-Bonding Network with Graph Theory

A hydrogen-bonding network is a target of graph-theoretical approaches. A digraph rather than an undirected graph is appropriate for representing a hydrogen-bonding network, because a digraph expresses not only the connectivity but also the direction of a hydrogen bond. In this case, vertices represent components forming hydrogen bonds, and arcs stand for hydrogen bonds from hydrogen donors to hydrogen accepters (Fig. 3.3).

One of the most famous examples of hydrogen-bonding networks is found in water. Since a water molecule can form up to four hydrogen bonds, a maximum of two hydrogen donors and two hydrogen acceptors, the hydrogen-bonding networks become very complicated even if they are formed in clusters.

Water clusters have local minimum structures on the potential energy surfaces, among which the lowest energy one is the global minimum structure. The local minimum structures are often regarded as representative structures of the cluster. The number of local minima increases with the cluster size, and searching for all the local minima and the global minimum is a laborious problem.

The number of internal degrees of freedom of water clusters is quite high because of the independency of each component molecule. When the hydrogen-bonding network is specified, however, the configurations are almost defined except for the orientation of the dangling OH.

In 1991, Radhakrishnan and Herndon [8] used the graph representation of water clusters and conducted regression analyses using several graph invariants, in which the interaction energy of water clusters was fitted as a function of the graph invariants. The correlation is very good if proper graph invariants are selected for the analyses. The selected graph invariants include not only the number of arcs, which represents the number of the hydrogen bonds formed in the cluster, but also information about the network, e.g., the numbers of paths of different lengths, the number of three- and four-membered rings, and the total number of double donation or acceptance of arcs at each vertex. This result indicates that the cooperativity of hydrogen bonds is inherently associated with the hydrogen-bonding network.

The structure generation of an isomer is another application of the graph representation of water clusters. A typical procedure is as follows. First, an undirected graph corresponding to a particular topology of clusters under study is selected. Then, digraphs representing different topologies of isomers are generated by the replacement of the edges with arcs in the undirected graph. If there are any, the duplications, i.e., isomorphic digraphs, are removed. The final structures are constructed using the remaining digraph, and are used for the following studies, such as the geometry optimization. For example, cage, book, prism, chair, and boat structures for $(H_2O)_6$, cube structures for $(H_2O)_8$, fused cube structures for $(H_2O)_{12}$, and dodecahedral structures for $(H_2O)_{20}$ have been studied [9–13]. For the cubic octamer, there are 14 topologically distinct isomers, each of which has the corresponding local minimum structure.

3.3 Hydrogen-Bonding Pattern of Water Clusters

3.3.1 Enumeration and Mapping

When the number of the digraphs corresponding to a water cluster is enumerated, we can obtain all the possible topologically distinct hydrogen-bonding patterns of the water cluster. A digraph satisfying the following three conditions is considered

Table 3.1 The number of digraphs corresponding to water clusters

Vertex	Digraphs
2	1
3	5
4	22
5	161
6	1,406
7	14,241
8	164,461
9	2,115,335
10	29,903,139
11	460,066,726
12	7,644,586,673

as representing a water cluster: (1) the maximum number of arcs directed toward a vertex is 2 and the maximum number of arcs directed from a vertex is 2; (2) up to one arc is allowed between any two vertices; (3) the digraph must be connected. Miyake and Aida [14] enumerated the number of digraphs satisfying the above-mentioned conditions by means of adjacency matrices up to eight vertices. Furthermore, Vukičević et al. [15] extended this up to 12 vertices using a more sophisticated algorithm. The results of the enumerations are summarized in Table 3.1. The numbers guarantee the upper limits of the hydrogen-bonding patterns of water clusters; in other words, there are no other topologically distinguishable isomers. This is an advantageous property of the hydrogen-bonding pattern compared with the local minimum structures, the number of which is not easy to enumerate.

If a definition of a hydrogen bond is given, the structure of a water cluster can be mapped to the corresponding hydrogen-bonding pattern, although it is difficult to systematically assign the structure of a water cluster to the corresponding local minimum structure when the structure is geometrically far from the local minimum. Miyake and Aida [16] applied this idea to water octamers at finite temperature by means of Monte Carlo simulation. They demonstrated that the classification to the hydrogen-bonding pattern corresponds to the division of the configurational space of the water cluster structure, which does not depend on whether local minimum structures exist or not.

3.3.2 Helmholtz Energy, Internal Energy, and Entropy

We consider a system of a water cluster in the canonical ensemble that is characterized by a constant number of molecules, constant volume, and constant temperature T. The canonical ensemble is created by means of Monte Carlo simulation. The partition function Q of the system is given by

$$Q = \int \rho(E) e^{-\beta E} \, dE, \tag{3.1}$$

where $\rho(E)$ is the density of states, and $\beta = 1/k_B T$. The Helmholtz free energy A is related to the partition function in the canonical ensemble:

$$A = -k_B T \ln Q. \tag{3.2}$$

Since the system can be divided into a set of hydrogen-bonding patterns, the partition function is expressed as follows:

$$Q = \sum_i \int \rho_i (E) e^{-\beta E} \, dE$$
$$= \sum_i Q_i. \tag{3.3}$$

The subscript i donates hydrogen-bonding pattern i. Now, we define the Helmholtz free energy of hydrogen-bonding pattern i, as follows:

$$A_i = -k_B T \ln Q_i$$
$$= U_i - T S_i. \tag{3.4}$$

Here, U_i is the internal energy of hydrogen-bonding pattern i, and S_i is the entropy of hydrogen-bonding pattern i. However, it is not so straightforward to compute the absolute value of the partition function. In practice, we can evaluate the relative free energies ΔA_{ij} between hydrogen-bonding patterns i and j from the probabilities P_i and P_j at which hydrogen-bonding patterns i and j are sampled in the canonical ensemble by means of molecular dynamics or Monte Carlo simulations, namely,

$$\Delta A_{ij} = -k_B T \ln \left(Q_i / Q_j \right) = -k_B T \ln \left(P_i / P_j \right)$$
$$= \Delta U_{ij} - T \Delta S_{ij}. \tag{3.5}$$

The internal energy differences between the hydrogen-bonding patterns can be obtained from ensemble averages of the potential energy; thus,

$$\Delta U_{ij} = \langle U_i \rangle - \langle U_j \rangle. \tag{3.6}$$

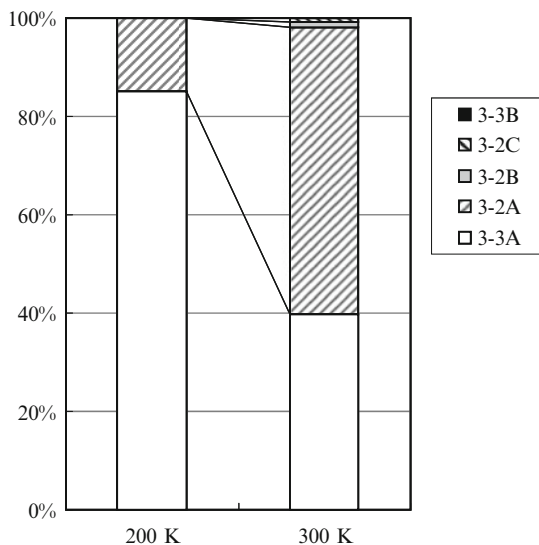The relative entropies are calculated using Eq. 3.5.

3.3.3 Water Trimer

Five hydrogen-bonding patterns of the water trimer are depicted in Fig. 3.4. The global minimum structure is found in cyclic hydrogen-bonding pattern 3-3A, in
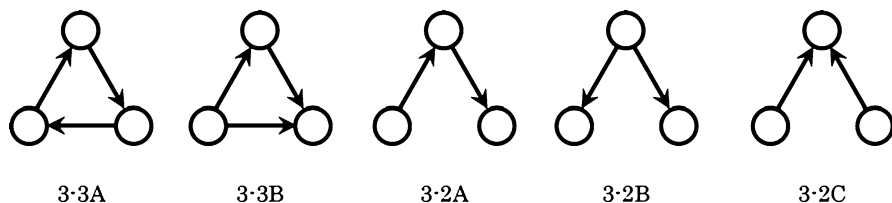
Fig. 3.4 Digraph representation of a water trimer

Fig. 3.5 Relative population of water trimers at 200 and at 300 K

which all water molecules act as both a hydrogen donor and a hydrogen acceptor. This pattern also contains another local minimum structure, which is different from the global minimum one in the orientation of the dangling OH [17]. In linear hydrogen-bonding pattern 3-2A, to the best of our knowledge, there are no local minima on the ab initio molecular orbital (MO) potential energy surface. Two linear local minimum structures [18] are classified as patterns 3-2B and 3-3C, respectively. These two structures are almost isoenergetic.

The relative populations of the hydrogen-bonding patterns of water trimers at 200 K and at 300 K are shown in Fig. 3.5. The energies are shown in Table 3.2. At 200 K, cyclic pattern 3-3A is the lowest in free energy, or is the most populated. The stability is due to it having the lowest internal energy, which is the average of the interaction energies of the structures classified into the pattern. The pattern with the second-lowest energy is 3-2A, followed by 3-2B and 3-2C.

At 300 K, linear pattern 3-2A becomes the lowest in free energy. Cyclic pattern 3-3A is higher in free energy, although the internal energy is still the lowest. The result indicates that the configurational space of hydrogen-bonding pattern 3-2A is generally placed at a higher area than that of 3-3A on the potential energy surface.

Table 3.2 Relative Helmholtz free energies, internal energies, and entropic terms of hydrogen-bonding patterns of $(H_2O)_3$	200 K			300 K		
Pattern	ΔA	ΔU	$-T\Delta S$	ΔA	ΔU	$-T\Delta S$
3-3A	0.00	0.00	0.00	0.23	−2.86	3.09
3-2A	0.69	2.20	−1.51	0.00	0.00	0.00
3-2B	3.35	6.01	−2.66	2.40	2.72	−0.32
3-2C	3.44	5.82	−2.38	2.50	2.74	−0.25
3-3B	3.96	4.78	−0.81	3.84	1.63	2.21

The energy values are in kilocalories per mole

3.3.4 Water Octamer

Although the enumeration by means of the digraph representation of a water cluster revealed that 164,461 hydrogen-bonding patterns of the water octamer are possible, not all the patterns can be formed because of the geometry limitation, i.e., the shape of water molecules, the conditions of hydrogen bonds, and so on. As mentioned already, the number is the maximal value. In fact, tens of thousands of patterns are observed in a typical Monte Carlo simulation of the water octamer. From various theoretical studies [19–22], it is known that two cubic structures, one has D_{2d} symmetry and the other has S_4 symmetry (Fig. 3.3), are especially stable, and either of which is the global minimum structure on the potential energy surface of the water octamer. Other cubic or noncubic local minimum structures, such as a cyclic single ring isomer, have higher potential energies than the two cubic isomers.

The Monte Carlo simulation using the TIP3P potential by Miyake and Aida [16] showed that the Helmholtz energies of double-ring hydrogen-bonding patterns are lower than those of two cubic hydrogen-bonding patterns (8-12A and 8-12B in Fig. 3.3) corresponding to the D_{2d} and S_4 structures at 200 K. The internal energies of the two patterns remain low. Furthermore, the cyclic single-ring hydrogen-bonding pattern is the lowest in Helmholtz energy at 300 K. The results were qualitatively supported by a thermodynamic simulation based on the 164 local minimum structures with the harmonic approximation by Maeda and Ohno [23], where double-ring structures are more abundant than cubic structures at higher temperatures.

3.3.5 Dipole Moment of Water Clusters

The dipole moment of a hydrogen-bonding pattern can be a characteristic quality. The orientation of each molecule constituting the cluster, which is inherently obscured in a hydrogen-bonding pattern, is reflected in the dipole moment as an ensemble average.

The dipole moments of pattern 3-3A at 200 and 300 K are calculated to be 1.4 and 1.6 D, respectively. The temperature dependence is due to the variation of the

structure distribution among the hydrogen-bonding pattern. The cyclic hydrogen-bonding network tends to restrict the structure, and this leads to a decrease in the dipole moment of the cluster. The dipole moments of pattern 3-2A at 200 and 300 K are 2.1 and 2.9 D, respectively.

3.4 Assessment of Potential Functions for Water

3.4.1 Potential Functions for a Water Molecule

Nowadays, ab initio MO or density functional theory (DFT) calculations can be routinely performed for clusters and the condensed phase with the periodic boundary condition using a small unit cell. These calculations are computationally too expensive to apply for much larger systems and simulations for long times. Therefore, the water potential functions are still important, and their accuracy and transferability are comparable to those of high-level ab initio methods and the computational cost is relatively low.

Many potential functions describing water–water interaction have been developed since Bernal and Fowler [24] proposed the first interaction potential in 1933. We do not intend to delve here into the details of the models and the parameters used to calculate the interaction. There are two types of potential functions: one is the empirical potential and the other is the ab initio potential. Most empirical models have been composed of simple pairwise additive interaction terms, e.g., the charge–charge Coulomb terms and Lennard-Jones terms. The number of interaction sites and the geometries depend on the model, resulting in a variety of potential functions.

The potential functions for water were reviewed previously [25]. A list of potential functions for the water molecule which have been developed since 2002 is given in Table 3.3.

3.4.2 Distribution of the Water Molecules in a Water Dimer

The assessment of the water potential energy functions is often done by comparing the simulation results with available experimental data. Here we show a different aspect for the assessment. In solution or in a crystal, the oxygen atom of a water molecule accepts at most two hydrogen bonds. We show whether water potential functions can represent this feature or not.

The distribution of a water molecule around another water molecule is evaluated by the interaction free energy (ΔA) landscape. Here we show the distribution of a water molecule in a water dimer. The free energy landscape represents the stability and distribution of a ligand molecule around the target molecule at finite temperature [46–48].

Table 3.3 Potential functions for water which have been developed since 2002
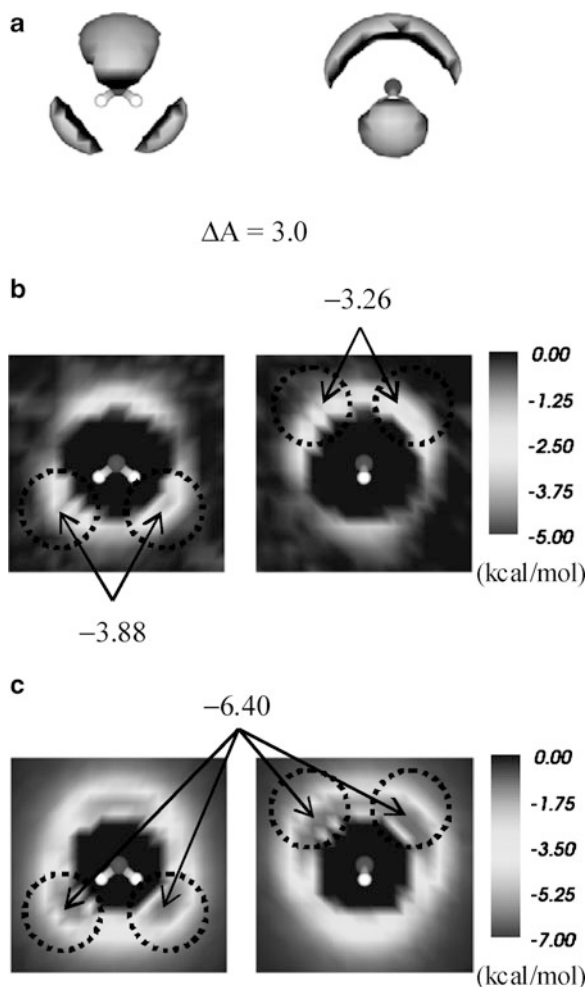
Model	References	Year	Status	Sites	Rigid/flexible	Polarizable/ nonpolarizable
SPC/A	[26]	2002	Empirical	3	Rigid	Nonpolarizable
SPC/L	[26]	2002	Empirical	3	Rigid	Nonpolarizable
TTM2-R	[27]	2002	Ab initio	4	Rigid	Polarizable
TTM2-F	[28]	2002	Ab initio	4	Flexible	Polarizable
SPC/S	[29]	2003	Empirical	3	Rigid	Nonpolarizable
COS/B2	[30]	2003	Empirical	4	Rigid	Polarizable
AMOEBA	[31]	2003	Empirical	3	Flexible	Polarizable
SWM4-DP	[32]	2003	Empirical	5	Rigid	Polarizable
SAPT-5s + 3B	[33]	2003	Ab initio		Rigid	Polarizable
TIP4P-Ew	[34]	2004	Empirical	4	Rigid	Nonpolarizable
TIP5P-E	[35]	2004	Empirical	5	Rigid	Nonpolarizable
COS/G2	[36]	2004	Empirical	5	Rigid	Polarizable
COS/G3	[36]	2004	Empirical	5	Rigid	Polarizable
TIP4P/Ice	[37]	2005	Empirical	4	Rigid	Nonpolarizable
TIP4P/2005	[38]	2005	Empirical	4	Rigid	Nonpolarizable
TTM2.1-F	[39]	2006	Ab initio	4	Flexible	Polarizable
SSDQO	[40]	2006	Empirical	1	Rigid	Nonpolarizable
SDFT-5s	[41]	2006	Ab initio		Rigid	Nonpolarizable/ polarizable
TTM3-F	[42]	2008	Ab initio	4	Flexible	Polarizable
CC-pol	[43]	2008	Ab initio		Rigid	Polarizable
CC-pol-8s	[44]	2008	Ab initio		Rigid	Polarizable
DMIP	[45]	2009	Empirical	3	Flexible	Polarizable

We calculate and compare ΔA landscapes of a water dimer: one is from an ab initio MO energy calculation at the HF/STO-3G level of theory, and the other is from a force field energy calculation using TIP3P.

The configurations are sampled by Metropolis Monte Carlo simulations of 10^7 steps. One of the water molecules (water A) is kept fixed during the simulation, and the oxygen atom (O_A) of water A is at the origin. Another water molecule (water B) moves around in the simulation box of 10.0 Å^3. To sample interaction configurations efficiently, a periodic boundary condition is imposed on the oxygen atom (O_B) of water B. This is the constant NVT MC simulation with $T = 300$ K. In the current simulations, we assume that a water molecule is rigid and has TIP3P geometric parameters. Simulation results are visualized as a map and an isosurface (Fig. 3.6 for STO-3G and Fig. 3.7 for TIP3P). ΔA_i of cell i represents both the O_B distribution around a water molecule and the stability of the system at 300 K. During Monte Carlo simulation, minimum interaction energies for small cubic cells are also stored. These are visualized as a ΔE_{min} map and this represents the O_B distribution around a water molecule at 0 K.

The results from Monte Carlo simulations with STO-3G and TIP3P potentials are shown in Figs. 3.6 and 3.7, respectively. On the ΔE_{min} map in either figure,

Fig. 3.6 Distribution of the water oxygen atom in water dimer from Monte Carlo simulation with HF/STO-3G: (**a**) ΔA isosurface; (**b**) ΔA map; (**c**) ΔE_{min} map. Energies are in kilocalories per mole

$\Delta A = 3.0$

four minima are observed with the same stability. This indicates that the four tetrahedrally located sites, which are potential hydrogen-bonding sites, are identical at 0 K. On the ΔA map in either figure, the ΔA values around the hydrogen atoms of water A and O_A are different. These are common characteristics of Monte Carlo simulation results from ab initio MO calculations and TIP3P calculations.

On the other hand, there is a striking difference in the distribution around O_A between the ab initio MO simulation and the TIP3P simulation: there are clearly two minima in the ΔA map of the ab initio MO simulation (Fig. 3.6), whereas there is only one minimum in the ΔA map of the force field simulation (Fig. 3.7). In the case of TIP3P, it seems that the two minima around O_A on the ΔE_{min} map collapse to one toward the bisector of the H–O–H angle of water A on the ΔA map. In the ΔA

Fig. 3.7 Distribution of the water oxygen atom in a water dimer from Monte Carlo simulation with TIP3P: (**a**) ΔA isosurface; (**b**) ΔA map; (**c**) $\Delta E_{\min}$ map. Energies are in kilocalories per mole
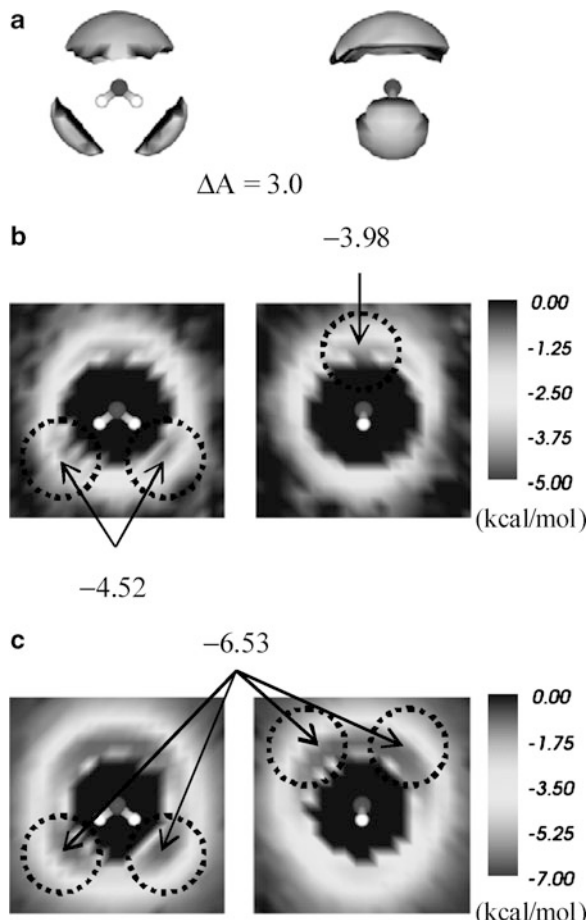
isosurface of the TIP3P simulation, a hemispherical distribution is seen around O_A. This may indicate that TIP3P cannot reproduce the angle dependency in hydrogen bonding in simulations.

Caution is needed when a three-dimensional water network is treated with a force field in finite-temperature simulations.

3.5 Protonated Water Cluster

3.5.1 Rooted Digraphs and Restrictive Rooted Digraphs

A rooted digraph is used to represent the features of a protonated water (PW) cluster [49, 50]. A graph is a set of vertices and edges, and a graph corresponding to a PW cluster is a kind of rooted graph, since a PW molecule is distinguished from other
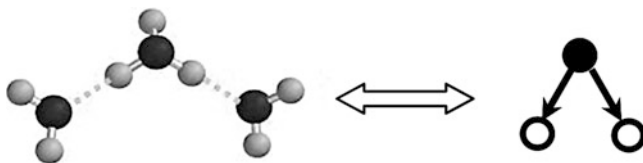
Fig. 3.8 Structure of a protonated water cluster and the corresponding rooted digraph

water molecules in the PW cluster. For a rooted graph with n vertices, the adjacency matrix $\mathbf{A}$ is the nth-order square matrix, whose element a_{ij} is equal to 1 for a pair of vertices i and j which are connected by an edge, and 0 otherwise. Since the hydrogen bond possesses direction and corresponding vertices, to represent the feature of the hydrogen bond in a PW cluster we use a rooted directed graph (digraph). A rooted digraph is a set of vertices and arrows (Fig. 3.8). A rooted digraph has a corresponding matrix representation. For a rooted digraph with n vertices, the directed adjacency matrix $\mathbf{H}$ is the nth-order square matrix, whose element h_{ij} is equal to 1 for an arrow directed from vertex i to vertex j, and 0 otherwise. PW clusters can be represented by rooted digraphs, where the vertices correspond to PW molecules or water molecules, and arrows correspond to hydrogen bonds from the proton donor to the proton acceptor. We call the representative adjacency matrix the "HB matrix." All possible structures which are topology-distinct can be obtained by means of the HB matrix, i.e., by counting up all the possible rooted digraphs with the conditions for forming PW clusters.

The numbers of enumerated rooted graphs and rooted digraphs of PW clusters of $H_3O^+(H_2O)_{n-1}$ ($n = 2–7$) are given in Table 3.4. Various initial geometries for a PW cluster corresponding to these possible rooted digraphs (for $n = 2–4$) were constructed and each of the trial geometries was optimized by means of the ab initio MO method. As seen in Table 3.4, although the number of possible topology-distinct rooted digraphs increases rapidly with cluster size, the number of stable topology-distinct structures is very limited; e.g., only one local minimum out of nine rooted digraphs and only three local minima out of 63 rooted digraphs are found for the trimer and for the tetramer, respectively. Making use of these results as well as those from other works [51–57], we extracted four structural rules (given below), and found the criteria that a rooted digraph corresponding to a stable structure for PW clusters should fulfill. Here, we call a vertex that corresponds to a PW molecule a P-vertex and a vertex that corresponds to a water molecule a W-vertex.

RRDG-1:	There is no arrow directed toward the P-vertex.
RRDG-2:	There are two or three arrows directed from the P-vertex.
RRDG-3:	When two arrows are directed from the P-vertex, no W-vertex which accepts an arrow from the P-vertex can accept an arrow from another vertex.
RRDG-4:	When three arrows are directed from the P-vertex, up to two of the W-vertices, each of which accepts an arrow from the P-vertex, can accept an arrow from another vertex.

Table 3.4 The numbers of rooted graphs, rooted digraphs, and restrictive rooted digraphs of protonated water clusters of $H_3O^+(H_2O)_{n-1}$ ($n = 2$–7) and the number of stable structures of protonated water clusters of $H_3O^+(H_2O)_{n-1}$ ($n = 2$–6)

| | | n | | | | | |
		2	3	4	5	6	7
Rooted graphs		1	3	11	58	294	1,806
Rooted digraphs		2	9	63	561	5,843	68,696
Restrictive rooted digraphs			1	5	39	338	3,523
Topology-distinct local minimum structures	MP2/6-31G**	1	1	3	9	43	
	MP2/aug-cc-pVDZ	1	1	3	8	30	
	B3LYP/6-31G**	1	1	3	9	31	
	B3LYP/aug-cc-pVDZ	1	1	3	5	25	

We remove those hydrogen-bonding patterns which do not fulfill these criteria from all possible topology-distinct hydrogen-bonding patterns and generate the restrictive rooted digraphs.

We have enumerated the rooted graphs, rooted digraphs, and restrictive rooted digraph ($n \geq 3$), which correspond to PW clusters of $H_3O^+(H_2O)_{n-1}$ ($n = 2$–7). The numbers of the generated rooted graphs, the generated rooted digraphs, and the generated restrictive rooted digraphs, and the corresponding number of local minima are summarized in Table 3.4. It should be noted here that we are dealing with only topology-distinct geometries in the current work. We do not take account of any fine structures of PW clusters, such as the direction of a free O–H bond.

3.5.2 Topology-Distinct Protonated Water Clusters

PW clusters are common in nature and play important roles in many fields of science, including atmospheric chemistry, solution chemistry, and biological chemistry. There are a lot of stable structures in PW clusters with various arrangements of the constituent water molecules. The number of the available structures (the hydrogen-bonding patterns) plays an important role in thermodynamic properties of PW clusters. The number of local minima increases rapidly with the cluster size.

It is not trivial to present all of the possible structures or to claim that a structure is indeed the global minimum. The number of local minima might vary when a different level of theory or a different potential function is used for the calculation of the potential energy surface. The important point is that we know all the possible topology-distinct hydrogen-bonding patterns of the PW cluster after the enumeration; i.e., we know that there cannot be other patterns.

For the PW clusters of $H_3O^+(H_2O)_{n-1}$ ($n = 2$–5), all the optimized geometries are shown in Fig. 3.9. Only topology-distinct geometries are dealt with here. Any fine structures of PW clusters, such as the direction of a free O–H bond, are not
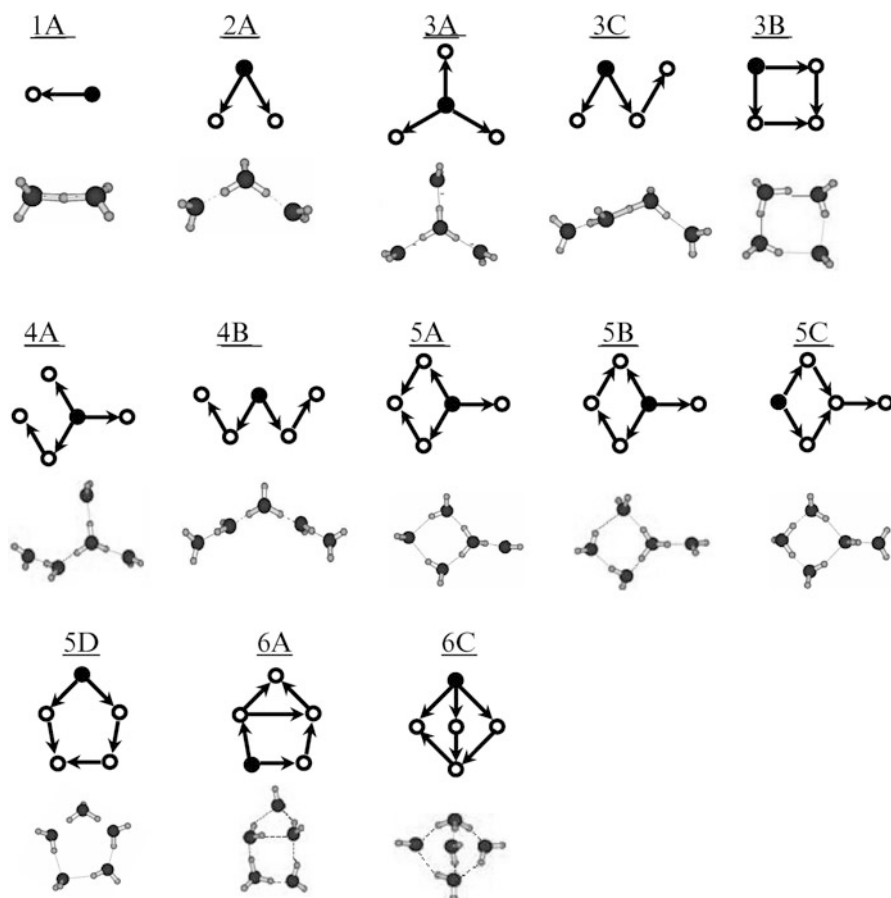
Fig. 3.9 Rooted digraphs of protonated water clusters of $H_3O^+(H_2O)_{n-1}$ ($n = 2$–5) and the optimized geometries at the MP2/aug-cc-pVDZ level of theory

taken into consideration. All water molecules in PW clusters up to a heptamer are classified according to the difference in the contribution in the hydrogen-bonding pattern. The O–H bond stretching frequency depends on the class of the water molecule as well as on the classes of the water molecules to/from which hydrogen bonds are directed [50].

For a PW dimer, the optimized structure (1A in Fig. 3.9) has C_2 symmetry, and is the Zundel cation. The PW dimer from the topological point of view is shown in Fig. 3.10a. In the figure, P1 denotes a PW molecule which donates one hydrogen bond; 1A denotes a water molecule which accepts one hydrogen bond. Because of the symmetry, a hydrogen-bonding pattern in which there is an arrow from P1 toward 1A is equal to one with an arrow where P1 and 1A are exchanged. Z0 denotes a Zundel-type water molecule with no other water molecules attached. At the global minimum, two Z0 water molecules are symmetrically the same.
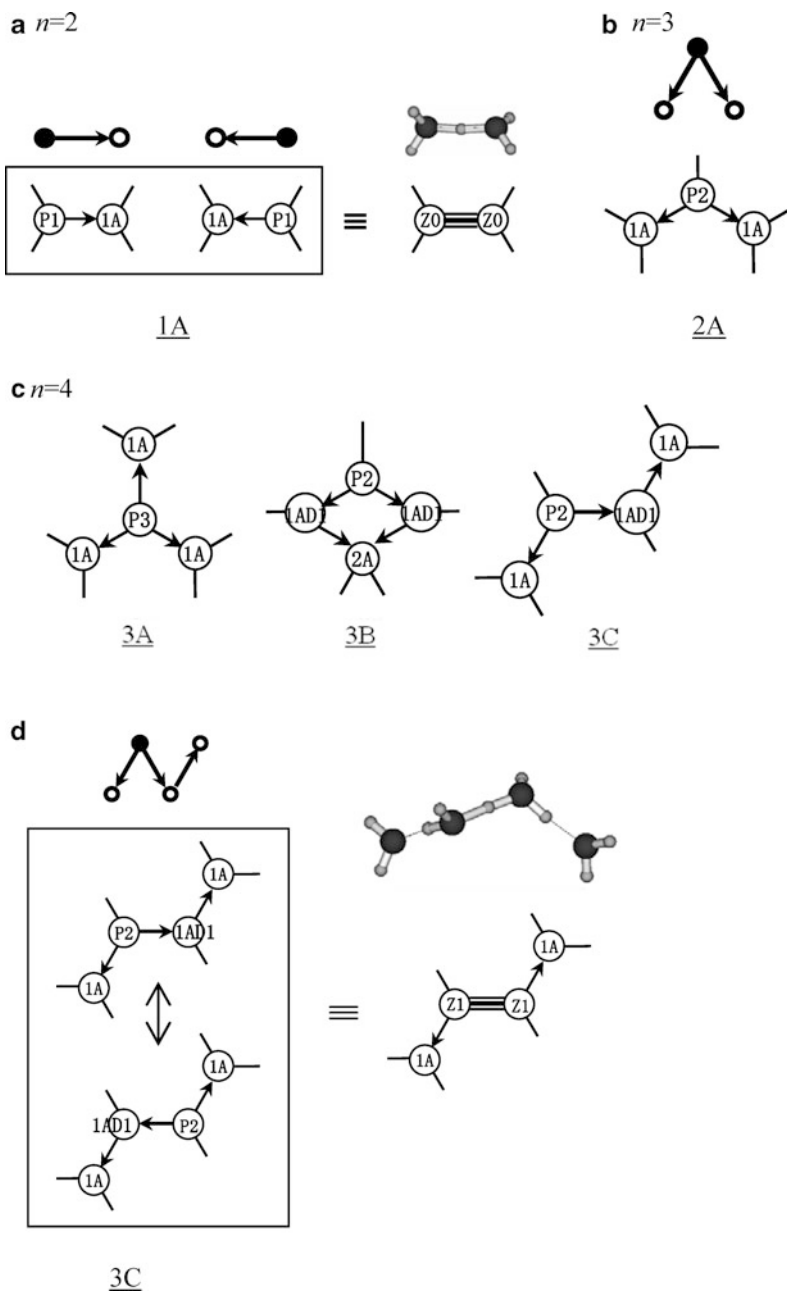
Fig. 3.10 Classification of water molecules into protonated water clusters: (**a**) Protonated water dimer; (**b**) Protonated water trimer; (**c**) Protonated water tetramer; (**d**) Zundel-type protonated water tetramer
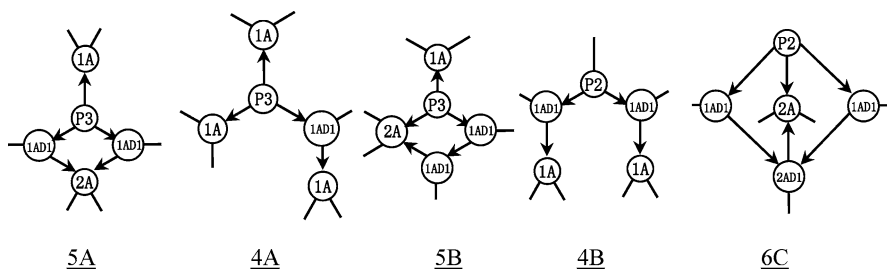
Fig. 3.11 Classification of water molecules into protonated water pentamers

For the PW trimer, there are nine topology-distinct rooted digraphs with three vertices, and there is only one restrictive rooted digraph (2A in Fig. 3.9). The corresponding structure of this restrictive rooted digraph is just the global minimum of the PW trimer. A schematic drawing of the PW trimer is given in Fig. 3.10b. In the figure, P2 denotes a PW molecule which donates two hydrogen bonds.

For the PW tetramer, there are 63 topology-distinct rooted digraphs with four vertices, and there are five restrictive rooted digraphs (Table 3.4). We have found that three of the five restrictive rooted digraphs correspond to the stable structures of PW tetramers; the optimized structures and the corresponding rooted digraphs of $H_3O^+(H_2O)_3$ are given in Fig. 3.9 (3A, 3B, and 3C). Schematic drawings of the PW tetramer are given in Fig. 3.10c and d. Pattern 3C is the one in which two O–H bonds on both sides of the Zundel-type PW dimer are hydrogen-bonded with two water molecules. Each of the water molecules which share a proton between them is called Z1 here. As shown in Fig. 3.10d, although 3C does not have C_2 symmetry at the local minimum, we can consider the two Z1 water molecules as being quasi-symmetrical.

For the PW pentamer, 39 restrictive rooted digraphs among 561 possible rooted digraphs were generated. Various initial geometries were constructed for a PW pentamer with a hydrogen-bonding topology corresponding to each of the restrictive rooted digraphs, followed by the geometry optimization by means of the ab initio MO method and the DFT method with various basis sets. We found nine local minima out of 39 restrictive rooted digraphs by means of both MP2(full)/6-31G** and B3LYP/6-31G**, and eight and five local minima out of 39 restrictive rooted digraphs with MP2(full)/aug-cc-pVDZ and B3LYP/aug-cc-pVDZ levels of theory, respectively (Table 3.4). The optimized structures with MP2/aug-cc-pVDZ and the corresponding rooted digraphs of eight local minima of PW pentamers are given in Fig. 3.9. PW pentamer 4B (Fig. 3.11) has an H_3O^+ Eigen core and is a unique pattern with C_s symmetry, in which two water molecules are hydrogen-bonded to two free O–H bonds on two dangling water molecules of Eigen-type PW trimer 2A (Fig. 3.10).

For the PW hexamer, 338 restrictive rooted digraphs among 5,843 possible rooted digraphs were generated. Various initial geometries were constructed for a PW hexamer with a hydrogen-bonding topology corresponding to each of the

above-mentioned restrictive rooted digraphs, followed by geometry optimization by means of the ab initio MO method and the DFT method with various basis sets. We found 43, 30, 31, and 25 local minima out of 338 restrictive rooted digraphs at the MP2(full)/6-31G**, MP2(full)/aug-cc-pVDZ, B3LYP/6-31G**, and B3LYP/aug-cc-pVDZ levels of theory, respectively (Table 3.4).

By means of the anharmonic downward distortion following algorithm, isomers of PW clusters of $H_3O^+(H_2O)_{n-1}$ ($n = 5$–7) have been explored [58]. They located, 9, 24, and 131 isomers for $n = 5$, 6, and 7, respectively, by the automatic exploration.

3.6 Future Perspective

Progress in the implementations of ab initio MO theory and in computer power enable various large-scale computations. To understand the complex computational results, the importance of graphs, including digraphs and rooted digraphs, will increase more and more. A graph-theoretical consideration provides a theoretical framework, even when the computational results may differ depending on the levels of the computational methods used.

References

1. Cayley A (1874) Philos Mag 47:444–446
2. Wiener H (1947) J Am Chem Soc 69:17–20
3. Hosoya H (1971) Bull Chem Soc Jpn 44:2332–2339
4. Hosoya H (2002) Internet electron. J Mol Des 1:428–442
5. Ohno K, Shimoaka T, Akai N, Katsumoto Y (2008) J Phys Chem A 112:7342–7348
6. Fujita S (2008) Bull Chem Soc Jpn 81:193–219
7. Fujita S (2010) Bull Chem Soc Jpn 83:1–18
8. Radhakrishnan TP, Herndon WC (1991) J Phys Chem 95:10609–10617
9. McDonald S, Singer SJ, Ojamäe L (1998) J Phys Chem A 102:2824–2832
10. Tissandier MD, Singer SJ, Coe JV (2000) J Phys Chem A 104:752–757
11. Kuo J-L, Coe JV, Singer SJ, Band YB, Ojamäe L (2001) J Chem Phys 114:2527–2540
12. Shi Q, Kais S, Francisco JS (2005) J Phys Chem A 109:12036–12045
13. Belair SD, Francisco JS, Singer SJ (2005) Phys Rev A 71:013204/1-10
14. Miyake T, Aida M (2002) Chem Phys Lett 363:106–110
15. Vukičević D, Grubeša T, Graovac A (2005) Chem Phys Lett 416:212–214
16. Miyake T, Aida M (2006) Chem Phys Lett 427:215–220
17. Keutsch FN, Cruzan JD, Saykally RJ (2003) Chem Rev 103:2533–2577
18. Xantheas SS (2000) Chem Phys 258:225–231
19. Tsai CJ, Jordan KD (1993) J Phys Chem 97:11227–11237
20. Gruenloh CJ, Carney JR, Hagemeister FC, Arrington CA, Zwier TS, Fredericks SY, Wood John TI, Jordan KD (1998) J Chem Phys 109:6601–6614
21. Lee HM, Suh SB, Lee JY, Tarakeshwar P, Kim KS (2000) J Chem Phys 112:9759–9772
22. Xantheas SS, Aprà E (2004) J Chem Phys 120:823–828
23. Maeda S, Ohno K (2007) J Phys Chem A 111:4527–4534
24. Bernal JD, Fowler RH (1933) J Chem Phys 1:515–548
25. Guillot B (2002) J Mol Liq 101:219–260

26. Glattli A, Daura X, van Gunsteren WF (2002) J Chem Phys 116:9811–9828
27. Burnham CJ, Xantheas SS (2002) J Chem Phys 116:1500–1510
28. Burnham CJ, Xantheas SS (2002) J Chem Phys 116:5115–5124
29. Glattli A, Daura X, Van Gunsteren WF (2003) J Comput Chem 24:1087–1096
30. Yu H, Hansson T, van Gunsteren WF (2003) J Chem Phys 118:221–234
31. Ren P, Ponder JW (2003) J Phys Chem B 107:5933–5947
32. Lamoureux G, MacKerell Alexander DJ, Roux B (2003) J Chem Phys 119:5185–5197
33. Mas EM, Bukowski R, Szalewicz K (2003) J Chem Phys 118:4386–4403
34. Horn HW, Swope WC, Pitera JW, Madura JD, Dick TJ, Hura GL, Head-Gordon T (2004) J Chem Phys 120:9665–9678
35. Rick SW (2004) J Chem Phys 120:6085–6093
36. Yu H, van Gunsteren WF (2004) J Chem Phys 121:9549–9564
37. Abascal JLF, Sanz E, Garcia Fernández R, Vega C (2005) J Chem Phys 122:234511/1-9
38. Abascal JLF, Vega C (2005) J Chem Phys 123:234505/1-12
39. Fanourgakis GS, Xantheas SS (2006) J Phys Chem A 110:4100–4106
40. Ichiye T, Tan M-L (2006) J Chem Phys 124:134504/1-10
41. Bukowski R, Szalewicz K, Groenenboom G, van der Avoird A (2006) J Chem Phys 125:044301/1-8
42. Fanourgakis GS, Xantheas SS (2008) J Chem Phys 128:074506/1-11
43. Bukowski R, Szalewicz K, Groenenboom GC, van der Avoird A (2008) J Chem Phys 128:094313/1-15
44. Cencek W, Szalewicz K, Leforestier C, van Harrevelt R, van der Avoird A (2008) Phys Chem Chem Phys 10:4716–4731
45. Walsh TR, Liang T (2009) J Comput Chem 30:893–899
46. Pichierri F, Aida M, Gromiha MM, Sarai A (1999) J Am Chem Soc 121:6152–6157
47. Yoshida T, Nishimura T, Aida M, Pichierri F, Gromiha MM, Sarai A (2002) Biopolymers 61:84–95
48. Sayano K, Kono H, Gromiha M, Sarai A (2000) J Comput Chem 21:954–962
49. Jieli M, Miyake T, Aida M (2007) Bull Chem Soc Jpn 80:2131–2136
50. Jieli M, Aida M (2009) J Phys Chem A 113:1586–1594
51. Headrick JM, Diken EG, Walters RS, Hammer NI, Christie RA, Cui J, Myshakin EM, Duncan MA, Johnson MA, Jordan KD (2005) Science 308:1765–1769
52. Wei D, Salahub DR (1997) J Chem Phys 106:6086–6094
53. Hodges MP, Wales DJ (2000) Chem Phys Lett 324:279–288
54. Valeev EF, Schaefer Henry FI (1998) J Chem Phys 108:7197–7201
55. Ojamäe L, Shavitt I, Singer SJ (1998) J Chem Phys 109:5547–5564
56. Christie RA, Jordan KD (2002) J Phys Chem B 106:8376–8381
57. Mella M, Kuo J-L, Clary DC, Klein ML (2005) Phys Chem Chem Phys 7:2324–2332
58. Luo Y, Maeda S, Ohno K (2009) J Comput Chem 30:952–961

Chapter 4
Generalized-Ensemble Algorithms for Simulations of Complex Molecular Systems

Hisashi Okumura, Satoru G. Itoh, and Yuko Okamoto

Abstract In molecular simulations of complex systems with many degrees of freedom, conventional Monte Carlo and molecular dynamics simulations in canonical ensemble or isobaric-isothermal ensemble suffer from a great difficulty, in which simulations tend to get trapped in states of energy local minima. A simulation in generalized ensemble performs a random walk in specified variables and overcomes this difficulty. In this chapter, we review the generalized-ensemble algorithms. Replica-exchange method, multicanonical algorithm, and their extensions are described. Some simulation results based on these generalized-ensemble algorithms are also presented.

H. Okumura • S.G. Itoh
Department of Theoretical and Computational Molecular Science, Institute for Molecular Science, Okazaki, Aichi 444-8585, Japan

Research Center for Computational Science, Okazaki, Aichi 444-8585, Japan

Department of Structural Molecular Science, The Graduate University for Advanced Study, Okazaki, Aichi 444-8585, Japan
e-mail: hokumura@ims.ac.jp; itoh@ims.ac.jp

Y. Okamoto (✉)
Department of Physics, Graduate School of Science, Nagoya University, Nagoya, Aichi 464-8602, Japan

Structural Biology Research Center, Graduate School of Science, Nagoya University, Nagoya, Aichi 464-8602, Japan

Center for Computational Science, Graduate School of Engineering, Nagoya University, Nagoya, Aichi 464-8603, Japan
e-mail: okamoto@phys.nagoya-u.ac.jp

4.1 Introduction

In complex molecular systems such as biomolecular systems, conventional Monte Carlo (MC) and molecular dynamics (MD) simulations at low temperatures in the canonical ensemble and those at low temperatures or high pressures in the isobaric-isothermal ensemble tend to get trapped in states of energy local minima, giving results in error. In order to overcome this difficulty, a class of simulation methods, which are referred to as the *generalized-ensemble algorithms*, are often employed (for reviews, see e.g., Refs. [1–5]). In a generalized-ensemble simulation, each state is weighted by a non-Boltzmann probability weight factor so that a random walk in potential energy space may be realized. The random walk allows the simulation to overcome any energy barrier and to sample much wider conformational space than by conventional methods. The generalized-ensemble algorithm was introduced to the molecular simulation field almost 20 years ago [6].

One of the most well-known generalized-ensemble algorithms is perhaps *replica-exchange method* (REM) [7] (see Ref. [8] for the MD version). Multiple replicas of the system in the canonical ensemble at different temperatures are simulated simultaneously, and every few steps, a pair of replicas at neighboring temperatures is exchanged. This causes a random walk in temperature for each replica, and the simulation can avoid getting trapped in states of energy local minima.

REM was extended to multidimensions/multivariables so that not only temperature but also other parameter values of the system are exchanged, and the method is referred to as *multidimensional replica-exchange method* (MREM) [9]. Various special cases of MREM were then proposed [10–15] (MREM is also known as *Hamiltonian replica-exchange method* [10]).

Another widely used generalized-ensemble algorithm is *multicanonical algorithm* (MUCA) [16, 17] (for a textbook, see, e.g., Ref. [18]; see also Refs. [19, 20] for the MD version). The probability weight factor, which is referred to as the multicanonical weight factor, is defined to be inversely proportional to the density of states so that a flat distribution in potential energy may be obtained. The uniform distribution induces a free random walk in the potential energy space, and the multiple-minima problem is overcome.

MUCA was extended so that flat distributions in parameters other than potential energy and/or multidimensional parameter space may be realized [21–28].

We remark that general formulations for multidimensional/multivariable generalized-ensemble algorithms (including REM and MUCA) were recently worked out [29–31].

In this chapter, we describe both REM and MUCA. We then present several of newly developed generalized-ensemble algorithms that are multidimensional/multicomponent extensions of REM and MUCA. The first algorithm is an example of MREM and referred to as the *van der Waals replica-exchange method* (vWREM) [32], where different values of van der Waals radius are exchanged. The second one is the *multioverlap algorithm* (MUOV), which performs a random walk

in the overlap space instead of the potential energy space [33–35]. Further extension of MUOV, which is referred to the *multicanonical-multioverlap algorithm* (MUCA-MUOV) [36–38] and realizes a random walk both in the potential energy space and the overlap space, is then given. The fourth method that we present here is the *multibaric-multithermal algorithm* (MUBATH), which realizes a random walk both in the potential energy space and in the volume space [39–45]. We remark that other generalized-ensemble algorithms for the isobaric-isothermal ensemble have also been developed [46–49]. Finally, examples of some simulation results based on these methods are presented.

4.2 Generalized-Ensemble Algorithms

4.2.1 Replica-Exchange Method

Let us consider a system of N atoms of mass m_k ($k = 1, \ldots, N$) with their coordinate vectors and momentum vectors denoted by $q \equiv \{\boldsymbol{q}_1, \ldots, \boldsymbol{q}_N\}$ and $p \equiv \{\boldsymbol{p}_1, \ldots, \boldsymbol{p}_N\}$, respectively. The Hamiltonian $H(q, p)$ of the system is the sum of the kinetic energy $K(p)$ and the potential energy $E(q)$:

$$H(q, p) = K(p) + E(q), \tag{4.1}$$

where

$$K(p) = \sum_{k=1}^{N} \frac{\boldsymbol{p}_k{}^2}{2m_k}. \tag{4.2}$$

In the canonical ensemble at temperature T, each state $x \equiv (q, p)$ with the Hamiltonian $H(q, p)$ is weighted by the Boltzmann factor:

$$W_{\mathrm{B}}(x; T) = \exp\left(-\beta H(q, p)\right), \tag{4.3}$$

where the inverse temperature β is defined by $\beta = 1/k_{\mathrm{B}}T$ (k_{B} is the Boltzmann constant). The average kinetic energy at temperature T is then given by

$$\langle K(p) \rangle_T = \left\langle \sum_{k=1}^{N} \frac{\boldsymbol{p}_k{}^2}{2m_k} \right\rangle_T = \frac{3}{2} N k_{\mathrm{B}} T. \tag{4.4}$$

Because the coordinates q and momenta p are decoupled in Eq. 4.1, we can suppress the kinetic energy part and can write the Boltzmann factor as

$$W_{\mathrm{B}}(x; T) \propto W_{\mathrm{B}}(E; T) = \exp(-\beta E). \tag{4.5}$$

The canonical probability distribution of potential energy $P_{\text{NVT}}(E;T)$ is then given by the product of the density of states $n(E)$ and the Boltzmann weight factor $W_{\text{B}}(E;T)$:

$$P_{\text{NVT}}(E;T) \propto n(E)W_{\text{B}}(E;T). \tag{4.6}$$

Because $n(E)$ is a rapidly increasing function and the Boltzmann factor decreases exponentially, the canonical ensemble yields a bell-shaped distribution of potential energy which has a maximum around the average potential energy at temperature T. The conventional MC or MD simulations at constant temperature are expected to yield $P_{\text{NVT}}(E;T)$. A MC simulation based on the Metropolis algorithm [50] is performed with the following transition probability from a state x of potential energy E to a state x' of potential energy E':

$$w(x \to x') = \min\left(1, \frac{W_{\text{B}}(E';T)}{W_{\text{B}}(E;T)}\right) = \min\left(1, \exp\left(-\beta \Delta E\right)\right), \tag{4.7}$$

where

$$\Delta E = E' - E. \tag{4.8}$$

A MD simulation, on the other hand, is based on the following Newton equations of motion:

$$\dot{\boldsymbol{q}}_k = \frac{\boldsymbol{p}_k}{m_k}, \tag{4.9}$$

$$\dot{\boldsymbol{p}}_k = -\frac{\partial E}{\partial \boldsymbol{q}_k} = \boldsymbol{F}_k, \tag{4.10}$$

where $\boldsymbol{F}_k$ is the force acting on the kth atom ($k = 1, \cdots, N$). This set of equations actually yield the microcanonical ensemble, however, and we have to add a thermostat in order to obtain the canonical ensemble at temperature T. Here, we just follow Nosé's prescription [51, 52], and we have

$$\dot{\boldsymbol{q}}_k = \frac{\boldsymbol{p}_k}{m_k}, \tag{4.11}$$

$$\dot{\boldsymbol{p}}_k = -\frac{\partial E}{\partial \boldsymbol{q}_k} - \frac{\dot{s}}{s}\boldsymbol{p}_k = \boldsymbol{F}_k - \frac{\dot{s}}{s}\boldsymbol{p}_k, \tag{4.12}$$

$$\dot{s} = s\frac{P_s}{Q}, \tag{4.13}$$

$$\dot{P}_s = \sum_{k=1}^{N} \frac{\boldsymbol{p}_k{}^2}{m_k} - 3Nk_{\text{B}}T = 3Nk_{\text{B}}\left(T(t) - T\right), \tag{4.14}$$

where s is Nosé's scaling parameter, P_s is its conjugate momentum, Q is its mass, and the "instantaneous temperature" $T(t)$ is defined by

$$T(t) = \frac{1}{3Nk_{\mathrm{B}}} \sum_{k=1}^{N} \frac{p_k(t)^2}{m_k}. \tag{4.15}$$

However, in practice, it is very difficult to obtain accurate canonical distributions of complex systems at low temperatures by conventional MC or MD simulation methods. This is because simulations at low temperatures tend to get trapped in one or a few of local-minimum-energy states. This difficulty is overcome by, for instance, the generalized-ensemble algorithms, which greatly enhance conformational sampling.

The *replica-exchange method* (REM) [7] is one of effective generalized-ensemble algorithms. The system for REM consists of M *noninteracting* copies (or replicas) of the original system in the canonical ensemble at M different temperatures T_m ($m = 1, \ldots, M$). We arrange the replicas so that there is always exactly one replica at each temperature. Then there exists a one-to-one correspondence between replicas and temperatures; the label i ($i = 1, \ldots, M$) for replicas is a permutation of the label m ($m = 1, \ldots, M$) for temperatures, and vice versa:

$$\begin{cases} i = i(m) \equiv f(m), \\ m = m(i) \equiv f^{-1}(i), \end{cases} \tag{4.16}$$

where $f(m)$ is a permutation function of m and $f^{-1}(i)$ is its inverse.

Let $X = \left\{ x_1^{[i(1)]}, \ldots, x_M^{[i(M)]} \right\} = \left\{ x_{m(1)}^{[1]}, \ldots, x_{m(M)}^{[M]} \right\}$ stand for a "state" in this generalized ensemble. Each "substate" $x_m^{[i]}$ is specified by the coordinates $q^{[i]}$ and momenta $p^{[i]}$ of N atoms in replica i at temperature T_m:

$$x_m^{[i]} \equiv \left(q^{[i]}, p^{[i]} \right)_m. \tag{4.17}$$

Because the replicas are noninteracting, the weight factor for the state X in this generalized ensemble is given by the product of Boltzmann factors for each replica (or at each temperature):

$$W_{\mathrm{REM}}(X) = \prod_{i=1}^{M} \exp\left\{ -\beta_{m(i)} H\left(q^{[i]}, p^{[i]} \right) \right\} = \prod_{m=1}^{M} \exp\left\{ -\beta_m H\left(q^{[i(m)]}, p^{[i(m)]} \right) \right\}, \tag{4.18}$$

where $i(m)$ and $m(i)$ are the permutation functions in Eq. 4.16.

We now consider exchanging a pair of replicas in this ensemble. Suppose we exchange replicas i and j which are at temperatures T_m and T_n, respectively:

$$X = \{ \ldots, x_m^{[i]}, \ldots, x_n^{[j]}, \ldots \} \longrightarrow X' = \{ \ldots, x_m^{[j]'}, \ldots, x_n^{[i]'}, \ldots \}. \tag{4.19}$$

Here, i, j, m, and n are related by the permutation functions in Eq. 4.16, and the exchange of replicas introduces a new permutation function f':

$$\begin{cases} i = f(m) \longrightarrow j = f'(m), \\ j = f(n) \longrightarrow i = f'(n). \end{cases} \tag{4.20}$$

The exchange of replicas can be written in more detail as

$$\begin{cases} x_m^{[i]} \equiv \left(q^{[i]}, p^{[i]}\right)_m \longrightarrow x_m^{[j]'} \equiv \left(q^{[j]}, p^{[j]'}\right)_m, \\ x_n^{[j]} \equiv \left(q^{[j]}, p^{[j]}\right)_n \longrightarrow x_n^{[i]'} \equiv \left(q^{[i]}, p^{[i]'}\right)_n, \end{cases} \tag{4.21}$$

where the definitions for $p^{[i]'}$ and $p^{[j]'}$ will be given below.

In the original implementation of the REM [7], Monte Carlo method was used, and only the coordinates q (and the potential energy function $E(q)$) had to be taken into account. In molecular dynamics method, on the other hand, we also have to deal with the momenta p. We proposed the following momentum assignment in Eq. 4.21 [8]:

$$\begin{cases} p^{[i]'} \equiv \sqrt{\dfrac{T_n}{T_m}} \, p^{[i]}, \\[4mm] p^{[j]'} \equiv \sqrt{\dfrac{T_m}{T_n}} \, p^{[j]}, \end{cases} \tag{4.22}$$

which we believe is the simplest and the most natural. This assignment means that we just rescale uniformly the velocities of all the atoms in the replicas by the square root of the ratio of the two temperatures so that the temperature condition in Eq. 4.4 may be satisfied immediately after replica exchange is accepted. We remark that general momentum rescaling formulae were derived for various thermostats in Ref. [53].

The transition probability of this replica-exchange process is given by the usual Metropolis criterion:

$$w(X \to X') \equiv w\left(x_m^{[i]} \mid x_n^{[j]}\right) = \min\left(1, \frac{W_{\text{REM}}(X')}{W_{\text{REM}}(X)}\right) = \min\left(1, \exp\left(-\Delta\right)\right), \tag{4.23}$$

where in the second expression (i.e., $w(x_m^{[i]}|x_n^{[j]})$), we explicitly wrote the pair of replicas (and temperatures) to be exchanged. From Eq. 4.22, the kinetic energy terms all cancel out in Eq. 4.23, and Δ becomes

$$\Delta = \beta_m \left(E\left(q^{[j]}\right) - E\left(q^{[i]}\right)\right) - \beta_n \left(E\left(q^{[j]}\right) - E\left(q^{[i]}\right)\right), \tag{4.24}$$

$$= (\beta_m - \beta_n)\left(E\left(q^{[j]}\right) - E\left(q^{[i]}\right)\right). \tag{4.25}$$

Here, i, j, m, and n are related by the permutation functions in Eq. 4.16 before the replica exchange:

$$\begin{cases} i = f(m), \\ j = f(n). \end{cases} \tag{4.26}$$

Note that after introducing the momentum rescaling in Eq. 4.22, we have the same Metropolis criterion for replica exchanges, i.e., Eqs. 4.23 and 4.25, for both MC and MD versions.

Without loss of generality, we can assume $T_1 < T_2 < \cdots < T_M$. The lowest temperature T_1 should be sufficiently low so that the simulation can explore the global-minimum-energy region, and the highest temperature T_M should be sufficiently high so that no trapping in an energy-local-minimum state occurs. A REM simulation is then realized by alternately performing the following two steps:

1. Each replica in canonical ensemble of the fixed temperature is simulated *simultaneously* and *independently* for a certain MC or MD steps.
2. A pair of replicas at neighboring temperatures, say $x_m^{[i]}$ and $x_{m+1}^{[j]}$, is exchanged with the probability $w\left(x_m^{[i]} \middle| x_{m+1}^{[j]}\right)$ in Eq. 4.23.

A random walk in "temperature space" is realized for each replica, which in turn induces a random walk in potential energy space. This alleviates the problem of getting trapped in states of energy local minima.

After a long production run of a REM simulation, the canonical expectation value of a physical quantity A at temperature T_m $(m = 1, \ldots, M)$ can be calculated by the usual arithmetic mean:

$$\langle A \rangle_{T_m} = \frac{1}{n_m} \sum_{k=1}^{n_m} A\left(x_m(k)\right), \tag{4.27}$$

where $x_m(k)$ $(k = 1, \ldots, n_m)$ are the configurations obtained at temperature T_m and n_m is the total number of measurements made at $T = T_m$. The expectation value at any intermediate temperature T $(= 1/k_B\beta)$ can also be obtained as follows:

$$\langle A \rangle_T = \frac{\sum_E A(E) P_{NVT}(E; T)}{\sum_E P_{NVT}(E; T)} = \frac{\sum_E A(E) n(E) \exp(-\beta E)}{\sum_E n(E) \exp(-\beta E)}. \tag{4.28}$$

Here, the explicit form of the physical quantity A should be known as a function of potential energy E. For instance, $A(E) = E$ gives the average potential energy $\langle E \rangle_T$ as a function of temperature, and $A(E) = \beta^2 (E - \langle E \rangle_T)^2$ gives specific heat.

The density of states $n(E)$ in Eq. 4.28 is given by the multiple-histogram reweighting techniques [54, 55] as follows (an extension of the multiple-histogram method is also referred to as the *weighted histogram analysis method* (WHAM) [55]). Let $N_m(E)$ and n_m be respectively the potential energy histogram and the total number of samples obtained at temperature $T_m = 1/k_B \beta_m$ ($m = 1, \cdots, M$). The best estimate of the density of states is then given by [54, 55]

$$n(E) = \frac{\displaystyle\sum_{m=1}^{M} g_m^{-1} N_m(E)}{\displaystyle\sum_{m=1}^{M} g_m^{-1} n_m \exp(f_m - \beta_m E)}, \qquad (4.29)$$

where we have for each $m \ (= 1, \ldots, M)$

$$\exp(-f_m) = \sum_E n(E) \exp(-\beta_m E). \qquad (4.30)$$

Here, $g_m = 1 + 2\tau_m$, and τ_m is the integrated autocorrelation time at temperature T_m. For many systems, the quantity g_m can safely be set to be a constant in the reweighting formulae [55], and hereafter, we set $g_m = 1$. Note that Eqs. 4.29 and 4.30 are solved self-consistently by iteration [54, 55] to obtain the density of states $n(E)$ and the dimensionless Helmholtz free energy f_m.

Moreover, the ensemble averages of any physical quantity A (including those that cannot be expressed as functions of potential energy) at any temperature T ($=1/k_B \beta$) can now be obtained from the "trajectory" of configurations of the production run. Namely, we first obtain f_m ($m = 1, \cdots, M$) by solving Eqs. 4.29 and 4.30 self-consistently, and then we have [56]

$$\langle A \rangle_T = \frac{\displaystyle\sum_{m=1}^{M}\sum_{k=1}^{n_m} A(x_m(k)) \frac{1}{\displaystyle\sum_{\ell=1}^{M} n_\ell \exp[f_\ell - \beta_\ell E(x_m(k))]} \exp[-\beta E(x_m(k))]}{\displaystyle\sum_{m=1}^{M}\sum_{k=1}^{n_m} \frac{1}{\displaystyle\sum_{\ell=1}^{M} n_\ell \exp[f_\ell - \beta_\ell E(x_m(k))]} \exp[-\beta E(x_m(k))]}, \qquad (4.31)$$

where $x_m(k)$ ($k = 1, \cdots, n_m$) are the configurations obtained at temperature T_m.

4.2.2 Extensions of the Replica-Exchange Method

4.2.2.1 Multidimensional Replica-Exchange Method

We now describe the *multidimensional replica-exchange method* (MREM) [9]. The crucial observation that led to this algorithm is as follows: As long as we have *M noninteracting* replicas of the original system, the Hamiltonian $H(q, p)$ of the system does not have to be identical among the replicas, and it can depend on a parameter with different parameter values for different replicas.

Let us consider a generalized potential energy function $E_{\boldsymbol{\lambda}}(x)$, which depends on L parameters $\boldsymbol{\lambda} = (\lambda^{(1)}, \ldots, \lambda^{(L)})$, of a system in state x. The system for MREM consists of M noninteracting replicas of the original system in the "canonical ensemble" with $M (= M_0 \times M_1 \times \cdots \times M_L)$ different parameter sets $\boldsymbol{\Lambda}_m$ ($m = 1, \ldots, M$), where $\boldsymbol{\Lambda}_m \equiv (T_{m_0}, \boldsymbol{\lambda}_m) \equiv (T_{m_0}, \lambda_{m_1}^{(1)}, \ldots, \lambda_{m_L}^{(L)})$ with $m_0 = 1, \ldots, M_0, m_\ell = 1, \ldots, M_\ell$ ($\ell = 1, \ldots, L$). Because the replicas are noninteracting, the weight factor is given by the product of Boltzmann-like factors for each replica:

$$W_{\text{MREM}} \equiv \prod_{m_0=1}^{M_0} \prod_{m_1=1}^{M_1} \cdots \prod_{m_L=1}^{M_L} \exp\left(-\beta_{m_0} E_{\boldsymbol{\lambda}_m}\right). \tag{4.32}$$

Without loss of generality, we can order the parameters so that $T_1 < T_2 < \cdots < T_{M_0}$ and $\lambda_1^{(\ell)} < \lambda_2^{(\ell)} < \cdots < \lambda_{M_\ell}^{(\ell)}$ (for each $\ell = 1, \cdots, L$). A MREM simulation is realized by alternately performing the following two steps:

1. For each replica, a "canonical" MC or MD simulation at the fixed parameter values is carried out simultaneously and independently for a certain steps.
2. We exchange a pair of replicas i and j which are at the parameter sets $\boldsymbol{\Lambda}_m$ and $\boldsymbol{\Lambda}_{m+1}$, respectively. The transition probability for this replica-exchange process is given by

$$w(\boldsymbol{\Lambda}_m \leftrightarrow \boldsymbol{\Lambda}_{m+1}) = \min(1, \exp(-\Delta)), \tag{4.33}$$

where we have

$$\Delta = (\beta_{m_0} - \beta_{m_0+1})\left(E_{\boldsymbol{\lambda}_m}\left(q^{[j]}\right) - E_{\boldsymbol{\lambda}_m}\left(q^{[i]}\right)\right), \tag{4.34}$$

for T-exchange, and

$$\Delta = \beta_{m_0}\left[\left(E_{\boldsymbol{\lambda}_{m_\ell}}(q^{[j]}) - E_{\boldsymbol{\lambda}_{m_\ell}}(q^{[i]})\right) - \left(E_{\boldsymbol{\lambda}_{m_\ell+1}}(q^{[j]}) - E_{\boldsymbol{\lambda}_{m_\ell+1}}(q^{[i]})\right)\right], \tag{4.35}$$

for $\lambda^{(\ell)}$-exchange (for one of $\ell = 1, \cdots, L$). Here, $q^{[i]}$ and $q^{[j]}$ stand for configuration variables for replicas i and j, respectively, before the replica exchange.

4.2.2.2 van der Waals Replica-Exchange Method

We now describe a special example of MREM, which we refer to as the *van der Waals Replica-Exchange Method* (vWREM) [32].

We consider a system consisting of solute molecule(s) in explicit solvent. We can write the total potential energy as follows:

$$E_\lambda(q) = E_p(q_p) + E_{ps}(q_p, q_s) + E_s(q_s), \tag{4.36}$$

where E_p is the potential energy for the atoms in the solute only, E_{ps} is the interaction term between solute atoms and solvent atoms, and E_s is the potential energy for the atoms of the solvent molecules only. Here, $q = \{q_p, q_s\}$, where q_p and q_s are the coordinate vectors of the solute atoms and the solvent atoms, respectively, and denoted by $q_p \equiv \{q_1, \ldots, q_{N_p}\}$ and $q_s \equiv \{q_{N_p+1}, \ldots, q_N\}$. ($N_p$ is the total number of atoms in the solute.)

We are more concerned with effective sampling of the conformational space of the solute itself than that of the solvent molecules. The steric hindrance of the solute conformations are governed by the van der Waals radii of each atom in the solute. Namely, when the van der Waals radii are large, the solute molecule is bulky, and we have more steric hindrance among the solute atoms by the Lennard-Jones interactions, and when it is small, the solute molecule can move more freely. We thus introduce a parameter λ that scales the van der Waals radius of each atom in the solute by

$$\sigma_{k\ell} \longrightarrow \lambda\sigma_{k\ell} \tag{4.37}$$

and write the Lennard-Jones energy term within E_p in Eq. 4.36 as follows:

$$V_\lambda\left(q_p\right) = \sum_{k=1}^{N_p-1} \sum_{\ell=k+1}^{N_p} 4\epsilon_{k\ell} \left\{ \left(\frac{\lambda\sigma_{k\ell}}{r_{k\ell}}\right)^{12} - \left(\frac{\lambda\sigma_{k\ell}}{r_{k\ell}}\right)^6 \right\}, \tag{4.38}$$

where $r_{k\ell}$ is the distance between atoms k and ℓ in the solute and $\epsilon_{k\ell}$ and $\sigma_{k\ell}$ are the corresponding Lennard-Jones parameters. The original potential energy is recovered when $\lambda = 1$, and the steric hindrance of solute conformations is reduced when $\lambda < 1$. We remark that this is the only λ-dependent term in E_λ in Eq. 4.36.

We prepare M values of λ, λ_m ($m = 1, \ldots, M$). Without loss of generality, we can assume that the parameter values are ordered as $\lambda_1 < \cdots < \lambda_M$. Here, we consider the case in which temperature is fixed to be $T_0 = 1/k_B\beta_0$. The vWREM is realized by alternately performing the following two steps:

1. For each replica, a canonical MC or MD simulation at the corresponding parameter value λ_m is carried out simultaneously and independently for a certain steps with the corresponding Boltzmann factor of Eq. 4.3 for each replica.

2. We exchange a pair of replicas i and j which are at the neighboring parameter values λ_m and λ_{m+1}, respectively. The transition probability for this replica-exchange process is given by Eq. 4.33, where Δ in Eq. 4.35 now reads

$$\Delta = \beta_0 \left[\left(V_{\lambda_m}\left(q_{\mathrm{p}}^{[j]}\right) - V_{\lambda_m}\left(q_{\mathrm{p}}^{[i]}\right) \right) - \left(V_{\lambda_{m+1}}\left(q_{\mathrm{p}}^{[j]}\right) - V_{\lambda_{m+1}}\left(q_{\mathrm{p}}^{[i]}\right) \right) \right]. \tag{4.39}$$

Here, V_λ is the Lennard-Jones potential energy in Eq. 4.38 among the solute atoms only.

Note that because the λ dependence of E_λ exists only in V_λ, the rest of the terms have been canceled out in Eq. 4.35.

We see that Eq. 4.39 includes only the coordinates q_{p} of the atoms in the solute only and is independent of the coordinates q_{s} of solvent molecules. Because $N_{\mathrm{p}} \ll N$ usually holds, the difficulty in the usual REM that the number of required replicas increases with the number of degrees of freedom is much alleviated in this formalism.

We remark that in order to further enhance the conformational sampling, we can perform a two-dimensional REM in both temperature and λ, using Eqs. 4.34 and 4.35.

4.2.2.3   Reweighting Techniques

The results from MREM simulations with different parameter values can be analyzed by the reweighting techniques [54, 55]. Suppose that we have carried out a MREM simulation at a constant temperature T_0 with M replicas corresponding to M parameter values λ_m ($m = 1, \ldots, M$).

For appropriate reaction coordinates ξ_1 and ξ_2, the canonical probability distribution $P_{T,\lambda}(\xi_1, \xi_2)$ with any parameter value λ at any temperature T can be calculated from

$$P_{T,\lambda}(\xi_1, \xi_2) = \sum_{E_{\lambda_1}, \ldots, E_{\lambda_M}} \frac{\displaystyle\sum_{m=1}^{M} N_m(E_{\lambda_1}, \ldots, E_{\lambda_M}; \xi_1, \xi_2) e^{-\beta E_\lambda}}{\displaystyle\sum_{m=1}^{M} n_m e^{f_{T_0, \lambda_m} - \beta_0 E_{\lambda_m}}}, \tag{4.40}$$

and

$$e^{-f_{T_0, \lambda_m}} = \sum_{\xi_1, \xi_2} P_{T_0, \lambda_m}(\xi_1, \xi_2). \tag{4.41}$$

Here, $N_m(E_{\lambda_1}, \ldots, E_{\lambda_M}; \xi_1, \xi_2)$ is the histogram of the M-dimensional energy distributions at the parameter value λ_m and the reaction coordinate values (ξ_1, ξ_2), which was obtained by the MREM simulation, and n_m is the total number of samples obtained at the parameter value λ_m. Note that this probability distribution is not normalized. Equations 4.40 and 4.41 are solved self-consistently by iteration. Note also that these equations can be easily generalized to any reaction coordinates $(\xi_1, \xi_2, \ldots)$.

From the probability distribution $P_{T,\lambda}(\xi_1, \xi_2)$ in Eq. 4.40, the expectation value of a physical quantity A with any parameter value λ at any temperature T is given by

$$\langle A \rangle_{T,\lambda} = \frac{\displaystyle\sum_{\xi_1,\xi_2} A(\xi_1, \xi_2) P_{T,\lambda}(\xi_1, \xi_2)}{\displaystyle\sum_{\xi_1,\xi_2} P_{T,\lambda}(\xi_1, \xi_2)}. \tag{4.42}$$

We can also calculate the free energy (or the potential of mean force) as a function of the reaction coordinates ξ_1 and ξ_2 with any parameter value λ at any temperature T from

$$F_{T,\lambda}(\xi_1, \xi_2) = -k_{\mathrm{B}} T \ln P_{T,\lambda}(\xi_1, \xi_2). \tag{4.43}$$

By utilizing these equations, therefore, we can obtain various physical quantities from the MREM simulations with the original and non-original parameter values. We remark that although we wrote *any* T in Eqs. 4.40, 4.42, and 4.43 above, the valid T value is limited in the vicinity of T_0. We also need the T-exchange process in Eq. 4.34 in order to have accurate average quantities for a wide range of T values.

4.2.3   Multicanonical Algorithm

The next generalized-ensemble algorithm that we present is the *multicanonical algorithm* (MUCA) [16, 17]. In the multicanonical ensemble, each state is weighted by a non-Boltzmann weight factor $W_{\mathrm{MUCA}}(E)$ (which we refer to as the *multicanonical weight factor*) so that a uniform potential energy distribution $P_{\mathrm{MUCA}}(E)$ may be obtained:

$$P_{\mathrm{MUCA}}(E) \propto n(E) W_{\mathrm{MUCA}}(E) \equiv \text{constant}. \tag{4.44}$$

The flat distribution implies that a free one-dimensional random walk in the potential energy space is realized in this ensemble. This allows the simulation to escape from any local-minimum-energy states and to sample the configurational space much more widely than the conventional canonical MC or MD methods.

The definition in Eq. 4.44 implies that the multicanonical weight factor is inversely proportional to the density of states, and we can write it as follows:

$$W_{\text{MUCA}}(E) \equiv \exp\left[-\beta_0 E_{\text{MUCA}}(E; T_0)\right] = \frac{1}{n(E)}, \tag{4.45}$$

where we have chosen an arbitrary reference temperature, $T_0 = 1/k_B \beta_0$, and the "*multicanonical potential energy*" is defined by

$$E_{\text{MUCA}}(E; T_0) \equiv k_B T_0 \ln n(E) = T_0 S(E). \tag{4.46}$$

Here, $S(E)$ is the entropy in the microcanonical ensemble. Because the density of states of the system is usually unknown, the multicanonical weight factor has to be determined numerically by iterations of short preliminary runs [16, 17].

A multicanonical MC simulation is performed, for instance, with the usual Metropolis criterion [50]: The transition probability of state x with potential energy E to state x' with potential energy E' is given by

$$w(x \rightarrow x') = \min\left(1, \frac{W_{\text{MUCA}}(E')}{W_{\text{MUCA}}(E)}\right) = \min\left(1, \frac{n(E)}{n(E')}\right)$$

$$= \min\left(1, \exp\left(-\beta_0 \Delta E_{\text{MUCA}}\right)\right), \tag{4.47}$$

where

$$\Delta E_{\text{MUCA}} = E_{\text{MUCA}}(E'; T_0) - E_{\text{MUCA}}(E; T_0). \tag{4.48}$$

The MD algorithm in the multicanonical ensemble also naturally follows from Eq. 4.45, in which the regular constant temperature MD simulation (with $T = T_0$) is performed by replacing E by E_{MUCA} in Eq. 4.12 [19, 20]:

$$\dot{p}_k = -\frac{\partial E_{\text{MUCA}}(E; T_0)}{\partial q_k} - \frac{\dot{s}}{s}\, p_k = \frac{\partial E_{\text{MUCA}}(E; T_0)}{\partial E}\, F_k - \frac{\dot{s}}{s}\, p_k. \tag{4.49}$$

Let $N_{\text{MUCA}}(E)$ be the histogram of potential energy distribution $P_{\text{MUCA}}(E)$ obtained by the production run. The best estimate of the density of states can then be given by the single-histogram reweighting techniques [57] as follows (see the proportionality relation in Eq. 4.44):

$$n(E) = \frac{N_{\text{MUCA}}(E)}{W_{\text{MUCA}}(E)}. \tag{4.50}$$

By substituting this quantity into Eq. 4.28, one can calculate ensemble averages of physical quantity $A(E)$ as a function of temperature. Moreover, the ensemble averages of any physical quantity A (including those that cannot be expressed as functions of potential energy) at any temperature $T\ (= 1/k_B \beta)$ can also be obtained

as long as one stores the "trajectory" of configurations from the production run. Namely, we have

$$\langle A \rangle_T = \frac{\displaystyle\sum_{k=1}^{n_s} A(x_k) W_{\mathrm{MUCA}}^{-1}(E(x_k)) \exp\left[-\beta E(x_k)\right]}{\displaystyle\sum_{k=1}^{n_s} W_{\mathrm{MUCA}}^{-1}(E(x_k)) \exp\left[-\beta E(x_k)\right]}, \tag{4.51}$$

where x_k is the configuration at the kth MC (or MD) step and n_s is the total number of configurations stored.

4.2.4 Extensions of Multicanonical Algorithm

4.2.4.1 Multioverlap Algorithm and Multicanonical-Multioverlap Algorithm

While MUCA yields a flat distribution in potential energy and performs a random walk in potential energy space, we can, in principle, choose any other variable and induce a random walk in that variable. One such example is the *multioverlap algorithm* (MUOV) [33–35]. Here, we choose a protein system and define the overlap in the space of dihedral angles by [58]

$$O = 1 - d, \tag{4.52}$$

where d is the dihedral-angle distance given by

$$d = \frac{1}{n\pi} \sum_i d_a(\theta_i, \theta_i^0). \tag{4.53}$$

θ_i is the dihedral angle i, and θ_i^0 is the dihedral angle i of the reference conformation. The distance $d_a(\theta_i, \theta_i^0)$ between two dihedral angles is defined by

$$d_a(\theta_i, \theta_i^0) = \min(|\theta_i - \theta_i^0|, 2\pi - |\theta_i - \theta_i^0|). \tag{4.54}$$

The dihedral-angle distance d in Eq. 4.53 takes a value in the range $0 \le d \le 1$. If $d = 0$, all dihedral angles are coincident with those of the reference conformation. The dihedral-angle distance is thus an indicator of how similar the conformation is to the reference conformation. As one can see in Eq. 4.52, the dihedral-angle distance d is equivalent to the overlap O. We will deal with the dihedral-angle distance instead of the overlap hereafter.

In the multioverlap ensemble at a constant temperature T_0, the probability distribution is given by the following non-Boltzmann weight factor, which we refer to as the multioverlap weight factor:

$$W_{\text{muov}}(d, E; T_0) = e^{-\beta_0 E_{\text{muov}}}, \qquad (4.55)$$

where E_{muov} is the "multioverlap potential energy" defined by

$$E_{\text{muov}}(d, E; T_0) = E - k_B T_0 f(d; T_0). \qquad (4.56)$$

The function $f(d; T_0)$ is the dimensionless free energy at dihedral-angle distance d.

The generalization to the multidimensional dihedral-angle distance space is straightforward, and the multioverlap weight factor is given by

$$W_{\text{muov}}(d_1, \ldots, d_L, E; T_0) = e^{-\beta_0 E_{\text{muov}}} \equiv e^{-\beta_0 E + f(d_1, \ldots, d_L; T_0)}, \qquad (4.57)$$

where L is the number of the reference conformations and d_i is the dihedral-angle distance, with respect to reference conformation i ($i = 1, \ldots, L$). The function $f(d_1, \ldots, d_L; T_0)$ is the dimensionless free energy with the fixed value of dihedral-angle distances $d_1, \cdots, d_L$. The dimensionless free energy $f(d_1, \ldots, d_L; T_0)$ is defined so that the probability distribution of dihedral-angle distances $P_{\text{muov}}(d_1, \ldots, d_L; T_0)$ is flat:

$$\begin{aligned}
P_{\text{muov}}(d_1, \ldots, d_L; T_0) &= \int dE \, P_{\text{muov}}(d_1, \ldots, d_L, E; T_0) \\
&\propto \int dE \, n(d_1, \ldots, d_L, E) W_{\text{muov}}(d_1, \ldots, d_L, E; T_0) \\
&= \int dE \, n(d_1, \ldots, d_L, E) e^{-\beta_0 E + f(d_1, \cdots, d_L; T_0)} \\
&\equiv \text{constant}, \qquad (4.58)
\end{aligned}$$

where $P_{\text{muov}}(d_1, \ldots, d_L, E; T_0)$ is the probability distribution of potential energy and dihedral-angle distances, and $n(d_1, \ldots, d_L, E)$ is its density of states.

The MD algorithm in the multioverlap ensemble also naturally follows from Eq. 4.57, in which the regular constant temperature MD simulation (with $T = T_0$) is performed by replacing E by E_{muov} in Eq. 4.12 [35, 36]:

$$\begin{aligned}
\dot{p}_k &= -\frac{\partial E_{\text{muov}}}{\partial q_k}(d_1, \ldots, d_L, E; T_0) - \frac{\dot{s}}{s} \, p_k \\
&= F_k + k_B T_0 \frac{\partial f}{\partial q_k}(d_1, \ldots, d_L; T_0) - \frac{\dot{s}}{s} \, p_k. \qquad (4.59)
\end{aligned}$$

The multioverlap weight factor, or the dimensionless free energy, is not a priori known and has to be determined by the usual iterations of short simulations [2, 18]. Suppose that we have determined an appropriate dimensionless free energy $f(d_1, \ldots, d_L; T_0)$ at temperature T_0 and that we have made a production run at this temperature. The results of the multioverlap production run can then be analyzed by the reweighting techniques [57]. Namely, the expectation value of a physical quantity A at any temperature T is given by

$$
\langle A \rangle_T = \frac{\displaystyle\sum_{d_1, \cdots, d_L, E} A(d_1, \cdots, d_L, E) N_{\mathrm{muov}}(d_1, \cdots, d_L, E) W_{\mathrm{muov}}(d_1, \cdots, d_L, E; T_0)^{-1} e^{-\beta E}}{\displaystyle\sum_{d_1, \cdots, d_L, E} N_{\mathrm{muov}}(d_1, \cdots, d_L, E) W_{\mathrm{muov}}(d_1, \cdots, d_L, E; T_0)^{-1} e^{-\beta E}}
$$

$$
= \frac{\displaystyle\sum_{d_1, \cdots, d_L, E} A(d_1, \cdots, d_L, E) N_{\mathrm{muov}}(d_1, \cdots, d_L, E) e^{-(\beta - \beta_0)E - f(d_1, \cdots, d_L; T_0)}}{\displaystyle\sum_{d_1, \cdots, d_L, E} N_{\mathrm{muov}}(d_1, \cdots, d_L, E) e^{-(\beta - \beta_0)E - f(d_1, \cdots, d_L; T_0)}}, \qquad (4.60)
$$

where $N_{\mathrm{muov}}(d_1, \ldots, d_L, E)$ is the histogram of the probability distribution $P_{\mathrm{muov}}(d_1, \ldots, d_L, E; T_0)$ of potential energy and dihedral-angle distances that was obtained by the multioverlap production run.

The multioverlap algorithm can further be combined with the multicanonical algorithm as follows (this method is referred to as the *multicanonical-multioverlap algorithm* (MUCA-MUOV)) [36]. In analogy with the multicanonical ensemble in Eq. 4.44 or the multioverlap ensemble in Eq. 4.58, by employing the non-Boltzmann weight factor $W_{\mathrm{mcmo}}(d_1, \ldots, d_L, E)$, which we refer to as the multicanonical-multioverlap weight factor, a uniform probability distribution with respect to the potential energy and dihedral-angle distances is obtained:

$$
P_{\mathrm{mcmo}}(d_1, \ldots, d_L, E) \propto n(d_1, \ldots, d_L, E) W_{\mathrm{mcmo}}(d_1, \ldots, d_L, E) \equiv \text{constant.} \tag{4.61}
$$

In this method, we obtain a random walk not only in the dihedral-angle distance space but also in the potential energy space.

4.2.4.2 Multibaric-Multithermal Algorithm

Besides the canonical ensemble, molecular simulations in the isobaric-isothermal ensemble are also commonly used. This is because most experiments are carried out under the constant pressure and constant temperature conditions. The canonical probability distribution $P_{\mathrm{B}}(E; T_0)$ in Eq. 4.6 is here replaced by the isobaric-isothermal distribution $P_{\mathrm{NPT}}(E, V; T_0, P_0)$ for potential energy E and volume V:

$$
P_{\mathrm{NPT}}(E, V; T_0, P_0) \equiv n(E, V) e^{-\beta_0 \mathcal{H}}. \tag{4.62}
$$

Here, the density of states $n(E, V)$ is given as a function of both E and V, and $\mathcal{H}$ is the "enthalpy" (without the kinetic energy contributions):

$$\mathcal{H} = E + P_0 V, \tag{4.63}$$

where P_0 is the pressure at which simulations are performed. This weight factor produces an isobaric-isothermal ensemble at constant temperature (T_0) and constant pressure (P_0). This ensemble has bell-shaped distributions in both E and V.

As for the MD methods in this ensemble, we just present the Nosé-Andersen algorithm [51, 52, 59]. The equations of motion in Eqs. 4.11–4.14 are now generalized as follows:

$$\dot{\boldsymbol{q}}_k = \frac{\boldsymbol{p}_k}{m_k} + \frac{\dot{V}}{3V}\,\boldsymbol{q}_k, \tag{4.64}$$

$$\dot{\boldsymbol{p}}_k = -\frac{\partial \mathcal{H}}{\partial \boldsymbol{q}_k} - \left(\frac{\dot{s}}{s} + \frac{\dot{V}}{3V}\right)\boldsymbol{p}_k = \boldsymbol{F}_k - \left(\frac{\dot{s}}{s} + \frac{\dot{V}}{3V}\right)\boldsymbol{p}_k, \tag{4.65}$$

$$\dot{s} = s\,\frac{P_s}{Q}, \tag{4.66}$$

$$\dot{P}_s = \sum_{i=1}^{N} \frac{\boldsymbol{p}_i^2}{m_i} - 3Nk_{\mathrm{B}}T_0 = 3Nk_{\mathrm{B}}\left(T(t) - T_0\right), \tag{4.67}$$

$$\dot{V} = s\,\frac{P_V}{M}, \tag{4.68}$$

$$\dot{P}_V = s\left\{\frac{1}{3V}\left(\sum_{i=1}^{N} \frac{\boldsymbol{p}_i^2}{m_i} - \sum_{i=1}^{N} \boldsymbol{q}_i \cdot \frac{\partial \mathcal{H}}{\partial \boldsymbol{q}_i}\right) - \frac{\partial \mathcal{H}}{\partial V}\right\} = s\left[P(t) - P_0\right], \tag{4.69}$$

where M is the artificial mass associated with the volume, P_V is the conjugate momentum for the volume, and the "instantaneous pressure" $P(t)$ is defined by

$$P(t) = \frac{1}{3V}\left(\sum_{i=1}^{N} \frac{\boldsymbol{p}_i(t)^2}{m_i} - \sum_{i=1}^{N} \boldsymbol{q}_i(t) \cdot \frac{\partial \mathcal{H}}{\partial \boldsymbol{q}_i}(t)\right)$$

$$= \frac{1}{3V}\left(\sum_{i=1}^{N} \frac{\boldsymbol{p}_i(t)^2}{m_i} + \sum_{i=1}^{N} \boldsymbol{q}_i(t) \cdot \boldsymbol{F}_i(t)\right). \tag{4.70}$$

We now introduce the idea of the multicanonical technique into the isobaric-isothermal ensemble method and refer to this generalized-ensemble algorithm as the *multibaric-multithermal algorithm* (MUBATH) [39, 40, 42, 43]. The molecular simulations in this generalized ensemble perform random walks both in the potential energy space and in the volume space.

In the multibaric-multithermal ensemble, each state is sampled by the multibaric-multithermal weight factor $W_{\mathrm{mbt}}(E, V) \equiv \exp\{-\beta_0 \mathcal{H}_{\mathrm{mbt}}(E, V)\}$ ($\mathcal{H}_{\mathrm{mbt}}$ is referred to as the multibaric-multithermal enthalpy) so that a uniform distribution in both potential energy and volume may be obtained:

$$P_{\mathrm{mbt}}(E, V) \propto n(E, V) W_{\mathrm{mbt}}(E, V) = n(E, V) \exp\{-\beta_0 \mathcal{H}_{\mathrm{mbt}}(E, V)\} \equiv \text{constant.} \tag{4.71}$$

In order to perform the multibaric-multithermal MD simulation, we just solve the above equations of motion (Eqs. 4.64–4.69) for the regular isobaric-isothermal ensemble (with $T = T_0$ and $P = P_0$), where the enthalpy $\mathcal{H}$ is replaced by the multibaric-multithermal enthalpy $\mathcal{H}_{\mathrm{mbt}}$ in Eqs. 4.65 and 4.69 [42].

The multibaric-multithermal weight factor is, however, not a priori known and has to be determined by the usual iterations of short simulations [2, 18]. After an optimal weight factor $W_{\mathrm{mbt}}(E, V)$ is obtained, a long production simulation is performed for data collection. We employ the reweighting techniques [57] for the results of the production run to calculate the isobaric-isothermal-ensemble averages. The probability distribution $P_{\mathrm{NPT}}(E, V; T, P)$ of potential energy and volume in the isobaric-isothermal ensemble at the desired temperature T and pressure P is given by

$$P_{\mathrm{NPT}}(E, V; T, P) = \frac{N_{\mathrm{mbt}}(E, V) \, W_{\mathrm{mbt}}(E, V)^{-1} \, \mathrm{e}^{-\beta(E+PV)}}{\displaystyle\sum_{E,V} N_{\mathrm{mbt}}(E, V) \, W_{\mathrm{mbt}}(E, V)^{-1} \, \mathrm{e}^{-\beta(E+PV)}}, \tag{4.72}$$

where $N_{\mathrm{mbt}}(E, V)$ is the histogram of the probability distribution $P_{\mathrm{mbt}}(E, V)$ of potential energy and volume that was obtained by the multibaric-multithermal production run. The expectation value of a physical quantity A at T and P is then obtained from

$$\langle A \rangle_{T,P} = \sum_{E,V} A(E, V) \, P_{\mathrm{NPT}}(E, V; T, P). \tag{4.73}$$

4.3 Examples of Simulation Results

We now present several examples of the simulation results by the generalized-ensemble algorithms described in the previous section.

The first example is a vWREM simulation of a small peptide [32]. In order to demonstrate the effectiveness of vWREM, in which we exchange pairs of the van der Waals radius parameter values, we applied the vWREM MD algorithm, which we refer to as the *vWREMD*, to the system of an alanine dipeptide in explicit water solvent and compared the results with those obtained by the replica-exchange MD (REMD) simulation [8] and conventional canonical MD simulations. The N-terminus and the C-terminus were blocked by the acetyl group and the N-methyl
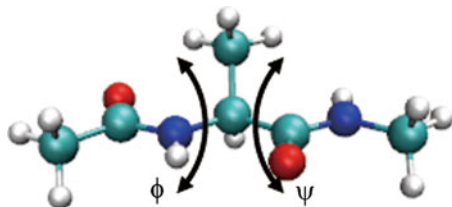
Fig. 4.1 The common initial conformation of the alanine dipeptide for the vWREMD, REMD, and canonical MD simulations. Reprinted from Ref. [32] with kind permission of © The American Institute of Physics (2010)

group, respectively. The number of water molecules was 67. The force field that we adopted was the AMBER parm96 parameter set [60], and the model for the water molecules was the TIP3P rigid-body model [61]. The vWREMD, REMD, and canonical MD simulations were carried out with the symplectic integrator with rigid-body water molecules, in which the temperature was controlled by the Nosé-Poincaré thermostat [44,45,62–65]. The system was put in a cubic unit cell with the side length of 13.4 Å, and we imposed the periodic boundary conditions.

In the vWREMD simulation, we needed only four replicas ($M = 4$). That is, we employed four different parameter values λ_m ($m = 1, \ldots, 4$), and their values were $\lambda_1 = 0.85$, $\lambda_2 = 0.9$, $\lambda_3 = 0.95$, and $\lambda_4 = 1.0$. The original potential energy corresponds to the scale factor $\lambda_4 = 1.0$. The temperature of the system T_0 was set to be 300 K for all the replicas in the vWREMD simulation. We also employed four replicas for the REMD simulation to compare the sampling efficiency with those of the vWREMD simulation, and the four different temperatures were 300 K, 315 K, 335 K, and 360 K, and these temperatures were determined so that exchanges between pairs of replicas were accepted sufficiently. Moreover, we carried out four canonical MD simulations at 300 K, and the difference among these four simulations was initial velocities. We employed the original parameter value $\lambda = 1.0$ for the REMD and canonical MD simulations. The initial conformations were the same for all the simulations, and the initial backbone dihedral angles ϕ and ψ of the alanine dipeptide were set $(\phi, \psi) = (180°, 180°)$, as shown in Fig. 4.1. The total time of the MD simulations was 2.5 ns per replica for the vWREMD and REMD simulations and 2.5 ns for each canonical simulation, including equilibration for 0.1 ns.

Figure 4.2 shows the time series of the backbone dihedral angles ϕ for the vWREMD, REMD, and the conventional canonical MD simulations. From the figure, we see that the samplings in the ϕ space in the vWREMD simulation were the most effective, then those in the REMD simulation, and the least effective in the conventional MD simulation.

The second example is a multioverlap MD simulation of the system of a pentapeptide, Met-enkephalin, in vacuum [34]. The amino-acid sequence is Tyr-Gly-Gly-Phe-Met. The N-terminus and the C-terminus were blocked with the acetyl group and the N-methyl group, respectively. The force field that we adopted is the CHARMM param 22 parameter set [66]. Our multioverlap MD simulations
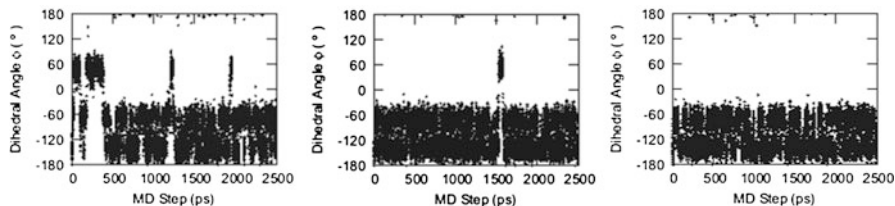
Fig. 4.2 Time series of the dihedral angle ϕ during the vWREMD simulation (*left*), REMD simulation (*center*), and canonical MD simulation (*right*)
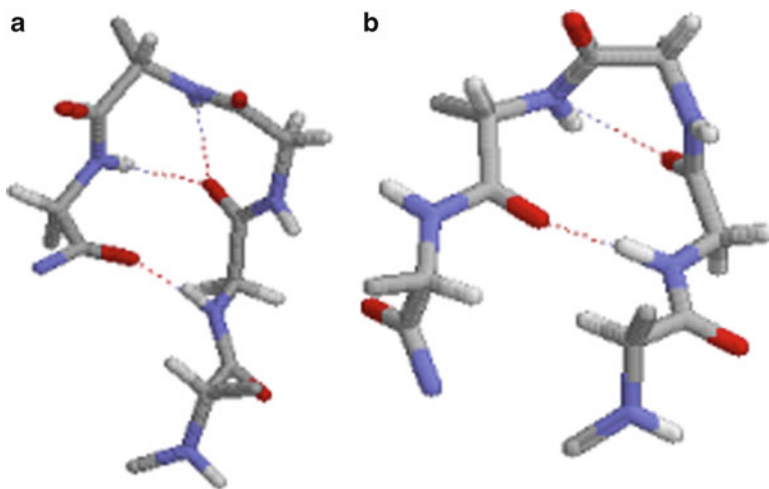
Fig. 4.3 (**a**) Reference conformation 1 and (**b**) reference conformation 2. The side chains are suppressed, and only backbone structures are shown. The *dotted lines* denote the hydrogen bonds. The N-terminus and the C-terminus are on the *right-hand side* and on the *left-hand side*, respectively

were performed by implementing the method in the CHARMM macromolecular mechanics program [67].

We considered two energy-local-minimum states of Met-enkephalin as reference conformations. In Fig. 4.3, we show these two reference conformations. We then set $L = 2$ in Eq. 4.57, and the dimensionless free energy is expressed as $f(d_1, d_2; T_0)$. The multioverlap MD simulation was carried out at $T_0 = 300$ K with a time step of 0.5 fs.

Figure 4.4 shows the time series of the dihedral-angle distances with respect to each of the two reference conformations. While Fig. 4.4a, b shows the results of the conventional canonical MD simulation at $T_0 = 300$ K, Fig. 4.4c, d shows the results of the multioverlap MD simulation at the same temperature. When $d_1 = 0$, the values of dihedral angles of backbone completely coincide with those of reference conformation 1 and $d_2 = 0.122$. Conversely, when $d_2 = 0$, $d_1 = 0.122$. When d_1 (d_2) is near zero, the conformation is similar to reference conformation 1 (2). Therefore, Fig. 4.4 implies that the multioverlap MD simulation performed a
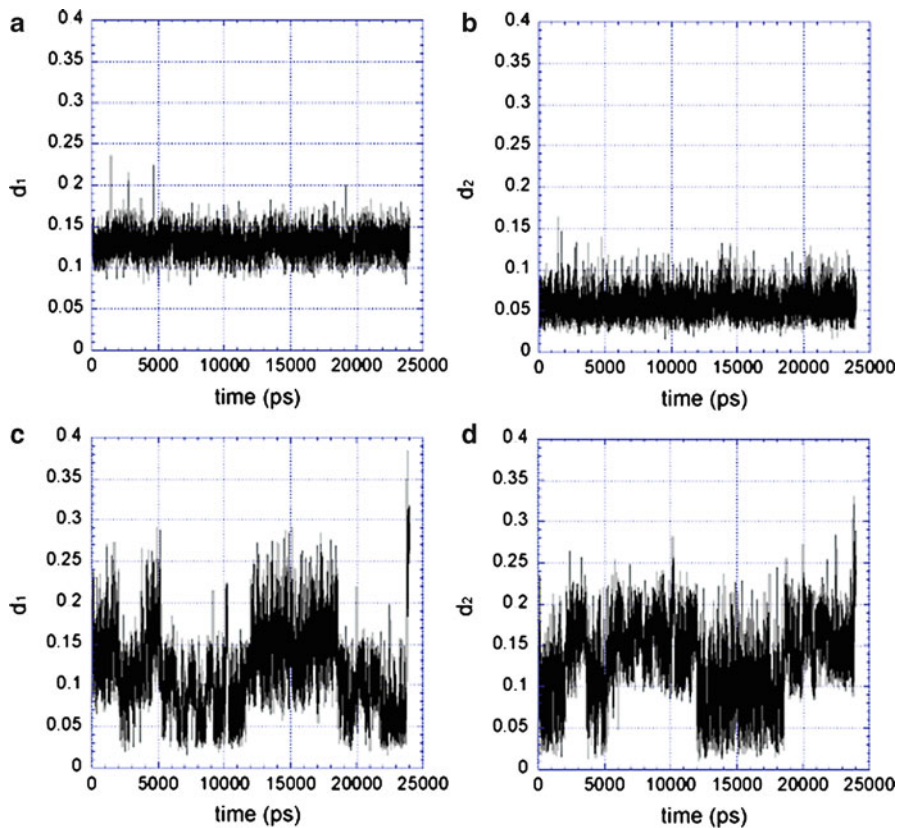
Fig. 4.4 The time series of the dihedral-angle distances d_1 and d_2. (a) and (b) are from the conventional canonical MD simulation, and (c) and (d) are the results from the multioverlap MD simulation at $T_0 = 300$ K

random walk in the dihedral-angle distance space between reference conformation 1 and reference conformation 2, whereas the usual canonical MD simulation got trapped in a local-minimum state near conformation 2.

The free energy $F(d_1, d_2; T)$ (or the potential of mean force) at temperature T is defined by

$$F(d_1, d_2; T) = -k_{\mathrm{B}}T \ln P_{\mathrm{B}}(d_1, d_2; T), \tag{4.74}$$

where $P_{\mathrm{B}}(d_1, d_2; T)$ is the reweighted canonical probability distribution of d_1 and d_2 at T and given by (see Eq. 4.60)

$$P_{\mathrm{B}}(d_1, d_2; T) = \frac{\displaystyle\sum_{E} N_{\mathrm{muov}}(d_1, d_2, E)e^{-(\beta-\beta_0)E-f(d_1,d_2;T_0)}}{\displaystyle\sum_{d_1,d_2,E} N_{\mathrm{muov}}(d_1, d_2, E)e^{-(\beta-\beta_0)E-f(d_1,d_2;T_0)}}. \tag{4.75}$$
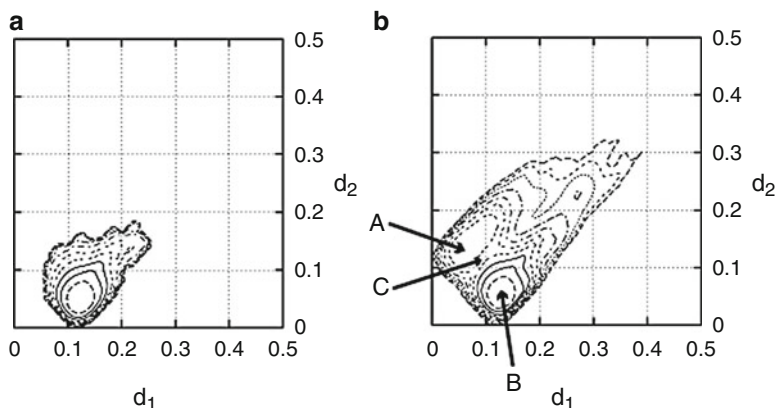
Fig. 4.5 The free-energy landscape obtained from (**a**) the conventional canonical MD simulation and (**b**) the multioverlap MD simulation at $T_0 = 300$ K. *Contour lines* are drawn every 1 kcal/mol. The labels A and B locate the local-minimum states. The label C stands for the *saddle point*, or the transition state, between these two local-minimum states

In Fig. 4.5, we illustrate the free-energy landscapes with respect to the dihedral-angle distances that were calculated from the results of the conventional canonical MD simulation and those of the multioverlap MD simulation. While in Fig. 4.5a only one local-minimum state exists near reference conformation 2, in Fig. 4.5b, we find a local-minimum state A and a local-minimum state B near reference conformation 1 and reference conformation 2, respectively. This result again implies that the canonical MD simulation got trapped in the latter local-minimum state. The local-minimum state B near reference conformation 2 corresponds to the global-minimum state at 300 K. The local-minimum state A near reference conformation 1 is another local-minimum state at 300 K. The free-energy difference between the global-minimum state (B) and the local-minimum state (A) is about 3 kcal/mol.

The saddle point C in Fig. 4.5b corresponds to the transition state between the global-minimum state (B) and the local-minimum state (A). The free-energy difference between B and C is about 5 kcal/mol and that between A and C is 2 kcal/mol. Because $k_B T \approx 0.6$ kcal/mol at $T = 300$ K, these barrier heights are rather high. This is why the conventional canonical MD simulation got trapped in the vicinity of the global-minimum state B.

Our next simulation is the multicanonical-multioverlap MD simulation of Alzheimer's amyloid-β (Aβ) peptide fragment [37]. The amino-acid sequence was Ace-GAIIGLMVGGVVIA-Nme. In multicanonical-multioverlap simulations, we must have a reference conformation. We adopted the conformation that was obtained from the corresponding part in the conformation whose PDB ID code is 2BEG. Here, we took into account only the backbone dihedral angles ϕ (the rotation angles around the N–C$_\alpha$ bonds) and ψ (the rotation angles around the C$_\alpha$–C bonds) of the residues 30–41 of Aβ(29–42) as the reference dihedral angles in our simulations. The force field that we adopted is the CHARMM 22 parameter
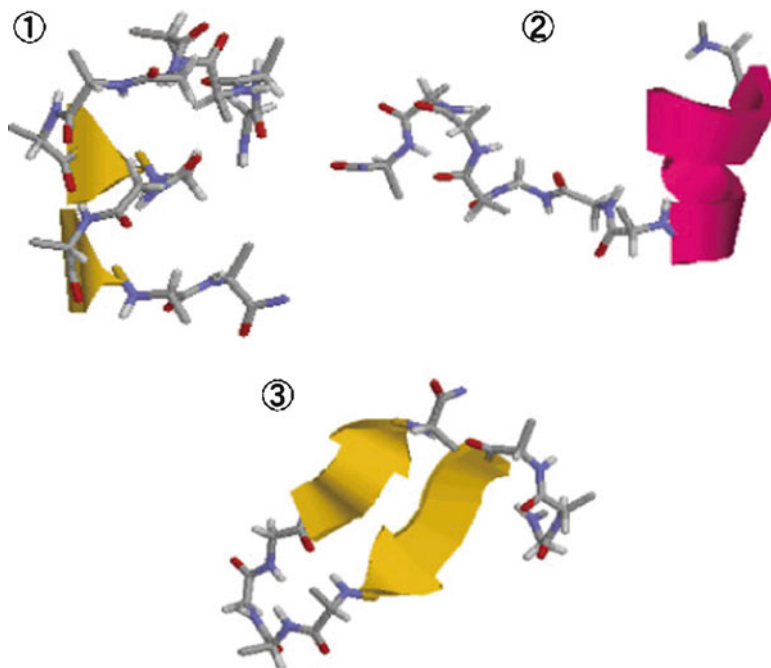
Fig. 4.6 Typical conformations of the Aβ(29–42) molecule at 300 K when two molecules are spatially separated. Reprinted from Ref. [37] with kind permission of © The American Chemical Association (2008)

set [66]. We employed the GB/SA model [68–70] as an implicit solvent model. We also introduced the harmonic constraint $k(r - r_0)^2/2$ when the distance between the center of mass of two Aβ(29–42) molecules exceeded 20 Å in order to avoid the states in which two molecules are too much spatially separated. Here, r is the distance between the center of mass of two molecules, and k is a force constant whose value is 200 kcal/(mol Å^2), and the value of r_0 is set 20 Å.

In Fig. 4.6, we show conformations of Aβ(29–42) monomer in the case when the distance between the center of mass of two peptides is more than 15 Å at 300 K. We identified three major metastable states. These states correspond to low concentrations of Aβ(29–42) peptides or to their monomeric states. Conformation 1 in Fig. 4.6 is a β-helix-like structure, conformation 2 is an α-helix (or sometimes π-helix) structure, and conformation 3 is an intramolecular antiparallel β-sheet (β-hairpin) structure. When the Aβ(29–42) peptide is in a monomeric state, therefore, it seems that the conformations of Aβ(29–42) peptides have the same structure as those in Fig. 4.6.

We show the free-energy landscape of the dimer system at 300 K in Fig. 4.7a. The free-energy landscape was obtained from the results of the multicanonical-multioverlap MD simulation by the reweighting techniques. The abscissa is the number of backbone C$_\alpha$ intermolecular contacts, and we regard a pair of C$_\alpha$ atoms
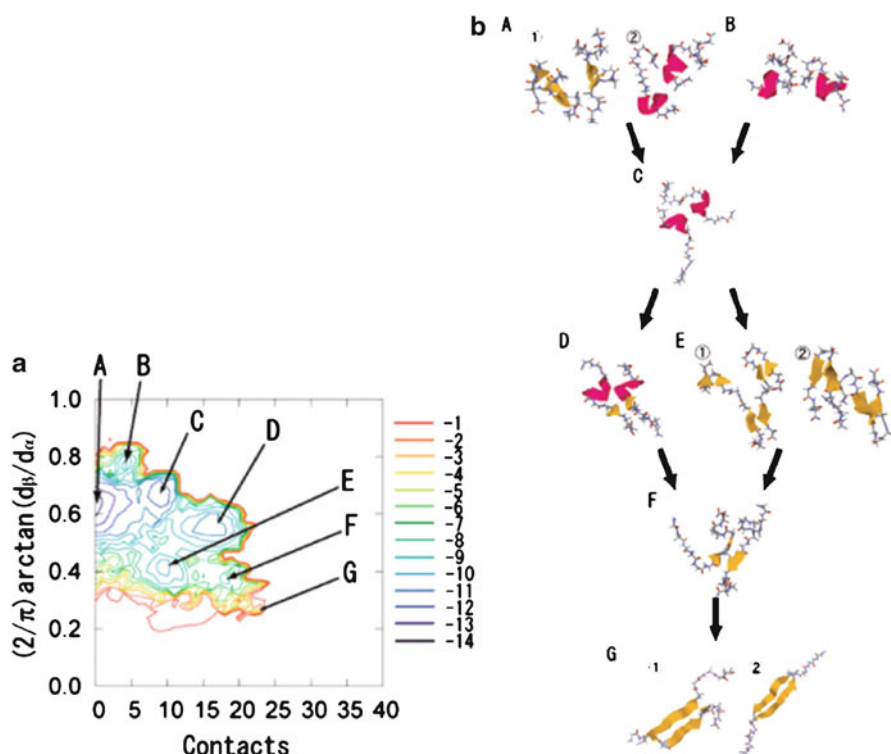
Fig. 4.7 (**a**) Free-energy landscape of an Aβ(29–42) dimer system at 300 K. The ordinate is an indicator of structure for helix and strand. When the value of the ordinate is close to 1, conformations of Aβ(29–42) become helical. Conversely, if the value is close to 0, the conformations have extended forms. The abscissa is the number of backbone C$_\alpha$ intermolecular contacts. *Contour lines* are drawn every 1 kcal/mol. (**b**) Typical structures in the corresponding local-minimum states in (**a**). The *arrows* indicate possible pathways of the early stages of amyloidogenesis. Reprinted from Ref. [37] with kind permission of © The American Chemical Association (2008)

as being in contact if the distance between the two atoms is within 6.5 Å. d_α and d_β in the label of the ordinate are dihedral-angle distances, which we introduced to set the reaction coordinates of the free-energy data analysis. When the value of d_α (d_β) is close to 0, the structures of Aβ(29–42) molecules are helical (extended strand). From the free-energy landscape in Fig. 4.7a, we identified seven local-minimum states. In Fig. 4.7b, we show typical conformations of the Aβ(29–42) in each local-minimum state.

From Figs. 4.6 and 4.7, we deduce the dimerization (oligomerization) process, which corresponds to a seeding process in amyloidogenesis, for Aβ(29–42) peptides as follows: Stage 1: When the Aβ(29–42) peptides are in the monomeric state, the peptides are mainly in one of the three conformational states in Fig. 4.6. Stage 2: Aβ(29–42) peptides come close to each other and create dimers (or oligomers) as a

result of hydrophobic effects. If the structures are intramolecular antiparallel β-sheet structures before dimerization, such as conformation 3 in Fig. 4.6, the conformation after dimerization will correspond to conformation 2 in the local-minimum state E in Fig. 4.7b. If the structures are like conformation 1 or 2 in Fig. 4.6, on the other hand, the Aβ(29–42) dimer will have structures like those of the conformations in A or B in Fig. 4.7b. Stage 3: If the conformations in stage 2 are in states A or B in Fig. 4.7b, then the peptides have helical conformations with extended parts like those in C. If the conformations in stage 2 are already in E in Fig. 4.7b, on the other hand, this corresponds to Stage 4 below. Stage 4: The extended parts will create intermolecular β-ladders such as those in D or E. Stage 5: The intramolecular secondary structures are broken, and the peptides will have a fully extended form such as those in F. Stage 6: The Aβ(29–42) dimer has intermolecular parallel or antiparallel β-sheet structure like those in G. These pathways are summarized in Fig. 4.7b (see the arrows). In the early process of amyloidogenesis, these intermolecular parallel or antiparallel β-sheet structure can be a seed of amyloid fibrils.

We now present the results of a multibaric-multithermal MD simulation [42]. We considered a Lennard-Jones 12–6 potential system. The length and the energy are scaled in units of the Lennard-Jones diameter σ and the depth of the potential ϵ, respectively. We use an asterisk ($*$) for quantities reduced by σ and ϵ.

We used 500 particles ($N = 500$) in a cubic unit cell with periodic boundary conditions. We started the multibaric-multithermal weight factor determination from a regular isobaric-isothermal simulation at $T_0^* = 2.0$ and $P_0^* = 3.0$ (the multibaric-multithermal production run was also performed at this set of temperature and pressure values). These temperature and pressure values are respectively higher than the critical temperature T_c^* and the critical pressure P_c^* [71,72]. Recent reliable data are $T_c^* = 1.3207(4)$ and $P_c^* = 0.1288(5)$ [72]. The cutoff radius r_c^* was taken to be $r_c^* = 4.0$. A cutoff correction was added for the pressure and the potential energy.

In order to carry out the multibaric-multithermal MD simulation in Eqs. 4.64–4.69 with the replacement of $\mathcal{H}$ by $\mathcal{H}_{\mathrm{mbt}}$, we employed the Nosé-Poincaré formalism [44,45,62–65]. This gives the same equations of motion as the Nosé thermostat and provides a symplectic integrator. Therefore, it has an advantage that the secular deviation of the Hamiltonian is suppressed. We have recently shown that this integrator is also very effective for rigid-body molecules [64]. We performed a long production run of 10^6 MD steps.

In Fig. 4.8a, we show the probability distribution $P_{\mathrm{NPT}}(E^*/N, V^*/N)$ from the isobaric-isothermal simulation that was carried out first. It is a bell-shaped distribution. As the iteration of the multibaric-multithermal weight factor determination proceeds, $P_{\mathrm{mbt}}(E^*/N, V^*/N)$ will become flat and broad gradually. Figure 4.8b depicts the probability distribution $P_{\mathrm{mbt}}(E^*/N, V^*/N)$ from the multibaric-multithermal simulation that was finally performed. It shows a flat distribution, and the multibaric-multithermal MD simulation indeed sampled the conformational space in wider ranges of E^*/N and V^*/N than the conventional isobaric-isothermal MD simulation.
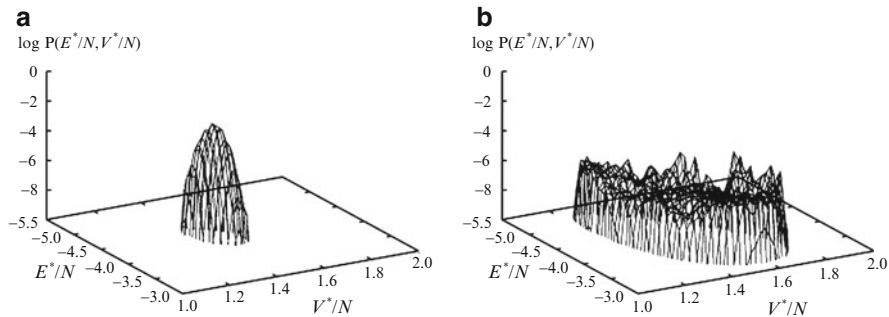
Fig. 4.8 (**a**) The probability distribution $P_{\mathrm{NPT}}(E^*/N, V^*/N)$ in the isobaric-isothermal MD simulation at $(T_0^*, P_0^*) = (2.0, 3.0)$ and (**b**) the probability distribution $P_{\mathrm{mbt}}(E^*/N, V^*/N)$ in the multibaric-multithermal MD simulation. Reprinted from Ref. [42] with kind permission of © Elsevier (2004)
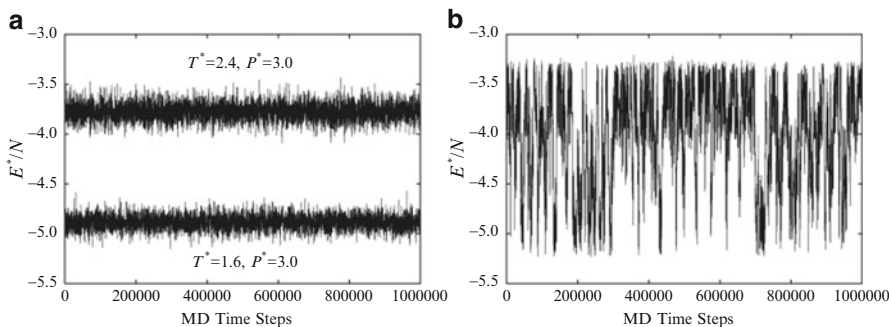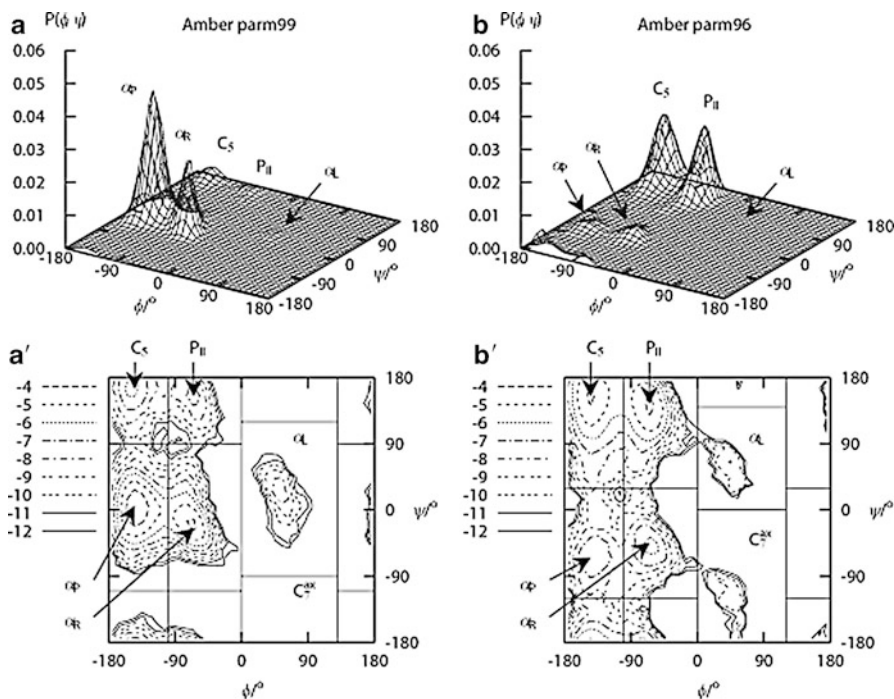

Fig. 4.9 The time series of E^*/N from (**a**) the conventional isobaric-isothermal MD simulations at $(T_0^*, P_0^*) = (2.4, 3.0)$ and at $(T_0^*, P_0^*) = (1.6, 3.0)$ and (**b**) the multibaric-multithermal MD simulation. Reprinted from Ref. [42] with kind permission of © Elsevier (2004)
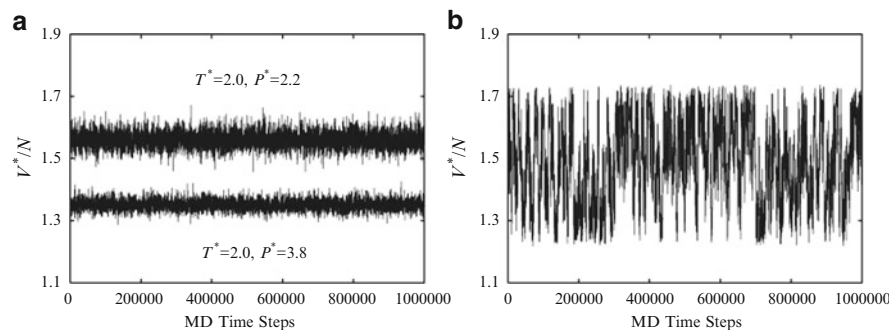
Fig. 4.10 The time series of V^*/N from (**a**) the conventional isobaric-isothermal MD simulations at $(T_0^*, P_0^*) = (2.0, 2.2)$ and at $(T_0^*, P_0^*) = (2.0, 3.8)$ and (**b**) the multibaric-multithermal MD simulation. Reprinted from Ref. [42] with kind permission of © Elsevier (2004)

Fig. 4.11 The probability distributions $\mathcal{P}(\phi, \psi)$ of the backbone dihedral angles ϕ and ψ at $T = 298$ K and $P = 0.1$ MPa, which were obtained by the reweighting techniques from the results of the multibaric-multithermal MD simulation (**a**) in the AMBER parm99 force field and (**b**) in the AMBER parm96 force field. (**a′**) and (**b′**) are the contour map of (**a**) and that of (**b**), respectively. Reprinted from Ref. [45] with kind permission of © The American Chemical Society (2008)

The time series of E^*/N from two conventional isobaric-isothermal MD simulations at $(T_0^*, P_0^*) = (1.6, 3.0)$ and $(2.4, 3.0)$ are given in Fig. 4.9a. The potential energy fluctuates in narrow ranges of $E^*/N = -4.0 \sim -3.5$ at the higher temperature of $T_0^* = 2.4$ and in the ranges of $E^*/N = -5.1 \sim -4.7$ and at the lower temperature of $T_0^* = 1.6$. On the other hand, Fig. 4.9b shows that the multibaric-multithermal MD simulation realizes a random walk in the potential energy space and covers a wide energy range.

A similar situation is observed in V^*/N. In Fig. 4.10a the time series of two conventional isobaric-isothermal MD simulations at $(T_0^*, P_0^*) = (2.0, 2.2)$ and $(2.0, 3.8)$, is shown. The volume fluctuations are only in the range of $V^*/N = 1.3 \sim 1.4$ and $V^*/N = 1.5 \sim 1.6$ at $P_0^* = 3.8$ and at $P_0^* = 2.2$, respectively. On the other hand, the multibaric-multithermal MD simulation performs a random walk that covers even a wider volume range, as shown in Fig. 4.10b.

We applied the MUBATH MD algorithm to a system consisting of one alanine dipeptide molecule and 63 water molecules. We used enough water molecules so that the alanine dipeptide molecule was always held perfectly within the
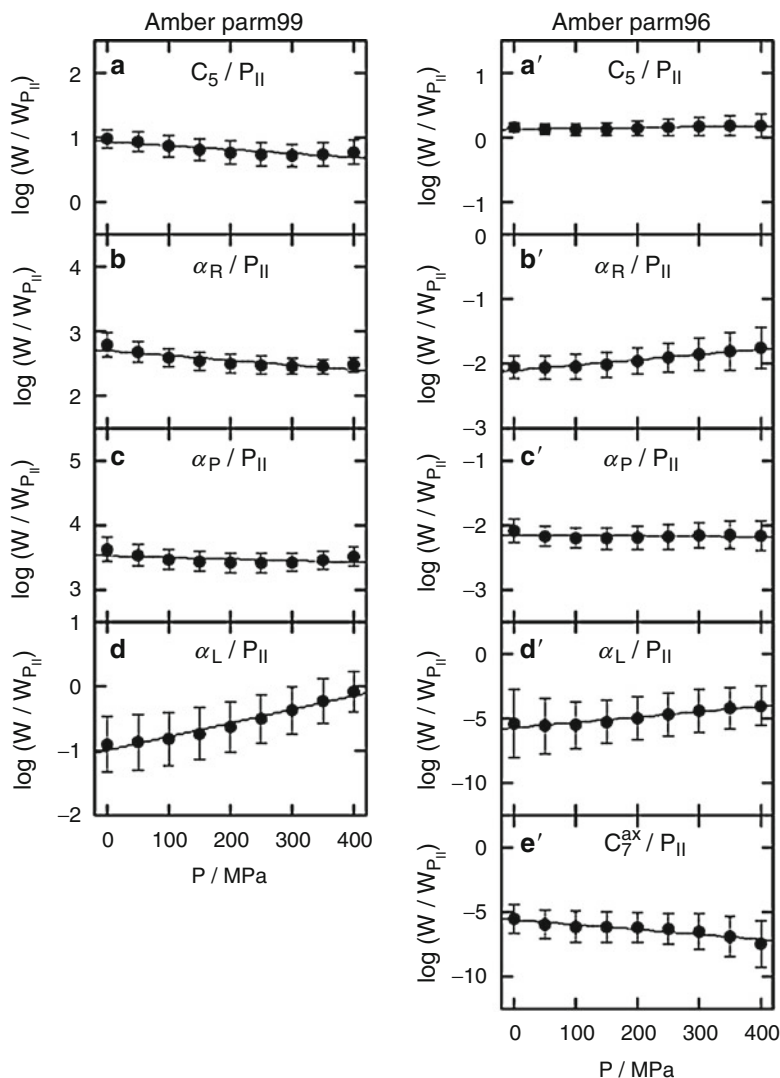
Fig. 4.12 The population ratios $W/W_{P_{II}}$ against the P_{II} state as functions of pressure P at constant temperature of $T = 298$ K, which was obtained by the reweighting techniques from the results of the multibaric-multithermal MD simulation. Reprinted from Ref. [45] with kind permission of © The American Chemical Society (2008)

simulation box. We used both AMBER parm99 [73] and AMBER parm96 [60] force fields for the alanine dipeptide molecule and the TIP3P [61] rigid-body model for the water molecules. We employed a cubic unit cell with periodic boundary conditions. The electrostatic potential was calculated by the Ewald method. We calculated the van der Waals interaction, which is given by the Lennard-Jones 12–6

Table 4.1 Differences ΔV / (cm^{3}mol^{-1}) in partial molar volume of the $C_5, \alpha_R, \alpha_P, \alpha_L$, and C_7^{ax} states from that of the P_{II} state calculated by the MUBATH MD simulations. Raman experimental data are taken from Ref. [75]

State	AMBER parm99	AMBER parm96	Raman
C_5	1.5 ± 0.9	-0.3 ± 0.9	0.1 ± 0.3
α_R	1.8 ± 0.8	-2.0 ± 2.0	1.1 ± 0.2
α_P	0.6 ± 0.8	0.1 ± 1.2	–
α_L	-5.2 ± 1.0	-10.2 ± 5.6	–
C_7^{ax}	–	9.4 ± 4.1	–

term, for all pairs of the atoms within the minimum image convention instead of introducing the spherical potential cutoff. The time step was taken to be $\Delta t = 0.5$ fs.

Figure 4.11 shows $\mathcal{P}(\phi, \psi)$ obtained from the MUBATH MD simulations by the reweighting techniques at $T = 298$ K and $P = 0.1$ MPa. In the case of longer peptides or proteins, the α_R state corresponds to an α-helix structure, and the P_{II} and C_5 states correspond to a β-strand structure. It is known that, in general, the AMBER parm99 force field tends to form an α-helix structure, and the AMBER parm96 force field tends to form a β-sheet structure [74]. The distributions $\mathcal{P}(\phi, \psi)$ in Fig. 4.11 are consistent with this feature.

Figure 4.12 shows the population ratio of each state and the P_{II} state as a function of P at the constant temperature of $T = 298$ K. A pressure increase at constant temperature generally causes a decrease in the volume. The decreases in the population ratio of some state and the P_{II} state mean that the volume of that state is larger than that of the P_{II} state. The difference in partial molar volume ΔV of the C_5 state from that of the P_{II} state, for example, is calculated from the derivative of $\log(W_{C_5}/W_{P_{II}})$ with respect to P by

$$\Delta V = -RT \left[\frac{\partial \log(W_{C_5}/W_{P_{II}})}{\partial P} \right]_T . \tag{4.76}$$

The difference between the partial molar volume of the other states and that of the P_{II} state was also obtained in the same way. The values of ΔV are shown in Table 4.1. Note that all the experimental data lie in between the corresponding simulation results with the two force fields.

4.4 Conclusions

In this chapter, we described two powerful generalized-ensemble algorithms, namely, replica-exchange method (REM) and multicanonical algorithm (MUCA), which are effective for molecular simulations. We also introduced multidimensional/multivariable extensions of the two methods, namely, MREM, vWREM, MUOV, MUCA-MUOV, and MUBATH. These generalized-ensemble algorithms are particularly useful for biomolecular simulations.

References

1. Hansmann UHE, Okamoto Y (1999) New Monte Carlo algorithms for protein folding. Curr Opin Struct Biol 9:177–183
2. Mitsutake A, Sugita Y, Okamoto Y (2001) Generalized-ensemble algorithms for molecular simulations of biopolymers. Biopolymers 60:96–123
3. Sugita Y, Okamoto Y (2002) Free-energy calculations in protein folding by generalized-ensemble algorithms. In: Schlick T, Gan HH (eds) Lecture notes in computational science and engineering, computational methods for macromolecules: challenges and applications. Springer, Berlin, pp 304–332. e-print: arXiv:cond-mat/0102296
4. Itoh SG, Okumura H, Okamoto Y (2007) Generalized-ensemble algorithms for molecular dynamics simulations. Mol Simul 33:47–56
5. Okamoto Y (2009) Generalized-ensemble algorithms for studying protein folding. In: Kuwajima K, Goto Y, Hirata F, Kataoka M, Terazima M (eds) Water and biomolecules. Springer, Berlin, pp 61–95
6. Hansmann UHE, Okamoto Y (1993) Prediction of peptide conformation by multicanonical algorithm – new approach to the multiple-minima problem. J Comput Chem 14:1333–1338
7. Hukushima K, Nemoto K (1996) Exchange Monte Carlo method and application to spin glass simulations. J Phys Soc Jpn 65:1604–1608
8. Sugita Y, Okamoto Y (1999) Replica-exchange molecular dynamics method for protein folding. Chem Phys Lett 314:141–151
9. Sugita Y, Kitao A, Okamoto Y (2000) Multidimensional replica-exchange method for free-energy calculations. J Chem Phys 113:6042–6051
10. Fukunishi F, Watanabe O, Takada S (2002) On the Hamiltonian replica exchange method for efficient sampling of biomolecular systems: application to protein structure prediction. J Chem Phys 116:9058–9067
11. Liu P, Kim B, Friesner RA, Bern BJ (2005) Replica exchange with solute tempering: a method for sampling biological systems in explicit water. Proc Natl Acad Sci USA 102:13749–13754
12. Affentranger R, Tavernelli I, Di Iorio EE (2006) A novel Hamiltonian replica exchange MD protocol to enhance protein conformational space sampling. J Chem Theory Comput 2:217–228
13. Lou H, Cukier RI (2006) Molecular dynamics of apo-adenylate kinase: a distance replica exchange method for the free energy of conformational fluctuations. J Phys Chem B 110:24121–24137
14. Kannan S, Zacharias M (2007) Enhanced sampling of peptide and protein conformations using replica exchange simulations with a peptide backbone biasing-potential. Proteins 66:697–706
15. Mu Y (2009) Dissociation aided and side chain sampling enhanced Hamiltonian replica exchange. J Chem Phys 130:164107
16. Berg BA, Neuhaus T (19991) Multicanonical algorithms for 1st order phase transitions. Phys Lett B 267:249–253
17. Berg BA, Neuhaus T (1992) Multicanonical ensemble: a new approach to simulate first-order phase transitions. Phys Rev Lett 68:9–12
18. Berg BA (2004) Introduction to Monte Carlo simulations and their statistical analysis. World Scientific, Singapore

19. Hansmann UHE, Okamoto Y, Eisenmenger F (1996) Molecular dynamics, Langevin and hybrid Monte Carlo simulations in a multicanonical ensemble. Chem Phys Lett 259:321–330
20. Nakajima N, Nakamura H, Kidera A (1997) Multicanonical ensemble generated by molecular dynamics simulation for enhanced conformational sampling of peptides. J Phys Chem B 101:817–824
21. Berg BA, Hansmann UHE, Neuhaus T (1993) Simulation of an ensemble with varying magnetic field: a numerical determination of the order-order interface tension in the $D = 2$ Ising model. Phys. Rev. B 47:497–500
22. Janke W, Kappler S (1995) Multibondic cluster algorithm for Monte Carlo simulations of first-order phase transitions. Phys Rev Lett 74:212–215
23. Berg BA, Janke W (1998) Multioverlap simulations of the 3D Edwards-Anderson Ising spin glass. Phys Rev Lett 80:4771–4774
24. Kumar S, Payne P, Vásquez M (1996) Method for free-energy calculations using iterative techniques. J Comput Chem 17:1269–1275
25. Bartels C, Karplus M (1997) Multidimensional adaptive umbrella sampling: applications to main chain and side chain peptide conformations. J Comput Chem 18:1450–1462
26. Higo J, Nakajima N, Shirai H, Kidera A, Nakamura H (1997) Two-component multicanonical Monte Carlo method for effective conformation sampling. J Comput Chem 18:2086–2092
27. Iba Y, Chikenji G, Kikuchi M (1998) Simulation of lattice polymers with multi-self-overlap ensemble. J Phys Soc Jpn 67:3327–3330
28. Bachmann M, Janke W (2003) Multicanonical chain-growth algorithm. Phys Rev Lett 91:208105
29. Mitsutake A, Okamoto Y (2009) From multidimensional replica-exchange method to multidimensional multicanonical algorithm and simulated tempering. Phys Rev E 79:047701
30. Mitsutake A, Okamoto Y (2009) Multidimensional generalized-ensemble algorithms for complex systems. J Chem Phys 130:214105
31. Mitsutake A (2009) Simulated-tempering replica-exchange method for the multidimensional version. J Chem Phys 131:094105
32. Itoh SG, Okumura H, Okamoto Y (2010) Replica-exchange method in van der Waals radius space: overcoming steric restrictions for biomolecules. J Chem Phys 132:134105
33. Berg BA, Noguchi H, Okamoto Y (2003) Multioverlap simulations for transitions between reference configurations. Phys Rev E 68:036126
34. Itoh SG, Okamoto Y (2004) Multi-overlap molecular dynamics methods for biomolecular systems. Chem Phys Lett 400:308–313
35. Itoh SG, Okamoto Y (2006) Theoretical studies of transition states by the multioverlap molecular dynamics methods. J Chem Phys 124:104103
36. Itoh SG, Okamoto Y (2007) Effective sampling in the configurational space of a small peptide by the multicanonical-multioverlap algorithm. Phys Rev E 76:026705
37. Itoh SG, Okamoto Y (2008) Amyloid-β(29–42) dimer formations studied by a multicanonical-multioverlap molecular dynamics simulation. J Phys Chem B 112:2767–2770
38. Itoh SG, Tamura A, Okamoto Y (2010) Helix-hairpin transitions of a designed peptide studied by a generalized-ensemble simulation. J Chem Theor Comput 6:979–983
39. Okumura H, Okamoto Y (2004) Monte Carlo simulations in multibaric-multithermal ensemble. Chem Phys Lett 383:391–396
40. Okumura H, Okamoto Y (2004) Monte Carlo simulations in generalized isobaric-isothermal ensembles. Phys Rev E 70:026702
41. Okumura H, Okamoto Y (2004) Liquid-gas phase transitions studied by multibaric-multithermal Monte Carlo simulations. J Phys Soc Jpn 73:3304-3311
42. Okumura H, Okamoto Y (2004) Molecular dynamics simulations in the multibaric-multithermal ensemble. Chem Phys Lett 391:248–253
43. Okumura H, Okamoto Y (2006) Multibaric-multithermal ensemble molecular dynamics simulations. J Comput Chem 27:379–395
44. Okumura H, Okamoto Y (2007) Multibaric-multithermal molecular dynamics simulation of alanine dipeptide. Bull Chem Soc Jpn 80:1114–1123

45. Okumura H, Okamoto Y (2008) Temperature and pressure dependence of alanine dipeptide studied by multibaric-multithermal molecular dynamics simulations. J Phys Chem B
    112:12038–12049
46. Nishikawa T, Ohtsuka H, Sugita Y, Mikami M, Okamoto Y (2000) Replica-exchange Monte
    Carlo method for Ar fluid. Prog Theor Phys Suppl 138:270–271
47. Okabe T, Kawata M, Okamoto Y, Mikami M (2001) Replica-exchange Monte Carlo method
    for the isobaric-isothermal ensemble. Chem Phys Lett 335:435–439
48. Paschek D, Garcia AE (2004) Reversible temperature and pressure denaturation of a protein
    fragment: a replica exchange molecular dynamics simulation study. Phys Rev Lett 93:238105
49. Mori Y, Okamoto Y (2010) Generalized-ensemble algorithms for the isobaric-isothermal
    ensemble. J Phys Soc Jpn 79:074003
50. Metropolis N, Rosenbluth AW, Rosenbluth MN, Teller AH, Teller E (1953) Equation of state
    calculations by fast computing machines. J Chem Phys 21:1087–1092
51. Nosé S (1984) A molecular dynamics method for simulations in the canonical ensemble. Mol
    Phys 52:255–268
52. Nosé S (1984) A unified formulation of the constant temperature molecular dynamics methods.
    J Chem Phys 81:511–519
53. Mori Y, Okamoto Y (2010) Replica-exchange molecular dynamics simulations for various
    constant temperature algorithms. J Phys Soc Jpn 79:074001
54. Ferrenberg AM, Swendsen RH (1989) Optimized Monte Carlo data analysis. Phys Rev Lett
    63:1195–1198
55. Kumar S, Bouzida D, Swendsen RH, Kollman PA, Rosenberg JM (1992) The weighted
    histogram analysis method for free-energy calculations on biomolecules. 1. The method.
    J Comput Chem 13:1011–1021
56. Mitsutake A, Sugita Y, Okamoto Y (2003) Replica-exchange multicanonical and multicanonical replica-exchange Monte Carlo simulations of peptides. I. Formulation and benchmark test.
    J Chem Phys 118:6664–6675
57. Ferrenberg AM, Swendsen RH (1988) New Monte Carlo technique for studying phase
    transitions. Phys Rev Lett 61:2635–2638
58. Hansmann UHE, Masuya M, Okamoto Y (1997) Characteristic temperatures of folding of a
    small peptide. Proc Natl Acad Sci USA 94:10652–10656
59. Andersen HG (1980) Molecular dynamics simulations at constant pressure and/or temperature.
    J Chem Phys 72:2384–2393
60. Kollman PA, Dixon R, Cornell W, Fox T, Chipot C, Pohorille A (1997) The development/application of a 'minimalist' organic/biochemical molecular mechanic force field using
    a combination of ab initio calculations and experimental data. In: Wilkinson A, Weiner P, van
    Gunsteren WF (eds) Computer simulation of biomolecular systems, vol 3. Elsevier, Dordrecht,
    pp 83–96
61. Jorgensen WL, Chandrasekhar J, Madura JD, Impey RW, Klein ML (1983) Comparison of
    simple potential functions for simulating liquid water. J Chem Phys 79:926–935
62. Bond SD, Leimkuhler BJ, Laird BB (1999) The Nosé-Poincaré method for constant temperature molecular dynamics. J Comput Phys 151:114–134
63. Nosé S (2001) An improved symplectic integrator for Nosé-Poincaré thermostat. J Phys Soc
    Jpn 70:75–77
64. Okumura H, Itoh SG, Okamoto Y (2007) Explicit symplectic integrators of molecular
    dynamics algorithms for rigid-body molecules in the canonical, isothermal-isobaric, and
    related ensembles. J Chem Phys 126:084103
65. Okumura H (2008) Partial multicanonical algorithm for molecular dynamics and Monte Carlo
    simulations. J Chem Phys 129:124116
66. MacKerell AD Jr, Bashford D, Bellott M, Dunbrack RL Jr, Evanseck JD, Field MJ, Fischer
    S, Gao J, Guo H, Ha S, Joseph-McCarthy D, Kuchnir L, Kuczera K, Lau FTK, Mattos C,
    Michnick S, Ngo T, Nguyen DT, Prodhom B, Reiher WE III, Roux B, Schlenkrich M, Smith
    JC, Stote R, Straub J, Watanabe M, Wiórkiewicz-Kuczera J, Yin D, Karplus M (1998) All-atom
    empirical potential for molecular modeling and dynamics studies of proteins. J Phys Chem B
    102:3586–3616

67. Brooks BR, Bruccoleri RE, Olafson BD, States DJ, Swaminathan S, Karplus M (1983) CHARMM: a program for macromolecular energy, minimization, and dynamics calculations. J Comput Chem 4:187–217
68. Still WC, Tempczyk A, Hawley RC, Hendrickson T (1990) Semianalytical treatment of solvation for molecular mechanics and dynamics. J Am Chem Soc 112:6127–6129
69. Dominy BN, Brooks CL III (1999) Development of a generalized-Born model parametrization for proteins and nucleic acids. J Phys Chem B 103:3765–3773
70. Feig M, Brooks CL III (2002) Evaluating CASP4 predictions with physical energy functions. Proteins 49:232–245
71. Okumura H, Yonezawa F (2000) Liquid-vapor coexistence curves of several interatomic model potentials. J Chem Phys 113:9162–9168
72. Okumura H, Yonezawa F (2001) Reliable determination of the liquid-vapor critical point by the NVT plus test particle method. J Phys Soc Jpn 70:1990–1994
73. Wang J, Cieplak P, Kollman PA (2000) How well does a restrained electrostatic potential (RESP) model perform in calculating conformational energies of organic and biological molecules? J Comput Chem Phys 21:1049–1074
74. Yoda T, Sugita Y, Okamoto Y (2004) Comparisons of force fields for proteins by generalized-ensemble simulations. Chem Phys Lett 386:460–467
75. Takekiyo T, Imai T, Kato M, Taniguchi Y (2004) Temperature and pressure effects on conformational equilibria of alanine dipeptide in aqueous solution. Biopolymers 73:283–290

Chapter 5
Atomistic Mechanism of Carbon Nanostructure Self-Assembly as Predicted by Nonequilibrium QM/MD Simulations

**Stephan Irle, Alister J. Page, Biswajit Saha, Ying Wang,
K.R.S. Chandrakumar, Yoshio Nishimoto, Hu-Jun Qian,
and Keiji Morokuma**

> *What can be controlled is never completely real; what is real
> can never be completely controlled.*
>
> Vladimir V. Nabokov [1]

Abstract We review our quantum chemical molecular dynamics (QM/MD)-based studies of carbon nanostructure formation under nonequilibrium conditions that were conducted over the past 10+ years. Fullerene, carbon nanotube, and graphene formation were simulated on the nanosecond time scale, considering experimental conditions as closely as possible. An approximate density functional method was employed to compute energies and gradients on the fly in direct MD simulations, while the simulated systems were pushed away from equilibrium via carbon concentration or temperature gradients. We find that carbon nanostructure formation from feedstock particles involves a phase transition of sp to sp^2 carbon phases, which begins with the formation of Y-junctions, followed by a nucleus consisting of pentagons, hexagons, and heptagons. The dominance of hexagons in the synthesized

S. Irle (✉) • Y. Wang • Y. Nishimoto • H.-J. Qian
Institute for Advanced Research and Department of Chemistry, Nagoya University,
Nagoya 464-8602, Japan
e-mail: sirle@chem.nagoya-u.ac.jp; ywang@iar.nagoya-u.ac.jp;
yoshio.nishimoto@a.mbox.nagoya-u.ac.jp; hujunqian@gmail.com

A.J. Page • B. Saha • K.R.S. Chandrakumar
Fukui Institute for Fundamental Chemistry, Kyoto University, Kyoto 606-8103, Japan
e-mail: alisterpage@gmail.com; bisajit@gmail.com; krschandrakumar@gmail.com

K. Morokuma (✉)
Cherry L. Emerson Center for Scientific Computation and Department of Chemistry,
Emory University, Atlanta, GA 30322, USA

Fukui Institute for Fundamental Chemistry, Kyoto University, Kyoto 606-8103, Japan
e-mail: morokuma@emory.edu

products is explained via annealing processes that occur during the cooling of the grown carbon structure, accelerated by transition-metal catalysts when present. The dimensional structures of the final synthesis products (0D spheres – fullerenes, 1D tubes – nanotubes, 2D sheets – graphenes) are induced by the shapes of the substrates/catalysts and their interaction strength with carbon. Our work prompts a paradigm shift away from traditional anthropomorphic formation mechanisms solely based on thermodynamic stability. Instead, we conclude that nascent carbon nanostructures at high temperatures are dissipative structures described by nonequilibrium dynamics in the manner proposed by Prigogine, Whitesides, and others. As such, the fledgling carbon nanostructures consume energy while increasing the entropy of the environment and only gradually anneal to achieve their familiar, final structure, maximizing hexagon formation wherever possible.

5.1   Introduction

Nanotechnology started out as a vision that involved arranging atoms "one by one, just as we want them," following Richard Feynman's "There's plenty of room at the bottom" speech [2]. The basic idea was to use atom-positioning techniques for writing the contents of entire encyclopedias on the head of a pin. Feynman thereupon developed the concepts of atomic-scale computing and molecular machinery, a theme that was enthusiastically picked up most notably by K. Eric Drexler in his 1986 book "*Engines of Creation*" [3]. The concept of the molecular machines, assembled with atomic precision, culminated in Drexler's idea of self-replicating "nanofactories" [4], where the molecular equivalents of industrial robots build the next generation of molecular robots. This so-called top-down atom assembly approach, based on the ideas of Feynman and Drexler, was closely related to a view of the nanoscale where Newtonian mechanics dictate the motions and interactions of molecules and atoms as scaled-down versions of scaffolds and billiard balls. Initially, the top-down approach met success: using the tip of a scanning tunneling microscope (STM), which had been invented in 1981 [5], Don Eigler and Erhard Schweizer wrote the letters I-B-M on a nickel (110) surface using 35 Xenon atoms. However, it was soon realized that such an approach would be difficult to extend to three dimensions, would be too laborious on an industrial scale, and, most importantly, inevitably impeded by physical and chemical interactions between those molecules and atoms. Rick Smalley – one of the discoverers of buckminsterfullerene C_{60}, and perhaps the most outspoken advocate for the use of nanotechnology as part of a solution to global problems – is well known for his criticism of Drexler's molecular assemblers [6, 7]. This criticism rests on the grounds that precise positioning control is impossible due to, what he called, the "fat finger" and "sticky finger" problems. Chemical and van der Waals forces are the major culprits, plaguing the top-down approach to nanotechnology. The debate continued on without conclusion, but Drexler's nanofactories have not materialized thus far, nearly 20 years after their initial conception.

A practical solution to the problems highlighted by Smalley was to engage the "enemy forces" of the top-down approach as "prime enablers" in a "bottom-up" nanotechnology. This technology is rooted in supramolecular chemistry, a field that was pioneered by Jean-Marie Lehn, Donald Cram, Fraser Stoddard, and others in the 1970s and 1980s. Chemical and van der Waals forces between the supramolecular constituents are now exploited to direct chemical systems into spontaneous self-assembly following "instructions" (molecular regions endowed with specific interactions) encoded in their chemical constituents [8]. Biological nanomolecules such as DNA and proteins similarly create form and function based on distinct sequences of smaller molecular entities, namely, nucleobases and amino acids. The bottom-up approach can be most easily appreciated when molecules self-assemble into monolayers on two-dimensional surfaces, where weak intermolecular forces, namely, van der Waals and hydrogen-bonding interactions, orchestrate the assembly of sometimes stunningly beautiful patterns [9, 10]. Weak covalent bond formation between adsorbates and metal surface, as in the case of self-assembled monolayers (SAMs) of thiols [11], or strong covalent bond formation between monomer units, as in the recently reported bottom-up synthesis of graphene [12], can also be used for directed structure formation. The assemblies are certainly not restricted to two dimensions, as molecular tweezers [13] and DNA-based nano-origami [14] show. The full range of the chemistry toolbox is used in bottom-up nanotechnology. It is thus potentially possible to create ever-new custom-designable materials and functions [15] and to expand into the so-called adjacent possible regime, in which molecular machines create functional materials of higher complexity [16].

A different type of bottom-up nanotechnology, not based on supramolecular chemistry but on nanomorphology [17], also relies on the principle of directed self-assembly. In this less chemical but more physical approach, the principles of aggregation and coarsening during crystal growth are exploited in the creation of zero- and one-dimensional nanoparticles with specific shapes and electronic properties. These structures typically contain few chemical elements and became popularly known as quantum dots (QDs) or quantum wires (QWs) [18, 19]. Among such structures, nanoparticles composed of carbon are arguably the most fascinating. Carbon is perhaps the most important chemical element in the universe after hydrogen: Its atoms have the unique ability to bind to each other with strong covalent bonds in one-, two- and three-dimensional molecular structures, ranging in size from small diatomics to large polymers and crystals. Its rich hydrocarbon chemistry occurring in interstellar dust clouds is crucial for the cooling of star formation processes [20]. On Earth, carbon plays the center stage role in biochemistry, essential to terrestrial life. To mankind, elemental carbon in the form of charcoal was essential to harness the power of fire for making iron-based tools, and carbon-based fossil fuel plays a central role for heating and energy production to this day. The development of nanotechnology received a great boost by the discovery of the pure carbon compound buckminsterfullerene in 1985 [21]. The family of fullerenes demonstrated for the first time elemental carbon's powerful ability to form an infinite array of allotropes beyond graphite and diamond. The most familiar ones are, of course, zero-dimensional fullerenes [22], one-dimensional

carbon chains [23] and carbon nanotubes (CNTs) [24], two-dimensional graphenes [25], and three-dimensional graphites and nanodiamonds (NDs) [26]. In addition, there is a plethora of other allotropes that are intermediates between these basic three categories, such as haeckelites [27], nanoscrolls [28], nanohorns [29], CNT helices [30, 31], CNT-graphene hybrids [32], and Schwarzites [33], to name just a few. Extensive reviews of these and more structures can be found in [34–36]. The basic difference between carbon-based nanostructures and conventional QDs and QWs is the fact that the covalent bonds between constituent atoms in the case of carbon are exceptionally strong. This gives rise to high mechanical stability and thermal conductivity. The resulting macromolecular structures thus possess diverse electronic band structures ranging from insulators (diamonds) to metals (graphenes, haeckelites, certain CNTs, etc.). The combination of these properties makes carbon-based nanomaterials potentially ideal candidates for a wide range of applications that not only include Feynman's original concepts of molecular computing and molecular machinery [37] but also more daring ones, such as the use of CNT ropes for the construction of space elevators [38].

Knowledge of the detailed mechanisms of nanostructure formation is crucial for the further successful development of bottom-up nanotechnologies. In the case of supramolecular chemistry, it is often possible to study the sequence of individual steps leading up to structure formation, since the self-assembly reactions are typically carried out in solution and therefore occur under relatively "mild" conditions [8, 39]. Consequently, similar to other wet "flask-and-beaker" chemistry, thermodynamic stabilities and kinetic reaction rates can be extracted from experiment, and computation of minimum energy reaction pathways connecting reactants, transition states, intermediates, and final products [40] are possible using traditional approaches that involve the efficient optimization of stationary points on the Born–Oppenheimer potential energy surfaces. However, in the case of carbon nanostructure formation, it is often necessary to employ extraordinarily high temperatures in which small carbon fragments condense into larger complexes along a steep temperature gradient [41]. This is especially true in the case of laser evaporation [21] and Krätschmer–Huffman carbon arc [42] methods of fullerene and CNT synthesis, and the laser-evaporation synthesis of single-walled carbon nanohorns (SWCNH) [29]. A common aspect of all of these methods is that graphite patches are transformed into carbon plasma or vapor at temperatures exceeding the sublimation point of graphite (around 3,900 K [43]) [44], which rapidly cools down to temperatures between 1,000 and 2,000 K. NDs are nowadays often produced using chemical vapor deposition techniques around 3,000 K [45], where gas-phase pyrolytic decomposition of the carbon feedstock species also plays a crucial role [46]. Under such extreme conditions, it becomes clearly impossible to know the major chemical species involved in the elementary reactions, let alone to study all the individual chemical reaction steps leading to the gradual nanostructure formation. Time-resolved spectroscopic diagnostics of single-walled CNT (SWCNT) growth in laser-evaporation synthesis [47] have not been able to shed light on the atomic level details of CNT nucleation and growth. Even under the much less dramatic reaction conditions employed, for instance, in catalytic chemical vapor deposition (CCVD)

synthesis of CNTs [48–50] and graphenes [51, 52], where catalysts are thought to reduce the barriers for the decomposition of the carbon feedstock [53], it is clear that the precursor gas chemistry determines the crystallinity of CNTs at low temperature [54]. Unfortunately, the precursor gas chemistry is highly complex and usually left out in the kinetic modeling of CNT nucleation, growth, and growth termination [55]. For all of these reasons, unsurprisingly, the formation mechanisms of fullerenes, CNTs, and graphenes remain a topic of "heated" discussions to this day.

Theoretical studies of the fullerene, CNT, and graphene formation mechanisms have been carried out in great numbers, and it is impossible to list even a small fraction of them in this review. Unfortunately, the vast majorities of these studies and formation mechanism proposals tacitly assume that the carbon nanostructure formation would occur akin to traditional organic or organometallic chemistry, where each intermediate along the reaction step is close to thermodynamic equilibrium with the reaction medium and the other constituents of the reaction mix. As an example, we will highlight some of these postulated reaction mechanisms, namely, the ring stacking mechanism of fullerene formation by Wakabayashi and Achiba from 1992 [56], Smalley's pentagon road of fullerene formation [57], and the screw-dislocation growth model of SWCNTs by Ding and Yakobson [58]. In the history of buckminsterfullerene C_{60}, the greatest mystery has been how nature achieves to materialize, without fail, its characteristic high icosahedral point group symmetry in each single molecule. Such "precision engineering" stands juxtaposed against the backdrop of the high-temperature and the chaotic gas-phase chemistry of its synthesis process. Achiba and Wakabayashi reasoned that, based on their time-of-flight mass spectrometry (TOF-MS) observation of abundant carbon macrocycle anions C_n^- ($n = 10, 12, 14, 16$) in laser-evaporated carbon vapor, carbon rings might stack along ordered sequences such that the end product would result in the familiar I_h–C_{60} or D_{5h}–C_{70} fullerene cages. The precision required for such stacking is mind-boggling: To construct the I_h–C_{60} cage, the proposed stacking sequence reads C_{10}–C_{18}–C_{18}–C_{12}–C_2. Not only are C_{18} rings almost entirely absent from TOF-MS spectra, the original C_{10} ring must also first collapse into a carbon equivalent of naphthalene (*sans* hydrogen atoms), a structure that is energetically many electron volts higher than the macrocyclic isomer, or the ring structure. Moreover, in contrast to C_{60}, the stacking sequence for C_{70} needs to be substantially modified to yield its familiar D_{5h} isomer: C_{10}–C_{18}–C_{20}–C_{16}–C_2–C_2–C_2. Not only is C_{20} almost entirely absent from the TOF-MS, it seems also strange to assume the presence of C_2 at the final stage of fullerene formation, since these highly reactive species should have been previously consumed in the formation of the macrocyclic carbon rings. Rick Smalley avoided such pitfalls and postulated that C_2 molecules would stack in carbon clusters that would *maximize* the number of isolated pentagons in the structure. Thermodynamics is at work here: isolated pentagons are known to be energetically more stable by about 1 eV compared to fused pentagons, which provide the justification of the empirical isolated-pentagon rule (IPR) [59]. This rule states that experimentally observed (empty) fullerene cages avoid fused pentagons. However, Smalley never explained how these C_2 molecules would construct the different molecular structures of C_{60} versus C_{70}. Once the cage size is "decided," the

C_2's would have to stack in different position sequences without help from the IPR, since both cages have no fused pentagons. Somewhat related to Smalley's pentagon road is the proposal by Ding and Yakobson [58] that SWCNT sidewalls grow in such a way that C_2 units always settle at the "cozy corner" (in analogy to the screw-dislocation growth in crystallization processes described by Frank and coworkers in 1949 [60]). Although it is undeniable that thermodynamically C_2 molecules would prefer to aggregate at the position that would result in an extension of the outermost hexagon layer around the open rim, the difference between Frank's crystal growth theory and SWCNT growth is the difference in the binding strength between the constituent atoms. As mentioned above, the carbon-carbon bond in CNTs is among the strongest found in nature; once formed, excess reaction energy is quickly dissipated away from the addition site via the high thermal conductivity of CNTs, and it is therefore unlikely that the C_2 molecule would detach and migrate along the rim after it had "discovered" that it was attached in the "incorrect" position. The potential energy surfaces of Coulombic or van der Waals crystals are up to orders of magnitudes shallower! Moreover, it is not clear whether CNT growth in CVD synthesis is really occurring by means of naked C_2 molecules, or whether C_2H or C_2H_2 species play an important role, as postulated for instance in [61].

These three examples demonstrate a desire to explain growth of highly ordered carbon nanostructures as a consequence of a central principle of order, whether this be thermodynamical stability (Smalley/Ding-Yakobson) or anthropomorphic creation of order by molecules following precise reaction roadmaps in analogy to construction staff following the architect's blueprints (Wakabayashi-Achiba). The theme of a central principle of order is followed in nearly all theoretical studies of carbon nanostructure formations; we have reviewed a number of these works in [62] in the context of fullerene formation and in [63] in the context of SWCNT nucleation and growth. In retrospect, it is easy to dismiss proposals of anthropomorphic formation mechanisms on the grounds that diffusion processes are inherently random. It is *not* easy to evaluate how far away from thermodynamic equilibrium the self-assembly processes occur: if all growth processes were reversible, performed for instance at infinitely slow cooling rates, the end result would always be highly oriented graphite [41]. We wish to stress once more at this point that fullerene and CNT formation occurs either in the presence of large temperature and carbon concentration gradients (in the case of laser ablation/carbon arc synthesis), driving the systems away from thermodynamic equilibrium, or occurs at still relatively high temperatures between 800 and 1,500 K (in the case of CCVD synthesis). In both cases, the exact composition of the carbon feedstock is unknown, and the effects of large entropy and random diffusion cannot be ignored. It depends on the individual case whether principles applicable to thermodynamic equilibrium can be used to understand the creation of molecular order, and it is difficult to estimate how much of a system's formation mechanism is based on nonequilibrium phenomena.

It is now well accepted that irreversible processes occurring in systems far from thermodynamic equilibrium may cause the emergence of order [64–66], in particular when autocatalysis is involved and coupled with feedback networks [16]. The low-entropic structures created in such processes form due to the consumption

of energy and consequent dissipation of entropy to the outside world. The constituents of dissipative structures change over time while their overall appearance remains practically unchanged. Examples for such so-called dynamic self-assembly are abundant and include the autocatalytic process of star formation in galaxies [20], self-organized critical systems near phase transitions [67], sand dunes, clouds in the atmosphere, tornadoes and hurricanes, the processes occurring inside and among biological cells [16], and biological and geological morphogenesis, to name just a few. *None of these self-organized systems requires central management, and none is directly associated with minima on potential energy surfaces,* since the constituents of the dissipative structures change dynamically over time. Furthermore, systems in thermodynamic equilibrium appear unchanged over time and can therefore not be immediately used to study growth processes that naturally follow an arrow of time [65].

Since carbon nanostructure formation occurs under "nonequilibrium" conditions and involves complex chemical reaction networks that change over time, we felt compelled to study the atomistic dynamics of fullerene, SWCNT, and graphene formation by taking temperature and/or carbon concentration gradients explicitly or implicitly into account. A study of such dynamic systems necessarily requires that its time evolution be accurately followed. The most straightforward way to follow time evolution of chemical systems in computer simulations can be achieved by numerically solving Newton's equation of motion for the atomic (classical) nuclei in so-called molecular dynamics (MD) simulations. Although Newtonian trajectories of individual particles appear identical under propagation in positive or negative time, Newtonian trajectories of ensembles of particles do not, due to collisions creating correlations between these particles. The succession of these correlations causes the ensemble of particles to become "Poincaré nonintegrable" [65], and propagation forward and backward in time will necessarily lead to different trajectories, introducing the notion of an "arrow of time" [65]. The result is that unidirectional growth processes involving *ensembles of particles* can be studied in such many-body systems even though the MD trajectory of an *individual particle* on a potential energy surface is, in principle, time reversible. Boltzmann's arrow of time emerges in these simulations naturally! Quite naturally, numerical simulations of nanostructure formation involve a great number of atoms and the propagation of their positions and velocities over a long period of time. For this reason, computationally efficient Tersoff-type [68, 69] reactive empirical bond order (REBO) [70–72] force fields have been employed in the early studies of fullerene [73, 74] and SWCNT formation [75–83]. However, fullerenes, SWCNTs, and graphenes consist of sp^2-hybridized carbon atoms where quantum mechanical delocalization of π-conjugation becomes important. Moreover, when a metal catalyst is involved as, for instance, in SWCNT and graphene growth simulations, charge transfer and the effects of variable electronic states of the catalyst nanoparticles play an important role. It is therefore desirable to perform direct MD simulations on the fly on potential energy surfaces (PESs) that are obtained from quantum chemical electronic structure calculations. But not even

massively parallel computers are fast enough to perform direct quantum chemical MD (QM/MD) simulations based on density functional theory (DFT) electronic structure theory, which is the computationally *least demanding* of the traditional quantum chemical methodologies.

When we entered the field of carbon nanostructure growth simulations, we set out to perform such QM/MD simulations of ensembles of C atoms and C_2 and C_2H_2 molecules using an approximate DFT method, which will be explained in the following section. Aside from a few isolated attempts that employed conventional DFT in BOMD simulations shorter than 50 ps [84–86], our series of QM/MD simulations approaching the nanosecond timescale now stands unrivaled. In Sect. 5.2, we briefly describe the employed quantum chemical method in detail, and in the subsequent sections, we review our nonequilibrium QM/MD simulations of fullerene formation (Sect. 5.3), SWCNT nucleation and growth (Sect. 5.4), and graphene growth (Sect. 5.5), before drawing general conclusions on the formation mechanisms of carbon nanostructures (Sect. 5.6).

5.2 Computational Methodology of Nonequilibrium QM/MD Simulations

In this section, we present a brief account of the main theoretical methods and algorithms employed in the QM/MD simulations that are presented in Sects. 5.3, 5.4 and 5.5. Our approach is based on the density-functional tight-binding (DFTB) method. This method is essentially a two-center approximation to the popular DFT method, which had its first great successes starting in the 1990s [87, 88]. For systems containing a few hundred atoms, DFTB is, in practice, ca. three orders of magnitude faster than traditional DFT methods. In DFTB theory, the atomic/molecular energy is given as

$$E_{\text{DFTB}} = \sum_{i}^{\text{occ.}} \varepsilon_i + \frac{1}{2} \sum_{A \neq B}^{\text{atoms}} E_{\text{rep}}^{\text{AB}} \qquad (5.1)$$

where ε_i is the ith Kohn–Sham (KS) eigenvalue (obtained from the diagonalization of the Hamiltonian matrix in a non-orthogonal pseudo-atomic orbital basis) and $E_{\text{rep}}^{\text{AB}}$ describes the repulsive force between nuclei A and B, a function of nuclear geometry alone. The matrix elements of the two-center Hamiltonian, from which the ε_i's are computed, as well as the $E_{\text{rep}}^{\text{AB}}$ potentials do not need to be computed as integrals over the pseudo-atomic orbital basis functions and operators since they are only read into memory once for each molecular geometry from tabulated data. This results in a significant reduction in the computation time compared to traditional DFT. However, effects of charge polarization are not included in this 0th order approximation. To alleviate this problem, the self-consistent-charge DFTB (SCC-DFTB) method was developed [89]. The SCC-DFTB energy is given as

$$E_{\text{SCC–DFTB}} = \sum_{i}^{\text{atoms}} \varepsilon_i + \frac{1}{2} \sum_{A \neq B}^{\text{atoms}} E_{\text{rep}}^{AB} + \frac{1}{2} \sum_{A \neq B}^{\text{atoms}} \gamma_{AB} \Delta q_A \Delta q_B \qquad (5.2)$$

The SCC-DFTB energy includes a second-order contribution to the DFTB energy involving the charge fluctuation, $\Delta q_\alpha = q_\alpha - q_\alpha^0$, where q_α and q_α^0 are the effective atomic populations of the atom α in the molecule and in the free atom, respectively, typically computed from Mulliken population analysis. The SCC-DFTB KS molecular orbitals (MOs) are iteratively optimized until the corresponding energy of Eq. (5.2) becomes self-consistent with respect to Δq_A and Δq_B. Although all Hamiltonian matrix elements are kept in memory at each molecular geometry, the iterative procedure incurs an increase in computational time of approximately one order of magnitude with respect to non-charge-consistent DFTB [Eq. (5.1)] because matrix diagonalization of the one-electron Hamiltonian needs to be performed for each charge iteration. We note in passing that spin-splitting energies can be introduced in a similar way using on-center spin-spin interaction energies. In this case, the self-consistent solutions with respect to both charge density and spin densities are computed using different MOs for different spin [90], which incurs an additional doubling of the required computational time. When the gap between highest occupied MO (HOMO) and lowest unoccupied MO (LUMO) is small, or the density of states near the Fermi level is large, it occurs frequently that self-consistency with respect to charge and/or spin densities cannot be attained. This happens nearly always in metallic or near-metallic systems. However, the convergence issue is improved dramatically by introducing a finite electronic temperature during the convergence of the MOs. In such a case, the variational SCC-DFTB energy becomes the Mermin free energy [91]

$$E_{\text{SCC–DFTB}} + T_e 2 k_B \sum_{i}^{\text{orbitals}} [f_i \ln f_i + (1 - f_i) \ln (1 - f_i)] \qquad (5.3)$$

where T_e is the electronic temperature and the population of the ith MO, f_i, is now defined at each SCC iteration using the Fermi-Dirac (FD) distribution

$$f_i = \frac{1}{\exp{[(\varepsilon_i - \mu)/k_B T_e + 1]}} \qquad (5.4)$$

The FD distribution is, in principle, a continuous function determining specific values for the ith MO energy, ε_i. μ is the chemical potential and is numerically determined so that the sum of all fractional MO occupations is equal to the total number of electrons N_e: $N_e = 2\Sigma_i f_i$. The FD distribution varies continuously over the [0,1] interval near the Fermi level, with larger values closer to the HOMO and smaller values closer to the LUMO. The application of the FD distribution to SCC-DFTB wavefunction effectively allows the description of ensembles of electronic states in an average sense, and we did not include spin polarization in our QM/MD simulations of metallic or near-metallic systems where its effects are small due to the

high density of states near the Fermi level. Since DFTB is based on DFT, it inherits both the strengths and weaknesses of DFT. Molecular geometries and vibration frequencies [92] calculated using DFTB are therefore generally reliable. Extensions to include dispersion interactions have been reported as early as 2001 [93]. On the other hand, DFTB is subject to the self-interaction error of DFT [94, 95].

The MD method essentially involves the discrete integration of Newton's equations of motion as a function of time. Since its conception [96, 97], it has been applied with great success in fields as diverse as molecular physics, materials science, and biological sciences. The discretization of time in MD integration may be achieved in a number of different ways. One such method is the Velocity–Verlet algorithm [98], which is perhaps the most popular MD integration scheme today. In this algorithm, both the nuclear coordinates and velocities are updated at each iteration of the integration, using coordinates/velocities of the previous iteration

$$x\left(t+\Delta t\right) \approx x(t) + v(t)\Delta t - \frac{1}{2m}\nabla U\left(x(t)\right)\Delta t^2 \tag{5.5a}$$

$$v\left(t+\Delta t\right) \approx v(t) - \frac{1}{2m}\left[\nabla U\left(x(t)\right) + \nabla U\left(x\left(t+\Delta t\right)\right)\right]\Delta t \tag{5.5b}$$

where U is the derivative of the electronic potential energy (in this case calculated using DFTB or SCC-DFTB). Discrete integration of the equations of motion in this fashion results in the microcanonical, or NVE, ensemble (in which the number of atoms, N, the volume, V, and the total energy, E, of the system are held constant). We will limit the present discussion to MD in which N, V, and the system temperature, T, are held constant throughout the simulation. Placing these restrictions on the MD system results in what is otherwise known as the NVT ensemble. There are several popular methods (more commonly known as thermostats) by which the MD temperature is maintained, and each results in the rescaling of nuclear velocities in some way. Of particular note are the thermostats of Anderson [99], Berendsen [100], and the method of velocity scaling [101], which is most simple in its formulation. In the present context, we most often employ the Nosé–Hoover chain thermostat [102–105], in which the nuclear Hamiltonian of the system is augmented with a term representing a heat-bath that is coupled to the degrees of freedom of the system. The augmented equations of motion thus sample microcanonical and canonical distributions in the extended and original systems, respectively. However, care must be taken when deciding the strength at which the Nose–Hoover chain thermostat is coupled to the MD system. Too weak coupling will result in inadequate temperature control, whereas too strong coupling is known to result in high-frequency temperature oscillations.

The nonequilibrium conditions are imposed in our simulation systems either by periodic addition of reactive carbon species such as C atoms, C_2 or C_2H_2 molecules, or by placing systems that are in equilibrium at much higher temperature, such as ensembles of C_2 molecules, in a comparatively low-temperature environment. Occasionally, we also remove particular atom species from a system. Moreover, carbon concentration can be varied in open systems in various ways. Which of

these techniques is employed in our simulations depends on the specific case, and therefore, we will introduce these respective methodologies in the corresponding individual sections.

5.3 Fullerene Formation

5.3.1 Background and Experimental Synthesis

Kroto, Smalley, Curl, and coworkers synthesized fullerenes C_{60} and C_{70} in 1985 by applying the then newly available high-power laser technology for the evaporation of graphite [21]. Higher helium pressure and longer annealing time gave higher relative yield of these two particular species over the other C_n clusters. The authors proposed the soccer ball structure for C_{60} for the following two reasons: First, that in a spherical carbon cage, there are no highly reactive unsatisfied edge valences and, second, that the structure of the truncated icosahedron is aesthetically pleasing. They postulated that pentagons are energetically only favorable if they are completely surrounded by hexagons [59]. For this structural proposal, later verified by spectroscopic measurements, and the consequent discovery of the entire family of fullerenes, the Nobel Prize in Chemistry was awarded to Sir Harry Kroto, Richard E. Smalley, and Robert F. Curl in 1996. Eric A. Rohlfing et al. had published the characteristic bimodal TOF-MS distribution of laser-evaporated graphite soot already in 1984 [106] but did not provide a convincing explanation for the magic C_{60} peak. Earlier than Kroto et al., they had found that for small C_n^+ clusters $1 \leq n \leq 30$, all values of n are allowed, while for larger C_n^+ clusters $n \geq 36$, only even-sized $n = 2$ m species are visible in the TOF-MS. A "forbidden zone" appears between $n = 30$ and 36. Extended Hückel [107] and higher-level ab initio calculations [108] predict that regular polygonal rings are energetically more favorable than open chains from $n > 10$. The low-mass distribution shows magic peaks for C_{11}^+, C_{15}^+, C_{19}^+, and C_{23}^+ species [106]. Wakabayashi et al. independently demonstrated a high abundance of C_{10}^- rings in their TOF-MS experiment for negative anions [56]. Apparently, the $\Delta n = 4$ periodicity can be attributed to Hückel's rule if one assumes that a π-electron was ionized in these cations, leaving 10, 14, 18, and 22 π-electrons in these all-carbon macrocycles. From $n = 36$ onward to higher masses, fullerene cages are the likely structures underlying the observed mass peaks. Today, we therefore interpret the TOF-MS distribution as linear carbon chains in the region $1 \leq n < \sim 10$ [109], macrocyclic rings $\sim 10 \leq n < 30$ [56, 108], and fullerenes $n \geq 36$ [57]. It is clear that the magic peaks at C_{60} and C_{70} are not the result of thermodynamic stability, since the cohesion energy of fullerenes continuously increases with the cage size approaching infinity (and thus graphite) [110, 111]. Moreover, any fullerene synthesis operates under nonequilibrium conditions with a continuous energy and carbon input. The surprising abundance of C_{60} and C_{70} must therefore have a kinetic origin [112, 113].

For higher yield fullerene synthesis, the Krätschmer–Huffman carbon arc process is more suitable [42] than the original laser-evaporation technique. Commercially, combustion of benzene or other hydrocarbons [114] is employed for mass production of C_{60} on the scale of tons/year. Irrespective of the synthesis method, carbon must be exposed to very high temperatures, so that the condensation process of the carbon vapor or hydrocarbon fragments may facilitate the self-assembly of the fullerene cages.

Attempts to rationalize the high abundance of C_{60} and C_{70} were perhaps unconsciously guided by architectural principles, which are rather understandable since the fullerene pentagon-hexagon carbon network immediately bears strong resemblance to the geodesic domes created by American architect Richard Buckminster Fuller [115]. Moreover, Euler's 12-pentagon closure principle combined with the chemical stability conferred by pentagon nonadjacency (the IPR rule), provided a structurally based stability criteria perfectly realized in the I_h–C_{60} and D_{5h}–C_{70} fullerene isomers as the smallest members of cages satisfying both criteria. However, how carbon atoms "find" their locations during the growth of these highly symmetric structures in the chaotic environment of cooling carbon vapor had puzzled experimentalists and theoreticians for a long time. Proposed routes for cage self-assembly involved the orderly stacking of C_2 units ("pentagon road") [57] or C_{10} rings ("ring stacking" mechanism) [56], following rather precisely defined stacking sequences. A single stacking mistake would lead to the wrong cage isomer! The "party line" [116] and "ring fusion spiral zipper" mechanism [117] proposed that linear carbon chains and rings would aggregate to form small closed carbon cages with sizes from C_{38}, after which the highly strained non-IPR cage would grow by C_2 insertion to C_{60} and C_{70}. Such a less directed, more "organic" self-assembly mechanism has the advantage that it can explain the striking absence of cluster sizes between and including C_{29} and C_{37} [57], which would correspond to half-opened carbon basket structures that have many dangling bonds on their edges and are therefore more reactive. A variety of other, partially more exotic self-assembly mechanisms have been proposed, and we refer the reader to an excellent review by Nancy Goroff [118].

5.3.2 Dynamic Self-Assembly of Giant Fullerenes

Theoretical studies based on quantum chemical modeling of reaction pathways have attempted to follow the aforementioned proposed formation mechanisms by identifying their associated transition states and intermediates. We gave a brief overview of these studies in [62]. Starting in 2005, our own quantum chemical molecular dynamics (QM/MD) simulations of cooling carbon vapor began with placing ensembles of C_2 molecules into periodic boundary boxes at 2,000 K temperature, causing spontaneous carbon condensation since this temperature simulates a "shock freezing" of the C_2 molecules that are only in thermodynamic equilibrium at temperatures around 5,500 K. Another aspect of imposing nonequilibrium
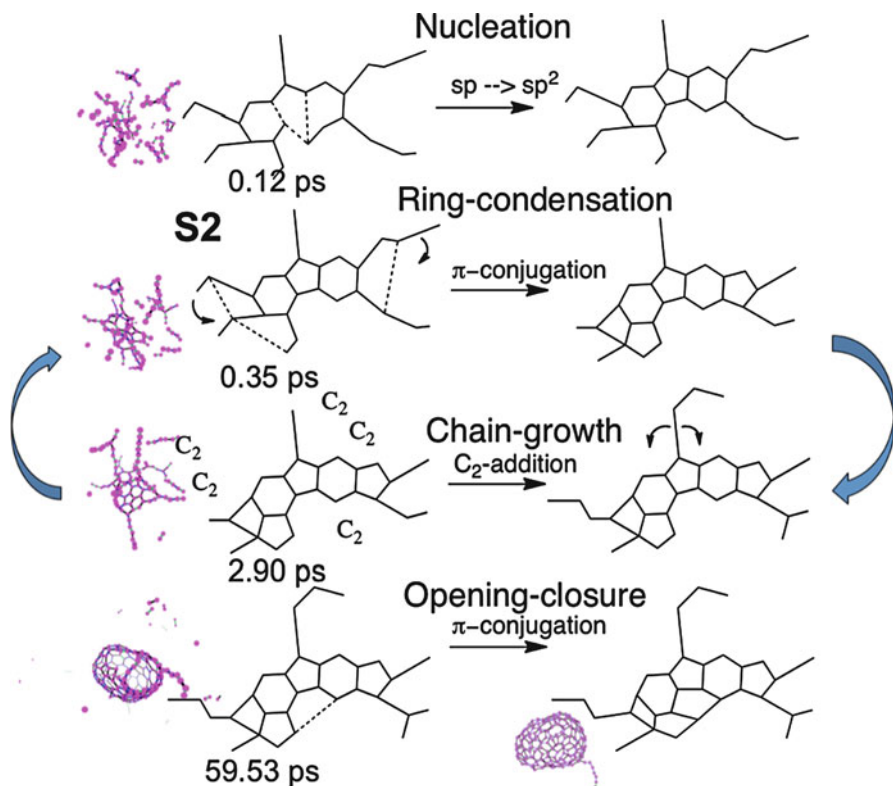
Fig. 5.1 Snapshots of trajectory S2, (modified from Irle et al. [119]) and schematic illustration of irreversible steps during dynamic giant fullerene self-assembly. Note that ring condensation and chain growth may occur simultaneously and repeatedly

conditions was achieved by the periodic addition of more C_2's during the simulation. We observed that giant fullerene (GF) cages with sizes of C_{121} to C_{208} spontaneously self-assembled within 40–110 ps with a yield of approximately 23%, deduced by counting the number of "successful" trajectories [119]. The carbon density in these simulations was increased from 0.09 to 0.18 g/cm^3 as a result of C_2 feeding. Beginning QM/MD simulations with an initial carbon density of 0.20 g/cm^3 and increasing it to 0.35 g/cm^3 dramatically reduced the fullerene cage yield to approximately 5%, while at the same time reducing the cage size to the range C_{74}–C_{96} and producing more amorphous carbon clusters instead [120]. Irrespective of the carbon density, we found that the mechanism of dynamic self-assembly essentially follows three stages: (i) nucleation, (ii) cage growth, and (iii) cage closure. Figure 5.1 depicts schematically the irreversible events occurring during these three stages of GF self-assembly. Stage (i), nucleation, involves the reactive collision of carbon chains that were rapidly created from individual C_2 molecules during the first few picoseconds of the simulations. Covalent bond formation between the chains and

subsequent ring transformations are associated with highly exothermic sp- to sp^2-carbon rehybridization (upper panel of Fig. 5.1). It is important that a large number of strained divalent carbon atoms are avoided in this process: Y-junctions with short arms are better suited to react with each other to produce a high sp^2/sp carbon ratio in the initial condensed ring system, compared to long linear carbon chains. Once a stable "nucleus" of about three fused pentagons and/or hexagons forms, stage (ii), growth, ensues, and the condensed ring system grows rather quickly via ring collapse of attached polyyne chains (second panel of Fig. 5.1). Nearly equal numbers of pentagons and hexagons with a smaller fraction of heptagons are created here. Together, these events resemble closely the party line [116] and ring fusion spiral zipper mechanisms [117]. The carbon chains attached to the nucleus regrow during ring collapse by assimilation of C_n chains from the environment (third panel of Fig. 5.1), and ring collapse proceeds simultaneously. We have named these bowls with attached carbon chains "octopus-on-the-rock" structures and found this very flexible, dynamic, and reactive intermediate also during carbon nanotube growth as well. If the "arms of the octopus" exceed a critical chain length of about ten carbon atoms, it can be found that they form macrocyclic half-ring structures at the boundary of the sp^2 structure (the "body of the octopus"). In GF self-assembly, ring collapse and chain growth are accompanied with annealing of pentagons and heptagons to hexagons and repeated until the remaining cage opening can be closed (bottom panel of Fig. 5.1 in stage iii). It appears that at least for carbon densities between 0.09 and 0.20 g/cm^3, as much carbon as immediately available from the environment is incorporated into the fullerene cage. Higher carbon densities are likely not realized in experiment, while lower carbon densities may indeed favor the creation of smaller fullerene cages as found recently by Ueno et al. [121]. The dynamic self-assembly of GF was also simulated by Yamaguchi et al. [122] using tight-binding MD techniques in 2007. We have recently revisited the dynamic self-assembly mechanism by explicitly including helium carrier gas in our QM/MD simulations by combining DFTB energies with He–He and He–C Lennard Jones potentials and found that the carbon diffusion is indeed slowed down at high carrier gas pressures due to its caging effect, previously postulated based on experimental studies [123]. The caging effect shifts the size distribution of the initially self-assembled GFs toward smaller cage sizes. However, at experimentally optimum helium pressures of around half atmosphere, we still find that the average cage size is larger than 70 atoms, and that shrinking is an important factor for the formation of kinetically stable fullerene cages.

5.3.3   Hot Giant Fullerene Shrinking

To us and others, it was puzzling that only GFs self-assembled in nonequilibrium simulations, although we already mentioned that from a thermodynamic point of view, larger fullerene cages are more stable than smaller ones [110, 111] and require less curvature buildup during the cage self-assembly stage. Subsequent heating of
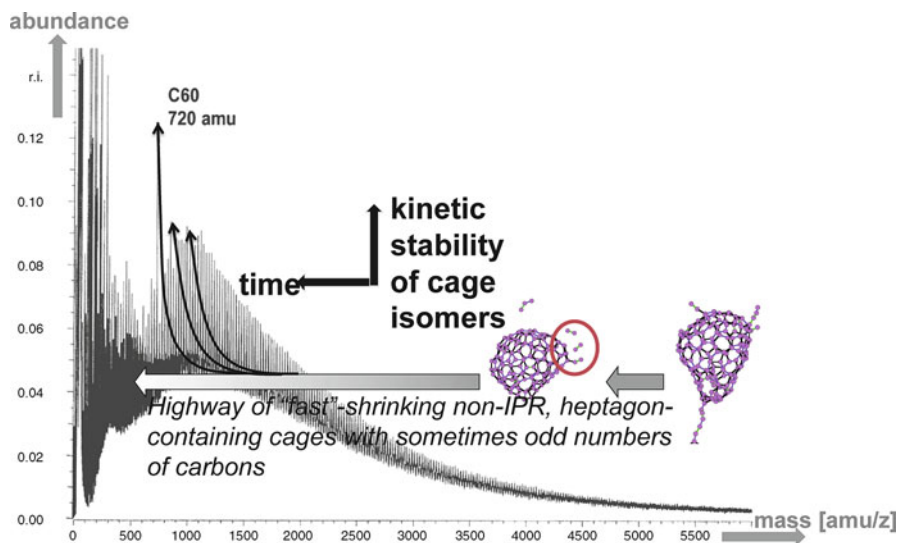
Fig. 5.2 Schematic view of giant fullerene shrinking along the "highway of fast-shrinking, non-IPR, heptagon containing cages" with progressing time from the right to the left, and kinetic stability on the vertical axis, overlying a typical mass spectrum of black soot from Johnson et al. [277]. In this view, the shrinking process is envisioned to lead to smaller, rounder, less defective, and therefore kinetically increasingly stable fullerene isomers. Structures from giant fullerene S3 during shrinking taken from Zheng et al. [125]

these defect-rich giant cages in continued QM/MD simulations demonstrated that they are easily deformable and lose at first attached polyyne antennas ("fall-off") and later C_2 (and to a much smaller amount other small C_n chains) via the same window mechanism first reported for tight-binding MD simulations of C_{60} at temperatures around 5,600 K [124]. In comparison, C_2 evaporation from defect-rich GFs is easier and already occurs on the order of ∼100 ps at temperatures between 2,000 and 3,000 K [41, 120, 125]. During annealing, defect healing occurs on a similar time scale as cage shrinking, and thus, it becomes gradually more difficult for the cages to evaporate C_2 ("pop-out" events). Figure 5.2 shows schematically how a typical mass spectrum of black soot with magic fullerene peaks for sizes C_{60}, C_{70}, C_{76}, C_{78}, and C_{84} can be interpreted as a result of the shrinking process. The initial self-assembled fullerenes themselves possess a size distribution that depends on carbon density and temperature; a TOF-MS of clusters produced by expansion of a supersonic carbon beam into ultracold He indeed showed no special abundance of C_{60} or C_{70} but rather a steady increase in the abundance of higher fullerenes, and the presence of clusters with odd number of carbon atoms [126]. Beginning with these defect-rich GFs, C_2 evaporation leads to cage shrinking. As the GFs are diffusing in the carbon plume or combustion flame, the overall density of carbon material becomes smaller, and therefore, cage growth by C_2 assimilation can be expected to become less efficient than the shrinking process (albeit being exothermic). The latter is fueled by the

abundance of kinetic energy carried by the inert gas required for high yield of C_{60} and C_{70} [127]; the increase in C_{60} and C_{70} yield due to the simple introduction of an "integration cup" by Kroto et al. [21] is another piece of evidence for the importance of annealing and cage shrinking. "C_2 swapping," recently proposed by Curl et al. [128], is not necessarily required for cage shrinking, as we showed in long-term NVT dynamics of GFs at 2,000 K [41, 125]. The ejected C_2 molecules need not be absorbed by other fullerene cages but can be lost to the wall or in soot particles, in particular when the carbon concentration reduces over time as is the case for the expansion of the carbon vapor plume in laser ablation and carbon arc synthesis. In the light of these QM/MD simulations, C_{60} and C_{70} as the *smallest* possible fullerene cages obeying the IPR rule possessing *highest kinetic stability* are the ultimate survivors of a grueling *shrinking* process [62], provided that the synthesis is carried out at sufficiently high temperature and carrier gas pressure [123]. In agreement with the original assumption by Bob Curl [112, 113], the surprising abundance of C_{60} and C_{70} does therefore have a kinetic origin.

5.3.4 The "Shrinking Hot Giant" Road of Fullerene Formation

In the light of the simulation results and discussions given above, one could say that the beautiful molecular structure of the highly ordered and I_h-symmetrical C_{60} molecule simply happens to be a consequence of the fact that it is the smallest member of the Goldberg series (which follows the IPR by construction) of near-spherical, icosahedral carbon cages with closed surface, a closed-shell electronic configuration, and large energetic stabilization [129]. At first, GFs dynamically self-assemble in a three stage autocatalytic process from polyyne chains during irreversible exothermic $sp \rightarrow sp^2$ rehybridization, where occasional pentagons incorporated in growing graphene sheets lend modest curvature to the growing superstructure, ultimately producing closed spherical cages without open edges or dangling bonds. These GFs are highly defective and can lose C_2 units rather easily due to thermal excitations. Between most C_2 pop-out events, the fullerene cage has time to undergo Stone–Wales and related transformations that eventually may lead to the energetically most stable isomer, as Osawa [130] and Maruyama [73] have impressively shown previously in generalized Stone–Wales reaction pathway and reactive empirical bond order (REBO) MD simulations, respectively. Elimination of C_2 molecules from buckminsterfullerene is associated with genuinely high energy barriers since its cage possesses such a strong, rigid framework (the original motivation for Buckminster Fuller to create lightweight yet very stable large dome structures). The high temperatures required for pyrolytic decomposition of I_h–C_{60} (2,650 K) and D_{5h}–C_{70} (2,440 K) [131] demonstrate that these cages, once formed, are extremely hard to destroy. The Stone–Wales transformation for I_h–C_{60} with barriers of 6–8 eV (depending on the choice of the DFT method) requires a temperature exceeding 1,100 K [132], and it can be

assumed that, once a perfect I_h–C_{60} cage was obtained by the combination of C_2 elimination and Stone–Wales transformations, no more structural transformations should occur below this temperature. The cage shrinking via C_2 pop-out therefore necessarily reaches an endpoint at either D_{5h}–C_{70} or I_h–C_{60}, providing the basis for Curl's kinetic origin argument for its abundance as described in [112, 113]. Since there is no IPR fullerene smaller than C_{60}, smaller cages – if formed via routes not involving I_h–C_{60} – most likely disintegrate and become "recycled" in a new dynamic self-assembly process. The I_h-symmetric structure of buckminsterfullerene is therefore the ultimate survivor of the bombardment by carrier gas and other hot carbon fragments, since it does not easily lose C_2 molecules in further pop-out events. The soccer ball as archetype of a nearly round sphere with a minimum number of vertices can be kicked around without much damage to its structure! The argumentation for the abundance of the almost spherical, thermodynamically also favorable closed-shell C_{70} fullerene (the C_{70}:C_{60} ratio is typically 0.1–0.3 [133]) follows similar lines, in particular when considering the fact that C_{60} and C_{70} are the only and therefore smallest IPR satisfying C_n fullerenes with $n \leq 70$. This fact, as well as recent high-resolution transition electron microscopy (HRTEM) evidence of GF cage shrinking [134], clearly supports the validity of the continued shrinking with C_{60} and C_{70} species as the product "of some nozzle process which is removing the other clusters from the beam," as Smalley et al. already suggested in their original works [135]. We named the combination of dynamic GF self-assembly and cage shrinking the "shrinking hot giant" (SHG) road of fullerene formation. Our more recent QM/MD simulations [136, 137] of combustion fullerene synthesis [114] confirmed that SHG applies also in the case where hydrocarbon fuels are burnt in an oxygen-lean environment. The presence of hydrogen was found to effectively delay ring condensation, which is stage (ii) described in Sect. 5.3.2, as it proves more difficult for radical sites to find divalent carbon reaction partners along oligoacetylenic chains or at the edges of polyaromatic hydrocarbon flakes [137]. Only when the H/C ratio drops to about 5–10%, fast polygonal network formation via ring condensation reactions was observed, leading to the self-assembly of GFs in analogy to the pure carbon simulations [137].

5.3.5 Growth of Fullerene Cages

Although thermal shrinking is now a widely accepted mechanism, recent HRTEM observations of direct fullerene formation from a graphene flake [138] and of catalyst-free fullerene growth inside nanotubes [139], as well as the symmetric smooth size distributions of fullerene laser coalescence products around main buckminsterfullerene dimer (C_{118}), trimer (C_{178}), etc., peaks [140] are seemingly at odds with the SHG road. We note, however, that in the growth and coalescence experiments, a tightly sealed environment is required, and that C_2 can presumably not escape in such an experimental setup. It therefore appears that in addition to C_2 evaporation, the reverse process, namely, C_2 capture, should exist as well and

was "overlooked" by our previous QM/MD simulations of cage shrinking, which were performed in free vacuum [120, 125]. Curl and coworkers recently proposed a "spreading the distribution" mechanism based on C_2 exchange between fullerene cages with the goal to explain the experimentally observed abundance patterns [128]. Such line of thinking follows an earlier theoretical work by Yi et al. who reported a possible $C_{58} + C_{62} \rightarrow 2C_{60}$ coproportionation mechanism [141]. Indeed, if the system was in chemical equilibrium as it is in a *tightly closed environment*, the principle of microcanonical reversibility would apply, and C_2 ejection and capture reactions should occur at equal chemical reaction rates.

To verify this hypothesis, we recently performed constant temperature/constant density direct quantum chemical/molecular mechanics (QM/MM) molecular dynamics (MD) simulations of dynamically self-assembled, hot GFs with their attached polyyne antennas on the nanosecond timescale. In the microcanonical ensemble (NVE simulations), we included explicit ambient buffer gas helium or argon atoms at high pressures, and in constant temperature simulations, we employed a velocity scaling thermostat, keeping the system pressure relatively low. It was found that hot GFs are able to grow as well as shrink during continued high temperature simulations, on the order of several carbon atoms per nanosecond. Growth of GF occurred via end-on attack of C_2, followed by either destruction of its C–C bond or by capture of its dangling bond by cage carbon atoms. *A concerted insertion of C_2 into six-membered rings as in the Endo–Kroto mechanism* [142, 143] *was not observed in our simulations.* On the other hand, C_2 ejection followed the previously described routes, namely, a window mechanism [41, 120, 124, 125] or, for instance, a carbene defect-catalyzed pathway. It was observed that larger GFs (>100 cage carbons) have a tendency to shrink whereas smaller GFs (<100 cage carbons) tend to grow. However, the C_2 ejection and insertion rates depend strongly on the concentration of available carbon outside the cages: a larger number of free carbons increase the growth rate, whereas a smaller number increase the shrinking rate. Nevertheless, given this observation from constant density simulations, it seems reasonable that the fullerene cage size abundance should peak at a certain GF size, as obtained by kinetic modeling based on the assumption of a C_2 swapping equilibrium system [128]. The presence of explicit buffer gas and the resulting higher pressure favor the shrinking process, in agreement with experimental increased yield for C_{60} and C_{70} with higher buffer gas pressure [21].

5.3.6 Novel Aspects of the SHG Mechanism

In realistic pure carbon-based systems, in particular in the first stages after laser ablation and production of the carbon vapor plume, the carbon concentration is high. Small cage formation may play an important part at this stage, as was shown by Ueno and Saito in the C_{10} collision simulations [121]. However, our simulations including helium carrier gas at experimental pressures show that large cage growth (>70 atoms) via dynamic self-assembly prevails, and that the number of directly

formed C_{60} and sub-C_{60} fullerene cages is not very large. As the carbon vapor plume expands and is carried away and cooled by the buffer gas, the carbon concentration gradually reduces, and the hot GFs will tend to shrink as a result of the nonequilibrium conditions enforced by the carbon density gradient. The energy required for the endothermic shrinking process is available since the formation of GFs is highly exothermic. Our results indicate that fullerene formation under typical conditions is a kinetically controlled shrinking and annealing process. On the other hand, the present simulations can explain the fact that fullerene molecules can grow inside carbon nanotubes [139], and that fullerene coalescence [140] experiments in a *tightly sealed environment* can produce oligomers with a higher number of carbon atoms as present in the component monomers. Most intriguingly, we extrapolate from our simulations that C_2 swapping between GFs after cage self-assembly may lead to total replacement of all constituent carbon atoms of the initial GF cage, since the experimental time of fullerene synthesis is on the order of $1,000\,\mu s$ [144]. If this does indeed happen, it becomes literally true that fullerene cages are dissipative structures formed under nonequilibrium conditions, similar to atmospheric clouds or biological systems. This would then be the first time that the formation of a molecular, covalently bound structure is explained in terms of Prigogine's theory of self-organization in nonequilibrium systems [64, 145].

5.4 Carbon Nanotube Formation

We turn now to a discussion of our recent QM/MD simulations of SWCNT nucleation, growth, and healing. This discussion will focus on the mechanism of SWCNT nucleation on a number of different catalyst nanoparticles, including Fe, Ni, SiO_2, SiC, and Si. SWCNT nucleation resulting from both model CVD and arc-discharge processes will also be discussed. In this way, we will demonstrate that, at the atomic level, the mechanism of SWCNT nucleation is surprisingly invariant to both the experimental method employed and several pertinent environmental factors. Similar as for the fullerenes, we begin with a brief description of the popular experimental synthesis methods.

5.4.1 Background and Experimental Synthesis

The laser-evaporation technique that was employed first in the discovery of buckminsterfullerene [21] can also be used to generate both SWCNTs [146, 147] and multi-walled CNTs (MWCNTs) [148]. Carbon arc-discharge [149–151] and solar furnace methods [152] may also be employed. Common to all these methods is the fact that a graphite target containing a transition metal (TM) (ultimately the catalyst for the synthesis of SWCNTs) is used. In fact, Bethune had initially tried to generate endohedral metallofullerenes containing cobalt when he discovered

that the Krätschmer-Huffman carbon arc process in this case produced webs of carbon fibers instead of the expected metallofullerenes [153]. Multiple pulses are found to produce higher SWCNT yields and greater purities in case of pulsed laser vaporization (PLV) [154] and to produce double-walled CNTs (DWCNTs) in case of high-temperature pulsed arc discharge (HT-PAD) [155]. It is thought that the first pulse produces many large graphene fragments, and that subsequent pulses further decompose these carbon clusters [156]. However, without doubt, the processes occurring in the immediate ablation zone are very complex and still not well understood [157]. For fullerene and CNT synthesis, subsequent heating after the initial pulse(s) is always required, and furnace temperatures vary typically between 1,000 and 1,500 K. If on the other hand the carbon plumes are allowed to cool to room temperature immediately after a pulse, single-walled nanohorns (SWNHs), in the case of laser evaporation [29], or amorphous carbon, in the case of HT-PAD, are produced [155]. In contrast to fullerene synthesis, where He is most efficient, Ar and N_2 [158] are excellent carrier gases in both PLV and carbon arc syntheses of SWCNTs. The task of the carrier gas is likely to evenly distribute kinetic energy and thus "thermostat" the carbon plumes. By-products of SWCNTs in PLV synthesis are frequently fullerenes, giant fullerenes, as well as graphite onions [159, 160], but the amount of amorphous carbon produced in carbon arc methods is typically somewhat greater.

Apart from these "pure carbon"–based CNT synthesis methods, catalytic CVD (CCVD) SWCNT syntheses are nowadays widely used in particular because they are more promising for industrial-style continuous nanotube production. Perhaps most famous is the high-pressure CO conversion (HiPco) synthesis developed at Rice University, which relies on the Bouduard charcoal reaction: $2\,CO \rightarrow C + CO_2$ [49]. In early times, $Fe(CO)_5$ and $Mo(CO)_6$ were used as the gaseous source for both metal catalyst and carbon (floating catalysts) in the HiPco process, but ferrocene, ethylene, acetylene, and other feedstock species have gradually replaced the carbonyl compounds [48, 161]. Only recently has CO staged a comeback in the context of chirality control when employed in combination with NH_3 [162]. When the metal catalyst is deposited on a substrate like Al_2O_3 or SiO_2, vertically aligned nanotube arrays (VANTAs) of SWCNTs and MWCNTs can be grown in high yield on the catalyst surface [163]. H_2 is commonly mixed in the carrier gas in order to continually reduce the metal catalyst, to etch the metal catalyst particle surfaces, and to promote hydrogen abstraction from the hydrocarbon feedstock by virtue of an anti-Le Chatelier behavior common to open dynamic nonequilibrium systems. In CCVD synthesis, oven temperatures are typically lower than in the case of laser ablation or carbon arc syntheses, namely, around 500–900 K, but can go up as high as 1,500 K [164].

Following different approaches, Maruyama et al. [50] and Hata et al. [165] found that the presence of oxygen during the CCVD synthesis leads to increased yield and tube lengths, by the admixture of water vapor or the use of ethanol (alcohol CCVD or short ACCVD) as carbon source, respectively. Also, sulfur has been successfully used to increase the yield of SWCNTs [166] or prompt SWCNT Y-junction formation [167]. It is believed that the role of the chalocogens is to burn

away amorphous carbon [168, 169], or to capture hydrogen radical atoms, which would favor the formation of amorphous carbon by sp^3-carbon production [170]. As to the latter argument, it has recently been demonstrated that the presence of atomic hydrogen is in fact important for both nucleation and growth mechanisms [171]. Recent evidence points to the prevention of Ostwald ripening of the metal catalyst as a major role of water in the vertically allowed SWCNT carpet growth [172]. A hybrid method combining both laser-evaporation and CCVD syntheses is laser-assisted CCVD (LCCVD), which is a high-quality, albeit expensive, SWCNT synthesis method [173].

5.4.2 SWCNT Nucleation: Acetylene Oligomerization on Metal Particles

Today, CVD synthesis of SWCNTs from hydrocarbon feedstock is perhaps the most popular method of choice on the commercial scale. The most typically employed gaseous precursors include acetylene, ethanol, and methane (almost always in the presence of some inert buffer/carrier gas). Yet little is known regarding the atomistic mechanism of such carbonaceous CVD processes. Here, we will focus on the mechanism of Fe-catalyzed acetylene CVD elucidated from our recent QM/MD simulations [174].

   In order to investigate the Fe-catalyzed acetylene (C_2H_2) CVD process, we employed an Fe_{38} catalyst nanoparticle. The diameter of this nanoparticle is ca. 0.9 nm and so is at the lower end of the experimental SWCNT diameter distributions [175]. Thirty C_2H_2 molecules were initially supplied at periodic intervals onto the equilibrated catalyst nanoparticle (see Fig. 5.3a), after which the resultant $(C_2H_2)_{30}Fe_{38}$ model complex was annealed at 1,500 K for 500 ps. During the C_2H_2 adsorption process, the occasional abstraction of atomic H by the Fe-catalyst surface was observed, leading to the presence of C_2H radicals on the particle surface. Similarly, abstraction of atomic H by adjacent C_2H_2 molecules was also observed, resulting in both C_2H and C_2H_3 species. Both abstraction processes are endothermic, with barriers between ca. 20 and 35 kcal mol^{-1}. The direct formation of H_2 was not observed, despite the abstraction of atomic H by the catalyst surface. This is not surprising, considering the high endothermicity of the H_2 formation process (using SCC-DFTB, this barrier is estimated to be ca. 35–50 kcal/mol^{-1}). Such endothermic processes are inherently difficult to observe in unbiased MD simulations on this time scale. The radical products C_2H and C_2H_3 are extremely reactive and therefore rapidly initiated oligomerization between adjacent C_2H_x species. Such oligomerization is exothermic by ca. 18 kcal mol^{-1} (see Fig. 5.3b). Following these oligomerization reactions, extended sp^2-hybridized carbon networks ultimately form on the catalyst surface via cross-linking of neighboring oligoacetylene-like chains, resulting in the formation of pentagonal and hexagonal carbon rings. In all cases, pentagonal rings were formed first – an
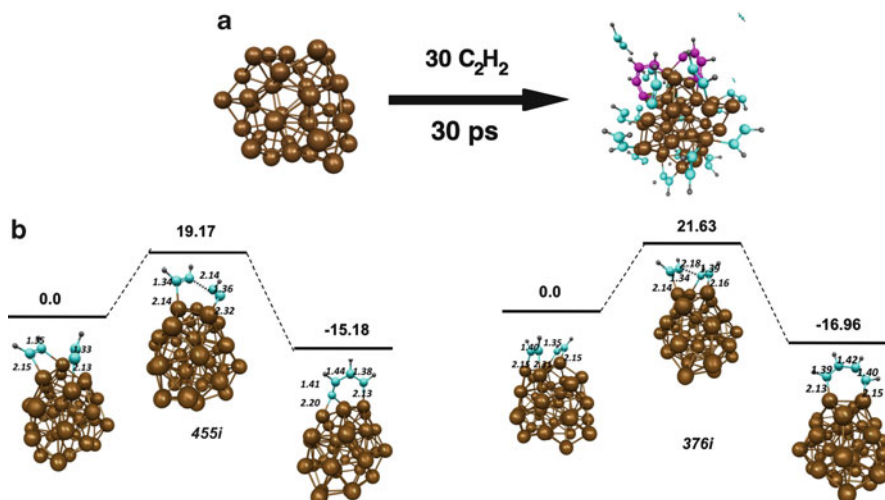
Fig. 5.3 The initial stages of simulated acetylene CVD on Fe_{38} catalyst nanoparticles at 1,500 K. (**a**) Oligomerization results in the formation of extended polyyne chains on the catalyst surface within 30 ps. (**b**) Examples of C_2 oligomerization and their associated energetics. Examples of both the $C_2H_2 + C_2H \rightarrow C_4H_3$ and $C_2H_2 + C_2H_2 \rightarrow C_4H_4$ oligomerization reactions are depicted. The C_2H precursors here are occasionally produced via the abstraction of atomic H onto the catalyst surface. All energies and bond lengths given in kcal mol^{-1} and Å, respectively. Energies of transition state frequencies are given in cm^{-1}

observation that will frequently recur in Sects. 5.4.3, 5.4.4 and 5.4.5. Such a cross-linking process is depicted schematically in Fig. 5.4. Also depicted in Fig. 5.4 is the polyyne cross-linking mechanism (pertaining to SWCNT growth) proposed by Eres [61]. While both processes are distinctly similar, no pure hexagonal ring networks were formed in the cross-linking processes observed in our QM/MD simulations.

Figure 5.5 shows the ultimate products of the H-abstraction and oligoacetylene oligomerization/cross-linking processes, namely, the formation of an extended sp^2-hybridized carbon network. The structure of this network generally fell into one of three categories. The most "successful" structure regarding SWCNT nucleation is structure (i), in which the network extends over the catalyst surface. In essence, such a structure constitutes a SWCNT cap fragment, similar to the "yarmulke" cap proposed by Smalley and coworkers [176]. However, structure (i) was only observed at relatively low H/C ratios (see Sects. 5.4.3 and 5.4.4 for examples of SWCNT nucleation in the absence of H). In cases of higher H/C ratios (i.e., more H), structure (ii) was typically observed due to the passivating effect of H at the unsaturated edge of the carbon network. It is assumed that this graphene-like sheet may coalesce to form an open nanotube according to the mechanism proposed by Eres [61] (cf. Fig. 5.4), and we point out that polyacetylenic species and polyaromatic hydrocarbons represent a large fraction of the exhaust gas during CCVD SWCNT synthesis. Structure (iii) was also observed as a result of the
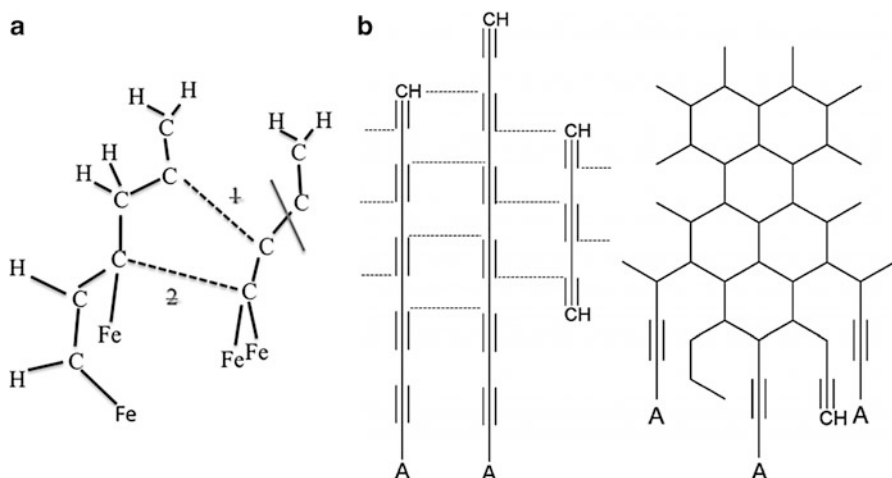
Fig. 5.4 Cross-linking of extended polyyne chains on the catalyst surface leads to carbon ring formation. (**a**) Explicit example of cross-linking observed in QM/MD simulations. Numbers *1* and *2* indicate reaction step. (**b**) Cross-linking reaction proposed by Eres et al. [61], resulting in the formation of a graphene-type structure (Reprinted from Eres et al. [61] with kind permission of © The American Chemical Society (2009))
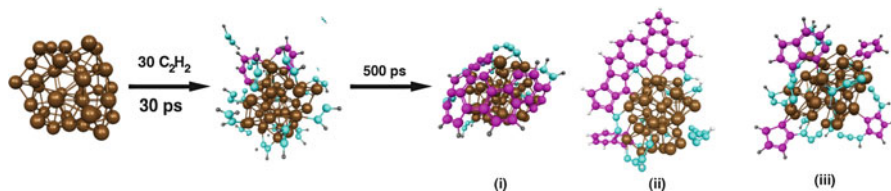
Fig. 5.5 An extended sp^2-hybridized carbon network is formed on the catalyst surface following polyyne oligomerization. QM/MD simulations indicate that structures (*i*), (*ii*), and (*iii*) are typically formed. Structure (*i*) is akin to the "yarmulke" SWCNT cap fragment proposed by Smalley et al. [176]. Structure (*ii*) is typically formed in the presence of higher H concentrations and points to the possibility that SWCNT nucleation may take place in the absence of a SWCNT cap fragment. Structure (*iii*) features a catalyst nanoparticle covered with sp^2-hybridized carbon "islands"

polyyne oligomerization/cross-linking process. In this case, the process yielded "islands" of sp^2-hybridized carbon. The presence of hydrogen at the edges of the growing sp^2 carbon network substantially slows down the ring collapse mechanism that was rapid in stage (ii) of the fullerene self-assembly mechanism described in Sect. 5.3.2. The origin of the growth inhibition by hydrogen in this case is identical to the delay of stage (ii) ring collapse reactions during fullerene combustion synthesis [136, 137], described in Sect. 5.3.3. Assumedly, QM/MD annealing of hydrogen-rich structures over longer time scales (i.e., several nanoseconds) and in the presence of hydrogen atoms acting as hydrogen scavengers might yield a more consistent network after hydrogen removal, such as that typical of structure

(i). Nevertheless, we wish to stress here that SWCNT nucleation is not *necessarily* preceded by a carbon cap structure, or a liquid carbide phase, as structure (ii) demonstrates. The latter observation will be corroborated in Sect. 5.4.3.

5.4.3 SWCNT Nucleation: Metal Type and Size Effect

It was observed in Sect. 5.4.2 that the removal/sequestration of hydrogen from feedstock acetylene molecules was – somewhat surprisingly – the most problematic issue in these QM/MD simulations. Presumably, the same problem would exist regardless of the type of carbonaceous precursor employed in this respect (be it acetylene, methane, ethanol, etc.). This difficulty arises due to a problem inherent to MD methods since such methods have difficulty overcoming large energy barriers on the global potential energy surface (PES). Although, in the limit of infinite time, an MD simulation will sample all possible geometrical configurations and consequently will have overcome all such barriers on the global PES. In practice however, this is not possible considering the relatively short time span achievable with MD simulations. To this end, we will discuss an alternative QM/MD approach to the problem of SWCNT nucleation on Fe catalysts [177].

In the present approach, the hydrogen was simply removed from the gas-phase carbonaceous molecules prior to their interaction with the catalyst nanoparticle. This left us with atomic carbon or C_2 molecules as carbon supply, the latter of which has been confirmed to be an abundant and important species during laser ablation SWCNT synthesis [178, 179]. It should be mentioned that such an approach represents a deviation from both CVD and pure carbon-based experimental conditions. On one hand, in hydrocarbon CVD synthesis, it is clear and we have shown in Sect. 5.4.2 that hydrogen may play an important role in the SWCNT nucleation process (and similarly, during continued SWCNT growth). On the other hand, in pure carbon SWCNT synthesis methods such as carbon arc or laser evaporation, it is assumed that the catalyst particles are either supersaturated with carbon dissolved at the time of metal/carbon co-condensation from the plasma from which carbon caps segregate [180–182], or that hemi-spherical fullerene fragments form caps on condensing metal or metal carbide particles [183, 184]. The vapor–liquid–solid (VLS) mechanism [185, 186] is often quoted for this type of SWCNT growth, but details of the mechanism depend strongly on the type of catalyst, temperature profiles, and prevailing pressures in the various experimental setups. By adding carbon atoms or C_2 molecules onto pure metal particles, we are closer to the simulation of laser ablation or carbon arc SWCNT synthesis, yet neglect the fact that the metal particles possibly contain a large amount of carbon, and that the carbon environment is certainly more complex and consists of more than a single feedstock species. Nevertheless, for the sake of manageability of the simulations at a stage where we could no longer perform an accurate modeling of experimental conditions, we resorted to the periodic supply of 30 C_2 molecules onto a pure metal nanoparticle. Figure 5.6 depicts this adsorption process and the process of
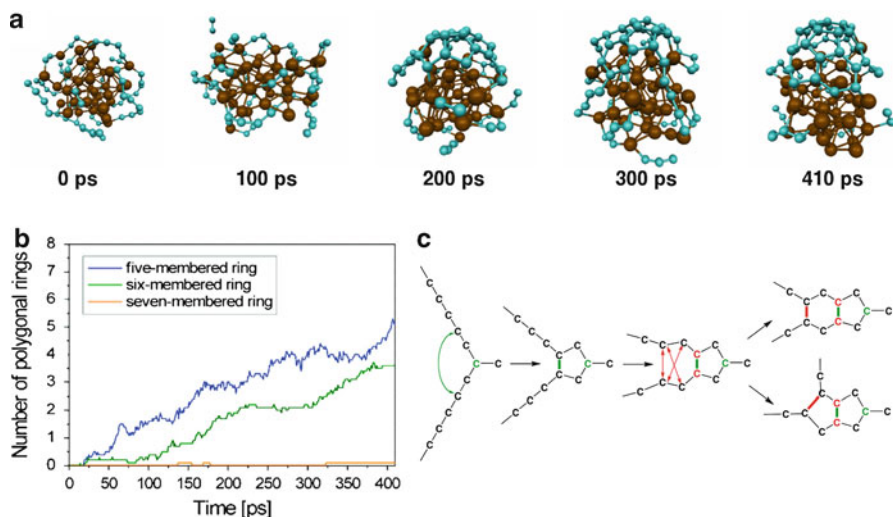
Fig. 5.6 SWCNT nucleation occurs via three distinct stages according to QM/MD simulations. (**a**) QM/MD relaxation of a 30 C_2 – Fe_{38} model system at 1,500 K yields a distinct SWCNT cap fragment after 410 ps. (**b**) SWCNT nucleation is driven by successive ring condensation events on the catalyst surface. The preferential formation of pentagonal rings in this structure is attributed to the curvature of the catalyst surface and the diffusion dynamics of extended polyyne chains. (**c**) The SWCNT nucleus. A single sp^2-hybridized carbon atom acts as the cornerstone of all subsequent ring formation events in the nascent SWCNT structure (Adapted from Ohta et al. [177] with kind permission of © American Chemical Society (2009))

constant temperature annealing that followed. In this case, the MD relaxation of this Fe_{38}-carbon system was continued for 410 ps. Figure 5.6a shows that the SWCNT nucleation process may be partitioned into three distinct stages. Initially, C_2 units bound to the Fe_{38} catalyst surface from the gas phase. The relatively weak Fe–C interaction energy facilitated the subsequent diffusion of these C_2 units over the catalyst surface. As a natural consequence of this diffusion, C_2 units ultimately began to interact with each other, coalescing to form longer polyyne chains (i.e., Fe–C_n–Fe structures) and "Y-junctions" (sp^2 carbon atoms with three short linear C_n chains attached, the so-called tri-furcates mentioned in [122]). This was apparently the rate-limiting step of the nucleation process, in that it was ca. 100 ps before the second stage of the nucleation mechanism took place (Fig. 5.6b). This second stage featured the initial ring condensation processes on the catalyst surface, while the subsequent third stage consisted entirely of additional ring condensation events, resulting in the formation of a SWCNT cap fragment. The exact mechanism of the initial ring condensation process from a single Y-junction is depicted in Fig. 5.6c. Figure 5.6b shows that there was generally a preference for the formation of pentagonal rings, as opposed to hexagonal or heptagonal rings, during the initial stages of SWCNT nucleation. Indeed, the initial ring structure formed was pentagonal as shown in Fig. 5.6c. This fact is consistent with our simulations

regarding the formation mechanism of fullerenes at high temperatures as described in Sect. 5.3.2, where Y-junctions are also the precursors of polygonal ring networks. The longevity of these pentagonal rings, however, is attributed to the high positive curvature of the catalyst nanoparticle surface (due to its small diameter) [187]. In effect, our simulation results seem to suggest that the growing sp^2-hybridized carbon network attempts to "mold" itself to its supporting catalyst substrate from its very beginnings.

The initial pentagonal ring observed in Fig. 5.6 acted as an anchor, or corner-stone, for all subsequent ring condensation events. This period of ring condensation (stage three of the nucleation process) consisted of a periodic process (Fig. 5.6c) in which adjacent polyyne chains interacted on the catalyst surface due to their diffusion, thus extending the sp^2-hybridized carbon structure. This process is best illustrated by the initial ring condensation event, in which two adjacent polyyne chains coalesced, resulting in the above mentioned "Y-junction." This initial sp^2-hybridized open-shell carbene with one carbon atom was, in essence, the nucleus of the final SWCNT itself since all subsequent ring condensation was based around it. The first pentagonal ring formed following the movement of two Y-junction branches toward each other. With respect to the original sp^2-hybridized carbon atom, the most energetically favorable interaction corresponded to the interaction between the second carbon atoms of each arm. In this way, only two divalent carbon atoms, unfavorably bent to 108°, become members of the first pentagonal ring. The bending causes these divalent carbon atoms to take the electronic configuration of a open-shell carbene with one π-electron participating in the π-conjugation of the carbon ring and one unpaired σ-electron that will receive significant stabilization by metal-carbon bonds from the catalyst surface. If one simply considers only carbon-carbon bonds to determine the valence hybridization of the carbon atoms in the carbon structures on the catalyst, the sp/sp^2 ratio of the first pentagon ring is 2/3 (since the original Y-junction has three branches); if a hexagon had formed, this ratio would be $3/3 = 1$ and therefore require greater stabilization from the catalyst. However, the catalyst should not come "too close" to the growing sp^2 carbon network, as the latter only weakly binds via van der Waals forces to the metal particle: carbon atoms with three carbon-carbon bonds do not interact strongly with the metal surface. We therefore observed that the initial pentagon was formed on top of a metal vacancy and "clamped" in between metal atoms that could both be considered a "step edge." In subsequent ring collapse events leading to condensed ring systems, pentagons as well as hexagons had similar probabilities of formation because the formation of a hexagon from an already existing pentagon with two attached carbon chains has an sp/sp^2 ratio of 2/3, equal to that of the formation of the *first* pentagon.

As mentioned in Sect. 5.3 and will be discussed in Sects. 5.4.6 and 5.5, extended polyyne chains play a dominant role not only in fullerene formation and SWCNT nucleation but also in the subsequent "continued" growth of SWCNT structures, and the formation of graphenes. In this sense, SWCNT growth is therefore very similar to the dynamic self-assembly of fullerenes (ring condensation growth via the "arms of the octopus" see Fig. 5.1) [62, 119]. This leads to the conclusion
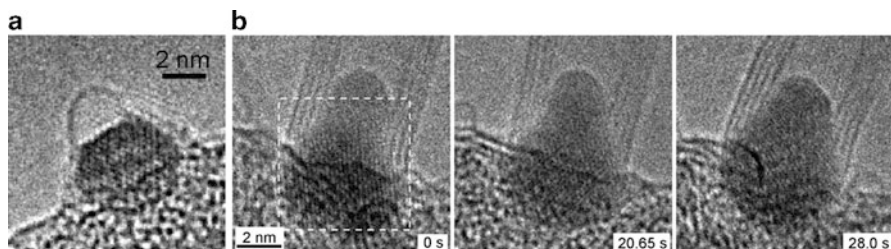
Fig. 5.7 TEM images of intermediate structures observed during SWCNT growth experiments. (**a**) A SWCNT cap fragment bound to a crystalline Fe_3C nanoparticle with an approximate diameter of 2 nm (Adapted from Yoshida et al. [191] with kind permission of © The American Chemical Society (2008)). (**b**) A MWCNT growing from a $(Fe, Mo)_{23} C_6$ nanoparticle catalyst. In this case, the nanoparticle diameter is ca. 6 nm (Adapted from Yoshida et al. [191] with kind permission of © The American Chemical Society (2009))

that such polyyne chains are essential for both the conception and the extension of any sp^2-hybridized carbon network. Of course, the crucial difference between SWCNT and fullerene nucleation here is the presence of the catalyst nanoparticle. In particular, it is noted that the QM/MD simulation presented in Fig. 5.6 once again verifies the original proposal of Smalley et al., namely, that one of the fundamental roles of the catalyst nanoparticle is to prevent the closure of the growing sp^2-hybridized structure [147]. We note that the carbon network growth via ring collapse of short carbon chain mirrors the mechanism of SWCNT sidewall destruction, studied by us in [188, 189]. The image of short polyyne chains attached to the open end of a growing or disintegrating SWCNT was probably first invoked by Rick Smalley in his comparison to the unraveling of the sleeve of a sweater [190].

5.4.4 Nucleation from Transition-Metal Carbide

According to the VLS mechanism [185, 186], CNT nucleation and growth are preceded by a gaseous carbon/catalyst phase which co-condenses, forming a catalyst-carbide nanoparticle. Images of transition-metal carbide nanoparticles during SWCNT growth have been obtained using transmission electron microscopy (TEM) on several occasions [191, 192] (see Fig. 5.7). Yet, to date, there is no experimental evidence indicating that this carbide phase *necessarily* precedes the nucleation and growth of SWCNTs, and indeed, environmental TEM images have also supported the existence of pure metal phases during growth in the case of nickel [193]. Anisimov et al. went in fact so far to say that cementite (Fe_3C) particles are catalytically inactive [194]. Our QM/MD simulations discussed in Sects. 5.4.2 and 5.4.3 indicate that, for nanoparticle catalysts of ca. 1 nm, a carbide phase is not formed at 1,500 K when carbon is added from the outer environment and is not necessary for the SWCNT cap formation process. Recently, even the thermodynamic stability of bulk transition-metal carbide nanoparticles have
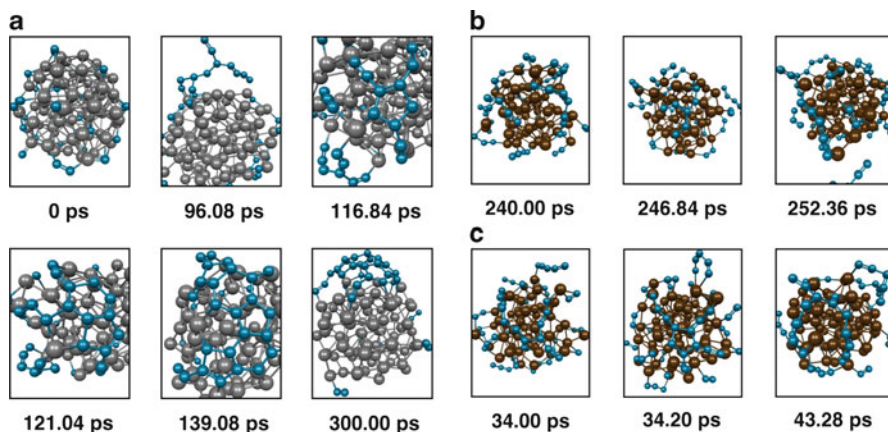
Fig. 5.8 The kinetics of SWCNT nucleation from Ni–carbide is enhanced relative to those from Fe–carbide. Nevertheless, the mechanism of SWCNT nucleation is identical in both cases. (**a**) The evolution of a computed SWCNT nucleation trajectory from a $Ni_{77}C_{39}$ carbide nanoparticle at 1,400 K. The SWCNT cap fragment is formed within 300 ps following repeated ring condensation events. (**b**), (**c**) The evolution of two $Fe_{58}C_{58}$ carbide nanoparticles at 1,400 K. The stronger Fe–C interaction impedes the formation of C–C bond and therefore impedes the SWCNT nucleation process itself. Both trajectories show examples of the formation, and subsequent destruction, of pentagonal carbon rings (Adapted from Page et al. [196] with kind permission of © The American Chemical Society (2010))

been drawn into question from a number of independent approaches [194, 195]. Assumedly then, SWCNT nucleation may occur in the *absence* of a carbide phase. Such disparities between theoretical and experimental assertions give reason for further study of the role of the carbide phase to SWCNT nucleation and growth.

QM/MD simulations of SWCNT nucleation from amorphous Fe- and Ni-carbide nanoparticles of ca. 1.3 nm size at 1,400 K are depicted in Fig. 5.8. It is evident from this figure that, upon MD annealing at constant temperature, the amorphous carbide phase almost immediately decomposes (within ca. 5–10 ps), yielding segregated Fe/Ni-carbon systems. This phenomenon is known to take place regardless of temperature or the carbon concentration in the amorphous carbide phase [196]. Figure 5.8 also indicates that the SWCNT cap nucleation mechanism in this case (from a Ni-carbide) is the same as that presented in Sect. 5.4.3. For example, the almost immediate precipitation of carbon from the nanoparticle bulk to the surface leads to the formation of extended polyyne chains over the nanoparticle surface. The oligomerization/cross-linking, etc., of these chains then leads to the formation of primarily pentagonal and hexagonal rings (Fig. 5.8a) as the SWCNT cap fragment is formed. The initial ring structure in all cases here is invariably a pentagonal ring and is created by the Y-junction dynamics of Fig. 5.6c. Thus, the SWCNT nucleation mechanism on Fe/Ni catalysts is evidently independent of the type of metal catalyst, the temperature, and the origin/type of the feedstock carbon employed. We find the invariance of the SWCNT nucleation mechanism with respect to these pertinent experimental factors remarkable.
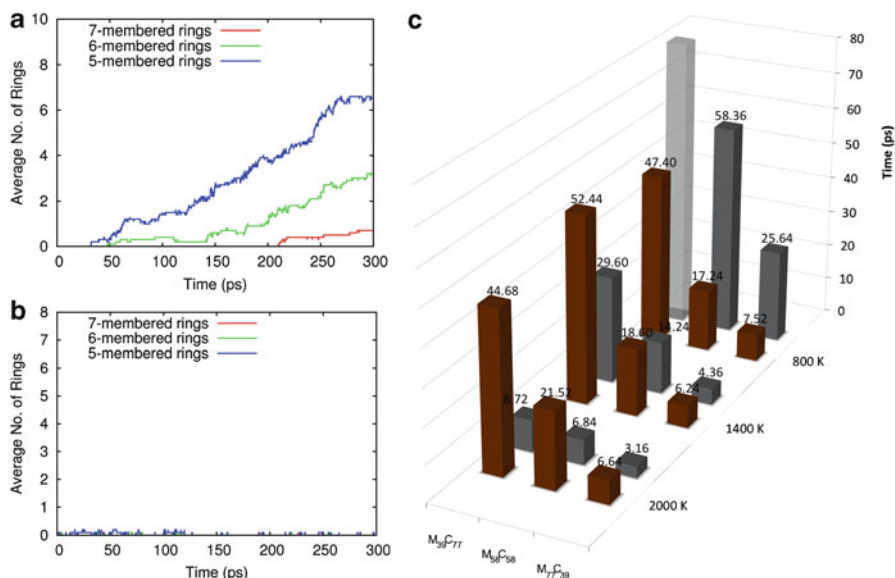
Fig. 5.9 The kinetics of SWCNT nucleation from Ni–carbide is enhanced relative to those from Fe–carbide. Average polygonal carbon rings formed from (**a**) $Ni_{58}C_{58}$ and (**b**) $Fe_{58}C_{58}$ at 1,400 K. (**c**) Average carbon precipitation times (in ps) for Fe- and Ni-carbide nanoparticles between 800 and 2,000 K. Fe-carbide carbon remains within the nanoparticle bulk for a longer time period, compared to Ni-carbide carbon, due to the stronger Fe–C interaction. At 800 K, the trend is reversed since Ni–carbide exists in the solid phase. All data averaged over ten trajectories (Adapted from Page et al. [196] with kind permission of © The American Chemical Society (2010))

Despite this invariance, differences in the ultimate product of the nucleation process are evident with respect to both the catalyst type and the simulation temperature. The kinetics of SWCNT nucleation was also affected by the type of catalyst employed – explicitly, SWCNT nucleation from the decomposition of Ni-carbide proceeded more quickly, compared to that from Fe-carbide (see Figs. 5.8 and 5.9). It was observed that at higher temperatures (2,000 K, as opposed to 800 or 1,400 K), the populations of pentagonal and hexagonal rings in the SWCNT cap fragment were approximately equal. On the other hand, at lower temperatures, a distinct preference toward pentagonal ring formation existed. These differing ring populations were ascribed to the effect of temperature on the SWCNT nucleation dynamics. At higher temperatures, the growing polyyne chains on the catalyst surface are more thermally excited and thus exhibited larger amplitude vibrational motion. Considering the pentagonal ring mechanism given in Fig. 5.6c, this increased motion makes the formation of a C–C bond between tertiary carbon atoms (with respect to the sp^2-hybridized "cornerstone" carbon atom) more likely. It also allows metal atoms to leave the nanoparticle surface and bind more tightly to the divalent bent carbon atoms of the initial carbon polygon. Hence, hexagonal ring formation is more probable in this case. Perhaps the most

important difference observed between the kinetics of SWCNT nucleation from Fe- and Ni-carbide nanoparticles, however, pertains to the relative rates of SWCNT nucleation. It was recently established that SWCNT nucleation is significantly more labile on Ni catalysts, compared to Fe catalysts. This observation may be directly attributed to the relative strengths of the catalyst-carbon interactions. This theme recurred throughout the present work, as it dominates many aspects of both SWCNT nucleation and growth. For example, the catalyst-carbon interaction strengths between cap fragments and M_{55} nanoparticles, calculated using SCC-DFTB, are 1.78 and 1.06 eV for Fe-C and Ni-C, respectively [197]. For comparison, the C–C interaction strength is 5.84 eV. Therefore, Fe–C bond formation is more favorable than Ni–C bond formation in a thermodynamic sense. Consequently, C–C bond formation during the decomposition of Fe-carbide nanoparticles is impeded, which in turn impedes the nucleation of the sp^2-hybridized carbon network. This argument also explains other phenomena related to SWCNT nucleation, such as the lifetimes of the bulk and subsurface carbide intermediate species [196] (see Fig. 5.9). In particular, the average time required for precipitation of all carbon from the nanoparticle bulk to the nanoparticle surface/subsurface in the case of Fe-carbide always exceeds that for Ni-carbide, except at low temperatures. At 800 K, the reverse is the case since the Ni-carbide nanoparticle enters the solid phase, while the Fe-carbide nanoparticle remains liquid. These QM/MD findings therefore support recent claims that a subsurface carbide structure (in which a high density of carbon exists at, or just below, the nanoparticle surface) precedes SWCNT nucleation and growth [195, 198–201].

5.4.5 Nucleation from Nonmetal Nanoparticles

The mechanism of SWCNT nucleation on traditional, transition-metal catalysts such as Fe, Ni, and Co has now been the subject of both experimental and theoretical scrutiny for approximately a decade. Since 2009, however, a number of experimental reports [202–210] have established nontraditional nanomaterials to be catalytically active in the context of SWCNT nucleation and growth from methane and ethanol CVD. Si-based materials, and in particular SiO_2, have been remarkably successful in this respect. Yet it has only been since 2010 that the atomistic mechanisms of SiO_2-, SiC-, and Si-catalyzed SWCNT nucleation have been clarified [211, 212]. These QM/MD investigations will be the focus of this section.

QM/MD simulations of methane CVD on SiO_2 nanoparticles at 1,200 K [211] are outlined in Fig. 5.10. Due to the inherently low catalytic activity of SiO_2 itself, CH_x radicals ($x = 0$–3 and is chosen randomly) were supplied to the SiO_2 instead of CH_4. This approach was motivated by the prior conclusion that CH_4 decomposes pyrolytically prior to adsorption on the SiO_2 surface [206]. In contrast to CVD using traditional transition-metal catalysts, a complex chemical process was revealed in the simulation on SiO_2. Most notably, CO was produced as the
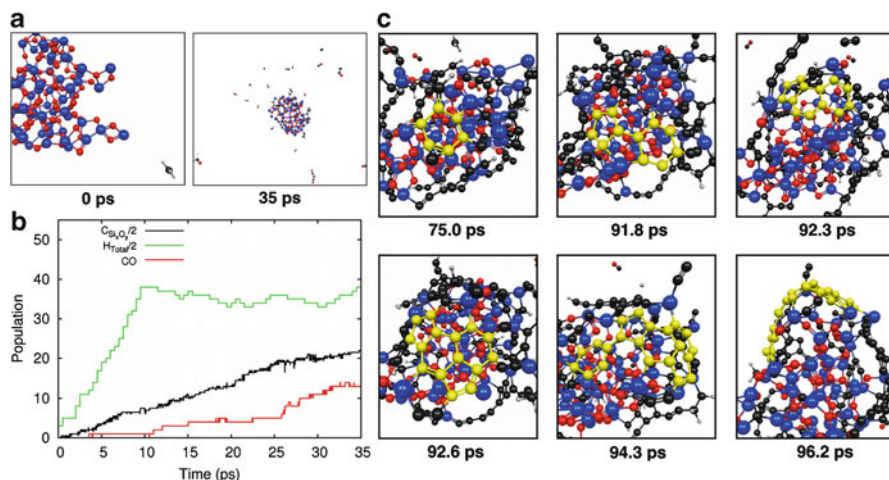
Fig. 5.10 CH_4 CVD on SiO_2 nanoparticles at 1,200 K leads to SWCNT nucleation via a VSS mechanism. (**a**) Snapshots at 0 and 35 ps showing the CVD process. (**b**) CO is the major chemical product of the CH_4 CVD process. The production of CO first requires the natural removal of H from the CO carbon atom. C_{SixOy} and H_{SixOy} are the concentration of C and H on the SiO_2 nanoparticle, respectively. (**c**) Evolution of SWCNT nucleation on SiO_2 nanoparticles. Contrary to nucleation on transition-metal catalysts, nucleation here requires the saturation of the solid-phase catalyst with carbon (Adapted from Page et al. [212]. Reprinted with permission © 2011 American Chemical Society)

primary chemical product via the carbothermal reduction of the SiO_2 nanoparticle, a fact that is consistent with recent experimental observations [203]. The production of each CO molecule first required hydrogen abstraction from neighboring C, Si, or O atoms. Ultimately, the insertion of carbon into/removal of oxygen from the SiO_2 nanoparticle resulted in the local formation of amorphous SiC. However, this carbothermal reduction was limited to the outer regions of the catalyst, with the core of the particle remaining "oxygen rich." The amorphous SiC regions were composed predominantly of extended polyyne chains "anchored" in place by native Si atoms. Consequently, these polyyne chains exhibit restricted vibrational and translational mobility, compared to the equivalent precursor structures observed during transition-metal-catalyzed SWCNT nucleation. A more detailed discussion of the thermodynamic reasons underpinning these phenomena is given below. At high concentrations of surface polyyne chains, SWCNT nucleation was observed. This observation supports the previous claim by Homma and coworkers that SWCNT nucleation on solid, covalent catalysts requires a "carbon-covered" catalyst nanoparticle in order for nucleation to take place [207]. The pentagon-first mechanism, established by QM/MD simulations of pure carbon on transition-metal catalysts and discussed in Sects. 5.4.3 and 5.4.4, played a lesser role in the current context. This is primarily due to two reasons: (a) higher initial carbon density will cause a lower overall sp/sp^2 ratio due to the increased presence of carbon atoms with

three carbon-carbon bonds and (b) the stronger substrate-carbon interaction will more effectively stabilize the triplet-carbene-like carbon atoms in the initial carbon polygon. Similarly, the liquid carbide phase that is central to the VLS mechanism of SWCNT, discussed in Sect. 5.4.4, is absent in the case of SiO_2-catalyzed SWCNT nucleation. This conclusion followed an analysis of the instantaneous Lindemann index [213] of the SiO_2 nanoparticle during the CVD process. The Lindemann index [213], δ, is defined as

$$\delta = \frac{1}{N} \sum_i \delta_i \qquad (5.6a)$$

where

$$\delta_i = \frac{1}{N-1} \sum_{j \neq i} \frac{\sqrt{\left\langle r_{ij}^2 \right\rangle_T - \left\langle r_{ij} \right\rangle_T^2}}{\left\langle r_{ij} \right\rangle_T} \qquad (5.6b)$$

Here, N is the number of atoms in the relevant system, r_{ij} is the instantaneous distance between atoms i and j, and the brackets denote thermal averaging over a finite interval of time. It is noted here that δ describes all atoms in the system and is thus generally referred to as the "global" Lindemann index. On the other hand, δ_i pertains only to the motion of atom i and is therefore referred to as the "atomic" Lindemann index. In the current discussion, we will make reference to both δ and δ_i. The Lindemann index has been used with particular success in the investigation of transition and main group metal species (both bulk and nanoparticle structures) [214–217]. From these investigations, the particular efficacy of the Lindemann index in the prediction of nanoparticle melting points has been established. For example, it is now generally accepted that the "threshold" δ value, which signifies the transition between the solid and liquid phases is between 0.10 and 0.15 [214–217]. Thus, any system exhibiting a δ below this threshold value may be considered to be solid, whereas those with δ above this threshold value are considered to be liquid. At all times, the Lindemann index revealed that the SiO_2 nanoparticle existed as a solid-phase structure. Moreover, QM/MD relaxation of this nanoparticle at elevated temperatures (up to 3,000 K) indicated that nanoparticle SiO_2 decomposes from the solid phase at sufficiently high temperatures [212]. This sublimative phenomenon here rules out the VLS mechanism as an explanation of SiO_2-catalyzed SWCNT nucleation and growth entirely. Instead, QM/MD simulations point to a vapor–solid– solid (VSS) mechanism explaining SWCNT nucleation and growth in this case. The mechanisms of SWCNT nucleation and growth on traditional and nontraditional catalysts are therefore of fundamentally different natures. Subsequent experimental results [210] have since corroborated this proposed VSS mechanism.

The observation that the catalytically relevant region of the SiO_2 nanoparticle is effectively devoid of oxygen motivated the subsequent QM/MD investigation of SWCNT nucleation on pure Si nanoparticles. To this end, a Si_{58} nanoparticle of approximate dimension $0.9 \times 0.9 \times 0.9$ nm^3 was employed as a CVD catalyst
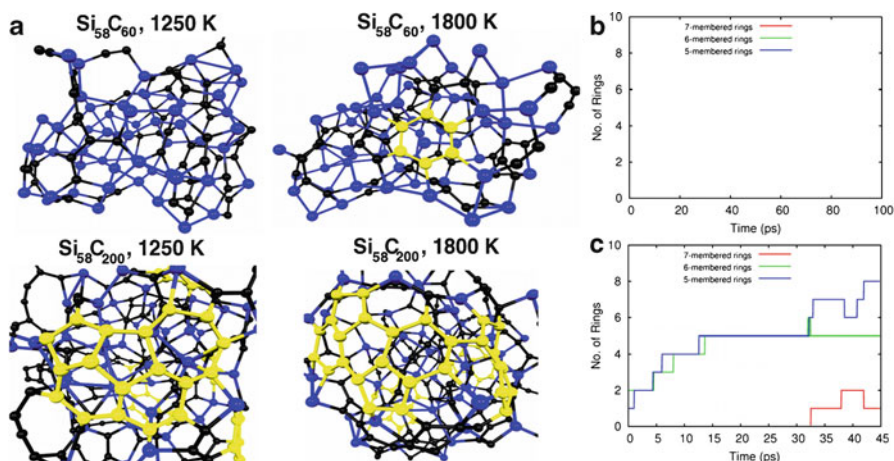
Fig. 5.11 SWCNT nucleation on Si catalyst nanoparticles following the adsorption of gas-phase C_2. (**a**) Structures of $Si_{58}C_{60}$ and $Si_{58}C_{200}$ model complexes at 1,200 and 1,800 K. (**b**) Polygonal ring populations observed using low [C] conditions (i.e., a $Si_{58}C_{60}$ model system). (**c**) Polygonal ring populations observed using high [C] conditions (i.e., $Si_{58}C_{200}$ model system). It is evident that the initial saturation of the Si catalyst surface with carbon is necessary in order for SWCNT nucleation to proceed

at 1,200 and 1,800 K. Gas-phase C_2 moieties were adsorbed on the surface of this catalyst nanoparticle in the manner described in Sect. 5.4.3. Two different concentrations of carbon, namely, 60 and 200, were employed here, following the observation made regarding the dependence of SWCNT nucleation on surface carbon concentration on SiO_2 catalyst nanoparticles. The structures of these $Si_{58}C_{60}$ and $Si_{58}C_{200}$ model systems after 100 and 45 ps annealing, respectively, are shown in Fig. 5.11. Upon adsorption on the Si_{58} surface, these C_2 moieties generally coalesced, forming extended polyyne chains, in an identical fashion to nucleation on Fe, Ni, and SiO_2 catalysts. However, the mobility of these polyyne chains in the case of Si_{58} was notably restricted, as was observed in the case of SiO_2. This was also the case at a higher annealing temperature of 1,800 K, leading to the conclusion that the effect of temperature (at least below 2,000 K) on this SWCNT nucleation process is effectively negligible. Once formed, these polyyne chains themselves gradually coalesced on the nanoparticle surface, ultimately forming extended branched carbon networks. While this is similar to the initial steps in SWCNT nucleation discussed in Sects. 5.4.2, 5.4.3 and 5.4.4 in an atomistic sense, it is noted that the kinetics of this coalescence on Si_{58} is significantly slower, compared to traditional, transition-metal catalysts. In particular, in the latter case, the rate-limiting step of SWCNT nucleation may be considered to be the formation of the SWCNT "nucleus" (the initial polygonal carbon ring structure). Figure 5.11a shows that, following the formation of the SWCNT nucleus on Si_{58}, the subsequent extension of the sp^2-hybridized carbon network proceeded at a significantly slower rate. Figure 5.11a also illustrates the effect of surface carbon concentration on SWCNT nucleation.
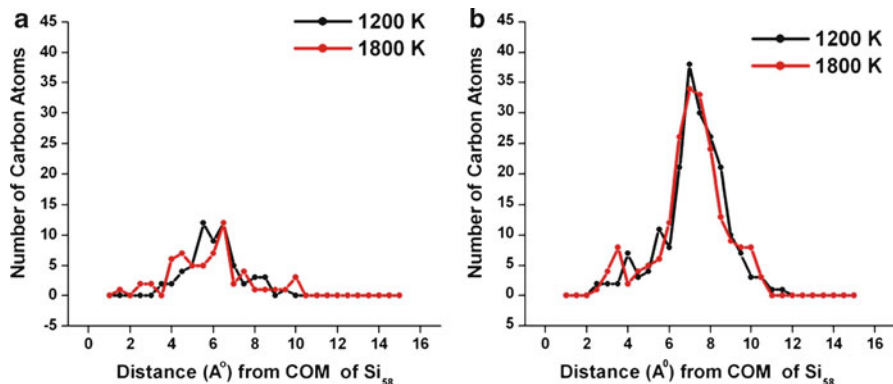
Fig. 5.12 Radial distributions of carbon in (**a**) $Si_{58}C_{60}$ and (**b**) $Si_{58}C_{200}$ model complexes at 1,200 and 1,800 K. The inability of carbon to freely diffuse through the bulk region of the Si nanoparticle is evident. Consequently, the majority of the carbon in both cases resides on the nanoparticle surface, the latter of which is solid. SWCNT nucleation cannot therefore proceed via a VLS mechanism

For example, the formation of polygonal carbon rings in the $Si_{58}C_{60}$ complex (following the adsorption of 30 C_2 species) is limited to a single hexagonal ring structure after 100 ps. Conversely, an extended network of carbon ring structures was formed in the $Si_{58}C_{200}$ model complex after only 50 ps. Thus, as was the case regarding SiO_2 catalyst nanoparticles, it is evident that the saturation of the Si nanoparticle surface with carbon is a prerequisite for SWCNT nucleation. In this sense then, SWCNT nucleation on SiO_2 and Si_{58} seemingly proceeds via an identical route – this point will be discussed at greater length below.

Following the adsorption of C_2 onto the Si_{58} nanoparticle surface, the resultant surface structure resembled an amorphous SiC phase, while the core of the Si nanoparticle remained pristine. This is evident from Fig. 5.12a, which shows the radial distribution of carbon within the Si nanoparticle as SWCNT nucleation proceeds. This figure also shows that, at higher temperature, the penetration of the Si nanoparticle by adsorbed carbon atoms becomes more probable and is independent of the surface carbon concentration. Yet, the free diffusion of carbon through the nanoparticle bulk and surface in this case is restricted below 2,000 K. The latter observation may be explained with recourse to an analysis of the nanoparticle phase during SWCNT nucleation. In the case of the pristine Si_{58} catalyst nanoparticle, δ at 1,200 and 1,800 K were 0.298 and 0.372, respectively. However, upon the adsorption of C_2 on the Si_{58} surface, a dramatic decrease in this Lindemann index was observed. At low carbon concentrations (i.e., the $Si_{58}C_{60}$ model complex), these same δ values were 0.093 and 0.231, while at high concentrations (i.e., the $Si_{58}C_{200}$ model complex), they were 0.049 and 0.088, respectively. This decrease indicates that the phase of the catalyst nanoparticle here changes from a liquid (when pristine) to solid (when carbon-doped). The VLS mechanism therefore clearly does not apply in this case. Considering this impasse, and the atomistic similarity between SWCNT
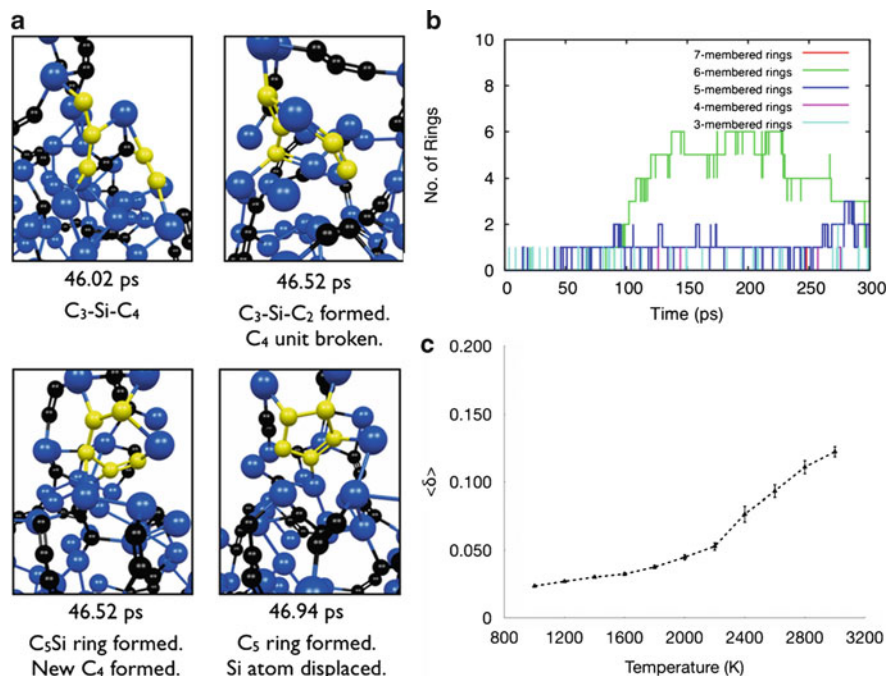
Fig. 5.13 Thermal annealing at constant temperature (2,500 K) leads to the structural deformation of SiC nanoparticles, ultimately producing SWCNT nucleation. (**a**) The first polygonal ring formation event due to the free diffusion of C_n units within the SiC nanoparticle. (**b**) Polygonal ring formation formed from the structural decomposition of the SiC nanoparticle at 2,500 K. (**c**) Time-averaged δ values of the SiC nanoparticle between 1,000 and 3,000 K, computed over an interval of 50 ps. SWCNT nucleation below 2,600 K evidently occurs while the SiC nanoparticle is in the solid phase. Thus, SWCNT nucleation can be explained with recourse to a VSS mechanism

nucleation from Si and SiO_2 nanoparticles, it is apparent that both proceed via the VSS mechanism, as opposed to the VLS mechanism.

The production of an amorphous SiC nanoparticle following the adsorption of C_2 on Si nanoparticles warrants further investigation of the possibility of SWCNT nucleation from SiC itself. Moreover, following the conclusion discussed above, namely, that SWCNT nucleation on both SiO_2 and Si occur via identical pathways, it is reasonable to anticipate that the same applies to SiC. To this end, we have investigated nucleation of SWCNT cap fragments as a result of the constant temperature thermal annealing of SiC nanoparticles alone. In this case, a model $Si_{96}C_{96}$ nanoparticle was annealed between 1,000 and 3,000 K. An example of SWCNT nucleation observed at 2,500 K is illustrated in Fig. 5.13. It is noted that this temperature is approximately that employed in relevant experiments which demonstrate SWCNT growth following the high temperature vacuum decomposition of SiC crystal surfaces [218]. These QM/MD simulations indicated that SWCNT nucleation in this case followed the degradation of the SiC crystalline structure. Indeed, upon annealing even at temperatures as low as 1,000 K, a well-

defined crystallinity was not evident in the model SiC nanoparticle even after a relatively short simulation time (i.e., 10–20 ps). The result of this degradation was the cleavage of C–Si bonds, yielding an increase in the number of C–C bonds. The pure carbon species exhibited free diffusion through/over the SiC nanoparticle. This diffusion causes the elongation/oligomerization of polyyne chains. However, the frequency of these interactions was concomitantly slower at lower temperatures, such as 1,000 K. As is evident from Fig. 5.13a, b, polygonal ring formation occurred after the initial period in which the oligomerization of polyyne chains took place. In this case, the initial polygonal ring formation was the result of the diffusion and subsequent interaction of neighboring C_3 and C_2 species. Figure 5.13b shows that subsequent ring condensation then proceeded reasonably rapidly, with a definite cap structure being formed within ca. 200 ps. However, after the formation of this cap structure, the population of polygonal rings here then decreased – such phenomena have not been observed in the case of traditional, transition-metal catalyst nanoparticles. In a kinetic sense, therefore, SWCNT nucleation resulting from thermal degradation of SiC is anticipated to be less favorable, compared to other traditional catalysts. SWCNT nucleation, at the atomic level, is essentially no more than the continual formation of carbon bonds between mono- and divalent carbons. The origin for these inhibited SWCNT nucleation kinetics can therefore be found in thermodynamics, which, at high temperatures, dominates SWCNT nucleation. In this sense then, SWCNT nucleation is in effect a "thermodynamic sink." From Sect. 5.4.4, it is evident that thermal annealing of amorphous Fe- and Ni-carbide nanoparticles yielded well-defined SWCNT cap structures, similar to those observed here. However, SWCNT nucleation from Fe- and Ni-carbide nanoparticles also resulted in cap structures exceeding the size of those observed using SiC, both on shorter timescales (generally within ca. 100 ps) and at lower temperatures (below 2,000 K). The strengths of the Fe–C, Ni–C, and Si–C interactions are 1.78, 1.06, and 6.88 eV/atom, respectively, at the SCC-DFTB level of theory [196] (to re-iterate, the strength of the C–C interaction is 5.48 eV using SCC-DFTB). The weaker interaction of the Fe/Ni catalyst with carbon therefore correlates directly with an increased rate of SWCNT nucleation. Once a C–C bond forms in the latter case, it is rarely broken due to its greater thermodynamic stability (even if it is not the most energetically stable ring structure – this is the deciding difference to Frank's screw-dislocation crystal growth [60], invalidating its application to SWCNT growth as promoted by Ding and Yakobson [58]). On the other hand, the Si–C and C–C interactions are, thermodynamically, comparable to each other. Consequently, C–C bonds are more frequently broken during nucleation on SiC nanoparticles.

The dependence of $<\delta>$ on simulation temperature for the SiC nanoparticle is depicted in Fig. 5.13c. From this figure, it is evident that the SiC nanoparticle existed in the solid state below 2,600 K. However, Fig. 5.13a,b suggests that there was undoubtedly some liquid-like character in the SiC nanoparticle at temperatures above 2,600 K. In particular, $<\delta_i>$ values indicate that, between 1,000 and 3,000 K, the SiC nanoparticle exhibited three distinct behaviors depending on the temperature. First, at lower temperatures ($<1,400$ K), the SiC nanoparticle was unquestionably solid. At intermediate temperatures (between 1,400 and 2,600 K) a gradual increase

in $<\delta_i>$ for atoms residing close, or near to, the nanoparticle surface was evident. Surface premelting therefore became prevalent at these temperatures, ultimately causing $<\delta>$ to increase slightly. Such surface premelting has been shown to be a prominent phenomenon in the melting dynamics of transition-metal nanoparticle species [216]. In this respect therefore, transition metals and SiC nanoparticles appear to be equivalent. According to established trends regarding transition-metal nanoparticle melting, by increasing the temperature further, this surface premelting is followed by the complete liquefaction of the nanoparticle. However, rather than undergoing this solid–liquid phase transition, the SiC nanoparticle instead became quasi-solid at temperatures above 2,600 K. One probable cause of this unexpected behavior is ascribed to the influence of surface chemistry (the formation of C–C bonds, polyyne chains, and polygonal carbon rings, etc.) on the Lindemann index itself. In extreme cases, the formation of an extended sp^2-hybridized carbon network on the SiC nanoparticle surface, in part, solidified the SiC nanoparticle surface, therefore retarding the melting process.

A pronounced similarity is therefore observed regarding the SWCNT nucleation mechanisms on SiO_2, SiC, and Si catalysts. The results discussed here constitute the first evidence of a catalyst independent mechanism with respect to Si-based catalysts. In addition, these results indicate the mechanism of SWCNT nucleation on these Si-based catalysts is remarkably different to that established for transition-metal catalysts and centers around a solid-phase catalyst nanoparticle. Since the independence of the SWCNT nucleation mechanism has been established and accepted in the case of transition-metal catalysts, this conclusion is seemingly unremarkable. However, we point out here that with respect to the majority of "nontraditional" catalysts such as SiO_2, SiC, Si, Al_2O_3, ZrO_2, and so on, the precise mechanisms of SWCNT nucleation remains are in fact unknown at present. Moreover, at first glance, there is no reason to suspect that the SWCNT nucleation mechanism on such a diverse range of catalyst species should be in any way related, considering their respective physicochemical properties.

5.4.6 Continued Sidewall Growth: Nanoparticle Effect

We now consider the phenomenon of continued SWCNT growth. This is generally defined as the extension of the nanotube sidewall (by the addition of newly created polygonal ring structures) parallel to the axis of growth. Note that this process differs from the process of SWCNT nucleation, in which the nascent nanotube cap fragment is formed. This partitioning of what is actually (in reality) a continuous process is somewhat arbitrary. Nonetheless, it has enabled the precise atomistic mechanism of SWCNT growth to be identified and studied.

Continued SWCNT growth has been modeled using QM/MD simulations on a number of occasions (see [219] and references therein). The approach employed in these investigations typically was similar to that described in Sect. 5.4.3 (see Fig. 5.14). Fe-catalyst nanoparticles were thus first annealed at 1,500 K, after
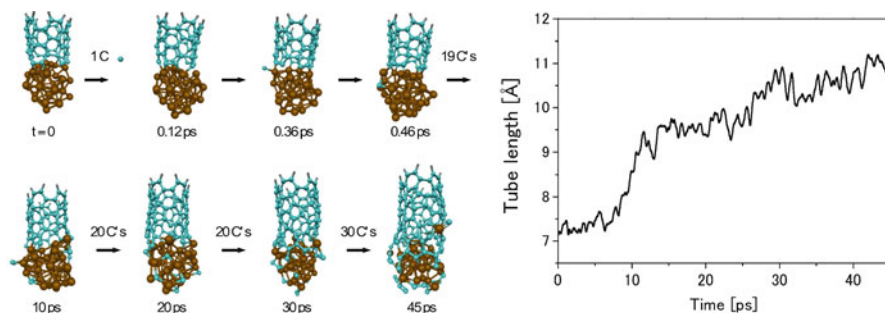
Fig. 5.14 Continued growth from a (5,5) SWCNT fragment on an Fe_{38} catalyst nanoparticle at 1,500 K. (**a**) The adsorption of gas-phase carbon atoms at a rate of 1 C/0.5 ps at the base of the SWCNT structure leads to the extension of the sp^2-hybridized carbon network via the formation of new polygonal rings at the nanotube base. Growth is mediated entirely by the catalyst surface in this case. (**b**) The SWCNT length as a function of time at 1,500 K. Adsorption of gas-phase carbon atoms results in the addition of ca. 4 Å to the base of the SWCNT (Adapted from Ohta et al. [271] with kind permission of © The American Chemical Society (2008))

which "simulated" gas-phase carbon feedstock (in this case, atomic C or C_2) was supplied at various rates to the base of the growing SWCNT or onto the nanoparticle surface itself. Two such nanoparticles have been employed, namely, Fe_{38} and Fe_{55}. In both cases, a model SWCNT cap fragment (a C_{40} cap of (5,5) chirality), or short SWCNT segment (depicted in Fig. 5.14), was employed to approximate a SWCNT cap fragment formed in situ (such as that shown in Fig. 5.6). The effect of the nanoparticle diameter on the mechanism and kinetics of continued SWCNT growth has therefore been considered. Somewhat unsurprisingly, the increase in nanoparticle diameter from 0.70 nm (Fe_{38}) to 0.94 nm (Fe_{55}) has no effect on the atomistic mechanism of continued SWCNT growth. This mechanism is depicted in Fig. 5.15. From this figure, it is evident that, like cap nucleation, the continued nanotube growth process was driven by the extension of the sp^2-hybridized carbon network. This extension itself was driven by the formation of polygonal carbon rings at the base of the nanotube structure (at the interface between the nanotube and the catalyst nanoparticle), thereby extending the SWCNT cap in a unidirectional manner. From Fig. 5.14, it can be seen that the SWCNT growth process took place almost entirely on the catalyst surface; the original hexagonal network of the tube remained intact and was pushed away from the metal due to the addition of new polygonal carbon network growth at the tube-metal interface. Only very rarely did carbon penetrate the catalyst surface and diffuse through the subsurface region. Similarly, carbon was never observed to freely diffuse through the bulk of the catalyst nanoparticle. Unsurprisingly, this behavior was not different from the behavior observed during SWCNT nucleation on Fe_{38}, a fact that is attributed to the nanoparticle's relatively small diameter, which exhibits a relatively high surface energy. It is also noted here that Fe_{38} and Fe_{55} are both "magic number" metal clusters and so exhibit unusual stability. We also performed a systematic comparison
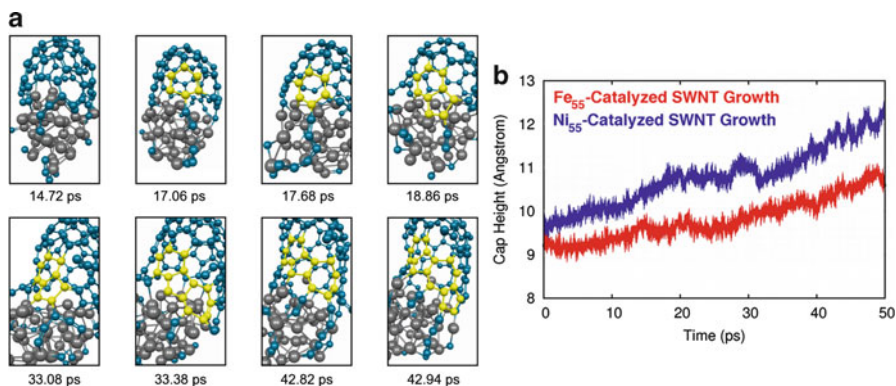
Fig. 5.15 Continued nanotube sidewall growth from a (5,5) SWCNT C_{40} cap on a Ni_{38} catalyst nanoparticle at 1,500 K. (**a**) In this case, the extension and collapse of a single bridging polyyne chain results in the formation of an extended conjugated system at the base of the SWCNT, including a hexagonal, heptagonal, and two pentagonal carbon rings. (**b**) Depending on the size of the catalyst nanoparticle, Ni-catalyzed SWCNT growth is found to be ca. 69–106% faster than Fe-catalyzed SWCNT growth at 1,500 K (Adapted from Page et al. [197] with kind permission of © The American Chemical Society (2010))

of continued SWCNT growth on an Fe_{38} particle at different temperatures, namely, 1,000, 1,500, and 2,000 K [220]. We found that 1,500 K was optimum for fast growth since catalyst encapsulation by the ring collapse of longer polyyne chains was more prevalent at the lower temperature, while loss of carbon fragments to the vacuum reduced the growth rate noticeably at the higher temperature.

While the SWCNT growth mechanisms on Fe_{38} and Fe_{55} were observed to be the same, this is not so with respect to the kinetics of SWCNT growth. QM/MD simulations [221] indicate that the growth slows with increasing catalyst nanoparticle diameter – a conclusion that parallels that of others based on experimental evidence [182, 222, 223]. This phenomenon is ascribed primarily to the relative surface areas and volumes of the two catalyst nanoparticles. In particular, although the diameter of Fe_{55} is only slightly larger than that of Fe_{38}, the increases in surface area and volume are more substantial. Thus, the domain over/through which adsorbed C_n species may migrate, before being incorporated into the growing SWCNT, is concomitantly larger in the case of Fe_{55}. Nanotube growth employing the former, smaller catalyst nanoparticle is therefore ca. 19% faster compared to that on Fe_{55}. It is conceded that both of these growth rates exceed those determined experimentally [47, 224–228] by several orders of magnitude. This is a natural consequence of the relatively unnatural carbon supply model that has been employed here. Nevertheless, the error thus induced is systematic, and so, these relative trends in growth rates likely remain valid. Although the growth depicted in Figs. 5.14 and 5.15 is an example for growth from a "floating" catalyst, it is likely that the mechanism of SWCNT "root"/"tip" growth on supported catalyst nanoparticles is similar since the majority of nanotube growth chemistry is mediated by the nanoparticle surface itself and not by its support.

5.4.7 *Defect Healing*

As has been shown in the preceding sections, there have been significant advances in both experimental and theoretical understanding of SWCNT nucleation and growth on a number of different catalyst species, with different carbon feedstock. Yet there are still outstanding issues regarding phenomena associated with SWCNT growth. The most notable issue at present is that of "chirality-controlled" growth. That is, a method by which a single particular, arbitrarily chosen (n, m) chirality-type tube [or, at most a narrow distribution around (n, m)] may be synthesized in situ remains elusive to date. At the atomistic scale, chirality-controlled growth is equivalent to growth in which first a particular cap establishing the (n, m) chirality is somehow created, after which only hexagonal rings are incorporated into the growing SWCNT sidewall. The fundamental principles guiding such chirality-specific synthesis are, as yet, largely unknown. Such chirality-controlled growth is extremely desirable since the physical, electrical, and optical properties of a SWCNT are determined entirely by its (n, m) chiral indices. Current experimental SWCNT synthesis techniques (such as CVD and arc discharge) are known to produce a broad distribution of (n, m) SWCNTs. While it is possible to subsequently isolate a narrow distribution of (n, m) SWCNTs, such techniques invariably damage the SWCNT structures by either chemical or physical means [229, 230]. Such damage potentially limits the application of these SWCNTs in nanoscale devices. An understanding of how to control a SWCNT's chirality in situ is therefore critical in this respect. In the following subsections, we will concentrate on the question how purely hexagonal sidewall growth can be achieved despite the fact that initially formed polygons exhibit distributions of pentagons, hexagons, and heptagons that depend on the carbon concentration, temperature, and possibly other factors.

5.4.7.1 SWCNT Growth: The Defect Problem

It was shown in the preceding sections that, similar to giant fullerene formation, SWCNT nucleation and growth processes are far from linear, ordered processes. On the contrary, they proceed via complex pathways, resulting in unpredictable dynamics attributable to the phase transition from linear sp carbon chains to fused ring networks composed of sp^2 carbon. Moreover, we find that entropy plays an important role in the formation mechanism, favoring the formation of defects. Considering the temperature at which SWCNTs nucleate and grow in CVD and arc-discharge environments (i.e., typically 1,000 K or higher), this in itself is not so surprising. Indeed, by revisiting the discussion of Sects. 5.4.2 and 5.4.3, it is apparent that the inclusion of defects (such as polyyne chains, non-hexagonal ring structures, and vacancies in the sp^2-hybridized carbon network) is inherent to the SWCNT nucleation process itself. The very first "nucleus" of the SWCNT on a transition-metal catalyst is actually a pentagonal ring "defect." The subsequent ring condensation process, by which the SWCNT cap fragment is formed, also produces

a majority of non-hexagonal ring defects. Although this is attributed to the curvature of the catalyst surface imposing itself onto the growing sp^2-hybridized carbon network, the further formation of defect structures during growth (see Sects. 5.4.2, 5.4.3, 5.4.4, 5.4.5 and 5.4.6) cannot be rationalized in this manner. Nevertheless, the incorporation of defect structures into a growing SWCNT effectively alters its chirality and therefore physical properties. Since it is apparent that SWCNT nucleation and growth are inherently defect-inducing processes, it is important to understand the mechanisms by which such defects are removed in situ. The defects may heal if the temperature during synthesis exceeds that required for cascades of Stone–Wales transformations [231, 232]. However, in most of our QM/MD simulations, such healing appears to be slow compared to chaotic growth. QM/MD simulation of defect removal on transition-metal catalysts is the subject of the following section.

5.4.7.2   SWCNT Chirality-Controlled Growth: The Healing Solution

The removal of SWCNT defect structures during growth has been investigated previously using QM/MD [233]. To induce growth, gas-phase carbon atoms were adsorbed at the region between a model C_{40} cap and its supporting Fe_{38} catalyst surface. The hypothesis of this approach took into account the inherent stability of the C–C bond (relative to the Fe–C bond) and therefore the greater stability of the SWCNT as a whole. Due to this stability, the removal, or healing, of defects during growth was anticipated to occur over longer time scales than those considered in prior QM/MD simulations (ca. 50 ps). Three gas-phase carbon adsorption rates were therefore employed, namely, 1 C/0.5 ps 1 C/10 ps and 1 C/20 ps (rates denoted using "fast," "slow," and "very slow"). It is noted here that the former of these adsorption rates is the same as that employed in the simulations discussed in Sects. 5.4.2, 5.4.3, 5.4.4, 5.4.5 and 5.4.6.

Comparison of the three carbon adsorption rates is made in Fig. 5.16. It is immediate from this figure that the ability of the SWCNT to heal itself during growth is directly correlated to the rate of carbon adsorption. As this rate decreases, the number of polygonal ring defects in the growing sp^2-hybridized carbon network decreases. Moreover, the active removal of defects from the growing SWCNT structure resulting in hexagonal ring formation is observed for slow and very slow carbon adsorption. This suggests that the kinetics of SWCNT growth is more favorable compared to those of defect removal. Figure 5.17 shows the reason explaining why this is indeed the case. This figure depicts schematically two examples of defect removal during slow SWCNT growth. The first of these defects is a conjugated pentagonal-heptagonal ring defect, and the second is an adatom defect. In both cases, the defect is removed solely by the self-isomerization of the SWCNT cap structure itself. For example, the adatom defect shown in Fig. 5.17b is formed following the adsorption of a carbon atom onto an existing hexagonal ring at the nanotube base. This adatom defect quickly converted to a heptagonal ring defect, which is evidently significantly more stable (lasting for ca. 15 ps). The addition
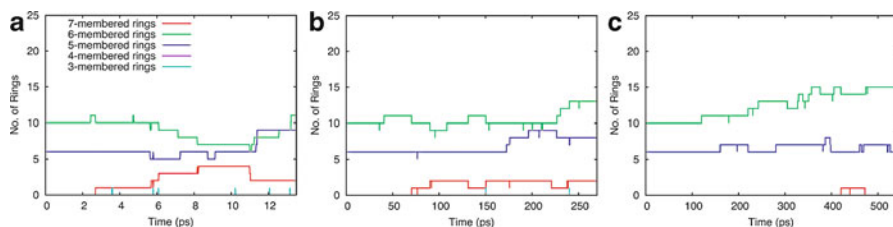
Fig. 5.16 SWCNT healing is directly correlated with the rate of carbon adsorption at the nanotube base. Polygonal rings formed in a single SCC-DFTB/MD trajectory using adsorption rates of 1 C/(**a**) 0.5 ps, (**b**) 10 ps, and (**c**) 20 ps. At the fastest adsorption rate considered, SWCNT growth incorporates several defect ring structures into the carbon nanostructure. Slowing the adsorption rate to 1 C/10 ps, the incorporation of defects is suppressed due to the action of the self-isomerization of the sp^2-hybridized carbon network. At the slowest rate considered, SWCNT growth occurs solely due to hexagonal ring addition, thereby illustrating chirality-controlled SWCNT growth (Adapted from Page et al. [233] with kind permission of © The American Chemical Society (2009))

of a second carbon atom results in a heptagonal-hexagonal ring rearrangement, which ultimately forms a C_2 defect at the base of the SWCNT. After a further ca. 10 ps, this C_2 unit detaches from the cap and diffuses away over the catalyst surface. Both instances of SWCNT defect removal depicted in Fig. 5.17 occur in the vicinity of the catalyst surface. The assistance of the catalyst surface is therefore implicated in these cases of SWCNT healing. The timescales over which these two examples of self-isomerization take place are between 5 and 25 ps, respectively. This observation is indicative of a fundamental principle regarding the in situ control of SWCNT chirality. That is, the rate at which defect structures are incorporated into the SWCNT structure depends on the relative rates of defect addition (due to growth) and defect removal (due to SWCNT self-isomerization).

5.4.7.3 SWCNT Healing: Effects of Catalyst Composition and Size

In Sects. 5.4.3 and 5.4.6, it was established that a number of kinetic and mechanistic phenomena associated with SWCNT nucleation and growth can be understood with recourse to the relative carbon-catalyst interaction strengths. For example, a stronger carbon-catalyst interaction leads to slower growth rates and changes the mechanisms of SWCNT nucleation and growth. From the previous section, it was seen that the catalyst nanoparticle is implicated in the defect healing process. It therefore seems reasonable to hypothesize that the carbon-catalyst interaction may also play some role regarding the relative ability of different catalysts to assist in SWCNT healing processes. We will presently discuss such a proposal with respect to Fe- and Ni-catalyst nanoparticles.

QM/MD simulations of SWCNT growth were carried out using Fe_{38}, Ni_{38}, Fe_{55}, and Ni_{55} catalyst nanoparticles [221]. Growth was induced at 1,500 K using a slow
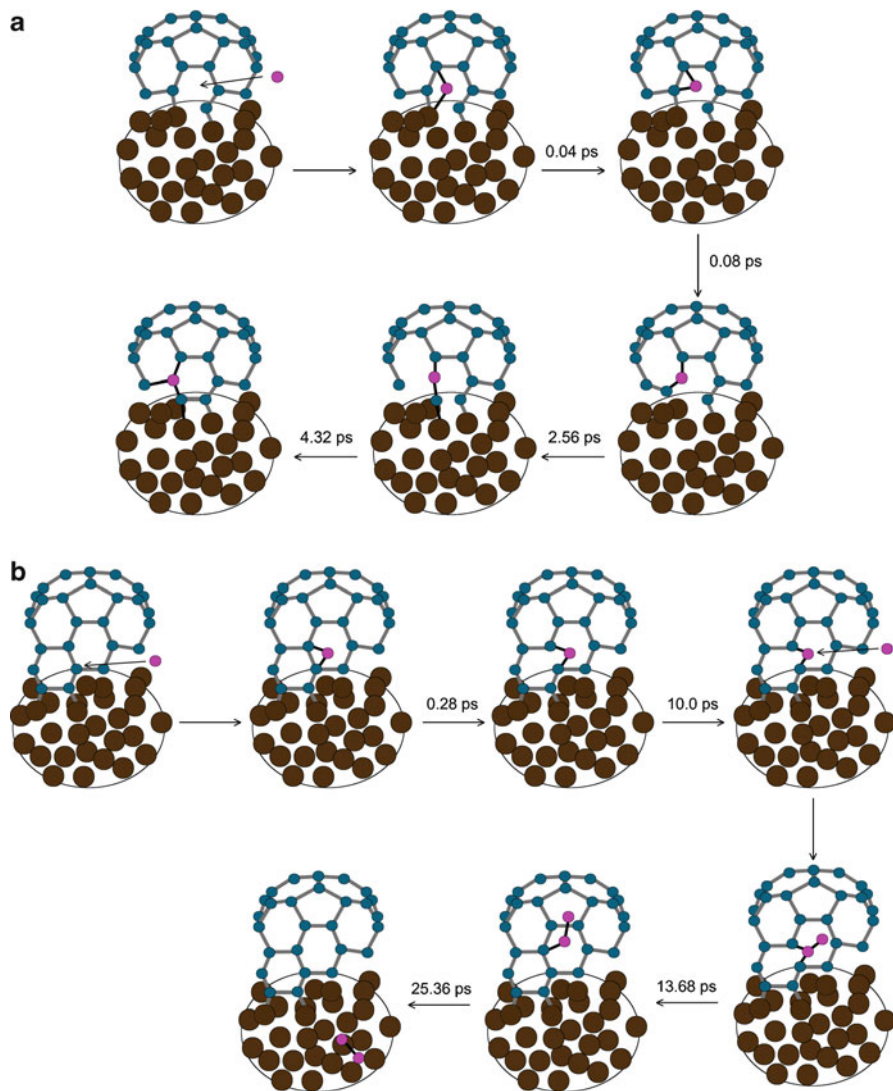
Fig. 5.17 Examples of SWCNT healing observed during SWCNT growth on Fe_{38} catalysts at 1,500 K. In both cases, defects are removed from the growing SWCNT cap solely by the self-isomerization of the sp^2-hybridized carbon network. (**a**) A conjugated pentagonal-heptagonal defect is removed, resulting in the formation of two hexagonal rings at the base of the SWCNT cap. (**b**) An adatom defect is removed, forming a hexagonal ring via a heptagonal ring defect intermediate structure (Adapted from Page et al. [233] with kind permission of © The American Chemical Society (2009))

carbon supply rate (i.e., 1 C/10 ps). The average defect formation and defect removal statistics after 300 ps are given in Table 5.1. For the purpose of this analysis, "defect formation" is defined here as the formation of a new pentagonal or heptagonal ring, the conversion of a hexagonal ring to a pentagonal-heptagonal ring, or the

Table 5.1 SWCNT healing statistics on Fe- and Ni-catalyst nanoparticles for a carbon adsorption rate of 1 C/10 ps. The net rate of SWCNT healing may be considered as the difference between the rates of defect formation and defect removal. All data averaged over ten SCC-DFTB/MD trajectories, following 300 ps of simulation

		Fe_{38}	Ni_{38}	Fe_{55}	Ni_{55}
Defect formation	Pentagonal formation	3.2	6.1	2.2	4.6
	Heptagonal formation	0.2	0.4	0.3	0.2
	Hexagonal→heptagonal transformation	2.7	2.8	2.3	2.9
	Hexagonal→deformation	1.0	0.2	0.6	0.2
	Hexagonal→pentagonal transformation	0.1	0.3	0.6	0.1
	Total defects formed (Σ_1)	7.2	9.8	6.0	8.0
Defect removal	Hexagonal formation	3.4	3.3	3.4	2.9
	Heptagonal→hexagonal transformation	1.1	1.0	0.8	1.3
	Pentagonal→hexagonal transformation	1.2	1.7	1.5	1.6
	Total defects removed (Σ_2)	5.7	6.0	5.7	5.8
Net healing ($\Sigma_2 - \Sigma_1$)		−1.5	−3.8	−0.3	−2.2

destruction of a hexagonal ring (i.e., ring opening). Conversely, "defect removal" is defined here as essentially the opposite of defect formation, i.e., the formation of new hexagonal rings and the conversion of a pentagonal-heptagonal ring to a hexagonal ring. From Table 5.1, it is evident that the rate of defect removal in the case of the four catalysts considered is essentially equivalent after 300 ps. Thus, there is little dependence of the defect removal process on the size or elemental composition of the catalyst. This is reasonable since the catalyst nanoparticle was never explicitly involved in the process of healing (as discussed in Sect. 5.4.7.2). Rather, it plays an implicit role, by saturating dangling bonds at the edge of the SWCNT structure, thereby supporting the self-isomerization process. On the other hand, Table 5.1 shows that the size and, more obviously, the elemental composition of the catalyst nanoparticle directly affect the rate of defect formation during growth. For example, for an equivalent catalyst size, SWCNT growth on a Ni catalyst induces ca. 30–35% more total defects, compared to SWCNT growth on an Fe catalyst. For a particular type of metal, Table 5.1 also shows that the number of defects formed during SWCNT growth decreases with increasing nanoparticle diameter. It is noted here that these two correlations are consistent with the effect of nanoparticle size and composition on the total SWCNT growth rate. That is, *faster growth leads to more defects, whereas slower growth leads to a smaller number of defects by comparison*.

5.4.8 Conclusion from Nonequilibrium QM/MD Simulations of SWCNT Nucleation and Growth

We have reviewed our own recent investigations into the phenomena of SWCNT nucleation and growth using state-of-the-art QM/MD methods. Admittedly, our

models represent deviations from experimental setups: (i) hydrogen and/or oxygen, usually present in alcohol CVD synthesis, is typically absent in our simulations for the reason that the hydrogen abstraction is a rare event on MD time scales; (ii) addition by carbon atoms constitutes the supply of species with excessive energy and reactivity, while addition of C_2 seems to be more realistic at least for the modeling of laser-evaporation synthesis [178, 179]; (iii) employed catalyst nanoparticles are at the lower end of the experimentally employed size distribution; (iv) substrate effects are missing; and (v) most severely, our carbon addition rates are often one to three orders of magnitude too fast in comparison to experimentally observed growth rates. Nevertheless, it is evident that QM/MD simulations of the nonequilibrium, high-temperature processes occurring during SWCNT nucleation and synthesis can provide fundamental knowledge that complements experimental understanding. Moreover, considering the spatial and temporal resolutions furnished by QM/MD methods (i.e., nanometers and picoseconds, respectively), such simulations can predate, or correct, experimental understanding of these phenomena. This is certainly the case with respect to models of SWCNT nucleation and growth. For example, the VLS mechanism of SWCNT nucleation and growth on a variety of transition-metal catalysts is very widely accepted. Yet it is only since the application of QM/MD in this area that true understanding of various aspects of the VLS mechanism has come to light. One such aspect regards the atomistic processes of SWCNT nucleation and growth, which are dominated by the formation and coalescence of extended polyyne chains, and the interaction of these chains with the supporting catalyst surface. Another aspect, which remains under debate at the time of writing, regards the existence and role of the transition-metal carbide phase in the context of SWCNT nucleation and growth. In particular, our QM/MD simulations and recent experiments and theoretical studies have challenged the traditional role ascribed to this carbide phase in the SWCNT nucleation process. The presented QM/MD simulations of Sect. 5.4.7 have also uncovered the phenomenon of catalyst-assisted defect healing during continued SWCNT growth. This phenomenon, by which a SWCNT structure consisting entirely of hexagons can be attained, has since been implicated in models of chirality-controlled growth. Most recently, QM/MD simulations have led the way in understanding the manner in which SWCNTs nucleate and grow on "nontraditional" catalysts including SiO_2, SiC, and Si. They have also revealed the atomistic mechanism underpinning the CVD process on the former catalyst species. In this context, QM/MD methods alone have uncovered the remarkable fact that SWCNT nucleation on these solid-phase catalysts proceeds according to an entirely different mechanism, compared to the traditional picture of SWCNT nucleation/growth on transition-metal nanoparticles. Our "VSS" (vapor–solid–solid) model is now being recognized by experimentalists in these cases [210].

5.5   Graphene Formation

5.5.1   Background and Experimental Synthesis

The 2010 Nobel Prize in Physics was awarded jointly to Andre Geim and Konstantin Novoselov for their "groundbreaking experiments" regarding the two-dimensional material graphene [234]. Graphene is the name chosen by these Nobel laureates for a single layer of graphite. Since graphite is a well-studied material, it comes with little surprise that both the metal-catalyzed synthesis of such graphene sheets [51, 235] as well as their structures [236] had been reported before the publication of the Nobel Prize winning paper in 2004. The single graphene layer is a semimetal or zero-gap semiconductor and has excellent electronic properties, for instance, high mobility (15,000 cm^2 V^{-1} s^{-1} and higher) and a room-temperature quantum Hall effect [237]. Narrow single graphene ribbons show peculiar metallic and semiconducting behaviors depending on the edge type and width, analogous to the dependence of CNT conductivity on the roll-up vector [147]. Since chirality-specific CNT synthesis has yet to be achieved, as discussed in Sect. 5.4, the exquisite characteristics of graphene open new possibilities of application in many electronic devices, such as flexible film transistors, touch panels, solar panels, and so on.

Albeit easier than chirality-specific CNT synthesis, large-scale production of graphene also turns out to be a formidable task. The central problem is to synthesize a large-area graphene flake with a minimum number of defects at a reasonable cost and efficiency. So far, the following methods have been used to synthesize graphene flakes: (a) cumbersome micromechanical cleavage [234], (b) vacuum decomposition of SiC (0001) surfaces at very high temperatures (>1,350°C) [238, 239], (c) carburization and annealing of a metal carbide substrate [235, 240], and (d) chemical vapor decomposition (CVD) of hydrocarbons on metal surfaces [241–252]. At present, it seems that out of these four synthetic routes, similar as for CNT synthesis (Sect. 5.4.1), the CVD technique has the greatest promise as it can be potentially scaled up and does not require the high temperatures of SiC evaporation and carburization techniques, which typically induce defects. Indeed, over recent years, several reports of successful CVD synthesis of graphene on metal surfaces appeared in the scientific literature. Different types of hydrocarbon feedstock were employed (such as acetylene [242], propylene [243], acetaldehyde, and acetone [244]), and graphene was grown on a variety of metal surfaces (nickel seems most popular [242, 243, 245, 247, 252] but other metals such as rhodium [244], cobalt [248], ruthenium [241, 246], iridium [249, 250] and copper [251]).

Despite practical advances in synthesis techniques resulting from phenomeno-logical growth models, the atomistic mechanism by which graphene nucleates on catalyst surfaces remains the topic of fierce debate. It is clear that carbon solubility plays an important role; Ni has generally a higher C solubility than, for instance, Cu, and consequently carbide formation is well documented for Ni surfaces [235] but does not seem to play a role for Cu [251]. Temperature is equally important: Lahiri et al. [252] reported low-temperature conversion of a surface carbide to

graphene below 460°C, while at higher temperatures, carbon atoms [251] [for instance, on Cu(111) or Ni(111)], C_2 units on Rh-YSZ-Si(111) [244], or linear carbon chains [241] [on Ir(111)] attach to graphene islands. Evidence was found that graphene growth on Ni(111) [193, 243], Ru(0001) [241], and Ir(111) [250] begins with carbon atoms adsorbed at step edges, while it appears that graphene islands nucleate spontaneously on terraces in case of Ir(111) [250], Rh(111) [253], and Cu(111) [251]. Undoubtedly, Smoluchowski ripening via island coalescence plays an important role in the graphene growth process [249, 250, 253], and Wang et al. have even identified actual coronene-like C_{24} units as dominant islands performing the surface migration on Rh(111) [253]. Although much work has been done, a systematic study investigating the role of metal-carbon binding energy, carbon solubility, carbide formation, feedstock concentration, temperature, etc., for the formation mechanism is clearly required.

5.5.2 *Haeckelite and Graphene Nucleation on Ni(111)*

Previous theoretical investigations of graphene nucleation at step edges [254, 255] or terraces [241, 255, 256] have either employed static models, neglecting irreversible dynamic processes occurring during nonequilibrium growth, or only captured ultrashort dynamics of individual C–C bond formation in DFT-based MD simulations [25]. We have therefore employed the computationally efficient SCC-DFTB/MD method to study graphene nucleation on a Ni(111) surface at a nuclear temperature of 1,180 K throughout the simulation. We chose to study the nucleation of the first sp^2 carbon ring systems from *sp* carbon on a terrace, at a constant and rather large 83.3 mol% of the carbon density of a perfect, continuous sheet of graphene. Horizontally aligned C_2 units were randomly placed on a Ni(111) surface without initial polygonal order (see Fig. 5.18a) in a set of ten "H" trajectories. In another set of ten "G" trajectories, we replaced 12 C_2 units by a domelike C_{24} carbon cluster with coronene skeleton (mimicking observations in [250, 253]) to investigate a possible template effect by its hexagonal network. The nonequilibrium character of the simulations in this case is achieved by the use of C_2 units at a temperature far below that at which this species is at equilibrium with its environment.

As was the case in fullerene and SWCNT cap nucleation, the high density of the C_2 units initiated spontaneous *sp* carbon chain formation, which was followed by an almost instantaneous interchain networking process during the first 2.5 ps of annealing. Following this initial period of "reactive network formation" was a more subdued period of annealing. Essentially, all carbon rings that were generated after 50 ps were formed within the first 5 ps of simulation. Figure 5.18a–c shows that carbon ring formation proceeded via the interaction of adjacent polyyne chains on the Ni(111) surface. The presence of a Y-shaped junction, formed between two adjacent polyyne chains, preceded the majority of ring formation events observed in this work. The motion of the "arms" of this junction structure, driven by the diffusion of the constituent carbon atoms on the Ni(111) surface, was then observed
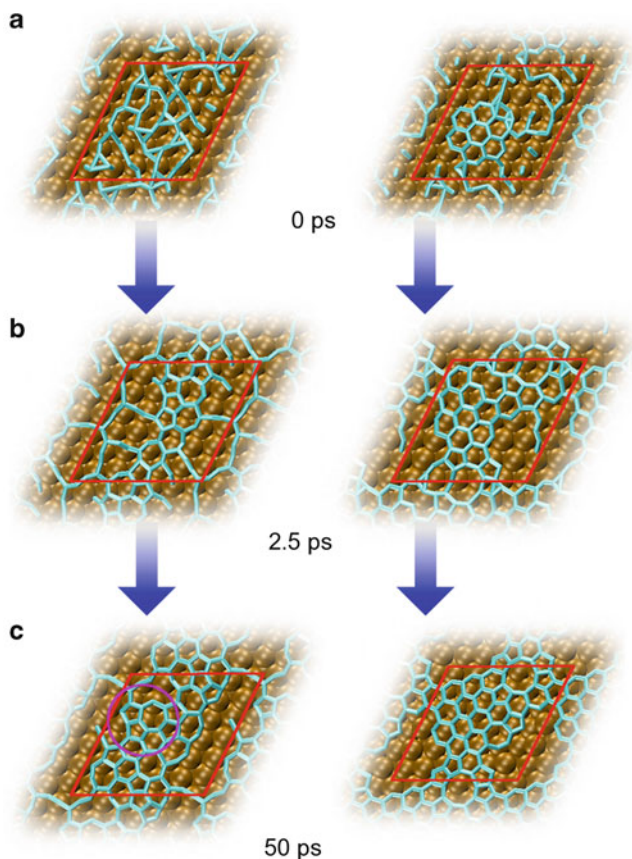
Fig. 5.18 Snapshots of "H" trajectories (**a–c**, *left*) and "G" trajectories (**d–f**, *right*) at 0, 2.5, and 50 ps, respectively. The location of the periodic boundary is indicated by the *red line*. The *circle* in 1(**c**) denotes an area of late ring collapse from a Y-junction

to initiate the ring formation process. Figure 5.18b, c shows an explicit example of this process between 2.5 and 50 ps. In this case, a single Y-junction (encircled) was generated on the Ni(111) at 2.5 ps. Its subsequent collapse to a pentagon, and its interaction with neighboring polyyne structures, culminated in the formation of a conjugated 6–5–5–7 carbon ring structure (i.e., adjoined 6-, 7-, and two 5-membered carbon rings).

The reader may notice that this ring formation mechanism resembles closely the SWCNT cap nucleation mechanism on transition-metal nanoparticles (Sects. 5.4.2, 5.4.3 and 5.4.4), as well as the initial steps of fullerene nucleation from polyyne chains (Sect. 5.3). Notably, all observed sp^2 carbon network nucleation events in vacuum and on transition-metal catalysts begin with the formation of a Y-junction, followed by five-membered ring formation. The motion of two Y-junction arms drives the latter process as shown for SWCNT cap nucleation in Fig. 5.6c. In

the context of graphene nucleation, the shortest Y-junctions have also been called C_4 "star conformations" in [256]. Interestingly, curvature of the catalyst surface does not seem to play a role for the initial pentagon that results from the Y-junction collapse. However, on a flat surface with a high polyyne concentration in a single layer as in our simulations, the positive curvature of the pentagon needs to be compensated by an adjacent polygon with negative curvature. Heptagons are therefore the ideal polygonal shapes that are preferred in the immediate vicinity of a pentagon. Thus, the structures formed in "H" trajectories resembled closely that of haeckelite patches [27], i.e., they were composed predominantly of five- and seven-membered rings. The curvature of the networked carbon structure was therefore effectively zero and hence matched that of the Ni(111) surface. In the case of the template-containing "G" model system, we found that the coronene-like fragment acted as a "template," which facilitated a more exclusive production of six-membered rings at the expense of five- and seven-membered rings.

Already, Shelton et al. stressed in 1974 the similarity of graphite formation on carbon-saturated Ni(111) to a phase transition process [235]. For a more quantitative understanding of this possibility, we have analyzed the phase transition from linear carbon chains to sp^2 carbon networks observed here in terms of random graph theory [257, 258]. Figure 5.19 displays for both "H" and "G" trajectories a plot of carbon cluster size per unit cell versus n_{C-C}/N_C, where n_{C-C} is the number of C–C bonds and N_C is the number of carbon atoms. As with other phase transitions described by random graph theory, the plot confirms the existence of a critical n_{C-C}/N_C value just before 1.0, above which the further conversion of linear carbon chains to sp^2 carbon polygons leads to the emergence of a fully networked carbon structure. *Thus*, *it is justifiable to discuss the sp^2 network formation from sp chains in the context of critical phase transition phenomena* [259]. In fact, similar phase transition behavior can clearly be identified in fullerene formation simulations from C_2 ensembles, and SWCNT cap nucleation simulations on transition-metal catalysts. Furthermore, the dynamics of haeckelite and graphene growth both obey nearly identical power laws. It is therefore possible to consider these phenomena in the context of self-organized criticality (SOC), alongside other phenomena as diverse as earthquake magnitudes, traffic jams, and modern city populations [67, 260]. Apparently, the employed temperature of 1,180 K is at the lower border to allow for a full conversion of pentagons and heptagons to hexagons via Stone–Wales transformations [261], as discussed in Sect. 5.3.3. We can only speculate that the haeckelite patches, although kinetically favored by the "pentagon-first" mechanism, will eventually anneal on microsecond time scales to a hexagonal graphene network. *Thus, the ensembles of carbon chains up to a critical concentration, as well as the haeckelite patches that are nucleated in the absence of a hexagonal network, can be interpreted as intermediate metastable states. It then appears that graphene crystallization, at least in the limit of high surface carbon concentrations, follows Ostwald's "rule of stages"* [262].
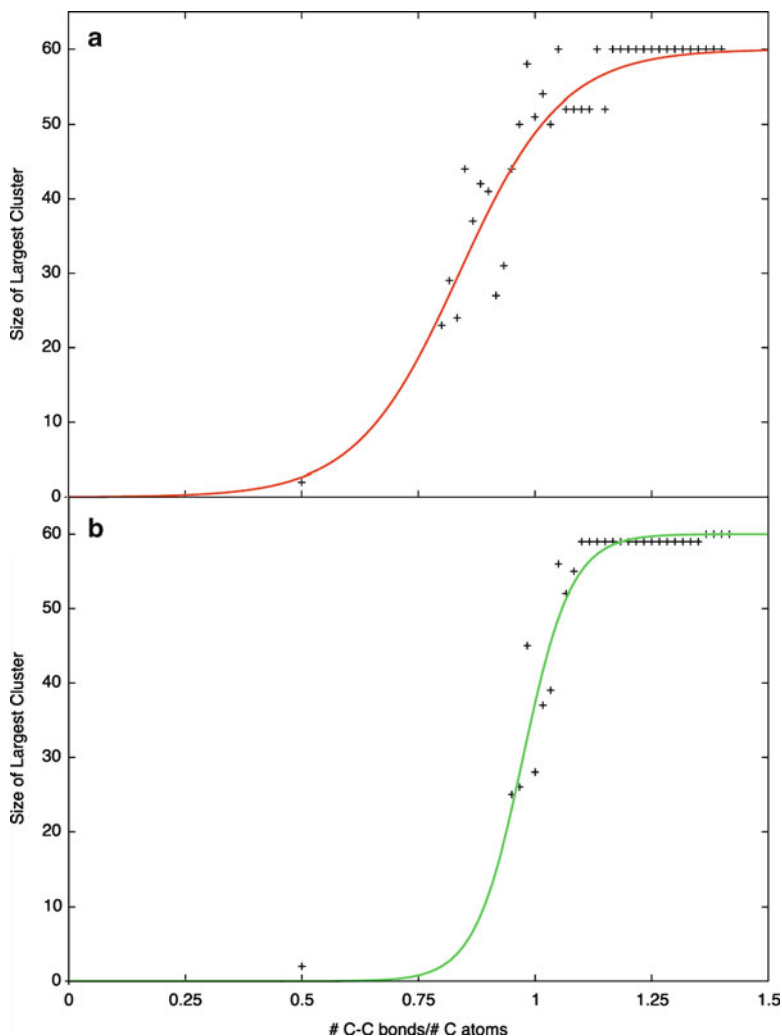
Fig. 5.19 Phase transitions for "H" trajectories (**a**) and "G" trajectories (**b**). As the ratio of the number of carbon bonds per carbon atom passes a critical value smaller than 1.0, the size of the largest connected cluster slowly increases until it reaches a phase transition and a giant component crystallizes. The data points were collected during the entire length of all trajectories

5.6 Common Features in Fullerene, Nanotube, and Graphene Self-Assembly

We have thus far summarized our nonequilibrium QM/MD simulations of fullerene (Sect. 5.3), SWCNT (Sect. 5.4), and graphene (Sect. 5.5) formation in both the presence and absence of various catalysts, such as transition-metal

nanoparticles/surfaces and nontraditional Si-containing "catalyst" nanoparticles. Following these simulations, we have proposed for the first time that carbon nanostructure formation corresponds to a phase transition from linear *sp* carbon chains to fused polygon networks composed of sp^2 carbon that occurs at a critical carbon concentration and corresponding carbon chain length distribution (Sect. 5.6). Usually, periods of random growth are followed by periods of stability, which justifies the classification of carbon nanostructure formation as growth by "punctuated equilibrium" behavior [263], usually discussed in the context of the evolution of the biosphere [264]. This surprising finding then displays with overwhelming clarity that the mode of structural self-assembly of inanimate matter (carbon) bears similarity to that of animate matter (biomolecules). In both cases, the molecular systems in question are held together by bond networks with great variability: In the case of carbon, these are the covalent bonds that can more or less effortlessly rearrange when temperatures are high enough to overcome associated barriers. In the case of biomolecules, these are the hydrogen bond networks, which already may rearrange at room temperature. In both cases, the structures encountered are not static but dynamic. As mentioned in Sect. 5.1, the nonequilibrium conditions of carbon nanostructure formation, in particular that of fullerenes, result in the formation of dissipative structures where constituents (atoms and polygonal bond networks in the case of fullerenes, bond networks in the case of SWCNTs and graphenes) are continually replaced in an entropy-producing process, while the overall structure remains intact. Akin to clouds in the atmosphere, these structures are in constant exchange with the environment (via heat and matter) during their growth and deserve to be called "dissipative structures." Needless to say, in such a case, carbon nanostructure formation at high temperatures has little, if any, resemblance to ordinary, thermodynamically controlled structure formation, such as crystal growth [60]. Attempts to explain the former by the latter, as, for instance, proposed by Ding and Yakobson, [58] are therefore apparently misguided. We will now discuss more general features that we observed in our studies.

5.6.1 *sp^2 Carbon Network Nucleation: Pentagon First?*

Much speculation has surrounded the question whether the first polygonal structure formed during fullerene formation should be a pentagon, hexagon, or even a square [117]. In these early days, it was apparent from TOF-MS that macrocyclic carbon *rings* are abundant in the early stages of fullerene formation [56]. Clearly, these are more stable than linear chains when the size of the carbon cluster exceeds roughly ten carbon atoms [108], and it therefore did not seem reasonable to propose that a pentagon would be created first since its odd number of vertices does not allow that attached carbon chains close upon themselves into rings (see Fig. 5.20a). However, when we performed our first nonequilibrium QM/MD fullerene formation simulations starting from ensembles of C$_2$ units, we noticed the abundance of carbon chains as opposed to macrocyclic rings, which we attributed to the high-temperature
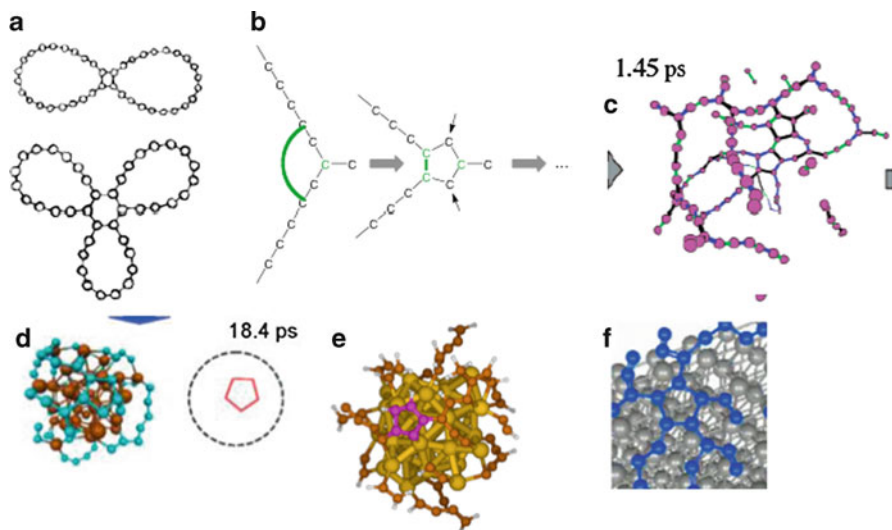
Fig. 5.20 Pentagon first. (**a**) Proposed structures from van Helden et al. [117]. Note that a pentagon is *absent* since it does not allow all attached carbon chains to be arranged in macrocycles. (**b**) Schematics of sp to sp^2 carbon conversion as initial stage of network nucleation, redrawn from Fig. 5.6c. *Black arrows* indicate intermediate divalent carbon atoms possessing unpaired σ-electrons. (**c**) Initial pentagon-containing structure during fullerene formation from Irle et al. [119]. (**d**) Initial pentagonal structure during SWCNT cap nucleation on an iron nanoparticle from Ohta et al. [177]. (**e**) Initial pentagonal structure during the oligomerization of acetylene on an iron nanoparticle. (**f**) Initial pentagonal structure during haeckelite nucleation on Ni(111)

environment where entropy strongly favors the former over the latter structures. Before us, nobody had explicitly considered the role of entropy in the fullerene formation process, only with the exception of Maruyama and coworkers in their REBO/MD simulations [74]. The latter chose not to elaborate on their finding possibly because their potential energy function was too crude to allow such detailed discussions. Whittaker had shown already in 1978 that carbyne forms of carbon might be stable between 2,600 and 3,800 K [265]. Since graphite lies adjacent to the region of carbyne in this famous carbon phase diagram [43], a mechanism of transition between the sp^2 and sp phases must exist. The hypothetical "party line" [116] and "ring fusion spiral zipper" mechanism [117] of fullerene formation come close to the ring condensation via carbon chain collapse observed in our QM/MD simulations (see Fig. 5.1). Actually, for the reverse reaction, namely, the disintegration of sp^2 carbon networks into carbon chains due to external pulling forces, evidence was recently found in experiment [266] and theory [188, 189, 267, 268]. In our earliest simulations of open-ended SWCNT self-capping, we had termed the developing short linear chains at the tube openings "wobbling C_2 units" [188, 189].

We first noticed the importance of carbon chain Y-junctions in our 2009 study of SWCNT cap nucleation [269] (see Figs. 5.6c and 5.20b). A Y-junction represents

a single sp^2 defect surrounded by sp^1 carbon. The smallest Y-junction is the aforementioned C_4 "star conformation," recently stressed in the context of graphene formation in [256]. Larger Y-junctions had been observed in 2007 by Yamaguchi et al., who referred to them as "tri-furcates" [122], and preceded fullerene formation in their TBMD simulations. Inspecting our own QM/MD trajectories from 2003 [119], we also found abundant Y-junctions that we had failed to identify earlier. Apparently, the sp to sp^2 transition starts with the single sp^2 corner stone carbon atom, marked green in Fig. 5.20b. Since squares are too highly strained, the smallest possible carbon cluster with an increase in the number of sp^2 carbons is the pentagon, possessing only two open-shell-carbene-like carbon atoms (indicated by a black arrow in Fig. 5.20b), as discussed in Sect. 5.4.3. Formation of a hexagon would not have alleviated ring strain much yet increased the number of unfavorable open-shell-carbene-like carbon atoms to three. In vacuum, even the formation of a pentagon as shown in Fig. 5.20b is endothermic by more than 2.5 eV, and we therefore never observe such pentagons. Rather, what we observe during fullerene formation are condensed ring systems, comprised of pentagons and hexagons, as shown in Fig. 5.20c. However, if a chemical environment is present that can stabilize the σ-radical electrons at the edge of the first polygon formed from a single Y-junction, we do observe the formation of single pentagons (Fig. 5.20d–f). We conjecture that the role of step edges on metal surfaces in the case of graphene growth, and on metal particles in the case of SWCNT cap nucleation, serves to stabilize the first generation of carbon polygons, which would otherwise suffer from dangling σ-bonds at their edge. On substrates with low carbon adhesion strength, such as transition metals, we find the formation of relatively long carbon chains. Subsequently, Y-junctions emerge during surface diffusion of the carbon chains, and in a process that apparently requires simulation times on the order of 100 ps, a single pentagon is created from this Y-junction [177, 196]. Subsequent polygons formed are pentagons, hexagons, and heptagons, very rarely quadrangles, and they are formed in rapid succession until the carbon chains attached to the first pentagon are too short to engage in sp^2 network growth by ring collapse. The formation of the first pentagon requires a long time since the condition has to be right such that its three sp^2 carbon atoms are located over a hollow site, and that its two open-shell-carbene-like carbon atoms can favorably interact with step-edge-like metal atoms. It was particularly revealing, and at first sight counterintuitive, that the first polygon created on a flat metal surface such as Ni(111) was always a pentagon, prompting the increased production of heptagons (and the creation of a haeckelite, see Sect. 5.5.2) in subsequent steps to maintain a near-zero sp^2 carbon curvature.

On substrates where the substrate-carbon interaction is comparable to the carbon-carbon interaction, such as Si, SiO_2, and SiC, much higher carbon concentrations are required [211] (see Sect. 5.4.5). The carbon binds strongly with surface Si atoms possessing dangling bonds due to the elimination of CO or structural defects. The carbon network formation in such cases does not follow the Y-junction collapse to pentagon structures and resembles more the segregation process of a carbide to yield separated Si and carbon phases. No particular preference for either pentagons or hexagons as initial pure carbon polygon was evident in our QM/MD simulations.

5.6.2 Causality Dilemma: Curvature or Polygon?

Since the proposal of the soccer ball structure for buckminsterfullerene C_{60}, [21] it was stressed that, according to the famous Euler theorem, 12 pentagons are required to achieve closure of any fullerene cage [115]. Smalley reasoned that annealing would *maximize* the number of pentagons in a growing structure [57]. Since hexagons have lower energies than pentagons, this assumption is definitely incorrect. Annealing has to produce all-hexagonal graphite, as it does when ample time for annealing and energy is provided to overcome Stone–Wales barriers (the pentagon/hexagon ratio is always decreasing over time in our QM/MD simulations of GFs at high temperature [41, 62, 120, 125, 136]). To halt the annealing process at the moment when the pentagons have found their right position, as Smalley suggested [57], is an arbitrary, goal-aware step that could only be achieved by an external organizer who possesses advance knowledge of the final fullerene cage architecture. This line of thinking is as misguided as the screw-dislocation growth model of SWCNT growth [58] and entirely overlooks the fact that fullerene formation occurs in an open environment, far from equilibrium, where dissipative, ever-changing structures take over the domain of inanimate, lifeless crystal structures. In the preceding section, we have elaborated on how carbon chooses pentagons as the first polygonal structure in the transition from sp to sp^2 phases. It then appears that one should not ask how nature puts the 12 pentagons into the fullerene or SWCNT but how the hexagons are created in the final, low-temperature, "dead" products. Since fullerenes, SWCNTs, and graphenes are dissipative structures that can change their polygonal composition almost arbitrarily at temperatures above the threshold for Stone–Wales transformations, it is now clear that the final polygonal makeup of a carbon nanostructure is the result of annealing during slow cooling from elevated synthesis temperatures. That is, we find that the shape of the dissipative high-temperature structure dictates the eventual positions of pentagons and hexagons and not the other way around. This shape is determined by two factors: catalyst geometry and catalyst-carbon interaction strength. In Fig. 5.21, we show three limiting cases. Figure 5.21a depicts the situation in vacuum (no catalyst) for the processes of fullerene cage closure [119] and SWCNT self-capping [189]. Figure 5.21b depicts a SWCNT cap formed on an Fe_{38} nanoparticle [269] (spherical catalyst, weak catalyst-carbon interaction). Figure 5.21c shows SWCNT cap formation on a SiO_2 nanoparticle [211] (spherical catalyst, strong catalyst-carbon interaction). Figure 5.21d depicts a SWCNT grown on the C-face of SiC (000-1) during high-temperature vacuum deposition, modeled via periodic removal of Si atoms [270] (flat catalyst, strong catalyst-carbon interaction). Finally, Fig. 5.21e shows haeckelite and graphene growth on Ni(111) (flat catalyst, weak catalyst-carbon interaction). For the ease of understanding, we have augmented these figures by schemes where green octopuses symbolize sp/sp^2 hybrid structures, as was done in Fig. 5.1 for the "octopus-on-the-rock" intermediate structures before cage closure. We find the following relationships:
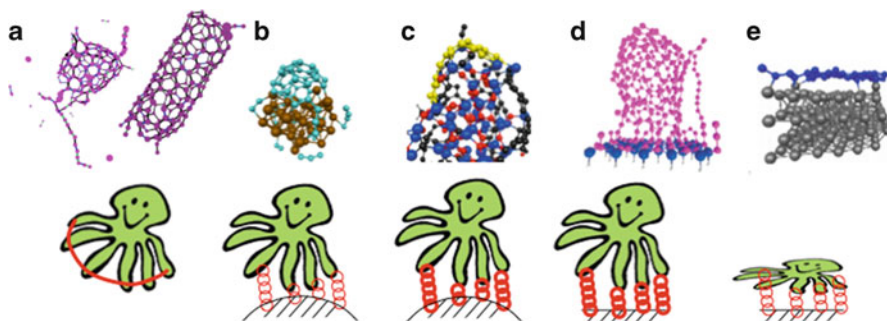
Fig. 5.21 Importance of catalyst shape and interaction strength with carbon for the shape adopted by the dissipative carbon superstructure during high-temperature synthesis. The octopus symbol in the schematic figures of the lower panel represents the sp/sp^2 hybrid nanostructure during self-assembly. (**a**) Vacuum, no catalyst in the process of fullerene cage closure [119] and SWCNT self-capping [189]. (**b**) SWCNT cap formation on an Fe$_{38}$ nanoparticle [269]. (**c**) SWCNT cap formation on an SiO$_2$ nanoparticle [211]. (**d**) SWCNT nucleation and growth on the C-face of SiC (000-1) during high-temperature vacuum deposition, modeled via periodic removal of Si atoms [270]. (**e**) Haeckelite and graphene growth on Ni(111)

1. Pure carbon (Fig. 5.21a) will achieve sp to sp^2 phase transition via the formation of a pentagon-rich polygon network formation, where spherical structures form as a result of the curvature induced by the randomly created pentagons. The process completes with the saturation of dangling edges via cage or cap closure of the curved carbon structure.

2. Weak to strong substrate-carbon interactions and a curved substrate (Fig. 5.21b, c) will prompt the formation of a carbon dome, followed by tube growth. This is because the system has to solve an optimization problem between two competing factors: weak or strong edge binding to the substrate on one hand, and the tendency of carbon to anneal to hexagonal structures, associated with zero curvature. The tube structure is the compromise structure that satisfies both constraints at the same time and preserves the original curved cap structure to the end. The requirement for initial dome formation is that catalyst-carbon interactions should be strong enough to overcome the strain energy of the curved π-conjugated carbon cap. In catalyst where this is not the case, for instance, in the case of gold, chemical modifications have to be made to the Au particles to enforce stronger catalyst-carbon interactions.

3. Strong catalyst-carbon interactions and a flat catalyst (Fig. 5.21d) also lead to the formation of a carbon dome, followed by the growth of a tube structure. The reason is the same as for (2), the shape of the particle in this case is of lesser importance when the edge binding is so strong that it easily can overcome the strain energy of the curved π-conjugated carbon cap.

4. Weak catalyst-carbon interactions and a flat catalyst (Fig. 5.21e) prompt the formation of a flat haeckelite or graphene structure. This is because the driving force for dome formation, namely, the edge stabilization by the catalyst, is not

Fig. 5.22 Conceptual depiction of (n, m) chirality imprinted from an already annealed, colder area onto the hot, defectively grown polygonal sp^2 carbon network near the tube-metal interface
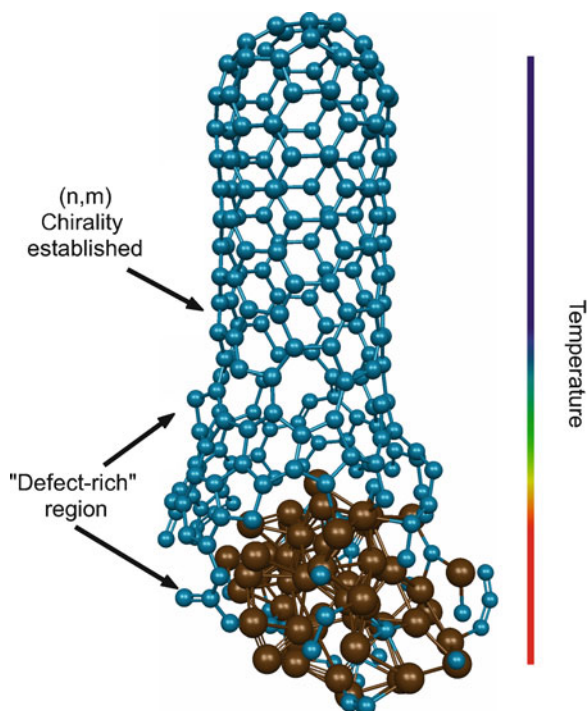
acting in this case. Thus, the growing carbon structure settles to form a planar haeckelite structure in the absence of a hexagonal seed network or graphene in its presence. We conjecture that the presence of a step edge, or the abundance of C_4 "star" cluster, may also favor graphene formation over haeckelite. At any rate, if temperature is high enough, haeckelite will quickly anneal to graphene on experimental time scales.

In the context of SWCNT nucleation, our observations imply that one has to ensure the thermal stability of a specific (n, m) chiral initial tube fragment, which can *imprint* its chirality on the subsequently growing sp^2 network (see Fig. 5.22 from [219]). Early on we noticed that long, straight SWCNT sidewalls correlate well with a high hexagon formation rate [271]. We now understand that the origin of these hexagons is the prevailing superstructure of the nascent carbon nanostructure and not vice versa.

5.7 Conclusions

Our simulations have shown that carbon nanostructure formation processes at high temperatures are processes occurring away from thermodynamic equilibrium and cannot be understood by applying methods that were developed for the study of the

latter. We have found a common phase transition mechanism for carbon cooling from sp to sp^2 phase that shows the importance of pentagons as first polygons created in the structural transformations. The structures formed are dissipative in nature and undergo constant changes regarding their composition, as they grow and consume matter and energy while distributing entropy to the outside world. Most importantly, nonequilibrium dynamics imply the occurrence of irreversible processes [65], such as the carbon-carbon bond formation and the almost instantaneous dissipation of heat of reaction into the environment (tube or carrier gas). The very nonequilibrium nature of these processes excludes equilibrium growth mechanisms, which rely on the reversibility of the crystallization processes, such as crystal growth. Carbon comes and attaches to existing carbon, producing either a hexagon or, almost equally likely, a polygonal defect. Consequently, in all carbon nanostructure formation processes, gradual defect healing from pentagons to hexagons has to take place, as described in Sect. 5.4.7, and we find that such annealing will follow the shape established by the dissipative structure, as shown in Fig. 5.21. We find that transition metals are very efficient in this annealing, as they keep boundary carbon mobile and lower the barrier for Stone–Wales transformations of carbon in their vicinity. If we are to master the challenge of (n, m) chirality-specific SWCNT growth, the targeted synthesis of specific metallofullerenes, or the efficient production of graphene nanoribbons with specific edge structures, we better acknowledge the fact that their synthesis occurs at high temperatures under nonequilibrium dynamics. At present, discussions are too often centered on the underlying thermodynamics, which is of course important, but does not give appropriate guidelines as to how to create carbon nanostructures with current methods of synthesis. We hope that this chapter has paved the way toward a new understanding of nonequilibrium synthesis, and that nanotechnology will benefit from the insights our QM/MD simulations have brought.

5.7.1 Future Perspectives

An important, if not *the* most important, issue that has remained unaddressed by our studies thus far is the question of how the (n, m) chirality of the first stable tube fragment (cap or short tube coalesced from polyyne chains) arises. There are good reasons why we did not tackle this apparently very important question yet: (a) As the success of the "very slow" carbon supply simulations reported in Sect. 5.4.7.2 shows with clarity, the rate of carbon addition has to be controlled so that slow Stone–Wales and other healing transformations can occur before more carbon is added that would stabilize existing defects. Therefore, to model defect-free growth, the nucleation and growth simulations would have to be performed for simulation times exceeding the presently possibly time scale by about one order of magnitude, which is nearly an impossible task since time is not parallelizable, and the currently employed DFTB algorithm does not scale well with the number of CPUs; (b) the nucleation of chiral caps of specific type likely requires the presence of stable crystal

facets with particular crystallographic surfaces. The simulation of nucleation on nanoparticles with specific shape requires that the simulations are performed below the melting temperature of the particles, and that the particles are large enough to support the stability of such facets. Low temperatures translate computationally to slower reactions and longer simulation times, while the use of larger catalyst particles translates to tremendously increased CPU time requirements by virtue of the $O(N^3)$ scaling of the currently employed DFTB algorithm. For these reasons, a new approach to calculating accurate potential energies and gradients on the fly is required to study the factors giving rise to specific (n, m) chirality in the first stable tube fragment. One such possibility is the use of Liouville-von Neumann MD (LvNMD) [272] based on the DFTB potential, which avoids diagonalization of the Hamiltonian while retaining the possibility to employ an electronic temperature regulating fractional orbital occupations according to Eq. (5.4). Another possibility might be the use of semiempirical reactive force fields such as ReaxFF [273], which was recently demonstrated to reproduce high-level first principles reaction data with good accuracy [274]. Another possibility is the use of an integrated method such as ONIOM [275, 276], employing DFTB and ReaxFF potentials for spatially separated areas such as bulk and surface. We are currently exploring all of these avenues while hoping that experimentalists find ways to synthesize small, stable tube fragments by means of organic chemistry approaches such as exemplified in the recent virtuous synthesis of [n]cycloparaphenylenes, representing so to speak the smallest segments of (n, n) armchair SWCNTs. It is our conviction that, if inexpensive mass production of high-quality SWCNTs with arbitrary (n, m) chirality could be achieved, SWCNTs would surely outperform graphenes in terms of durability, variability of electronic properties, ease of mechanical handling, and so on, when employed in future nanoscale electronic devices.

References

1. Nabokov VV (1974) Look at the harlequins! McGraw-Hill, New York
2. Feynman R (1959) There's plenty of room at the bottom: an invitation to enter a new world of physics. Paper presented at the annual meeting of the American Physical Society, Pasadena
3. Drexler KE (1986) Engines of creation. Anchor Books, New York
4. Drexler KE (1992) Nanosystems: molecular machinery, manufacturing, and computation. Wiley, New York
5. Binnig G, Rohrer H, Gerber C, Weibel E (1982) Tunneling through a controllable vacuum gap. Appl Phys Lett 40:178–180
6. Smalley RE (2001) Of chemistry, love, and nanobots. Sci Am 285:76–77
7. Baum R (2003) Nanotechnology. Chem Eng News 81(48):37–42
8. Lehn J-M (1995) Supramolecular chemistry: concepts and perspectives. Wiley-VCH, Weinheim
9. Pawin G, Wong KL, Kwon K-Y, Bartels L (2006) A homomolecular porous network at a Cu(111) surface. Science 313:961–962
10. Hoster HE, Roos M, Breitruck A, Meier C, Tonigold K, Waldmann T, Ziener U, Landfester K, Behm RJ (2007) Structure formation in Bis(terpyridine) derivative adlayers: molecule-substrate versus molecule-molecule interactions. Langmuir 23:11570–11579
11. Love JC, Estroff LA, Kriebel JK, Nuzzo RG, Whitesides GM (2005) Self-assembled monolayers of thiolates on metals as a form of nanotechnology. Chem Rev 105:1103–1169
12. Cai J, Ruffieux P, Jaafar R, Bieri M, Braun T, Blankenburg S, Muoth M, Seitsonen AP, Saleh M, Feng X, Müllen K, Fasel R (2010) Atomistically precise bottom-up fabrication of graphene nanoribbons. Nature 466:470–473
13. Petitjean A, Khoury RG, Kyritsakas N, Lehn J-M (2004) Dynamic devices. Shape switching and substrate binding in ion-controlled nanomechanical molecular tweezers. J Am Chem Soc 126:6637–6647
14. Seeman NC (2010) Structural DNA nanotechnology: growing along with nano letters. Nano Lett 10:1971–1978
15. Kinbara K, Aida T (2005) Toward intelligent molecular machines: directed motions of biological and artificial molecules and assemblies. Chem Rev 105:1377–1400
16. Kauffman S (2000) Investigations. Oxford University Press, Oxford
17. Seyed-Razavi A, Snook IK, Barnard AS (2010) Origin of nanomorphology: does a complete theory of nanoparticle evolution exist? J Mater Chem 20:416–421
18. Alivisatos AP (1996) Semiconductor clusters, nanocrystals, and quantum dots. Science 271:933–937
19. Xu X, Zhuang J, Wang X (2008) SnO2 Quantum dots and quantum wires: controllable synthesis, self-assembled 2D architectures, and gas-sensing properties. J Am Chem Soc 130:12527–12535
20. Smolin L (1997) The life of the cosmos. Oxford University Press, Oxford
21. Kroto HW, Heath JR, O'Brien SC, Curl RF, Smalley RE (1985) C60: buckminsterfullerene. Nature 318:162–163
22. Fowler PW, Manopoulous DE (1995) An atlas of fullerenes. Oxford University Press, Oxford
23. Fantini C, Cruz E, Jorio A, Terrones M, Terrones H, Van Lier G, Charlier J-C, Dresselhaus MS, Saito R, Kim YA, Hayashi T, Muramatsu H, Endo M, Pimenta MA (2006) Resonance Raman study of linear carbon chains formed by the heat treatment of double-wall carbon nanotubes. Phys Rev B 73:193408/193401–193404
24. Saito R, Dresselhaus MS, Dresselhaus G (1998) Physical properties of carbon nanotubes. Imperial College Press, London
25. Wu YH, Yu T, Shen ZX (2010) Two-dimensional carbon nanostructures: fundamental properties, synthesis, characterization, and potential applications. J Appl Phys Rev 108:071301/071301–071338
26. Krüger A (2008) The structure and reactivity of nanoscale diamond. J Mater Chem 18:1485–1492

27. Terrones H, Terrones M, Hernandez E, Grobert N, Charlier JC, Ajayan PM (2000) New metallic allotropes of planar and tubular carbon. Phys Rev Lett 84:1716–1719
28. Shioyama H, Akita T (2003) A new route to carbon nanotubes. Carbon 41:179–198
29. Iijima S, Yudasaka M, Yamada R, Bandow S, Suenaga K, Kokai F, Takahashi K (1999) Nano-aggregates of single-walled graphitic carbon nano-horns. Chem Phys Lett 309:165–170
30. Itoh S, Ihara S, Kitakami J (1993) Toroidal form of carbon C360. Phys Rev B 47:1703–1704
31. Amelinckx S, Zhang XB, Bernaerts D, Zhang XF, Ivanov V, Nagy JB (1994) A formation mechanism for catalytically grown helix-shaped graphite nanotubes. Science 265:635–639
32. Lee JM, Choung JW, Yi J, Lee DH, Samal M, Yi DK, Lee C-H, Yi G-C, Paik U, Rogers JA, Park WI (2010) Vertical pillar-superlattice array and graphene hybrid light emitting diodes. Nano Lett 10:2783–2788
33. Zakhidov AA, Baughman RA, Iqbal Z, Cui C, Khayrullin I, Dantas SO, Marti J, Ralchenko VG (1998) Carbon structures with three-dimensional periodicity at optical wavelengths. Science 282:897–901
34. Terrones H, Terrones M (2003) Curved nanostructure materials. New J Phys 5:126/121–137
35. Terrones M, Botello-Mendez AR, Campos-Delgado J, Lopez-Urias F, Vega-Cunti YI, Rodriguez-Marcias FJ, Elias AL, Munoz-Sandoval E, Cano-Marquez AG, Charlier J-C, Terrones H (2010) Graphene and graphite nanoribbons: morphology, properties, synthesis, defects and applications. Nano Today 5:351–372
36. Krüger A (2010) Carbon materials and nanotechnology. Wiley-VCH, Weinheim
37. Baughman RA, Zakhidov AA, de Heer WA (2002) Carbon nanotubes – the route toward applications. Science 297:787–792
38. Mamalis AG, Vogtländer LOG, Markopoulos A (2004) Nanotechnology and nanostructured materials: tends in carbon nanotubes. Precis Eng 28:16–30
39. Ma JC, Dougherty DA (1997) The cation-pi interaction. Chem Rev 97:1303–1324
40. Fukui K (1981) The path of chemical reactions – the IRC approach. Acc Chem Res 14:363–368
41. Irle S, Zheng G, Wang Z, Morokuma K (2007) Theory-experiment relationship of the "shrinking hot giant" road of dynamic fullerene self-assembly in hot carbon vapor. Nano 2:21–30
42. Krätschmer W, Lamb LD, Fostiropoulos K, Huffman DR (1990) Solid C60: a new form of carbon. Nature 347:354–358
43. Whittaker AG (1978) The controversial carbon solid-liquid-vapour triple point. Nature 276:695–696
44. Sasaki K (2011) Spectroscopic studies on laser-produced carbon vapor. In: Laszlo N, Irle S (eds) Spectroscopy, dynamics and molecular theory of carbon plasmas and vapors. World Scientific, Singapore
45. Ashfold MNR, May PW, Rego CA, Everitt NM (1994) Thin film diamond by chemical vapour deposition methods. Chem Soc Rev 23:21–30
46. Cheesman A, Harvey JN, Ashfold MNR (2008) Studies of carbon incorporation on the diamond 100 surface during chemical vapor deposition using density functional theory. J Phys Chem A 112(45):11436–11438
47. Puretzky AA, Geohegan DB, Schittenhelm H, Fan X, Guillorn MA (2002) Time-resolved diagnostics of single wall carbon nanotube synthesis by laser vaporization. Appl Surf Sci 197–198:552–562
48. Cheng HM, Li F, Su G, Pan HY, He LL, Sun X, Dresselhaus MS (1998) Large-scale and low-cost synthesis of single-walled carbon nanotubes by the catalytic pyrolysis of hydrocarbons. Appl Phys Lett 72:3282–3284
49. Nikolaev P, Bronikowski MJ, Bradley RK, Rohmund F, Colbert DT, Smith KA, Smalley RE (1999) Gas-phase catalytic growth of single-walled carbon nanotubes from carbon monoxide. Chem Phys Lett 313:91–97
50. Maruyama S, Kojima R, Miyauchi Y, Chiashi S, Kohno M (2002) Low-temperature synthesis of high-purity single-walled carbon nanotubes from alcohol. Chem Phys Lett 360:229–234
51. Nagashima A, Tejima N, Oshima C (1994) Electronic states of the pristine and alkali-metal-intercalated monolayer graphite/Ni(111) systems. Phys Rev B 50(23):17487–17495

52. Choi W, Lahiri I, Seelaboyina R, Kang YS (2010) Synthesis of graphene and its applications: a review. Crit Rev Solid State 35(1):52–71
53. Charlier J-C, Iijima S (2001) Growth mechanisms of carbon nanotubes, vol 80, Carbon nanotubes: synthesis, structure, properties, and application. Springer, New York
54. Nessim GD, Seita M, Plata DL, O'Brien KP, Hart AJ, Meshot ER, Reddy CM, Gschwend PM, Thompson CV (2011) Precursor gas chemistry determines the crystallinity of carbon nanotubes synthesized at low temperature. Carbon 49:804–810
55. Puretzky AA, Geohegan DB, Jesse S, Ivanov IN, Eres G (2005) In situ measurements and modeling of carbon nanotube array growth kinetics during chemical vapor deposition. Appl Phys A 81(2):223
56. Wakabayashi T, Achiba Y (1992) A model for the C60 and C70 growth mechanism. Chem Phys Lett 190(5):465–468
57. Smalley RE (1992) Self-assembly of the fullerenes. Acc Chem Res 25:98–105
58. Ding F, Harutyunyan AR, Yakobson BI (2009) Dislocation theory of chirality-controlled nanotube growth. Proc Natl Acad Sci 106:2506–2509
59. Kroto HW (1987) The stability of the fullerenes C_n, with n = 24, 28, 32, 36, 50, 60 and 70. Nature 384:529–531
60. Burton WK, Cabrera N, Frank FC (1949) Role of dislocations in crystal growth. Nature 163:398–399
61. Eres G, Rouleau CM, Yoon M, Puretzky AA, Jackson JJ, Geohegan DB (2009) Model for self-assembly of carbon nanotubes from acetylene based on real-time studies of vertically aligned growth kinetics. J Phys Chem C 113:15484–15491
62. Irle S, Zheng G, Wang Z, Morokuma K (2006) The C60 formation puzzle "solved": QM/MD simulations reveal the shrinking hot giant road of the dynamic fullerene self-assembly mechanism. J Phys Chem B 110:14531–14545
63. Irle S, Ohta Y, Okamoto Y, Page AJ, Wang Y, Morokuma K (2009) Milestones in molecular dynamics simulations of single-walled carbon nanotube formation: a brief critical review. Nano Res 2:755–767
64. Prigogine I, Stengers I (1984) Order out of chaos: man's new dialogue with nature. Bantam Books, Toronto
65. Prigogine I (1997) The end of certainty – time, chaos, and the new laws of nature. The Free Press, New York
66. Fialkowsy M, Bishop KJM, Klajn R, Smoukov SK, Campbell CJ, Grzybowski BA (2006) Principles and implementations of dissipative (dynamic) self-assembly. J Phys Chem B 110:2482–2496
67. Bak P (1996) How nature works: the science of self-organised criticality. Copernicus Press, New York
68. Tersoff J (1988) New empirical approach for the structure and energy of covalent systems. Phys Rev B 37:6991–7000
69. Tersoff J (1989) Modeling solid-state chemistry: Interatomic potentials for multicomponent systems. Phys Rev B 39:5566–5568
70. Brenner DW (1990) Empirical potential for hydrocarbons for use in simulating the chemical vapor deposition of diamond films. Phys Rev B 42:9458–9471
71. Brenner DW (1992) Empirical potential for hydrocarbons for use in simulating the chemical vapor deposition of diamond films. [Erratum to document cited in CA114(6):53045x]. Phys Rev B 46:1948
72. Brenner DW (2000) The art and science of an analytical potential. Phys Status Solidi B 217:23–40
73. Maruyama S, Yamaguchi Y (1998) A molecular dynamics demonstration of annealing to a perfect C60 structure. Chem Phys Lett 286:343–349
74. Yamaguchi Y, Maruyama S (1998) A molecular dynamics simulation of the fullerene formation process. Chem Phys Lett 286:336–342
75. Shibuta Y, Maruyama S (2002) Molecular dynamics simulation of generation process of SWNTs. Phys B 323:187–189

76. Shibuta Y, Maruyama S (2003) Molecular dynamics simulation of formation process of single-walled carbon nanotubes by CCVD method. Chem Phys Lett 382:381–386

77. Shibuta Y, Maruyama S (2004) Molecular dynamics of nucleation process of single-walled carbon nanotubes. Therm Sci Eng 12(4):79–80

78. Ding F, Bolton K, Rosen A (2004) Nucleation and growth of single-walled carbon nanotubes: a molecular dynamics study. J Phys Chem B 108(45):17369–17377

79. Ding F, Bolton K, Rosen A (2004) Iron-carbide cluster thermal dynamics for catalyzed carbon nanotube growth. J Vac Sci Technol A 22(4):1471–1476

80. Ding F, Rosen A, Bolton K (2004) Molecular dynamics study of the catalyst particle size dependence on carbon nanotube growth. J Chem Phys 121(6):2775–2779

81. Ding F, Rosen A, Bolton K (2004) The role of the catalytic particle temperature gradient for SWNT growth from small particles. Chem Phys Lett 393:309–313

82. Ding F, Rosen A, Bolton K (2005) Dependence of SWNT growth mechanism on temperature and catalyst particle size: bulk versus surface diffusion. Carbon 43:2215–2217

83. Ding F, Rosen A, Campbell CJ, Falk LKL, Bolton K (2006) Graphitic encapsulation of catalyst particles in carbon nanotube production. J Phys Chem B 110:7666–7670

84. Charlier J-C, De Vita A, Blase X, Car R (1997) Microscopic growth mechanisms for carbon nanotubes. Science 275:646–649

85. Gavillet J, Loiseau A, Journet C, Willaime F, Ducastelle F, Charlier J-C (2001) Root-growth mechanism for single-wall carbon nanotubes. Phys Rev Lett 87(27):275504–275501

86. Raty J-Y, Gygi F, Galli G (2005) Growth of carbon nanotubes on metal nanoparticles: a microscopic mechanism from ab initio molecular dynamics simulations. Phys Rev Lett 95:096103/096101–096104

87. Porezag D, Frauenheim T, Köhler T, Seifert G, Kaschner R (1995) Construction of tight-binding-like potentials on the basis of density-functional theory: application to carbon. Phys Rev B 51:12947–12957

88. Seifert G, Porezag D, Frauenheim T (1996) Calculations of molecules, clusters, and solids with a simplified LCAO-DFT-LDA scheme. Int J Quantum Chem 58:185–192

89. Elstner M, Porezag D, Jungnickel G, Elsner J, Haugk M, Frauenheim T, Suhai S, Seifert G (1998) Self-consistent-charge density-functional tight-binding method for simulations of complex materials properties. Phys Rev B 58:7260–7268

90. Kohler C, Seifert G, Gerstmann U, Elstner M, Overhof H, Frauenheim T (2001) Approximate density-functional calculations of spin densities in large molecular systems and complex solids. Phys Chem Chem Phys 3:5109–5114

91. Weinert M, Davenport JW (1992) Fractional occupations and density-functional energies and forces. Phys Rev B 45(23):13709–13712

92. Witek H, Irle S, Morokuma K (2004) Analytical second-order geometrical derivatives of energy for the self-consistent-charge density-functional tight-binding method. J Chem Phys 121:5163

93. Elstner M, Hobza P, Frauenheim T, Suhai S, Kaxiras E (2001) Hydrogen bonding and stacking interactions of nucleic acid base pairs: a density-functional-theory based treatment. J Chem Phys 114:5149–5155

94. Hourahine B, Sanna S, Aradi B, Köhler C, Niehaus T, Frauenheim T (2007) Self-interaction and strong correlation in DFTB. J Phys Chem A 111:5671–5677

95. Rapacioli M, Spiegelman F, Scemama A, Mirtschink A (2010) Modeling charge resonance in cationic molecular clusters: combining DFT-tight binding with configuration interaction. J Chem Theory Comput 7:44–55

96. Alder BJ, Wainwright TE (1957) Phase transition for a hard sphere system. J Chem Phys 27:1208–1209

97. Rahman A (1964) Correlations in the motion of atoms in liquid argon. Phys Rev 136:A405–A411

98. Swope WC, Andersen HC, Berens PH, Wilson KR (1982) A computer simulation method for the calculation of equilibrium constants for the formation of physical clusters of molecules: application to small water clusters. J Chem Phys 76(1):637–649

99. Andersen HC (1980) Molecular dynamics simulations at constant pressure and/or temperature. J Chem Phys 72:2384–2393
100. Berendsen HJC, Postma JPM, van Gunsteren WF, DiNola A, Haak JR (1984) Molecular dynamics with coupling to an external bath. J Chem Phys 81:3684–3690
101. Woodcock LV (1971) Isothermal molecular dynamics calculations for liquid salts. Chem Phys Lett 10:257–261
102. Hoover WG (1985) Canonical dynamics: equilibrium phase-space distributions. Phys Rev A 31:1695–1697
103. Martyna GJ, Klein ML, Tuckerman M (1992) Nose-Hoover chains: the canonical ensemble via continuous dynamics. J Chem Phys 97:2635–2643
104. Martyna GJ, Tobias DJ, Tuckerman M, Klein ML (1996) Explicit reversible integrators for extended systems dynamics. Mol Phys 87:1117–1157
105. Nose S (1984) A unified formulation of the constant temperature molecular dynamics methods. J Chem Phys 81:511–519
106. Rohlfing EA, Cox DM, Kaldor A (1984) Production and characterization of supersonic carbon cluster beams. J Chem Phys 81(7):3322–3330
107. Hoffmann R (1966) Extended Hückel theory – V: cumulenes, polyenes, polyacetylenes and Cn. Tetrahedron 22:521–538
108. Parasuk V (2011) Electronic and molecular structures of small- and medium-sized carbon clusters. In: Nemes L, Irle S (eds) Spectroscopy, dynamics and molecular theory of carbon plasmas and vapors. World Scientific, Singapore
109. Kroto HW, Heath JR, O'Brien SC, Curl RF, Smalley RE (1987) Long carbon chain molecules in circumstellar shells. Astrophys J 314(1):352–355
110. Dunlap BI, Boettger JC (1996) Local-density-functional study of the fullerenes, graphene, and graphite. J Phys B At Mol Opt Phys 29(21):4907–4913
111. Calaminici P, Geudtner G, Koster AM (2009) First-principle calculations of large fullerenes. J Chem Theory Comput 5:29–32
112. Curl RF, Haddon RC (1993) On the formation of the fullerenes. Philos Trans R Soc London Ser A 343:19–32
113. Mintmire JW (1996) Fullerene formation and annealing. Science 272:45–46
114. Howard JB, McKinnon JT, Makarovsky Y, Lafleur AL, Johnson ME (1991) Fullerenes C60 and C70 in flames. Nature 352:139–141
115. Kroto HW (1992) C60: buckminsterfullerene, the celestial sphere that fell to earth. Angew Chem Int Ed 31(2):111–129
116. Heath JR, Zhang Q, O'Brien SC, Curl RF, Kroto HW, Smalley RE (1987) The formation of long carbon chain molecules during laser vaporization of graphite. J Am Chem Soc 109(2):359–363
117. van Helden G, Gotts NG, Bowers MT (1993) Experimental evidence for the formation of fullerenes by collisional heating of carbon rings in the gas phase. Nature 363:60–63
118. Goroff NS (1996) Mechanism of fullerene formation. Acc Chem Res 29:77–83
119. Irle S, Zheng G, Elstner M, Morokuma K (2003) From C2 molecules to fullerenes in quantum chemical molecular dynamics. Nano Lett 3:1657–1664
120. Zheng G, Irle S, Morokuma K (2005) Towards formation of buckminsterfullerene C60 in quantum chemical molecular dynamics. J Chem Phys 122:014708
121. Ueno Y, Saito S (2008) Geometries, stabilities, and reactions of carbon clusters: towards a microscopic theory of fullerene formation. Phys Rev B 77:085403/085401–085411
122. Yamaguchi Y, Colombo L, Piseri P, Ravagnan L, Milani P (2007) Growth of sp-sp2 nanostructures in a carbon plasma. Phys Rev B 76:134119/134111–134117
123. Wakabayashi T, Kasuya D, Shiromaru H, Suzuki S, Kikuchi K, Achiba Y (1997) Towards the selective formation of specific isomers of fullerenes: T- and p-dependence in the yield of various isomers of fullerenes C60-C84. Z Phys D Atom Mol Cl 40:414–417
124. Xu CX, Scuseria GE (1994) Tight-binding molecular dynamics simulations of fullerene annealing and fragmentation. Phys Rev Lett 72:669–672
125. Zheng G, Wang Z, Irle S, Morokuma K (2007) Quantum chemical molecular dynamics simulations of "shrinking" of hot giant fullerenes. J Nanosci Nanotechnol 7:1662–1669

126. Bogana M, Ravagnan L, Casari CS, Zivelonghi A, Baserga A, Bassi AL, Bottani CE, Vinati S, Salis E, Piseri P, Barborini E, Colombo L, Milani P (2005) Leaving the fullerene road: presence and stability of sp chains in sp2 carbon clusters and cluster-assembled solids. New J Phys 7(81):1–8

127. Guangshi T, Hengjian Z, Chuanbao C, Rongzhi L, Hesun Z (1995) The effect of the atmosphere on the formation of fullerene. J Beijing Inst Technol 4(2):141–147

128. Curl RF, Lee MK, Scuseria GE (2008) C60 buckminsterfullerene high yields unraveled. J Phys Chem A 112(46):11951–11955

129. Fowler PW (1986) How unusual is C60? Magic numbers for carbon clusters. Chem Phys Lett 131(6):444–450

130. Osawa E, Ueno H, Yoshida M, Slanina Z, Zhao X, Nishiyama M, Saito H (1998) Combined topological and energy analysis of the annealing process in fullerene formation. Stone–Wales interconversion pathways among IPR isomers of higher fullerenes. J Chem Soc, Perkin Trans 2 . 1998:943–950

131. Sommer T, Kruse T, Roth P (1996) Thermal stability of fullerenes: a shock tube study on the pyrolysis of C60 and C70. J Phys B At Mol Opt Phys 29:4955–4964

132. Bettinger HF, Yakobson BI, Scuseria GE (2003) Scratching the surface of buckminster-fullerene: the barriers for Stone-Wales transformation through symmetric and asymmetric transition states. J Am Chem Soc 125:5572–5580

133. Saito S, Oshiyama A (1991) Electronic and geometric structures of C70. Phys Rev B 44(20):11532–11535

134. Huang JY, Ding F, Jiao K, Yakobson BI (2007) Real time microscopy, kinetics, and mechanism of giant fullerene evaporation. Phys Rev Lett 99:175503/175501–175504

135. Zhang QL, O'Brien SC, Heath JR, Liu Y, Kroto HW, Smalley RE (1986) Reactivity of large carbon clusters: spheroidal carbon shells and their possible relevance to the formation and morphology of soot. J Phys Chem 90(4):525–528

136. Saha B, Shindo S, Irle S, Morokuma K (2009) Quantum chemical molecular dynamics simulations of dynamic fullerene self-assembly in benzene combustion. ACS Nano 3:2241–2257

137. Saha B, Irle S, Morokuma K (2010) Formation mechanism of polycyclic aromatic hydro-carbons in benzene combustion: quantum chemical molecular dynamics simulations. J Chem Phys 132:224303/224301–224303/224311

138. Chuvilin A, Kaiser U, Bichoutskaia E, Besley NA, Khlobystov AN (2010) Direct transforma-tion of graphene to fullerene. Nature Chem 2:450–453

139. Koshino M, Niimi Y, Nakamura E, Kataura H, Okazaki T, Suenaga K, Iijima S (2010) Analysis of the reactivity and selectivity of fullerene dimerization reactions at the atomic level. Nature Chem 2:117–124

140. Hansen K, Yeretzian C, Whetten RL (1994) A simple rate equation for fullerene coalescence. Chem Phys Lett 218:462–466

141. Yi J-Y, Bernholc J (1993) Reactivity, stability, and formation of fullerenes. Phys Rev B 48(8):5724–5727

142. Endo M, Kroto HW (1992) Formation of carbon nanofibers. J Phys Chem 96:6941–6944

143. Yoshida M, Osawa E (1995) Formalized drawing of fullerene nets. 2. Applications to map-ping of pyracylene rearrangements, C2-insertion/elimination pathways, and leapfrog/carbon cylinder operations. Bull Chem Soc Jpn 68:2083–2092

144. Suzuki S, Yamaguchi H, Ishigaki T, Kataura H, Kratschmer W, Achiba Y (2001) Time evolution of emission by carbon nanoparticles generated with a laser furnace technique. Eur Phys J D 16:369–372

145. Nicolis G, Prigogine I (1977) Self-organization in nonequilibrium systems: from dissipative structures to order through fluctuations. Wiley, New York

146. Guo T, Nikolaev P, Thess A, Colbert DT, Smalley RE (1995) Catalytic growth of single-walled carbon nanotubes by laser vaporization. Chem Phys Lett 243:49–54

147. Thess A, Lee R, Nikolaev P, Dai H, Petit P, Robert J, Xu C, Lee YH, Kim SG, Rinzler AG, Colbert DT, Scuseria GE, Tomanek D, Fischer JE, Smalley RE (1996) Crystalline ropes of metallic carbon nanotubes. Science 273:483–487

148. Guo T, Nikolaev P, Rinzler AG, Tomanek D, Colbert DT, Smalley RE (1995) Self-assembly of tubular fullerenes. J Phys Chem 99:10694–10697
149. Iijima S (1993) Single-shell carbon nanotubes of 1-nm diameter. Nature 363:603–605
150. Bethune DS, Kiang CH, DeVries MS, Gorman G, Savoy R, Beyers R (1993) Cobalt-catalysed growth of carbon nanotubes with single-atomic-layer wall. Nature 363:605–607
151. Journet C, Maser WK, Bernier P, Loiseau A, Lamy de la Chapelle M, Lefrant S, Deniard P, Lee R, Fischer JE (1997) Large-scale production of single-walled carbon nanotubes by the electric-arc technique. Nature 388:756–758
152. Guillard T, Cetout S, Alvarez L, Sauvajol JL, Anglaret E, Bernier P, Flamant G, Laplaze D (1999) Production of carbon nanotubes by the solar route. Eur Phys J 5:251–256
153. Shinohara H (2011) Montreal (private communication)
154. Rinzler AG, Liu J, Dai H, Nikolaev P, Huffman CB, Rodriguez-Marcias FJ, Boul PJ, Lu AH, Heymann D, Colbert DT, Lee RS, Fischer JE, Rao AM, Eklund PC, Smalley RE (1998) Large-scale purification of single-wall carbon nanotubes. Process, product, and characterization. Appl Phys A-Mater 67(1):29–37
155. Sugai T, Okazaki T, Yoshida H, Shinohara H (2004) Syntheses of single- and double-wall carbon nanotubes by the HTPAD and HFCVD methods. New J Phys 43(2):431–436
156. Journet C, Bernier P (1998) Production of carbon nanotubes. Appl Phys A-Mater 67(1):1–9
157. Scott CD, Arepalli S, Nikolaev P, Smalley RE (2001) Growth mechanisms for single-wall carbon nanotubes in a laser-ablation process. Appl Phys A-Mater 72(5):573–580
158. Nishide D, Kataura H, Suzuki S, Tsukagoshi K, Aoyagi Y, Achiba Y (2003) High-yield production of single-wall carbon nanotubes in nitrogen gas. Chem Phys Lett 372(1, 2):45–50
159. Ramesh S, Brinson B, Johnson MP, Gu Z, Saini RK, Willis P, Marriott T, Billups WE, Margrave JL, Hauge RH, Smalley RE (2003) Identification of large fullerenes formed during the growth of single-walled carbon nanotubes in the HiPco process. J Phys Chem B 107(6):1360
160. Sadana AK, Liang F, Brinson B, Arepalli S, Farhat S, Hauge RH, Smalley RE, Billups WE (2005) Functionalization and extraction of large fullerenes and carbon-coated metal formed during the synthesis of single wall carbon nanotubes by laser oven, direct current arc, and high-pressure carbon monoxide production methods. J Phys Chem B 109:4416
161. Cheng HM, Li F, Sun X, Brown SDM, Pimenta MA, Marucci A, Dresselhaus G, Dresselhaus MS (1998) Bulk morphology and diameter distribution of single-walled carbon nanotubes synthesized by catalytic decomposition of hydrocarbons. Chem Phys Lett 289(5–6):602–610
162. Zhu Z, Jiang H, Susi T, Nasibulin AG, Kauppinen EI (2011) The use of NH3 to promote the production of large-diameter single-walled carbon nanotubes with a narrow (n, m) distribution. J Am Chem Soc 133:1224–1227
163. Jackson JJ, Puretzky AA, More KL, Rouleau CM, Eres G, Geohegan DB (2010) Pulsed growth of vertically aligned nanotube arrays with variable density. ACS Nano 4:7573–7581
164. Shukla B, Saito T, Yumura M, Iijima S (2009) An efficient carbon precursor for gas phase growth of SWCNTs. Chem Commun 2009:3422–3424
165. Hata K, Futaba DN, Mizuno K, Namai T, Yumura M, Iijima S (2004) Water-assisted highly-efficient synthesis of impurity-free single-walled carbon nanotubes. Science 306:1362–1364
166. Ren WC, Li F, Cheng HM (2005) Shell control and growth mechanism of carbon nanotubes by sulfur-enhanced floating catalyst method. Paper presented at the NASA/Rice University 2nd workshop on nucleation and growth of single-wall carbon nanotubes, Boerne, 8–12 April 2005
167. Valles C, Perez-Mendoza M, Castell P, Martinez MT, Maser WK, Benito AM (2006) Towards helical and Y-shaped carbon nanotubes: the role of sulfur in CVD processes. Nanotechnology 17:4292–4299
168. Scott CD, Arepalli S (2005) Second NASA/Rice University workshop on SWNT nucleation and growth mechanisms. In: 2nd NASA/Rice University workshop on SWNT nucleation and growth mechanisms, Boerne, 2005
169. Ago H, Uehara N, Yoshihara N, Tsuji M, Yumura M, Tomonaga N, Setoguchi T (2006) Gas analysis of the CVD process for high yield growth of carbon nanotubes over metal-supported catalysts. Carbon 44:2912–2918

170. Zhang G, Mann D, Zhang L, Javey A, Li Y, Yenilmez E, Wang Q, McVittie JP, Nishi Y, Gibbons J, Dai H (2005) Ultra-high-yield growth of vertical single-walled carbon nanotubes: hidden roles of hydrogen and oxygen. Proc Natl Acad Sci 102(45):16141–16145

171. Xu Y-Q, Flor E, Schmidt H, Smalley RE, Hauge RH (2006) Effects of atomic hydrogen and active carbon species in 1 mm vertically aligned single-walled carbon nanotube growth. Appl Phys Lett 89:123116/123111–123116/123113

172. Amama PB, Pint CL, McJilton L, Kim SM, Stach EA, Murray PT, Hauge RH, Maruyama B (2009) Role of water in super growth of single-walled carbon nanotube carpets. Nano Lett 9:44–49

173. Alexandrescu R, Crunteanu A, Morjan R-E, Morjan F, Rohmund F, Falk LKL, Ledoux G, Huisken F (2003) Synthesis of carbon nanotubes by CO2-laser-assisted thermal CVD. Infrared Phys Techn 44:43–47

174. Wang Y, Gao X, Eres G, Ohta Y, Qian H-J, Morokuma K, Irle S (2011) Acetylene oligomerization and oligoyne cross-linking on an iron particle: quantum chemical molecular dynamics simulations inspired by experiment. Submitted

175. Sugai Y, Yoshida H, Shimada T, Okazaki T, Shinohara H (2003) New synthesis of high-quality double-walled carbon nanotubes by high-temperature pulsed arc discharge. Nano Lett 3(6):769–773

176. Dai H, Rinzler AG, Nikolaev P, Thess A, Colbert DT, Smalley RE (1996) Single-wall nanotubes produced by metal-catalyzed disproportionation of carbon monoxide. Chem Phys Lett 260(3–4):471–475

177. Ohta Y, Okamoto Y, Page AJ, Irle S, Morokuma K (2009) Quantum chemical molecular dynamics simulation of single-walled carbon nanotube cap nucleation on an iron particle. ACS Nano 3(11):3413–3420

178. Arepalli S, Scott CD (1999) Spectral measurements in production of single-wall carbon nanotubes by laser ablation. Chem Phys Lett 302:139–145

179. Moodley MK, Coville NJ (2010) Experimental evidence for the early nucleation of single-walled carbon nanotubes. Chem Phys Lett 498:140–144

180. Yudasaka M, Yamada R, Sensui N, Wilkins T, Ichihashi T, Iijima S (1999) Mechanism of the effect of NiCo, Ni and Co catalysts on the yield of single-wall carbon nanotubes formed by pulsed Nd:YAG laser ablation. J Phys Chem B 103:6224–6229

181. Yudasaka M, Kasuya Y, Kokai F, Takahashi K, Takizawa M, Bandow S, Iijima S (2002) Causes of different catalytic activities of metals in formation of single-wall carbon nanotubes. Appl Phys A-Mater 74:377–385

182. Cau M, Dorval N, Cao B, Attal-Tretout B, Cochon JL, Loiseau A, Farhat S, Scott CD (2006) Spatial evolutions of Co and Ni atoms during single-walled carbon nanotubes formation: measurements and modeling. J Nanosci Nanotechnol 6:1298–1299

183. Kataura H, Kumuzawa Y, Maniwa Y, Ohtsuka Y, Sen R, Suzuki S, Achiba Y (2000) Diameter control of single-walled carbon nanotubes. Carbon 38(11–12):1691–1697

184. Nikolaev P, Holmes W, Sosa E, Boul P, Arepalli S (2009) Effect of the laser heating of nanotube nuclei on the nanotube type population. Nano Res 2:818–827

185. Saito Y (1995) Nanoparticles and filled nanocapsules. Carbon 33(7):979–988

186. Harris PJF (2007) Solid state growth mechanisms for carbon nanotubes. Carbon 45:229–239

187. Fan X, Buczko R, Puretzky AA, Geohegan DB, Howe JY, Pantelides ST, Pennycook SJ (2003) Nucleation of single-walled carbon nanotubes. Phys Rev Lett 90(14):145501/145501–145501/145504

188. Irle S, Zheng G, Elstner M, Morokuma K (2003) Formation of fullerene molecules from carbon nanotubes: a quantum chemical molecular dynamics study. Nano Lett 3(4):465–470

189. Zheng G, Irle S, Elstner M, Morokuma K (2004) Quantum chemical molecular dynamics model study of fullerene formation from open-ended carbon nanotubes. J Phys Chem A 108:3182–3194

190. Rinzler AG, Hafner JA, Nikolaev P, Lou L, Kim SG, Tomanek D, Nordlander P, Colbert DT, Smalley RE (1996) Unraveling nanotubes: field emission from an atomic wire. Science 269:1550–1553

191. Yoshida H, Takeda S, Uchiyama T, Kohno H, Homma Y (2008) Atomic-scale in-situ observation of carbon nanotube growth from solid state iron carbide nanoparticles. Nano Lett 8(7):2082–2086

192. Yoshida H, Shimizu T, Uchiyama T, Kohno H, Homma Y, Takeda S (2009) Atomic-scale analysis on the role of molybdenum in iron-catalyzed carbon nanotube growth. Nano Lett 9:3810–3815

193. Hofmann S, Sharma R, Ducati C, Du G, Mattevi C, Cepek C, Cantoro M, Pisana S, Parvez A, Cervantes-Sodi F, Ferrari AC, Dunin-Borkowski R, Lizzit S, Petaccia L, Goldoni A, Robertson J (2007) In situ observations of catalyst dynamics during surface-bound carbon nanotube nucleation. Nano Lett 7(3):602–608

194. Anisimov AS, Nasibulin AG, Jiang H, Launois P, Cambedouzou J, Shandakov SD, Kauppinen EI (2010) Mechanistic investigations of single-walled carbon nanotube synthesis by ferrocene vapor decomposition in carbon monoxide. Carbon 48:380–388

195. Harutyunyan AR, Awasthi N, Jiang A, Setyawan W, Mora E, Tokune T, Bolton K, Curtarolo S (2008) Reduced carbon solubility in Fe nanoclusters and implications for the growth of single-walled carbon nanotubes. Phys Rev Lett 100:195502/195501–195504

196. Page AJ, Yamane H, Ohta Y, Irle S, Morokuma K (2010) QM/MD simulation of SWCNT nucleation on transition metal carbide nanoparticles. J Am Chem Soc 132:15699–15707

197. Page AJ, Irle S, Morokuma K (2010) Polyyne chain growth and ring collapse drives Ni-catalyzed SWNT growth: a QM/MD investigation. J Phys Chem C 114:8206–8211

198. Amara H, Bichara C, Ducastelle F (2006) Formation of carbon nanostructures on nickel surfaces: a tight-binding grand canonical Monte Carlo study. Phys Rev B 73(11):113404

199. Amara H, Bichara C, Ducastelle F (2008) Understanding the nucleation mechanisms of carbon nanotubes in catalytic chemical vapor deposition. Phys Rev Lett 100:056105/056101–056104

200. Amara H, Bichara C, Ducastelle F (2008) A tight-binding grand canonical Monte Carlo study of the catalytic growth of carbon nanotubes. J Nanosci Nanotechnol 8:6099–6104

201. Amara H, Roussel JM, Bichara C, Gaspard JP, Ducastelle F (2009) Tight-binding potential for atomistic simulations of carbon interacting with transition metals: application to the Ni-C system. Phys Rev B 79(1):014109

202. Takagi D, Hibino H, Suzuki S, Kobayashi Y, Homma Y (2007) Carbon nanotube growth from semiconductor nanoparticles. Nano Lett 7(8):2272–2275

203. Bachmatiuk A, Börrnert F, Grobosch M, Schäffel F, Wolff U, Scott A, Zaka M, Warner JH, Klingeler R, Knupfer M, Büchner B, Rümmeli MH (2009) Investigating the graphitization mechanism of SiO2 nanoparticles in chemical vapor deposition. ACS Nano 3(12):4098–4104

204. Huang S, Cai Q, Chen J, Qian Y, Zhang L (2009) Metal-catalyst-free growth of single-walled carbon nanotubes on substrates. J Am Chem Soc 131(6):2094–2095

205. Liu B, Ren W, Gao L, Li S, Pei S, Liu C, Jiang C, Cheng HM (2009) Metal-catalyst-free growth of single-walled carbon nanotubes. J Am Chem Soc 131(6):2082–2083

206. Liu B, Ren W, Liu C, Sun C-H, Gao L, Li S, Jiang C, Cheng H-M (2009) Growth velocity and direct length-sorted growth of short single-walled carbon nanotubes by a metal-catalyst-free chemical vapor deposition process. ACS Nano 3(11):3421–3430

207. Homma Y, Liu H, Takagi D, Kobayashi Y (2009) Single-walled carbon nanotube growth with non-iron-group "catalysts" by chemical vapor deposition. Nano Res 2(10):793–799

208. Liu H, Takagi D, Chiashi S, Chokan T, Homma Y (2010) Investigation of catalytic properties of Al2O3 particles in the growth of single-walled carbon nanotubes. J Nanosci Nanotechnol 10:4068–4073

209. Liu H, Takagi D, Chiashi S, Homma Y (2010) The growth of single-walled carbon nanotubes on a silica substrate without using a metal catalyst. Carbon 48:114–122

210. Liu B, Tang D-M, Sun C, Liu C, Ren W, Li F, Yu W-J, Yin L-C, Zhang L, Jiang C, Cheng H-M (2011) Importance of oxygen in the metal-free catalytic growth of single-walled carbon nanotubes from SiOx by a vapor-solid-solid mechanism. J Am Chem Soc 133:197–199

211. Page AJ, Chandrakumar KRS, Irle S, Morokuma K (2011) SWNT nucleation from carbon-coated SiO2 nanoparticles via a vapor−solid−solid mechanism. J Am Chem Soc 133(3):621–628

212. Page AJ, Chandrakumar KRS, Irle S, Morokuma K (2011) Do SiO2 and carbon-doped SiO2 nanoparticles melt? Insights from QM/MD simulations and ramifications regarding carbon nanotube growth. Chem Phys Lett 508:235–241

213. Lindemann FA (1910) Z Phys 11:609

214. Ding F, Rosen A, Curtarolo S, Bolton K (2006) Modeling the melting of supported clusters. Appl Phys Lett 88:133110/133111–133113

215. Wen Y-H, Zhang Y, Zheng J-C, Zhu Z-Z, Sun S-G (2009) Orientation-dependent structural transition and melting of Au nanowires. J Phys Chem C 113:20611–20617

216. Neyts EC, Bogaerts A (2009) Numerical study of the size-dependent melting mechanisms of nickel nanoclusters. J Phys Chem C 113:2771–2776

217. Puri P, Yang V (2007) Effect of particle size on melting of aluminum at nano scales. J Phys Chem C 111:11776–11783

218. Kusunoki M, Rokkaku M, Suzuki T (1997) Epitaxial carbon nanotube file self-organized by sublimation decomposition of silicon carbide. Appl Phys Lett 71(18):2620–2622

219. Page AJ, Ohta Y, Irle S, Morokuma K (2010) Mechanisms of single-walled carbon nanotube nucleation, growth and healing determined using QM/MD methods. Acc Chem Res 43:1375–1385

220. Ohta Y, Okamoto Y, Irle S, Morokuma K (2009) Temperature dependence of iron-catalyzed continued single-walled carbon nanotube growth rates: density functional tight-binding molecular dynamics simulations. J Phys Chem C 113(1):159–169

221. Page AJ, Minami S, Ohta Y, Irle S, Morokuma K (2010) Comparison of single-walled carbon nanotube growth from Fe and Ni nanoparticles using QM/MD simulations. Carbon 48:3014–3026

222. Huang ZP, Wang DZ, Wen JG, Sennett M, Gibson H, Ren ZF (2002) Effect of nickel, iron and cobalt on growth of aligned carbon nanotubes. Appl Phys A-Mater 74:387–391

223. Mora E, Harutyunyan AR (2008) Study of single-walled carbon nanotubes growth via the catalyst lifetime. J Phys Chem C 112(13):4805–4812

224. Futaba DN, Hata K, Yamada T, Mizuno K, Yumura M, Iijima S (2005) Kinetics of water-assisted single-walled carbon nanotube synthesis revealed by a time-evolution analysis. Phys Rev Lett 95:056104/056101–056104

225. Sharma R, Rez P, Reacy MMJ, Stuart SJ (2005) In situ observation of the growth mechanisms of carbon nanotubes under diverse reaction conditions. J Electron Microsc 54:231–237

226. Geohegan DB, Puretzky AA, Styers-Barnett D, Hu H, Zhao B, Cui H, Rouleau CM, Eres G, Jackson JJ, Wood RF, Pannala S, Wells JC (2007) In situ time-resolved measurements of carbon nanotube and nanohorn growth. Phys Status Solidi B 244:3944–3949

227. Yao Y, Liu R, Zhang J, Jiao L, Liu Z (2007) Raman spectral measuring of the growth rate of individual single-walled carbon nanotubes. J Phys Chem C 111:8407–8409

228. Xiang R, Einarsson E, Okawa J, Miyauchi Y, Maruyama S (2009) Acetylene-accelerated alcohol catalytic chemical vapor deposition growth of vertically aligned single-walled carbon nanotubes. J Phys Chem C 113:7511–7515

229. Li X, Tu X, Zaric K, Welsher K, Seo WS, Zhao W, Dai H (2007) Selective synthesis combined with chemical separation of single-walled carbon nanotubes for chirality selection. J Am Chem Soc 129:15770–15771

230. Zheng M, Semke ED (2007) Enrichment of single chirality carbon nanotubes. J Am Chem Soc 129:6084–6085

231. Yakobson BI (1998) Mechanical relaxation and "intramolecular plasticity" in carbon nanotubes. Appl Phys Lett 72:918–920

232. Ding F (2005) Theoretical study of the stability of defects in single-walled carbon nanotubes as a function of their distance from the nanotube end. Phys Rev B 72:245409/245401–245407

233. Page AJ, Ohta Y, Okamoto Y, Irle S, Morokuma K (2009) Defect healing during single-walled carbon nanotube growth: a density-functional tight-binding molecular dynamics investigation. J Phys Chem C 113(47):20198–20207

234. Novoselov KS, Geim AK, Morozov SV, Jiang D, Zhang Y, Dubonos SV, Grivorieva LV, Firsov AA (2004) Electric field effect in atomically thin carbon films. Science 306:666–669

235. Shelton JC, Patil HR, Blakely JM (1974) Equilibrium segregation of carbon to a nickel (111) surface: a surface phase transition. Surf Sci 43:493–520
236. Gan Y, Chu W, Qiao L (2003) STM investigation on interaction between superstructure and grain boundary in graphite. Surf Sci 539:120–128
237. Castro Neto AH, Guinea F, Peres NMR, Novoselov KS, Geim AK (2009) The electronic properties of graphene. Rev Mod Phys 81:136–162
238. Forbeaux I, Themlin J-M, Debever J-M (1998) Heteroepitaxial graphite on 6H-SiC(0001): interface formation through conduction-band electronic structure. Phys Rev B 58:16396–16406
239. Kusunoki M, Suzuki T, Hirayama M, Shibata N, Kaneko K (2000) A formation mechanism of carbon nanotube films on SiC(0001). Appl Phys Lett 77(4):531–533
240. Land TA, Michely T, Behm RJ, Hemminger JC, Comsa G (1992) STM investigation of single layer graphite structures produced on Pt(111) by hydrocarbon decomposition. Surf Sci 264:261–270
241. Loginova E, Bartelt NC, Feibelman PJ, McCarty KF (2008) Evidence for graphene growth by C cluster attachment. New J Phys 10:093026/1–16
242. Chae SJ, Güneş F, Kim KK, Kim ES, Han GH, Kim SM, Shin H-J, Yoon S-M, Choi J-Y, Park MH, Yang CW, Pribat D, Lee YH (2009) Synthesis of large-area graphene layers on poly-nickel substrate by chemical vapor deposition: wrinkle formation. Adv Mater 21(22):2328–2333
243. Grüneis A, Kummer K, Vyalikh DV (2009) Dynamics of graphene growth on a metal surface: a time-dependent photoemission study. New J Phys 11(7):073050
244. Müller F, Sachdev H, Hüfner S, Pollard AJ, Perkins EW, Russell JC, Beton PH, Gsell S, Fischer M, Schreck M, Stritzker B (2009) How does graphene grow? Easy access to well-ordered graphene films. Small 5:2291–2296
245. Pollard AJ, Nair RR, Sabki SN, Staddon CR, Perdigao LMA, Hsu CH, Garfitt JM, Gangopadhyay S, Gleeson HF, Geim AK, Beton PH (2009) Formation of monolayer graphene by annealing sacrificial nickel thin films. J Phys Chem C 113(38):16565–16567
246. Sutter E, Albrecht P, Sutter P (2009) Graphene growth on polycrystalline Ru thin films. Appl Phys Lett 95:133109/133101–133103
247. Juang Z-Y, Wu C-Y, Lo C-W, Chen W-Y, Huang C-F, Hwang J-C, Chen F-R, Leou K-C, Tsai C-H (2009) Synthesis of graphene on silicon carbide substrates at low temperature. Carbon 47:2026–2031
248. Sanchez-Barriga J, Varykhalov A, Scholz MR, Rader O, Marchenko D, Rybkin A, Shikin AM, Vescovo E (2010) Chemical vapour deposition of graphene on Ni(111) and Co(0001) and intercalation with Au to study Dirac-cone formation and Rashba splitting. Diam Relat Mater 19:734–741
249. Coraux J, N'Diaye AT, Engler M, Busse C, Wall D, Buckanie N, Meyer zu Heringdorf F-J, van Gastel R, Poelsema B, Michely T (2009) Growth of graphene on Ir(111). New J Phys 11:023006/023001–023022
250. Lacovig P, Pozzo M, Alfe D, Baraldi A, Lizzit S (2009) Growth of dome-shaped carbon nanoislands on on Ir(111): the intermediate between carbidic clusters and quasi-free-standing graphene. Phys Rev Lett 103:166101/166101–166104
251. Li X, Cai W, Colombo L, Ruoff RS (2009) Evolution of graphene growth on Ni and Cu by carbon isotope labeling. Nano Lett 9:4268–4272
252. Lahiri J, Miller T, Adamska K, Oleynik II, Batzill M (2011) Graphene growth on Ni(111) by transformation of a surface carbide. Nano Lett 11:518–522
253. Wang B, Ma X, Caffio M, Schaub R, Li W-X (2011) Size-selective carbon nanoclusters as precursors to the growth of epitaxial graphene. Nano Lett 11(2):424–430
254. Saadi S, Abild-Pedersen F, Helveg S, Sehested J, Hinnemann B, Appel CC, Norskov JK (2010) On the role of metal step-edges in graphene growth. J Phys Chem C 114:11211–11227
255. Gao J, Yip J, Zhao J, Yakobson BI, Ding F (2011) Graphene nucleation on transition metal surface: structure transformation and role of the metal step edge. J Am Chem Soc 133:5009–5015

256. Cheng D, Barcaro G, Charlier JC, Hou M, Fortunelli A (2011) Homogenous nucleation of graphitic nanostructures from carbon chains on Ni(111). J Phys Chem C 115:10537–10543
257. Erdös P, Renyi A (1960) On the evolution of random graphs. Magyar Tud Akad Mat Kutato Int Közl 5:17–61
258. Bollobas B (1984) The evolution of random graphs. Trans Am Math Soc 286:257–274
259. Luczak T (1990) The phase transition in the evolution of random graphs. J Graph Theor 14:217–223
260. Bak P, Tang C, Wiesenfeld K (1987) Self-organized criticality: an explanation of 1/f noise. Phys Rev Lett 59:381–384
261. Stone AJ, Wales DJ (1986) Theoretical studies of icosahedral C60 and some related species. Chem Phys Lett 128(5, 6):501–503
262. Ostwald W (1897) Studien uber die Bildung und Umwandlung fester Korper. Z Phys Chem 22:289–330
263. Bak P, Sneppen K (1993) Punctuated equilibrium and criticality in a simple model of evolution. Phys Rev Lett 71:4083–4086
264. Gould SJ, Eldredge N (1977) Punctuated equilibria: the temp and mode of evolution reconsidered. Paleobiology 3:115–151
265. Whittaker AG (1978) Carbon: a new view of its high-temperature behavior. Science 200:763–764
266. Jin C, Lan H, Peng L, Suenaga K, Iijima S (2009) Deriving carbon atomic chains from graphene. Phys Rev Lett 102:205501/205501–205504
267. Wang Y, Lin Z-Z, Zhang W, Zhuang J, Ning X-J (2009) Pulling long linear atomic chains from graphene: molecular dynamics simulations. Phys Rev B 80:233403/233401–233404
268. Hobi EJ, Pontes RB, Fazzio A, da Silva AJR (2010) Formation of atomic carbon chains from graphene nanoribbons. Phys Rev B 81:201406R/201401–201404
269. Ohta Y, Okamoto Y, Irle S, Morokuma K (2009) Single-walled carbon nanotube growth from a cap fragment on an iron nanoparticle: density-functional tight-binding molecular dynamics simulations. Phys Rev B 79(19):195415
270. Wang Z, Irle S, Zheng G, Kusunoki M, Morokuma K (2007) Carbon nanotubes grow on the C face of SiC (000–1) during sublimation decomposition: quantum chemical molecular dynamics simulations. J Phys Chem C 111:12960
271. Ohta Y, Okamoto Y, Irle S, Morokuma K (2008) Rapid growth of a single-walled carbon nanotube on an iron cluster: density-functional tight-binding moleculer dynamics simulations. ACS Nano 2:1437–1444
272. Jakowski J, Morokuma K (2009) Liouville–von Neumann molecular dynamics. J Chem Phys 130:224106/224101–224112
273. van Duin ACT, Dasgupta S, Lorant F, Goddard WA III (2001) Reactive force field for hydrocarbons. J Phys Chem A 105:9396–9409
274. Nielson KD, van Duin ACT, Oxgaard J, Deng W-Q, Goddard WA III (2005) Development of the ReaxFF reactive force field for describing transition metal catalyzed reactions, with application to the initial stages of the catalytic formation of carbon nanotubes. J Phys Chem A 109:493–499
275. Svensson M, Humbel S, Froese RDJ, Matsubara T, Sieber S, Morokuma K (1996) ONIOM: a multilayered integrated MO + MM method for geometry optimizations and single point energy predictions. A test for Diels-Alder reactions and Pt(P(t-Bu)$_3$)$_2$ + H$_2$ oxidative addition. J Phys Chem 100:19357–19363
276. Dapprich S, Komaromi I, Byun KS, Morokuma K, Frisch MJ (1999) A New ONIOM implementation in Gaussian 98: part I. The calculation of energies, gradients, vibrational frequencies and electric field derivatives. J Mol Struct (THEOCHEM) 461–462:1–21
277. Johnson MP, Donnet JB, Wang TK, Wang CC, Locke RW, Brinson BE, Marriott T (2002) A dynamic continuum of nanostructured carbons in the combustion furnace. Carbon 40(2):189–194

Chapter 6
Modeling of Chemical Reactivity of Carbon Nanotubes: A Review

Takashi Yumura and Miklos Kertesz

Abstract In this review, we summarize recent progress on quantum mechanical (QM) computational studies of single wall carbon nanotubes (SWCNs) functionalized covalently. In particular, we focus on the additions of carbene into SWCNs and the associated changes in the carbon-carbon (CC) bonds. A variety of functionalizations are discussed: inner (endo-) and outer (exo-) additions, and additions into bonds that are at various orientations with respect to the tube axis across a wide range of research groups active in the field. Substituents studied ranged from alkyl radicals, amidogen, and a wide range of carbenes to bifunctional organic molecules.

The methods used in the reviewed literature are dominated by density functional theory (DFT). Other methods included QM/MM modeling (ONIOM) and some widely used wave function methods such as MP2 and the occasional semi-empirical quantum chemical method. Both periodic boundary condition (PBC) and cluster models were employed. Some of the results from different laboratories are compared in tabular form. Methodological and computational convergency issues are also discussed.

Two types of modification patterns on the tube surface near the addition site were obtained in a number of studies due to carbene addition, depending on whether the original CC bond in the honeycomb network is retained or broken. There are also subtle surface modifications in the neighborhood of the addition, which in turn modulates the electronic properties as well as has the power to direct a functional

T. Yumura

Department of Chemistry and Materials Technology, Kyoto Institute of Technology, Matsugasaki, Sakyo-ku, Kyoto 606-8585, Japan
e-mail: yumura@chem.kit.ac.jp

M. Kertesz (✉)
Department of Chemistry, Georgetown University, 37th and O streets, NW, Washington D.C. 20057-1227, USA
e-mail: kertesz@georgetown.edu

group into a specific preferred site. Patterns of the surface modification correlate with whether the CC bond at the carbene attachment remains connected or is cleaved. The correlation can be understood by counting the π electrons of the carbon nanotube and by using Clar's simple valence bond concept. Strategies to control structural and electronic properties of functionalized SWCNs are also reviewed.

6.1 Introduction

Carbon nanotubes [1–4] can be solubilized by covalent functionalization [5–15]. Thanks to enhancing the solubility of carbon nanotubes, researchers can apply functionalized nanotubes to many fields such as sensors, applications in medicinal chemistry, creation of new materials such as polymeric composites, and uses in solar conversion systems, to name only a few. Up to now, covalent functionalization of a sidewall of SWCNs can be roughly categorized into two subgroups: cycloadditions [16–31] and radical additions [32–88]. In the cycloadditions, divalent reagents such as carbenes and nitrenes have been utilized, whereas in the radical reactions, monovalent reagents, whose precursors are alkylhalides, diazonium-salts, alkyl-lithium, and so on, can attach onto carbon nanotube surfaces. Another type of covalent bond functionalization can be found in metal clusters deposited on nanotubes [89–92, 178]. For example, nanotubes can act as supports for platinum cluster catalysts by utilizing metal-nanotube interactions. Only highly reactive species make covalent bonds with nanotubes successfully. However, high reactivity of the reagents prohibits them from binding into a carbon nanotube in a site-selective manner. If one could line up ordered functional groups on a carbon nanotube surface in a specific pattern, functionalized carbon nanotubes could become candidates for building blocks constructing nanoscaled devices [93, 94], owing to their unique mechanical and electronic properties.

Functionalization of a carbon nanotube disrupts its sp^2-bonded network. The surface disruption can be observed by resonance Raman spectroscopy, where intensity of the D-band around 1,300 cm^{-1} increases and the intensity of the G-band around 1,500 cm^{-1} decreases upon covalent functionalization [5–15]. The changes in Raman spectra can be interpreted by the appearance of sp^3-hybridized carbon atoms near the binding sites. Some researchers focused on the electron mobility of a functionalized carbon nanotube. Measurements indicated that metallic conductivity is suppressed by the functionalization [95, 96]. The experimental findings suggest that the surface disruption should have a crucial impact on modulation of its electronic properties. Here we review our current understanding of the covalent functionalization of carbon nanotubes by organic-functional groups and the consequences of the partial disruption of the CC network of the tubes. Differences among tubes with different chiralities are also pointed out. Quantum mechanical modeling,

Clar aromatic pattern   Kekule pattern   Butadiene pattern   Quinonoid pattern
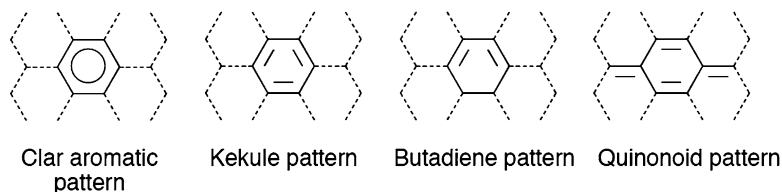
Chart 6.1 Important valence bond representation of sp^2 carbon surfaces

as pursued in various laboratories over the world, is particularly well suited for obtaining insights into the energetics and structural modifications of bond making and bond breaking in these carbon-based materials.

To better understand the electronic changes of carbon nanotubes by functionalization, one should investigate on the atomic scale how functional groups interact with a carbon nanotube as well as how the resultant interactions perturb the carbon nanotube surface. In this direction, recent quantum chemistry calculations, especially by using density functional theory (DFT) methods, will help us to understand the covalent bond formation. In fact, standard DFT methods, such as general gradient approximation (GGA) and hybrid functionals (e.g., B3LYP functional), can describe accurately how the CC network is affected in various carbon materials. There is no unanimity in the choice of methods in the literature. Generally, the accuracy of recent DFT methods has increased due to improvements in the quality of exchange-correlation functional. Due to these positive developments, several researchers have studied the important problem of organic functionalization of carbon nanotubes mostly by DFT methods with the aim to obtain microscopic mechanistic insights.

In this review, we will summarize recent progress on computational studies of covalent functionalization of carbon nanotubes, especially DFT studies with a focus on the disruption of a carbon nanotube surface by functionalization. To interpret the disruption of a carbon nanotube surface, we will utilize a basic idea of organic chemistry, the "Clar aromatic sextet" [97, 98] and review how π electron counts based on Clar valence representations provide a useful tool not only to explain property changes of a carbon nanotube upon functionalization, but also to devise a strategy toward site-selectivity. Chart 6.1 illustrates the most important valence bond (VB) representations, which will be referred to subsequently. Non-covalent functionalization of carbon nanotubes is also important in practical applications, but these will not be reviewed here [11, 15, 177]. In this review, we focus on comparing different computational methodologies applied to the covalent functionalization problem and aim to describe the trends and general understanding obtained in various laboratories.

6.2   Computational Methods

A number of papers discussing the formation of covalent bonds on an SWCN surface have been published [99–135]. First, we briefly summarize in Table 6.1 the computational methods and carbon nanotube models in the published papers. These computational studies differ from one another in two general ways. First, they model different chemical processes. Second, the models differ systematically with respect to the computational parameters. These key computational parameters belong to six major categories:

1. Periodic boundary conditions (PBC) versus finite cluster calculations.
2. Level of theory, such as the choice of density functional or the level of semiempirical versus Hartree Fock theory. (High-level wave function calculations are too expensive at the moment for sufficiently large clusters or units cells.)
3. Basis set or kinetic energy cutoff.
4. Number of atoms in the finite cluster and, similarly, number of atoms in the supercell in the PBC calculations.
5. An alternative to larger number of atoms is exploited in the quantum mechanics/molecular mechanics (QM/MM) combined methods, such as ONIOM, which depend on various additional parameters.
6. Other convergency parameters of the computations, such as number of k-points in PBC, geometry convergency parameters, etc.

To the best of our knowledge, the first paper on the subject was published in 2003 by Lu et al. who used a two-layer ONIOM approach [99, 100]. Later, more reliable results were obtained from a cluster approach based on B3LYP/6–31G* level by Chen et al. [101] and Bettinger [102]. As shown in Table 6.1, both types of calculations, the cluster approach and the periodic boundary condition (PBC) approach are well represented. The PBC calculations are mostly DFT based, whereas the cluster calculations rely on a variety of methods including semiempirical AM1 and PM3 methods, ab initio Hartree Fock (HF) method, DFT method with various functionals (GGA functionals such as PW91 and PBE and hybrid functionals such as B3LYP), and a two-layer QM/MM (ONIOM) method. In the ONIOM calculations, functional groups and their neighboring carbon atoms of a carbon nanotube are treated by a higher theoretical level such as a DFT method, whereas the rest of the functionalized carbon nanotube is treated at a lower level like AM1 or PM3.

Another key factor affecting the reliability of computations is the number of atoms contained in a finite-length tube model. Finite-length tubes have discrete energy levels, being in contrast to PBC (infinite-length) models. The number of energy levels of a tube model increases with its length [136–138]. Accordingly, the tube length affects the electronic properties, and thus it plays a crucial role in determining energy for the interactions with a functional group. Another important factor is that the edges of a finite-length tube strongly affect orbital shapes for the crucial frontier orbitals. If a functional group is situated near an edge, the

Table 6.1 Overview of published papers discussing functionalization of carbon nanotubes by organic compounds

Methods	Boundary condition	Addends	Tube model and chirality	Basis sets	Reference
Carbene additions					
ONIOM	Cluster	CH_2, SiH_2, GeH_2	$C_{130}H_{20}$ (5,5)	6-31G*	[99]
ONIOM	Cluster	H_2CNHCH_2	$C_{130}H_{20}$ (5,5)	6-31G*	[100]
B3LYP, HF, AM1,ONIOM	Cluster	O, CH_2, SiH_2, NH	$C_{130}H_{20}$ (5,5)	6-31G*/3-21G	[101]
PBE, B3LYP	Cluster	CH_2	$C_{210}H_{20}$ (5,5)	6-31G*/3-21G	[102]
ONIOM	Cluster	CH_2, SiH_2, GeH_2	$C_{130}H_{20}$ (5,5)	6-311G*	[103]
PW91	PBC	NCOOEt	C_{96}(6,6), C_{72}(9,0), C_{80} (10,10)	Double numerical BS	[104]
PBE	PBC	O, CH_2, SiH_2, NH	(19,0) (n,n); $n=5, 6, 10$–12	PW (240 eV)	[105]
B3LYP	Cluster	CH_2 SiH_2 GeH_2	$C_{130}H_{20}$(5,5)	LANL2DZ	[106]
B3LYP or PBE	Cluster and PBC	CH_2, CCl_2	(5,5), (10,0) $C_{90}H_{20}$ (5,5)	PBC: 6-31G*/3-21G; cluster: 6-31G*/6-311G**	[107]
PBE	PBC	CCl_2	C_{120} (5,5)	PW (408 eV)	[108]
Extend Hückel	Green function	CH_2, NH, COOH	(6,6)	Min. valence	[109]
B3LYP	Cluster	O, CH_2, SiH_2, NH	$C_{110}H_{20}$ (5,5), $C_{120}H_{20}$ (5,5), $C_{88}H_{16}$ (4,4), $C_{132}H_{24}$ (6,6), $C_{154}H_{28}$ (7,7), $C_{176}H_{32}$ (8,8)	6-31G*	[110]
PBE	PBC	2 CCl_2	(5,5), (9,0), (10,0), (7,3)	PW (280 eV)	[111]
B3LYP, DFTB	Cluster	O, CH_2, NH	$C_{130}H_{20}$ (5,5)	6-31G*	[112]
PBE	PBC	1–10 CCl_2	C_{60} (5,5)	PW (240 eV)	[113]
PBE	PBC	NH	(7,0), (8,0), (9,0), (10,0)	PW (precise set)	[114]

(continued)

Table 6.1 (continued)

Methods	Boundary condition	Addends	Tube model and chirality	Basis sets	Reference
ONIOM	Cluster	CH_2N_2	(7,0), (8,0), (9,0), (10,0)	6-31G*	[115]
PW91	PBC	2 CH_2	(5,5)	PW (349 eV)	[116]
PW91	PBC	CH_2, C_1-C_{59}	(10,10)	PW (349 eV)	[117]
PBE	PBC	$C(NO_2)_2$	(5,5), (8,8),	PW (408 eV)	[118]
PBE	PBC	NH	$(n,0)$; $n = 7-17$	PW (420 eV)	[119]
PBE	PBC	Phenyl, CCl_2	(5,5)	PW (400 eV)	[120]
PBE	PBC	Azomethine ylides, $H_2C = N^+RC^-H_2$ ($R = H,C_7H_{15}O_3$)	(4,4) (6,6) (8, 0) (9, 0)	PW (120 Ry)	[121]
LDA-Perdue-Zunger	Green function	Phenyl, CCl_2	(6,6), (10,10)	Split-valence Double-ζ BS	[122]
B3LYP	Cluster	O, CH_2	$C_{110}H_{20}$, $C_{120}H_{20}$	6-31G*	[123]
B3LYP	Cluster	CH_2, F	$C_{96}H_{22}$ (6,4), $C_{96}H_{22}$ (6,5)	3-21G	[124]
PW91	Cluster PBC	Bismalonate ($C_{10}H_{10}O_8$)	(10,10), $C_{380}H_{40}$ (10,10)	PW (349 eV) 3-21G	[125]
PBE	Cluster	C_4H_6, C_8H_8	$C_{150}H_{20}$ (5,5) $C_{180}H_{24}$ (9,0) $C_{160}H_{22}$ (6,5)	Double-ζ plus polarization BS	[126]
ONIOM	Cluster	C_4H_6, C_4NH_5	$C_{140}H_{20}$ (5,5) $C_{168}H_{24}$ (6,6)	6-31G*	[127]
PBE B3LYP	Cluster PBC	CH, CH_2, CH_3	C_{200}(PBE) C_{120} (B3LYP)	PW (no data) 6-31G	[128]

PBE	PBC	Azomethine ylides, $H_2CN(C_2H_4H)CH_2$	(5,5)	Double-ζ plus polarization BS	[129]
Radical additions					
LDA, GGA, and B3LYP (cluster) PBE (PBC)	Cluster PBC	PhN_2	C_{100} (5,5), C_{72} (9,0)	3-21G PW (400 eV)	[130]
PBE	PBC	Phenyl	(n, n); $n = 4$–10, $(m, 0)$; $m = 8$–16	Double numerical BS plus p polarization	[131]
PBE	PBC	CH_3	(5,5)	Double-ζ BS	[132]
ONIOM	Cluster	PhN_2	$C_{100}H_{20}$ (5,5)	6-31G*	[133]
B3LYP	Cluster	PhCl	$C_{60}H_{12}$ (3,3), $C_{60}H_{10}$ (5,0)	3-21G	[134]
PW91	PBC	CH_3, C_2H_4, C_3H_6, C_4H_8	(n, n); $n = 8, 10, 12$	PW (349 eV)	[135]

dependence on the relative position of the substituent and the edge can significantly modulate the orbital interactions relevant for reactivity of the group. Thus, the tube length of a model is required to be sufficiently long in order to obtain representative results for the addition processes that occur not near the edge. The cluster-based calculations listed in Table 6.1 used Gaussian-type basis sets. The standard basis sets are 6-311G*, 6-31G*, 3-21G basis sets, as well as effective core potential plus LANL2dz, which consist of, respectively, 18, 15, 9, and 9 contracted Gaussian basis functions per carbon atom.

Plane-wave-type basis sets were often used in the PBC calculations. Here the cut-off energy, ranging from 280 to 408 eV in Table 6.1, and k-point samplings are key parameters determining the accuracy of the PBC computation. In the PBC calculations, the supercell size is also important [107]. A sufficiently long supercell along the tube axis is required to avoid interactions between adjacent functional groups located on neighboring supercells. For example, unit cells used in our previous papers [125, 135] contain up to 240 carbon atoms of a carbon nanotube plus a few functional groups. In such large-scale calculations, DFT methods are preferred to wave-function-based methods, such as the second-order Møller–Plesset perturbation theory (MP2) and couple cluster (CC) methods. The advantage of DFT methods is that they include electron correlation to describe their properties in a relatively accurate manner, and at the same time are relatively less time-consuming. Hence, various researchers have investigated the interactions between carbene-derivatives and a carbon nanotube surface by using DFT methods (see Table 6.1). A key parameter throughout these studies is the binding energy, which is defined for a single addend as

$$E_{\text{bind}} (X) = E_{\text{tot}} (X - NT) - E_{\text{tot}} (NT) - E_{\text{tot}} (X).$$

Here NT stands for the carbon nanotube model (either a supercell for PBC or a H-terminated cluster), E_{tot} is the total energy calculated by the quantum mechanical model in question, which is the triplet state for CH_2.

6.3 Results and Discussion

6.3.1 Clar Representation of Pristine Carbon Nanotube Surfaces

SWCNs can be constructed by rolling up a single-graphene sheet [1–4] characterized by the index pair (n, m). These two integer parameters characterize the roll-up with a chiral vector $na_1 + ma_2$, where a_1 and a_2 denote lattice vectors of two-dimensional graphene. The electronic properties of carbon nanotubes (metallic or semiconducting characters) are determined by the chiral index (n, m). Up to now, theoretical work has mostly focused on special, achiral carbon nanotubes,
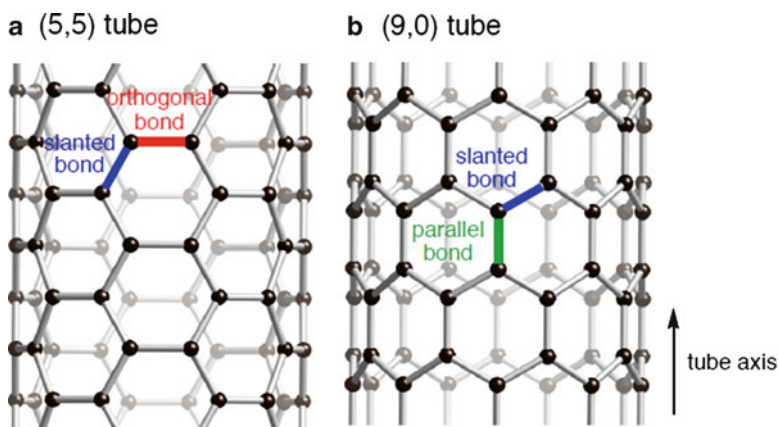
Fig. 6.1 The structures of an armchair and a zigzag carbon nanotube. (**a**) (5,5) Armchair carbon nanotube and (**b**) (9,0) zigzag carbon nanotube. Types of CC bonds in a carbon nanotube are also indicated. Bond directions are abbreviated in the text as S (slanted), O (orthogonal), and P (parallel) to the tube axis

characterized by either $m = n$ cases, the so-called armchair (n, n) nanotubes that are always metallic, and on the $m = 0$ cases, the so-called zigzag $(n, 0)$ nanotubes that are metallic if n is divisible by 3 [3]. In a few cases, chiral tubes that do not belong to these two special categories were also considered [124, 126]. As shown in Fig. 6.1, there are two types of CC bonds at each achiral nanotube with respect to the tube axis; an orthogonal (O) and a slanted (S) CC bond along the axis of an armchair nanotube, whereas a parallel and a S CC bond in a zigzag nanotube. PBC PW91 calculations showed that the lengths of the two types of CC bonds in armchair nanotubes are very close to each other (Fig. 6.2) [139–141]. The calculated CC bond lengths are around 1.425 Å, as shown in Fig. 6.2 [139]. Differences between O and S bonds (Δ) are small but vary systematically (Fig. 6.2). On the other hand, in zigzag $(n, 0)$ nanotubes one can distinguish between the two types of bonds in terms of bond lengths. The deviations Δ between the two bonds range from 0.05 to 0.01 Å as shown in Fig. 6.2. Interestingly, with an increase of m, the Δ values decrease in an oscillatory manner with a periodicity of three.

To understand qualitatively the changes in CC bonds of carbon nanotubes, Clar VB representations are helpful [126, 142–150]. For example, Matsuo et al. [142] and Ormsly et al. [146, 147] applied the Clar concepts to elucidate aromaticity of pristine carbon nanotubes with finite lengths and infinite lengths, respectively. In fact, they calculated nucleus-independent chemical shifts (NICS) and interpreted the degree of aromaticity at a certain position of the carbon nanotubes based on the VB representations. Ormsly and King considered a carbon nanotube to be constructed by rolling-up a graphene sheet whose π electrons are represented by aromatic sextets. According to the Clar VB representation, the (n, m) nanotubes with $n - m = 3k$ possess fully benzenoid structures, and their π electrons are aromatic
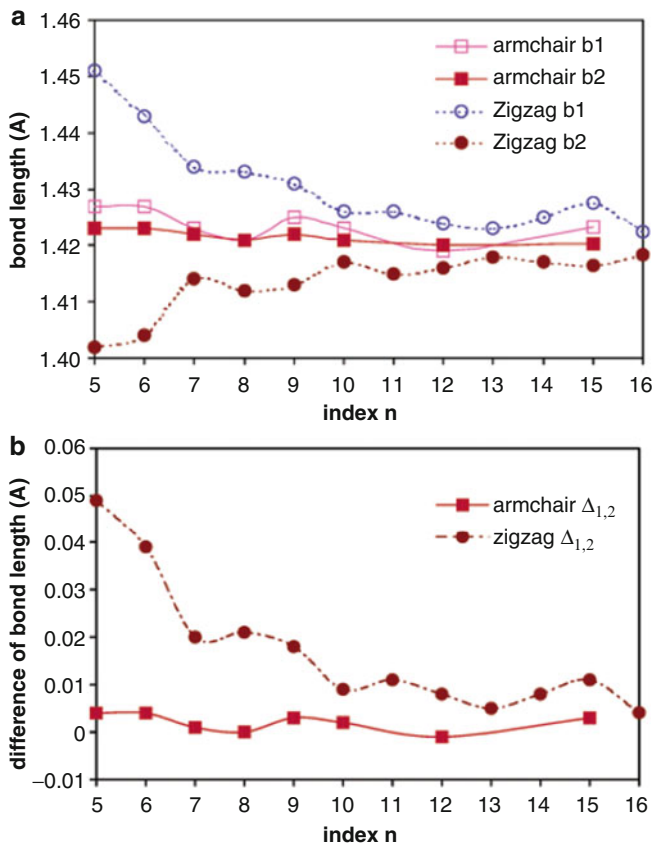
Fig. 6.2 (**a**) Variations of CC bond lengths in armchair (n, n) and zigzag (n, 0) carbon nanotubes as a function of n. The b1 and b2 bonds in armchair carbon nanotubes correspond to orthogonal (O) and slanted (S) bonds in Fig. 6.1, respectively. In zigzag carbon nanotubes, the b1 and b2 bonds represent slanted (S) and parallel (P) bonds in Fig. 6.1, respectively. (**b**) Differences between the two types of bonds (Δ) are also given as a function of n (Reproduced from Sun et al. [139] with kind permission of © The American Chemical Society (2003))

sextets given by circles in Fig. 6.3 [146, 147]. Qualitatively, these are exactly the conditions for n and m that are associated with metallic carbon nanotubes [151]. Also, this VB picture is consistent with the DFT calculations where two O and S CC bonds are equivalent in terms of their lengths [139]. In the other nanotubes ($m - n \neq 3\,k$), their π electrons cannot be represented only by aromatic sextets. Instead, a wrapping seam of double bonds appears in their tubes. Since the VB representations can discern three types of nanotubes in terms of the structural features, it is interesting to analyze structural changes of nanotubes due to functionalization with the aid of the Clar concept [116, 146, 147].
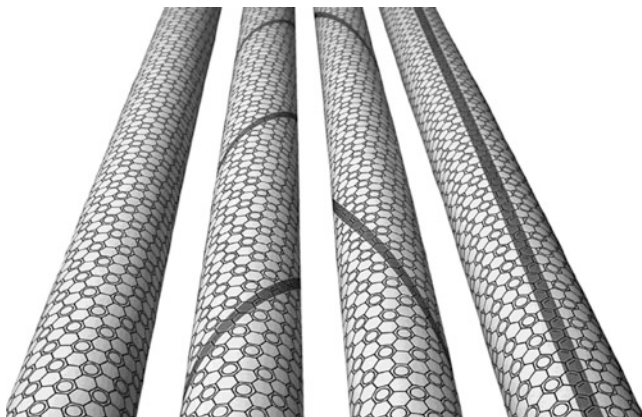
Fig. 6.3 Clar valence bond (VB) representation of (12,9), (12,8), (12,7), and (19,0) carbon nanotubes from left to right (Reproduced from Ormsby and King [147] with kind permission of © The American Chemical Society (2004))

6.3.2 Addition of an Organic Reagent into the Inner or Outer Surface of a Carbon Nanotube

In this section, we discuss the functionalization of a nanotube by two types of organic molecules: a carbene or an alkyl radical. The functionalization can occur on the inner or outer surface. Due to the different curvatures for inner versus outer functionalizations, especially for smaller diameter tubes, different reactivities are expected. In the formation of two covalent bonds between a nanotube and carbene, two electrons participate, whereas one electron contributes to the alkylation leading to completely different chemistries for the two types of reactions.

6.3.2.1 Addition of an Alkyl Radical

First we turn to functionalization of the (10,10) nanotube by an alkyl radical (methyl, ethyl, isopropyl, and tert-butyl radicals). Figure 6.4 shows that an inner or outer methyl radical attacks at one carbon (orange) atom of the nanotube. Due to the formation of one covalent bond, an sp^2 carbon of the tube is transformed into an sp^3 carbon. The DFT findings support the prediction by experimentalists [152, 153] in terms of the sp^2 to sp^3 transformation, as mentioned above. A further insight on the alkylation of a carbon nanotube was obtained in a recent DFT study [135] illustrated in Fig. 6.5, which displays the CC bond lengths and the binding energy depending on types and location of the alkyl radicals. The calculated binding energies in Fig. 6.5 show that the outer (exohedral) alkylation is energetically more stable relative to the inner (endohedral) alkylation, suggesting that the inner nanotube surface is less reactive than the outer surface. The inertness of inner tube surfaces

a inner methly radical bound to (10,10) tube   **b** outer methly radical bound to (10,10) tube
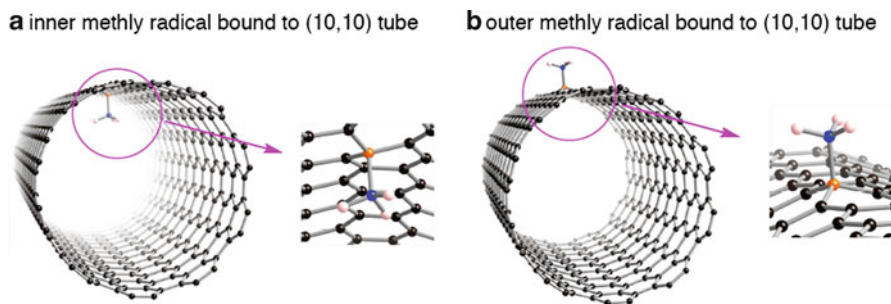
Fig. 6.4 PW91-optimized structures for a methyl radical bound to the (**a**) inner or the (**b**) outer surface of the (10,10) carbon nanotube. The carbon of the radical is in *blue*, and the C atom attached by the radical is in *orange* (Reproduced from Yumura [135] with kind permission of © The Royal Chemistry Society (2011))

has been also found in the addition of a single atom (H, N, and F atoms) [154] as well as that of amidogen (NH_2) [155]. In particular, Zhao et al. calculated the potential energy profile for the binding of NH_2 into an inner or outer surface of (5,5) nanotube, as shown in Fig. 6.6 [155]. In the outer addition, there is one local minimum. In contrast, an amidogen inside a nanotube has two stable configurations; one configuration has an amidogen located at the center of the tube (separate form), whereas the other has an amidogen bound to its inner surface (bound form). Between the two stable configurations, there is a noticeable barrier. The energy profile clearly indicates that the separate form is more preferable than the bound form, suggesting that an inner NC bond is weak.

The calculated binding energies (Fig. 6.5) are smaller than the binding energies of usual single CC bonds. In addition, the CC bond strength is strongly modulated by the number of methyl groups in the reactant radical: the CC bond between an inner alkyl radical and a tube surface becomes weaker for a more bulky radical. We also see in Fig. 6.5 the diameter-dependencies of the calculated binding energies. In terms of the diameter-dependencies, there is a different trend between the inner and outer additions. In the inner addition, the CC bonds are strengthened with an increase of tube diameter, whereas those in the outer addition are weakened. Both calculated binding energies will converge to the corresponding values in graphene (given by horizontal lines in Fig. 6.5), with an increase in the tube diameter. The differences between the outer and inner alkylation can link to how easily a tube surface is modified while forming a CC bond with an alkyl radical. Note that modification of a tube surface is an endothermic step-part of the total interaction energy [154]. Similar results were obtained by Chen et al., who investigated the addition of H or F atom into the inner or outer surfaces of a nanotube [154]. More importantly, Chen et al. correlated the differences in chemical reactivity among armchair (*n*, *n*) tubes by using π-orbital axial vector (POAV, see Chart 6.2) [156]. In other words, the binding energy for the outer F or H addition into an armchair nanotube has essentially a linear relationship with the θ_P value that characterizes the direction of the POAV [154]. To be more precise, a wider tube that has a smaller θ_P
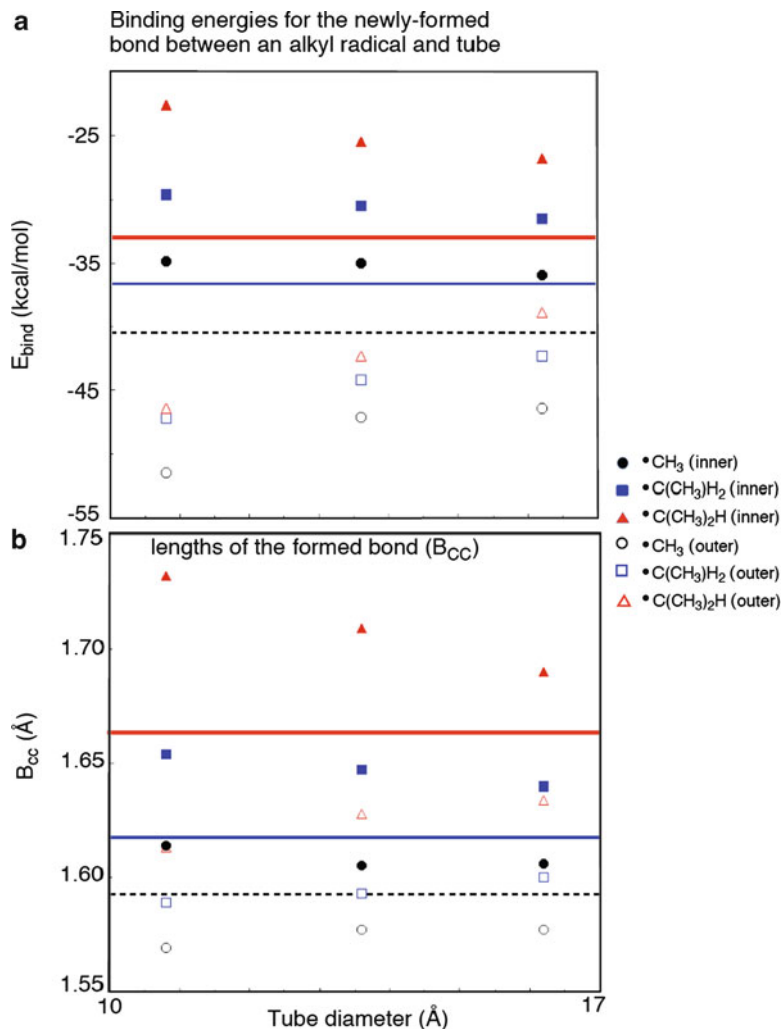
Fig. 6.5 Properties of the (8,8), (10,10), and (12,12) carbon nanotubes attached by an alkyl radical (methyl (*black circles*), ethyl (*blue squares*), and isopropyl (*red triangles*) radicals). In the alkylation, calculated binding energies (**a**) and CC bond lengths (**b**) are given as a function of tube diameter. *Horizontal lines* indicate respective graphene values that correspond to an infinite diameter tube. Inner radical species are given by *closed marks*, and outer species are given by *open marks* (Reproduced from Yumura [135] with kind permission of © The Royal Chemistry Society (2011))

value is less reactive toward the outer F or H addition. Furthermore, nanotube and fullerene chemistry can be distinguished by using the θ_P value. For example, the reactivity of the (5,5) tube is less pronounced than that of C_{60}, although both have a similar diameter. The different reactivities can be related to the different θ_P values. In fact, the θ_P value of a certain carbon atom in the (5,5) nanotube is less than half of that of C_{60}.

Fig. 6.6 Potential energy profiles for amidogen approaching one carbon atom of (5,5) carbon nanotube as a function of its separation from the tube center (denoted by Distance). The data were obtained from BLYP calculations. (**a**) Outer amidogen addition and (**b**) inner amidogen addition (Reproduced from Zhao et al. [155] with kind permission of © The American Chemical Society (2004))
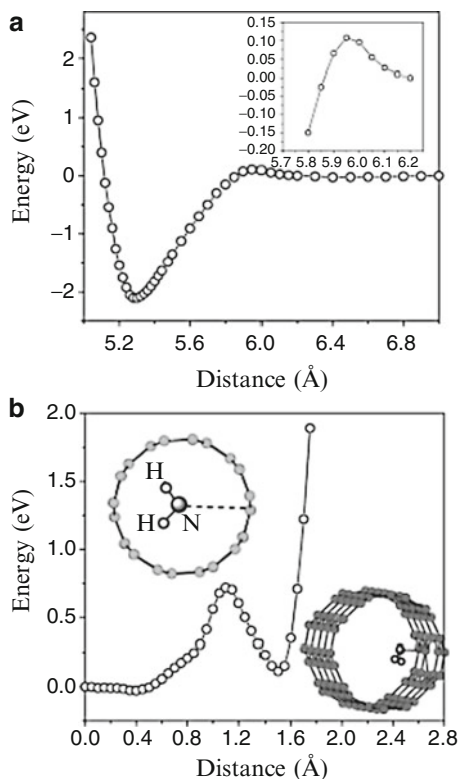
Chart 6.2 Illustration of the π-orbital axial vector (POAV)
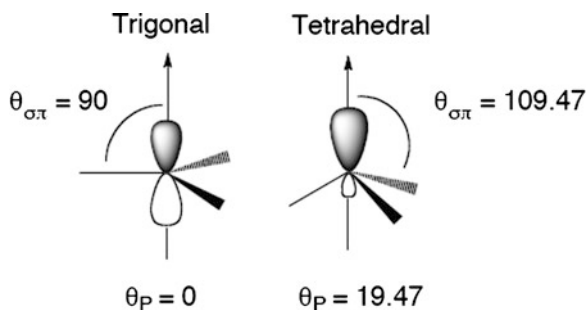
6.3.2.2 Addition of Carbenes

Properties of the surface affect the outcome whether a CC bond is completely broken or not at the binding site. As an example, Fig. 6.7 shows different types of the addition of an inner or outer carbene into a (5,5) nanotube. For the additions where two covalent bonds are newly formed, there are two possible binding sites: O or S with respect to the axis of an armchair tube. The O and S sites behave differently:
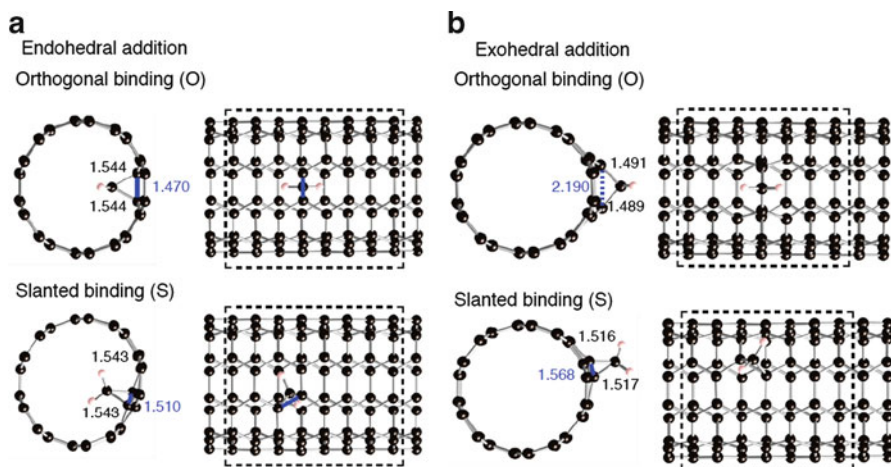
Fig. 6.7 Two optimized geometries for the addition of the CH_2 molecule into the inner (**a**) (outer (**b**)) surface of the (5,5) carbon nanotube. At the top, two CH_2 groups are attached to a CC bond orthogonal to the tube axis (*O*); at the bottom, two CH_2 groups are attached to a CC bond slanted to the tube axis (*S*). The binding sites are in *blue* (Reproduced from Yumura and Kertesz [116] with kind permission of © The American Chemical Society (2007))
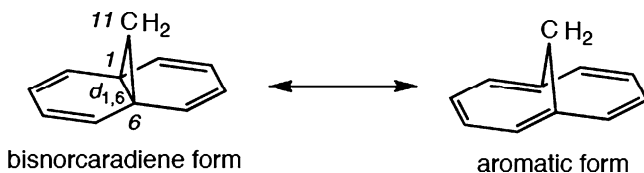
Scheme 6.1 1,6-methano[10]annulene

in the inner addition, the CC bond at the binding site is retained, irrespective of whether the site is O or S. However, for outer addition the orthogonal bond of the nanotube is cleaved, while an S bond is retained.

Breaking or retaining a CC bond at the site of carbene binding into a carbon nanotube is reminiscent of the valence tautomerization of 1,6-methano[10]annulene, which is created by the addition of divalent atom (labeled by C11, see Scheme 6.1) of carbene into the C1 and C6 atoms of naphthalene [157, 158]. In the valence tautomerization shown in Scheme 6.1, two isomers exist depending on the separation between the C1 and C6 atoms ($d_{1,6}$ bond). (We retain this numbering for the more complex cases where C11 will be the carbon of the attacking carbene and C1 and C6 will refer to the adjacent carbons in the tube.) One tautomer is the bisnorcaradiene form retaining the $d_{1,6}$ σ-bond, and the other is the aromatic form in which the $d_{1,6}$ bond is broken. The two tautomers have different number of π electrons in the naphthalene-moiety: in the aromatic form there are ten π electrons, while in the bisnorcaradiene form only eight π electrons remain, the other two being used for

Fig. 6.8 Potential energy surface scan along the $d_{1,6}$ bond of 1,6-methano[10]annulene and its derivatives as calculated with HF/6-31G* (Reproduced from Choi and Kertesz [157] with kind permission of © The American Chemical Society (1998))
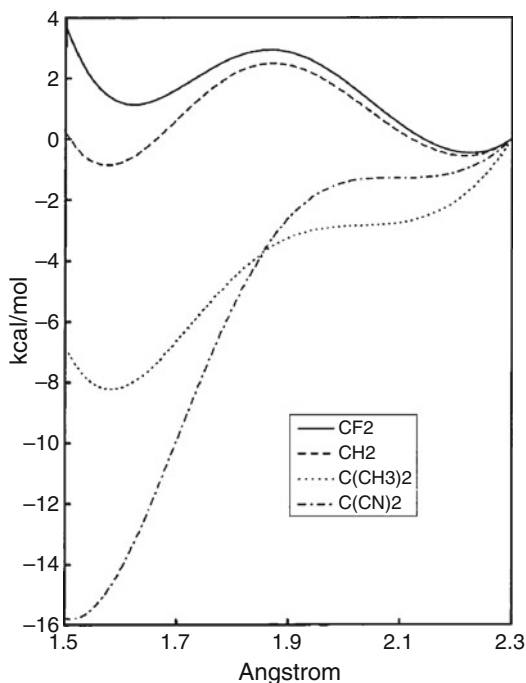
a C1-C6 σ-bond. The relative stability of the two tautomers depends sensitively on the chemical environment. Figures 6.8 and 6.9 display the HF and B3LYP potential energy surfaces of the tautomerization, respectively [157]. The energy scan analyses found that the $d_{1,6}$ value is a key parameter determining the relative stability of the two tautomeric forms and since bond breaking is involved, electron correlation is an important part of its energetics. As shown in Figs. 6.8 and 6.9, computational methods strongly affect the shapes of these potential energy surfaces. In fact, there are two local minima in the HF evaluation of 1,6-methano[10]annulene (Fig. 6.8), whereas only one stable conformation exists at $d_{1,6} = \sim 2.2$ Å (Fig. 6.9) in the B3LYP DFT evaluation. The DFT results can be reproduced by the MP2 calculations. The differences are due to important electron correlation effects as expected when comparing tautomeric forms with different numbers of σ- and π-electrons.

Here, we review key results of cyclopropanized carbon nanotubes reported in the literature. So far, researchers investigated mostly the addition of carbene into special nanotubes (armchair, i.e., $n = m$, and zigzag, i.e., $m = 0$, tubes). We emphasize the all important $d_{1,6}$ values (Tables 6.2, 6.3, and 6.4) as well as the respective binding energies (E_{BE}) (Tables 6.5 and 6.6). Note, that in carbene addition $d_{1,6}$ can indicate a broken bond, as in the case of attachments to S bonds, or bonds that are essentially retained, as in the case of attachments to parallel bonds. In an early study, Bettinger evaluated energies in the adsorption of carbene into a finite-length

Fig. 6.9 Potential energy surface scan along the $d_{1,6}$ bond of 1,6-methano[10] annulene and its derivatives as calculated with B3LYP/6-31G* (Reproduced from Choi and Kertesz [157] with kind permission of © The American Chemical Society (1998))
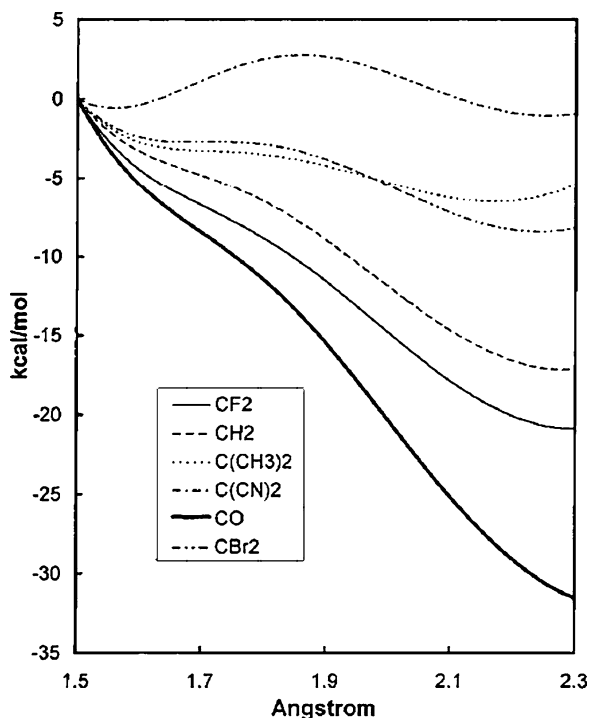
(5,5) tube ($C_{30+10n}H_{20}$) [107]. According to the B3LYP study, the binding energy shows an oscillatory behavior with a period of three as a function of n which likely comes from the strong n-dependence of the HOMO–LUMO gap of $C_{30+10n}H_{20}$. The values converge around −98 kcal/mol in $n \geq 6$. Accordingly, $C_{90}H_{20}$ is the smallest finite-length tube that can model infinite tubes appropriately. Bettinger also investigated a reaction mechanism for the CCl_2 addition into $C_{90}H_{20}$ [107]. The B3LYP calculation found that a diradicaloid complex is formed as a reaction intermediate. Despite the interesting conclusion, the formation of the diradicaloid intermediate was not found by Chu and Su, who analyzed the mechanism for the reaction between CH_2 using a longer tube model ($C_{130}H_{20}$) by an ONIOM approach [103]. As shown in Table 6.2, many researchers have separately discussed cyclopropanation of armchair nanotubes. Their studies found that at O sites, the carbene breaks a CC bond whose length of around 2.20 Å is indicative of bond breaking, whereas at S sites, the bond expands from an aromatic CC bond to an ordinary σ-bond with a bond length around 1.55 Å. Similar trends were obtained in PBC calculations, as shown in Table 6.4.

Within the cluster approach, the two-layer ONIOM method has been applied to treat nanocarbon materials as an economic alternative. The ONIOM results, as expected with any QM/MM computations, need to be evaluated with care. This is because the number of atoms treated at the higher level of theory as well as the types

Table 6.2 The $d_{1,6}$ values in cyclopropanized carbon nanotubes, obtained from cluster approaches based on PM3, AM1, HF, or DFT methods. All addends in Table 6.2 are on the outside of the nanotube

Method	Basis set	Tube model and chirality	Addends	Bond types[a]	$d_{1,6}$ values	Reference
PM3	–	$C_{100}H_{20}$ (5,5)	CH_2	O	2.238	[115]
AM1	–	$C_{130}H_{20}$ (5,5)	CH_2	O	2.224	[101]
HF	3-21G	$C_{130}H_{20}$ (5,5)	CH_2	O	2.140	[101]
PBE	3-21G	$C_{30}H_{20}$ (5,5)	CH_2	O	2.439	[107]
PBE	3-21G	$C_{60}H_{20}$ (5,5)	CH_2	O	2.163	[107]
PBE	3-21G	$C_{110}H_{20}$ (5,5)	CH_2	O	2.200	[107]
B3LYP	LANL2DZ	$C_{60}H_{20}$ (5,5)	$C(CH_3)_2$	O	2.167	[103]
B3LYP	6-31G*	$C_{100}H_{20}$ (5,5)	CH_2	O	2.217	[115]
B3LYP	6-31G*	$C_{130}H_{20}$ (5,5)	CH_2	O	2.186	[101]
PM3	–	$C_{100}H_{20}$ (5,5)	CH_2	S	1.544	[115]
B3LYP	6-31G*	$C_{100}H_{20}$ (5,5)	CH_2	S	1.564	[115]

[a]Definition of bond types is given in Fig. 6.1

Table 6.3 The $d_{1,6}$ values in cyclopropanized carbon nanotubes, obtained from cluster approaches based on ONIOM calculations. All addends in Table 6.3 are on the outside of the nanotube

Method	Basis set	Model	Addend	Bond type[a]	Atoms[b]	$d_{1,6}$ values	Reference
B3LYP:AM1	6-31G*: –	$C_{130}H_{20}$ (5,5)	CCl_2	O	16	1.64	[99]
B3LYP:AM1	6-31G*: –	$C_{130}H_{20}$ (5,5)	CCl_2	S	16	1.60	[99]
B3LYP:AM1	6-31G*: –	$C_{130}H_{20}$ (5,5)	CH_2	O	16	1.694	[101]
B3LYP:AM1	6-31G*: –	$C_{130}H_{20}$ (5,5)	CH_2	O	28	1.687	[101]
B3LYP:AM1	6-31G*: –	$C_{130}H_{20}$ (5,5)	CH_2	O	32	1.706	[101]
B3LYP:HF	6-31G*: 3-21G	$C_{130}H_{20}$ (5,5)	CH_2	O	16	1.651	[101]
B3LYP:HF	6-31G*: 3-21G	$C_{130}H_{20}$ (5,5)	CH_2	O	28	1.682	[101]
B3LYP:HF	6-31G*: 3-21G	$C_{130}H_{20}$ (5,5)	CH_2	O	32	1.712	[101]
B3LYP: B3LYP	6-31G*: STO-3G	$C_{130}H_{20}$ (5,5)	CH_2	O	16	2.176	[101]
B3LYP: B3LYP	6-31G*: STO-3G	$C_{130}H_{20}$ (5,5)	CH_2	O	28	2.182	[101]
B3LYP: B3LYP	6-31G*: STO-3G	$C_{130}H_{20}$ (5,5)	CH_2	O	32	2.176	[101]
B3LYP: PM3	6-31G*: –	$C_{130}H_{20}$ (5,5)	CH_2	O	16	2.167	[103]
B3LYP: PM3	6-31G*: –	$C_{100}H_{20}$ (5,5)	CH_2	O	16	2.167	[115]
B3LYP:/PM3	6-31G*: –	$C_{100}H_{20}$ (5,5)	CH_2	S	16	1.572	[115]

[a]Definition of bond types is given in Fig. 6.1
[b]The number of atoms treated at the higher-level theory in the ONIOM approach

Table 6.4 The $d_{1,6}$ values in cyclopropanized carbon nanotubes, obtained from PBC approaches. Addends on the inside of the nanotube are designated as "inner." Otherwise, addends in this table are on the outside of the tube

Method	Basis set	Chirality of model	Addend	Bond types[a]	$d_{1,6}$ values	References
PW91	Double numeric	(6,6)	CCl_2	O	2.18	[104]
PW91	Double numeric	(9,0)	CCl_2	S	2.16	[104]
PW91	Double numeric	(10,0)	CCl_2	S	2.19	[104]
PBE	PW (240 eV)	(5,5)	CH_2	O	2.17	[105]
PBE	PW (240 eV)	(10,10)	CH_2	O	2.08	[105]
PBE	PW (240 eV)	(11,11)	CH_2	O	1.65	[105]
PBE	PW (240 eV)	(12,12)	CH_2	O	1.67	[105]
PBE	PW (240 eV)	(19,0)	CH_2	P	1.68	[105]
PBE	3-21G	(3,3)	CH_2	O	2.26	[107]
PBE	3-21G	(12,12)	CH_2	O	2.15	[107]
PBE	3-21G	(3,0)	CH_2	S	2.10	[107]
PBE	3-21G	(3,0)	CH_2	P	1.50	[107]
PBE	3-21G	(12,0)	CH_2	S	2.29	[107]
PBE	3-21G	(12,0)	CH_2	P	1.56	[107]
PBE	PW (30 Ry)	(n, n); $3 \leq n \leq 12$	CH_2	O	$2.24 \sim 2.1$	[108]
PBE	PW (280 eV)	(9,0)	CCl_2	P	1.53	[111]
PBE	PW (280 eV)	(9,0)	CCl_2	S	1.82	[111]
PBE	PW (280 eV)	(10,0)	CCl_2	P	1.54	[111]
PBE	PW (280 eV)	(10,0)	CCl_2	S	2.12	[111]
PBE	PW (280 eV)	(5,5)	CCl_2	O	2.21	[111]
PBE	PW (280 eV)	(5,5)	CCl_2	S	1.57	[111]
PBE	PW (30 Ry)	(5,5)	$C(NO_2)_2$	O (1b)[b]	~ 2.19	[118]
PBE	PW (30 Ry)	(5,5)	$C(NO_2)_2$	O (1a)[b]	~ 2.22	[118]
PBE	PW (30 Ry)	(8,8)	$C(NO_2)_2$	O (1b)[b]	~ 1.56	[118]
PBE	PW (30 Ry)	(8,8)	$C(NO_2)_2$	O (1a)[b]	~ 2.19	[118]
PW91	PW (349 eV)	(5,5)	CH_2	O	2.190	[116]
PW91	PW (349 eV)	(5,5)	CH_2	S	1.568	[116]
PW91	PW (349 eV)	(5,5)	CH_2	O (inner)[c]	1.470	[116]
PW91	PW (349 eV)	(5,5)	CH_2	S (inner)[c]	1.510	[116]
PW91	PW (349 eV)	(10,10)	$C(COOH)_2$	O	2.126	[125]
PW91	PW (349 eV)	(10,10)	$C(COOH)_2$	S	1.535	[125]

[a]Definition of bond types is given in Fig. 6.1
[b]Definition of orientations of two NO_2 groups is given in Fig. 6.11
[c]The description of inner or outer refers to the location of the carbene attachment (see Fig. 6.7)

Table 6.5 The binding energies for carbene additions obtained from a cluster approach. The unit is in kcal/mol. All addends in Table 6.5 are on the outside of the nanotube

Method	Basis set	Tube model and chirality	Addend	Bond types[a]	E_{BE}[b]	Reference
B3LYP//PBE	6-31G*/3-21G	$C_{90}H_{20}$ (5,5)	CH_2	O	−98.5	[107]
ONIOM (B3LYP:PM3)	6-311G*	$C_{130}H_{20}$ (5,5)	CH_2	O	−93	[103]
B3LYP	LANL2DZ	$C_{60}H_{20}$ (5,5)	$C(CH_3)_2$	O	−60.1	[106]

[a]Definition of bond types is given in Fig. 6.1
[b]E_{BE} represents the binding energy for carbene addition

Table 6.6 The binding energies for carbene additions obtained from a PBC approach. The unit is in kcal/mol

Method	Basis	Model	Addend	Bond type[a]	E_{BE}[b]	Reference
PW91	Double numeric	(6,6)	CCl_2	O	−33.12	[104]
PW91	Double numeric	(9,0)	CCl_2	S	−24.63	[104]
PW91	Double numeric	(10,0)	CCl_2	S	−17.32	[104]
PBE	3-21G	(5,5)	CH_2	O	∼−98[b]	[107]
PBE	3-21G	(5,5)	CH_2	S	∼−70[c]	[107]
PBE	3-21G	(9,0)	CH_2	S	∼−90	[107]
PBE	3-21G	(9,0)	CH_2	P	∼−80	[107]
PBE	PW (280 eV)	(9,0)	CCl_2	P	−28.6	[111]
PBE	PW (280 eV)	(9,0)	CCl_2	S	−24.4	[111]
PBE	PW (280 eV)	(10,0)	CCl_2	P	−20.6	[111]
PBE	PW (280 eV)	(10,0)	CCl_2	S	−20.5	[111]
PBE	PW (280 eV)	(5,5)	CCl_2	O	−21.0	[111]
PBE	PW (280 eV)	(5,5)	CCl_2	S	−27.4	[111]
PW91	PW (349 eV)	(5,5)	CH_2	O	−117[d]	[116]
PW91	PW (349 eV)	(5,5)	CH_2	S	−87.3[d]	[116]

[a]Definition of bond types is given in Fig. 6.1
[b]E_{BE} represents the binding energy for carbene addition
[c]The value was obtained using the spin-unrestricted method (the energy of the cyclopropanized carbon nanotube relative to the dissociation limit toward a carbon nanotube and triplet CH_2)
[d]The value was obtained from the spin-restricted method (the energy of the cyclopropanized carbon nanotube relative to the dissociation limit toward a carbon nanotube and singlet CH_2)

of the combination between lower- and higher-level treatments influence sensitively the $d_{1,6}$ values, as shown in Table 6.3. For example, Lu et al. [99] investigated the addition of CCl_2 into a finite-length (5,5) tube ($C_{130}H_{20}$) by the ONIOM (B3LYP/6-31G*:AM1) method, and obtained the $d_{1,6}$ value of 1.64 Å at the O attachment corresponding to a lengthened yet unbroken bond. The value is significantly smaller than those obtained by other methods in Tables 6.2 and 6.4, all of which indicate a cleaved bond. In the ONIOM calculations, 16 atoms near the binding site are treated by the DFT method, and the other atoms by the AM1 method. Later, Chen et al. [101] investigated dependences of methods at lower level (AM1, HF/3-21G, and B3LYP/STO-3G) on the $d_{1,6}$ values of the CH_2-functionalized (5,5) tube. In the comparative studies [101], carbon atoms near the binding site are treated

Fig. 6.10 Optimized lengths of the $d_{1,6}$ bond in armchair (n, n) carbon nanotubes attached by CH_2 or NH, where n ranges from 3 to 12. O and S represent orthogonal and slanted (skewed) bonds with respect to the tube axis, respectively, given in Fig. 6.1. Similar values are also displayed for the functionalization of bent graphene (Reproduced from Lee and Marzari [108] with kind permission of © The American Physical Society (2006))
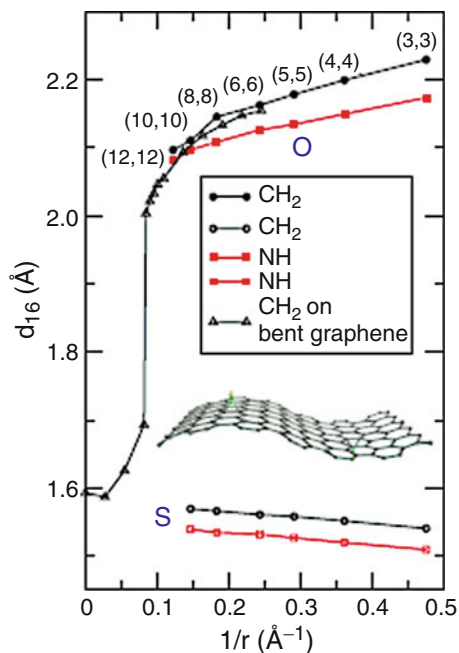
at B3LYP/6-31G* level as the higher-level treatment. As a result, the ONIOM (B3LYP/6-31G*:B3LYP/STO-3G) calculation obtained an open $d_{1,6}$ bond ($\sim$2.2 Å) in the optimized geometry, being similar to that obtained from full B3LYP/6-31G* optimization. On the other hand, the other two ONIOM methods cannot reproduce the B3LYP/6-31G* result, because both ONIOM optimized structures have a closed $d_{1,6}$ bond ($\sim$1.7 Å).

Besides the cluster approach, many researchers have employed PBC calculations to study interactions of carbon nanotubes with carbenes and its derivatives. Within the PBC approach, Bettinger investigated the minimum size of a supercell acceptable for describing the interactions of the SWCN with carbenes [107]. Accordingly supercells of three (two) ordinary unit cells in an armchair (a zigzag) nanotube are large enough for the calculations of the binding energy in cyclopropanation. The converged value is -98 kcal/mol with respect to the dissociation limit toward the triplet CH_2 and the (5,5) tube in Table 6.5. In terms of the geometrical feature, Lee and Marzari investigated diameter-dependencies of the $d_{1,6}$ value in the O and skewed attachments, as shown in Fig. 6.10 [108]. Their DFT studies found that opening an O bond at the carbene binding site can be seen in the (n, n) tubes, when n ranges from 3 to 12. Furthermore, they predicted the transition from an open to a closed form in a nanotube whose diameter is around 2.4 nm. Similar diameter-dependences of the $d_{1,6}$ values were found in the nitrene functionalization study of a nanotube by Zurek et al. [119].

Although CH_2- or CCl_2-functionalized carbon nanotubes have been extensively studied, a limited number of studies on the functionalization by other
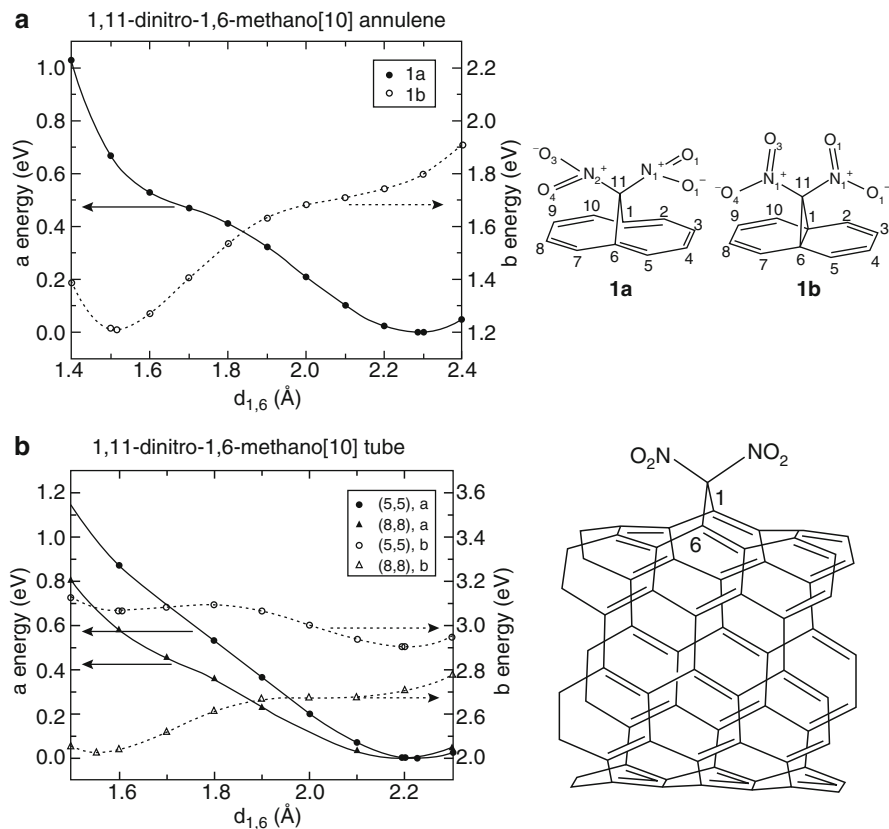
Fig. 6.11 Potential energy surface scan along the $d_{1,6}$ bond of 11,11-dinitro-1,6-methano[10]annulene (**a**) and dinitro-carbene-functionalized carbon nanotubes (**b**) obtained from PBE PBC calculations. The "1a" configuration of 11,11-dinitro-1,6-methano[10]annulene has C_{2v} symmetry and the four NO bonds are equivalent. In the "1b" configuration, two NO_2 groups are forced to rotate and are placed in a plane perpendicular to the naphthalene moiety (Reproduced from Lee and Marzari [118] with kind permission of © The American Chemical Society (2008))

carbene-derivatives have been published. Lee and Marzari used in their modeling studies dinitro-carbene as the addend to control the breaking of the $d_{1,6}$ bond [118]. In fact, they analyzed the potential energy surfaces of dinitro-carbene-functionalized tubes as well as 11,11-dinitro-1,6-methano[10]annulene, as shown in Fig. 6.11 [118]. In the study, two types of orientations of two NO_2 groups (1a and 1b in Fig. 6.11) were considered. Based on the PBE calculations of 11,11-dinitro-1,6-methano[10]annulene, the C11 atom with the 1a orientation cleaves the $d_{1,6}$ bond, whereas the bond remains unbroken in the 1b orientation. Similar argument can be applied to a relatively larger diameter tube (e.g., (8,8) tube) functionalized by dinitro-carbene. However, more complicated situations were found in the case of a
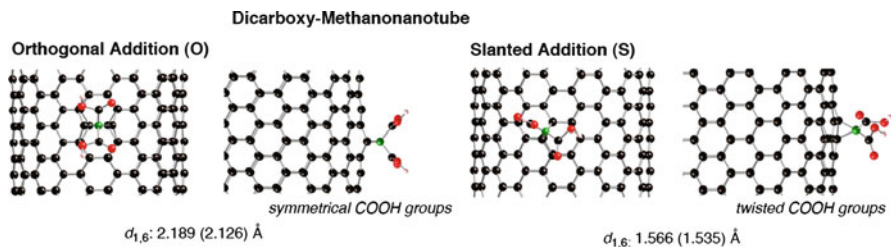
Fig. 6.12 Optimized structures for dicarboxy-methanocarbon nanotubes. In structure on the *left*, the divalent (*green*) C atom binds into an orthogonal (*O*) bond of the (10,10) carbon nanotube. The divalent atom is attached to two COOH groups symmetrically. In structure on the *right*, the divalent atom binds into a slanted (*S*) bond, and it is bound to a twisted COOH groups. Oxygen atoms are in *red*. Optimized $d_{1,6}$ bond lengths from PW91 cluster approach are given, and bond length values from PW91 PBC calculations are in parentheses (Reproduced from Yumura and Kertesz [125] with kind permission of © The American Chemical Society (2009))

narrow tube (e.g., (5,5) tube) because of the increased curvature effects. As a result, an open form with the dinitro orientation 1b is stable relative to its closed form, although the two forms are energetically very close. The role of the orientation of dicarboxy-carbene in determining the relative stability between an open and closed form has been analyzed subsequently in [125]. In the dicarboxy-carbene functionalization, there are mainly two types of binding orientations; one has the two dicarboxyl groups symmetrical with respect to a mirror plane perpendicular to the tube axis, whereas the other lacks such a symmetry due to the twisting of the COOH groups. As shown in Fig. 6.12, the dicarboxy-carbene with the symmetric orientation splits an O CC bond of the (10,10) nanotube, whereas a S CC bond remains unbroken after the addition of dicarboxy-carbene. The relationship between the dicarboxy binding orientation and the $d_{1,6}$ bond length is consistent with that found for 11,11-dicarboxy-1,6-methano[10]annulene and shown in Fig. 6.13. In the tautomerization, the twisted orientation has two isoenergetic local minima around the $d_{1,6}$ value of ∼1.6 and ∼2.2 Å in Fig. 6.13. On the other hand, there is one local minimum at $d_{1,6} = $∼2.3 Å in the symmetrical orientation. The dependence of the $d_{1,6}$ value on the orientation of the bond will be important in enhancing the site-selectivity of the functionalization of carbon nanotubes by bismalonate with a 2,3-butanediol tether, as will be discussed in Sect. 6.3.5.

6.3.3 Addition of Metal or Metal Clusters

Metal-nanotube interactions have been also well investigated by various theoretical researchers [159–167]. In cases where a single metal atom interacts with a nanotube, various metal-nanotube interactions occur. Typical locations include a site above a hexagon (hollow-site), a site above a CC bond, and a site above a tube carbon atom. The character of the metal-nanotube bonding dramatically depends on types of
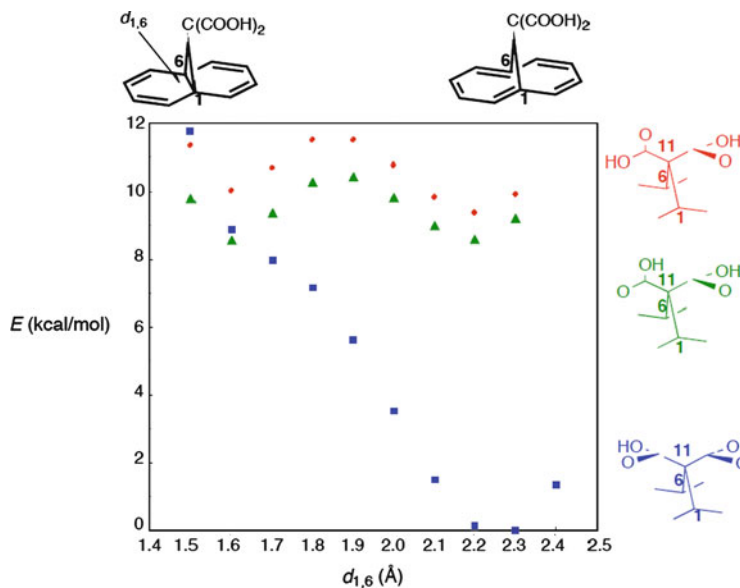
Fig. 6.13 Potential energy surface scan along the $d_{1,6}$ bond of 11,11-dicarboxy-1,6-methano[10]annulene at the PW91/6-31G* level of theory, showing dependency on the orientations of the two carboxyl groups. *Blue diamonds* indicate two carboxyl groups that are symmetric with respect to a mirror plane, whereas *red dots* and *green triangles* indicate twisted carboxyl groups (Reproduced from Yumura [135] with kind permission of © The Royal Chemistry Society (2011))

metal atoms [161]. When a metal cluster is attached to a nanotube surface, the shape and size of cluster are a key factor determining the interactions with a nanotube [163–167]. For example, Choug et al. estimated the stabilization energy by the binding of a Td–Pt$_4$ cluster onto a (10, 0) nanotube, and found that the stabilization energy increases when the number of Pt atoms in the cluster being in contact with the tube increases. Furthermore, the stabilization energy can be enhanced by using a boron-substituted nanotube [162] as well as tubes with defects [165]. Further work in this area is anticipated given the potential of such metal clusters attached to nanotubes in catalysis [168].

6.3.4 Surface Modification Induced by Organic Functionalization of Carbon Nanotubes

The surface does not remain unaffected during covalent functionalization. We discuss some systematic changes that happen to the carbon network of a nanotube induced by the carbene functionalization in connection with the variations in the $d_{1,6}$ CC bond length as a relevant parameter. From the analogy to

1,6-methano[10]annulene, whether the $d_{1,6}$ CC bond retained or not is directly related to the number of π electrons of a carbon nanotube to which the carbene is attached [116, 117]. According to [147], the pristine armchair (10,10) tube has aromatic sextets, based on the Clar VB concept. As discussed in the previous section, the inner O addition does not cleave the $d_{1,6}$ bond, and thus two π electrons are transferred from the tube surface to make two covalent bonds with carbene. In contrast, the number of π electrons is preserved after the outer O addition, where the $d_{1,6}$ bond is broken. As a result of these two different scenarios, in the inner cyclopropanized nanotube case, the geometrical features are similar to those of the bisnorcaradiene form of 1,6-methano[10]annulene, whereas in the outer cyclopropanized case, the geometry of the functionalized nanotube resembles that of the aromatic form of 1,6-methano[10]annulene. Corresponding to the number of π electrons that are the result of these two addition patterns, two different binding patterns can be identified using Clar's sextets. In the inner addition, two butadiene-like (B and B') patterns as well as one quinonoid (Q) patterns can be constructed, as shown in Fig. 6.14. Roughly speaking, the DFT-obtained surface modification can be considered to arise from a combination of the B, B', and Q Clar patterns. With respect to the Q pattern obtained from PW91 calculations, the bond-length alternation in the circumferential direction is significant only near the binding site [116]. Similar modification patterns are found in a nanotube attached by an inner defected C_{60} buckyball. This defected C_{60} (C_1–C_{59}) is formed initially from C_{60} with a high barrier of 8.4 eV [169]. In related experiments, the formation of a defective fullerene species has been suggested from transmission electron microscopy of nanopeapods, where fullerene buckyballs are encapsulated inside carbon nanotubes [170].

On the other hand, the outer O addition does not substantially perturb the π system of the nanotube. The Clar patterns as shown in Fig. 6.14 as C are retained except for the six-membered rings nearest to the binding site. The nearest six-membered rings have Kekulé structures indicated by K and K' in Fig. 6.14. The surface modification by the carbene attachment is completely different from that in the radical additions that have a nearly perfect D_{3h} symmetry [135]. The differences in the surface relaxations can be explained qualitatively by referring to the different numbers of π electrons migrating as a consequence of the two different kinds of functionalizations. In fact, one π electron migrates in the radical addition, while two (zero) π electrons participate in making two covalent bonds between carbene and inner (outer) tube surface.

As discussed above, π electron counts based on Clar VB representation can nicely explain the tube surface modified by the covalent functionalization, obtained from relatively accurate DFT calculations. Clar representations have been used by various researchers to aid in the understanding of the properties of functionalized nanotubes [116, 117, 124, 126, 146]. Clar representations can also shed light on the conductance of carbene-attached nanotubes [108]. For example, Marzari et al. reported that the conductance of the carbene-attached nanotube with an open C1C6 bond ($d_{1,6} > 2$ Å) is comparable to that of the pristine tube, but that with a closed
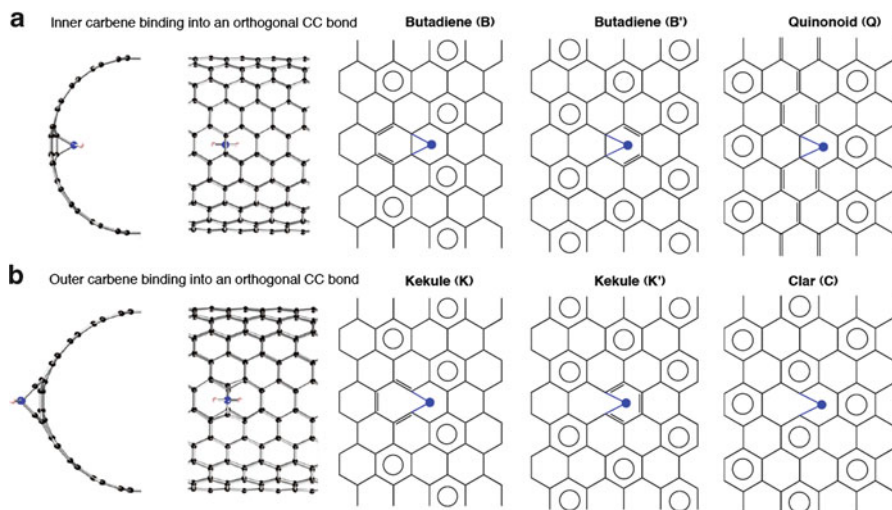
Fig. 6.14 Clar valence bond (VB) representations for the addition of CH_2 into an orthogonal CC bond on the inner (**a**) and outer (**b**) carbon nanotube surfaces. The *purple dots* represent binding sites for the CH_2 molecule. Aromatic sextets are indicated by *circles*. The tubes are presented as planar projections; only the vicinity of the addition site is shown (Reproduced from Yumura and Kertesz [116] with kind permission of © The American Chemical Society (2007))

C1C6 ($d_{1,6} < 1.7$ Å) significantly diminishes relative to the pristine unsubstituted case [108]. Thus, the Clar analysis, prior to performing large-scale and accurate DFT calculations or making extensive experimental efforts, might aid in predicting qualitatively the behavior of carbon nanotubes upon chemical modifications and additions.

6.3.5   Multiple Carbene Addition

A few studies have modeled double addition into SWCNs as a first step to elucidate any collective effects, in other words, deviations from two simple independent additions. If the surface modification induced by the first addition is sufficiently large to modify the parameters of the second addition, one might obtain design principles for selective functionalization. In order to separate the steric requirements from the electronic effects, a useful model is obtained by considering an inner addition followed by an outer addition.

As discussed in Sect. 6.3.4, the first inner carbene addition creates sites with double-bond character near the binding site. Since carbenes generally prefer to attack at a CC bond with higher electron densities, CC bonds with double-bond characters are good candidates for a site of the second carbene attachment. In other words, the inner carbene addition can direct the next carbene into specific CC bonds.

The interaction energy is a useful parameter in quantitatively evaluating the site-selectivity of the double addition:

$$E_{\text{interact}}(X) = E_{\text{double-bind}}(C11(X) - NT - C11(0)) - E_{\text{single-bind}}(C11(X) - NT)$$
$$- E_{\text{single-bind}}(NT - C11(0)).$$

Here, C11(X)-NT-C11(0) is a tube functionalized by the inner carbene as well as a second outer carbene, C11(X)-NT is a tube functionalized by an outer carbene at location X (measured relative to the first addition at the site designated as 0), and NT-C11(0) is a tube functionalized by inner carbene at the reference site, 0. $E_{\text{single-bind}}$ and $E_{\text{double-bind}}$ refer to the binding energies at single and double addition, respectively. If the electrons were completely localized in the two addition reactions, $E_{\text{interact}}(X)$ would be very small – close to zero. In PW91 calculations [116], significant $E_{\text{interact}}(X)$ values are with negative sign at well-defined X sites, with the absolute value of $E_{\text{interact}}(X)$ decreasing as X is located farther away from the 0 site. Of course, $E_{\text{interact}}(X)$ depends not only on the 0X distance. For example, relatively stable C11(X)-NT-C11(0) configurations have large negative E_{interact} values in Fig. 6.15 [116]. A negative $E_{\text{interact}}(X)$ value indicates to what extent the first inner addition stabilizes the addition of an outer carbene into a certain site. These data indicate strong local cooperative behavior in the double carbene additions.

In contrast, the addition of a carbene into the outer surface of a nanotube perturbs only two 6-membered rings nearest to the binding site along the tube axis, where double-bond characters appear [116, 125]. In this case, due to the proximity of the second addend, the double bonds cannot serve as a binding site for the second carbene. Nevertheless, some sites are more preferable than others for the second carbene after the first outer addition. In the search for an additional strategy for enhancing site-selectivity of outer functionalization of carbon nanotubes, some geometrical restrictions of the functional groups can be helpful. Fullerene chemistry helps to find functional groups that can selectively bind into a nanotube [171–175] by offering analogies. For example, Diederich et al. reported that a bismalonate with a 2,3-butanediol tether adds to C_{60} by a Bingel reaction to form only a cis-3 adduct, as shown in Scheme 6.2. With respect to the Bingel reaction, Gao et al. investigated a possible mechanism for its simple case, the reaction between CCl_3^- and C_{60}. Also, they compared its energy profile with that for carbene reaction [176]. According to Gao et al., the first step of the Bingel reaction is that CCl_3^- adds into a carbon atom of C_{60}. After that, one Cl^- ion cleaves in a transition state, and, at the same time, a new CC bond is formed to result in a cyclopropanized fullerene. On the other hand, in the carbene mechanism, CCl_2 carbene, formed preliminary from CCl_3^-, binds into C_{60} to create a cyclopropanized fullerene with a small barrier. These DFT calculations indicate that both mechanisms are competitive in energy.

Following previous experimental and theoretical studies, extensive DFT calculations on the stability of the cycloaddition of diethylbutane-2,3-diyl to the outer surface of a (10,10) nanotube were performed. [125] Out of the 12
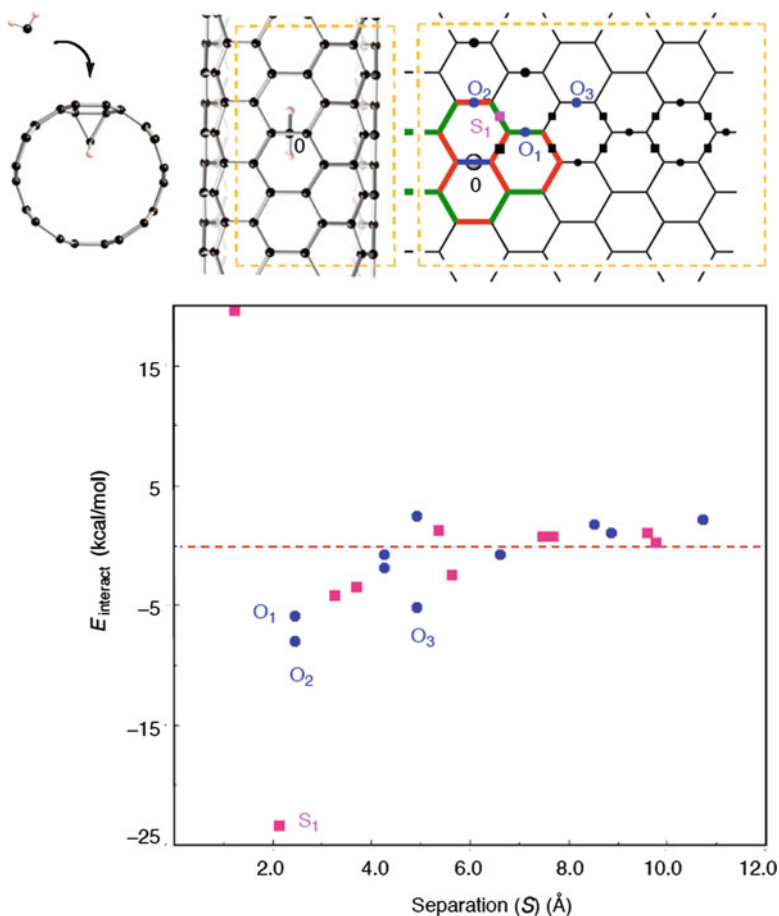
Fig. 6.15 Interaction energies $E_{interact}$ as a function of separation (S) of the two binding sites between the first (inner) and second (outer) attachment projected upon graphene (see the text for the definition of $E_{interact}$). *Purple squares* and *blue circles* represent the second attachment at a slanted and an orthogonal site, respectively. *Green and red bonds* indicate approximate double and approximate single bonds, respectively (Reproduced from Yumura and Kertesz [116] with kind permission of © The American Chemical Society (2007))

configurations considered, only two stable configurations were found for the bismalonate-functionalized nanotube, which are shown in Fig. 6.16. This specificity is in strong contrast to the double outer carbene additions. The DFT calculations found that replacement of CH_2 by the bismalonate enhances the site-selectivity of bisfunctionalization of the nanotube. The enhancement in the site-selectivity is explainable, because preferences of an O site over a S site as a second attachment are significantly weakened in the bismalonate functionalization [125]. The most important factor differentiating the bismalonate functionalization from double
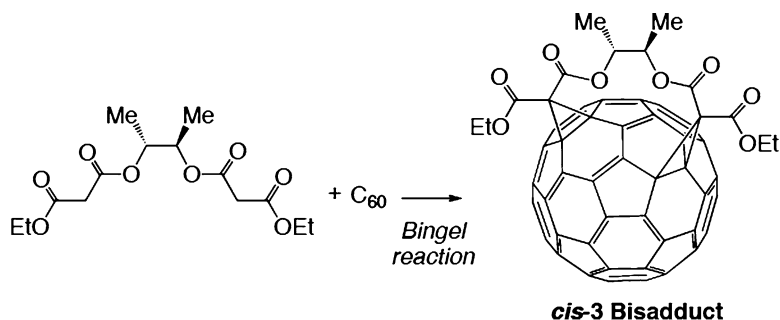
Scheme 6.2 Reaction between C_{60} and a bismalonate with 2,3-butanediol tether

a The most stable orthogonal configuration

b The most stable slanted configuration

$d_{1,6}$: 2.185 (2.126)Å
$d_{1,6}$: 2.186 (2.126)Å

$d_{1,6}$: 2.178 (2.130)Å
$d_{1,6}$: 1.567 (1.544)Å
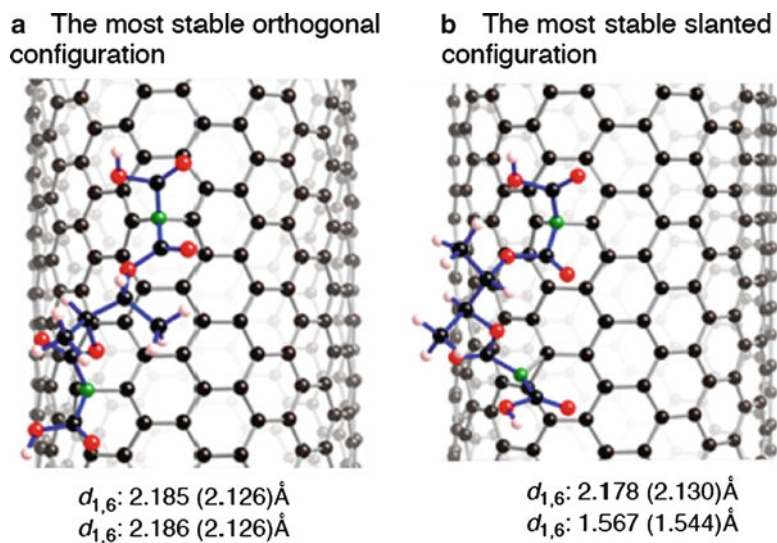
Fig. 6.16 Two stable conformations of the addition of the bismalonate with the 2,3-butanediol tether into the (10,10) carbon nanotube. The C atoms attached to the carbon nanotube (C11) are given by *green*. Optimized $d_{1,6}$ lengths in the finite-length calculations are given, and those in the infinite-length (PBC) calculations are given in parentheses. The optimized geometry in (**a**) shows the most stable conformation, where the divalent atoms are attached to O bonds of the nanotube. The optimized structure in (**b**) is the next most stable conformation, where one divalent atom binds to a O bond, and the other binds to a S bond (Reproduced from Yumura and Kertesz [125] with kind permission of © The American Chemical Society (2009))

carbene addition is conformational restriction of the bismalonate due to the 2,3-butanediol tether. The two C11 atoms are constrained by the 2,3-butanediol tether from freely binding into any available site on the nanotube. Another factor is the binding orientations of dicarboxyl-groups, as shown in Fig. 6.12. In O additions, only symmetric form is allowed, whereas symmetric and twisted forms are possible in S additions.
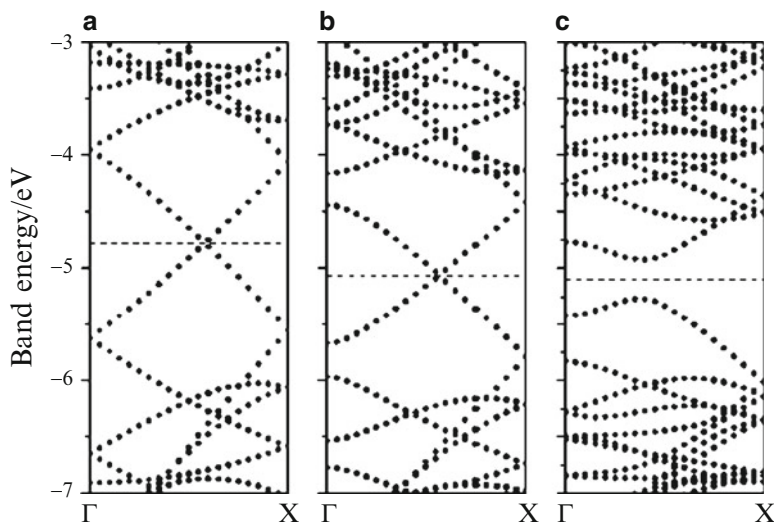
Fig. 6.17 Band structures of CCl$_2$-attached carbon nanotubes with different Cl:C modification ratio obtained from PW91 PBC calculations. In (**a**) Cl:C ratio is 0, in (**b**) Cl:C ratio is 12.5%, and in (**c**) Cl:C ratio is 25% (Reproduced from Zhao et al. [104] with kind permission of Wiley-VCH Verlag GmbH & Co. KGaA (2005))

Finally, we look at how the electronic properties of a carbon nanotube change upon multiple carbene additions. Zhao et al. analyzed band structures of CCl$_2$-attached (6,6) nanotubes with different Cl:C ratios (Cl:C = 0.0, 12.5, and 25%, where the ratio is calculated as the number of Cl atoms divided by the number of tube C atoms) [104]. According to their PW91 calculations, metallic characters of the (6,6) tube retain in the modification ratio of 12.5%, as shown in Fig. 6.17 [104]. In fact, two bands cross at Fermi level in the lower modification ratio, indicating that the functionalization does not significantly perturb the electronic properties of the pristine tube. The finding is consistent with the Clar view, because Clar patterns remain almost unchanged after the single divalent functionalization. In contrast, at the modification ratio of 25%, the CCl$_2$-susbstituted nanotube has a calculated band gap of ∼0.34 eV. In addition, they found that a metal-insulator transition might occur at the modification ratio of 18%. Consequently, they concluded that one could control the electronic properties of a tube by changing the degree of functionalization. These results were confirmed by Lu et al. who evaluated the modulation of band structures of CCl$_2$-functionalized (5,5) carbon nanotubes with the modification ratio ranging from 0% to 33% [113]. Similar conclusions on the high computed conductivity maintained upon addition of SWCNs were obtained by Lee et al. [108].

6.4   Conclusions

Density functional theory (DFT) calculations provide an atomic-scale insight of pristine and organic functionalized carbon nanotubes. Since π electrons migrate from a nanotube upon functionalization, electron correlation plays an essential role in accurately describing this process. In this review, we have highlighted recent DFT findings on the addition of prototypical organic molecules (carbene, its derivatives, and alkyl radicals) into a nanotube obtained by various computational treatments. The methodological approaches used by various groups to attack diverse problems contain – appropriately – a variety of tools that complement each other. These include cluster and periodic boundary condition (PBC) approaches, QM/MM modeling, and a variety of density functionals. A few calculations based on wave function method calculations provided some balance in the literature, but high-level calculations such as CCSD(T) are not feasible because the minimum size of an appropriate nanotube segment would be too large for this modeling.

All calculations are consistent with the finding that the number of π electrons participating in the functionalization determines the key features of the functionalized nanotube. In radical addition, one π electron contributes to making the new covalent bonds. In contrast, there are two stable forms of nanotube attached by carbene from a viewpoint of the number of π electrons. One is that carbene addition retains the CC bond at the attachment, and then two π electrons migrate from the tube to form the new bonds. In the other case, the CC σ-bond breaks after carbene addition, whereas the number of π electrons of the nanotube remains unchanged. One can see the two types of additions when a carbene is attached to the inner versus outer surface of a carbon nanotube. In addition, the relative stability of the two forms can be easily changed, depending on types of carbene-derivatives as well as the specific carbon nanotube. In this valence tautomerization problem, analogies to the valence tautomerization of 1,6-methano[10]annulene, where the CC bond at the attachment corresponds to $d_{1,6}$ bond, are helpful. In fact, the stable forms in carbene-functionalized nanotubes can be differentiated by whether the $d_{1,6}$ bond is retained or not. Cleaving or retaining the $d_{1,6}$ bond directly links to the number of π electrons migrating upon the functionalization. Similarly, the π electron count argument rationalizes that a carbon nanotube surface is modified differently, depending on the $d_{1,6}$ bond length.

Different groups consistently found that the orientation of the bonds attacked in the nanotube by the reactants has a small but noticeable effect on the energetics of the reaction and the relaxation pattern of the remaining bonds in the nanotube. Similar differences are obtained between inner and outer functionalizations. These differences might be exploitable for periodic patterning of carbon nanotubes in the future.

According to DFT calculations, the surface modification induced by carbene attachment is subtle, but has a strong impact on the modulation of the properties of a carbon nanotube. In particular, the surface modification induced by inner carbene

addition is limited near the first attachment, and thus one can utilize it to enhance site-selectivity for further carbene additions. To explain the DFT findings, the simple concept of Clar VB representation proved to be a useful interpretative tool. In addition, the Clar concept can provide a helpful insight on the change of the band structure of a nanotube upon the functionalization, and its conductivity.

References

1. Iijima S (1991) Nature 354:56
2. Iijima S, Ichihashi T (1993) Nature 363:603
3. Dresselhaus MS, Dresselhaus G, Eklund PC (1996) Science of fullerenes and carbon nanotubes. Academic, San Diego
4. Saito R, Dresselhaus G, Dresselhaus MS (1998) Physical properties of carbon nanotubes. Imperial College Press, London
5. Haddon RC (2002) Acc Chem Res 35:997
6. Niyogi S, Hamon MA, Hu H, Zhao B, Bhowmik P, Sen R, Itkis ME, Haddon RC (2002) Acc Chem Res 35:1105
7. Bahr JL, Tour JM (2002) J Mater Chem 12:1952
8. Hirsch A (2002) Angew Chem Int Ed 41:1853
9. Dyke CA, Tour JM (2004) J Phys Chem A 108:11151
10. Hirsch A, Vostrowsky O (2005) Top Curr Chem 245:193
11. Tasis D, Tagmatarchis N, Bianco A, Prato M (2006) Chem Rev 106:1105
12. Prato M, Kostarelos K, Bianco A (2008) Acc Chem Res 41:60
13. Vazquez E, Prato M (2009) ACS Nano 3:3819
14. Strano MS, Boghossian AA, Kim WJ, Barone PW, Jeng ES, Heller DA, Nair N, Jin H, Sharma R, Lee CY (2009) MRS Bull 34:950
15. Karousis N, Tagmatarchis N, Tasis D (2010) Chem Rev 110:5366
16. Chen Y, Haddon RC, Fang S, Rao AM, Eklund PC, Lee WH, Dickey EC, Grulke EA, Pendergrass JC, Chavan A, Haley BE, Smalley RE (1998) J Mater Res 13:2423
17. Chen J, Hamon MA, Hu H, Chen Y, Rao AM, Eklund PC, Haddon RC (1998) Science 282:95
18. Holzinger M, Vostrowsky O, Hirsch A, Hennrich F, Kappes M, Weiss R, Jellen F (2001) Angew Chem Int Ed 40:4002
19. Georgakilas V, Kordatos K, Prato M, Guldi DM, Holzinger M, Hirsch A (2002) J Am Chem Soc 124:760
20. Georgakilas V, Voulgaris D, Vazquez E, Prato M, Guldi DM, Kukovecz A, Kuzmany H (2002) J Am Chem Soc 124:14318
21. Kamarás K, Itkis ME, Hu H, Zhao B, Haddon RC (2003) Science 301:1501
22. Pantarotto D, Partidos CD, Graff R, Hoebeke J, Briand J-P, Prato M, Bianco A (2003) J Am Chem Soc 125:6160
23. Coleman KS, Bailey SR, Fogden S, Green MLH (2003) J Am Chem Soc 125:8722
24. Hu H, Zhao B, Hamon MA, Kamarás K, Itkis ME, Haddon RC (2003) J Am Chem Soc 125:14893
25. Pantarotto D, Singh R, McCarthy D, Erhardt M, Briand J-P, Prato M, Kostarelos K, Bianco A (2004) Angew Chem Int Ed 43:5242
26. Worsley KA, Moonoosawmy KR, Kruse P (2004) Nano Lett 4:1541
27. Wu W, Wieckowski S, Pastorin G, Benincasa M, Klumpp C, Briand J-P, Gennaro R, Prato M, Bianco A (2005) Angew Chem Int Ed 44:6358
28. Singh R, Pantarotto D, McCarthy D, Chaloin O, Hoebeke J, Partidos CD, Briand J-P, Prato M, Bianco A, Kostarelos K (2005) J Am Chem Soc 127:4388

29. Umeyama T, Tezuka N, Fujita M, Matano Y, Takeda N, Murakoshi K, Yoshida K, Isoda S, Imahori H (2007) J Phys Chem C 111:9734
30. Brunetti FG, Herrero MA, Munoz JDM, Diaz-Ortiz A, Alfonsi J, Meneghetti M, Prato M, Vazquez E (2008) J Am Chem Soc 130:8094
31. Georgakilas V, Bourlinos A, Gournis D, Tsoufis T, Trapalis C, Mateo-Alonso A, Prato M (2008) J Am Chem Soc 130:8733
32. Bahr JL, Yang J, Kosynkin DV, Bronikowski MJ, Smalley RE, Tour JM (2001) J Am Chem Soc 123:6536
33. Bahr JL, Tour JM (2001) Chem Mater 13:3823
34. Holzinger M, Hirsch A (2001) Curr Appl Phys 1:149
35. Kukovecz A, Kramberger C, Holzinger M, Kuzmany H, Schalko J, Mannsberger M, Hirsch A (2002) J Phys Chem B 106:6374
36. Strano MS, Dyke CA, Usrey ML, Barone PW, Allen MJ, Shan H, Kittrell C, Hauge RH, Tour JM, Smalley RE (2003) Science 301:1519
37. Dyke CA, Tour JM (2003) Nano Lett 3:1215
38. Dyke CA, Tour JM (2003) J Am Chem Soc 125:1156
39. Peng H, Reverdy P, Khabashesku VN, Margrave JL (2003) Chem Commun 2003:362
40. Guldi DM, Holzinger M, Hirsch A, Georgakilas V, Prato M (2003) Chem Commun 2003:1130
41. Stevens JL, Huang AY, Peng H, Chiang IW, Khabashesku VN, Margrave JL (2003) NanoLett 3:331
42. Saini RK, Chiang IW, Peng H, Smalley RE, Billups WE, Hauge RH, Margrave JL (2003) J Am Chem Soc 125:3617
43. Holzinger M, Abraham J, Whelan P, Graupner R, Ley L, Hennrich F, Kappes M, Hirsch A (2003) J Am Chem Soc 125:8566
44. Ying Y, Saini RK, Liang F, Sadana AK, Billups WE (2003) Org Lett 5:1471
45. Peng H, Alemany LB, Margrave JL, Khabashesku VN (2003) J Am Chem Soc 125:15174
46. Dyke CA, Stewart MP, Maya F, Tour JM (2004) SynLett 155
47. Zhu J, Peng H, Rodriguez-Macias F, Margrave JL, Khabashesku VN, Imam AM, Lozano K, Barrera EV (2004) Adv Funct Mater 14:643
48. Dyke CA, Tour JM (2004) Chem Eur J 10:813
49. Liang F, Sadana AK, Peera A, Chattopadhyay J, Gu Z, Hauge RH, Billups WE (2004) Nano Lett 4:1257
50. Zhang L, Kiny VU, Peng H, Zhu J, Lobo RFM, Margrave JL, Khabashesku VN (2004) Chem Mater 16:2055
51. Baik S, Usrey M, Rotkina L, Strano MS (2004) J Phys Chem B 108:15560
52. Khairoutdinov RF, Doubova LV, Haddon RC, Saraf L (2004) J Phys Chem B 108:19976
53. Chattopadhyay J, Sadana AK, Liang F, Beach JM, Xiao Y, Hauge RH, Billups WE (2005) Org Lett 7:4067
54. Liang F, Alemany LB, Beach JM, Billups WE (2005) J Am Chem Soc 127:13941
55. Price BK, Hudson JL, Tour JM (2005) J Am Chem Soc 127:14867
56. Usrey ML, Lippmann ES, Strano MS (2005) J Am Chem Soc 127:16129
57. Herranz MA, Martin N, Campidelli S, Prato M, Brehm G, Guldi DM (2006) Angew Chem Int Ed 45:4478
58. Bonifazi D, Nacci C, Marega R, Campidelli S, Ceballos G, Modesti S, Meneghetti M, Prato M (2006) Nano Lett 6:1408
59. Graupner R, Abraham J, Wunderlich D, Vencelova A, Lauffer P, Rohrl J, Hundhausen M, Ley L, Hirsch A (2006) J Am Chem Soc 128:6683
60. Price BK, Tour JM (2006) J Am Chem Soc 128:12899
61. Hudson JL, Jian H, Leonard AD, Stephenson JJ, Tour JM (2006) Chem Mater 18:2766
62. Stephenson JJ, Sadana AK, Higginbotham AL, Tour JM (2006) Chem Mater 18:4658
63. Hirsch A (2006) Phys Status Solidi B 243:3209
64. Chakraborty S, Chattopadhyay J, Peng H, Chen Z, Mukherjee A, Arvidson RS, Hauge RH, Billups WE (2006) J Phys Chem B 110:24812

65. Müller M, Maultzsch J, Wunderlich D, Hirsch A, Thomsen C (2007) Phys Status Solidi RRL 1:144
66. Kim WJ, Usrey ML, Strano MS (2007) Chem Mater 19:1571
67. Nair N, Kim WJ, Usrey ML, Strano MS (2007) J Am Chem Soc 129:3946
68. Müller M, Maultzsch J, Wunderlich D, Hirsch A, Thomsen C (2007) Phys Status Solidi B 244:4056
69. Stephenson JJ, Hudson JL, Leonard AD, Price BK, Tour JM (2007) Chem Mater 19:3491
70. Chattopadhyay J, Chakraborty S, Mukherjee A, Wang R, Engel PS, Billups WE (2007) J Phys Chem C 111:17928
71. Fantini C, Usrey ML, Strano MS (2007) J Phys Chem C 111:17941
72. Engel PS, Billups WE, Abmayr DW Jr, Tsvaygboym K, Wang R (2008) J Phys Chem C 112:695
73. Wunderlich D, Hauke F, Hirsch A (2008) J Mater Chem 18:1493
74. Wunderlich D, Hauke F, Hirsch A (2008) Chem Euro J 14:1607
75. Pekker A, Wunderlich D, Kamarás K, Hirsch A (2008) Phys Status Solidi B 245:1954
76. Müller M, Maultzsch J, Wunderlich D, Hirsch A, Thomsen C (2008) Phys Status Solidi B 245:1957
77. Syrgiannis Z, Hauke F, Rohrl J, Hundhausen M, Graupner R, Elemes Y, Hirsch A (2008) Euro J Org Chem 2008:2544
78. Doyle CD, Rocha J-DR, Weisman RB, Tour JM (2008) J Am Chem Soc 130:6795
79. Mukherjee A, Combs R, Chattopadhyay J, Abmayr DW, Engel PS, Billups WE (2008) Chem Mater 20:7339
80. Kim WJ, Nair N, Lee CY, Strano MS (2008) J Phys Chem C 112:7326
81. Fantini C, Pimenta MA, Strano MS (2008) J Phys Chem C 112:13150
82. Ni C, Chattopadhyay J, Billups WE, Bandaru PR (2008) Appl Phys Lett 93:243113
83. Doyle CD, Tour TM (2009) Carbon 47:3215
84. Usrey ML, Strano MS (2009) J Phys Chem C 113:12443
85. Müller M, Meinke R, Maultzsch J, Syrgiannis Z, Hauke F, Pekker Á, Kamarás K, Hirsch A, Thomsen C (2010) ChemPhysChem 11:2444
86. Syrgiannis Z, Gebhardt B, Dotzet C, Hauke F, Graupner R, Hirsch A (2010) Angew Chem Int Ed 49:3322
87. Gebhardt B, Graupner R, Hauke F, Hirsch A (2010) Euro J Org Chem 2010:1494
88. Hamilton CE, Lomeda JR, Sun Z, Tour JM, Barron AR (2010) Nano Res 3:138
89. Ajayan PM, Iijima S (1993) Nature 361:333
90. Che G, Lakshmi BB, Fisher ER, Martin CR (1998) Nature 393:346
91. Zhang Y, Franklin NW, Chen RJ, Dai H (2000) Chem Phys Lett 331:35
92. Joo SH, Choi SJ, Oh I, Kwak J, Liu Z, Terasaki O, Ryoo R (2001) Nature 412:169
93. Globus A, Bauschlicher C, Han J, Jaffe R, Levit C, Srivastave D (1998) Nanotechnology 9:192
94. Han J, Globus A (1997) Nanotechnology 8:95
95. Goldsmith BR, Coroneus JG, Khalap VR, Kane AA, Weiss GA, Collins PG (2007) Science 315:77
96. Kanungo M, Lu H, Malliaras GG, Blanchet GB (2009) Science 323:234
97. Clar E (1972) The aromatic sextet. Wiley, London
98. Portella G, Poater J, Sola M (2005) J Phys Org Chem 18:785
99. Lu X, Tian F, Zhang Q (2003) J Phys Chem B 107:8388
100. Lu X, Tian F, Xu X, Wang N, Zhang Q (2003) J Am Chem Soc 125:10459
101. Chen ZF, Nagase S, Hirsch A, Haddon RC, Thiel W, PvR S (2004) Angew Chem Int Ed 43:1552
102. Bettinger HF (2004) Org Lett 6:731
103. Chu YY, Su MD (2004) Chem Phys Lett 394:231
104. Zhao JJ, Chen ZF, Zhou Z, Park H, Schleyer PvR, Lu JP (2005) ChemPhysChem 6:598
105. Lu J, Nagase S, Zhang X, Maeda Y, Wakahara T, Nakahodo T, Tsuchiya T, Akasaka T, Yu D, Gao Z, Han R, Ye H (2005) J Mol Struc (Theochem) 725:255

106. Su MD (2005) J Phys Chem B 109:21647
107. Bettinger HF (2006) Chem Euro J 12:4372
108. Lee YS, Marzari N (2006) Phys Rev Lett 97:116801
109. Park H, Zhao J, Lu JP (2006) Nano Lett 6:916
110. Li J, Jia G, Zhang Y, Chen Y (2006) Chem Mater 18:3579
111. Cho E, Kim H, Kim C, Han S (2006) Chem Phys Lett 419:134
112. Zheng GS, Wang Z, Irle S, Morokuma K (2006) J Am Chem Soc 128:15117
113. Lu J, Wang D, Nagase S, Ni M, Zhang X, Maeda Y, Wakahara T, Nakahodo T, Tsuchiya T, Akasaka T, Gao Z, Yu D, Ye H, Zhou Y, Mei WN (2006) J Phys Chem B 110:5655
114. Zurek E, Pickard CJ, Autschbach J (2007) J Am Chem Soc 129:4430
115. Wanno B, Du AJ, Ruangpornvisuti V, Smith SC (2007) Chem Phys Lett 436:218
116. Yumura T, Kertesz M (2007) Chem Mater 19:1028
117. Yumura T, Kertesz M, Iijima S (2007) Chem Phys Lett 444:155
118. Lee YS, Marzari N (2008) J Phys Chem C 112:4480
119. Zurek E, Pickard CJ, Autschbach J (2008) J Phys Chem C 112:9267
120. Margine ER, Bocquet M-L, Blase X (2008) Nano Lett 8:3315
121. Cho E, Shin S, Yoon Y-G (2008) J Phys Chem C 112:11667
122. Lopez-Bezanilla A, Triozon F, Latil S, Blase X, Roche S (2009) Nano Lett 9:940
123. Jia G-X, Li J-Q, Chen L-G, Li Y, Ding K-N, Zhang Y-F (2009) Int J Quantum Chem 109:668
124. Baldoni M, Selli D, Sgamellotti A, Mercuri F (2009) J Phys Chem C 113:862
125. Yumura T, Kertesz M (2009) J Phys Chem C 113:14184
126. Mercuri F, Sgamellotti A (2009) Phys Chem Chem Phys 11:563
127. Osuna S, Houk KN (2009) Chem – A Euro J 15:13219
128. Wu JH, Hagelberg F (2010) Phys Rev B 81:155407
129. Denis PA, Iribarne F (2010) Int J Quantum Chem 110:1764
130. Sumpter BG, Jiang DE, Meunier V (2008) Small 4:2035
131. Zhao J-X, Ding Y-H (2008) J Phys Chem C 112:13141
132. Kim S, Cho E, Han S, Cho Y, Cho SH, Kim C, Ihm J (2009) Solid State Commun 149:670
133. Wang H, Xu J (2009) Chem Phys Lett 477:176
134. Martinez A, Francisco-Marquez M, Galano A (2010) J Phys Chem C 114:14734
135. Yumura T (2011) Phys Chem Chem Phys 13:337
136. Rochefort A, Salahub DR, Avouris P (1999) J Phys Chem B 103:641
137. Cioslowski J, Rao N, Moncrieff D (2002) J Am Chem Soc 124:8485
138. Zhou Z, Steigerwald M, Hybertsen M, Brus L, Friesner RA (2004) J Am Chem Soc 126:3597
139. Sun GY, Kürti J, Kertesz M, Baughman RH (2003) J Phys Chem B 107:6924
140. Sun GY, Kürti J, Kertesz M, Baughman RH (2002) J Am Chem Soc 124:15076
141. Kertesz M, Choi CH, Yang S (2005) Chem Rev 105:3448
142. Matsuo Y, Tahara K, Nakamura E (2003) Org Lett 5:3181
143. Yumura T, Hirahara K, Bandow S, Yoshizawa K, Iijima S (2004) Chem Phys Lett 386:38
144. Yumura T, Bandow S, Yoshizawa K, Iijima S (2004) J Phys Chem B 108:11426
145. Yumura T, Nozaki D, Bandow S, Yoshizawa K, Iijima S (2005) J Am Chem Soc 127:11769
146. Ormsby JL, King BT (2007) J Org Chem 72:4035
147. Ormsby JL, King BT (2004) J Org Chem 69:4287
148. Mercuri F (2008) Mol Simulat 34:905
149. Martin-Martinez FJ, Melchor S, Dobado JA (2008) Org Lett 10:1991
150. Baldoni M, Sgamellotti A, Mercuri F (2007) Org Lett 9:4267
151. Mintmire JW, Dunlap BI, White CT (1992) Phys Rev Lett 68:631
152. Kim UJ, Furtado CA, Liu X, Chen G, Eklund PC (2005) J Am Chem Soc 127:15437
153. Yi B, Rajagopalan R, Foley HC, Kim UJ, Liu X, Eklund PC (2006) J Am Chem Soc 128:11307
154. Chen ZF, Thiel W, Hirsch A (2003) ChemPhysChem 4:93
155. Zhao MW, Xia YY, Lewis JP, Mei LM (2004) J Phys Chem B 108:9599
156. Haddon RC (1998) J Comput Chem 19:139
157. Choi CH, Kertesz M (1998) J Phys Chem A 102:3429

158. Vogel E, Roth HD (1964) Angew Chem Int Ed 3:228
159. Duffy DM, Blackman JA (1998) Phys Rev B 58:7443
160. Fagan SB, Mota R, da Silva AJR, Fazzio A (2003) Phys Rev B 67:205414
161. Durgun E, Dag S, Bagci VMK, Gülseren O, Yildirim T, Ciraci S (2003) Phys Rev B 67:201401
162. Acharya CK, Turner CH (2006) J Phys Chem B 110:17706
163. Chi DH, Cuong NT, Tuan NA, Kim Y-T, Bao HT, Mitani T, Ozaki T, Nagao H (2006) Chem Phys Lett 432:213
164. Yang SH, Shin WH, Lee JW, Kim SY, Woo SI, Kang JK (2006) J Phys Chem B 110:13941
165. Kim SJ, Park YJ, Ra EJ, Kim KK, An KH, Lee YH, Choi JY, Park CH, Doo SK, Park MH, Yang CW (2007) Appl Phys Lett 90:023114
166. Krasnov PO, Ding F, Singh AK, Yakobson BI (2007) J Phys Chem C 111:17977
167. Cuong NT, Sugiyama A, Fujiwara A, Mitani T, Chi DH (2009) Phys Rev B 79:235417
168. Stoyanov SR, Titov AV, Kral P (2009) Coord Chem Rev 253:2852
169. Yumura T, Kertesz M, Iijima S (2007) J Phys Chem B 111:1099
170. Urita K, Sato Y, Suenaga K, Gloter A, Hashimoto A, Ishida M, Shimada T, Shinohara H, Iijima S (2004) Nano Lett 4:2451
171. Diederich F, Thilgen C (1996) Science 271:317
172. Kessinger R, Thilgen C, Mordasini T, Diederich F (2000) Helv Chim Acta 83:3069
173. Sergeyev S, Diederich F (2004) Angew Chem Int Ed 43:1738
174. Sergeyev S, Schar M, Seiler P, Lukoyanova O, Echegoyen L, Diederich F (2005) Chem Euro J 11:2284
175. Thilgen C, Diederich F (2006) Chem Rev 106:5049
176. Gao X, Ishimura K, Nagase S, Chen ZF (2009) J Phys Chem A 113:3673
177. Chen RJ, Zhang Y, Wang D, Dai H (2001) J Am Chem Soc 123:3838
178. Kim Y-T, Ohshima K, Higashimine K, Uruga T, Takata M, Suematsu H, Mitani T (2006) Angew Chem Int Ed 45:407

Chapter 7
Advancing Understanding and Design of Functional Materials Through Theoretical and Computational Chemical Physics

Jingsong Huang, Jacek Jakowski, Ariana Beste, Jarod Younker, Alvaro Vazquez-Mayagoitia, Eduardo Cruz-Silva, Miguel Fuentes-Cabrera, Alejandro Lopez-Bezanilla, Vincent Meunier, and Bobby G. Sumpter

Abstract Theoretical and computational chemical physics and materials science offers great opportunity toward helping solve some of the grand challenges in science and engineering, because structure and properties of molecules, solids, and liquids are direct reflections of the underlying quantum motion of their electrons. With the advent of semilocal and especially nonlocal descriptions of exchange and correlation effects, density functional theory (DFT) can now describe bonding in molecules and solids with an accuracy which, for many classes of systems, is sufficient to compare quantitatively to experiments. It is therefore becoming possible to develop a semiquantitative description of a large number of systems and processes. In this chapter, we briefly review DFT and its various extensions to include nonlocal terms that are important for long-range dispersion interactions that dominate many self-assembly processes, molecular surface adsorption processes, solution processes, and biological and polymeric materials. Applications of DFT toward problems relevant to energy systems, including energy storage materials, functional nanoelectronics/optoelectronics, and energy conversion, are highlighted.

J. Huang • M. Fuentes-Cabrera • B.G. Sumpter (✉)
Computer Science and Mathematics Division, and Center for Nanophase Materials Sciences,
Oak Ridge National Laboratory, Oak Ridge, TN 37831, USA
e-mail: huangj3@ornl.gov; fuentescabma@ornl.gov; sumpterbg@ornl.gov

J. Jakowski
National Institute for Computational Sciences, University of Tennessee, Oak Ridge,
TN 37831, USA
e-mail: jjakowsk@utk.edu

A. Beste
Joint Institute for Computational Sciences, University of Tennessee, Oak Ridge, TN 37831, USA
e-mail: bestea@ornl.gov

J. Younker
Computer Science and Mathematics Division, Oak Ridge National Laboratory, Oak Ridge,
TN 37831, USA
e-mail: younkerjm@ornl.gov

7.1 Introduction

In the twenty-first century, one of the forefront world problems is to develop safe, renewable, and sustainable energy [1]. Most sustainable energy systems rely on the energy influx from the sun. Sunlight is diffuse and intermittent, and it is essential to be able to store the energy chemically as a fuel. This is needed in order to provide energy for the transportation sector and decentralized applications and in order to even out temporal variations. The key to providing an efficient transformation of energy to a chemical form or from one chemical form into another is the availability of suitable catalysts [2]. In essentially all possible sustainable energy technologies, the lack of efficient and economically viable catalysts is a primary factor limiting their use.

Clearly, computational chemistry, physics, and materials science has continually provided a foundation for the investigation of the fundamental physics and chemistry underlying complex materials processes [3]. This is largely due to the fact that structure and properties of molecules, solids, and liquids are direct reflections of the underlying quantum motion of the indigenous electrons. However, the Schrödinger equation governing the electronic structure of an interacting set of electrons is generally too complicated to be solved for all but the simplest systems. Therefore, most systems of interest in materials physics, chemistry, and biochemistry are typically treated using an approximate description based on density functional theory (DFT) [4–7]. This approach has recently been improved with the introduction of semilocal and especially nonlocal descriptions of electron exchange and correlation effects. It follows that DFT can often describe bonding in molecules and solids accurately enough to compare quantitatively to experiments. This type of capability can effectively drive materials and chemical innovation by guiding molecular design. Indeed, it has long been a dream to be able to design materials directly on the basis of electronic structure calculations. The first examples of

---

A. Vazquez-Mayagoitia
Leadership Computing Facility, Argonne National Laboratory, Argonne, IL 60439,
USAalvaro@anl.gov

E. Cruz-Silva
Department of Polymer Science and Engineering, University of Massachusetts, Amherst,
MA 01003, USA
e-mail: cruzse@rpi.edu

A. Lopez-Bezanilla
National Center for Computational Sciences, Oak Ridge National Laboratory, Oak Ridge,
TN 37831, USA
e-mail: lopezbezania@ornl.gov

V. Meunier
Department of Physics, Applied Physics, and Astronomy, Rensselaer Polytechnic Institute,
Troy, NY 12180, USA
e-mail: meuniv@rpi.edu

materials design based partially on insight from electronic structure theory have appeared recently, but the systems considered until now have been simple. Several further developments are required before electronic structure-based design can be done more broadly. There are at least two major requirements for a general approach to a quantum-based strategy for materials design:

1. In a number of cases, we need higher accuracy than current DFT methods can provide in order to have predictive power. In addition, we need methods and associated computer codes that are more efficient computationally in order to be able to treat the complexity that characterizes most technically interesting systems and their environments – real materials including defects and two- or three-phase systems.

2. There is a need to build links between the quantum phenomena at the atomic scale and the functionality of the material at the macroscopic scale. This approach effectively defines an *atomistically informed mesoscale and macroscopic prediction/design/optimization capability*. Such a "from electrons to materials and devices" approach can be a key to enabling new breakthrough capabilities for sustainable energy systems.

Many groups around the world are intensely pursuing the first requirement [8–13], but much less effort is devoted to the second. Since we are interested in catalytic and energy storage/conversion materials and the underlying interfacial processes, the macroscopic properties are those manifested through the performance of the material. For example, in heterogeneous catalysis where atoms and molecules adsorb on a solid surface and undergo reactions, the microscopic properties are quantities like adsorption energies and activation energies for elementary surface processes. The link to the macroscopic catalytic properties as measured in a catalytic converter, for example, is a microkinetic model. There are now several examples where the macroscopic kinetics of a catalytic reaction has been modeled successfully on the basis of electronic structure calculations. These are important benchmarks showing that the theoretical methods work, but the procedure of calculating all energy parameters for all possible elementary steps under all possible conditions remains extremely demanding.

The same procedure can in principle be used to search for new energy storage or transmission materials and for improved catalysts for energy conversion. Development of suitable models of surface reactivity and their utilization for pinpointing the most important microscopic properties of materials are enabling characteristics for determining the catalytic properties as well as energy storage properties.

We note that computational simulation of many processes, especially those related to fabrication of materials, often require using direct molecular dynamics simulations or methods that allow treatment of extreme environments. Progress is still required in designing electronic structure algorithms that can speed up the required evaluation of energy and forces. In this regard, very promising new computer architectures and programming paradigms such as general programming of graphical processing units (GPGPU) may offer new opportunities. In this chapter, we outline some of our recent efforts and developments toward advancing

the computational design and understanding of nanoscale material systems, an "electrons to real devices" approach [14], with potential applicability for improved energy systems and processes [15, 16]. A number of application examples are highlighted, which are targeted toward advancing the understanding of materials properties relevant to energy science.

7.2 Computational Methods and Approach

Proper selection of a theoretical/computational model for simulation of materials or dynamical processes requires the consideration of the following issues:

1. Is the character of the processes quantum mechanical in its nature? If so, then accurate modeling will require using electronic structure methods. Also, if the nature of the internal interactions has significant contributions that are nonlocal or involve very strong electron correlation, one may need to consider many-body quantum approaches, self-interaction corrections, RPA-DFT, or modified DFT functionals.
2. What is the system size? Often typical system size of interest for modeling is a few hundred atoms or more (i.e., thousands of electrons). Chemistry of reactive bulk materials is intrinsically different from the chemistry of single molecules and thus requires different theoretical approaches. *In the latter case, the electronic state can be controlled with spectroscopic accuracy, and the long-term decay leads to a well-defined state (eigenstate of Hamiltonian). In the former case (bulk phase), the coupling between electronic and nuclei and electrons is nonadiabatic and leads to constant energy exchange between these degrees of freedom. The electronic state of the system is likely a superposition of the electronic eigenstates.*
3. What are the environmental conditions being simulated? Nanomaterials (i.e., graphitic materials such as nanotubes, fullerenes, graphene) are often produced under very harsh experimental conditions, including high temperature, pressure, and external electric fields. High temperature and concentration of reactant carbons in bulk-phase materials mean that the individual molecular carbon atoms or molecular fragments are moving fast and have a high probability of collision. Thus, a significant transfer of energy between electronic and nuclear degrees of freedom is likely. It seems unrealistic to assume that reaction occurs on the ground-state electronic surface without transfer of energy between nuclear and electronic degrees of freedom. The chemistry of such systems needs to involve electronically excited states and is intrinsically nonadiabatic.
4. What is the nature of transition state(s): static transition state methods versus molecular dynamics treatment of the chemical reactions? Standard "static" transition state theory methods of predicting the direction of chemical reactions and measuring the reactivity of chemical compounds are usually impractical in modeling bulk-phase material reactions. Such an approach is feasible only for small molecules (with limited number of possible transition state structures)

or for systems in which the reaction is localized to a small reaction region, while the structure and connectivity of the remaining parts of the system stay unchanged. The number of possible transition states and intermediate topologies grows exponentially with the number of atoms and quickly becomes too large to rigorously explore. Molecular dynamics approaches provide a convenient alternative in which out of the plethora of all possible intermediate states, only those which are energetically accessible and experimentally meaningful are studied.

5. What statistics are important for the process being modeled? Experimental observations are statistical in nature; thus, statistics are required for modeling/simulation in order to reproduce the experimental observation. For example, single trajectory simulations may not lead to qualitatively correct results. Performing several trajectory simulations with statistically varied initial conditions to match an experimental setup is generally required to be representative of the experimental observations.

6. What is the computational cost of a chosen theoretical model? Electronic structure-based evaluation of forces and energy is far more expensive than any classical force field-based calculation. The timescale for processes related to synthesis of carbon materials is in the range of several picoseconds. The electronic structure methods used for the evaluation of energy and forces must be very cheap to enable affordable MD simulations. For example, 2 min spent for one evaluation of the energy and forces translates into 2 weeks spent for 10,000 steps of MD. As a rule of thumb, computational cost of one electronic structure calculation of energy and forces (one time step of MD) should be on the order of 1 min (or less) of the computer time.

7.2.1 DFT and DFT-Based Methods

Density functional theory proposes to solve electronic structure problems using the electron charge density, $\rho(r)$, as the fundamental variable [17] which is formally based on the Hohenberg and Kohn theorems [18]. In practice, DFT is applied using the Kohn–Sham method (KS), using a mean-field approach [19]. The KS method represents the density as a linear combination of the inner products of spin-orbital functions and the energy as a functional of $\rho(r)$ as

$$E^{\mathrm{DFT}}[\rho] = T_{\mathrm{o}}[\rho] + J[\rho] + E_{\mathrm{xc}}[\rho] + \int \rho\left(\overrightarrow{r}\right) v_{\mathrm{ext}}\left(\overrightarrow{r}\right) \mathrm{d}\overrightarrow{r} + V_{\mathrm{NN}}, \qquad (7.1)$$

where the first and second terms are the kinetic energy of independent particles, $T_{\mathrm{o}}[\rho]$, and the Coulomb interaction energy, $J[\rho] = \frac{1}{2} \iint \mathrm{d}r' \mathrm{d}r \rho(r') \rho(r)/|r' - r|$. The term $v_{\mathrm{ext}}(r)$ is the external potential generated by the nuclei and felt by the electrons, and V_{NN} is the nuclear repulsion energy for a fixed nuclear configuration. In Eq. 7.1, the contribution $E_{\mathrm{xc}}[\rho]$ is the exchange-correlation energy, which includes the

electron exchange interaction as well as the many-body contribution to the kinetic and electron–electron repulsion potentials ($V_{ee}[\rho]$) that are not included in $T_o[\rho]$ or $J[\rho]$, that is, $E_{xc}[\rho] = V_{ee}[\rho] + T[\rho] - J[\rho] - T_o[\rho]$. The explicit expression of E_{xc} remains unknown, but there are many approaches that have shown satisfactory results. Such approaches are grouped according to their treatment of the density into "generations" or "ladder's rungs" [20]. The most common are based on the local density approximation (LDA) or generalized gradient approximation (GGA) [21]. Although some functionals have shown impressive results, those are not always transferable for every problem and can often fail for the description of long-range interactions and excited states. The origins of these difficulties are attributed to the incorrect cancellation of electron self-interaction [22] and incorrect treatment of dynamic correlation, among others. There are many strategies to avoid these problems, some of which involve the inclusion of explicit terms from wavefunction theories (hybrid functionals), treatments with optimized effective potentials, an adjustment to the asymptotic correction exchange-correlation potentials, and the addition of empirical energy terms.

The pervasiveness of hydrogen bonding and London forces among biological [23–25] and supramolecular [26–28] entities has motivated persistent efforts to develop reliable computational methodologies for noncovalent interactions (NCI) [29, 30]. Extensive work has established the importance of high levels of electron correlation, as embodied by coupled cluster through perturbative triples, CCSD(T) [31], for the proper characterization of dispersion attractions, yet achieving this "gold standard" of chemical accuracy [32] presents a formal cost of $O(N^7)$, where N is proportional to system size. Meanwhile, the attractively efficient DFT [formally $O(N^3)$–$O(N^4)$, or $O(N^5)$ for double hybrids] can falter for even qualitative descriptions [33–36]. The introduction of the DFT+dispersion (DFT-D) and exchange-hole dipole moment (XDM) [37–42] methods and the crafting of several long-range functionals [43–52] have transformed the vista of quantum chemical techniques available for nonbonded systems. These are among some of the most promising approaches emerging from a very active field that strives to improve performance for classes of NCI governed by disparate intermolecular forces and spanning broad-length scales.

Density functionals developed for covalent systems are often successful in treating hydrogen bonding and other electrostatically dominated noncovalent interactions that act over similarly short-length scales (<2 Å) [53]. In contrast, the dispersion attraction, which arises from correlated motions of electrons, is prominent chiefly over longer distances [<2–5 Å (medium-range) and >5 Å (long-range)], and none of the typical components of a functional, the local electron density ($\rho\sigma$), its gradient ($\nabla\rho\sigma$, present in semilocal generalized gradient approximation (GGA) functionals), or its kinetic energy ($\tau\sigma$, present in nonlocal meta-GGA functionals), is fully capable of acting over a suitable span. Hybrid functionals include long-range behavior (nonlocality) through Hartree–Fock exchange but remain local in correlation and, therefore, are also unable to correctly describe the R^{-6} asymptotic distance dependence of dispersion forces. The consequent

challenges to adapting affordable-scaling wavefunction and DFT methods for dispersion are amply reviewed in the recent literature [47, 54–58]. Among the more empirical treatments developed are dispersion-corrected atom-centered potentials (DCACP) [59] and DFT-D [43, 60–62]. For common implementations of the former, a pseudopotential optimized to replicate reference interaction energies is placed over each atom, thereby incorporating medium-range correlation but not capturing the correct asymptotic form, while for the latter, a damped atom–atom dispersion term is appended to the total DFT energy, thereby accurately encoding the long-range attraction yet necessitating a carefully tuned damping function to evenhandedly address double counting of the correlation energy across all system configurations and types of interaction. The exchange-hole dipole moment (XDM) is constructed similarly to DFT-D as a correction to the base electronic energy but, by modeling the instantaneous dipole that arises between an electron and its exchange hole, generates dispersion coefficients that are aware of the chemical environment. Also active are efforts to include medium-range dispersion in conventional semilocal DFT or to incorporate correlation components from wavefunction theory [49–52]; both approaches sometimes address long-range effects through an additional DFT-D-like term. A more complex task is the development of explicitly nonlocal correlation functionals from first principles. Currently at the forefront are vdW-DF [63] and VV09 [64].

The local or semilocal character of conventional density functionals necessarily leads to neglect of the long-range correlation interactions that capture attractive van der Waals forces. Initially proposed by Yang [60a] for ab initio DFT after its first introduction into the tight binding DFT approach by Elstner et al. [60b], and assiduously developed by Grimme [43, 61, 62], the DFT+dispersion (DFT-D) method appends to the base functional a scaled, damped, and fitted leading term to the well-known dispersion energy series,

$$E_{\text{disp}} = -C_6/R^6 - C_8/R^8 - C_{10}/R^{10} \tag{7.2}$$

Many calculations follow the DFT-D2 variant, where the correction takes the explicit form

$$E_{\text{disp}}^{\text{D2}} = -s^6 \sum_{i,j>i}^{N_{\text{at}}} \frac{C_6^{ij}}{R_{ij}^6} f_{\text{damp}}(R_{ij}). \tag{7.3}$$

Here, dispersion coefficients, C_{ij}^6, obtained from the geometric mean of tabulated elemental values, are summed over interatomic distances, R_{ij}, modulated by a damping function, $f_{\text{damp}}(R_{ij})$, that gradually activates the dispersion correction over a distance characterized by the sum of the two atomic vdW radii, while an overall scaling term, s^6, is optimized to be unique to each DFT exchange functional. The scaling factors employed are $s^{\text{B2PLYP6}} = 0.55$, $s^{\text{PBE06}} = 0.6$, $s^{\text{PBE6}} = 0.75$, $s^{\text{B9706}} = 0.7564$, $s^{\text{BP866}} = 1.05$, $s^{\text{B3LYP6}} = 1.05$, and $s^{\text{B976}} = 1.25$. Grimme recently presented a refined method, DFT-D3 [62], which incorporates an additional R^{-8}

term in the dispersion series and adjusts the C_{ij}^6 combination formula and damping function. The individual atomic C_i^6 are interpolated from several reference values based upon coordination numbers extracted from the molecular structure, rather than assigned solely by atomic identity as in DFT-D2, and thereby incorporate some awareness of the chemical environment into an otherwise largely heuristic correction. The -D3 dispersion has the form

$$E_{\text{disp}}^{\text{D3}} = -\sum_{n=6,8} s_n \sum_{i,j>i}^{N_{\text{at}}} \frac{C_n^{ij}}{R_{ij}^n} f_{\text{damp}}(R_{ij}, s_{r,n}), \tag{7.4}$$

where $s_{r,6}$ and s_8 are the customary nonunity parameters fitted for individual functionals and tabulated in Ref. [65].

A strategy to place dispersion corrections on a less-empirical footing than DFT-D is the "semiclassical" exchange-hole dipole moment model first formulated in 2005 by Becke and Johnson [37] (later placed on firmer theoretical foundations [39–41]) from the idea that the nonzero dipole moment of an exchange hole [66] can induce an instantaneous dipole moment, and thus dispersion interactions, between nonoverlapping systems. The method is notable for its first-principles calculation of dispersion coefficients and forms a wholly self-consistent and first-principles treatment of dispersion effects.

Recently we have performed a systematic study of techniques for treating noncovalent interactions within the computationally efficient DFT framework through comparison to benchmark-quality evaluations of binding strength compiled for molecular complexes of diverse size and nature [67]. Through comparison with available CCSD(T)/CBS benchmarks, the performance of DFT methods was evaluated both overall and for hydrogen-bonded, mixed-influence, and dispersion-bound subsets. Complete evaluations of test sets were conducted with aug-cc-pVDZ and aug-cc-pVTZ, and closer analyses with families of Dunning double-ζ and triple-ζ basis sets have permitted appraisal of these bases as well as the utility of the counterpoise correction. The efficiency and accuracy of functionals deliberately crafted to encompass long-range forces, a posteriori DFT+dispersion corrections (DFT-D2 and DFT-D3), and exchange-hole dipole moment (XDM) theory were assessed against a large collection of 469 energy points. For overall results, M05-2X, B97-D3, and B970-D2 yield superior values in conjunction with aug-cc-pVDZ, with a mean absolute deviation of 0.41–0.49 kcal/mol, and B3LYP-D3, B97-D3, ωB97X-D, and B2PLYP-D3 dominate with aug-cc-pVTZ, affording, together with XYG3/6-311+G(3df,2p), a mean absolute deviation of 0.33–0.38 kcal/mol. These results provide a rigorous benchmark for the various possible approaches for including dispersion into DFT and highlight the fact that chemical accuracy can be achieved for a nonbiased set of test systems. This is important as it allows the computational efficiency of DFT to be maintained while enabling accurate calculation of a much broader class of materials.

7.2.2 Beyond Static Calculations: Direct Dynamics Methods

A complete description of molecular systems requires solving the time-dependent Schrödinger equation for the constituent electrons and nuclei. This task is currently unfeasible. To simplify the problem, it is usually assumed that the motion of electrons (fast) and nuclei (slow) can be separated and that Born–Oppenheimer approximation is valid. As a consequence, the time-dependent Schrödinger equations are replaced by (a) classical Newton equations for nuclei and (b) time-independent Schrödinger equation for electrons. The resulting method is referred to as Born–Oppenheimer molecular dynamics (BOMD) [68–71] (or its extended Lagrangian variants [72]), in which nuclei move classically on the ground-state potential energy surface (or on its approximation) obtained on-the-fly self-consistently (or are propagated classically) from the stationary electronic structure. The high computational expense for the electronic structure calculation renders BOMD only practical in implementations of direct MD that are based on an independent particle model (Hartree–Fock, tight binding, and density functional theories). In these methods all nuclei are moving on the potential energy surface generated by the electronic structure, and the total "electronic" energy of the system can be expressed as a sum over occupied orbitals:

$$E = V_{NN} + \sum_i^{occ} \langle i|h|i \rangle + \frac{1}{2}\sum_{i,j}^{occ} \langle ij||ij \rangle, \tag{7.5}$$

or equivalently

$$E = V_{NN} + \mathrm{Trace}[H_{core}P + \frac{1}{2}G(P)P], \tag{7.6}$$

in which the electronic structure is represented by the density matrix P. V_{NN} represents interaction between nuclei and does not depend on electronic structure. The second, so-called one-electron term, H_{core}, depends linearly on P and represents kinetic energy of electrons and interaction of electrons with nuclei. The last term, $G(P)$, describes electron–electron repulsion and depends quadratically on P. The last equation can be used regardless of whether one solves a time-independent electronic structure (Born–Oppenheimer dynamics) problem or quantum dynamical time-dependent Schrödinger equation. It is orbital-free (but not basis-free) and is more general. The choice of the molecular orbitals is arbitrary and the electronic structure represented by the density matrix P may be described by many different choices of the molecular orbitals.

In the Born–Oppenheimer case, the electronic structure is determined through minimization of energy, thanks to variational principle. This is usually achieved by diagonalization of total Hamiltonian matrix ($F = H_{core} + G(P)$). Other alternatives to diagonalization methods exist (e.g., Fermi operator expansion or direct density

matrix minimization) and are described elsewhere (see Ref. [73] and references therein). Once the electronic structure and corresponding nuclear forces are known, the molecular motion is determined and related properties are described.

Alternatively to time-independent solutions of electronic structure problem in dynamics, one can integrate a time-dependent Schrödinger equation subject to initial electronic structure along with Newton equations of motion for the nuclei. It is also possible to include into dynamics a quantum dynamical treatment for selected nuclei. Possible approaches include quantum wavepacket dynamics, path integral, and Bohmian trajectory approaches. Quantum dynamical treatment plays an especially important role in proton transfer cases [74–76].

Here we focus on direct dynamics approaches in which quantum nuclear effects are neglected and all nuclei are treated classically. The theory described here is based on the density matrix representation of electronic structure and on localized atomic orbital basis sets. We summarize the theory of both time-independent and time-dependent quantum mechanical approaches in direct dynamics. Special attention is given to time-dependent quantum mechanical direct molecular dynamics.

7.2.3 Time-Independent Electronic Structure Approaches

In Born–Oppenheimer MD, the electronic structure (P) does not explicitly depend on time. Rather, it is assumed that electronic structure can instantaneously (and adiabatically) adjust to any changes in the position of nuclei. The solution to the stationary Born–Oppenheimer problem is found, thanks to variational principle, by minimization of electronic energy. Typically this is done by diagonalization of the electronic independent particle Hamiltonian (Fock matrix), F, followed by construction of the molecular orbitals and density matrix, P, from eigenvectors (C) of Hamiltonian (F):

$$FC = \varepsilon S C$$
$$P = CfC^+, \tag{7.7}$$

where f is a diagonal matrix of occupation numbers f_i. This is an iterative process; the electronic Hamiltonian, F, depends on electronic structure, P, itself. The resulting orbitals are fed back into the Hamiltonian, and the new, improved set of molecular orbitals is found. In principle, knowledge of the molecular orbitals is not required. Instead the electronic density matrix can be found directly from the electronic Hamiltonian using methods such as a conjugate-gradients density matrix search [73, 77]. The review of these methods is presented elsewhere [73].

In Born–Oppenheimer (BO) molecular dynamics (MD), the occupation numbers f_i are equal to 0 or 1, and the resulting density matrix is an idempotent matrix, or in the language of linear algebra, it is a projection operator. That is, any arbitrary molecular orbital (i.e., vector described as a combination of atomic orbitals basis

set) if multiplied by P will have a contribution that does not belong to space spanned by the occupied orbitals deleted, while the contribution that belongs to the occupied space will remain unchanged. Other related properties of BO density matrix are (a) idempotency and (b) N representability. Idempotency of density matrix means that the square of P is equal to P. N representability means that the trace of density matrix is equal to the number of electrons and thus density matrix collectively describes N electrons at once. The specific algebraic properties of density matrix lead to auxiliary techniques such as purification of density matrix and can be used in direct density matrix search. Properties of P can be also exploited in molecular dynamics [72, 73].

The total energy and forces in Born–Oppenheimer molecular dynamics is given by

$$E_{\text{tot}} = E_{\text{kin}} + V_{\text{NN}} + E_{\text{el}} \tag{7.8}$$

where E_{kin} is the kinetic energy for nuclei, V_{NN} is the nuclear energy, and E_{el} represents the electronic energy

$$E_{\text{el}} = \text{Tr}[H_{\text{core}} P + \tfrac{1}{2} G(P) P]. \tag{7.9}$$

The forces acting on nuclei R are equal to

$$F = -\frac{\partial E_{\text{pot}}}{\partial R} = -\frac{\partial V_{\text{NN}}}{\partial R} - \text{Tr}\left[\frac{\partial H_{\text{core}}}{\partial R} P + \frac{1}{2}\frac{\partial G(P)}{\partial R} P\right] - \text{Tr}\left[F\frac{\partial P}{\partial R}\right], \tag{7.10}$$

where $E_{\text{pot}} = V_{\text{NN}} + E_{\text{el}}$. The sum of the first two terms is so-called Hellmann–Feynman force. These terms describe, respectively, nuclear repulsion and contribution arising from derivatives of one-electron and two-electron integrals (first square bracket). The last term (second square bracket), in which F is the Fock matrix such that $F = H_{\text{core}} + G(P)$, is the so-called Pulay term and describes contribution to forces coming from derivate of electronic structure over R. It results from the time dependence of atomic basis set. It can be expressed as

$$F_{\text{Pulay}} = -\text{Tr}\left[F\frac{\partial P}{\partial R}\right] = -\text{Tr}\left[F\frac{\partial\left(CfC^+\right)}{\partial R}\right] = -\text{Tr}\left[F\frac{\partial C}{\partial R}fC^+ + FCf\frac{\partial C^+}{\partial R}\right], \tag{7.11}$$

in which the occupation numbers f_i are equal to 0 or 1 only and do not change during the dynamics, thus $\frac{\partial f}{\partial R} = 0$. Furthermore, the Pulay force can be expressed in terms of the overlap matrix derivative as

$$F_{\text{Pulay}} = \text{Tr}\left[W\frac{\partial S}{\partial R}\right], \tag{7.12}$$

where W is the energy weighted density matrix $W = Cf\varepsilon C^+$, with f and ε being diagonal matrices of occupation numbers and corresponding orbital energies. The final expression for the forces is

$$F = -\frac{\partial E_{\text{pot}}}{\partial R} = -\frac{\partial V_{\text{NN}}}{\partial R} - \text{Tr}\left[\frac{\partial H_{\text{core}}}{\partial R}P + \frac{1}{2}\frac{\partial G(P)}{\partial R}P\right] + \text{Tr}\left[W\frac{\partial S}{\partial R}\right]. \quad (7.13)$$

7.2.4 Mermin Dynamics

It is recognized that a realistic description of dynamics at metal surfaces and in the bulk phase must include the effect electronic excitations and of nonadiabatic (non-Born–Oppenheimer) transitions. Mermin generalization of Hohenberg–Kohn theory to finite electronic temperature T_{el} provides a practical way to approximate electronic excitations. Such effects can be approximated via the time-independent Mermin electronic energy functional [78, 79].

In this method the electronic structure does not evolve adiabatically but isothermally with electrons fractionally occupying electronic levels according to Fermi–Dirac distribution. Nuclei are moving in the mean field of free energy (electronic energy + electronic entropy), and the stationary time-independent electronic structure is instantaneously equilibrating at a given electronic temperature [78–80].

The total energy in Mermin dynamics is given by

$$E_{\text{tot}} = E_{\text{kin}} + V_{\text{NN}} + E_{\text{el}} - S_{\text{el}}T_{\text{el}}, \quad (7.14)$$

where the last two terms represent an electron free energy

$$E_{\text{free}} = E_{\text{el}} - S_{\text{el}}T_{\text{el}}. \quad (7.15)$$

The electronic energy is similar to the Born–Oppenheimer MD case and is equal to

$$E_{\text{el}} = \text{Tr}\left[H_{\text{core}}P + \frac{1}{2}G(P)P\right]. \quad (7.16)$$

The density matrix, P, can be obtained from the matrix of molecular orbitals coefficients as

$$P = CfC^+, \quad (7.17)$$

with diagonal matrix of occupations, and f is given by the Fermi–Dirac distribution

$$f_i = \frac{1}{1 + \exp\left(-\frac{\varepsilon_i - \mu}{kT_{\text{el}}}\right)}, \quad (7.18)$$

Fig. 7.1 Occupation numbers as a function of orbital energy from the Fermi–Dirac distribution. The chemical potential (Fermi level) is equal to 0. *Gray* area corresponds to the HOMO–LUMO gap in insulators (4 eV). Clearly, for insulators it would require a very high energy (equivalent of several thousands of K) to induce a noticeable electronic excitation
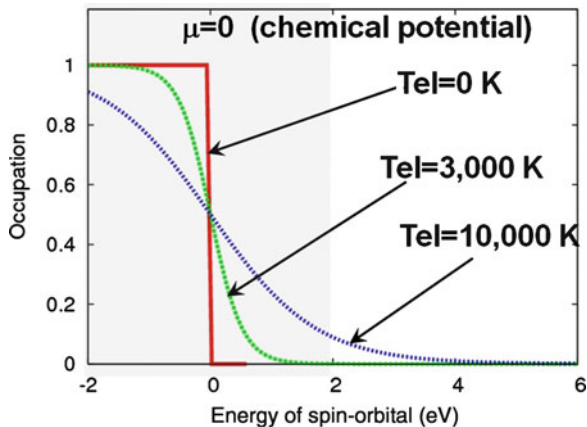
where μ is the chemical potential (or Fermi level). The important distinction of Mermin free energy dynamics compared to the BOMD case is that at finite electronic temperature, occupation numbers can be fractional. Thus the density matrix is no longer idempotent and is no longer a projection operator. The electronic entropy, S_{el}, depends only on the occupation numbers:

$$S_{el} = -k \sum_{i}^{M} [f_i \log f_i + (1 - f_i) \log(1 - f_i)]. \tag{7.19}$$

Clearly, at $T_{el} = 0$ K the entropy term vanishes due to the fact that occupation numbers f_i become equal to 1 when $\varepsilon_i < \mu$, and are equal to 0 otherwise. It can be easily verified that the only contribution to electronic entropy comes from the electronic levels with energy close to the Fermi level μ. The effect of electronic temperature is shown in Fig. 7.1.

From the perspective of density matrix properties, another consequence of using fractional occupancies is that, contrary to the BOMD case, the corresponding density matrix is not idempotent and describes mixed electronic state.

Forces in Mermin MD include the entropy contribution and are given by

$$\frac{\partial E}{\partial R} = -\frac{\partial V_{NN}}{\partial R} - \text{Tr} \left[\frac{\partial H_{core}}{\partial R} P - \frac{1}{2} \frac{\partial G(P)}{\partial R} P \right] - \text{Tr} \left[F \frac{\partial P}{\partial R} \right] - \frac{\partial S}{\partial R} T_{el}, \tag{7.20}$$

where, similarly to the BOMD case, the first two terms are Hellmann–Feynman forces, the third term is the Pulay term (contribution from derivative of electronic wavefunction), and the last term is a derivative of electronic entropy.

In Mermin dynamics, occupation numbers depend on time, through the changes in orbital energy in the Fermi–Dirac distribution functions. Thus the forces contain

contributions originating from the changes of occupation numbers with respect to position of nuclei. Pulay contribution to the forces is equal to

$$F_{\text{Pulay}} = -\text{Tr}\left[F\frac{\partial P}{\partial R}\right] = -\text{Tr}\left[F\frac{\partial C}{\partial R}fC^+ + FCf\frac{\partial C^+}{\partial R}\right] - \text{Tr}\left[FC\frac{\partial f}{\partial R}C^+\right].$$

$$(7.21)$$

The term in the first square bracket is identical with BOMD. The second term that depends on $\frac{\partial f}{\partial R}$ is new. It can be expressed in terms of an orbital energy as

$$\text{Tr}\left[FC\frac{\partial f}{\partial R}C^+\right] = \sum_i \varepsilon_i \frac{\partial f_i}{\partial R}.$$

$$(7.22)$$

We will now show that the above term cancels exactly with the derivate of entropy $\frac{\partial S}{\partial R}T_{\text{el}}$:

$$\frac{\partial(-T_{\text{el}}S_{\text{el}})}{\partial R} = -T_{\text{el}}\frac{\partial}{\partial R}\sum_i^M [f_i \log f_i + (1 - f_i)\log(1 - f_i)]$$

$$= -T_{\text{el}}\sum_i^M \frac{\partial f_i}{\partial R}\log\left(\frac{1}{f_i} - 1\right).$$

$$(7.23)$$

After inserting the expression for the Fermi–Dirac distribution, one can obtain

$$\frac{\partial(-T_{\text{el}}S_{\text{el}})}{\partial R} = -kT_{\text{el}}\sum_i^M \frac{\partial f_i}{\partial R}\frac{\varepsilon_i - \mu}{kT_{\text{el}}} = -\sum_i^M \frac{\partial f_i}{\partial R}\varepsilon_i + \mu\frac{\partial}{\partial R}\left(\sum_i^M f_i\right) = -\sum_i^M \frac{\partial f_i}{\partial R}\varepsilon_i,$$

$$(7.24)$$

in which we used the fact that the sum of occupation numbers f_i is constant and equal to total number of electrons; thus, its derivative vanishes. Comparison of the expression for $\frac{\partial(-T_{\text{el}}S_{\text{el}})}{\partial R}$ with the Pulay forces shows that it cancels exactly with the Pulay term $\left[FC\frac{\partial f}{\partial R}C^+\right]$. We can now write the final expression forces in Mermin dynamics:

$$F = -\frac{\partial E_{\text{pot}}}{\partial R} = -\frac{\partial V_{\text{NN}}}{\partial R} - \text{Tr}\left[\frac{\partial H_{\text{core}}}{\partial R}P + \frac{1}{2}\frac{\partial G(P)}{\partial R}P\right] + \text{Tr}\left[W\frac{\partial S}{\partial R}\right]. \quad (7.25)$$

The last expression is valid for nuclei moving classically in the field of free energy of electrons [80].

From the perspective of properties of the density matrix, using fractional occupancies in Mermin dynamics leads to non-idempotent density, which describes a mixed electronic state. This is in contrast with a conventional BOMD case in

which idempotent density matrix describes a pure electronic state. The mixed state density matrix in Mermin theory can always be represented as a combination of different pure-state (single determinants) density matrices spanned in the same N-electron and M-dimensional basis function Fock space in which the combination of coefficients is given by the Fermi–Dirac distribution. That is,

$$P_{\text{mixed}} = \sum_i P_{\text{pure}}^i w_i, \tag{7.26}$$

in which P_{mixed} and P_{pure}^i correspond to, respectively, N-electron mixed and pure state:

$$\sum_i w_i = 1,$$

$$\text{Tr}\left[P_{\text{mixed}}\right] = \text{Tr}\left[P_{\text{pure}}^i\right] = N_{\text{electrons}}. \tag{7.27}$$

The weighting factor w_i is equal to $f_i/N_{\text{electrons}}$ where $f_i = Tr[P_{\text{mixed}} P_{\text{pure}}^i]$. Thus, Mermin dynamics can be interpreted as a statistical ensemble of "independent" trajectories (each corresponding to different electronic states) with probability of finding a system in a given state equal to $f_i/N_{\text{electrons}}$.

Mermin dynamics is a generalization of BO dynamics to finite electronic temperature. It is a simple way to approximately include electronic excitation with a single factor (electronic temperature) and to fix SCF convergence problems plaguing the BOMD simulations for bulk and condensed phase systems. In fact, problems with convergence of SCF calculations in MD for bulk phase are very closely related to molecular systems passing via regions in which frequent crossing of near-Fermi level electronic states occurs and nonadiabatic transitions are expected to play an important role. In Mermin dynamics such states are averaged, which provides approximate multireference character of electronic structure provided via Fermi–Dirac thermal weighting parameters. Thus, Mermin dynamics can be thought of as an ideal "black body" system instantaneously equilibrating its energy.

Perhaps the biggest drawback of Mermin dynamics is that the changes of electronic structure (via occupation numbers changing with motion of nuclei) are incoherent. At any given time step, there is no track of electronic structure from the previous time step. This can lead to nonphysical (purely numerical) tunneling of electron charge between molecular systems which are very well separated and, in fact, noninteracting. Thus, for example, it can lead to oscillation of electron charge between two infinitely distant water molecules as the waters vibrate. This is the consequence of the fact that occupation numbers change with time (or more precisely with position of nuclei). This issue is also present in BOMD and can lead to fictitious electron "tunneling" between remote molecules. This is a serious problem in molecular systems that undergo a significant change in molecular topology (connectivity between atoms). It is a milder problem in systems in which

molecular topology is relatively stable with only few bonds being broken or formed, and can be prevented to some extent by reusing electronic structure from previous MD steps as an initial wavefunction.

The related issue is that in BOMD and Mermin dynamics, the electronic structure only depends on the position of nuclei but does not depend on the motion on nuclei (i.e., on nuclear momenta). The most natural way to include coupling dependence of the electronic structure on the motion of the nuclei is via the framework of time-dependent Schrödinger equation.

7.2.5 Time-Dependent Electronic Structure Approaches: Liouville–von Neumann Molecular Dynamics (LvNMD)

Introducing time-dependent Hamiltonians enables the description of (a) externally driven systems and molecules that are subject to strong laser fields for which linear response approximation is not valid, (b) processes with coupling and energy transfer between nuclear and electronic degrees of freedom, and (c) decoherence of quantum system from pure to mixed states.

Instead of solving time-independent Schrödinger equation for electrons at frozen positions of the nuclei as in the Born–Oppenheimer problem, one can integrate time-dependent Schrödinger equation. Here we use von Neumann representation of Schrödinger equation:

$$i\hbar \frac{dP(t)}{dt} = [F(t), P(t)], \qquad (7.28)$$

where $F(t)$ and $P(t)$ denote time-dependent Hamiltonian matrix for electrons and the density matrix [81]. In independent particle models (HF, DFT, tight binding), the Hamiltonian for electrons becomes a Fock matrix,

$$F = H_{\text{core}} + \frac{1}{2} G(P), \qquad (7.29)$$

where H_{core} describes interaction of electrons with nuclei, while $G(P)$ describes electron–electron interaction. To find a time evolution of density matrix, we integrate time-dependent Schrödinger equation. For that, knowledge of the following is required:

1. We need to know the initial density (initial value problem).
2. We need to know how the electronic Hamiltonian changes with time.
3. We need to know how to integrate the time-dependent Scrhödinger equation.

The initial density can be obtained from the SCF procedure, DFT, Mermin, or excited state density (linear response TDDFT), or as a direct product of densities for noninteracting systems.

7.2.6 Integration of the Time-Dependent Schrödinger Equation (Magnus Expansion)

At any given time t, density matrix $P(t)$ can be found from the time-evolution operator $U(t)$ as follows:

$$P(t) = U(t)P(0)U(t)^+, \tag{7.30}$$

where $U(t) = \exp(\Omega)$ is a unitary time-evolution operator and Hermitian conjugation is an inverse operator $U(t)^+ = U(t)^{-1} = \exp(-\Omega)$. Operator $\Omega(t)$ is given by Magnus expansion [82, 83]:

$$\Omega(t) = \Omega_1(t) + \Omega_2(t) + \cdots$$

$$\Omega(t) = \int_0^t dt' \frac{F(t')}{i\hbar} + \frac{1}{2} \int_0^t dt' \int_0^{t'} dt'' \left[\frac{F(t')}{i\hbar}, \frac{F(t'')}{i\hbar} \right] + \cdots \tag{7.31}$$

Regardless of the order of truncation in the above Magnus series, the operator $\Omega(t)$ is always Hermitian and the time-evolution operator $U(t)$ is always unitary. In large majority of ab initio molecular dynamics implementations of quantum dynamics, the Magnus series is truncated after the first-order term, leading to time-evolution operator given by:

$$U(t) = \exp\left(-\frac{i}{\hbar} \int_0^t F(t') dt' \right) \tag{7.32}$$

In principle, however, this expression is only valid when Hamiltonian F commute among themselves for all values of time. The effect of higher-order terms of Magnus expansion of molecular dynamics trajectory is not well understood. A promising recursive algorithm for implementation of Magnus series has been proposed by Oteo [83].

The most common implementation of quantum dynamics is based on so-called "midpoint" propagator:

$$U(t) = \exp\left(-\frac{i}{\hbar} \frac{(F(0) + F(t))}{2} \Delta t \right) \tag{7.33}$$

($\Delta t = t - t_0$; here $t_0 = 0$), which is equivalent to the assumption that F changes linearly with time t, and that corresponding operators $F(0)$ and $F(t)$ commute with each other.

In the current implementation of LvNMD, we truncated the Magnus expansion after the first term [81]. It is also assumed that the MD time steps are small enough that the matrix elements of the Fock operator change linearly between each two consecutive time steps. This leads to the expression for the time-evolution operator identical with the midpoint propagator.

7.2.7 Solution of LvN

Once the order of truncation of Ω in the Magnus expansion is decided, one can then focus on evaluation of time evolution of the density matrix (or on the wavefunction). It is always possible to directly find the exponential operator by diagonalizing Ω and then representing the time-evolution operator $\exp(\Omega)$ in terms of its eigenvectors of Ω. However, it is possible to avoid matrix diagonalization and directly express the effect of the time-evolution operator acting on density matrix via a matrix multiplication:

$$P(t) = P(0) + [\Omega, P(0)] + \frac{1}{2!}[\Omega, [\Omega, P(0)]] + \frac{1}{3!}[\Omega, [\Omega, [\Omega, P(0)]]] + \cdots \tag{7.34}$$

The derivation is very simple and follows the procedure of Baker, Campbell, and Hausdorff. The time-evolution operator is replaced with its parameterized version $U(t, \lambda) = \exp(\lambda\Omega)$ such that for $\lambda = 0$ the operator U becomes identity $(U(t, 0) = I)$ while taking $\lambda = 1$ leads to

$$U(t, 1) = \exp(\Omega). \tag{7.35}$$

Thus

$$P(t, \lambda) = \exp(\lambda\Omega) P(0) \exp(-\lambda\Omega), \tag{7.36}$$

such that for $\lambda = 0$ we have $P(\lambda = 0) = P(0)$ while $P(\lambda = 1) = P(t)$. We want to find $P(t) = P(\lambda = 1)$ via a Taylor expansion of $P(t, \lambda)$ around $\lambda = 0$. We need to determine the derivatives $\frac{d^n P(\lambda)}{d\lambda^n}$:

$$P(\lambda)^{(1)} = \frac{d}{dx}\left(e^{\lambda\Omega} P e^{-\lambda\Omega}\right) = e^{\lambda\Omega}\Omega P e^{-\lambda\Omega} + e^{\lambda\Omega} P(-\Omega)e^{-\lambda\Omega} = e^{\lambda\Omega}[\Omega, P]e^{-\lambda\Omega}, \tag{7.37}$$

$$P(\lambda)^{(2)} = \frac{d}{dx}\left(e^{\lambda\Omega}[\Omega, P]e^{-\lambda\Omega}\right) = e^{\lambda\Omega}\Omega[\Omega, P]e^{-\lambda\Omega} + e^{\lambda\Omega}[\Omega, P](-\Omega)e^{-\lambda\Omega}$$

$$= e^{\lambda\Omega}[\Omega, [\Omega, P]]e^{-\lambda\Omega}, \tag{7.38}$$

$$P(\lambda)^{(3)} = e^{\lambda \Omega} \left[\Omega, [\Omega, [\Omega, P]]\right] e^{-\lambda \Omega}, \tag{7.39}$$

$$P(\lambda)^{(n)} = \frac{\mathrm{d}^n P(\lambda)}{\mathrm{d}\lambda^n} = e^{\lambda \Omega} \underbrace{\left[\Omega, \dots [\Omega, [\Omega, P]]\right]}_{n \text{ times}} e^{-\lambda \Omega} \tag{7.40}$$

Now since we know all derivatives of $P(\lambda)$, we can now write

$$P(\lambda) = P(0) + \lambda P(0)^{(1)} + \frac{\lambda^2}{2!} P(0)^{(2)} + \frac{\lambda^3}{3!} P(0)^{(3)} + \frac{\lambda^4}{4!} P(0)^{(4)} \dots. \tag{7.41}$$

Thus

$$P(t, \lambda) = P(0) + \lambda[\Omega, P] + \frac{\lambda^2}{2!} [\Omega, [\Omega, P]] + \frac{\lambda^3}{3!} [\Omega, [\Omega, [\Omega, P]]] + \cdots, \tag{7.42}$$

where by setting $\lambda = 1$ we obtain the final expression. For the midpoint propagator $\Omega = -\frac{i}{\hbar} t \bar{F}$, this leads to

$$P(t) = P(0) - it \left[\bar{F}, P\right] - \frac{t^2}{2!} \left[\bar{F}, [\bar{F}, P]\right] + i \frac{t^3}{3!} \left[\bar{F}, [\bar{F}, [\bar{F}, P]]\right]$$

$$+ \frac{t^4}{4!} \left[\bar{F}, [\bar{F}, [\bar{F}, [\bar{F}, P]]]\right] \dots, \tag{7.43}$$

where $\bar{F}$ is an average (midpoint) operator such that $\bar{F} = \frac{1}{2}[F(0) + F(t)]$.

It is important to summarize the properties of time-evolution operator and of its action on $P(0)$. First, the time-evolution operator $\exp(\Omega)$ remains always unitary regardless of the order of the truncation of Magnus expansion. Unitary operators are norm conserving, and its action on any vector can be interpreted as a rotation of the basis set. Here the vector space is spanned by M single-electron pure-state densities P_{1el}^i such that $\text{Tr}[P_{\text{1el}}^i] = 1$. The occupation numbers f_i are linear combination coefficients:

$$P(t) = \sum_i^M P(t)_{\text{1el}}^i \cdot f_i. \tag{7.44}$$

The dot product in our space is then defined as $[P^k P^l]$. It is easy to verify that all one-electron densities $\{P_{\text{1el}}^j\}$ form an orthonormal basis set:

$$\text{Tr}[P_{\text{1el}}^i P_{\text{1el}}^j] = \delta_j^i. \tag{7.45}$$

The rotation due to time evolution is nonadiabatic but it is coherent:

$$P(t) = \exp(\Omega)\, P(0)\exp{(-\Omega)} = \exp(\Omega)\left(\sum_{i}^{M} P(0)^{i}_{\text{1el}} \cdot f_i\right)\exp{(-\Omega)}$$

$$= \sum_{i}^{M} \exp{(\Omega)}\, P(0)^{i}_{\text{1el}}\exp{(-\Omega)} \cdot f_i. \qquad (7.46)$$

That is, it is guaranteed that single-electron densities $P(t)^{i}_{\text{1el}}$, if idempotent at time $t = 0$, will remain idempotent after propagation and that their corresponding single-electron states (i.e., molecular orbitals) remain orthogonal. Also scalar coefficients f_i will remain unchanged during dynamics if propagation is performed correctly. In principle, any idempotent density matrix will always remain idempotent during the dynamics. Any pure state shall remain pure during the dynamics. Contrary to this, the single-electron densities $P(t)^{i}_{\text{1el}}$, although constructed at $t = 0$ from Born–Oppenheimer molecular orbitals (i.e., eigenvectors of F), do not need to stay on the Born–Oppenheimer surface, but their state can be described as a nonadiabatic superposition of BO states. The magnitude of deviation from BO surface is given by the commutator [F,P] and is a driving force of the dynamics itself.

The coherent character of density matrix propagation is an intrinsic property of unitarity of time-evolution operator. In order to describe decoherence of the wavefunction (or the density matrix) from a pure to a mixed state, one needs to include a non-Hermitian dephasing term to the Hamiltonian. As a consequence, the operator $\exp{(\Omega)}$ will no longer be unitary, and its action on P(0) no longer preserves length. An example of such nonunitary propagation is imaginary time propagation in which real time t is replaced with imaginary time it. Such a technique is often used to find a ground state in methods such as diffusion Monte Carlo. In consequence of action of a nonunitary operator $\exp{(-Ht)}$ on the random combination of all states, its contribution to the ground state is systematically amplified while coefficients corresponding to all other states decay exponentially with time.

Finally, it should be stressed that propagation of the wavefunction or density matrix on the time interval from 0 to t requires knowledge of the time dependence of the Hamiltonian operator. However, this information is not available. The operator F depends on the electronic structure through the two-electron term $G(P)$, and this is not known until the final electronic structure is found. We address this issue by performing an iterative SCF-like Fock refinement step in which the density matrix propagation for any given time step is performed repeatedly with an updated final Fock matrix from the previous cycle. This refinement procedure is continued until the Fock matrix is no longer changing. Then the final propagation is performed. This refinement effectively improves the stability of integration and allows for significantly extending the time step for integration for the time-dependent Schrödinger equation. To the knowledge of the authors, Liouville–von Neumann dynamics is the first implementation that employs SCF-like iterative refinement in the dynamics [81]. Our studies show that this is a crucial step that ensures a long-term stability of quantum dynamical propagation.

7.2.8   Implementation (Electronic Structure)

LvNMD method is general and can be used with Hartree–Fock, density functional theory, and tight binding methods (TB). The equation for electronic structure propagation in LvNMD is complex. Thus, contrary to BOMD and Mermin dynamics, the density matrix in LvNMD is always complex. One can expect that the Fock operator matrix is also complex since it directly depends on the density matrix through the electron repulsion term. However, it turns out that due to the cancellations, the Fock operator is always real for pure DFT functionals and for tight binding methods. In Hartree–Fock theory, the Fock operator becomes complex, but the only imaginary contribution comes from exchange part of the electron–electron interaction. Both the one-electron and Coulomb terms are always real.

The current implementation of LvNMD is based on a self-consistent-charge density functional tight binding theory (SCC-DFTB) [84]. This is an approximate DFT method in which only valence electrons are considered, while the remaining part (interaction between core electrons and nuclei) are described through the fitted repulsion E_{rep} term, which depends only on internuclear separation. Similar to DFT and Hartree–Fock methods, the interaction of valence electrons with core electrons and nuclei is described through a one-electron core Hamiltonian term (H_{core}). The electron repulsion term is described by a two-electron Hamiltonian. All integrals required to form the Fock matrix are parameterized from a DFT calculation and stored in a tabulated format. Integrals involving more than two centers are neglected.

An important part of solving von Neumann equation for density matrix propagation is the Fock refinement step. In order to propagate the density matrix from time t to time $t + \Delta t$, we need to know both the initial and final Fock operators. However, the final Fock operator depends on the final density matrix, and it is only known after the propagation of density matrix is completed. To solve this, the Fock matrix at time $t + \Delta t$ is formed using some guessed density matrix $P(t + \Delta t)$. Once the propagation $P(t) \rightarrow P(t + \Delta t)$ is performed, the better ("refined") Fock operator is formed, which is then used to perform a better propagation $P(t) \rightarrow P(t + \Delta t)$. This procedure is repeated until no further gain in improvement of the Fock matrix $F(t + \Delta t)$ is observed. The refined Fock operator is then used for the final propagation $P(t) \rightarrow P(t + \Delta t)$. The Fock refinement procedure is similar to the self-consistent field method, and it greatly improves the overall long-time stability of LvN dynamics [81]. It also allows us to use much larger steps as compared with other explicit time-dependent quantum mechanical ab initio dynamics. The typical time step in LvNMD is 0.1 fs, whereas in other methods explicit TD approaches, the typical time step is two orders of magnitude smaller.

It should be noted that propagation of the electronic structure through the time-dependent Schrödinger equation, if performed correctly, is intrinsically coherent and nonadiabatic. This is the consequence of the fact that the time-evolution operator is always unitary due to the Hermicity of the Hamiltonian operator. It would require adding a non-Hermitian term to allow dephasing from a pure to a mixed state. In case of propagation of the pure density matrix, it is very easy to verify whether the propagated density matrix still corresponds to a pure state or

not by monitoring idempotency of density matrix. Namely, the idempotency error, $\left\| P(t)^2 - P(t) \right\|$, should be close to zero. For the propagation of mixed states (e.g., initial density matrix from finite electronic temperature SCF), this simple formula cannot be used. Instead one can verify whether the dynamics remains coherent by making sure that there is no change in electronic entropy. This can be achieved through diagonalization of final and initial density matrices and comparison of their eigenvalues.

The unitary time evolution cannot change the eigenvalues (occupations) of the density matrix, but it rotates (mixes) underlying single-electron eigenstates (molecular orbitals). The occupied molecular orbitals do not need to be the same as the orbital obtained from the solution of Born–Oppenheimer problem. It is well known that the commutator [F,P] vanishes for the adiabatic electronic states which are eigenstates of the electronic Hamiltonian, and its nonzero value provides an insight how far is the electronic structure from its BO solution. In fact, the non-Born–Oppenheimer commutator [F,P] term appears on the right-hand side of von Neumann equation, and it is a driving term for time dependence of electronic structure. If the commutator on the right-hand side of von Neumann equation were equal to zero, then there would be no dynamics and the electronic were to remain in its initial adiabatic state.

It should be stressed that LvNMD is an orbital-free theory [81]. The total density matrix represents the entire electronic structure, and the individual orbitals are indistinguishable. Nevertheless, it is possible to exactly trace the time evolution of each initial molecular orbital set at $t = 0$ from BO electronic structure calculations by "tagging" them using a slightly altered occupation number (e.g., occupation numbers for the occupied orbitals would be assigned occupations of 1.00001, 1.00002, etc., instead of 1.0). Then one can trace back the results of time evolution by simply diagonalizing the final density matrix. The coefficients corresponding to eigenvalues of 1.00001, 1.00002 of final density matrix $P(t)$ then describe the propagated initial BO orbitals. The reason for this is that a coherent dynamics such as LvNMD (or other correct quantum dynamics) preserves the occupation numbers.

7.2.9 Initial Conditions

LvNMD is a method based on explicit integration of time-dependent Schrödinger equation subject to the initial electronic structure (density matrix). The initial density can be provided either from SCF calculations (ground or excited state density) or from an excited state density obtained from response theory. It is thus a very promising method for studies of excited states dynamics. The initial density matrix from SCF calculations can either be obtained at 0 K electronic temperature (Born–Oppenheimer density) or at finite electronic temperature (Mermin density). A notable difference between Mermin dynamics and LvNMD at finite temperature is that in Mermin dynamics the changes to electronic structure are incoherent with underlying assumptions that the molecular system can be thermalized infinitely fast.

For LvNMD at finite T_{el}, it can be interpreted as a closed system (or an ensemble of systems) with no interaction with an external environment with temperature-dependent probability of each system at time $t = 0$, which then evolves coherently with no external interaction. Furthermore, the initial density for the collection of noninteracting systems at time $t = 0$ can be prepared as a direct product of all densities. This gives a unique ability to prepare systems in various nonequilibrium initial states such that their chemical potentials (Fermi level) are not equal. This is important since the majority of chemical reactions, especially redox reactions (e.g., batteries), are driven by the difference in chemical potential. LvNMD is therefore very promising in real-time modeling of such processes, and it can be a useful tool in electrochemical energy storage research. Additionally, the matrix elements of the density matrix are very closely related to electron charge and corresponding dP/dt to electron current. It is thus very likely that direct dynamics can be used in molecular electronics simulations.

In the remainder of this chapter, we discuss a number of examples which demonstrate how the DFT and dynamics methods have been used to lend new insight into, or to guide, the design of functional nanostructured materials. These examples are mainly focused toward exploring fundamental material properties that are required for the efficient use of the underlying materials for energy science applications, including energy storage and conversion.

7.3 Application Examples

In this section we provide several examples of how computational chemistry and materials science has been used in collaboration with experiment to develop a detailed understanding of the structure and properties for materials where nanostructure is used to derive functional properties. These examples touch on the typical use of computational methods as (1) interpretation of experimental data; (2) prediction and design of new materials, properties, or processes; and (3) validation of a hypothesis or theory. Figure 7.2 provides a graphical overview of some of the examples discussed in more detail.

7.3.1 Supercapacitors and Interfaces

Electrical energy generated from renewable energy sources, such as solar and wind, offers enormous potential for meeting future energy demands [1]. However, the use of electricity generated from these intermittent sources requires efficient electrical energy storage. Electrochemical energy storage devices, that is, batteries and electrochemical capacitors or more conveniently "supercapacitors," are the leading electrical energy storage technologies today. Both are based on electrochemistry, but the fundamental difference between them is that batteries store energy in
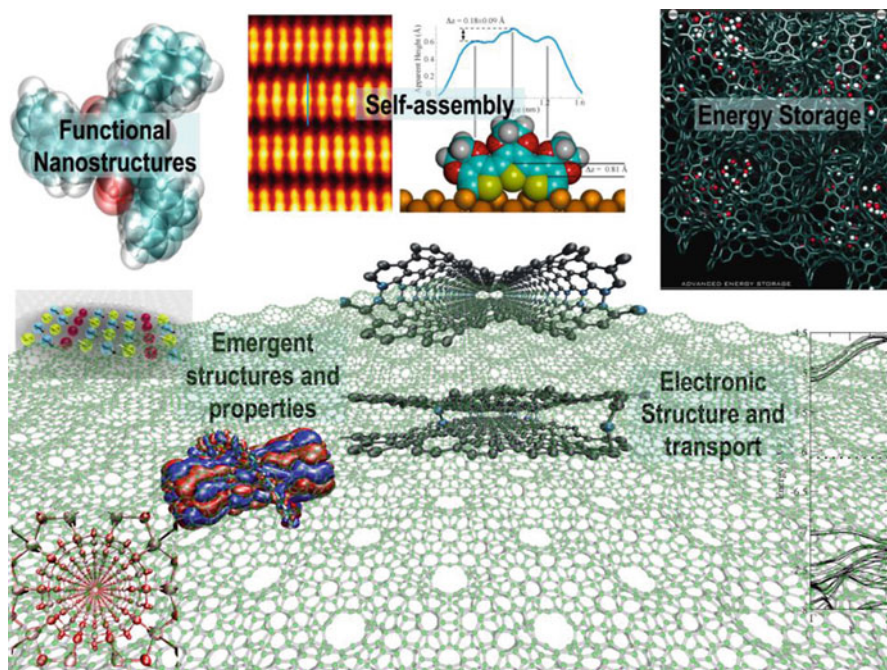
Fig. 7.2 Graphical overview of recent computational nanoscience projects

electrochemical reactants capable of generating charge, whereas supercapacitors store energy directly as charge [85]. Such a difference between batteries and supercapacitors manifests in their respective energy and power densities [85, 86]. Energy density measures how much energy is stored, whereas power density indicates how fast the energy can be released from or replenished into the system. For automotive transport applications, for instance, an ideal system would have both a large energy density and a large power density: The high energy density ensures sufficient energy for automobiles to travel a long distance, while the high power density enables the quick uptake of energy released by braking and the sudden release of the energy needed for accelerations. Because they store and release energy from electrochemical reactions, batteries have a large energy density but suffer from poor power density due to slow diffusion of active species and reaction kinetics. In contrast, supercapacitors are characterized by a high power density due to the absence of Faradaic processes, which also lead to other features of supercapacitors such as considerably longer lifetime and better safety compared to batteries. Fundamental limitations due to relatively slow electrochemical reactions in batteries make it hard to improve upon their power density characteristics. Instead of focusing on attempting to improve power density in conventional batteries, a great deal of research has been focused on attempting to increase the energy density of supercapacitors.
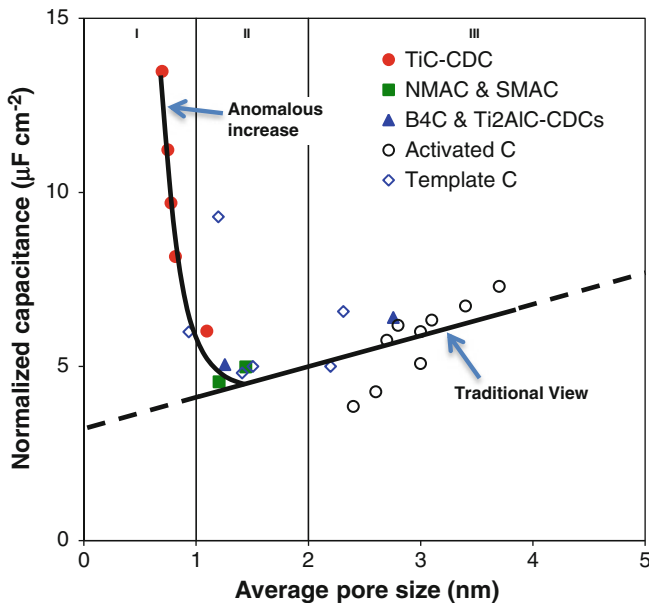
Fig. 7.3 Capacitance normalized by BET specific surface area for microporous carbide-derived carbons (pore size < 2 nm) and mesoporous activated and template carbons (pore size > 2 nm) in an organic electrolyte of tetraethylammonium tetrafluoroborate (TEABF$_4$) in acetonitrile (ACN). The normalized capacitance decreased with decreasing pore size until a critical value was reached. When the pore size is less than 1 nm, an anomalous increase by 100% in normalized capacitance was found (Adapted from Ref. [87]. With kind permission of © The American Association for the Advancement of Science 2006)

One of the worldwide research efforts on supercapacitors is aiming at increasing their energy density by optimizing the pore size distribution of nanoporous carbon materials. In their breakthrough work, Gogotsi and coworkers synthesized carbide-derived carbon (CDC) materials with unimodal micropores (pore size smaller than 2 nm) and found that these new materials exhibit an anomalous increase of normalized capacitance by 100% in an organic electrolyte of tetraethylammonium tetrafluoroborate (TEABF$_4$) in acetonitrile (ACN) (Fig. 7.3). In comparison, normalized capacitances of other mesoporous carbon materials (pore size > 2 nm) decrease slightly with decreasing pore size. These results speak against the application of the widely used electric double-layer capacitor (EDLC) model to nanoporous carbon materials, since this model dictates that the normalized capacitance is independent of pore size:

$$C/A = \varepsilon_r \varepsilon_0 / d \qquad (7.47)$$

where ε_r is the electrolyte dielectric constant, ε_0 is the permittivity of vacuum, A is the electrode specific surface area, and d is the effective thickness of the electric

double layer. The essence of the EDLC model lies in the compact layer of counterions that balance the charge on the planar electrode surfaces. More importantly, the new results for the microporous carbons challenge the long-held axiom that pores smaller than the size of solvated electrolyte ions are incapable of contributing to energy storage since solvated ions cannot enter such pores. These new experimental discoveries pose an opportunity to further optimize the capacitance of carbon supercapacitors. They also indicate possible new energy storage mechanisms that are different from the traditional view of electrical double layer.

To rationalize this anomalous increase in capacitance, we departed from the conventional EDLC model and consider the overlap of compact layers of counterions when the pore sizes are reduced to less than 1 nm. Depending on the pore shapes, which can be considered as cylindrical or slit pores, we proposed two alternative charge storage mechanisms. For cylindrical pores that have a pore curvature, partially desolvated counterions line up along the pore axes. Although the molecular geometries of the counterions could be anisotropic, the pore walls experience the average effect due to the translation or room-temperature rotation of the counterions along or with respect to the pore axes. Conversely, the counterions could experience the average effect as well although in reality the micropore shape may be distorted from an ideal cylinder. As a result, we proposed an electric wire-in-cylinder capacitor (EWCC) model:

$$C/A = \varepsilon_r \varepsilon_0 / \left[b \ln(b/a_0) \right], \tag{7.48}$$

where b is the pore radius and a_0 is the effective size of the counterions, that is, the extent of electron density around the ions. Since slit pores without pore curvature are also a possible pore shape, an electric sandwich capacitor (ESWC) model (Fig. 7.4, inset) may be proposed, assuming that the two compact layers of counterions next to the two opposing pore walls overlap into one layer of counterions sandwiched between the two pore walls [89]:

$$C/A = \varepsilon_r \varepsilon_0 / (b - a_0) \tag{7.49}$$

The common feature of the EWCC and ESWC models is that counterions are confined in subnanometer pores to form a single file of counterions, either as a 1D wire or a 2D layer. Accordingly, there is no space for diffuse layers, or even for solvent molecules, between the counterions and the pore walls. Note that solvent molecules could still be present along the 1D wire or in the 2D layer in the case of low charge density, unless the charge density approaches a pore saturation scenario, when the solvent molecules are displaced by counterions. Although there is no space for two-way traffic, the micropores can still be charged, as long as each micropore has two entrances in order for the electrolytes already inside to exit through one of them and for the counterions to charge the pores through the other one, given a nonuniform electric field along each pore.

The EWCC and ESWC models were applied to fit the experimental data taken from Ref. [90], where the total capacitances are dissected into capacitance
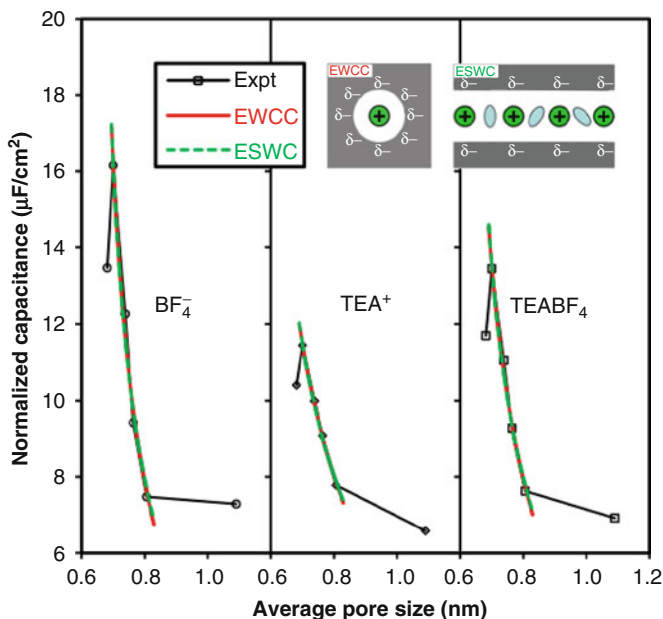
Fig. 7.4 Experimental data of microporous CDC supercapacitors with 1.5 M TEABF$_4$ in ACN fit by the electric wire-in-cylinder capacitor (EWCC) model and the electric sandwich capacitor (ESWC) model for the capacitance contributions from TEA$^+$, BF$_4$$^-$, and the total capacitance. The *inset* shows the schematic diagrams of counterions forming single file of 1D wire or 2D sandwich layer within a negatively charged cylindrical pore (EWCC) or slit pore (ESWC) (Adapted from Ref. [88]. With kind permission of © WILEY – VCH VERLAG GMBH & CO. KGAA 2008)

contributions of cations and anions (Fig. 7.4). Analysis of the experimental data for total capacitance of microporous CDCs shown in Fig. 7.3 gives comparable results [88, 91]. Note that in Fig. 7.4 only the data in a narrow pore size range can be analyzed using Eqs. 7.48 and 7.49. The data on the right of the fitting range have higher normalized capacitances than the extrapolation from the fit curve probably because of the solvent effect, which would increase the dielectric constant. The data on the left have lower normalized capacitances than the extrapolation because of pore saturation. As can be seen from Fig. 7.4, the anomalous increase in capacitance was well reproduced by both the EWCC and ESWC models. The main reason that these models work for micropores is that as the pore size decreases, the distance between the counterions and the pore walls, that is, the effective double-layer thickness *d*, decreases accordingly. Simply from the EDLC model that shows the capacitance is inversely proportional to *d*, an enhanced capacitance is justified. The overlapping fitting curves indicate that the differences of fitting results between the two fitting models are small. The small differences indicate that the confinement effect instead of the pore shape is responsible for the anomalous increase in capacitance. CDCs may prefer a certain pore shape than another, but the model simply cannot tell. Nevertheless, these models captured the confinement

Table 7.1 Fitting results using EWCC model and ESWC model for the experimental data of total capacitance and the contributions from cations and anions with 1.5 M TEABF$_4$ in ACN

Capacitance contribution[a]	Model	R^2	ε_r[b]	a_0 [Å][b]	Ionic radii [Å]
TEA$^+$	EWCC	0.997	2.37 (0.15)	2.08 (0.07)	3.37[c]
	ESWC	0.995	1.50 (0.07)	2.35 (0.07)	
BF$_4$$^-$	EWCC	0.989	1.06 (0.11)	2.97 (0.06)	2.32[c]
	ESWC	0.986	0.87 (0.08)	3.03 (0.05)	
Total	EWCC	0.993	1.44 (0.12)	2.67 (0.07)	–
	ESWC	0.991	1.09 (0.08)	2.79 (0.06)	

[a]Experimental data from [90]
[b]Numbers in parentheses are standard errors of fitting parameters
[c]Reference [92]

effect on the anomalous increase in capacitance. As can be seen in Table 7.1, the fitting qualities in terms of R^2 are excellent for all fitting cases. The dielectric constants ε_r obtained are ca. 1, which implies that counterions are at least partially desolvated so that the bare counterions can fit into the micropores. Comparing all of the fittings, we found that the EWCC fitting for BF$_4$$^-$ produces a ε_r value that is the closest to unity. In comparison, the TEA$^+$ fitting gives a ε_r value that deviates the most from unity. This difference may have come from the rigidity of BF$_4$$^-$ anion and the flexibility of TEA$^+$. This argument is further supported by the normalized capacitance of TEA$^+$ shown in Fig. 7.4, where the highest value achieved is only 11.5 μF/cm^2, compared to 16.2 μF/cm^2 for BF$_4$$^-$. As the pore size decreases, the radius of TEA$^+$ decreases as well. Consequently, the capacitance does not increase as sharply as it should, and the a_0 value is underestimated in the fit (Table 7.1).

   To corroborate the parameter a_0 obtained by the above fittings, we used DFT to calculate the radial charge distribution of electrolyte ions enclosed in nanotubes, that is, the radial electron density inside cylindrical electrodes. All DFT calculations were performed using the NWChem suite of programs [10] to obtain fundamental information that includes important quantum effects related to the confined geometries of micropores. Figure 7.5 shows the radial charge distributions of BF$_4$$^-$ in (6,6) and (8,8) nanotubes terminated with H atoms and in vacuum, and their corresponding integrated number of electrons, at the level of B3LYP/cc-pVDZ. a_0 is taken as the radius where 90% of the electron is enclosed from the curve of integrated number of electrons, which is 2.22, 2.31, and 2.31 Å for BF$_4$$^-$ enclosed in (6,6) and (8,8) nanotubes terminated with H atoms, and for the bare ion. These radii are in quite good agreement with the literature data and the fit results (Table 7.1). However, for the radius of TEA$^+$, the disparity between the literature data and the fitting results can be as large as 1.3 Å. By DFT calculations of the radial charge distribution of a TEA$^+$ enclosed in a (6,6) nanotube terminated with H atoms, we found that with its C_2' axis in alignment with the pore axis, TEA$^+$ has a radius of ca. 2.4 Å when confined inside a subnanometer pore, which is closer to the fitted value shown in Table 7.1. The literature radius of 3.4 Å is actually about the length of an ethyl arm on TEA$^+$. The projection of the four terminal C atoms of ethyl arms of TEA$^+$ onto a plane is a square. A rough estimate of the side length of
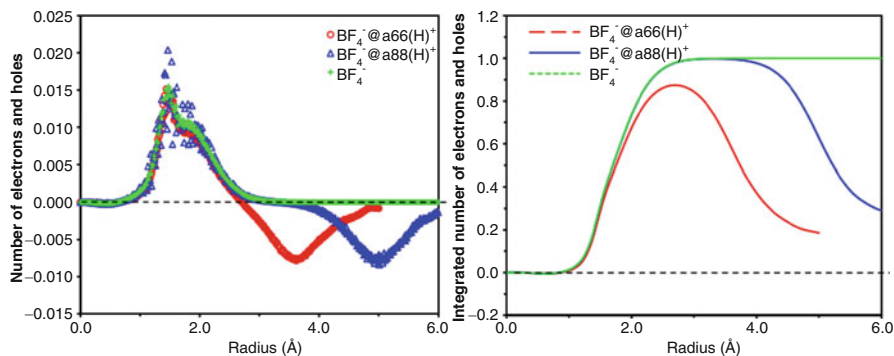
Fig. 7.5 The radial charge distributions (*left panel*) and the integrated radial charge distribution (*right panel*) as a function of radius within the boron-centered sphere for $BF_4^-@a66(H)^+$, $BF_4^-@a88(H)^+$, and BF_4^-. $BF_4^-@a66(H)^+$ and $BF_4^-@a88(H)^+$ denote BF_4^- in a (6,6) and (8,8) tube, respectively (Reproduced from Ref. [88]. With kind permission of © John Wiley & Sons, Inc. 2008)

the square by trigonal geometry using the ethyl arm length of 3.4 Å (Table 7.1) gives an a_0 value of 2.4 Å if the C_2' axis is assumed to be in alignment with the pore axis. These DFT calculations effectively confirm the fitting results obtained from the EWCC and the ESWC models, which in turn corroborate the new energy storage mechanism presented above.

We further calculated the solvation free energies $\Delta G°$ for TEA^+ and BF_4^- in ACN to provide additional evidence for the desolvation of counterions in micropores. Calculations of $\Delta G°$ were performed using the SM8 continuum solvation model [93] with the GAMESSPLUS module [94] interfaced with the GAMESS package [11]. The geometries optimized at the level of B3LYP/aug-cc-pVDZ were used in single-point SM8 solvation calculations in conjunction with class IV CM4 charges [95] at the level of B3LYP/6-31G(d). Since the experimental data of $\Delta G°$ for TEA^+ in ACN are not available, $\Delta G°$ for three other cations ($EtNH_3^+$, $Et_2NH_2^+$, and Et_3NH^+) with structures similar to that of TEA^+ were calculated in order to provide a validation of the theory used. The computed $\Delta G°$ for $EtNH_3^+$, $Et_2NH_2^+$, and Et_3NH^+ agree very well with the experimental data available from the Minnesota Solvation Database [96], showing small relative errors of only 1–5%. Under the conventional standard state of 1 atm and 298.15 K, the solvation free energies $\Delta G°$ are found to be only -51.2 and -45.1 kcal/mol for TEA^+ and BF_4^- in ACN, respectively [97]. These values are much smaller than those of typical monovalent inorganic ions in aqueous solutions (e.g., the solvation free energies of Na^+, K^+, F^-, and Cl^- ions are -98.3, -80.8, -103.8, and -75.8 kcal/mol, respectively) [98]. Another factor that facilitates the desolvation of organic ions is that the nonelectrostatic ion–electrode interactions (essentially the van der Waals attractions) are strong, which explains the contact adsorption of TEA^+ and BF_4^- at neutral and charged electrodes [97]. Although at present $\Delta G°$ for organic ions trapped in micropores have not been studied yet, it is expected that the relatively

small solvation energies in combination with the strong van der Waals interactions between organic ions and electrode atoms facilitate the desolvation of counterions when they enter micropores during charging process.

7.3.2   Investigating Properties of Nanostructured Materials

Some of the most revolutionary ideas in modern materials synthesis evolve from a realization that by harnessing the collective phenomena present on the molecular interaction length scale, $\sim$1 nm, materials with new and unique properties can be produced. This paradigm of materials synthesis is a consequence of not only the pair-wise interactions of molecules but also the many-body self-organizing behavior that is active in the formation of most inorganic, organic, and organic–inorganic hybrid material systems. The overarching goal is to understand the mechanism(s) whereby these unique assemblies are formed to enable the design and synthesis of materials with prescribed functional (physiochemical) properties.

In recent years, use of the terms nanoscience, nanoparticles, or nanostructures has grown in both the scientific community and society at large. This is principally because many important phenomena depend on the length scales from 0.1 to 100 nm or spatial confinement to these dimensions. In an article entitled "Nanoscience, Nanotechnology, and Chemistry" [99], it was noted that research and development must be focused on the development of science and technology at the "right scale." Investigations that provide insight into the effects of confinement in space and time, that span the classical and quantum regimes, and where the confining medium is either "hard" (zeolite, aerogel, or porous membrane) or "soft" (emulsions, micelle, or sol-gel network) will aid in making the leap from "strictly synthesis of nanostructured materials" to understanding the emergent properties of these materials [100].

When gases or liquids are adsorbed or entrained in an open framework such as activated carbon, aerogels, xerogels, zeolites, or silica glasses with pores of nanometer scale dimensions, unexpected phenomena emerge. For example, the freezing point of a liquid or glass transition can be significantly depressed when confined in nanometer-sized pores [101]. Phase transitions and the conformation of flexible moieties also exhibit behaviors significantly different from those exhibited in bulk materials [102]. Ordered mesoporous materials have attracted wide interest in fields such as catalysis, separation processes, regulated transport, and immobilization of biomolecules [103]. Here again, molecule–molecule (M–M) and molecule–substrate (M–S) interactions are important parameters to consider, as well as surface roughness, surface tension, pore diameter, wall morphology/composition, frictional losses, and fluctuations can all introduce dramatic changes in the behavior of the confined/adsorbed molecular species. The relative magnitude of the M–M and M–S interactions can vary markedly as the diameter of the pore is varied, so it should not be surprising that interesting new phenomena are observed in studies that systematically vary the pore dimensions and architecture in addition to the chemical composition of the base material (e.g., boron nitride, graphite, and MgO).
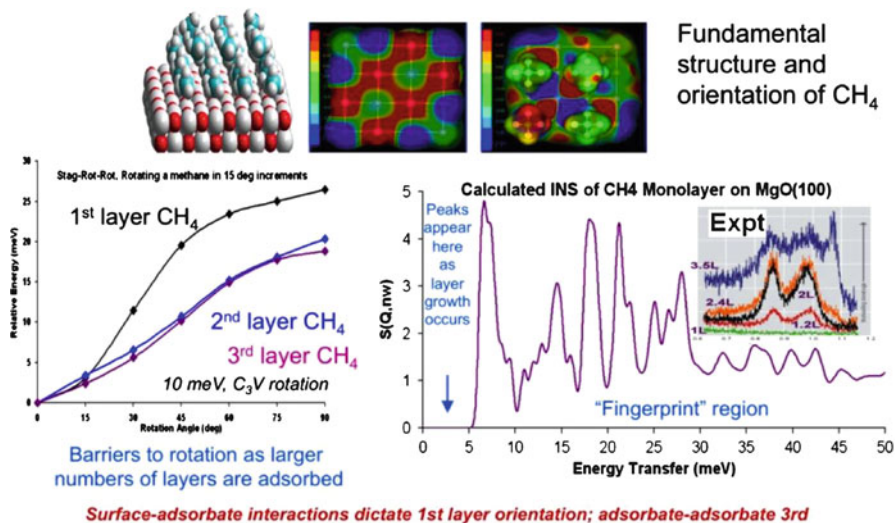
Fig. 7.6 Calculated structure factor based on ab initio calculations used to understand and visualize structure and dynamics of CH_4 adsorbed on MgO(100) (Reproduced from Ref. [104]. With kind permission of © The American Chemical Society 2007)

The nature of the fundamental interactions of materials confined at interfaces was explored using accurate first-principles electronic structure calculations in combination with thermodynamic and neutron scattering experiments. These studies are essential in order to develop a molecular-level understanding of the important forces that manipulate the structure and dynamics at interfaces (solid–solid, gas–solid, and liquid–solid), which in turn are the principle drivers of the bulk properties for heterostructured materials. In addition, the elucidation of the nanoscale structure of adsorbed molecules on an extended solid surface is of fundamental importance in phenomena such as adhesion, corrosion, and heterogeneous catalysis.

The adsorption of a species on a surface, as typified by the prototypical hydrocarbon methane adsorbed to the prototypical oxide MgO(100), was studied using first-principles DFT methods (Fig. 7.6) [104, 105]. Of prime interest in this system, as in all such interfaces, is the balance between surface–adsorbate and adsorbate–adsorbate interactions. The relative simplicity and regularity of this system, as well as the efficiency of the computational tools used, have combined to yield results that provide significant insight into both mono- and multilayered adsorbed systems. In this particular system, it was determined that only the structure of the first adsorbed layer is dominated by surface–adsorbate interactions, although adsorbate–adsorbate interactions still play a role even at the monolayer scale: The former effect selects for a structure wherein partially positive hydrogen atoms are oriented toward lattice oxygen sites, whereas the latter effect dictates the orientation of each methane with respect to its neighbor. The structural motif of an added second layer is consistent with that predicted solely based on interadsorbate repulsion, although, as this

structure is also favored by the electrostatic character of the surface, the relative roles of each effect cannot be fully judged. At the third layer, and presumably all higher-order layers, the minimization of close H–H contacts is found to determine the structure. *Ab initio* molecular dynamics simulations furthermore provided support to the highly influential role of repulsive interadsorbate interactions in determining structure.

The results shown in the Fig. 7.6 were obtained from DFT calculations for the adsorption of methane onto a MgO(100) surface. The relative orientation of the methane (C_{3v} and C_{2v}) and its adsorption site (atop oxygen, atop Mg, bridge, etc.) were previously unknown and difficult to determine from lower-level quantum calculations that tend to give the C_{3v} atop oxygen orientation. Electron correlation effects tend to give the C_{2v} methane atop Mg orientation as the lowest energy state, and the adsorption site is on the Mg instead of the O. (See Fig. 7.6, top 2 panels: Left panel shows C_{3v} on O as computed from Hartree–Fock calculations; right top panel shows C_{2v} atop Mg for 1st layer from DFT; MP2 also gives this orientation.) The effects of adding a monolayer of methane followed by a bi- and trilayer were also elucidated. The MgO electrostatic potential is what dictates the first and second layer adsorption, as shown in the top right panel; H atoms on methane orient toward the electronegative O and the C atoms aligns with Mg. The first layer alters the electrostatic potential as shown going from the middle top to the right top panel. The next layer of methane orients to align the H atoms toward the electronegative regions. The inelastic neutron scattering (INS) was directly computed from the quantum calculations using the normal modes. In addition the actual rotational energy barriers for methane were explicitly computed as a function of the number of methane layers (lower right panel). Overall, a reasonably complete understanding of the experimentally measured INS was possible, in particular, the reduction in the energy for the peaks as more layers of methane were adsorbed (bottom left panel with the experimental insert showing how at one monolayer, labeled 1L, the INS has a peak at higher energies, while as more layers of methane are added, 2L–3.5L, two peaks appear at the lower energies. These peaks could be directly assigned to the rotation motion of methane on MgO as determined from the calculations that show explicitly the vibrational motion and give the relative barriers for rotation). This work has been recently extended to the systems of n-butane, pentane, and cyclohexane on MgO.

The rotational motion of methane was a key point of interest and clearly shown to be hindered by the MgO surface for the first methane layer. As a second layer is added, the barrier for methane rotation is much lower and likely may occur in two separate ways; however, addition of a third layer of methane serves to substantially raise the rotational barrier for one of these methane rotational pathways. Third layer methane apparently can only rotate in one way, which was revealed via quantum molecular dynamics simulations. The details of this pathway, particularly the changes in rotational motion of second layer methane as it is covered, await further calculated INS spectra for verification.

B	C	N
[He] $2s^2\ 2p^1$	[He] $2s^2\ 2p^2$	[He] $2s^2\ 2p^3$
R_{cov}= 84pm	R_{cov}=76pm	R_{cov}=71pm

Si	P	S
[Ne] $3s^2\ 3p^2$	[Ne] $3s^2\ 3p^3$	[Ne] $3s^2\ 3p^4$
R_{cov}=111pm	R_{cov}=107pm	R_{cov}=105pm

Se
[Ar] $3d^{10}\ 4\ s^2\ 4p^4$
R_{cov}= 120pm

Fig. 7.7 Periodic table highlighting the elements applicable for substitution of carbon within a graphitic lattice

7.3.3 Tuning the Reactivity of Carbon Surfaces

From graphite to fullerenes to nanotubes, carbon displays the versatility of sp^2 hybridization coupled with the appropriate valence. By doping single-wall (SWNT) and multiwall (MWNT) carbon nanotubes, it is possible to significantly change their physical and chemical properties, and this fact can be used for developing novel materials [106]. The most studied doped carbon nanotubes are those containing boron (B) and nitrogen (N) [107]. B and N are the nearest neighbors of carbon (C) in the periodic table (see Fig. 7.7) that can provide *p*- and *n*-doping, respectively, their valence electrons being in the second shell, like carbon. Phosphorous (P) is another electron donor that can be incorporated into nanotubes [108], but fundamentally different from N because its valence electrons are in the third shell. Co-doping of P and N is also possible and was recently experimentally realized [109, 110]. Functionally, the substitutionally doped nanotubes offer enhanced chemical reactivity, a feature that is useful for molecular-level detection, polymer nanocomposites, and oxidation–reduction reactions [111].

Figure 7.8 shows the energetic preference for B, N, Si, P, S, and Se for substitution into different lattice sites of a representative carbon nanotube structure, which is termed the boomerang for brevity. Notable from this figure is that N prefers
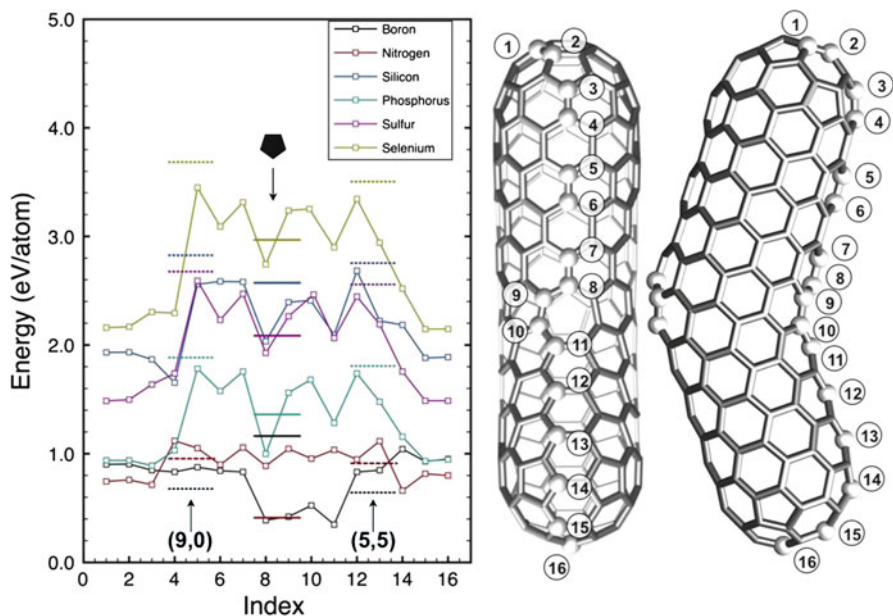
Fig. 7.8 *Left panel* shows the relative formation energy for C substitution with B, N, Si, P, S, and Se into the graphitic lattice at the sites numbered on the joined (9,0) and (5,5) carbon nanotube structure (*right panel*), which is termed a boomerang in the text

to substitute in regions with positive curvature, B on negative, while Si, S, P, and Se can promote either positive or negative curvature. Some experimental evidence for these trends was obtained via CVD growth of carbon nanotubes where it was explicitly observed that N tends to cause shorter and smaller-diameter "bamboo" nanotubes and S leads to branched and cone-stacked nanotubes [107, 112, 113].

A detailed natural bond order analysis was used to help understand the hybridization of the different atomic substitutions. The results are discussed with regard to four representative locations: C_{34} (zigzag), C_{176} (armchair), C_{P2} (knee pentagon), and C_{92} (heptagon). The connectivity for the bonds connecting these four atoms with the neighboring atoms C_A, C_B, and C_C is shown in Fig. 7.9. The valence structures are calculated using the NBO 5.0 program for all of the boomerangs without substitution (X = C) and with substitutions (X = B, Si, N, P, S, and Se) at the four locations in Fig. 7.9.

The natural bond orbital (NBO) analysis uses the one-electron density matrix to define the shape of the atomic orbitals in the molecular environment and to derive molecular bonds from the density between the atoms. The results in terms of hybridizations, Mayer bond orders, and natural atomic charges are tabulated in Table 7.2 for the all-C and the Si-, S-, and Se-substituted boomerangs which are closed-shell singlets, and in Table 7.3 for the B-, N-, and P-substituted boomerangs which are open-shell doublets.
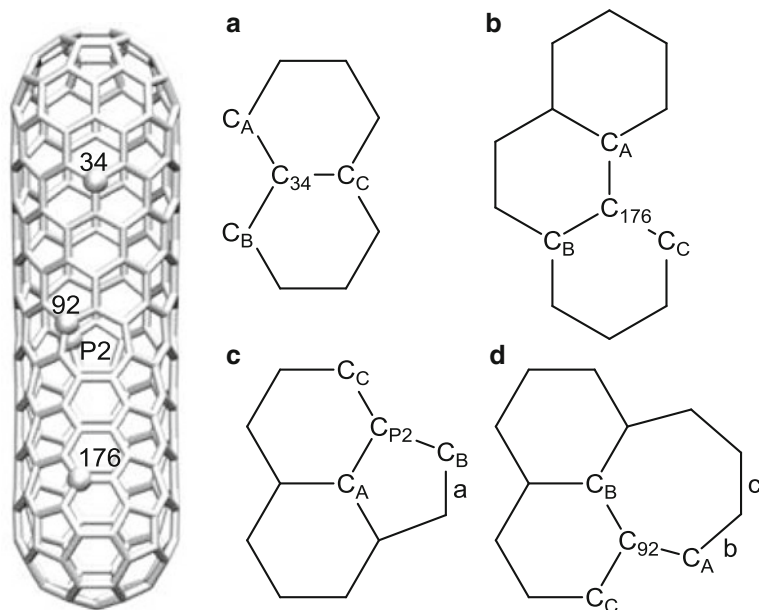
Fig. 7.9 Local structures of the all-C boomerang at the zigzag side (**a**), the armchair side (**b**), the knee pentagon (**c**), and at the heptagon (**d**). These four representative locations are selected for comparison so that the mirror plane passes through these local structures in the middle. The four atoms C_{34}, C_{P2}, C_{176}, and C_{92} are the sites of substitutions with X = B, Si, N, P, S, and Se

As can be seen in Table 7.2, the hybridizations of σ orbitals for the all-C structure are very similar to the typical hybridization for planar sp^2 C, with only a small deviation. The p orbitals not involved in the above hybridization participate in the π-bond formation. The Mayer bond orders of double bonds between X and C_C are only slightly larger than those of single bonds, in agreement with the observed small bond length alternations (BLAs) between single bonds and double bonds, which implies a high degree of delocalization. The delocalization is also reflected in the number of low-occupancy lone pairs (LP) and high-occupancy LP* orbitals. An ideal Lewis structure of the all-C boomerang is that, on the top of the σ-bond connected skeleton, each C may find an immediate neighbor to form a π bond so that every electron in the p orbital nearly perpendicular to the local surface is accounted for. However, the search for Lewis structure did not end up with this ideally localized structure. Instead, the NBO analysis found two LP and two LP* on the C network (Table 7.4). Using the resonance of 1,3-butadiene, this can be understood with ease. As can be seen from Fig. 7.10, the typical Lewis structure has alternating single bond and double bonds. A localized structure with two radical electrons located at both ends could also exist. There is additionally a third resonance structure, among other possibilities, that one end has an LP while the other end has an LP*. Normally the

Table 7.2 Valence structures in terms of hybridizations, Mayer bond orders, and natural atomic charges calculated by NBO analysis at the level of PBE/6-31G* for the all-C and the Si-, S-, and Se-substituted boomerangs which are closed-shell singlets

X	Site[a]	Hybridization[b]			LP on X	Mayer bond order			Natural charge
		$X–C_A$	$X–C_B$	$X–C_C$		$X–C_A$	$X–C_B$	$X–C_C$	
C	34	$sp^{2.02}–sp^{2.04}$	$sp^{2.02}–sp^{2.04}$	$sp^{1.97}–sp^{1.92}$, $s^0p^{1.00}–s^0p^{1.00}$	–	1.215	1.215	1.227	−0.006
	176	$sp^{2.04}–sp^{2.04}$	$sp^{2.03}–sp^{2.00}$	$sp^{1.94}–sp^{1.82}$, $s^0p^{1.00}–s^0p^{1.00}$	–	1.192	1.210	1.285	−0.003
	P2	$sp^{2.13}–sp^{2.12}$	$sp^{2.07}–sp^{2.07}$	$sp^{1.83}–sp^{2.00}$, $s^0p^{1.00}–s^0p^{1.00}$	–	1.177	1.177	1.282	0.003
	92	$sp^{1.91}–sp^{1.90}$	$sp^{2.00}–sp^{2.02}$	$sp^{2.01}–sp^{1.98}$, $s^0p^{1.00}–s^0p^{1.00}$	–	1.210	1.173	1.273	0.012
Si	34[c]	$sp^{2.05}d^{0.02}–sp^{2.78}$	$sp^{2.05}d^{0.02}–sp^{2.78}$	$sp^{2.25}d^{0.03}–sp^{2.06}$, $sp^{21.18}d^{0.03}–sp^{98.44}d^{0.01}$	–	1.033	1.033	1.174	1.417
	176[c]	$sp^{2.01}d^{0.02}–sp^{2.66}$	$sp^{2.15}d^{0.03}–sp^{2.60}$	$sp^{2.01}d^{0.02}–sp^{2.08}$, $sp^{37.63}d^{0.07}–sp^{62.37}d$	–	1.007	1.092	1.176	1.416
	P2	$sp^{2.06}d^{0.03}–sp^{2.55}$	$sp^{2.18}d^{0.03}–sp^{2.65}$	$sp^{1.75}d^{0.02}–sp^{3.02}$	$s^0p^{1.00*}$	0.943	0.993	1.014	1.192
	92	$sp^{2.10}d^{0.03}–sp^{2.42}$	$sp^{1.84}d^{0.02}–sp^{2.51}$	$sp^{2.02}d^{0.02}–sp^{2.41}$	$s^0p^{1.00*}$	1.152	1.080	1.126	1.619
S	34	$sp^{5.19}d^{0.03}–sp^{3.48}$	$sp^{5.19}d^{0.03}–sp^{3.48}$	$sp^{4.35}d^{0.03}–sp^{3.07}$	$sp^{1.03}$	0.844	0.844	0.940	1.014
	176	$sp^{5.76}d^{0.04}–sp^{3.62}$	$sp^{4.84}d^{0.03}–sp^{3.28}$	$sp^{4.36}d^{0.03}–sp^{2.91}$	$sp^{1.01}$	0.792	0.911	0.958	0.997
	P2	$sp^{5.30}d^{0.03}–sp^{3.59}$	$sp^{4.99}d^{0.03}–sp^{3.39}$	$sp^{4.90}d^{0.03}–sp^{3.55}$	$sp^{0.97}$	0.876	0.917	0.863	1.000
	92	$sp^{4.20}d^{0.04}–sp^{2.99}$	$sp^{5.14}d^{0.04}–sp^{3.41}$	$sp^{4.77}d^{0.03}–sp^{3.29}$	$sp^{1.11}$	0.956	0.814	0.881	1.029
Se	34	$sp^{7.45}d^{0.04}–sp^{3.95}$	$sp^{7.45}d^{0.04}–sp^{3.95}$	$sp^{6.10}d^{0.03}–sp^{3.41}$	$sp^{0.60}$	0.829	0.829	0.929	1.178
	176	$sp^{8.22}d^{0.04}–sp^{4.07}$	$sp^{6.85}d^{0.04}–sp^{3.68}$	$sp^{6.18}d^{0.03}–sp^{3.24}$	$sp^{0.60}$	0.780	0.898	0.947	1.158
	P2	$sp^{7.64}d^{0.04}–sp^{4.10}$	$sp^{7.12}d^{0.04}–sp^{3.82}$	$sp^{6.96}d^{0.03}–sp^{4.02}$	$sp^{0.57}$	0.859	0.904	0.845	1.142
	92	$sp^{6.09}d^{0.04}–sp^{3.38}$	$sp^{7.53}d^{0.04}–sp^{3.85}$	$sp^{7.02}d^{0.04}–sp^{3.73}$	$sp^{0.61}$	0.941	0.801	0.857	1.195

[a] Site indices are shown in Fig. 7.9

[b] The first hyphenated group is for a σ bond, and the second group, if any, is for a π bond

[c] Similar to the all-C structure, Si forms a double bond with C_C. This is, however, not the case for substitutions at Si_{P2} and Si_{92}, where Si has an LP* and C_C forms double bond with one of its other neighbors

[d] This can be renormalized to $s^{0.03}p^{0.97}–s^{0.02}p^{0.98}$, which is a p-rich orbital with a small admixture of s components (see the text)

Table 7.3 Valence structures in terms of hybridizations, Mayer bond orders, and natural atomic charges calculated by NBO analysis at the level of PBE/6-31G* for the B-, N-, and P-substituted boomerangs which are open-shell doublets

X	Site[a]	Hybridization[b]			LP	Mayer bond order			Natural charge
		$X–C_A$	$X–C_B$	$X–C_C$		$X–C_A$	$X–C_B$	$X–C_C$	
B	34	$sp^{1.99}–sp^{1.70}$, $sp^{1.99}–sp^{1.70}$	$sp^{1.99}–sp^{1.70}$, $sp^{1.99}–sp^{1.70}$	$sp^{2.03}–sp^{1.58}$, $sp^{2.02}–sp^{1.58}$	$s^0p^{1.00*}$, $s^0p^{1.00*}$	1.049	1.049	1.039	0.581
	92	$sp^{1.96}–sp^{1.64}$, $sp^{1.95}–sp^{1.63}$	$sp^{1.91}–sp^{1.67}$, $sp^{1.92}–sp^{1.67}$	$sp^{2.14}–sp^{1.71}$, $sp^{2.14}–sp^{1.72}$	$s^0p^{1.00*}$, $s^0p^{1.00*}$	1.030	1.041	1.029	0.614
	P2	$sp^{2.09}–sp^{1.81}$, $sp^{2.09}–sp^{1.80}$	$sp^{2.09}–sp^{1.76}$, $sp^{2.07}–sp^{1.75}$	$sp^{1.85}–sp^{1.73}$, $sp^{1.86}–sp^{1.73}$	$s^0p^{1.00*}$, $s^0p^{1.00*}$	1.005	1.007	1.083	0.642
	176	$sp^{1.99}–sp^{1.70}$, $sp^{1.99}–sp^{1.69}$	$sp^{2.07}–sp^{1.68}$, $sp^{2.07}–sp^{1.67}$	$sp^{1.96}–sp^{1.47}$, $sp^{1.95}–sp^{1.47}$	$s^0p^{1.00*}$, $s^0p^{1.00*}$	1.044	1.038	1.100	0.583
N	34	$sp^{2.06}–sp^{2.75}$, $sp^{2.07}–sp^{2.75}$	$sp^{2.06}–sp^{2.75}$, $sp^{2.07}–sp^{2.75}$	$sp^{1.96}–sp^{2.61}$, $sp^{1.95}–sp^{2.59}$	$s^0p^{1.00}$, $s^0p^{1.00}$	0.950	0.950	0.892	−0.292
	92	$sp^{1.85}–sp^{2.50}$, $sp^{1.85}–sp^{2.49}$	$sp^{2.15}–sp^{2.77}$, $sp^{2.13}–sp^{2.76}$	$sp^{2.16}–sp^{2.68}$, $sp^{2.14}–sp^{2.68}$	$sp^{69.08}$, $sp^{98.05}$	0.949	0.905	0.904	−0.309
	P2	$sp^{2.25}–sp^{2.81}$, $sp^{2.27}–sp^{2.81}$	$sp^{2.11}–sp^{2.73}$, $sp^{2.12}–sp^{2.73}$	$sp^{2.11}–sp^{2.80}$, $sp^{2.12}–sp^{2.80}$	$sp^{19.39}$, $sp^{18.40c}$	0.996	0.985	0.915	−0.307
	176	$sp^{2.12}–sp^{2.75}$, $sp^{2.13}–sp^{2.75}$	$sp^{2.07}–sp^{2.71}$, $sp^{2.08}–sp^{2.71}$	$sp^{1.97}–sp^{2.50}$, $sp^{1.96}–sp^{2.50}$	$sp^{57.81}$, $sp^{58.82}$	0.952	0.938	1.024	−0.287
P	34	$sp^{5.22}d^{0.05}–sp^{2.64}$, $sp^{5.02}d^{0.05}–sp^{2.75}$	$sp^{5.22}d^{0.05}–sp^{2.64}$, $sp^{5.02}d^{0.05}–sp^{2.75}$	$sp^{4.45}d^{0.05}–sp^{2.31}$, $sp^{4.82}d^{0.05}–sp^{2.31}$	$sp^{1.00}$, $sp^{1.00}$	0.889	0.889	0.982	1.061
	92	$sp^{4.38}d^{0.05}–sp^{2.35}$, $sp^{4.73}d^{0.05}–sp^{2.36}$	$sp^{5.30}d^{0.05}–sp^{2.61}$, $sp^{4.94}d^{0.05}–sp^{2.74}$	$sp^{5.11}d^{0.05}–sp^{2.54}$, $sp^{5.04}d^{0.05}–sp^{2.62}$	$sp^{1.01}$, $sp^{1.01}$	0.992	0.868	0.904	1.059
	P2	$sp^{5.65}d^{0.05}–sp^{2.70}$, $sp^{5.57}d^{0.05}–sp^{2.75}$	$sp^{5.31}d^{0.05}–sp^{2.56}$, $sp^{5.39}d^{0.05}–sp^{2.58}$	$sp^{5.42}d^{0.05}–sp^{2.76}$, $sp^{5.38}d^{0.05}–sp^{2.83}$	$sp^{0.85}$, $sp^{0.86}$	0.914	0.938	0.880	0.994
	176	$sp^{5.61}d^{0.05}–sp^{2.68}$, $sp^{5.23}d^{0.05}–sp^{2.89}$	$sp^{4.93}d^{0.05}–sp^{2.52}$, $sp^{5.09}d^{0.05}–sp^{2.50}$	$sp^{4.62}d^{0.04}–sp^{2.21}$, $sp^{4.76}d^{0.05}–sp^{2.27}$	$sp^{0.97}$, $sp^{0.97}$	0.869	0.936	0.985	1.039

[a] Site indices are shown in Fig. 7.9

[b] The first group is for α-spin, and the second group is for β-spin, corresponding to the "different Lewis structures for different spins" description for open-shell cases

[c] This can be renormalized to p-rich $s^{0.05}p^{0.95}$ (α) and $s^{0.05}p^{0.95}$ (β) (see the text)

Table 7.4 Number of LP and LP* for all boomerang structures calculated by NBO analysis at the level of PBE/6-31 G*

X	Site[a]	LP[b]	LP*[b]	Difference[b]
C[c]	34	2	2	0
	176	2	2	0
	P2	2	2	0
	92	2	2	0
Si[c]	34	1	1	0
	176	2	2	0
	P2	4	4	0
	92	3	3	0
S[c]	34	7	5	2
	176	8	6	2
	P2	3	1	2
	92	3	1	2
Se[c]	34	6	4	2
	176	6	4	2
	P2	4	2	2
	92	4	2	2
B[d]	34	2, 0	2, 2	0, −2
	176	3, 1	3, 3	0, −2
	P2	2, 1	2, 3	0, −2
	92	3, 1	3, 3	0, −2
N[d]	34	3, 2	1, 2	2, 0
	176	4, 1	2, 1	2, 0
	P2	4, 2	2, 2	2, 0
	92	3, 2	1, 2	2, 0
P[d]	34	2, 1	0, 1	2, 0
	176	3, 1	1, 1	2, 0
	P2	3, 2	1, 2	2, 0
	92	3, 2	1, 2	2, 0

[a]Site indices are shown in Fig. 7.9
[b]In the case of open-shell species, there are two numbers, one for the α-spin orbital and the other for the β-spin orbital
[c]Closed-shell species
[d]Open-shell species

LP is doubly occupied while the LP* empty. As a consequence of delocalization, both the LP and LP* have one electron in each orbital. This valence picture can be extended to 1,3,5-hexatriene and even longer polyenes. For a more complicated system such as the all-C boomerang that has a two-dimensional surface compared to the one-dimensional polyenes, there can be higher numbers of LP and LP*, as shown in Table 7.4. It is worth noting that for the all-C structure, one LP is coupled with one LP*, and therefore the number of LP is equal to that of LP* (Table 7.4). However, this may not be the case for structures with other substitution atoms, as shown in Table 7.4. Another reason for the presence of two LP and two LP* on the all-C structure lies at the PBE96 functional used. It is commonly found that DFTs

Fig. 7.10 Resonance structures of 1, 3-butadiene (qualitative discussions, not obtained by NBO calculations)
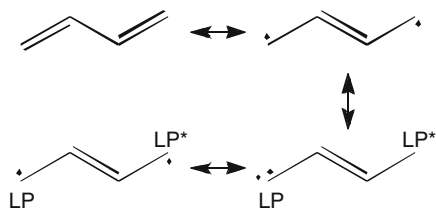
favors highly delocalized structures while greater mixing of Hartree–Fock exchange favors localized structures. Therefore, we also employed B3LYP, which has 20% Hartree–Fock exchange, for geometry optimization and NBO analysis, and found that an ideally localized structure can be obtained, which has no LP or LP*. Simply by comparing the bond lengths in the PBE- and B3LYP-optimized geometries (not shown), we found that the BLA of B3LYP is larger than that of PBE. Therefore it may be concluded that the numbers of LP and LP* are directly related to the BLA. In the following, we will focus on the PBE96 geometries for all substituted boomerang structures, since we are only concerned with the local valence structures at the four sites whereas the numbers of LP and LP* do not matter to our analysis.

For Si-substituted structures, the valence of Si is expected to be similar to that of C. However, we observe several differences. The substitution atom Si deviates from the local surface regardless of the substitution sites. It is also found that for this second-row atom, the hybridizations in the σ orbitals of Si are different from those of C structure in that there is a small admixture of d orbital in the sp^2 hybridization. Comparing all substitution atoms, we found that this is a common feature with second-row atoms including Si, P, and S (and with third-row atom Se), but is absent with first-row B, C, or N. Affected by the Si substitution, the immediate C neighbors have hybridization somewhere between sp^2 and sp^3. Another difference from all-C structure is that for Si$_{P2}$ and Si$_{92}$, Si does not form π bond with its immediate neighboring C atom. Its p orbital not involved in the above hybridization belongs to a non-Lewis LP* orbital. The observation that it is a non-Lewis rather than a Lewis LP orbital can be ascribed to the lower electronegativity of Si compared to C, which is also reflected by the natural atomic charges of more than one for Si. As we have addressed before, this LP* is not really an empty orbital but rather a high-occupancy non-Lewis orbital (occupancies for Si$_{P2}$ and Si$_{92}$ are 0.78 and 0.67, respectively). For Si$_{34}$ and Si$_{176}$, Si does form π bonds but the atomic orbitals of π bonds are not purely p orbitals, although the p components are rather high. Another way of presentation is to normalize the hybridization to the sum of 1. For example, for the Si$_{176}$ substitution, the NBO output of sp$^{37.63}$d$^{0.07}$–sp$^{62.37}$ for the π bond can be normalized as s$^{0.03}$p$^{0.97}$–s$^{0.02}$p$^{0.98}$, which in this case are p-rich orbitals with a small admixture of s components. The only similarity of Si with the all-C structure is that the number of LP is the same as that of LP* (Table 7.4).

With S and Se substitutions, similar to the Si-substitution cases, there are small degrees of d components in the hybridized σ orbitals of S and Se. In addition, the p components are rather high, giving rise to nontraditional hybridization type. Affected by this, even the neighboring C atoms have unusual hybridizations, with

p components higher than that of sp^3 in most cases. The LPs on S and Se are not of pure p character but rather appear to be sp hybridization. This can be ascribed to the fact that s orbital is not used up in the hybridized σ orbitals as can be seen from the relatively high p character in the hybridized σ orbitals; the residual s character is then used in the LPs. Comparing S and Se, it is interesting to find that Se has higher p components in the σ orbitals, which means lower s component, and therefore the LPs of Se have higher s and lower p components as compared to S. The occupancy numbers of LPs on S and Se are about 2 for all S and Se substitutions. The bond orders between S or Se and neighboring C atoms are all weaker than the C and Si cases, probably as a result of the absence of π bonds and larger deviation of the substituting atoms from the local surfaces in the S and Se substitutions. The most notable feature of S and Se substitutions is the natural atomic charge of about one. For a previously studied S-substituted C_{60}, that is, $C_{59}S$ [106], we have found that one of the three neighboring C atoms also has an LP and the natural atomic charge of S is also one. This valence of $C_{59}S$ may be depicted in a way that one of the σ bonds between S and a C is a dative bond, resulting in the atomic charge of one for S. In the boomerang structures, the LP on one of the three neighboring C atoms of S and Se is delocalized elsewhere. However, as can be seen in Table 7.4, the number of LP is higher than that of LP^* by two, which is the same as that found in $C_{59}S$.

Unrestricted calculations for open-shell species produce two sets of NBO results, one for the α-spin orbitals and the other for the β-spin orbitals (Table 7.3). The valence of B substitution is straightforward to understand. Each B undergoes sp^2 hybridization to form σ bonds. The p orbital not present in the above hybridization is left out as an empty orbital (α and β LP^*). The only unusual result is that the hybridizations of B's immediate carbon neighbors are slightly deviated from sp^2. Due to its lower electronegativity, B has positive natural charges regardless of substitution sites. Finally, for β-spin, in addition to B, one of its C neighbors also has an LP^* orbital. Therefore, the number of LP^* is higher than that of LP by two (Table 7.4).

The valence structures of N and P substitutions are similar to one another in the following terms. In both N and P substitutions, the hybridizations of C_A, C_B, and C_C are closer to sp^3 than to sp^2 category, which is also the case for Si substitution. In addition, as a result of the additional valence electron of N and P, as compared to C, there is no π bond between N or P with their immediate C neighbors. This is also the reason that the number of LP for α-spin orbitals is higher than that of LP^* by two, as can be seen in Table 7.4. The differences between N and P substitutions are summarized as follows: (a) Although the hybridization of N still belongs to sp^2 category, the p component of each P hybridization is greatly enhanced, giving rise to a nontraditional hybridization type with relatively low s components; (b) for second-row P atom, there are a small admixture of d orbital, which is a common feature found for second- and third-row atoms including Si, P, S, and Se; (c) the LPs on N are purely p orbitals in N_{34} substitution and are p-rich orbitals with a small admixture of s characters in other substitution cases [e.g., the NBO output of $sp^{19.39}$ (α) and $sp^{18.40}$ (β) for N_{P2} can be normalized to p-rich $s^{0.05}p^{0.95}$ (α) and $s^{0.05}p^{0.95}$ (β)] while the LPs on P are primarily sp category; and (d) finally, the difference in

natural atomic charges may be ascribed to the difference in electronegativity. On the basis of the present calculations, it can be seen that the valence structures of N and P in the boomerangs are similar to those in previously studied $C_{59}N$ and $C_{59}P$ [106].

7.3.4 Heterojunctions

Heterojunctions between different materials are of increasing interest in nanotechnology. For creating devices on the nanoscale, different structures have to be joined such as to obtain junctions with predefined properties. Junctions between carbon nanotubes (CNTs) and metal or semiconducting nanowires are not only desirable to exploit the electronic and mechanical properties of CNTs. In electronic devices, conductive contacts between the graphitic network of CNTs and metallic electrodes need to be established in order to link the nanotubes with each other and their periphery. To date, most results indicate that the behavior of such a device is dominated by the electronic processes taking place at the nanotube–metal contact. For instance, the resistance of the ohmic contact or Schottky barrier effects are influenced by the type of interface between metal and the graphitic structure. In some previous studies, multiwall carbon nanotube (MWNTs) interconnections with metal electrodes only occurred with the outermost wall of MWNTs. A robust mechanical connection in such a junction cannot be expected, nor can the inner walls of MWNTs participate considerably in charge transport. Therefore, detailed knowledge regarding the nature and strength of bonding as well as the morphology and electrical properties of contacts is important because it is vital to connect all concentric cylinders of a MWNT, across the entire cross section of the nanotube, to a metal particle. Hence, a covalent nanotube–metal junction would allow one to attach nanotubes firmly to metal pieces which is useful for achieving well-defined electrical contacts and also for attaching nanotubes firmly to metal supports for the realization of ultrastrong nanotube ropes in mechanical systems.

Recent studies have reported examples involving graphitic material interfaced with metal particles for Co crystals and nanotubes, Fe particles with amorphous carbon pillars, and W or Pt particles and MWNTs. An interface between carbon nanotubes and metal particles was also observed during the growth of nanotubes from catalytically active metals. However, the structure of the interface and the nature of bonding between metal and carbon remained unclear. This is not only important for predicting and understanding the electrical or mechanical properties of the junctions but also for exploring the growth of nanotubes from catalytically active metal particles where the nucleation and growth of the tube occurs through such an interface.

We recently reported the controlled formation and characterization of heterojunctions between carbon nanotubes and different metal nanocrystals (Fe, Co, Ni, and FeCo) [114]. The heterojunctions are formed from metal-filled multiwall carbon nanotubes (MWNTs) via intense electron beam irradiation at temperatures in the
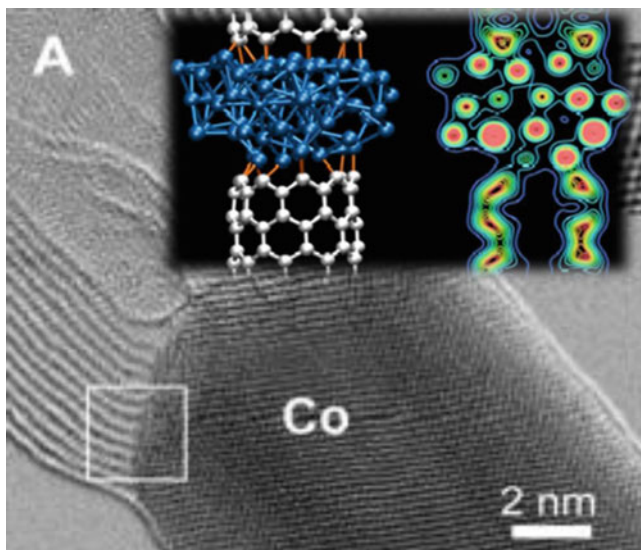
Fig. 7.11 HRTEM image of a heterojunction formed between multiwalled carbon nanotubes and cobalt metal following e-beam irradiation and thermal annealing. The overlay of the computed interface structure and charge density contours highlights that the interface is formed via covalent bonding (Reproduced from Ref. [114]. With kind permission of © PNAS 2009)

range of 450–700°C and observed in situ in a transmission electron microscope. Under irradiation, the segregation of metal and carbon atoms occurs, leading to the formation of heterojunctions between metal and graphite (see Fig. 7.11). Metallic conductivity of the metal–nanotube junctions was found using in situ transport measurements in an electron microscope. Density functional calculations show that these structures are mechanically strong (Table 7.5), the bonding at the interface is covalent (wavefunction showing localized electron density at the interface between the metal and carbon as seen in the figure), and the electronic states at and around the Fermi level are delocalized across the entire system. These properties are essential for the application of such heterojunctions as contacts in electronic devices and vital for the fabrication of robust nanotube–metal composite materials.

Table 7.5 lists the computed binding energies for a single benzyl radical on various transition metal surfaces and that for a (9,0) SWCNT–Co(111) interface. Note that it appears there is in general a chemical bond formed even for a single benzene radical, with binding energies larger for the metals with less filled d orbitals (left side of the periodic table; also these are more stable in a flat orientation, which are not shown in the table). For the Co-(9,0)–SWNT, the total binding energy is quite large, 68.46 eV, and if we assume that there are 9 bonds formed (# dangling bonds), the bond energies are 7.6 eV. From the interatomic distances, it actually appears that there are reasonably strong multicenter Co–C interactions (as many as 3 per/carbon), which is likely why the binding energy is so large. Taken

Table 7.5 Computed adsorption energy (eV) for a phenyl group on different transition metal surfaces and sites

Surface[a]	Lattice type	Upright E_{ad}[b]	Site
Ti(0001)	hcp	2.81	Bridge
V(111)	bcc	2.60	Atop
Fe(110)	bcc	1.78	Bridge
Cu(111)	fcc	1.21	Bridge
Au(111)	fcc	1.04	Atop
Pd(111)	fcc	1.62	Atop
Si(111):H[c]	Diamond	3.04	Atop
Co(111)	hcp	2.02	Atop
Ni(111)	ccp	2.10	Atop
Co(111)–CNT[d]	hcp	68.46	Mostly atop

[a]C_6H_5 coverage is at 0.111 molecule per surface atom for all surfaces here
[b]$E_{ad} = E(surface) + E(C_6H_5) - E(C_6H_5/surface)$, eV
[c]Hydrogenated Si(111) surface
[d]Interface between a 3-layer cluster of Co(111) and a single-walled (9,0) carbon nanotube (binding energy is given as the total)

together with the experimental data, the results computed demonstrate that robust interconnections can be efficiently formed between multiwall carbon nanotubes and demonstrate a heterojunction consisting of covalent bonding across the interface. This breakthrough provides a key step toward enabling carbon nanotube-based electronic devices as it allows a way to make the required connections to metallic contacts.

Graphene: The ability of carbon atoms to adopt sp^2 hybridization dictates many structural and physical properties of carbon materials, for example, the stability of a graphene sheet. Recent advances in graphene-based materials exemplify the many possibilities brought about by the simple hexagonal structure of a graphene sheet. Carbon-based materials have found an enormously wide range of practical applications. In particular, they have played a crucial role in fuel cells, molecular electronics, separations, and catalytic systems. One important means to further expand their potential is to functionalize their surfaces.

We have studied the interaction between a phenyl group (C_6H_5) and a graphene sheet using first-principles gradient-corrected DFT [115]. The results demonstrated that isolated C_6H_5 groups are weakly bonded to the basal plane, comparable to physisorption, whereas a pair of C_6H_5 molecules, located at the *para* positions of the same graphene ring, is significantly more stable. We also demonstrated the high reactivity of edge sites for aryl attachments: A 1,2-addition pair is predicted to be most stable for the armchair edge, whereas the zigzag edge, which possesses a unique localized state near the Fermi level, shows a higher affinity for an isolated phenyl group. Our calculations provide support for the experimental observation that edge sites of graphite are more reactive than the basal plane during the aryl

diazonium-grafting process. Such enhanced chemical reactivity can be useful for carbon-based catalysis processes or for the formation of robust heterostructures for composite materials.

The importance of an edge to a graphene sheet parallels that of a surface to a crystal. Cutting through an infinite graphene sheet, one first breaks C–C σ bonds and then obtains two semi-infinite graphene sheets, each with a one-dimensional edge. The dangling σ bonds at the edges can be saturated with hydrogen (so-called hydrogenated or hydrogen-terminated edges), and all the carbon atoms remain sp^2 hybridized. Depending on the cutting direction, two unique types of edges can be obtained: zigzag and armchair. The cutting also introduces a boundary at the edge to the previously fully delocalized π-electron system. The zigzag edge of a graphene nanoribbon possesses a unique electronic state that is near the Fermi level and localized at the edge carbon atoms. We have investigated the chemical reactivity of these zigzag edge sites by examining their reaction energetics with common radicals from first principles. The results show that the ground state of the zigzag-edged ribbons is antiferromagnetic (AFM) while the ferromagnetic state is only slightly higher in energy [116]. In the AFM phase, the carbon atoms at the edges are found to have a magnetic moment of ∼0.14 μB, and the local density of states at these carbon atoms shows a strong peak just below the Fermi level for the majority spin and another just above the Fermi level for the minority spin. These features result from the localized electronic state at the zigzag edges and led us to propose a "partial radical" concept to characterize the chemical reactivity of those zigzag edge carbons [117]. By computing the bond dissociation energy (BDE) of the bonds formed between the edge carbon and common radicals, we found that the edge C–X BDE (X = H, OH, CH3, F, Cl, Br, and I) is 40–80% of the experimental (sp3)–X BDE, and thus demonstrated the validity of this partial radical concept. By comparing the zigzag edge's C–H BDE with those of a graphene sheet, nanotubes, and the armchair edge, we showed that the zigzag edge is indeed unique in that it has the highest BDE, at least 1.2 eV stronger than the others, due to the presence of the edge state near the Fermi level.

Although graphene has novel and outstanding electronic properties, which could significantly advance nanoelectronics in the near future, variations in thickness (stacked sheets) and edge shape or the presence of defects could significantly modify the electronic properties of graphene [16]. It is therefore imperative to control both the number of stacked layers (thickness) and in particular the edge geometry, in order to optimize the electronic properties and in turn facilitate applied nanodevice design. Graphene can be synthesized by a variety of methods and subsequently modified by lithographic techniques in order to fabricate electronic devices at the nanoscale. .

Various techniques have been used to engineer and control the atomic structure of carbon nanostructures, such as electron and ion beam irradiation, as well as Joule heating. It has been shown that electron irradiation can be effective in removing graphene monolayers from a multilayer material. Subnanometer-scale defects, such as pentagons and heptagons within the honeycomb lattice, have been shown to be crucial for creating functional 1D, 2D, and 3D nano- and micromaterials via
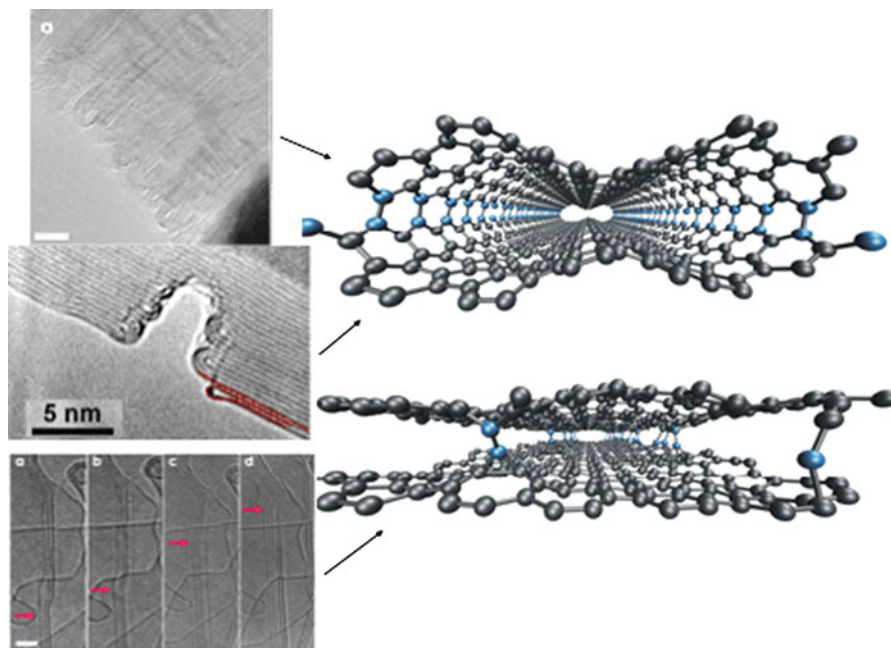
Fig. 7.12 Graphene ribbon structures formed under different experimental conditions: *left panels, top* showing loops formed following either thermal annealing or Joule heating, *bottom* showing edge reconstruction during Joule heating without loop formation heating. *Top right panel* shows a summary of quantum MD simulations where loop formation predominates unless the initial graphene layers have vacancies, interstitials, and Frenkel pairs presence (*bottom right*)

cross-linking carbon nanotubes and multilayer graphene and by graphene edge reconstruction. Important structural changes can also be induced by the controlled knock-on of individual carbon atoms, as illustrated recently with aberration-corrected scanning transmission electron microscopy (AC-STEM) experiments. A number of studies have shown that the *combined* effect of electron irradiation and high temperature could lead to structural modifications and functionalization of sp^2 hybridized carbon nanostructures. For instance, electron irradiation in the transmission electron microscope (TEM) at high temperature yields coalesced carbon nanotubes of large diameters, molecular junctions, and corrugated tubular structures from carbon nanopeapods. In striking contrast with these experiments, where the irradiation is applied locally and the temperature is controlled by heating the entire sample holder, sharp nanoribbon edges are formed when heat is provided by a controlled, directional high electrical current density after sample exposure to electron irradiation (see Fig. 7.12, bottom left). While the need for local heating has been rationalized using electronic transport theory, the role of electron irradiation has been largely ignored in existing models. Finally we note that experimental studies have reported that loops only form along zigzag edges and not along armchair edges, as observed in highly oriented pyrolytic graphite (HOPG) samples.

Treatment by Joule heating alone, that is, without prior irradiation, enables the reconstruction of individual edges in graphene by creating bilayer and even trilayer looped edges (Fig. 7.12, top and middle left), a situation that is also encountered with high-temperature thermal treatments, in contrast with the results discussed in Ref. [16]. These results may seem contradictory since no explanation had been provided to account for loop versus nonloop formation along the edges of graphene structures. In this respect, it is important to recognize that there are critical differences in the two studies, even though the samples were synthesized with identical procedures. Notably, the samples from Ref. [16] were first irradiated for 20 min using an electron beam with a current density of 100 A/cm^2 and accelerated at 200 keV.

We recently highlighted the critical role of electron irradiation in preventing the formation of bilayer loop edges in graphene materials (Fig. 7.12, right) [118]. The understanding was achieved by using extensive ab initio quantum molecular dynamics simulations and quantum transport calculations enabled through large-scale computing and demonstrates that vacancies and interstitials are key for keeping graphene layers parallel and preventing bilayer edge coalescence (looping). The role of vacancies is to increase the surface reactivity and interlayer interactions far from the edges. Interstitials, on the other hand, provide effective feedstock for interlayer link creation that keeps bilayers parallel and prevents looping. Notably, it is the combination of vacancies and interstitials that keeps the edges open and avoids loop formation. Quantum transport calculations confirm that cross-linking of bilayers increases the backscattering and creates significant transport between the layers. These cross-linking sites are key for the Joule heating defect cleansing and are susceptible to being healed during the process.

Overall, this work provided a rationale/mechanism explaining why loops do form if Joule heating is used alone and why adjacent nanoribbon layers do not coalesce when Joule heating is applied after high-energy electrons first irradiate the sample. Our work, based on large-scale quantum molecular dynamics and electronic transport calculations, shows that vacancies on adjacent graphene sheets, created by electron irradiation, inhibit the formation of edge loops (see Fig. 7.12).

7.3.5 Self-assembly and Optoelectronics

Recently, considerable effort has been devoted to studying nanoscale structure–property relations of π-conjugated organic polymers, as they may serve as active components in future large-area as well as nanoelectronic devices. Conventional organic synthesis can create conjugated polymers of practically any length and structure [119, 120], yet their controlled positioning on a surface presents an ongoing challenge. Individual polymers can be positioned using a scanning probe tip, but a device cannot be assembled in this manner within a practical timescale. Alternatively, surface-confined conjugated polymers can be grown directly on crystalline substrates. Although electrochemical polymerization on conducting surfaces

has long been used to prepare films of conjugated polymers such as polythiophene [121, 122], only recently the techniques for preparation *and* characterization of aligned arrays of the polymers have been developed. Promising results were obtained using UV irradiation [123] or scanning probe microscopy (SPM) tip pulsing [124] to form polydiacetylenes and, recently, surface-catalyzed coupling to form polyphenylene [15]. However, these polymers have not been demonstrated to be useful in a device context; most notably, they are not good conductors [125, 126]. More electronically relevant ordered polythiophene wires have been prepared by pulsed electrooxidative polymerization of substituted thiophenes [127, 128]. The symmetry of the employed Au(111)/I_2 substrate confines the polymer growth along one of the three crystallographic axes, although the linear structure of the polymer is perturbed by the kinks induced by occasional *syn* conformation of thiophene–thiophene links.

Poly(3,4-ethylenedioxythiophene) (PEDOT) is the most industrially important conducting polymer [121, 129, 130] due to its combined characteristics of high electrical conductivity, high transparency, and exceptional stability in its doped (conducting) state. It is widely used in the fabrication of electroactive devices [131], in particular for organic light-emitting diodes and photovoltaic cells, but also sensors, electrochromics [132], and as an oxygen reduction catalyst [133]. There has been a significant interest in using PEDOT in nanoelectronic devices, although the existing methods for preparing nanostructured PEDOT materials are limited to relatively large structures lacking molecular order.

Using in situ STM imaging combined with first-principles DFT calculations, we demonstrate the surface-confined growth of ordered arrays of poly(3,4-ethylenedioxythiophene) (PEDOT) chains [15]. This is achieved by using the 110 facet of copper simultaneously as a template and catalyst for polymerization. The method is demonstrated to provide a facile method to assemble aromatic building blocks into ordered structures and is extendable to other halogen-terminated molecules to produce the unique epitaxially aligned conjugated polymers. These types of systems could be of central importance to develop future electronic and optoelectronic devices with high-quality active materials. The very high resolution of *in situ* STM imaging combined with first-principles DFT calculations allowed the explicit polymerization process to be visually followed, from the formation of a reactive intermediate, to the formation of monomers, dimers, trimers, tetramers, and longer oligomers, one monomer unit at a time (see figure). The strong molecule–surface interactions dictate that all monomer units orient in an upright position with the sulfur atom pointing toward the substrate (see Fig. 7.13), leading to an unexpected and previously unobserved all-*cis* conformation of the PEDOT chain. The polymerization process is controlled by the classical Ullmann dissociative coupling mechanism, where the substrate itself acts as a catalyst, thus suggesting a general approach for this type of reaction. This demonstrated capability should be particularly useful in the controlled growth of novel 2D conjugated organic structures, which are currently the focus of widespread research in optoelectronics and light harvesting.
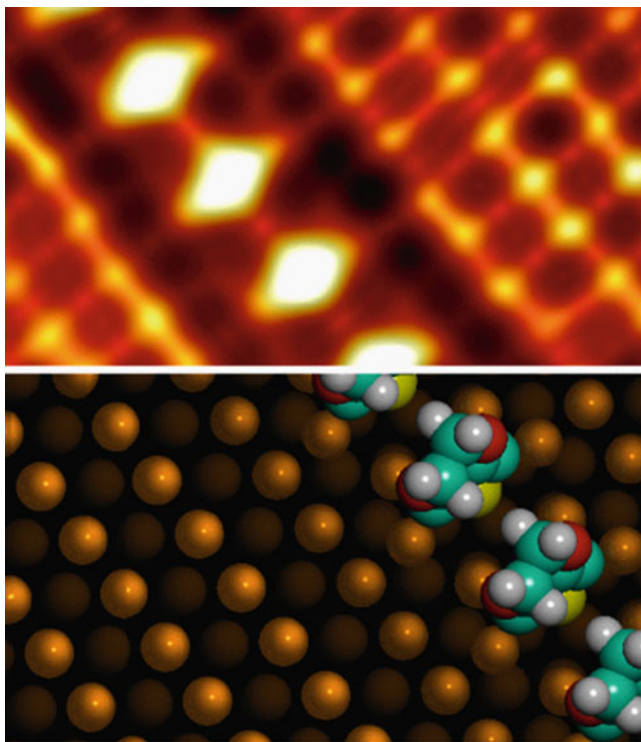
Fig. 7.13 STM image of a Cu(110) facet following epitacial self-assembly of DIEDOT monomers (*top*). Ab initio computed geometries and adsorption sites are shown in the *bottom panel*

7.3.6 Supramolecular Organic Wires and Modified DNA-Based Structures

"Unconventional" donor–acceptor molecules, 1-aza-adamantanetriones (AATs) **1**, have emerged as vehicles to probe through-bond interactions "beyond-the-molecule" and constitute a new class of organogelators [134–137]. Theoretical studies have explored the mechanism of AAT self-assembly and the electronic structure that arises should the molecules (e.g., **1a** and **1b**) organize into periodic 1D structures that feature close core-to-core interactions. With a goal to create well-ordered assemblies of the AATs and probe their supramolecular electronic properties, one approach is to enhance the interactions between the peripheral substituents (R groups in **1**). Some of the diverse possibilities are shown in **1**, each of which imparts different properties to the solid-state self-assembled structures. In order to explore this large diversity, computational methods have proven invaluable.
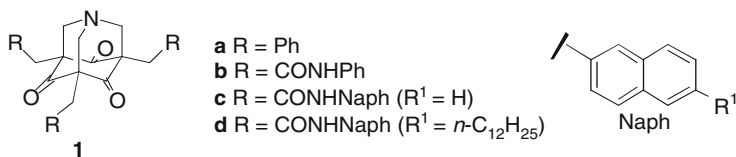
Overall this work has, through a joint theoretical and experimental effort, (a) developed efficient synthetic strategies to novel donor-σ-acceptor molecules (and their precursors) that form robust, networked assemblies in solution (organogels; see Fig. 7.14, bottom right panel), (b) shown that molecular-level structural perturbations that arise from or otherwise influence through-bond (hyperconjugative-type) donor–acceptor interactions have consequences on solid-state and supramolecular assembly structure, and (c) revealed that intermolecular orbital delocalization (Fig. 7.14, top left panel) is conceivable for self-assembled donor-σ-acceptor molecules where the accompanying electronic structure shows promise for semiconductive organic materials applications (Fig. 7.14, top right panel) [134, 135]. The results have clearly demonstrated that the one-dimensional arrangements of these molecules (Fig. 7.14, top right panel) have novel electronic properties that are tunable by either direct chemical substitution or by electron doping, thereby enabling this class of supramolecular materials to offer attractive opportunities for semiconductor devices [134].

In biological systems, self-assembly, organization, and molecular recognition are prominent, ranging from protein folding to antigen–antibody interactions. Nanobiotechnology holds the promise of heralding unprecedented advances in medicine and for understanding fundamental aspects of biology. We have recently explored aspects of these processes by focusing on the structural, optical, electronic, and conductivity properties of unnatural bases, base pairs, and the DNAs they make up, that is, size-expanded and metalated DNAs.

Size-expanded DNAs are composed of DNA base analogues that can be described as a fusion between benzene or naphthalene and a DNA natural base (see Fig. 7.15). There are three types of size-expanded DNAs. xDNA [138–144] and yDNA [145–147] are made of benzo-homologated bases (referred to here as x- and y-bases, respectively). yyDNA [148] is made up of naphtho-homologated bases (yy-bases). Our interest in size-expanded duplexes was motivated by two facts. On one hand, these duplexes preserve the recognition properties, a necessary requisite for creating DNA-like nanostructures. On the other hand, size-expanded DNAs have higher melting points than natural DNAs, which is a consequence of the former having stronger π–π stacking interactions than the latter. Having higher melting points implies higher stability, and having stronger π–π stacking interactions implies having a more efficient band conduction mechanism. Thus, we decided to investigate the unnatural duplexes using first-principles techniques. Due to the complexity of the problem, we decided to start by simpler systems, that is, the size-expanded bases, and investigate their structure and electronic properties.
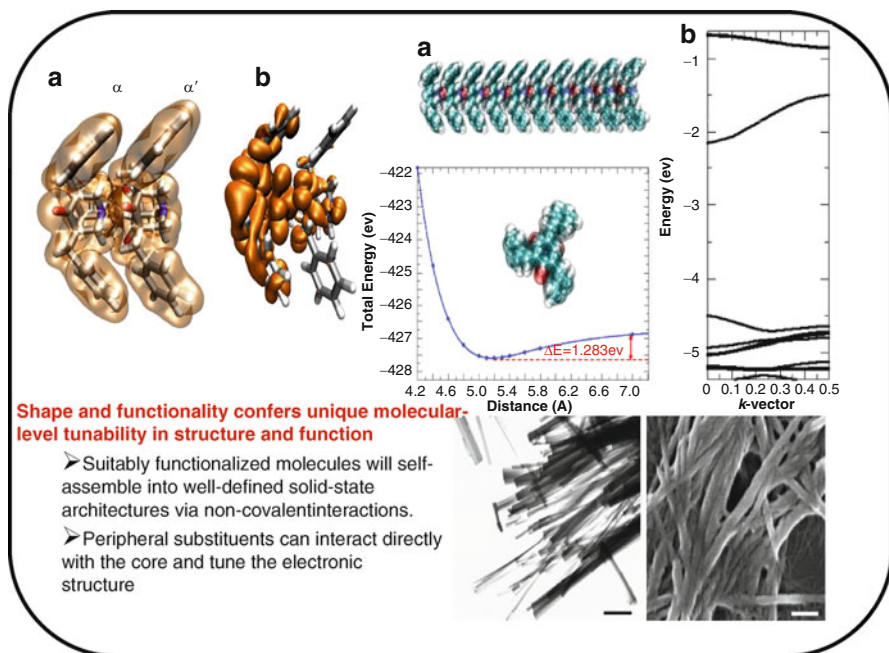
Fig. 7.14 Results summarizing a joint experimental and computational study of the self-assembly of a new class of donor–acceptor organic nanowires. The emergent electronic structure for these materials demonstrates tunable semiconducting properties (Reproduced from Ref. [134]. With kind permission of © The American Chemical Society 2007)
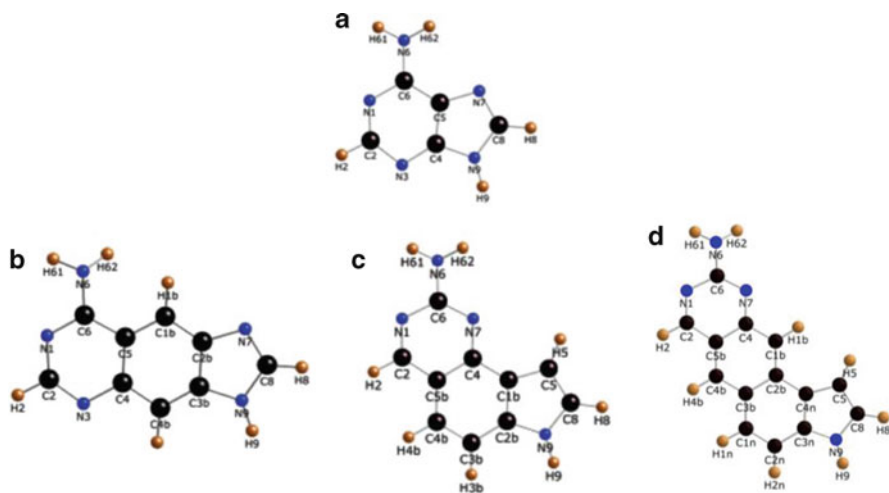
Fig. 7.15 Expansion of the adenine base. (**a**) Adenine, (**b**) xA, (**c**) yA, and (**d**) yyA

Table 7.6 HOMO and LUMO orbital energies and HOMO–LUMO gap (in eV) for the x-, y-, and yy-bases calculated at the LDA/6-31G** level

Base	HOMO	LUMO	Gap
Adenine			
A	0.56	4.44	3.88
xA	0.72	3.62	2.90
yA	1.21	4.09	2.89
yyA	1.35	3.52	2.17
Thymine			
T	0.10	3.97	3.87
xT	0.22	3.62	3.40
yT	0.00	3.55	3.55
yyT	0.37	3.15	2.78
Guanine			
G	0.81	4.81	4.00
xG	0.89	4.05	3.16
yG	1.46	3.95	2.50
yyG	1.62	3.38	1.76
yyG-AO3	1.04	3.55	2.51
Cytosine			
C	0.50	4.14	3.63
xC	0.58	3.62	3.04
yC	0.90	4.10	3.19
yyC	0.81	3.48	2.67
yyC-AO3	0.88	3.53	2.65

The energies are given relative to the HOMO of yT (-5.92 eV). For comparison purposes, we also show the HOMO and LUMO orbital energies and HOMO–LUMO gap for the natural bases

Table 7.6 shows the HOMO–LUMO gaps, as obtained with *ab initio* techniques, of the x-, y-, and yy-bases and that of their natural counterparts [149–153]. Figure 7.16 summarizes this data. Clearly, expanding the natural DNA bases, by fusing them to a benzene or naphthalene motif, reduces their HOMO–LUMO gap. The same is true for the whole duplex: Fig. 7.17 shows that xDNA has a smaller HOMO–LUMO gap than a natural DNA with the same sequence [155]. Whether or not size-expanded DNAs could be an alternative to DNA for molecular-wire applications remains to be seen. We hope that our studies will motivate experimental studies aimed at measuring the conductivity of these duplexes.

Metalated DNAs, and in particular M-DNA, are one of the other unnatural duplexes that we have considered. M-DNA was discovered by Lee et al. in 1993 [156], and in 1999 Aich et al. proposed that the structure of M-DNA is very similar to that of DNA, except for a chain of metal atoms that runs in the center M-DNA's helix [157]. The metals' atoms replaced the imino proton of G and A (the imino proton is released by raising the pH), and thus the metal atoms are intercalated in between the G-C and A-T base pairs, as in G-M-C and A-M-T, (M = Zn, Ni, Cu). In 2001, Rakitin et al. [158] showed, experimentally, that Zn–DNA conducts
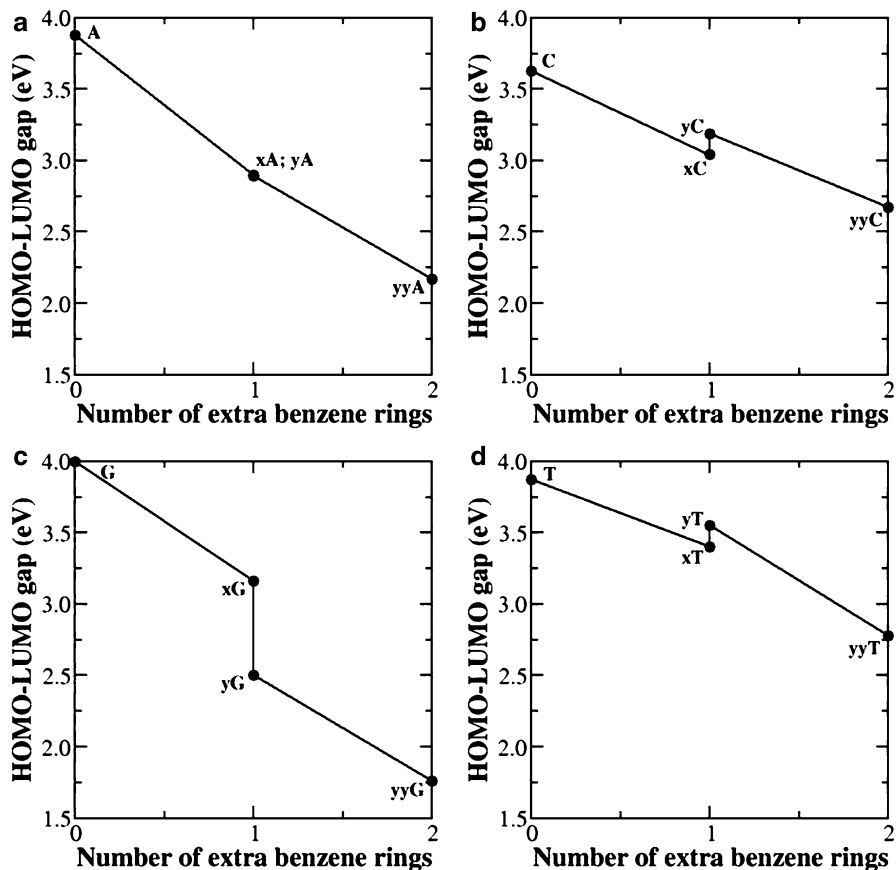
Fig. 7.16 HOMO–LUMO gap versus number of extra benzene rings for A, C, G, T, and their benzo- and naphtho-homologated analogues (Reproduced from Ref. [154]. With kind permission of © The American Chemical Society 2008)

better than a DNA duplex with the same sequence. If the experimental results were to be confirmed, M-DNA would certainly be very attractive for nanotechnological applications. For example, one can envision building any type of 2D structure made of DNA, raise the pH while adding metals, and convert this DNA-based nanostructure into a metallic one based on M-DNA. The problem is that to confirm the experimental results, one must first understand the structure of M-DNA, and this has not been done so far. Thus our first objective was to probe Lee's structural model for M-DNA. For simplicity, we decided to focus on the G-Zn-C base pair. In Ref. [159] we investigated eight models for this base pair, including the one proposed by Lee et al. We found that neither of the models remained planar: They all prefer to buckle, indicating that having metals in the duplex might render the helix unstable. Not only this, we also found that neither of the models has electronic properties suggestive of better conduction. In particular, Rakitin et al. argued that
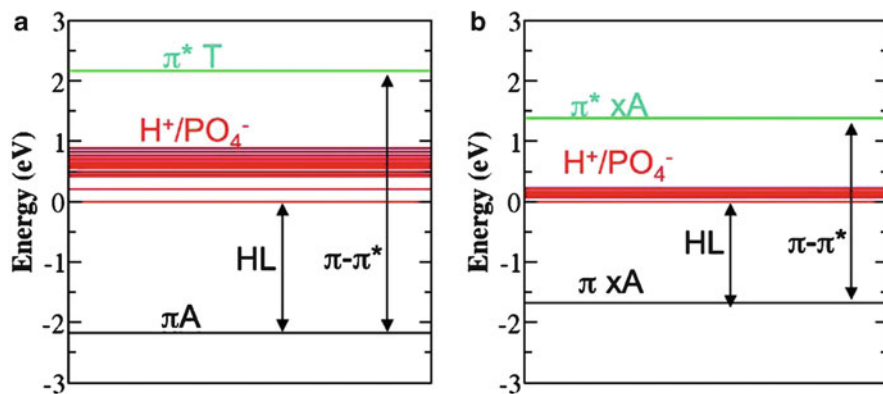
Fig. 7.17 Energy level diagram of (**a**) B-DNA and (**b**) xDNA. The energies are given relative to the LUMO. The HL and $\pi-\pi^*$ gaps are denoted by *arrows* (Reproduced from Ref. [155]. With kind permission of © The American Chemical Society 2007)

the better conductivity of M-DNA is due to the alignment of the Zn-d states with the Fermi level of the Au electrodes in between which M-DNA was sandwiched. We found that the Zn-d level states are deep into the valence band, making it difficult to argue that such states could ever be aligned with the Fermi level of the surrounding Au electrodes. It seems to us that the conductivity of M-DNA could be due to other factors. For example, it could very well be that the Zn metal atoms are attached to the phosphate backbone, and that this increases the conductivity. Any other structural model for M-DNA that places the metal inside of the helix seems to us less plausible.

Finally, we have considered the possibility of modifying DNAs by suitable chemical modifications that might enhance its conductivity properties. In particular, recently Salon et al. demonstrated that it is possible to make a DNA duplex with a thymine base that has one of the O atoms replaced by Se [160]. We used theoretical techniques to investigate the electronic properties of this Se–DNA duplex, and we found that this duplex could certainly be a good candidate for molecular-wire applications [154].

7.3.7 Thermal Decomposition of Lignin Model Compounds (Models for Biomass)

One possible route to a sustainable future is the use of biomass as an alternative energy and chemical supply. There are many advantages biomass has to offer over fossil fuels: Biomass is renewable, carbon dioxide release in the atmosphere is reduced by carbon dioxide consumption during plant growth, other harmful gas emission is low, and there is a wide range of raw material available. Essential for a successful integration of biomass in our economy is the creation of an infrastructure, including

Fig. 7.18 PPE (R_1,R_2, R_3,R_4,X,Y = H) and PPE derivatives with naturally occurring substituents

$$R_1, R_2, R_3, R_4 = H, OH, OCH_3$$
$$X = H, OH \quad Y = H, CH_2OH$$
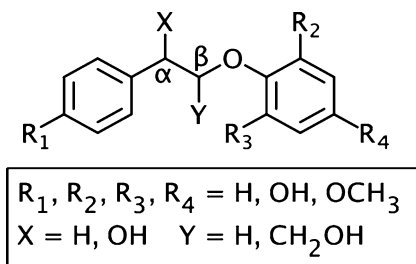
production, storage, waste management, and transportation. This requires the understanding of underlying reaction mechanisms, development of catalysts, and innovative engineering. An underused but major component of biomass is lignin, which is an amorphous, polyphenolic, three-dimensional network. Pyrolysis is one of the most important processing techniques of lignin, but is also highly complex due to the intricate structure of lignin and the dependence on origin and isolation technique. A common approach is to use model compounds, representing the various linkages in lignin, to obtain mechanistic insight into the thermal conversion process.

The β-O-4 linkage is by far the most common linkage in lignin, and its simplest model is phenethyl phenyl ether (PhCH$_2$CH$_2$OPh, PPE), shown in Fig. 7.18. Several mechanisms for the thermolysis of PPE were discussed in the literature [161–164]. At moderate temperatures (330–425°C), Britt et al. [165] determined that the thermal decomposition of PPE in the gas phase, in the neat liquid, and in solution proceeds through a radical chain mechanism. Two competitive pathways, defined as the α/β-selectivity, contribute to primary product formation through hydrogen abstraction on the α- and β-carbon, respectively; see Fig. 7.18. In a subsequent work, Britt et al. [166] studied the influence of substituents on the pyrolysis mechanism and found that the radical mechanism still holds with modified rates of reaction and α/β-selectivities. Substituents can perturb all key steps in the mechanism and are difficult to analyze experimentally.

In our computational studies, we probe individual steps of the radical chain mechanism, explain the origin of substituent effects, and provide kinetic data for major reaction steps. Depending on the substituent distribution, a simplified kinetic model is applicable to predict the α/β-selectivity. In other cases, kinetic data of all participating reactions is necessary to obtain product distributions through numerical integration of the corresponding rate equations.

Transition state theory (TST) in combination with cost-effective DFT provides a framework for the calculation of rate constants for medium-size systems. However, the computation of rate constants is a challenging task: Small inaccuracies in the activation energy result in large errors in absolute rate constants, the harmonic approximation for low-frequency vibrational modes can lead to significant discrepancies in entropic contributions, and errors intrinsic to TST include the neglect of barrier recrossing and tunneling (the latter is often accommodated with a correction factor). Fortunately, when a series of reactions is modeled, the product distribution depends on relative rates where we can profit from the cancellation of systematic

errors. Whereas errors in the calculation of energies are expected to be systematic, errors in the computation of the entropic contribution due to anharmonicities in low-frequency modes are not. We implemented anharmonic corrections for low vibrations (typically up to 110 cm^{-1}) within the independent mode approximation. Anharmonic potentials are obtained by displacement along the normal mode vector, and the vibrational partition function is calculated using the semiclassical Wigner–Kirkwood expansion. We found that the semiclassical partition function is an excellent approximation to the one-dimensional quantum partition function when we examined in detail various one-dimensional partition functions of a relevant transition state in the pyrolysis of PPE in the experimental temperature range [167].

We use the NWChem program package [10] for electronic structure calculations and our own Python code interfaced to NWChem for the computation of the TST rate constants including a Wigner tunneling and anharmonic corrections. In earlier works [168, 169], we utilized the B3LYP functional [170, 171], and in more recent studies [172–174], we use the M06-2X functional [47], which is more suitable to describe medium-range correlation. A mixed basis set is employed for optimizations and frequency analysis, where a 6-31G* basis is centered on each atom except where the unpaired electron is located, for which diffuse functions are added. A 6-311++G** basis set is used for energy calculations.

The initial step of the pyrolysis of PPE is the homolytic cleavage of the weakest bond in the system [165], the carbon–oxygen bond (PhCH$_2$CH$_2$–OPh) and to a smaller extent the carbon–carbon bond (PhCH$_2$–CH$_2$OPh). The homolysis rate and the carbon–oxygen/carbon–carbon selectivity depend primarily on the corresponding bond dissociation enthalpies because the reverse reactions are expected to have low reaction barriers. Both quantities can be strongly influenced by naturally occurring substituents. We calculated bond dissociation enthalpies (BDEs) for an array of PPE derivatives with substituent combinations derived from Fig. 7.18 [172, 175]. We found that the carbon–oxygen BDE for PPE is 7.6 kcal/mol lower than the carbon–carbon BDE at 618 K, which translates to an approximate C–O/C–C homolysis ratio of about 500:1. If a hydroxy substituent is located at the α-carbon position, the homolysis ratio is reduced to about 10:1. In contrast, if a methoxy substituent is located at the phenyl ring adjacent to the ether oxygen, the contribution of the carbon–carbon dissociation becomes vanishingly small. The carbon–oxygen BDEs are little altered by substituents on the phenethyl ring and by aliphatic substituents (0.1–1.7 kcal/mol). However, if substituents are located at the phenyl ring adjacent to the ether oxygen, the carbon–oxygen BDEs are significantly reduced (up to 8.6 kcal/mol for di-o-OCH$_3$ substituents) and the C–O homolysis rates increase by orders of magnitude depending on the temperature. The carbon–carbon BDEs are generally less sensitive to substituent effects (up to 2.4 kcal/mol increase or decrease compared to PPE). Often, substituent effects in BDEs are thought of as being additive. However, we found that if a hydroxy substituent is located at the α-carbon and a methoxy substituent at the *ortho* position of the phenyl ring adjacent to the ether oxygen, their effects cancel. This contradicts an argument in the literature [176] that DFT is insufficient to study lignin model compounds. No influence of o-methoxy groups in derivatives, where additional α-OH and β-CH$_2$OH

Fig. 7.19 PPE with multiple substituents; hydrogen bond lengths are given in Å
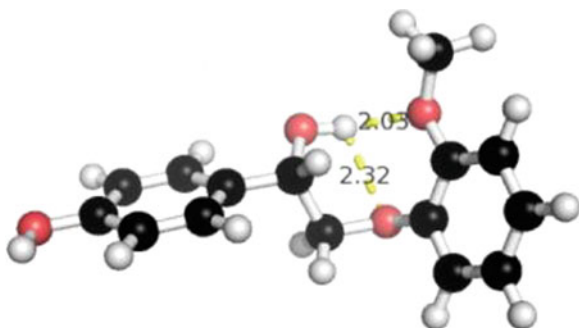
substituents were located on the ether bridge, were observed. Since higher-level methods were used in [176], the BDE reduction in our previous work [172] was attributed to the inability of DFT to predict BDEs in PPE derivatives. This is not the case, but in fact, the hydrogen bond formed between the α-hydroxy group and the *o*-methoxy substituent (see Fig. 7.19) decreases the effect of the methoxy group and increases the BDE by partially restoring the aromaticity, which is diminished by the methoxy substituent, and by the need to break an additional hydrogen bond during bond dissociation.

In a different study, we investigated the hydrogen abstraction reactions occurring in the pyrolysis of PPE and PPE derivatives, where a hydroxy and methoxy substituent is located in the R_1 position (see Scheme 7.1) [168]. The hydrogen abstraction reactions are the rate-determining steps of the radical chain propagation and proceed through two distinct channels, the α- and β-channels, as mentioned above. If the interconversion between the abstraction products, the α- and β-radicals, is negligible and if we assume steady-state conditions for intermediate radicals, we can derive a simplified kinetic model, where the α/β-selectivity of the entire PPE pyrolysis depends on the relative rate constants of the α- and β-hydrogen abstraction for each radical only. Because the computation of these rate constants involve reactions of the same reactants proceeding through similar transition states, cancellation of systematic errors can be exploited particularly effectively. To calculate the rate constants, we need to locate all contributing transition states. There are two equivalent α- and two equivalent β-hydrogen atoms in PPE, and each radical (phenoxy and benzyl) has two equivalent sides of radical attack. When substituents are introduced, the symmetry is reduced and the conformational space increases. Even for PPE, we find multiple transition states for each reaction channel, which are distinct by the angle at which the radical attacks. Assigning a reaction path to each transition state and calculating the rate constants yields the Arrhenius plots shown in Fig. 7.20.

The α-transition states are stabilized through delocalization of the unpaired electron into the phenyl ring, and we observe that the α-abstraction is faster than the β-abstraction for the phenoxy and the benzyl abstraction reactions. We find an opposing effect in the β-transition states of the phenoxy abstraction, where the
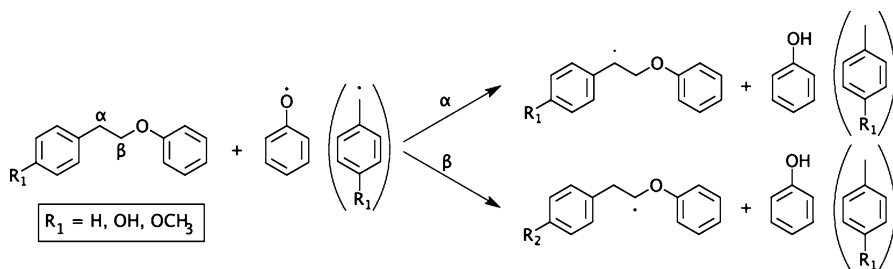
Scheme 7.1 Hydrogen abstraction reactions in the pyrolysis of PPE and PPE derivatives
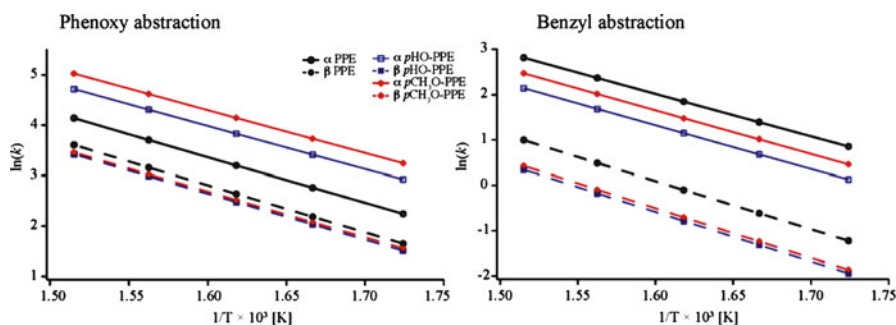
Fig. 7.20 Arrhenius plots for the hydrogen abstraction by the phenoxy and benzyl radicals in the temperature range of 580–660 K (Reproduced from Ref. [169]. With kind permission of © The American Chemical Society 2008)

electrophilic phenoxy radical polarizes the β-transition states by drawing charge from the adjacent ether oxygen into the aromatic ring, stabilizing the β-transition states. As a consequence, the gap between α- and β-rate constants is smaller for the phenoxy abstraction than for the benzyl abstraction. The effect of the substituents is the deceleration of the β-abstraction by the phenoxy radical and of the α- and β-abstraction by the benzyl radical. In contrast, we find that the α-abstraction by the phenoxy radical is accelerated by hydroxy and, to a larger extent, by methoxy substituents. Using the TST rate constants, we can calculate the α/β-selectivities for the hydrogen abstraction by the phenoxy and benzyl radicals, which are given as the ratio of the cumulative rate constants for the α- and β-pathways and listed in Table 7.7. Also reported in Table 7.7 are the total α/β-selectivities. We observe that the total α/β-selectivity is dominated by the α/β-selectivity of the phenoxy radical. Although the total α/β-selectivities underestimate the experimental values, the experimental trend is well reproduced.

Motivated by this success, we proceeded to study the hydrogen abstraction reactions for PPE derivatives, where methoxy substituents are located in R_2-, R_3-, and R_4- position of the phenyl ring adjacent to the ether oxygen [173]. However, this is a more complicated problem: Multiple conformers for the reactants are relevant,

Table 7.7 α/β-Selectivities for hydrogen abstraction by the phenoxy and benzyl radicals and total α/β-selectivities at 618 K (Experimental values are taken from [166])

	$R_1 = H$		$R_1 = OH$		$R_1 = OCH_3$	
	Comp.	Exp.	Comp.	Exp.	Comp.	Exp.
Phenoxy	1.8		3.9		5.1	
Benzyl	7.0		6.9		8.9	
Total	2.4	3.8 ± 0.3	4.3	5.1 ± 0.1	5.5	7.4 ± 0.3

Reproduced from Ref. [169]. With kind permission of © The American Chemical Society (2008)
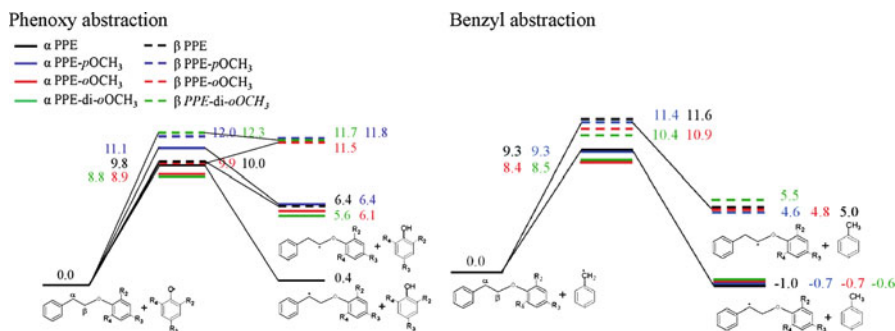
Fig. 7.21 Reaction profile for the hydrogen abstraction reactions by benzyl and phenoxy radicals on substituted PPE, energy differences in kcal/mol (Reproduced from Ref. [173]. With kind permission of © The American Chemical Society 2010)

the twofold symmetry of the α- and β-hydrogen atoms is not necessarily given, and the phenoxy radical has two distinct sides of attack for methoxy substituents located at *ortho* and *para* positions. In total, we located 117 transition states for the four investigated PPE derivatives, all with significant contributions to the rate constants. Figure 7.21 shows the reaction profiles for the hydrogen abstraction reactions, using only the lowest transition states. The most prominent feature of the reaction profile of substituted PPE compared to PPE is that the product energies for the hydrogen abstraction by the phenoxy radical are significantly increased due to the stabilization of the phenoxy radical and the destabilization of phenol by methoxy substituents, which are additive effects. This implies that the reverse reactions will have a significant contribution to the pyrolysis mechanism and the simplified kinetic model used to calculate the α/β-selectivities in Table 7.7 cannot be applied. We calculated the rate constants for the hydrogen abstraction reactions, but to predict product distribution, we need to consider all reactions participating in the pyrolysis mechanism. At a minimum, we need to include the β-scission and phenyl migration reactions.

We, therefore, studied the phenyl migration reaction, shown in Scheme 7.2. This reaction is also important to our investigations because it has to be fast ($>4.0 \times 10^5$ s^{-1} at 648 K [165]) for the assumption of negligible interconversion between
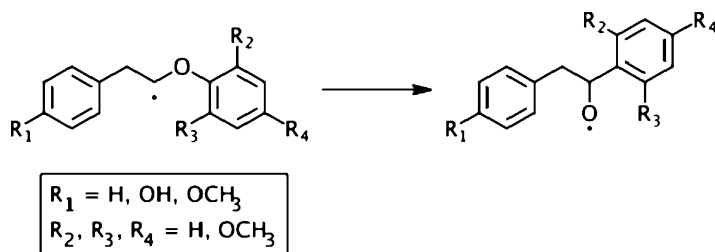
Scheme 7.2 Phenyl migration reaction in substituted PPE

Fig. 7.22 Intermediate of the phenyl migration reaction in hydroxy-substituted β-PPE
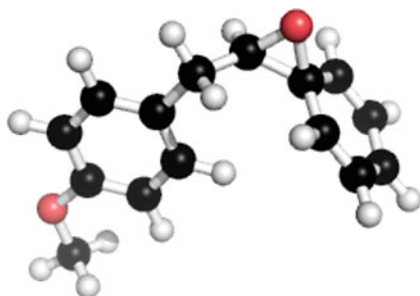
α- and β-PPE radicals in the simplified kinetic model to hold. The phenyl shift reaction of the β-PPE radical and derivatives with substituents located at the R_1, R_2, R_3, and R_4 positions proceed through a radical intermediate containing an epoxy ring, where multiple conformers contribute to the reaction [174]. An example is given in Fig. 7.22. In the reactant, the single electron is centered at the β-carbon atom. In the first transition states, the phenyl ring approaches the radical center leading to the epoxy intermediate. In the second transition state, the epoxy ring opens to form the product, where the radical center has shifted to the oxygen atom. The overall rate constant of the phenyl shift reaction is the rate constant of a series of first-order reactions. We use the steady-state condition for the intermediate to calculate the rate constants of the phenyl migration. The applicability of the steady-state condition was confirmed by numerical integration. The rate constant of the phenyl migration is on the order of 10^7 s^{-1} at 648 K, which is sufficiently fast for an effective suppression of the interconversion between α- and β-PPE radicals. Hydroxy and methoxy substituents in the R_1 position and methoxy substituents in the R_4 position have little influence on the rate constant compared to the migration in β-PPE. But methoxy substituents in the R_2 and R_3 position accelerate the phenyl shift reaction, by a factor of 18 at 618 K if both *ortho* positions are occupied by a methoxy substituent.

The continued investigation of individual reactions in the pyrolysis of substituted PPE will lead to the collection of all necessary date for a complete kinetic model and will provide the insight needed to chemically control the thermal degradation of PPE derivatives, which serve as model compounds for the most common
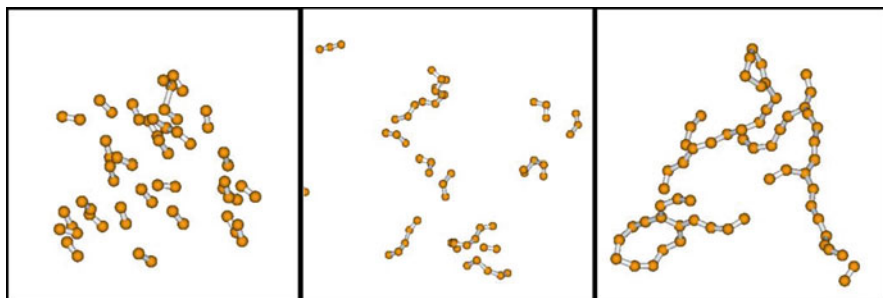
Fig. 7.23 Initial and final structures from BOMD and LvNMD simulations at $T_{el} = 0$ K. *Left*: initial structure for BO and LvN simulations. *Center*: final BOMD structure after 1 ps. *Right*: final LvNMD structure after 1 ps (Jakowski et al. [177], Royal Society of Chemistry, 2011) (Reproduced by permission of the PCCP Owner Societies)

linkage in lignin. Meanwhile, mechanistic details, kinetic and thermodynamic information, and knowledge of the effects of substituents are obtained by studying various reactions occurring in the thermolysis of PPE derivatives. This concerted methodology can then be extended to additional structural moieties present in lignin.

7.3.8 Dynamics of Carbon Dimers (C_2) Under Extreme Conditions

Vaporized carbon plays an important role in fabrication of carbon nanostructures, as it is fundamental to chemical vapor deposition (CVD) as well as laser ablation synthesis approaches. The first stage of this process is the formation of short carbon chains. These short carbon chains then condense into longer ones, often forked carbon chains, and subsequently reorganize into ring structures (see Fig. 7.23). In this regard, we have previously carried out extensive quantum molecular dynamics studies of a model system with gaseous C_2. The modeling of the C_2 vapor condensation via conventional BOMD is difficult because the system is very reactive and the formation of new CC bonds is exothermic. This adversely affects the conservation of energy (see Fig. 7.24, top left). Thus, we performed microcanonical (constant energy) simulation of gaseous $30C_2$ via LvNMD and BOMD methods. The C_2 molecules were set randomly inside the box of the size $30 \times 30 \times 30$ Å. But the system was not constrained during dynamics and could expand freely. The time step used in simulation was set to 0.1 fs. The total number of time steps was 10,000 (total simulation time 1 ps). In both LvNMD and BOMD cases, we used the same initial conditions (coordinates, velocities, electronic structure). The BOMD simulation was performed at $T_{el} = 0$ K. Thus the corresponding density matrix is idempotent and represents a pure state. The electronic structure from BOMD at time $t = 0$ and $T_{el} = 0$ K was used as an initial density matrix in LvNMD simulations.
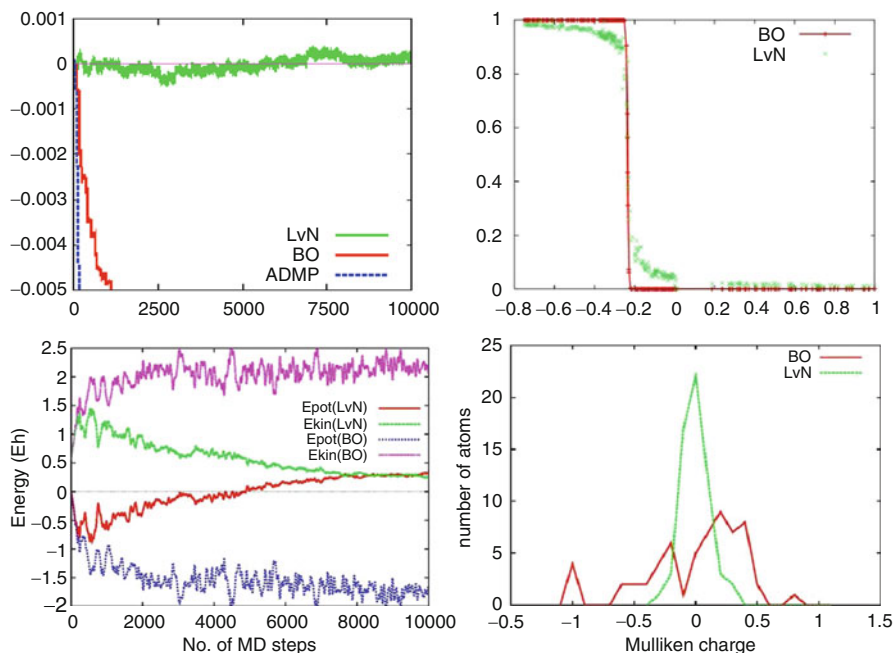
Fig. 7.24 Simulations of 30C$_2$ system at $T_{el} = 0$ K via BOMD and LvNMD. *Top left*: conservation of total energy (in mEh). *Top right*: projected "occupations" of LvN density (*green*) at 1 ps on the corresponding structure's BO states (*red*). ADMP is an implementation of a Car–Parrinello dynamics with the localized orbitals. *Bottom left*: time dependence of the potential and kinetic energy for BO and LvN dynamics. *Bottom, right*: total Mulliken charge from the LvN density (*green*) and BO density for the final structure (Jakowski et al. [177], Royal Society of Chemistry, 2011) (Reproduced by permission of the PCCP Owner Societies)

To control coherency of density matrix propagation, we measured the propagation error for the final density (at $t = 1$ ps) as L2 norm for differential matrix $\lVert P(t)^2 - P(t) \rVert$. The idempotency loss for the final density is very small in the order of magnitude 10^{-9}, thus ensuring that the final density matrix represented pure state and that the dynamics was coherent. Also the total energy for LvNMD simulation is conserved very well. Figure 7.24 (top left) shows comparison of energy for BOMD, LvNMD, and localized atomic orbitals implementation of Car–Parrinello dynamics (ADMP). No energy drift is observed, and the oscillations of total energy were on micro-Hartree level. We observe a drift of energy for the BOMD case. For atomic orbitals of Car–Parrinello dynamics, the energy conservation was very poor and we did not continue these simulations.

The initial and final molecular structures for LvNMD and BOMD are shown in Fig. 7.24. The results of simulations are rather striking. The number of carbon bonds formed during the LvNND simulations is significantly higher than in the BOMD case. The LvNMD simulations suggest that the rate of condensation of C$_2$

is higher than suggested by BOMD simulations. After 1 ps dynamics of LvNMD, we observed that 90% of carbons formed three large chain-like structures with two carbon rings (one six-membered ring and one ten-membered ring). The carbon structures are respectively built of 16, 17, and 22 carbons (the system contains 60 carbons). In the case of BOMD, we observed many short chains formed (average size is 5 carbons). See Fig. 7.23, center, for the details.

We observe a significant transfer of energy between electronic and nuclear degrees of freedom as a result of interaction between C_2 subunits. In principle, the energy released during the new –CC– bond formation can be transferred into kinetic energy of constituent nuclei or into electronic excitation or released as a radiation (neither BOMD nor LvNMD does not account for the radiation). In the BOMD case, the entire energy released from newly formed –CC– bond is converted into kinetic energy of nuclei; thus, the classical part of the system (nuclei) becomes strongly heated, while the electrons remain "cold." In the LvNMD case, only some portion of energy released from newly formed –CC– bond is converted into kinetic energy of nuclei, while the rest goes into electronic excitation.

The impact of this energy transfer on kinetics of reaction is pronounced. Since only some portion of CC bonding energy is converted into kinetic energy of nuclei (as compared to the BOMD case), hence the velocities of the nuclei after reaction are smaller than in the BOMD case. In consequence the probability that the C_4 reaction product will stay longer near the reaction chamber and get involved into subsequent reaction is much higher in the LvNMD case (small velocities) than in the BOMD case (high velocities). In the BOMD case, the reaction product quickly evaporates from the reaction location.

LvNMD simulation suggests that the process of condensation of C_2's into larger carbon structures has a nonadiabatic character. The suggested mechanism is the following: When two C_2 subunits approach each other, their HOMO orbitals are practically degenerate. As the intermolecular separation is large, the bonding and antibonding combinations of HOMO orbitals of each C_2 are very close in energy (the energy gap is zero for infinite separations), and thus the nonadiabatic transition is permitted. The new –CC– bonds are thus formed as a combination/superposition of adiabatic states rather than a single (lowest energy) Born–Oppenheimer state. The mixing coefficients are determined by temporal molecular orientation of C_2 units and values (and phases) of interacting (overlapping) orbitals.

$$i\hbar \frac{\partial}{\partial t} \begin{bmatrix} c_A \\ c_B \end{bmatrix} = \begin{bmatrix} E_A & <A\,|V|\,B> \\ <B\,|V|\,A> & E_B \end{bmatrix} \begin{bmatrix} c_A \\ c_B \end{bmatrix}. \tag{7.50}$$

Figure 7.24 (top, right) presents analysis of final LvNMD density matrix in terms of BO electronic structure. The BO calculations were performed for the final LvNMD geometry. We then projected the final density matrix from LVNMD onto orbitals of ground BO state for the comparison. The projected LvN "occupation" numbers are given by

$$f_k = \text{Trace}[P(t)P_k^{BO}], \tag{7.51}$$

where $P(t)$ is total N-electronic density matrix from LvN simulations, while P_k^{BO} is a single-electron density matrix obtained from kth BO molecular orbital (described by its $c_{k,j}$ coefficients) as follows:

$$P_k^{BO} = \begin{bmatrix} c_{k,1} \\ \vdots \\ c_{k,i} \end{bmatrix} \begin{bmatrix} c_{k,1} & \ldots & c_{k,i} \end{bmatrix}. \qquad (7.52)$$

Such projection describes in an approximate fashion an "overlap" of LvN electronic structure with ground BO state and hence a relative excitation of LvN electronic structure as compared with BO.

The resulting f_k numbers are plotted as a function of BO orbital energies and compared with BO occupations. The choice of BO energy is arbitrary, and the analysis provides only a qualitative picture of excitations. Another equally valid but different choice could be corresponding LvN "orbital" energy (calculated as trace $[FP_k^{BO}]$). Nevertheless, such qualitative analysis provides a useful intuitive picture. The projected LvN occupations resemble Fermi–Dirac distribution. The highest probability of excitation is for orbitals near Fermi level (highest occupied and lowest virtual orbitals). The mechanisms are such that due to the motion nuclei, the highest occupied orbitals get "swollen" and gain contribution from the lowest unoccupied orbitals of which energy is just above the Fermi level.

Another indication of non-Born–Oppenheimer character of $30C_2$ dynamics can be obtained from the analysis of Mulliken charges. Figure 7.24 (bottom, right) compares distribution of Mulliken charges from LvNMD simulations with analogous distribution (the same geometry) from adiabatic BO calculations. It is a histogram type plot, and it shows the number of atoms for a given total net charge obtained from Mulliken analysis. Interestingly the distribution of Mulliken charges from BO calculations looks "random" with much larger ionic character of carbon–carbon bonding (see Fig. 7.24, bottom right). Although our model system contains only carbons and thus no charge polarization is expected, four carbons from BO are anions with charge -1. In addition, there is a minimum of charge distribution near net charge equal to 0. This result is counter intuitive. Very likely such unphysical charging and sloshing between different carbon structures may be responsible for poor energy conservation in BOMD simulations. Contrary to BO-based charges, the Mulliken analysis of final electronic structure from time-dependent LvN simulations is much more physical. The charge distribution in the LvNMD case is narrow, and it centers at charge value equal to 0. The maximum deviation of net charge from most probable zero does not exceed $+/- 0.3$. Comparing Mulliken charges with nuclear velocities shows that the largest deviation of Mulliken charge from 0 coincides with very large nuclear velocity (see Fig. 7.25). Both "hot carbons" are members of the same carbon structure (see Fig. 7.25), and their violent vibration may lead to local electronic excitation (measured as a difference between BO and LvN based density). The correct behavior of electron charges in LvN is very encouraging.

Fig. 7.25 Distribution of velocity (arbitrary units) of the final LvN structure. The inset structure represents one of the three largest LvN structures and corresponding charges from a Mulliken analysis. "Hot" carbons are marked in *purple*, and the corresponding velocities are pointed on the distribution below (Jakowski et al. [177], Royal Society of Chemistry, 2011) (Reproduced by permission of the PCCP Owner Societies)
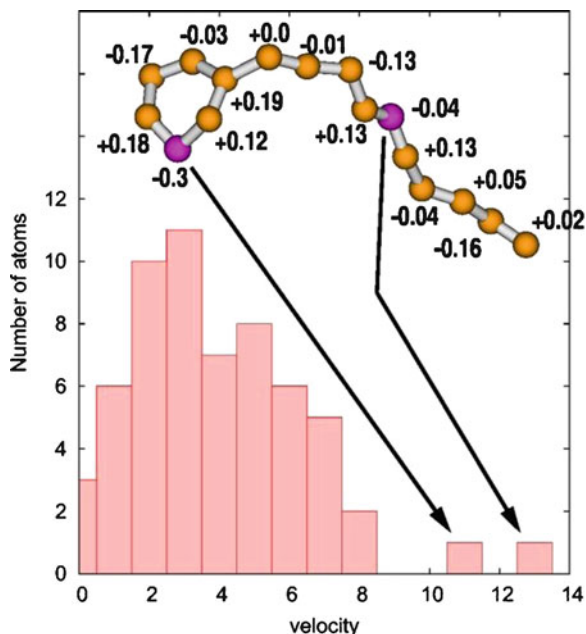
Finally, Fig. 7.24 (bottom left) shows the time dependence of the potential and kinetic energy for the nuclear motion for BOMD and LvNMD. The potential energy on the plot was shifted such that its value at $t = 0$ is equal. The behavior of LvN curve can be interpreted as a result of coupling between the electrons and nuclei that leads to the transfer and "equilibration" of energy between electronic and nuclear degrees of freedom, in correspondence with equipartition of energy theorem. In the BOMD case, no transfer is allowed; thus, regardless of velocity of constituent nuclei, the electrons are always staying on the ground electronic state.

7.4   Future Perspectives

Chemistry, physics, and materials science describes the structure, function, and transformation of the molecules and materials that are key to defining our "materials world." In a world attempting to balance energy usage, environmental quality, human health, and economic prosperity, chemistry and physics is, and will continue to be, a key science required to meet these challenges. While the current computer architectural shift toward multicore heterogeneous computing (CPU/GPGPU) poses challenges to the existing simulation paradigms, it opens up a tremendous opportunity to unify scalable mathematical algorithms, electronic structure methods, and advanced computing tools so as to enable the development of virtual microscopy tools capable of efficiently simulating material systems at scale. That capability
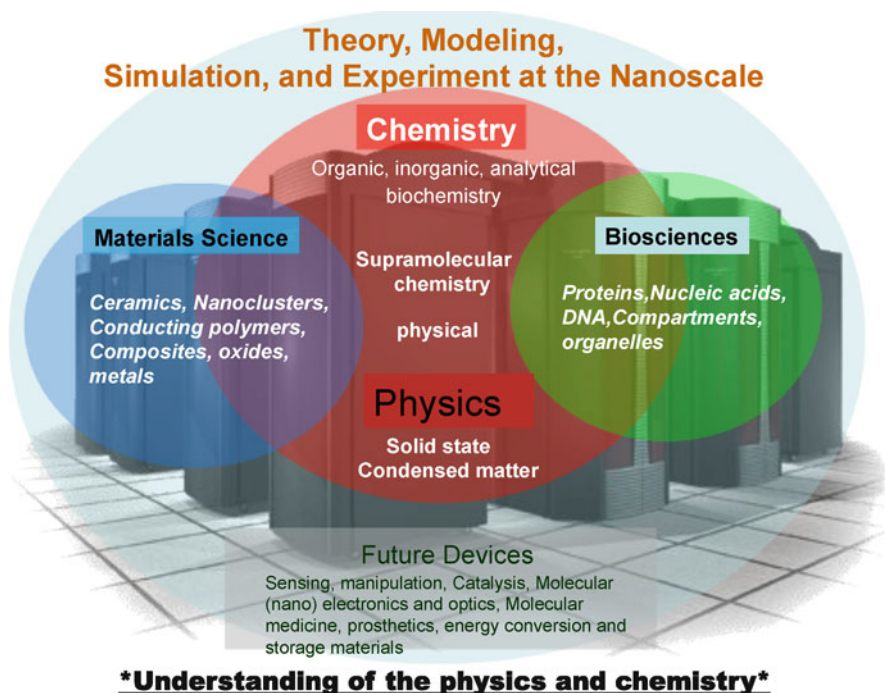
Fig. 7.26 Schematic diagram illustrating how predictive simulations can enable the efficient design of new materials and devices when combined with experiment and characterization

will enable predictive simulations of entire device structures from first principles that are critical to advancing the understanding of structure–property relationships, and will promote the virtual design of molecular and nanoscale assembly while providing new discovery tools for rapid prototyping (see Fig. 7.26). Such advances can potentially lead to the improved capability for discovery/understanding of novel phenomena and for providing principles for the design of efficient energy paradigms.

References

1. Goodenough JB, Abruna HD, Buchanan MV (2007) Basic research needs for electrical energy storage. Report of the basic energy sciences workshop on electrical energy storage, DOE-BES, 2007
2. Bell AT, Gates BC, Ray D (2007) Technical report. US Department of Energy
3. Report of the Department of Energy Workshop on Computational Materials Science and Chemistry for Innovation, http://www.ornl.gov/sci/cmsinn/CMSC_Workshop_Report.pdf, (2010)
4. Szabo A, Ostlund NS (1992) Modern quantum chemistry. McGraw-Hill, New York

5. McWeeny R (1992) Methods of molecular quantum mechanics. Academic, London
6. Simons J, Nichols J (1997) Quantum mechanics in chemistry. Oxford University Press, New York
7. Jensen F (2003) Introduction to computational chemistry. Wiley, New York
8. Giannozzi P, Baroni S, Bonini N, Calandra M, Car R, Cavazzoni C, Ceresoli D, Chiarotti GL, Cococcioni M, Dabo I, Corso AD, Gironcoli S, Fabris S, Fratesi G, Gebauer R, Gerstmann U, Gougoussis C, Kokalj A, Lazzeri M, Martin-Samos L, Marzari N, Mauri F, Mazzerello R, Paolini S, Pasquarello A, Paulatto L, Sbraccia C, Smogunov A, Umari P, Wentzcovitch RM (2009) J Phys Cond Matter 21:395502
9. Hafner J (2008) J Comput Chem 29:2044–2078
10. Valiev M, Bylaska EJ, Govind N, Kowalski K, Straatsma TP, Van Damm HJJ, Wang D, Nieplocha J, Apra E, Windust TL, de Jong WA (2010) Comput Phys Commun 181:1477–1489
11. Schmidt MW, Baldridge KK, Boatz JA, Elgert ST, Gordon MS, Jensen JH, Koseki S, Matsunaga N, Nguyen KA, Su SJ, Windus TL, Dupuis M, Montogomery JA (1993) J Comput Chem 14:1347–1363
12. Janssen CL, Nielsen IB, Leininger ML, Valeev EF, Seidl ET (2003) The massively parallel quantum chemistry program (MPQC). Sandia National Laboratories, Livermore
13. Turney JM, Simmonett AC, Parrish RM, Hohenstein EG, Evangelista FA, Fermann JT, Mintz BJ, Burns LA, Wilke JJ, Abrams ML, Russ NJ, Leininger ML, Janssen CL, Seidl ET, Allen WD, Schaefer HF, King RA, Valeev EF, Sherill CD, Crawford TD (2011) WIREs Comput Mol Sci (doi: 10.1002/wcms.93)
14. Yoo JJ, Balakrishnan K, Huang JS, Meunier V, Sumpter BG, Srivastava A, Conway M, Reddy ALM, Yu J, Vajtai R, Ajayan PM (2011) Nano Lett 11:1423–1427
15. Lipton-Duffin JA, Ivasenko O, Perepichka DF, Rosei F (2009) Small 5:592–597
16. Jia X, Hofmann M, Meunier V, Sumpter BG, Campos-Delgado J, Romo-Herrera JM, Son H, Hsieh Y-P, Reina A, Kong J, Terrones M, Dresselhaus MS (2009) Science 323:1701–1705
17. Parr R, Yang W (1989) Density functional theory of atoms and molecules. Oxford University Press, New York
18. Hohenberg P, Kohn W (1964) Phys Rev 136:B864–B871
19. Kohn W, Sham LJ (1965) Phys Rev 140:A1133–A1138
20. Perdew JP, Schmidt K (2001) Jacob's ladder of density functional approximations for the exchange-correlation energy. AIP, New York
21. Perdew JP, Kurth SA (2003) Primer in density functional theory. Springer, Berlin/Heidelberg
22. Perdew JP, Zunger A (1981) Phys Rev B 23:5048–5079
23. Meyer EA, Castellano RK, Diederich F (2003) Angew Chem Int Ed 42:1210–1250
24. Anbarasu A, Anand S, Babu MM, Sethumadhavan R (2007) Int J Biol Macromol 41:251–259
25. Jeffery GA, Saenger W (1991) Hydrogen bonding in biological structures. Springer, Berlin
26. Brunsveld L, Folmer BJB, Meijer EW, Sijbesma RP (2001) Chem Rev 101:4071–4097
27. Claessens CG, Stoddart JF (1997) J Phys Org Chem 10:254–272
28. Dinadayalane TC, Gorb L, Simeon T, Dodziuk H (2007) Int J Quantum Chem 107:2204–2210
29. Vazquez-Mayagoitia A, Sherill CD, Apra E, Sumpter BG (2010) J Chem Theory Comput 6:727–734
30. Sherrill CD, Sumpter BG, Sinnokrot MO, Marshall MS, Hohenstein EG, Walker RC, Gould IR (2009) J Comput Chem 30:2187–2193
31. Raghavachari K, Trucks GW, Pople JA, Head-Gordon M (1989) Chem Phys Lett 157:479–483
32. Lee TJ, Scuseria GE (1995) Achieving chemical accuracy with coupled-cluster theory. In: Langhoff SR (ed) Quantum mechanical electronic structure calculations with chemical accuracy. Kluwer Academic Publishers, Dordrecht, pp 47–108
33. Rappe AK, Bernstein ER (2000) J Phys Chem A 104:6117–6128
34. Tsuzuki S, Luthi HP (2001) J Chem Phys 114:3949–3957
35. Johnson ER, Wolkow RA, DiLabio GA (2004) Chem Phys Lett 394:334–338
36. Kannemann FO, Becke AD (2009) J Chem Theory Comput 5:719–727

37. Becke AD, Johnson ER (2005) J Chem Phys 122:154104
38. Becke AD, Johnson ER (2006) J Chem Phys 124:014104
39. Angyan JG (2007) J Chem Phys 127:024108
40. Becke AD, Johnson ER (2007) J Chem Phys 127:154108
41. Hesselmann A (2009) J Chem Phys 130:084104
42. Steinmann SN, Corminboeuf C (2010) J Chem Theory Comput 6:1990–2001
43. Grimme S (2006) J Comput Chem 27:1787–1799
44. Xu X, Goddard WA (2004) Proc Natl Acad Sci USA 101:2673–2677
45. Zhao Y, Schultz NE, Truhlar DG (2006) J Chem Theory Comput 2:364–382
46. Zhao Y, Truhlar DG (2008) Theor Chem Acc 120:215–241
47. Zhao Y, Truhlar DG (2008) Acc Chem Res 41:157–167
48. Chai J-D, Head-Gordon M (2008) Phys Chem Chem Phys 10:6615–6620
49. Grimme S (2006) J Chem Phys 124:034108
50. Schwabe T, Grimme S (2007) Phys Chem Chem Phys 9:3397–3406
51. Chai J-D, Head-Gordon M (2009) J Chem Phys 131:174105
52. Zhang Y, Xu X, Goddard WA (2009) Proc Natl Acad Sci USA 106:4963–4968
53. Koch W, Holthausen MC (2001) A chemist's guide to density functional theory. Wiley-VCH, New York
54. Johnson ER, Mackie ID, DiLabio GA (2009) J Phys Org Chem 22:1127–1135
55. Grafenstein J, Cremer D (2009) J Chem Phys 130:124105
56. Sherrill CD (2009) Computations of noncovalent pi interactions. Wiley, Hoboken
57. Foster ME, Sohlberg K (2010) Phys Chem Chem Phys 12:307–322
58. Riley KE, Pitonak M, Jurecka P, Hobza P (2010) Chem Rev 110:5023–5063
59. von Lilienfeld A, Tavernelli I, Rothlisberger U, Sebastiani D (2004) Phys Rev Lett 93:153004
60. (a) Wu Q, Yang W (2002) J Chem Phys 116:515–524; (b) Elstner M, Hobza P, Frauenheim T, Suhai S, Kaxiras E (2001) J Chem Phys 114:5149–5155
61. Grimme S (2004) J Comput Chem 25:1463–1473
62. Grimme S, Antony J, Ehrlich S, Krieg H (2010) J Chem Phys 132:154104
63. Langreth DC, Dion M, Rydberg H, Schroder E, Hyldgaard P, Lundqvist BI (2005) Int J Quantum Chem 101:599–610
64. Vydrov OA, Voorhis TV (2009) Phys Rev Lett 103:063004
65. See http://www.uni-muenster.de/Chemie.oc/grimme/ for a FORTRAN program implementing the DFT-D3 method and a file with available C6 coefficients. Westfalische Wilhelms-Universitat Munster, Organisch-Chemisches Institut, Theoretische Organische Chemie, Grimme Research Group, Corrensstrasse 40, D-48149 Munster, email: grimmes@unimuenster.de
66. Becke AD, Roussel MR (1989) Phys Rev A 39:3761–3767
67. Burns LA, Vazquez-Mayagoitia A, Sumpter BG, Sherill CD (2011) J Chem Phys 134:084107
68. Marx D, Hutter J (2000) Modern methods and algorithms of quantum chemistry. NIC, Julich
69. Hase WL, Song K, Gordon MS (2003) Comput Sci Eng 5:36–44
70. Niklasson AMN, Tymczak CJ, Challacombe M (2006) Phys Rev Lett 97:123001
71. Dolstsinis NL (2002) Quantum simulations of complex many-body systems: from theory to algorithms. NIC, Julich
72. (a) Car R, Parrinello M (1985) Phys Rev Lett 55:2471–2474; (b) Herbert JM, Head-Gordon M (2004) J Chem Phys 121:11542–11556; (c) Schlegel HB, Millam JM, Iyengar SS, Voth GA, Daniels AD, Scuseria G, Frisch MJ (2001) J Chem Phys 114:9758–9763
73. Godecker S (1999) Rev Mod Phys 71:1085–1123
74. Hayes RL, Paddison SJ, Tuckerman ME (2009) J Phys Chem B 113:16574–16589
75. Hwang JK, Warshel A (1996) J Am Chem Soc 118:11745–11751
76. Benkovic SJ, Hammes-Schiffer S (2003) Science 301:1196–1202
77. Millam JM, Scuseria GE (1997) J Chem Phys 106:5569–5577
78. (a) Mermin ND (1965) Phys Rev 137:A1441–A1443; (b) Sokoloff J (1967) Ann Phys 45:186–190
79. Kuhne TD, Krack M, Mohamed FR, Parrinello M (2007) Phys Rev Lett 98:066401

80. (a) Weinert M, Davenport JW (1992) Phys Rev B 45:13709–13712; (b) Wentzcovitch RM, Martins JL, Allen PB (1992) Phys Rev B 45:11372–11374
81. (a) Jakowski J, Morokuma K (2009) J Chem Phys 130:224106 (b) Jakowski J, Irle S, Morokuma K (2011) Quantum chemistry: Propagation of electronic structure on GPU. In Hwu W-M (ed) GPU computing gems. Emerald edition, Morgan Kauffmann Pub., pp. 59–74; (c) Jakowski J, Irle S, Sumpter BG, Morokuma K (2012) J Phys Chem Lett 3:1536–1542
82. Magnus W (1954) Commun Pure Appl Math 7:649–673
83. Oteo JA, Ros J (2000) J Math Phys 41:3268–3277
84. (a) Porezag D, Frauenheim T, Kohler T, Seifert G, Kaschner R (1995) Phys Rev B 51:12947–12957; (b) Elstner, Porezag D, Jungnickel G, Elsner J, Haugk M, Frauenheim T, Suhai S, Seifert G (1998) Phys Rev B 58:7260–7268; (c) Zheng G, Lundberg M, Jakowski J, Vreven T, Frisch MJ, Morokuma K (2009) Int J Quantum Chem 109:1841–1854; (d) Slater JC, Koster GF (1954) Phys Rev 94:1498–1524
85. Abruna HD, Kiya Y, Henderson JC (2008) Phys Today 61:43–47
86. Christen T, Ohler C (2002) J Power Sources 110:107–116
87. Chmiola J, Yushin G, Gogotsi Y, Portet C, Simon P, Taberna PL (2006) Science 313:1760–1763
88. Huang JS, Sumpter BG, Meunier V (2008) Chem Eur J 14:6614–6626
89. Feng G, Qiao R, Huang JS, Sumpter BG, Meunier V (2010) ACS Nano 4:2382–2390
90. Chmiola J, Largeot C, Taberna PL, Simon P, Gogotsi Y (2008) Angew Chem Int Ed 47:3392–3395
91. Huang JS, Sumpter BG, Meunier V (2008) Angew Chem Int Ed 47:520–524
92. Marcus Y (1994) Biophys Chem 51:111–127
93. Marenich AV, Olson RM, Kelly CP, Cramer CJ, Truhlar DG (2007) J Chem Theory Comput 3:2011–2033
94. Higashi M, Marenich AV, Olson RM, Chamberlin AC, Pu J, Kelly CP, Thompson JD, Xidos JD, Li J, Zhu T, Hawkins GD, Truhlar DG (2009) GAMESSPLUS – version 2009. University of Minnesota, Minneapolis
95. Kelly CP, Cramer CJ, Truhlar DG (2005) J Chem Theory Comput 1:1133–1152
96. Marenich AV, Kelly CP, Thompson JD, Truhlar DG (2009) Minnesota solvation database. University of Minnesota, Minneapolis
97. Feng G, Huang JS, Sumpter BG, Meunier V, Qiao R (2010) Phys Chem Chem Phys 12:5468–5479
98. Frese KW (1989) J Phys Chem 93:5911–5916
99. Whitesides GM (2005) Small 1:172–179
100. Koza M, Frick B, Zorn R (2007) 3rd international workshop on dynamics in confinement, The European Physical Journal Special Topics. Springer, New York
101. He F, Wang LM, Richert R (2007) Eur Phys J Spec Top 141:3–9
102. Love JC, Estroff LA, Kriebel JK, Nuzzo RG, Whitesides GM (2005) Chem Rev 105:1103–1169
103. Salimi A, Hallaj R, Soltanian S (2007) Biophys Chem 130:122–131
104. Drummond ML, Sumpter BG, Shelton WA, Larese J (2007) J Phys Chem C 111:966–976
105. Drummond ML, Sumpter BG, Shelton WA, Larese J (2006) Phys Rev B 73:195313
106. Sumpter BG, Huang JS, Meunier V, Romo-Herrera JM, Cruz-Silva E, Terrones H, Terrones M (2009) Int J Quantum Chem 109:97–118
107. Sumpter BG, Meunier V, Romo-Herrera JM, Cruz-Silva E, Cullen DA, Terrones H, Smith DJ, Terrones M (2007) ACS Nano 1:369–375
108. Marciel IO, Campos-Delgado J, Cruz-Silva E, Pimenta MA, Sumpter BG, Meunier V, Lopez-Urias F, Munoz-Sandoval E, Terrones H, Terrones M, Jorio A (2009) Nano Lett 9:2267–2272
109. Cruz-Silva E, Cullen DA, Gu L, Romo-Herrera JM, Munoz-Sandoval E, Lopez-Urias F, Sumpter BG, Meunier V, Charlier J-C, Smith DJ, Terrones H, Terrones M (2008) ACS Nano 2:441–448
110. Cruz-Silva E, Lopez-Urias F, Nunoz-Sandoval E, Sumpter BG, Terones H, Charlier J-C, Meunier V, Terrones M (2009) ACS Nano 3:1913–1921

111. Cruz-Silva E, Lopez-Urias F, Munoz-Sandoval E, Sumpter BG, Terrones H, Charlier J-C, Meunier V, Terrones M (2011) Nanoscale 3:1008–1013
112. Romo-Herrera JM, Cullen DA, Cruz-Silva E, Ramirez D, Sumpter BG, Meunier V, Terrones H, Smith DJ, Terrones M (2009) Adv Func Mater 19:1193–1199
113. Romo-Herrera JM, Sumpter BG, Cullen DA, Terrones H, Cruz-Silva E, Smith DJ, Meunier V, Terrones M (2008) Angew Chem Int Ed 47:2948–2953
114. Rodriguez-Manzo JA, Banhart F, Terrones M, Terrones H, Grobert N, Ajayan PM, Sumpter BG, Meunier V, Wang M, Bando Y, Golberg D (2009) Proc Natl Acad Sci USA 106:4591–4595
115. Jiang DE, Sumpter BG, Dai S (2006) J Phys Chem B 110:23628–23632
116. Jiang DE, Sumpter BG, Dai S (2007) J Chem Phys 127:124703
117. Jiang DE, Sumpter BG, Dai S (2007) J Chem Phys 126:134701
118. Cruz-Silva E, Botello-Mendez AR, Barnett ZM, Jia X, Dresselhaus MS, Terrones H, Terrones M, Sumpter BG, Meunier V (2010) Phys Rev Lett 105:045501
119. Tour JM (1996) Chem Rev 96:537–553
120. Tour JM (2007) J Org Chem 72:7477–7496
121. Groenendaal L, Zotti G, Aubert PH, Waybright SM, Reynolds JR (2003) Adv Mater 15:855–879
122. Roncali J (1992) Chem Rev 92:711–738
123. Grim PCM, De Feyter S, Gesquière A, Vanoppen P, Rücker M, Valiyaveettil S, Moessner G, Müllen K, De Schryver FC (1997) Angew Chem Int Ed 36:2601–2603
124. Okawa Y, Aono M (2001) Nature 409:683–684
125. Takami K, Mizuno J, Akai-Kasaya M, Saito A, Aono M, Kuwahara Y (2004) J Phys Chem B 108:16353–16356
126. Akai-Kasaya M, Shimizu K, Watanabe Y, Saito A, Aono M, Kuwahara Y (2003) Phys Rev Lett 91:255501
127. Sakaguchi H, Matsumura H, Gong H, Abouelwafa AM (2005) Science 310:1002–1006
128. Sakaguchi H, Matsumura H, Gong H (2004) Nat Mater 3:551–557
129. Heywang G, Jonas F (1992) Adv Mater 4:116–118
130. Groenendaal BL, Jonas F, Freitag D, Pielartzik H, Reynolds JR (2000) Adv Mater 12:481–494
131. Kirchmeyer S, Reuter K (2005) J Mater Chem 15:2077–2088
132. Sonmez G (2005) Chem Commun 42:5251–5259
133. Winther-Jensen B, Winther-Jensen O, Forsyth M, MacFarlane DR (2008) Science 321:671–674
134. Sumpter BG, Meunier V, Valeev EF, Lampkins AJ, Li H, Castellano RK (2007) J Phys Chem C 111:18912–18916
135. Sumpter BG, Meunier V, Vazquez-Mayagoitia A, Catellano RK (2007) Int J Quantum Chem 107:2233–2242
136. Yuan L, Sumpter BG, Abboud KA, Catellano RK, New J (2008) Chem 32:1924–1934
137. Li Y, Lampkins AJ, Baker MB, Sumpter BG, Huang JS, Abboud KA, Castellano RK (2009) Org Lett 11:4314–4317
138. Liu HB, Gao JM, Lynch SR, Saito YD, Maynard L, Kool ET (2003) Science 302:868–871
139. Liu HB, Gao JM, Kool ET (2005) J Org Chem 70:639–647
140. Liu HB, Lynch SR, Kool ET (2004) J Am Chem Soc 126:6900–6905
141. Liu HB, Gao JM, Maynard L, Saito YD, Kool ET (2004) J Am Chem Soc 126:1102–1109
142. Liu HB, Gao JM, Kool ET (2005) J Am Chem Soc 127:1396–1402
143. Gao JM, Liu HB, Kool ET (2005) Angew Chem Int Ed 44:3118–3122
144. Gao JM, Liu HB, Kool ET (2004) J Am Chem Soc 126:11826–11831
145. Lu HG, He KZ, Kool ET (2004) Angew Chem Int Ed 43:5834–5836
146. Lee AHF, Kool ET (2005) J Am Chem Soc 127:3332–3338
147. Lee AHF, Kool ET (2005) J Org Chem 70:132–140
148. Lee AHF, Kool ET (2006) J Am Chem Soc 128:9219–9230
149. Fuentes-Cabrera M, Sumpter BG, Wells JC (2005) J Phys Chem B 109:21135–21139

150. Fuentes-Cabrera M, Sumpter BG, Lipkowski P, Wells JC (2006) J Phys Chem B 110: 6379–6384
151. Fuentes-Cabrera M, Lipkowski P, Huertas O, Sumpter BG, Orozco M, Luque FJ, Wells JC, Leszczynski J (2006) Int J Quantum Chem 106:2339–2346
152. Huertas O, Poater J, Fuentes-Cabrera M, Orozco M, Sola M, Luque FJ (2006) J Phys Chem A 110:12249–12258
153. Vazquez-Mayagoita A, Huertas O, Fuentes-Cabrera M, Sumpter BG, Orozco M, Luque FJ (2008) J Phys Chem B 112:2179–2186
154. Vazquez-Mayagoitia A, Huertas O, Brancolini G, Migliore A, Sumpter BG, Orozco M, Luque FJ, Di Felice R, Fuentes-Cabrera M (2009) J Phys Chem B 113:14465–14472
155. Fuentes-Cabrera M, Zhao X, Kent PRC, Sumpter BG (2007) J Phys Chem B 111:9057–9061
156. Lee JS, Latimer LJP, Reid RS (1993) Biochem Cell Biol [Biochimie Et Biologie Cellulaire] 71:162–168
157. Aich P, Labiuk SL, Tari LW, Delbaere LJT, Roesler WJ, Falk KJ, Steer RP, Lee JS (1999) J Mol Biol 294:477–485
158. Rakitin A, Aich P, Papadopoulos C, Kobzar Y, Vedeneev AS, Lee JS, Xu JM (2001) Phys Rev Lett 86:3670–3673
159. Fuentes-Cabrera M, Sumpter BG, Sponer JE, Sponer J, Petit L, Wells JC (2007) J Phys Chem B 111:870–879
160. Salon J, Sheng J, Jiang JS, Chen GX, Caton-Williams J, Huang Z (2007) J Am Chem Soc 129:4862–4863
161. Gilbert KE, Gajewski JJ (1982) J Org Chem 47:4899–4902
162. Klein MT, Virk PS (1983) Ind Eng Chem Fundam 22:35–45
163. Brezny R, Mihalov V, Kovacik V (1983) Holzforschung 37:199–204
164. Kawamoto H, Horigoshi S, Saka S (2007) J Wood Sci 73:268–271
165. Britt PF, Buchanan AC, III, Malcolm EA (1995) J Org Chem 60:6523–6536
166. Britt PF, Kidder MK, Buchanan AC, III (2007) Energy Fuel 21:3102–3108
167. Beste A (2010) Chem Phys Lett 493:200–205
168. Beste A, Buchanan AC, III, Britt PF, Hathorn BC, Harrision RJ (2007) J Phys Chem A 111:12118–12126
169. Beste A, Buchanan AC, III, Harrison RJ (2008) J Chem Phys A 112:4982–4988
170. Becke AD (1993) J Chem Phys 98:5648–5652
171. Lee C, Yang W, Parr RG (1988) Phys Rev B 37:785–789
172. Beste A, Buchanan AC, III (2009) J Org Chem 74:2837–2841
173. Beste A, Buchanan AC, III (2010) Energy Fuel 24:2857–2867
174. Beste A, Buchanan, AC, III (2011) J Org Chem 76:2195–2203
175. Younker JM, Beste A, Buchanan AC, III (2011) Chem Phys Chem 12:3556–3565
176. Elder T (2010) Holzforschung 64:435–440
177. Jakowski J, Irle S et al (2012) Phys Chem Chem Phys 14:6273–6279

Chapter 8
New Advances in QSPR/QSAR Analysis of Nitrocompounds: Solubility, Lipophilicity, and Toxicity

Liudmyla N. Ognichenko, Victor E. Kuz'min, Leonid Gorb, Eugene N. Muratov, Anatoly G. Artemenko, Nikolay A. Kovdienko, Pavel G. Polishchuk, Frances C. Hill, and Jerzy Leszczynski

Abstract This chapter discusses QSAR/QSPR applications of the simplex representation of molecular structure (SiRMS) methodology. It has been determined that SiRMS proves to be quite an efficient tool for analyzing nitroaromatic aqueous solubility, lipophilicity, and toxicity. Using multiple linear regression (MLR) and random forest (RF) statistical methods at the 2D level of representation of molecular structure, models possessing high statistical characteristics (MLR: $R^2 = 0.85$, $Q^2 = 0.83$; RF: $R^2 = 0.99$, $R^2_{OOB} = 0.88$) were obtained for aqueous solubility of more than 2,800 organic compounds. The external validation set of 301 compounds (including 47 nitro-, nitroso-, and nitrogen-rich military compounds) was used for evaluation of the models' predictive ability.

A 2D QSPR model based on SiRMS and RF approaches has been developed to predict "structure of octanol-water partition coefficient ($\text{Log} K_{ow}$)" for a set of

L.N. Ognichenko • V.E. Kuz'min • E.N. Muratov • A.G. Artemenko • N.A. Kovdienko
• P.G. Polishchuk
Laboratory of Theoretical Chemistry, Department of Molecular Structure, A.V. Bogatsky
Physical-Chemical Institute National Academy of Sciences of Ukraine, Lustdorfskaya
Doroga 86, Odessa 65080, Ukraine
e-mail: ogni@icnanotox.org; theorchem@gmail.com; 00dqsar@ukr.net; artanat@ukr.net;
kovdienko@interchem.com.ua; pavel_polishchuk@ukr.net

L. Gorb
Badger Technical Services, LLC, 39180, Vicksburg, MS, USA
e-mail: lgorb@icnanotox.org

F.C. Hill
Environmental Laboratory, US Army ERDC, Vicksburg, MS 39180, USA
e-mail: Frances.C.Hill@usace.army.mil

J. Leszczynski (✉)
Interdisciplinary Center for Nanotoxicity, Department of Chemistry, Jackson State University,
P.O. Box 17910, Lynch Street, Jackson, MS 39217, USA

US Army ERDC, Vicksburg, MS 39180, USA
e-mail: jerzy@icnanotox.org

more than 10,970 organic compounds and has been successfully validated with two external test sets. This model predicts $\text{Log}K_{\text{ow}}$ values with the greatest accuracy among available modern models. $\text{Log}K_{\text{ow}}$ values of 29 military compounds with unknown experimental value of $\text{Log}K_{\text{ow}}$ have been predicted. The correspondence between observed and predicted toxicity values obtained using 1D and 2D models is quite high.

The most comprehensive consensus model allows for improved accuracy of toxicity predictions and has been shown to be an effective virtual screening tool. It was found that substitution of fluorine and hydroxyl groups into nitroaromatic compounds increases toxicity, whereas substitution of a methyl group has the opposite effect. The influence of chlorine on toxicity has not been determined unambiguously. The mutual influence of substituents in the benzene ring is substantially nonadditive and plays a crucial role regarding toxicity.

This chapter contains 5 subsections, 12 tables, and 8 figures. In the first and second subsections, a short introduction is presented, and applied methods are described. The third, fourth, and fifth subsections are devoted to the QSPR analysis of aqueous solubility, lipophilicity, and toxicity for nitroaromatic compounds with military interest.

Abbreviations

CART	Classification and regression trees algorithm
COSMO	Conductor-like screening model
CR	Continuum regression
DA	Applicability domain
GA	Genetic algorithm
HIT QSAR	Hierarchical QSAR technology
LD_{50}	50% lethal dose concentration
$\text{Log}K_{\text{ow}}$	Octanol-water partition coefficient
LUMO	Lowest unoccupied molecular orbital
MAE	Mean absolute error
MCI	Molecular connectivity indices
MLR	Multiple linear regression statistical method
MOE	Molecular Operating Environment
MP	Melting point
NN	Neural network
OOB	Out-of-bag set
PLS	Partial least squares or projection on latent structures statistical method
RF	Random forest statistical method
Q^2	Cross-validation determination coefficient
QSAR/QSPR	Quantitative structure-activity/property relationship

R^2	Determination coefficient for training set
R^2_{test}	Determination coefficient for test set
SE	Standard errors of prediction
SiRMS	Simplex representation of molecular structure
S_w	Aqueous solubility
TV	Trend-vector statistical method

8.1 Introduction

In order to correctly predict the environmental fate of real and possible contaminants, the methods that are able to evaluate molecular characteristics must also be able to predict environmentally related physical, chemical, and biological properties with high accuracy. Among these properties are:

1. Aqueous solubility that is also associated with an affinity for adsorption to solids in water, soil particles, or sediment.
2. Lipophilicity ($\text{Log}K_{\text{ow}}$, octanol/water partition coefficient) as extensively used parameter in risk assessment models. It predicts the distribution of chemicals between aqueous and organic media. Both those characteristics are essential for modeling the transport and fate of chemical contaminants and in understanding the pharmacokinetic behavior of toxicants in living organisms.
3. Numerous characteristics of toxicity (logLD_{50}, logLC_{50}, etc.) which are also of extreme interest in environmentally related studies.

Currently among the most efficient tools for such predictions are the techniques called quantitative structure–activity (property) relationships (QSAR/QSPR). A QSAR/QSPR are the mathematical models that quantify the relationships between the structure-related properties (descriptors) of chemical species and their physical, chemical, or biological properties (e.g., toxicological endpoint) [1–10]. Since their introduction more than 40 years ago [11], QSAR approaches have been widely used in the pharmaceutical industry, primarily for lead discovery and optimization. Likewise, they have been employed in toxicology [12, 13] and regulations [14–16] and have been particularly cost-effective for prioritizing untested chemicals for more extensive and costly experimental evaluations (for application of others than QSRP-based techniques to predict solubility and lipophilicity of energetic compounds, see our review in this book [17]). Traditional QSAR modeling involves three fundamental steps: (1) collect or, if necessary, design a training set of chemicals, (2) choose descriptors that can properly relate chemical structure to the property or activity, and (3) apply statistical regression methods that correlate changes in structure with changes in the target property. The final QSAR model is validated, internally, by a procedure known as leave-group-out cross validation, and externally, by a test set of compounds with experimentally measured properties that were not used to build the QSAR model.

The development and application of QSAR techniques for environmental science started with the prediction of toxicity caused by baseline toxicants [18–23]. Nitroaromatics, nitramines, nitroanisoles, nitrogen-rich compounds and their nitroso and amino derivatives are of potential interest for QSAR studies due to their use as explosives and propellants in military and industrial applications [24, 25]. Waste from nitroaromatic compounds can be disseminated during the manufacturing, storage, transportation, and utilization of munitions leading to a potential hazard for the environment [26]. A number of studies have shown that nitroaromatic compounds, as well as their degradation products, synthetic by-products, and products of incomplete combustion are harmful to the biosphere due to their toxicity [26–29]. Therefore, an understanding of the environmentally relevant physical, chemical, and biological properties of these contaminants is an important guide to the fate of these compounds in the environment. However, just few QSAR studies have been carried out in order to explain and/or predict the toxic influence of nitrocompounds on different living systems [30–33].

In the present work, we review the application of simplex representation of molecular structure (SiRMS) to predict physical, chemical, and biological properties of nitrocompounds. Recently, SiRMS [34] has been employed successfully in several studies to differentiate "structure–activity" relationships [35–37] and was used for the analysis of important properties of nitrocompounds—aqueous solubility, lipophilicity, and toxicity.

This chapter contains five subsections. In the first and second sections, a short introduction to the present work is given and applied methods and the review of related studies are represented. The third, fourth, and fifth sections are devoted to the QSPR analysis of aqueous solubility, lipophilicity, and toxicity for nitroaromatic compounds of military interest.

8.2   QSRP/QSAR Methods Used in This Chapter

8.2.1   Simplex Representation of Molecular Structure (SiRMS) Approach

Hierarchical technology for quantitative structure–activity relationships (HiT QSAR) [34, 38, 39], based on the simplex representation of molecular structure (SiRMS) method [34, 40, 41], was the method utilized for QSPR/QSAR analysis in the present study. This method has proven to be efficient in previous studies for solving a variety of "structure–activity" problems [35–37, 42]. Importantly, this approach allows for obtaining a solution for the problem specified in the QSAR, not ab ovo, but with the use of information received from a previous stage by means of the system of improved solutions. The application of HiT QSAR provides a set of related QSAR models that supplement each other (consensus strategy). Consensus QSAR modeling has gained in popularity and acceptance over the last decade and can be briefly described by the slogan "More models, good and different."

Advantage of this technique can be easily explained by the fact that the same predictions obtained by different and independent methods (either statistical or descriptors generation) are more preferable than single prediction made by even the best fitted and predictable model [39, 43].

Application of HiT QSAR methods allows one to derive a set of distinct QSAR models that complement each other. When combined, these models can solve problems related to virtual screening, evaluation of structural factors influence on activity, modification of known molecular structures, and design of new, potential high-performance drug agents.

The unique and principle feature of the HiT QSAR technology consists in applying multiaspects hierarchical strategy that includes the following steps: models of molecular structure description (1D → 2D → 3D → 4D); scales of activity estimation (binary → nominal → ordinal → continual); mathematical methods for the analysis of the structure–activity relationship (pattern recognition → rank → correlation → multivariate regression → PLS); and the final aims of QSAR research (prediction → interpretation → structure optimization → molecular design).

In the framework of SiRMS, any molecule can be represented as a system of different simplexes (tetratomic fragments of fixed composition, structure, chirality, and symmetry) [34, 36, 37, 40–42, 44]. Atoms in a simplex can be differentiated on the basis of differing characteristics, especially atom individuality, partial atom charge [45], lipophilicity of the atom [46], atomic refraction [47], and designation of the atom as possible hydrogen donor or acceptor during H-bond formation (A, hydrogen acceptor in H-bond; D, hydrogen donor in H-bond; I, indifferent atom).

Since only 1D and 2D models [34] are reviewed in this study, we present protocols to obtain information at the 1D and 2D levels only. 1D models consider only the gross formula of a molecule. Actually, such models reflect only the composition of a molecule. Obviously, it is quite impossible to solve the "structure–activity" tasks adequately using such approaches. Therefore, usually these models have an auxiliary role only, but sometimes they can also be used as independent virtual screening tools [48]. 2D models contain information about the structure of the compound and are based on its structural formula [49]. Such models reflect only the topology of the molecule. 2D models are very popular [35, 50]. The advantages of such approaches lie in fact that the topological model of molecular structure in an implicit form contains information about possible conformations of the compound. Over the years, experience has shown that the 2D level of representation of molecular structure is sufficient for the solution of more than 90% of existing QSAR/QSPR tasks.

8.2.2 Statistical Methods for Solution of QSPR Tasks

Below we will describe partial least squares or projection to latent structures (PLS) and random forest (RF) statistical approaches. These approaches have been used successfully for the development of QSAR/QSPR models. One also could use the

traditional QSAR tool—multiple linear regression (MLR) analysis; however, we will not describe it here, since it is well described elsewhere (see for instance [34]).

The large number of simplex descriptors was generated on the basis of the SiRMS approach. The PLS method [34, 45, 51, 52] is used for statistical model development as the most popular linear statistical method. The PLS method has proven to be efficient when a great number of variables is utilized. The removal of highly correlated and constant descriptors, genetic algorithm (GA) [53], trend-vector method (TV) [54, 55], and the automatic variable selection (AVS) strategy based on interactive [51] and evolutionary [52] selection of variables was used for selection of descriptors in PLS.

The results of the QSAR analysis can be extended to make predictions for compounds with unknown activity values (a process sometimes called "virtual screening"). With the purpose of analyzing the competence regions [56] of PLS models, "domain applicability" (DA) procedures, developed by us [34], have been successfully used in a number of applications.

RF is an effective nonparametric statistical technique for analysis involving large databases. The main features of RF are the following: it is possible to analyze compounds with different mechanism of action within one data set; there is no need to preselect descriptors; the method has its own reliable procedure for the estimation of both the model quality and its internal predictive ability; models obtained are tolerant to "noise" in the source experimental data. RF models can be constructed according to the methodology described in the literature for the original RF algorithm [57]. RF is an ensemble of single decision trees built by a classification and regression trees algorithm (CART) [58]. This ensemble produces a corresponding number of outputs. Outputs of all trees are aggregated to facilitate one final prediction. In regression, the final predicted value for a task is given as the average of the predictions from the individual trees. Each tree was grown as follows: (1) A bootstrap sample, which will be a training set for the current tree, is produced from the whole training set of N compounds. Compounds which are not in the current tree training set are placed in an out-of-bag (OOB) set (OOB set size is $N/3$). (2) The best split by CART algorithm [58] among the m randomly selected descriptors from the whole set of $M's$ in each node is chosen. The value of m is just one tuning parameter to which RF models are sensitive. (3) Each tree is grown to the largest possible extent. There is no pruning.

The tree approach [34] has been used for DA estimation. Such an approach for DA estimation is similar to some extent to methods described in Ref. [56]. As opposed to integral approaches [36] where usually the convex region (polyhedron, ellipsoid) that can contain vast cavities has been determined in the structural space, the applied approach is local. Actually, the space of structural parameters has been analyzed locally, i.e., regions around every training set point are analyzed. The presence of cavities in the structural space, which corresponds to DA, is undesirable, and it has been eliminated in the approach described here.

For the QSAR/QSPR statistical fit assessment determination coefficients for training and test sets R^2 and R^2_{test}, cross-validation determination coefficient Q^2 (in our studies, leave-group-out cross-validation algorithm has been used, where

amount of groups $= 7$), standard errors (SE) of prediction, and mean absolute error (MAE) have been used. $\mathrm{SE} = \sqrt{\sum_n (Y - \hat{Y})^2 / (n-1)}$, $\mathrm{MAE} = \sum_n |Y - \hat{Y}| / n$, where Y represents the observed property value, $\hat{Y}$ is the predicted property value, and n is the number of compounds in the corresponding set.

In addition, RF possesses its own reliable statistical characteristics, which could be used for validation and model selection. The major criterion for estimation of the predictive ability of the RF models and model selection is the value of R^2_{OOB}. The coefficient of determination for the OOB set is calculated similar to R^2_{test}: $R^2_{\mathrm{OOB}} = 1 - \sum_n (Y - \hat{Y})^2 / \sum_n (Y - \bar{Y})^2$, where Y is the observed property value, $\hat{Y}$ is the predicted property value, $\bar{Y}$ represents the average observed property value for training set, and n is the number of compounds in the OOB set.

8.3 Aqueous Solubility

Information on the solubility of new and emerging compounds is an important factor for environmental risk assessment, providing data for the modeling of transport and fate of chemical compounds and for understanding the pharmacokinetic behavior of contaminants in living organisms. The manufacturing, storage, transportation, and utilization of munitions can lead to the release of nitro- and nitroso-compounds into the environment. These compounds and their metabolites may have long-term environmental impact. In many cases, aqueous solubility (S_w) of new and emerging chemicals is the determinative property for the estimation of the environmental impact of these compounds, and it governs research related to remediation techniques. However, S_w experimental data, particularly on military crucial contaminants, often are not available and are only accessible as predicted values based on existing QSPR methodologies.

8.3.1 The Comparison of Recent Aqueous Solubility QSPR Models

Many attempts have been made to estimate S_w values using QSPR techniques beginning in the late 1970s [59]. During the last 35 years, various new methods have been proposed, and the accuracy of the predictions and coverage of chemical systems have been significantly improved.

Quantitative structure–property relationship (QSPR) investigations prior to 1990 [60–64] produced acceptable "structure–aqueous solubility" models, but only for small data sets with structurally similar molecules. One major limitation of these early approaches was that the factors that affect aqueous solubility for training set compounds were constrained to be similar for the test set data. For nonpolar compounds, aqueous solubility is controlled predominantly by solute molecular size

and shape [59]. Nevertheless, for polar solutes, other molecular properties, such as number of hydrogen bond donor and acceptor groups, atomic charges, polarizability, and polar surface area, must also be taken into account. Consequently, development of adequate QSPR models for diverse data sets was problematic. Quite often, only internal validation was used for the estimation of the predictive ability of models. This resulted in the development of over-fitted and, simultaneously, nonpredictive models. MLR methods represent the general statistical approaches used for the development of many of these early QSPR methods.

Advancement in computational methods and computer hardware in the last decade has made possible the creation of original descriptor sets for "structure–aqueous solubility" investigations, which have helped to improve the accuracy of S_W predictions. Great strides have been made particularly in modeling of the aqueous solubility of such multifunctional compounds as drugs [65, 66].

A brief description of the recent "structure–solubility" studies is presented in Table 8.1, along with an account of the number and type of descriptors used, and the statistics of the work set. Though the data do not represent an exhaustive listing of the recent advances, principle trends are clearly highlighted. Recent studies utilize a host of more powerful statistical techniques, e.g., PLS or artificial neural networks, as the foundation for QSPR investigations, along with the more traditional multiple linear regression approach. Genetic algorithms and other descriptor selection methods have also been heavily utilized. Diverse data sets have been employed more and more often, although some researchers have continued to investigate only specific classes of chemical compounds [67–69].

There are two main approaches applied to the development of QSAR methods used for aqueous solubility predictions. The first approach encompasses studies based on utilizing an experimental data (octanol/water partition coefficient, melting point, molecular volume, etc.) as descriptors for development of the QSPR models. Such methods are characterized by the use of global molecular features and small descriptor sets. Quite often, these approaches are based on specialized, expensive software and require supercomputer-level hardware to execute. The absence of corresponding experimental values for new compounds is their main limitation, which makes such approaches less attractive. Additionally, predictive ability of any approach still depends on the type and diversity of the compounds used in the training sets, the statistical methods employed, and the nature and availability of relevant descriptors. Comparative tests of software for aqueous solubility predictions have been carried out [59]. However, the results of such a comparison including an external set of 122 pharmaceutical compounds were mainly disappointing.

The second approach is based on obtaining information from the molecular structure of organic compounds. The more popular versions of these methods are "substructure" approaches, where a molecular structure is represented by atoms or fragment (atom groups) combinations. Very often, these approaches are based on the assumption that molecular properties could be represented as additive sums of the properties of their structural fragments. Thus, the "substructure" approaches are more practical because they allow for the calculation of S_w directly from the chemical structure. However, in reality, solubility does not obey an additive rule.

Table 8.1 Summary of recent aqueous solubility models

References	Compounds	Molecule count in		Statistics	Descriptors	Method	Comments
		Training	Test				
[68]	Diverse organic	930	177	$R^2 = 0.935$ $R^2_{test} = 0.911$	22 MOE and 65 structural	PLS, CR, NN	
[69]	Chlorinated hydrocarbons	50	73	$R^2 = 0.967$	3 MCI	MLR	Small work set Not suitable for military compounds
[70]	Diverse organic	949		$R^2 = 0.74$ $MAE = 0.58$	Log P and MP	MLR	Internal validation only
[71]	Polycyclic aromatic hydrocarbons	Not given	Not given	$R^2 = 0.97$ $Q^2 = 0.937$	Quantum chemical	PLS	Internal validation only
[72]	Polychlorinated dibenzo-p-dioxins	75		$R^2 = 0.978$	Mean molecular polarizability	MLR	Small work set Not suitable for military compounds No validation
[73]	Drugs	1,708		$Q^2 = 0.872$	Molecular surface	MLR	Internal validation only
[73]	Drugs	1,708		$Q^2 = 0.886$	Molecular surface and log P	MLR	Internal validation only
[74]	Diverse organic	3,664		$Q^2 = 0.832$	Atom type counts and log P	MLR	Internal validation only

(continued)

Table 8.1 (continued)

References	Compounds	Molecule count in		Statistics	Descriptors	Method	Comments
		Training	Test				
[75]	Drugs	110	40	$R^2_{\text{test}} = 0.9959$ RMSEP $= 0.096$	Log P, molecular volume, and H-bond-forming ability	MLR	Small work set
[76]	Diverse organic	108		$R^2 = 0.952$ SE $= 0.441$	Log P, MP, LUMO energy, and total molecular surface area (COSMO)	MLR	Small work set No validation
[76]	Diverse organic	21		$R^2 = 0.819$ SE $= 0.781$	Log P, MP, LUMO energy, and total molecular surface area (COSMO)	MLR	Small work set No validation
[76]	Diverse organic	10		$R^2 = 0.849$ SE $= 0.341$	Log P, MP, LUMO energy, and total molecular surface area (COSMO)	MLR	Small work set No validation

Reprinted from Kovdienko et al. [81]. With kind permission of © John Wiley & Sons (2010)

MOE molecular operating environment, *PLS* partial least squares, *CR* continuum regression, *NN* neural network, *MLR* multiple linear regression, *MCI* molecular connectivity indices, *MP* melting point, *MAE* mean absolute error, *RMSEP* root mean square error of prediction, *COSMO* conductor-like screening model, *LUMO* lowest unoccupied molecular orbital

This is the major reason why the accuracy of aqueous solubility estimations by such QSPR techniques is frequently unsatisfactory.

By analyzing the results of the QSPR studies [68–76] listed in Table 8.1, several important disadvantages of a traditional approach can be seen. In studies [71, 74, 77, 78], only the small data sets of specific classes of organic molecules were used. All the models listed in Table 8.1 are well fitted, and most of them are robust. The determination coefficient, R^2 values, listed in Table 8.1 are all ≥ 0.9, but a more important measure of model robustness, characterized by the "leave-one-out" determination coefficient, Q^2, yields a more realistic picture of the successes of the method. However, it was estimated only in a limited number of the studies [73, 75, 76]. Moreover, it is still necessary to test the ability of each method to predict the aqueous solubility of external validation sets of compounds. Unfortunately, some authors have ignored this fact and erroneously estimated the predictive ability of their method using only R^2 or Q^2 values. There are two examples [70, 79] of high-quality QSPR studies that resulted in robust and predictive QSPR models. Unfortunately, these models were mainly devoted to drug or drug-like compounds and thus cannot be used for solubility prediction of military compounds, which are structurally dissimilar. Finally, for computational methods that are based on a direct quantum-mechanical evaluation of solubility [74–78], it is still necessary to use physicochemical characteristics as descriptors and to employ potentially time-consuming software for solubility modeling. Sometimes, such approaches cannot be used to process large and diverse sets of compounds.

An application of the simplex representation of molecular structure (SiRMS) approach [38, 39] can overcome many of the deficiencies mentioned above. Particularly, usage of a SiRMS approach results in a greater flexibility in the description of the molecular structure of compounds. It also allows for the analysis of large and diverse data sets of organic chemicals. Consensus modeling implemented in HiT QSPR [39] can also increase the predictive reliability of subsequent QSPR models.

8.3.2 Application of Random Forest and Multiple Linear Regression Techniques to QSPR Prediction of an Aqueous Solubility for Nitroaromatic Compounds

This chapter focuses on a development of new QSPR equations for accurate prediction of S_w values for a diverse set of large (including a few thousand) organic compounds. Such a development was mirrored by the effort to improve the quality of the solubility predictions for a subset of the data set, explosives, and products of their environmental degradation, applying a SiRMS approach with subsequent validation of results using a broad spectrum of experimentally determined data.

For standardization, all aqueous solubilities [80] have been converted into mmol/L units, and final values are reported as log S_w [81]. The external test set of 301 molecules (entirely independent of the training set) was used for the estimation of accuracy of the predictive QSPR models. The training set contained nearly 190

nitro- and nitroso-compounds. 47 nitro-, nitroso-, and nitrogen-rich compounds (which are of interest for military applications as primary compounds or products of their environmental degradation) were included in the test set. The addition of such molecules in this work set provides an opportunity to develop well-fitted and robust models of aqueous solubility for nitroaromatic and nitrogen-rich compounds.

Log P [46] and molecular refraction [47] were used as two integral structural parameters added to the simplex descriptors differentiated by atom types. The most relevant 1,481 descriptors were selected from the initial pool by stepwise regression using the following protocol:

1. The first descriptor was selected (by maximum R^2 value) by complete enumeration of all the remaining (after elimination of nonsignificant and highly correlated variables) descriptors from the initial pool.
2. The second descriptor was selected in order to achieve maximum R^2 value in combination with the first selected descriptor by complete enumeration of all remaining descriptors.
3. The third descriptor was selected in a similar manner in order to achieve maximum R^2 value in combination with two previously selected descriptors.
4. This procedure was repeated until R^2 value started to increase, or until total number of selected descriptors reached number of molecules divided by 10 (Topliss rule).

Determination of optimal values of T (trees count) and m (descriptors count) represent the traditional starting points for every RF investigation. The following procedure is recommended for determination of an optimal T value: start from a small constant number of descriptors, increase the number of trees stepwise until R_{OOB}^2 does not change significantly. Once an optimal T value is identified, one builds models with the optimal number of trees by increasing the variable number in a stepwise manner. The final model is determined by the highest value of OOB set prediction accuracy. In the reviewed study, T and m values equal to 100 and 200, respectively, were found as optimal and were chosen for subsequent models.

A well-fitted RF model **I** based on 2D simplex descriptors ($R^2 = 0.99$, $R_{OOB}^2 = 0.88$) was obtained. The molecular fragments with significant influence on aqueous solubility are shown in Table 8.2. Data in Table 8.2 are arranged in decreasing order of Raw score [57, 58], which characterizes variable importance for a selected model. External validation by a diverse test set containing 301 molecules (including 47 nitro- and nitroso-compounds) shows an acceptable level of reliability and the high predictive ability for the derived model **I** ($R_{test}^2 = 0.82$).

The quality of the MLR model **II** obtained by the method of stepwise regression for "structure–aqueous solubility" investigation is also quite satisfactory—determination coefficient $R^2 = 0.85$, cross-validated determination coefficient $Q^2 = 0.83$. This model demonstrates the good predictive ability for the external test set compounds ($R_{test}^2 = 0.76$). Therefore, model **II** also can be used for estimation of the influence of various molecular fragments on solubility log S_w. The influence of some significant simplex descriptors is shown in Table 8.2 (data are arranged

Table 8.2 Descriptor importance of random forest model (**I**) and descriptor influences of MLR model (**II**)

Model I

#	Parameter	Raw score	#	Parameter	Raw score
1	Log P	0.749	13	[structure]	0.016
2	Molecular refraction	0.342	14	[structure]	0.014
3	[structure]	0.258	15	[structure Cl]	0.014
4	[structure]	0.231	16	[structure]	0.013
5	—O—H	0.076	17	[structure]	0.013
6	[structure]	0.068	18	[structure]	0.012
7	=O	0.068	19	—N	0.011
8	[structure]—Cl	0.062	20	[structure]	0.01
9	—Cl	0.051	21	N=	0.009
10	[structure]	0.036	22	[structure]	0.008
11	[structure]	0.03	23	H—N	0.008
12	[structure O—H]	0.022	24	[structure]	0.008

Model II

#	Variable name	Regression coefficient	β	#	Variable name	Regression coefficient	β
1	Log P	−0.526	−0.521	13	—N	0.266	0.060
2	Molecular refraction	−0.037	−0.344	14	[structure]	−0.051	−0.049
3	[structure]	−0.098	−0.213	15	[structure]	−0.553	−0.048
4	[structure]	0.164	0.152	16	[structure]	1.545	0.045
5	[structure]	0.708	0.113	17	[structure]	0.504	0.045
6	[structure]	−0.741	−0.091	18	[structure Cl]	−0.145	−0.042
7	[structure]	−0.217	−0.078	19	[structure]	2.149	0.031
8	[structure]	−0.758	−0.066	20	[structure N]	−1.566	−0.029
9	[structure]	−0.656	−0.063	21	[structure]	0.509	0.029
10	—O—H	0.158	0.061	22	[structure]	−0.681	−0.027
11	[structure]	−0.470	−0.049	23	[structure]	1.131	0.027
12	[structure]	−0.156	−0.044	24	[structure]	1.515	0.022

Reprinted from Kovdienko et al. [81]. With kind permission of © John Wiley & Sons (2010)

in decreasing order of normalized regression coefficients β [82]—characteristic of variable importance for MLR models).

It is significant that the magnitude of each regression coefficient for the derived models indicates the relative importance of each descriptor. Though it is possible to determine the degree of importance of descriptors for the RF model, it is absolutely impossible to establish what kind of influence (promoting or interfering action) the descriptors have on the final result. This is a direct consequence of the nonlinear character of the RF models. In studies such as that described, this problem can be overcome by joint consideration of results for both models obtained.
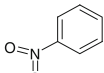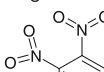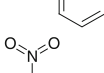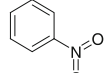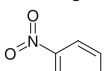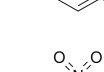
Therefore, the comparison of the results presented in Table 8.2 suggests that for this data set the **I** and **II** models reveal that lipophilicity is the most important contributor to aqueous solubility log S_w. This influence is highly interfering, i.e., these properties are inversely proportional quantities. Such effect conforms to the inversely proportional relationship between solubility log S_w and octanol-water partition coefficient log P [83]. Molecular refraction also has a largely interfering effect on aqueous solubility. This result steams from the fact that dispersion forces interfere with the transition of solute molecules into solution [84].

Analysis of the most important simplex parameters for the derived models demonstrates considerable negative influence of hydrophobic molecular fragments (parameters 3, 4, 6, 10, 11, 17 in Table 8.2) and positive effect of molecular fragments with polar substituents (parameters 5, 7, 12, 14, 19, 22–24 in Table 8.2). As a rule, many polar solutes have generally good solubility in water because of the presence of various hydrogen bond donor or acceptor groups.

The most important molecular fragments for the regulation of aqueous solubility of military compounds were identified and selected on the basis of aforementioned simplexes (see Table 8.3). As can be seen in Table 8.3 (*Section A*), an increase in the number of nitrogen atoms in the aromatic ring in the series benzene–pyridine–pyrimidine–pyridazine results in an increase in aqueous solubility. Correspondingly, an increase in the number of nitro groups causes a gradual decrease of aqueous solubility (Table 8.3, *Section B*). Analyzing trends in the data from Table 8.3 (*Section C*), it can be seen that amino and hydroxyl groups promote the dissolution process to a larger degree than the nitro- and nitroso groups. Most probably, this finding is due to the fact that amino and hydroxyl groups participate more readily in hydrogen bonding. The influence of selected fragments on lipophilicity and water solubility is shown in Table 8.3. As expected, an inverse relationship between lipophilicity and water solubility is observed.

Finally, in Table 8.4, we have collected solubility predictions for 47 nitro-, nitroso-, and nitrogen-rich compounds of military interest from the test set predicted by models **I** and **II**. Determination coefficients for this data set are $R^2_{\text{test}}(I) = 0.77$ and $R^2_{\text{test}}(II) = 0.38$ respectively. Additional investigation has shown the presence of two outliers in the observable test set (molecules 36, 37, Table 8.4) with $\sigma > 3$ [85]. Determination coefficients after outliers are removed are $R^2_{\text{test}}(I) = 0.86$, $R^2_{\text{test}}(II) = 0.84$.

Table 8.3 The comparative influence of some molecular fragments on aqueous solubility and lipophilicity for US Army interest compounds

Section	Fragment	Mean contribution to solubility	Mean contribution to lipophilicity
A	pyridazine	−0.111	−0.589
	pyridine	−0.851	0.578
	pyrimidine	−0.975	0.161
	benzene	−1.854	1.392
B	benzene	−1.789	1.031
	nitrobenzene	−2.012	1.178
	1,2-dinitrobenzene	−2.215	1.492
	1,3-dinitrobenzene	−2.259	1.250
	1,4-dinitrobenzene	−2.312	1.561
	1,3,5-trinitrobenzene	−2.417	1.379
C	H–N(H)–	−0.051	−0.357
	---O–	−0.196	0.354
	O=N–	−0.402	0.264
	O=N	−0.461	0.077

Reprinted from Kovdienko et al. [81]. With kind permission of © John Wiley & Sons (2010)

Table 8.4 Predicted values of the aqueous solubility log (S_w) for compounds of military interest

#	Compound	CAS number	Observed (log S_w)	Predicted (log S_w) **I**	Predicted (log S_w) **II**
1	2-Methyl-1,3-dinitrobenzene	606-20-2	0.040	0.075	0.512
2	4-Nitrobenzoic acid	62-23-7	0.077	1.322	0.904
3	3-Nitroaniline	99-09-2	0.940	1.240	1.254
4	2,6-Dichloro-4-nitroaniline	99-30-9	−1.466	−0.168	−0.084
5	1,3,5-Trinitrobenzene	99-35-4	0.112	0.689	0.193
6	1,2-Dichloro-4-nitrobenzene	99-54-7	−0.203	−0.741	−0.598
7	Ethyl-4-nitrobenzoate	99-77-4	−	0.293	0.612
8	4-Nitroaniline	100-01-6	0.720	1.240	1.254
9	4-Nitrophenol	100-02-7	1.917	1.736	1.537
10	1,2,4,5-Tetrachlor-3-nitrobenzol	117-18-0	−2,097	−2.135	−1.922
11	2-Methyl-1,3,5-trinitrobenzene	118-96-7	−0,246	0.408	0.084
12	3,5-Dinitrobenzamide	121-81-3	1.156	0.845	0.630
13	N-(3-Nitrophenyl)acetamide	122-28-1	0.835	1.125	0.849
14	Dimethoxy-(4-nitrophenoxy)-thioxo-phosphorane	298-00-0	−0.840	−0.587	−0.696
15	1-Bromo-4-nitrobenzene	586-78-7	−0.245	1,049	0.016
16	2-Nitrobenzamide	610-15-1	0.990	1,135	1,222
17	1-Ethyl 3,5-dinitrobenzoate	618-71-3	−0.010	0.315	0.184
18	3,5-Dinitroaniline	618-87-1	0.848	0.692	0.826
19	4-Nitrobenzamide	619-80-7	1,500	1,052	1,058
20	3-Nitrobenzamide	645-09-0	1.540	1.052	1.058
21	1,2,3,4-Tetrachloro-5-nitrobenzene	879-39-0	−1.557	−2.099	−2.066
22	2,4-Dichloro-1-(4-nitrophenoxy)benzene	1836-75-5	−2.453	−2.515	−2.524
23	1,3,5-Trichloro-2-(4-nitrophenoxy)benzene	1836-77-7	−2.623	−2.805	−3.102
24	2,6-Dinitro-N-propyl-4-(trifluoromethyl)-benzamine	2077-99-8	−1.457	−1.534	−2.176
25	Ethoxy-(4-nitrophenoxy)-phenyl-thioxo-phosphorane	2104-64-5	−2.019	−0.994	−2.665
26	N,N-Bis(2-chloroethyl)-4-methyl-2,6-dinitroaniline	26389-78-6	−2.328	−2.167	−2.814
27	N-(Cyclopropylmethyl)-2,6-dinitro-N-propyl-4-(trifluoromethyl)aniline	26399-36-0	−3.540	−3.333	−3.435
28	1-Bromo-2-chloro-4-nitrobenzene	29682-39-1	−1.094	−0.663	−0.656
29	N-(2-Chloroethyl)-2,6-dinitro-N-propyl-4-(trifluoromethyl)aniline	33245-39-5	−2.601	−2.966	−3.323
30	N-(1-Ethylpropyl)-3,4-dimethyl-2,6-dinitroaniline	40487-42-1	−3.009	−2.183	−2.351
31	Diethoxy-(4-nitrophenoxy)-thioxo-phosphorane	56-38-2	−1.424	−1.222	−1.304
32	4-Nitrotoluene	99-99-0	0.513	0.719	0.612

(continued)

Table 8.4 (continued)

#	Compound	CAS number	Observed (log S_w)	Predicted (log S_w) **I**	Predicted (log S_w) **II**
33	4-Methyl-3,5-dinitroaniline	19406-51-0	0.796	0.645	0.717
34	2-Methoxy-1,3,5-trinitrobenzene	606-35-9	−0.086	0.617	0.499
35	1-Methoxy-2,4-dinitrobenzene	119-27-7	−0.107	0.235	0.668
36	1,3,5,7-Tetranitro-1,3,5,7-tetrazocane	2691-41-0	−1.821	0.417	2.759
37	2,4,6,8,10,12-Hexanitro-2,4,6,8,10,12-hexaazatetracyclo[5.5.0.05,9.03,11]dodecane	135285-90-4	−2.081	0.165	2.764
38	N-Methyl-N-(2,4,6-trinitrophenyl)nitramide	479-45-8	−0.588	0.165	−0.286
39	1,4-Dinitrosobenzene	105-12-4	1.327	1.302	−0.538
40	Nitrosobenzene	586-96-9	1.301	1.561	0.470
41	1-Methyl-2,3,4-trinitrobenzene	602-29-9	−0.236	0.174	0.248
42	1-Methyl-2,4,5-trinitrobenzene	610-25-3	−0.166	0.354	0.084
43	1-Methyl-2,3-dinitrobenzene	602-01-7	0.080	−0.005	0.512
44	2-Methyl-1,4-dinitrobenzene	619-15-8	0.080	−0.011	0.348
45	2-Methyl-3,5-dinitroaniline	35572-78-2	0.796	0.652	0.717
46	1-Methoxy-3,5-dinitrobenzene	5327-44-6	0.183	0.463	0.410
47	2-Nitrotoluene	88-72-2	0.673	0.750	0.776

Reprinted from Kovdienko et al. [81]. With kind permission of © John Wiley & Sons (2010)

8.4   Lipophilicity

Lipophilicity plays a key role in many biochemical, pharmacological, and ecological processes. The octanol-water partition coefficient (LogK_{ow}) is widely applied in quantitative structure–activity/property relationship (QSAR/QSPR) studies. This property is used to provide invaluable information for overall understanding of the absorption, distribution, metabolism, and elimination of a wide variety of chemicals. However, experimental estimation of LogK_{ow} is expensive. Thus, there is a need to have reliable software that can be used for accurate prediction of lipophilicity for chemical compounds based on their structures.

Many approaches have been developed for the prediction of LogK_{ow} based on nonexperimental structural parameters. Such methods can be divided into two groups. The first group of methods are "substructure" approaches which use substructures where the molecular structure is represented by atoms (atom contribution methods) [86] or fragments (group contribution methods) [87]. In these approaches, LogK_{ow} values are obtained as a sum of the contributions of each atom or fragment of the molecules. Nevertheless, there are also nonadditive methods, in particular, ALOGPS [88], an approach that was recently developed on the basis of neural network ensemble analysis. In this method, the atom and bond-type E-state indices as well as the number of hydrogen and nonhydrogen atoms are used to represent the molecular structures.

The second group of methods is represented by "whole structure" approaches which use descriptors like topological indices [89] and/or integral molecular features [90] in calculating LogK_{ow}. However, these kinds of methods need experimental correction factors or complex correction terms.

In the past 10 years, many atom/group contribution approach type models for estimation of LogK_{ow} values have been developed and implemented in computational protocols. Most of these models are currently available as commercial software packages. For example, current popular LogK_{ow} models include XLog$P$ [86], ACD/Log$P$ [91], LogK_{ow} [92], CLog$P$ [87], KLog$P$ [93, 94], HLog$P$ [95], SMILELOG [96], CHEMICALC [97], and ALOGPS [88].

Majority of the existing theoretical methods for the calculation of LogK_{ow} are based on the assumption that the properties of a molecule could be represented as a sum of the properties of its structural fragments. But, in reality, lipophilicity does not obey the additive scheme. Some methods need experimental correction factors. This is the reason why the accuracy of such predictions using different QSPR methods is frequently unacceptably low for estimations of physical characteristics, including LogK_{ow}.

We expect that the application of simplex representation of molecular structure (SiRMS) [39, 48, 98] in combination with the random forest (RF) method [57, 58] will allow for the estimation of fragment contributions to lipophilicity in a nonlinear manner. Thus, it will be possible to overcome the described limitations and drawbacks of existing models.

8.4.1 QSPR Prediction of Lipophilicity for Nitroaromatic Compounds Using Random Forest Technique on the Basis of SiRMS Approach

The main goals of the recent activities were to develop new QSPR models for accurate prediction of LogK_{ow} values for different chemical compounds using a SiRMS approach and to define the influence of different structural factors on the studied property.

Experimental values for LogK_{ow} were obtained from the PHYSPROP database (version 2004) containing 13,474 compounds [99]. After removing compounds containing salts, mixtures of molecules, erroneous or wrong structures, and duplicates, a total number of 10,973 compounds, characterized by experimental LogK_{ow} values, were selected for the data set to be considered for the new SiRMS approach. LogK_{ow} values varied from -5.08 to 11.29, with an average value of 2.14.

In addition, two external test sets were used for evaluation of the models predictivity. 1,396 wrong structures from PHYSPROP database which had been excluded during the previous step were corrected according to their CAS registration

numbers using ChemSpider (http://www.chemspider.com), PubChemProject (http://pubchem.ncbi.nlm.nih.gov), and SciFinder(http://scifinder.cas.org) databases. Thus, the first external test set was formed from these 1,396 compounds.

The second test set contains 35 compounds which have strongly polar groups ($-NO_2$, $-N{=}O$) in their structures [98]. The presence of such groups often leads to errors in the $LogK_{ow}$ calculations.

In the reviewed study, the atoms were divided into groups corresponding to their (1) partial charge: $A < -0.17 < B < -0.05 < D < 0.06 < E < 0.17 < F < 0.28 < G < 0.40 < I$; (2) refraction: $A < 1.5 < B < 3 < C$; and (3) lipophilicity: $A < -1.51 < B < -0.96 < C < -0.42 < D < 0.13 < E < 0.68 < F < 1.23 < G$. For the atom H-bond characteristic, the atoms were divided into three groups: A (acceptor of hydrogen in H-bond), D (donor of hydrogen in H-bond), and I (indifferent atom). It should be noted that in this work lipophilicity ($XLog\,P$) was calculated by additive scheme [46].

Taking into account the popularity of different methods of estimation of additive lipophilicity, one considered that the analysis of structural factors which determine deviations from additivity is expedient. Using 7,900 integral parameters and 2D descriptors which were differentiated by lipophilicity, types, refraction, charges, and ability to be a donor or an acceptor of hydrogen bond, the well-fitted RF model **III** ($R^2_{OOB} = 0.930$, $SE = 0.47$, $MAE = 0.32$) was obtained. 79.9% of out-of-bag set compounds were predicted with $MAE < 0.5$. It should be noted that integral parameter of lipophilicity calculated by additive scheme presents about 33% of importance. This model approximates the database with high exactness.

In addition, two external test sets were used to compare our approach with current popular $LogK_{ow}$ models: KOWWIN v 1.67a [92] (EPI calc.), ACD lab v 10.04 [100] (ACD lab.), ALOGPS v 2.0 [88] (ALOGPS), $XLogP$ [46] ($XLogP$), and $LogP$ [95] (HyperChem). External validation by the first test set containing 1,396 organic molecules shows an acceptable level of reliability and demonstrates the high predictive ability for the developed model **III** ($R^2_{ext\_test\_1} = 0.856$, $SE = 0.64$, $MAE = 0.49$) along with best modern models (for **ALOGPS**[1]: $R^2_{ext\_test\_1} = 0.879$, $SE = 0.37$, $MAE = 0.57$; for **EPI calc.**: $R^2_{ext\_test\_1} = 0.864$, $SE = 0.39$, $MAE = 0.63$; for **XLogP**: $R^2_{ext\_test\_1} = 0.691$, $SE = 0.75$, $MAE = 1.0$; for **ACD lab.**: $R^2_{ext\_test\_1} = 0.815$, $SE = 0.46$, $MAE = 0.75$).

The predicted $LogK_{ow}$ values by different methods for 35 nitrogen-containing compounds of second test set are represented in Table 8.5. As it can be seen from Table 8.5, all models except HyperChem and XLogP provide good results for the prediction of values of octanol–water partition coefficient, i.e., the predicted $LogK_{ow}$ values are in good agreement with experimental ones for compounds of military interest.

---

[1]Most probably, the molecules of first external test were used for the construction of ALOGPS and EPI models.

Table 8.5 The prediction of $LogK_{ow}$ values by different methods for 35 military compounds of test set 2

#	Molecule	CAS	$LogK_{ow}$ (exp.)	Model III	EPI calc.	ACD lab.	ALOGPS	HyperChem	XLogP
1	Benzene, 2-methyl-1,3-dinitro-	606-20-2	2.10	2.18	2.18	2.08	1.81	−1.44	1.99
2	Benzoic acid, 4-nitro-	62-23-7	1.89	1.69	1.69	1.89	1.51	−0.23	1.41
3	Benzenamine, 3-nitro-	99-09-2	1.37	1.25	1.47	1.37	1.53	−0.72	1.09
4	Benzenamine, 2,6-dichloro-4-nitro-	99-30-9	2.80	2.73	2.76	3.54	3.01	0.32	2.33
5	Benzene, 1,3,5-trinitro-	99-35-4	1.18	1.64	1.45	1.22	1.54	−3.89	1.58
6	Benzene, 1,2-dichloro-4-nitro-	99-54-7	3.12	3.16	3.10	3.16	3.11	1.10	3.07
7	Benzoic acid, 4-nitro-, ethyl ester	99-77-4	2.33	2.39	2.14	2.33	2.25	0.14	2.16
8	Benzenamine, 4-nitro-	100-01-6	1.35	1.21	1.47	1.39	1.50	−0.72	1.09
9	Phenol, 4-nitro-	100-02-7	1.91	1.67	1.91	1.57	1.93	−0.22	1.46
10	Benzene, 1,2,4,5-tetrachloro-3-nitro-	117-18-0	4.38	4.42	4.39	3.73	4.09	2.14	4.31
11	Benzene, 2-methyl-1,3,5-trinitro-	118-96-7	1.73	1.86	1.99	1.68	1.50	−3.42	1.86
12	Benzamide, 3,5-dinitro-	121-81-3	0.83	0.56	0.37	0.55	0.52	−3.08	0.56
13	Acetamide, N-(3-nitrophenyl)-	122-28-1	1.47	1.49	1.64	1.47	1.18	−1.08	1.16
14	Phosphorothioic acid, O,O-dimethyl O-(4-nitrophenyl) ester	298-00-0	2.86	3.04	2.75	2.78	2.97	0.91	−1.06
15	Benzene, 1-bromo-4-nitro-	586-78-7	2.55	2.67	2.70	2.55	2.66	0.86	2.63
16	Benzamide, 2-nitro-	610-15-1	−0.12	0.46	−0.18	0.17	0.25	−1.10	0.69
17	Benzenamine, 3,5-dinitro-	618-87-1	1.89	1.13	1.29	1.74	1.57	−2.69	0.96
18	Benzamide, 4-nitro-	619-80-7	0.82	0.67	0.56	0.82	0.31	−1.10	0.69
19	Benzamide, 3-nitro-	645-09-0	0.77	0.69	0.56	0.68	0.21	−1.10	0.69
20	Benzene, 1,2,3,4-tetrachloro-5-nitro-	879-39-0	3.93	4.41	4.39	3.94	4.25	2.14	4.31
21	Benzene, 2,4-dichloro-1-(4-nitrophenoxy)-	1836-75-5	4.64	4.63	4.32	4.92	4.88	2.53	4.65

#	Compound	CAS							
22	Benzene, 1,3,5-trichloro-2-(4-nitrophenoxy)-	1836-77-7	4.97	5.19	4.96	5.33	5.26	3.05	5.27
23	Benzenamine, 2,6-dinitro-N-propyl-4-(trifluoromethyl)-	2077-99-8	3.65	3.24	3.78	4.98	3.32	−0.64	3.20
24	Phosphonothioic acid, phenyl-, O-ethyl O-(4-nitrophenyl) ester	2104-64-5	3.85	3.62	4.47	3.85	4.88	2.35	0.90
25	Benzenamine, N-(cyclopropylmethyl)-2,6-dinitro-N-propyl-4-(trifluoromethyl)-	26399-36-0	5.54	4.89	5.62	5.25	5.10	0.76	4.30
26	Benzene, 1-bromo-2-chloro-4-nitro-	29682-39-1	3.25	3.17	3.35	3.15	3.26	1.38	3.25
27	Benzenamine, N-(1-ethylpropyl)-3,4-dimethyl-2,6-dinitro-	40487-42-1	5.18	3.92	4.82	5.56	4.36	0.29	3.74
28	Phosphorothioic acid, O,O-diethyl O-(4-nitrophenyl) ester	56-38-2	3.83	3.60	3.73	3.84	3.76	1.59	−0.23
29	Benzene, 1-methyl-4-nitro-	99-99-0	2.37	2.36	2.36	2.41	2.34	0.54	2.12
30	Benzene, nitroso-	586-96-9	2.00	1.83	1.86	2.01	1.41	1.82	1.65
31	Benzene, 1-methyl-2-nitro-	88-72-2	2.30	2.33	2.36	2.41	2.32	0.54	2.12
32	Ethylene glycol dinitrate	628-96-6	1.16	0.55	1.17	1.16	1.17	−2.86	0.16
33	3-Nitrotoluene	99-08-1	2.45	2.35	2.36	2.41	2.32	0.54	2.12
34	2,4-Dinitrotoluene	121-14-2	1.98	2.18	2.18	2.08	1.90	−1.44	1.99
35	RDX	121-82-4	0.87	0.39	0.68	−2.19	1.07	3.46	−0.60
MAE				0.25	0.18	0.26	0.27	2.62	0.68
SE				0.37	0.24	0.62	0.36	2.93	1.22
$R^2_{ext\_test\_2}$				0.94	0.97	0.87	0.94	0.35	0.53

8.4.2 Analysis of the Influence of Structural Fragments on the Lipophilicity (2D QSPR Analysis Using SiRMS and PLS or RF Statistical Methods)

In the present study, 2D simplex descriptors for representations of molecular structure were utilized in the prediction of $\mathrm{Log}K_{\mathrm{ow}}$. The atoms were divided into groups corresponding to their (1) partial charge, $A < -0.17 < B < -0.07 < D < 0.03 < E < 0.14 < F < 0.24 < G < 0.35 < I$, and (2) refraction, $A < 1.5 < B < 3 < C$. The QSPR models were generated using a training set of 65 nitrogen-containing compounds (Table 8.6). Twenty-eight nitrogen-containing compounds from the PHYSPROP database [99] were added to 37 military compounds [98]. All of these compounds have polar groups ($-NO_2$, $-NH_2$, $N=O$, $-NH-OH$) in their structures. The presence of such groups often leads to errors at the $\mathrm{Log}K_{\mathrm{ow}}$ calculations.

At the initial step, 900 simplex descriptors were generated. The Y-scrambling test repeated 1,000 times revealed the absence of chance correlations ($Q_{\mathrm{YS}}^2 \leqslant 0.21 \pm 0.01$).

In modern QSAR analysis, the most effective predictions are achieved as the result of using consensus approaches [101–104], i.e., when several single models are used concurrently. In this study, the prognosis of the property of interest was developed by averaging the predictions generated by an ensemble of QSPR models.

For QSPR analysis, the training set was divided into five subsets in which each subset contained 20% of the molecules included in the test set. It should be noted that every molecule is included in a test set only one time. Statistical characteristics of the PLS models obtained are quite good ($Q^2 = 0.855–0.935$, $R_{\mathrm{test}}^2 = 0.833 - 0.878$). For average model **IV** (PLS (consensus)) with five subsets, MAE $= 0.27$; SE $= 0.34$. The model **IV** approximates the data with high exactness. Using 900 descriptors generated at initial step, the well-fitted RF model **V** ($R^2 = 0.987$; $R_{\mathrm{OOB}}^2 = 0.787$, SE $= 0.64$, MAE $= 0.44$) was obtained.

It was noted [34] that one of advantages of the SiRMS approach is that it can provide a good mechanistic interpretation. To test it, the influence of each atom (as a part of simplex) in the investigated property has been calculated on the basis of developed models **IV** and **V**. As shown in Table 8.7, the contributions of some fragments for these models vary in much the same way. The polar groups with potential hydrogen donor/acceptor of H-bond centers promote lipophilicity decrease ($-COOC_2H_5 > -OCH_3 > -OH > -COOH > -C=O > -CONHOH > -CONH_2 > -CH_2CH_2-NH_2 > -CH(CH_2NH_2)OH$). The contribution to lipophilicity of bromine and chlorine is higher than for fluorine. As expected, the accumulation of alkyl groups promotes lipophilicity increase: $-N(C_3H_7)(CH_2-C_3H_5) > -N(C_3H_7)(C_2H_4CL) > -NHCH(C_2H_5)_2 > -NHCH_2CH_2CH_3 > =NH$ $-NHOH > -NH_2 > -NHCONH_2$.

The current popular $\mathrm{Log}K_{\mathrm{ow}}$ models KOWWIN v 1.67a [92] (EPI calc.), ACD lab v 10.04 [100] (ACD lab.), ALOGPS v 2.0 [88] (ALOGPS), and XLogP [46] (XLogP) were used for calculations of the $\mathrm{Log}K_{\mathrm{ow}}$ values of the 65 molecules in this investigation (Table 8.6). As can be seen from the table, the developed models

Table 8.6 Observed and predicted LogK_{ow} values by different methods

#	Molecule	CAS number	Observed LogK_{ow}	Predicted			ALOGPS	ACDlab	XLogP
				IV	V	EPI calc.			
1	2-Methyl-1,3-dinitrobenzene	606-20-2	2.06	2.22	2.20	2.18	1.81	2.08	1.99
2	1,2,4,5-Tetrachloro-3-nitrobenzene	117-18-0	3.89	3.96	3.24	4.39	4.09	3.73	4.31
3	2-Methyl-1,3,5-trinitrobenzene	118-96-7	1.73	2.03	1.90	1.99	1.50	1.68	1.86
4	3,5-Dinitrobenzamide	121-81-3	0.83	0.64	0.86	0.37	0.52	0.55	0.56
5	N-(3-Nitrophenyl)acetamide	122-28-1	1.47	1.63	1.70	1.64	1.18	1.47	1.16
6	O,O-Dimethyl O-4-nitrophenyl phosphorothioate	298-00-0	2.86	2.52	3.11	2.75	2.97	2.78	−1.06
7	1-Bromo-4-nitrobenzene	586-78-7	2.55	2.34	2.22	2.70	2.66	2.55	2.63
8	2-Nitrobenzamide	610-15-1	−0.15	0.52	1.07	−0.18	0.25	0.17	0.69
9	3,5-Dinitroaniline	618-87-1	1.89	1.22	1.37	1.29	1.57	1.74	0.96
10	4-Nitrobenzamide	619-80-7	0.82	0.63	0.80	0.56	0.31	0.82	0.69
11	4-Nitrobenzoic acid	62-23-7	1.89	1.62	1.71	1.69	1.51	1.89	1.41
12	3-Nitrobenzamide	645-09-0	0.77	0.63	0.82	0.56	0.21	0.68	0.69
13	1,2,3,4-Tetrachloro-5-nitrobenzene	879-39-0	3.93	3.89	3.27	4.39	4.25	3.94	4.31
14	2,4-Dichloro-1-(4-nitrophenoxy)benzene	1836-75-5	4.64	4.35	3.57	4.32	4.88	4.92	4.65
15	1,3,5-Trichloro-2-(4-nitrophenoxy)benzene	1836-77-7	4.70	4.99	4.14	4.96	5.26	5.33	5.27
16	2,6-Dinitro-N-propyl-4-(trifluoromethyl)aniline	2077-99-8	3.65	3.63	3.54	3.78	3.32	4.98	3.20
17	O-Ethyl O-4-nitrophenyl phenylphosphonothioate	2104-64-5	3.85	3.79	3.35	4.47	4.88	3.85	0.90
18	N-(Cyclopropylmethyl)-2,6-dinitro-N-propyl-4-(trifluoromethyl)aniline	26399-36-0	5.54	5.22	4.31	5.62	5.10	5.25	4.30

(continued)

Table 8.6 (continued)

#	Molecule	CAS number	Observed $\text{Log}K_{ow}$	Predicted					
				IV	V	EPI calc.	ALOGPS	ACDlab	XLogP
19	1,2-Dichloro-4-nitrobenzene	29682-39-1	3.25	2.89	2.74	3.35	3.26	3.15	3.25
20	N-(2-Chloroethyl)-2,6-dinitro-N-propyl-4-(trifluoromethyl)aniline	33245-39-5	4.63	4.73	4.49	5.07	4.91	4.64	4.07
21	3-Nitroaniline	99-09-2	1.43	1.26	1.60	1.47	1.53	1.37	1.09
22	3,4-Dimethyl-2,6-dinitro-N-(pentan-3-yl)aniline	40487-42-1	5.18	5.33	3.33	4.82	4.36	5.56	3.74
23	O,O-Diethyl O-4-nitrophenyl phosphorothioate	56-38-2	3.83	3.69	3.18	3.73	3.76	3.84	−0.23
24	1-Methyl-4-nitrobenzene	99-99-0	2.37	2.16	2.32	2.36	2.34	2.41	2.12
25	1,3,5,7-Tetranitro-1,3,5,7-tetrazocane	2691-41-0	0.17	0.90	2.11	0.82	1.42	−2.92	−0.80
26	1,3,4,7,8,10-Hexanitrooctahydro-1H-5,2,6-(epiminomethanetriylimino)imidazo[4,5-b]pyrazine	135285-90-4	1.92	1.17	2.11	0.34	2.69	0.03	−1.57
27	2,6-Dichloro-4-nitroaniline	99-30-9	2.84	2.68	2.14	2.76	3.01	3.54	2.33
28	Nitrosobenzene	586-96-9	2.00	1.61	1.22	1.86	1.41	2.01	1.65
29	2-Methyl-1,4-dinitrobenzene	619-15-8	1.63	2.30	1.98	2.18	1.90	1.83	1.99
30	1-Methyl-2-nitrobenzene	88-72-2	2.30	2.15	2.29	2.36	2.32	2.41	2.12
31	1,3,5-Trinitrobenzene	99-35-4	1.18	1.64	1.80	1.45	1.54	1.22	1.58
32	1,2-Dichloro-4-nitrobenzene	99-54-7	3.05	3.07	2.65	3.10	3.11	3.16	3.07
33	Ethyl-4-nitrobenzoate	99-77-4	2.33	2.37	2.15	2.14	2.25	2.33	2.16
34	4-Nitroaniline	100-01-6	1.35	1.47	1.62	1.47	1.50	1.39	1.09

#	Name	CAS							
35	4-Nitrophenol	100-02-7	1.91	1.74	1.82	1.91	1.93	1.57	1.46
36	2,4-Dinitrophenol	51-28-5	1.67	1.72	1.77	1.73	1.89	1.74	1.93
37	4-(2-Amino-1-hydroxyethyl)benzene-1,2-diol	51-41-2	-1.24	-0.86	0.11	-1.16	-1.40	-0.88	-0.28
38	4-(2-Aminoethyl)benzene-1,2-diol	51-61-6	-0.98	-0.78	0.45	0.38	-0.40	0.12	0.55
39	2-(3,4,5-Trimethoxyphenyl)ethanamine	54-04-6	0.78	0.40	1.21	0.85	0.91	0.90	0.86
40	Benzamide	55-21-0	0.64	0.44	0.52	0.74	0.51	0.74	0.82
41	4-(Aminomethyl)benzoic acid	56-91-7	1.03	0.67	0.85	0.95	-2.05	0.77	0.77
42	1-*m*-Tolylurea	63-99-0	1.29	1.20	1.34	1.25	1.17	1.29	0.70
43	1,3-Dimethyl-2-nitrobenzene	81-20-9	2.95	2.50	2.48	2.91	2.76	2.87	2.40
44	1,2-Dimethyl-3-nitrobenzene	83-41-0	2.83	2.55	2.61	2.91	2.84	2.87	2.40
45	1-Chloro-2-methyl-3-nitrobenzene	83-42-1	3.09	2.69	2.43	3.00	2.87	3.10	2.73
46	2-Methoxy-3-nitroaniline	85-45-0	1.78	1.50	1.76	1.55	1.64	1.39	1.05
47	1-Chloro-2-nitrobenzene	88-73-3	2.24	2.48	2.56	2.46	2.48	2.34	2.45
48	2-Methoxyaniline	90-04-0	1.18	1.19	1.17	1.16	0.93	1.09	1.18
49	N-Phenylhydroxylamine	100-65-2	0.79	1.37	1.48	1.03	1.06	0.79	0.95
50	4-Nitrosophenol	104-91-6	1.29	1.40	1.62	1.38	1.12	1.27	1.27
51	1-Nitrosonaphthalen-2-ol	131-91-9	2.28	2.18	1.74	2.56	2.50	2.43	3.16
52	N-Hydroxybenzamide	495-18-1	0.26	0.70	1.28	0.61	0.17	0.26	1.07
53	2-(4-Butoxyphenyl)-N-hydroxyacetamide	2438-72-4	2.08	2.40	2.06	1.98	2.09	1.70	2.44
54	2-Methyl-4-nitrosophenol	6971-38-6	1.71	1.76	1.44	1.93	1.45	1.73	1.56
55	1-Hydroxy-3-phenylurea	7335-35-5	0.41	0.99	1.27	0.58	0.24	0.41	0.67

(continued)

Table 8.6 (continued)

#	Molecule	CAS number	Observed LogK_{ow}	Predicted					
				IV	V	EPI calc.	ALOGPS	ACDlab	XLogP
56	1-(2-Chloroethyl)-3-(3-methoxyphenyl)-1-nitrosourea	13909-21-2	2.66	2.14	2.63	2.57	2.49	2.66	1.68
57	1-(4-Chlorophenyl)-3-hydroxyurea	30085-34-8	1.39	1.64	1.72	1.23	0.81	1.39	1.29
58	3-Bromo-2-nitrosonaphthalen-1-ol	30922-52-2	2.93	2.65	2.47	3.45	3.11	2.93	3.95
59	2-Amino-4-nitrosophenol	75773-74-9	0.03	0.76	1.53	0.47	0.70	0.03	0.53
60	N-(4-Methoxybenzyl)-N-methylnitrous amide	84174-20-9	1.62	1.86	1.57	1.15	1.52	1.37	1.57
61	N-(3-Methoxybenzyl)-N-methylnitrous amide	98736-45-9	1.60	1.86	1.58	1.15	1.51	1.37	1.57
62	Ethane-1,2-diyl dinitrate	628-96-6	1.16	1.37	1.00	1.17	1.17	1.16	0.16
63	1-Methyl-3-nitrobenzene	99-08-1	2.45	2.16	2.27	2.36	2.32	2.41	2.12
64	1-Methyl-2,4-dinitrobenzene	121-14-2	1.98	2.16	1.86	2.18	1.90	2.08	1.99
65	1,3,5-Trinitro-1,3,5-triazinane	121-82-4	0.87	0.94	0.95	0.68	1.07	−2.19	−0.60
R^2				0.94	0.85	0.93	0.87	0.84	0.53
MAE				0.27	0.44	0.25	0.32	0.27	0.64
SE				0.34	0.64	0.37	0.53	0.66	1.07

Table 8.7 Influence of fragments

Fragment	Model IV (PLS)			Model V (RF)		
	Min	Max	Mean	Min	Max	Mean
$-COOC_2H_5$	0.599	0.599	0.599	0.096	0.096	0.096
$-OCH_3$	0.094	0.224	0.182	−0.083	0.142	0.021
$-OH$	−0.166	−0.041	−0.114	−0.221	0.041	−0.092
$-COOH$	−0.135	−0.135	−0.135	−0.162	−0.106	−0.134
$-C=O$	−0.446	−0.028	−0.236	−0.412	0.089	−0.169
$-CONHOH$	−0.736	−0.487	−0.593	−0.466	−0.030	−0.312
$-CONH_2$	−1.008	−0.633	−0.919	−0.938	−0.372	−0.76
$-CH_2CH_2-NH_2$	−1.133	−1.132	−1.132	−0.923	−0.689	−0.806
$-CH(CH_2NH_2)OH$	−1.629	−1.629	−1.629	−1.217	−1.217	−1.217
$-N(C_3H_7)(CH_2-C_3H_5)$	2.350	2.350	2.35	1.356	1.356	1.356
$-NHCH(C_2H_5)_2$	1.976	1.976	1.976	0.923	0.923	0.923
$-N(C_3H_7)(C_2H_4CL)$	1.864	1.864	1.864	0.950	0.950	0.95
$-NHCH_2CH_2CH_3$	0.914	0.914	0.914	0.327	0.327	0.327
$-NO_2$	−0.002	0.143	0.048	−0.094	0.262	0.045
$-N=O$	−0.001	0.050	0.014	−0.087	0.074	−0.017
$-NHCOCH_3$	−0.101	−0.101	−0.101	−0.228	−0.228	−0.228
$=NH$	−0.339	0.000	−0.145	−0.189	0.109	−0.071
$-NHOH$	−0.473	−0.143	−0.341	−0.289	−0.019	−0.2
$-NH_2$	−0.759	−0.237	−0.457	−0.527	−0.110	−0.326
$-NHCONH_2$	−0.735	−0.735	−0.735	−0.458	−0.458	−0.458
$-CL$	0.049	0.204	0.158	−0.008	0.174	0108
$-BR$	0.104	0.125	0.116	−0.029	0.198	0.101
$-F$	0.023	0.023	0.023	0.043	0.044	0.044
$-OPS(O)$	0.109	0.237	0.166	0.291	0.327	0.302
$-P$	0.062	0.171	0.114	0.105	0.132	0.115
$\overset{S}{\underset{}{\overset{\|}{P}}}$	0.062	0.171	0.114	0.220	0.238	0.227

IV and **V** have an acceptable level of reliability and high predictive ability and are comparable to the best modern models.

Based on the data from Table 8.6, one can conclude that all models except XLogP show reasonable values for the prediction of octanol-water partition coefficients, i.e., the predicted $LogK_{ow}$ values are in good agreement with experimental ones for military important compounds.

The next task includes predictions of the properties for compounds for which no experimental data exists. Using different methods, $LogK_{ow}$ values were predicted for 29 military compounds with unknown experimental $LogK_{ow}$. The predicted $LogK_{ow}$ values of these compounds are presented in Table 8.8. In this table, the $LogK_{ow}$ values are presented also for model **III** which was developed on the basis of PHYSPROP database (see above, Sect. 8.4.1). Interestingly, 60% of the molecules from this set were predicted by different methods with $\Delta_{Max-Min}$ less than 1.

Table 8.8 The prediction of $LogK_{ow}$ values by different methods for 29 military compounds with unknown experimental $LogK_{ow}$

#	Molecule	CAS	EPI calc.	ACD lab.	ALOGPS	Model III	Model IV	Model V	Mean value	Δ(Max−min)
1	Ethyl 3,5-dinitrobenzoate	618-71-3	1.95	1.91	2.07	2.25	2.37	2.83	2.23	0.92
2	N,N-Bis(2-chloroethyl)-4-methyl-2,6-dinitroaniline	26389-78-6	4.42	2.87	3.32	3.13	4.31	4.30	3.73	1.55
3	4-Methyl-3,5-dinitroaniline	19406-51-0	1.84	2.2	1.8	1.44	1.62	1.74	1.77	0.76
4	2-Methoxy-1,3,5-trinitrobenzene	606-35-9	1.53	1.04	1.29	1.56	2.23	1.68	1.56	1.19
5	1-Methoxy-2,4-dinitrobenzene	119-27-7	1.71	1.56	1.68	1.71	2.20	1.75	1.77	0.64
6	N-Methyl-N,2,4,6-tetranitroaniline	479-45-8	1.64	1.49	1.64	1.95	2.63	2.63	2.00	1.14
7	1,4-Dinitrosobenzene	105-12-4	1.73	1.7	1.31	1.48	1.63	1.73	1.60	0.42
8	1-Methyl-2,3,4-trinitrobenzene	602-29-9	1.99	2.12	1.43	1.9	2.64	3.26	2.22	1.83
9	1-Methyl-2,4,5-trinitrobenzene	610-25-3	1.99	1.65	1.52	1.88	2.38	1.41	1.81	0.97
10	1-Methyl-2,3-dinitrobenzene	602-01-7	2.18	2.3	1.88	2.1	2.39	2.29	2.19	0.51
11	2-Methyl-3,5-dinitroaniline	35572-78-2	1.84	2.2	1.83	1.47	1.59	1.88	1.80	0.73
12	1-Methoxy-3,5-dinitrobenzene	5327-44-6	1.71	2.14	1.68	1.83	1.97	2.16	1.92	0.48
13	2,3-Dinitroanisole	16315-07-4	1.71	1.92	1.63	1.69	2.27	1.94	1.86	0.64
14	2,5-Dinitroanisole	3962-77-4	1.71	1.45	1.68	1.74	2.27	1.77	1.77	0.82
15	2,3,6-Trinitrotoluene	18292-97-2	1.99	1.65	1.47	1.89	2.44	2.09	1.92	0.97
16	3,4-Dinitroanisole	4280-28-8	1.71	2.22	1.69	1.83	2.33	1.79	1.93	0.64
17	1,3,5-Trinitrosobenzene	–	1.6	1.77	1.29	1.24	1.81	1.16	1.48	0.65
18	1,3-Dinitrosobenzene	7259-71-4	1.73	1.86	1.31	1.58	1.68	1.40	1.59	0.55
19	1,3-Dinitro-5-nitroso-1,3,5-triazine	–	−0.7	−0.47	0.54	1.08	1.11	1.45	0.50	2.15
20	1,3-Dinitroso-5-nitro-1,3,5-Triazine	–	−0.64	−0.41	0.5	0.89	1.08	1.46	0.48	2.10

		CAS								
21	1,3,5-Trinitroso-1,3,5-triazine	–	−0.59	−0.35	0.95	0.67	1.06	1.32	0.51	1.91
22	1-Hydroxylamino-3,5-dinitro-1,3,5-triazine	–	−0.09	−1	0.2	0.44	0.84	1.21	0.27	2.21
23	1-Hydroxylamino-3-nitroso-5-nitro-1,3,5-triazine	–	−0.04	−0.94	0.12	0.27	0.82	1.21	0.24	2.15
24	1-Hydroxylamino-3,5-dinitroso-1,3,5-triazine	–	−0.56	−0.88	0.58	0.05	0.79	1.04	0.17	1.92
25	3-Amino-2,6-dinitrotoluene	10202-92-3	2.38	2.68	1.8	1.83	2.07	1.85	2.10	0.88
26	2-Hydroxylamino-4,6-dinitrotoluene	59283-76-0	1.79	1.96	1.44	1.27	1.86	1.62	1.66	0.69
27	FOX-7 or 1,1-diamino-2,2-dinitroethylene	145250-81-3	−2.86	−2.71	0.41	0.64	0.41	1.10	−0.50	3.96
28	HBT (C1(NNC2=NN=NN2)=NN=NN1)	74999-19-2	−2.97	−2.01	0.13	−0.38	0.96	1.02	−0.54	3.99
29	5-Nitro-1,10-phenanthroline	4199-88-6	2.11	1.56	2.31	2.38	2.45	2.39	2.20	0.89

8.5 Toxicity

Quantitative structure–activity relationships are widely used to predict toxicity of compounds based on the chemical structure and corresponding physicochemical properties. The development and application of QSAR started with the prediction of toxicity caused by baseline toxicants [20, 21]. A prerequisite for correct predictive assessment of chemical toxicity using QSAR is an accurate assignment of toxic action modes that could be caused by different factors related to the structure of molecules-toxicants in a complex system. The nitroaromatic compounds display complex mechanisms of toxicity, and numerous QSAR studies have been undertaken to explain and predict toxicity of nitrocompounds on different living systems [31, 32].

In spite of acceptable QSAR models being developed on the basis of topological and quantum-chemical indexes, many questions remain unanswered. One of them, addressed in this study in great detail, is the relationship between chemical structure and toxicity. This information could provide a basis for the formation of new hypotheses as to mechanisms of chemical toxic action. Therefore, the aim of the study reviewed in this section was to extend recent investigations [105] by applying the hierarchical technology for quantitative structure–activity relationships (HiT QSAR) for (1) evaluation of the influence of structure, including analysis of the substitution characteristics of nitroaromatic compounds on their toxicity, (2) and in vivo prediction of toxicity for new nitroaromatic derivatives.

8.5.1 The Effect of Nitroaromatics' Composition on Their Toxicity In Vivo (1D QSAR Analysis)

In recent papers [105, 106], the QSAR analysis of oral toxicity of a variety of compounds on rats has been developed for 28 selected nitroaromatic molecules. This study started with construction of descriptions of the structure-toxicity relationship for the same compounds using simpler descriptors. Therefore, analysis of the potential for toxicity of nitroaromatics through a preliminary virtual screening by QSAR models on the basis of their composition was undertaken. For this task, the 1D QSAR models based on the simplex representation of molecular structure (SiRMS) approach [40, 41] have been applied to predict the oral rat toxicity of selected nitroaromatic compounds.

In combination with the individuality markers of the atoms, their electronegativity and refraction have also been used [48]. The atoms have been divided depending on the mentioned above physicochemical characteristics into seven groups corresponding to their refraction $A \le 2 < B \le 3 < C \le 4 < D \le 6 < E \le 9 < F \le 12 < G$ and electronegativity $A \le 1.5 < B \le 2 < C \le 2.5 < D \le 3 < E \le 3.5 < F$. It is necessary to note that, for the QSAR analysis together with simplex descriptors, the other structural parameters corresponding to molecular fragments of different sizes can be

applied. Thus, in this work, molecular fragments containing from 1 to 7 atoms have been used. All fragmentary descriptors (except simplexes) have been differentiated only by an atom individuality.

Investigated structures [106] as well as their gross formulas obtained using different ways of atoms' differentiation (see above) are presented in Table 8.9. The experimentally determined (observed) values of toxicity of investigated structures as well as those predicted by the developed QSAR models are displayed in Table 8.10.

Approximately 1,200 descriptors have been calculated during the initial stage of this work. After the removal of highly correlated and constant descriptors and trend-vector procedure, only 32 of them remained for PLS models development using the procedures mentioned above.

Based on previous studies [36, 42, 59], one can conclude that in most cases QSAR tasks can be solved at the 2D level of representation of molecular structure. In this work, the possibility of usage of an additive 1D QSAR model as a virtual screening tool has been also considered. This was the first attempt to use 1D models on the basis of SiRMS as an independent tool for development of QSAR analysis.

Usually such models have only an auxiliary role and are used in preliminary stages of investigations because of the absence of molecular structure consideration even on a topological level. Despite these limitations, a satisfactory QSAR model **VI** ($R^2 = 0.81$; $Q^2 = 0.69$) was developed. It explains 81% of the total toxicity variation in the considered nitroaromatic set and has no outliers both by classical 3σ rule as well as Williams graph [107]. However, the quality of predictions for molecules 13 and 17 is poor. As can be seen in Table 8.11, in this model not only the number of atoms of certain elements but also their combinations differentiated by electronegativity and refraction have been used. This fact, in our opinion, governs the quality of the developed QSAR model. Such set of descriptors allows the consideration of interactions of contributions of different atoms into activity that, finally, leads to a nonadditive model. As can be seen in Fig. 8.1a, the range of separate atoms' contributions to toxicity is quite large.[2] One can conclude that the presence of nitrogen (belonging to the nitro group), oxygen (belonging to the nitro group, hydroxyl, and carboxyl), and fluorine atoms promotes an increase of toxicity. Interestingly, carbon atoms (in methyl groups) are predicted to decrease the toxicity.
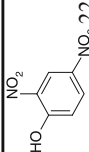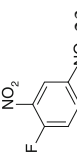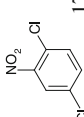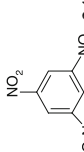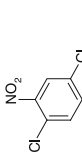
The additive QSAR model **VII** ($R^2 = 0.67$; $Q^2 = 0.53$) has been developed in order to compare with model **VI**. The numbers of atoms of different elements were used as structural descriptors here. Although this model is statistically significant, it is unfit for toxicity screening.
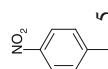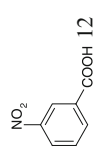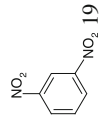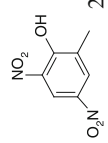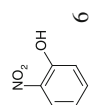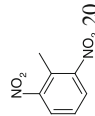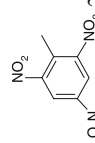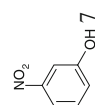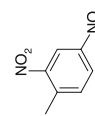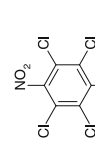
Understanding that the quality of model **VII** is too low to make any conclusions, we would like to note that, as obvious from Fig. 8.1b, in this case as well as in model **VI**, the presence of O, N, and F atoms increases toxicity and carbon atoms decrease it. Averaged influence of chlorine atoms is close to zero because there are both high and low toxic chlorine derivatives of nitrobenzene. Thus, this model reflects the same trends as the former one except the chlorine influence.

---

[2]For fluorine, there is only one contribution value because it occurs only in compound 23.

Table 8.9 Structures and gross formulas of investigated compounds

Structure	Gross formulas (element) (Electronegativity) (Refraction) (Model **VIII**)	Structure	Gross formulas (element) (Electronegativity) (Refraction) (Model **VIII**)	Structure	Gross formulas (element) (Electronegativity) (Refraction) (Model **VIII**)	Structure	Gross formulas (element) (Electronegativity) (Refraction) (Model **VIII**)
1	C_6H_6 / C_6D_6 / A_6B_6 / C_6H_6	8	$C_6H_5N_1O_3$ / $C_5D_6E_4$ / A_8B_7 / C_6H_4NO	15	$C_8H_9N_1O_2$ / $C_9D_8E_3$ / $A_{11}B_9$ / $C_6H_3NM_2$	22	$C_6H_4N_2O_5$ / $C_4D_6E_7$ / A_9B_8 / $C_6H_3N_2O$
2	C_7H_8 / C_8D_7 / A_8B_7 / C_6H_5M	9	$C_6H_4N_1O_2Cl$ / $C_4D_6E_4$ / A_6B_7D / C_6H_4NCl	16	$C_8H_9N_1O_2$ / $C_9D_8E_3$ / $A_{11}B_9$ / $C_6H_3NM_2$	23	$C_6H_3N_2O_4F$ / $C_3D_6E_6$ / A_8B_8 / $C_6H_3N_2F$
3	$C_6H_5N_1O_2$ / $C_5D_6E_3$ / A_7B_7 / C_6H_5N	10	$C_6H_4N_1O_2Cl$ / $C_4D_6E_4$ / A_6B_7D / C_6H_4NCl	17	$C_6H_3N_1O_2Cl_2$ / $C_3D_6E_5$ / $A_5B_7D_2$ / $C_6H_3NCl_2$	24	$C_6H_3N_3O_6$ / $C_3D_6E_9$ / A_9B_9 / $C_6H_3N_3$
4	$C_7H_7N_1O_2$ / $C_7D_7E_3$ / A_9B_8 / C_6H_4NM	11	$C_6H_4N_1O_2Cl$ / $C_4D_6E_4$ / A_6B_7D / C_6H_4NCl	18	$C_6H_3N_1O_2Cl_2$ / $C_3D_6E_5$ / $A_5B_7D_2$ / $C_6H_3NCl_2$	25	$C_6H_2N_1O_2Cl_3$ / $C_2D_6E_6$ / $A_4B_7D_3$ / $C_6H_2NCl_3$

5

$C_7H_5N_1O_3$
$C_7D_7E_3$
A_9B_8
C_6H_4NM

12

$C_7H_5N_1O_4$
$C_5D_7E_5$
A_9B_8
C_6H_4NK

19

$C_6H_4N_2O_4$
$C_4D_6E_6$
A_8B_8
$C_6H_4N_2$

26

$C_7H_6N_2O_5$
$C_6D_7E_7$
$A_{11}B_9$
$C_6H_2N_2MO$

6

$C_7H_5N_1O_3$
$C_5D_6E_4$
A_8B_7
C_6H_4NO

13

$C_7H_5N_1O_4$
$C_5D_7E_5$
A_9B_8
C_6H_4NK

20

$C_7H_6N_2O_4$
$C_6D_7E_6$
$A_{10}B_9$
$C_6H_3N_2M$

27

$C_7H_5N_3O_6$
$C_5D_7E_9$
$A_{11}B_{10}$
$C_6H_2N_2M$

7

$C_7H_5N_1O_3$
$C_5D_6E_4$
A_8B_7
C_6H_4NO

14

$C_7H_6N_1O_2Cl$
$C_6D_7E_4$
A_8B_8
C_6H_4ND

21

$C_7H_6N_2O_4$
$C_6D_7E_6$
$A_{10}B_9$
$C_6H_3N_2M$

28

$C_6N_1O_2Cl_5$
D_6E_8
$A_2B_7D_5$
C_6NCl_5

Table 8.10 Observed and predicted values of investigated nitroaromatics toxicity

Structure	$-\lg LD_{50}$(rats), mmol/kg										
	Observed	Predicted by model									
		VI	VII	VIII	IX	X	XI	XII	XIII	XIV	XV
1[a, c]	−1.86	−1.46	−1.19	−1.59	−1.66	−1.81	−1.37	−1.73	N/A	−1.78	−1.58
2	−1.78	−1.80	−1.49	−1.84	−1.55	−1.81	−1.88	−1.95	N/A	−1.90	−1.77
3	−0.69	−0.69	−0.67	−0.76	−0.67	−0.78	−0.67	−0.65	−0.60	−0.74	−0.71
4	−0.81	−0.83	−0.97	−1.03	−1.14	−0.97	−0.91	−0.92	−0.89	−0.86	−0.97
5[c]	−1.19	−0.83	−0.97	−1.03	−1.14	−0.97	−0.91	−1.02	−1.11	−1.07	−0.97
6	−0.38	−0.40	−0.42	−0.36	−0.49	−0.34	−0.33	−0.30	−0.06	−0.29	−0.39
7	−0.37	−0.40	−0.42	−0.36	−0.49	−0.34	−0.33	−0.34	−0.60	−0.46	−0.39
8[b]	−0.16	−0.40	−0.42	−0.36	−0.49	−0.34	−0.33	−0.15	−0.16	−0.17	−0.39
9[a]	−0.23	−0.63	−0.67	−0.45	−0.45	−0.38	−0.38	−0.24	−0.65	−0.26	−0.46
10[b]	−0.39	−0.63	−0.67	−0.45	−0.45	−0.38	−0.38	−0.36	−0.60	−0.48	−0.46
11[c]	−0.43	−0.63	−0.67	−0.45	−0.45	−0.38	−0.38	−0.55	−0.60	−0.63	−0.46
12[b, c]	−0.61	−0.45	−0.45	−0.74	−0.79	−0.67	−0.98	−0.84	−0.58	−0.75	−0.73
13[b]	−1.07	−0.45	−0.45	−0.74	−0.79	−0.67	−0.98	−0.98	−0.60	−1.03	−0.73
14[a]	−1.02	−1.26	−0.97	−1.03	−0.79	−0.67	−0.63	−0.93	−0.95	−0.98	−0.88
15	−1.12	−1.16	−1.26	−1.15	−1.01	−1.09	−1.18	−1.11	−1.18	−1.08	−1.12
16[b]	−1.21	−1.16	−1.26	−1.15	−1.01	−1.09	−1.18	−1.10	−0.89	−1.25	−1.12
17	−1.32	−0.71	−0.67	−0.72	−0.84	−0.64	−0.65	−1.29	−0.65	−0.75	−0.71
18	−0.52	−0.71	−0.67	−0.72	−0.84	−0.64	−0.65	−0.49	−0.60	−0.37	−0.71
19	0.31	−0.05	−0.16	0.16	0.44	0.16	0.07	0.19	−0.17	−0.14	0.16
20	−0.14	−0.07	−0.45	−0.27	−0.17	−0.26	−0.22	−0.09	−0.46	−0.26	−0.20
21[c]	−0.17	−0.07	−0.45	−0.27	−0.17	−0.26	−0.22	−0.13	−0.46	−0.31	−0.20
22[a]	0.41	0.21	0.10	0.71	0.24	0.72	0.45	0.50	0.37	0.43	0.47
23	0.57	0.86	0.87	0.68	0.58	−0.04	0.55	0.50	0.37	0.74	0.53
24	−0.11	0.15	0.36	0.05	0.14	0.10	−0.01	−0.08	0.26	0.01	0.08
25	−0.67	−0.83	−0.67	−0.71	−0.88	−0.69	−0.70	−0.78	−0.65	−0.63	−0.76
26[b, c]	0.52	0.26	−0.19	0.40	0.48	0.27	0.24	0.51	0.37	0.46	0.33
27[a]	−0.49	−0.52	0.07	−0.64	−0.24	−0.62	−0.59	−0.53	−0.03	−0.32	−0.52
28[a]	−0.57	−0.84	−0.67	−0.67	−0.99	−0.85	−0.84	−0.63	−0.70	−0.64	−0.84

Reprinted from Kuz'min et al. [48]. With kind permission of Elsevier (2008)

[a]This molecule have been used for model **IX** test set

[b]This molecule have been used for model **X** test set

[c]This molecule have been used for model **XI** test set

With the goal to describe investigated molecules at the 1D level in more details, the presence of the different substituents by their representation as pseudoatoms was considered explicitly. In other words, gross formulas of the compounds under consideration were expressed in the following way:

$$HhCcNaObMmKkDdFfCli,$$

where $N = NO_2$, $O = OH$, $M = CH_3$, $K = COOH$, $D = CH_2Cl$, $h = 0–6$; $c = 6–8$; $a = 0–3$; $b = 0–1$; $m = 0–2$; $k = 0–1$; $d = 0–1$; $f = 0–1$; $i = 0–5$.

Table 8.11 1D QSAR model **V1** descriptors and their relative influence on toxicity change

Descriptor (differentiation)	Corresponding atom combination	Relative contribution in activity (%)
Toxicity increase		
E (electronegativity)	N or O	28
A_2B (van der Waals attractive potential)	H_2O or H_2F	13
CFH_2 (element)	CFH_2	12
Toxicity decrease		
C_4 (element)	C_4	18
C_3N_3H (element)	C_3N_3H	14
AB_2D_2 (atomic refraction)	HC_2Cl_2, $HCNCl_2$, HN_2Cl_2, OC_2Cl_2, $OCNCl_2$, ON_2Cl_2	8
C_6Cl (element)	C_6Cl	
		7

Reprinted from Kuz'min et al. [39]. With kind permission of © Springer (2008)

Formally, because of such consideration of substituents, model **VIII**[3] represents ND QSAR level, where $1 < N < 2$. Practically, in this case, toxicity is determined by the number of substituents of different kind in benzene ring without taking their mutual positions into account. Nevertheless, even such molecular models are sufficient to develop QSAR relationship which quality is adequate for virtual screening of toxicity ($R^2 = 0.91$; $Q^2 = 0.83$).

The R^2 and Q^2 values provide necessary characteristics of model goodness-of-fit, robustness, and internal predictivity, but usually they cannot provide reliable information about its external predictive ability. Hence, for an additional validation, the initial set of 1–28 compounds was divided into training and test sets. Approximately 20% [85, 107] (6 compounds) representing different groups of activity were selected to the test set, and 22 remaining compounds were assigned to the training set. In order to enhance tests of the prediction power of the obtained QSAR model **VIII**, three different test sets were used during this analysis. Test set patterns were developed in the following way: dissimilarity matrix for all initial training set molecules was obtained on the basis of normalized structural descriptors of model **VIII**. Structural dissimilarity was estimated through Euclidean distances in multidimensional space of used molecular descriptors on the basis of this matrix. Thus, the total structural dissimilarity toward the rest of initial work set compounds can be calculated for every molecule as a sum of corresponding Euclidean distances. In the meanwhile, all the compounds were divided into groups depending on their toxicity, where the number of groups equals the number of molecules that one wants to include into the test set. One compound from each group was chosen for

[3]Differentiations of atoms by their refractions and electronegativities were not used in this model because of representation of the whole substituent like one pseudoatom.
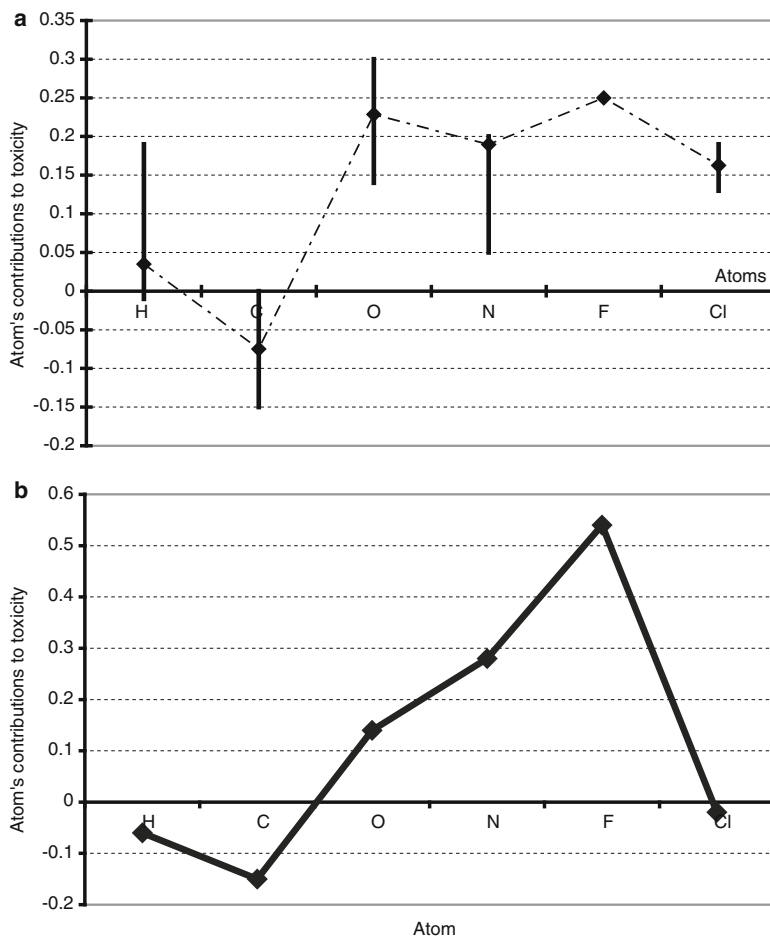
Fig. 8.1 Atom's contributions to toxicity change: (**a**) simplex 1D QSAR model **VI**; (**b**) additive model **VII** (Reprinted from Kuz'min et al. [48]. With kind permission of Elsevier 2008)

inclusion into the test set according to its maximal (or minimal) total Euclidean distance toward the other molecules from this group, or by random choice. Thus, the first test set was constructed to maximize its diversity with the training set (model **IX**), i.e., compounds with the maximal dissimilarity were chosen. The second test set was created in order to minimize it diversity with the training set (model **X**), i.e., less dissimilar compounds from each group were removed. And the last test set was chosen in a random manner, taking into account activity variation only (model **XI**). All of developed models **IX–XI** were well fitted and robust and have good internal and external predictivities ($R^2 = 0.84$–0.88; $Q^2 = 0.64$–0.80; $R^2_{\text{test}} = 0.84 - 0.87$). Thus, one can conclude that composition of nitroaromatics (with the

explicit consideration of substituents) contains sufficiently useful information for preliminary toxicity screening within the frameworks of nonadditive QSAR model.

The importance of nonadditivity is evident from the analysis of Fig. 8.2a. For example, it is apparent that the contribution of nitro groups into toxicity depends substantially on the presence/absence of other substituents and varies from highly positive to weakly negative. Only in one case involving one substituent (fluorine) that appears in the training set in only one molecule did we encounter a direction of change of toxicity values that could not be determined. The analysis of mean contributions depicts the same trend as previous QSAR models, i.e., nitro groups and hydroxyl groups increase toxicity, and the presence of methyl group decreases toxicity. The validity of this trend is confirmed by the results of the 2D QSAR model **XII** [106] which does not contain outliers and where the topological structure of the molecules is taken into account (see below, Sect. 8.5.2). An additional advantage of model XII is that partial atom charge, lipophilicity of the atom, atomic characteristics as possible donor or acceptor of H-bonds, and van der Waals attraction and repulsion potentials [108] were considered along with the presence of atoms, individuality, electronegativity, and refraction. Despite the fact that model **XII** is much more accurate ($R^2 = 0.98$, $Q^2 = 0.91$, plus additional external validation of its predictivity) than the 1D models, all trends of substituents' contributions to toxicity fluctuation are preserved in the latter (see Fig. 8.2b), with the only one exception—carboxyl group that is contained only in two compounds.

In additive[4] model **XIII**, the structural descriptors were expanded to include the number of substituents relative to their position toward nitro groups. Thus, every nitroaromatic compound was characterized by two *ortho*, two *meta*, and one *para* substituent(s). In the case of di- or trinitroaromatics, the second and the third nitro groups have been considered as an ordinary substituents. The first nitro group in the substituted meta-polynitroaromatic compounds is the group that has nonhydrogen substituent(s) in the *ortho* position. In the case of unsubstituted polynitroaromatic compounds, all nitrogroups were equal, and the numeration of nitro groups did not provide additional descriptors. Thus, this model has nearly a 2D level of representation of molecular structure and toxicity which was determined by constant substituents' contributions. Model **XIII** also reflects the trends mentioned above (Fig. 8.2c) but with much lesser accuracy ($R^2 = 0.71$, $Q^2 = 0.50$) that may prevent any subsequent application of this model.

Thus, it is important to emphasize that *the consideration of substituents mutual influence on toxicity of nitroaromatic compounds is the necessary condition for the development of adequate QSAR models*. To this purpose, one adds supplementary descriptors to the model **XIII** which take into account the number of substituents (n(OH), n(H), n(Cl), etc.) in the molecule as well as their mutual positions relative to each other. After calculation of all possible combinations for a substituent, this particular substituent is excluded from further descriptors' development. It allows

---
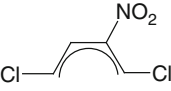
[4]This model is similar within certain limits to Free-Wilson approach.
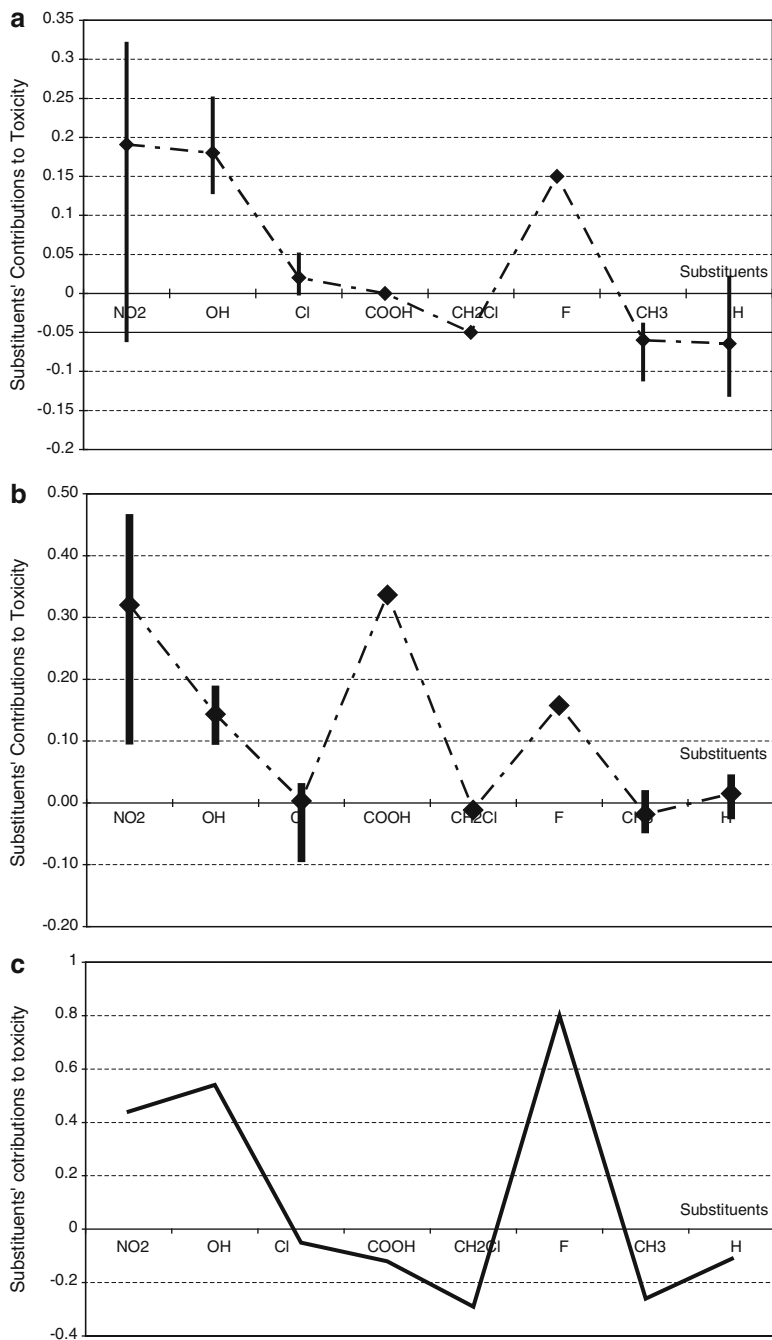
Fig. 8.2 Substituents contributions to toxicity change: (**a**) simplex 1D QSAR model **VIII**; (**b**) simplex 2D QSAR model **XII**; (**c**) additive model **XIII** (Reprinted from Kuz'min et al. [48]. With kind permission of Elsevier 2008)

one to avoid multiple consideration of any specific substituent. Such description of molecular structure provides closer description to the 2D level, than in the previous case (model **XIII**). This new model (**XIV**) is much more adequate ($R^2 = 0.92$; $Q^2 = 0.80$) than model **XIII**.

A comparison of toxicity values predicted by models **VI**, **VIII–XII**, and **XIV** shows very good agreement. Only compound 17 is poorly predicted by all these models (except model **XII**) because of the ambiguous effect of the Cl fragment on toxicity [106]. Evidently, consideration of only the composition of the molecule as well as the substituents' pair effects is not sufficient to describe toxicity in a meaningful manner. The errors of prediction for other compounds are small and usually have both positive and negative character, i.e., for the same compound some models overestimate, while the others underestimate the observed toxicity.

Because every model has its own advantages and shortcomings, we try to unite the former and avoid the latter. The toxicity values predicted by models **VI** and **VIII–XI** for each compound were averaged in consensus model **XV** ($R^2 = 0.90$). This provides the most accurate prediction of toxicity despite the fact that the test set compounds were also included in this model. It is necessary to note that compound 17 was not the statistical outlier in model **XV**. It is obvious that for both the training and the test set compounds the observed toxicity values are in a good agreement with the results of the simpler 1D QSAR models **VI** and **VIII–XI** and more complicated extended Free-Wilson analog **XIV**, as well as average model **XV**, and the most adequate 2D QSAR model **XII**. This demonstrates the good predictivity and ability of this method to be used as a virtual screening tool.

A detailed analysis of substituents' interferences and their contributions to toxicity as predicted by model **VIII** is presented in Fig. 8.3. The relative contributions to toxicity of nitro groups, aromatic carbon, and hydrogen (Fig. 8.3a) are significantly different in different molecules—benzene (1), nitrobenzene (3), 1,3-dinitrobenzene (19), and 1,3,5-trinitrobenzene (24). As expected, the minimal contributions to toxicity were observed for benzene (0 for NO_2 (it is absent) and C, and -0.15 for H). The insertion of one nitro group (compound 3) increases the contributions of all mentioned fragments. For 1,3-dinitrobenzene (19), their values increase even greater, but for 1,3,5-trinitrobenzene (24) the situation is dramatically different. The relative contribution of every nitro group is substantially lower; hydrogen contributions almost did not change, and the aromatic carbon atoms contributions to toxicity are seen to be slightly larger. The same trends for these compounds are observed in the most adequate 2D QSAR model **XII**, as well as in other approaches [106].

The interactions of substituents discussed in details for chlorosubstituted nitrobenzenes are demonstrated in Fig. 8.3b. The relative contributions to toxicity of nitro groups, chlorine, hydrogen, and aromatic carbon atoms are shown. It is evident that contributions of nitro groups to toxicity under the sequential insertion of chlorine decrease in the order: $3 > 9$, 10, $11 > 17$, $18 > 25 > 28$. Chlorine's contributions are maximal for monochloro derivatives of nitrobenzene, when for

Fig. 8.3 The analysis of structural fragments influence on toxicity for some: (**a**) nitrobenzenes; (**b**) chlorosubstituted nitrobenzenes (Reprinted from Kuz'min et al. [48]. With kind permission of Elsevier 2008)
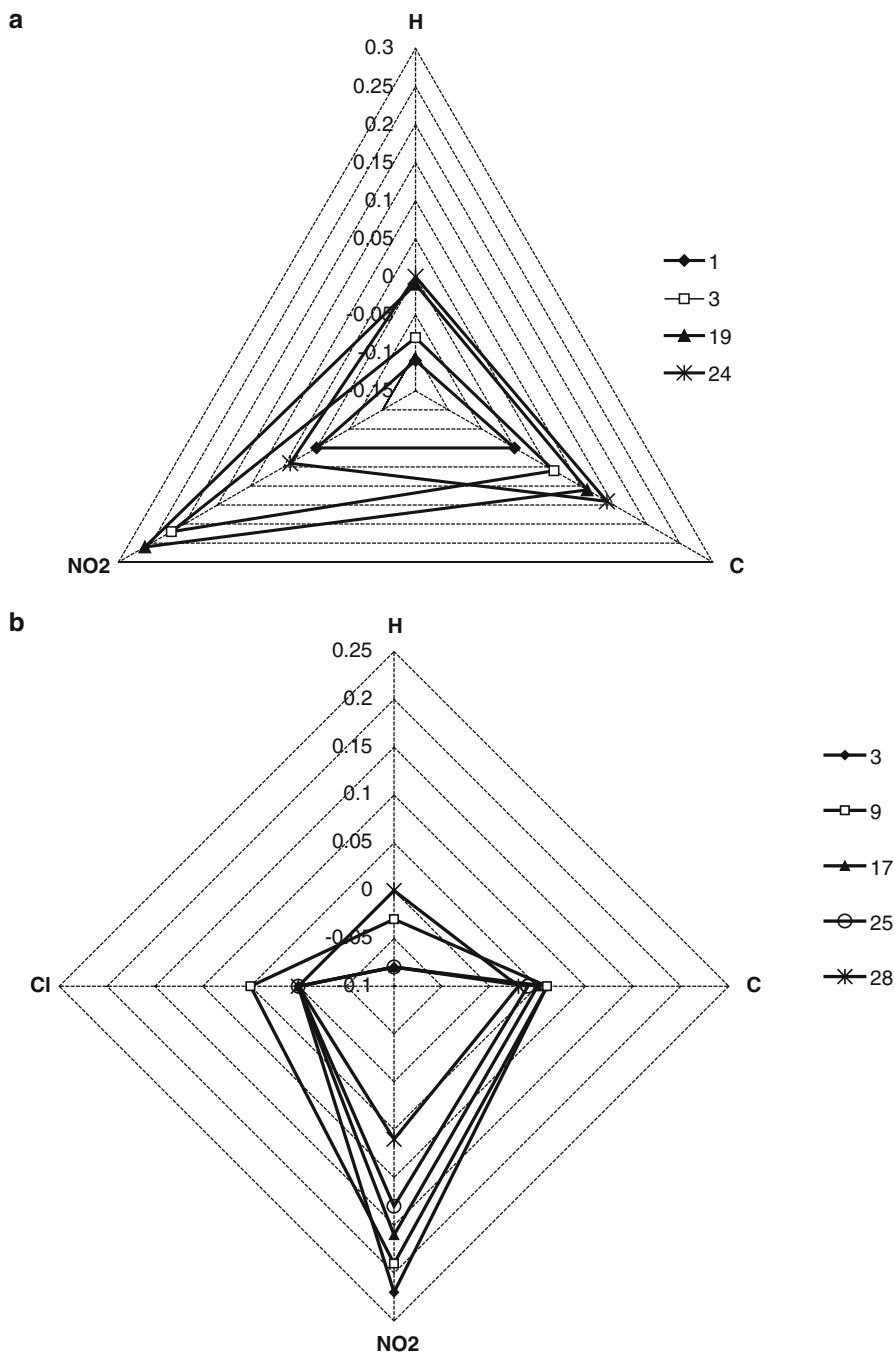
all the rest of the substituted nitrobenzenes they are close to 0. Aromatic carbons' contributions are nearly constant for all studied compounds, while hydrogen atoms have a small negative effect on toxicity. Their strongest influence is observed for di- and tri-substituted nitrobenzenes.[5]

Thus, even simple 1D QSAR models allow one to predict the trends of substituents' effects on the toxicity of nitroaromatics. Despite that these models cannot distinguish between isomers, nevertheless, they can estimate the toxicity values, i.e., they are useful for preliminary virtual screening. Seemingly, the reason of their successful application is their nonadditivity, i.e., the possibility of substituents' interference consideration.

8.5.2 The Effect of Characteristics of Substituents of the Nitroaromatics on Toxicity In Vivo (2D QSAR Analysis)

The preliminary 1D QSAR results show that even the information on the composition of molecules reveals the main tendencies of changes in toxicity. The reviewed study applies the HiT QSAR approach at 2D level of representation of molecular structure for (1) evaluation of the influence of the characteristics of 28 nitroaromatic compounds (some of which belong to a widely known class of explosives) as to their toxicity; (2) prediction of toxicity for new nitroaromatic derivatives; and (3) analysis of the effects of substituents in nitroaromatic compounds on their toxicity in vivo.

The initial work set (compounds 1–28, Fig. 8.4) was divided into training and test sets. Approximately 20% [107] (six compounds) from different groups of activity were selected to the test set; the 22 remaining compounds were assigned to the training set. In order to evaluate the predictive power of the obtained QSAR models, three different test sets were used during this analysis. Most likely, the usage of several (three is the sufficient minimum) test sets constructed by different principles and subsequent comparison and averaging (consensus modeling [101]) of the obtained results for the model validation is more preferable than the usage of only one set. In that way, the first test set was constructed to maximize its diversity with the training set, i.e., the compounds with the maximal dissimilarity were chosen. The second test set was created in order to minimize its diversity with the training set, i.e., less dissimilar compounds from each group were removed. And the last test set was chosen in random manner taking into account activity variation only. The procedure for forming the test sets has been described in detail in Ref. [39].

The experimentally determined (observed) values for toxicity of the investigated structures [59] are presented in Table 8.12. Approximately 3,100 simplex descriptors were calculated during the initial stage of work.

---

[5]The isomers cannot be distinguished by 1D QSAR models.
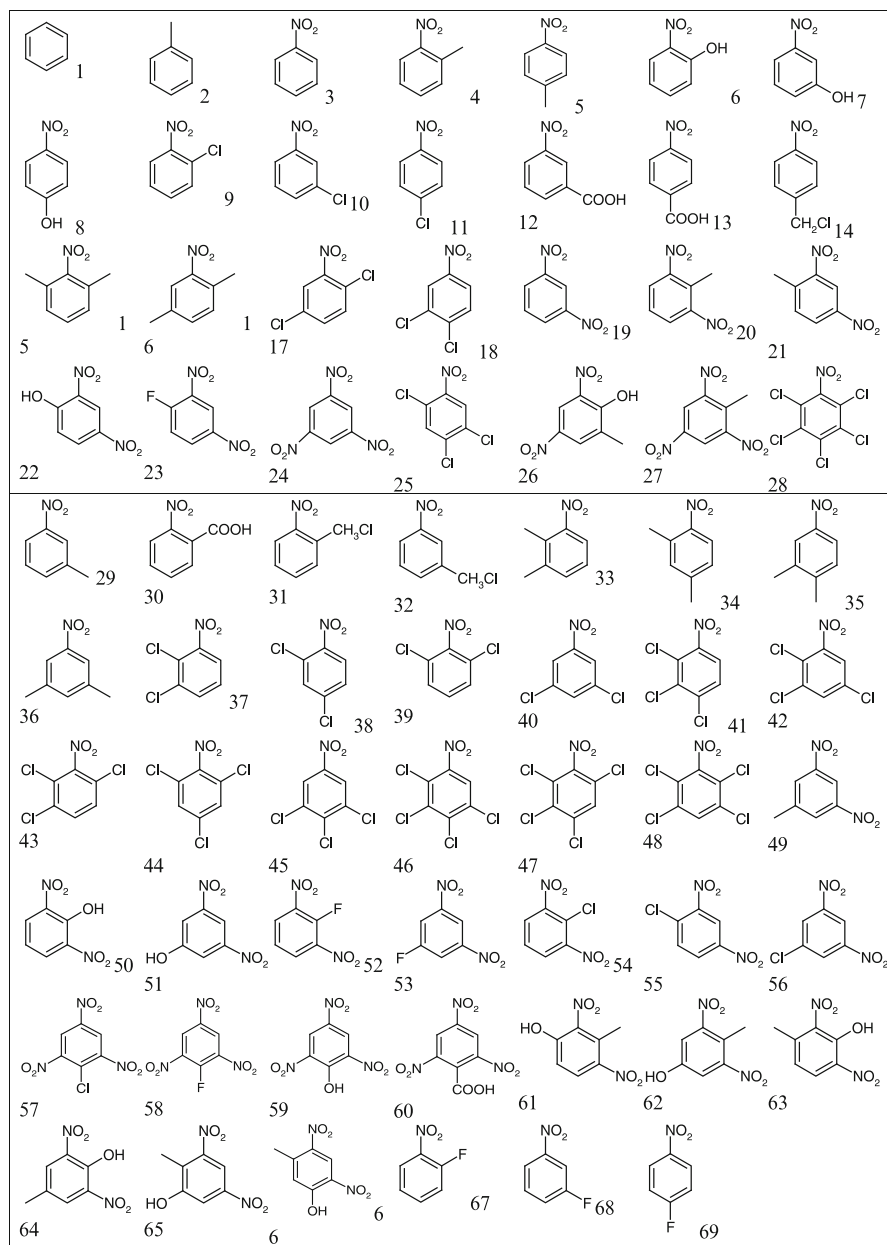
Fig. 8.4 Investigated compounds (Reprinted from Kuz'min et al. [39]. With kind permission of © Springer 2008)

Table 8.12 Observed and predicted values of investigated nitroaromatics toxicity

Structure	$-\lg LD_{50}$(rats), mmol/kg					
	Observed	Predicted model **XVI**	Predicted model **XVII**	Predicted model **XVIII**	Predicted model **XIX**	Consensus model **XX**
1	−1.86	−1.73	−1.76	−1.68	−1.65	−1.70
2[a, b, c]	−1.78	−1.95	−1.94	−1.68	−1.97	−1.87
3[a]	−0.69	−0.65	−0.69	−0.84	−0.66	−0.73
4	−0.81	−0.92	−0.94	−0.96	−0.86	−0.92
5[b]	−1.19	−1.02	−1.01	−1.08	−1.16	−1.08
6	−0.38	−0.30	−0.39	−0.45	−0.30	−0.38
7	−0.37	−0.34	−0.22	−0.15	−0.42	−0.26
8	−0.16	−0.15	−0.09	−0.32	−0.16	−0.19
9[a, c]	−0.23	−0.24	−0.56	−0.24	−0.52	−0.44
10[b]	−0.39	−0.36	−0.54	−0.52	−0.53	−0.53
11[a, c]	−0.43	−0.55	−0.59	−0.52	−0.35	−0.49
12	−0.61	−0.84	−0.89	−0.75	−0.92	−0.85
13[b, c]	−1.07	−0.98	−1.01	−0.78	−0.77	−0.85
14	−1.02	−0.93	−1.01	−1.04	−0.92	−0.99
15	−1.12	−1.11	−1.01	−1.08	−1.17	−1.09
16	−1.21	−1.10	−1.14	−1.16	−1.16	−1.15
17	−1.32	−1.29	−1.36	−1.24	−1.27	−1.29
18	−0.52	−0.49	−0.46	−0.64	−0.41	−0.51
19	0.31	0.19	0.23	0.23	0.15	0.20
20	−0.14	−0.09	−0.08	0.03	−0.22	−0.09
21[b]	−0.17	−0.13	−0.33	−0.12	−0.30	−0.25
22	0.41	0.50	0.56	0.57	0.62	0.58
23	0.57	0.50	0.46	0.57	0.56	0.53
24[b]	−0.11	−0.08	−0.08	−0.17	0.03	−0.07
25[b, c]	−0.67	−0.78	−0.61	−0.97	−0.66	−0.74
26[a, c]	0.52	0.51	0.13	0.47	0.38	0.33
27	−0.49	−0.53	−0.53	−0.57	−0.41	−0.50
28	−0.57	−0.63	−0.49	−0.43	−0.68	−0.53
29		−0.83	−0.89	−1.04	−1.13	−1.02
30		−0.92	−0.94	−0.50	−0.70	−0.71
31		−0.92	−0.94	−0.96	−0.84	−0.91
32		−0.83	−0.89	−1.04	−0.90	−0.94
33		−1.10	−1.14	−1.16	−1.14	−1.15
34		−1.06	−1.08	−1.18	−1.14	−1.13
35		−1.20	−1.21	−1.28	−1.63	−1.37
36		−0.84	−0.91	−1.24	−1.56	−1.23
37		−0.23	−0.37	−0.08	−0.61	−0.35
38		−0.53	−0.58	−2.20	−0.60	−1.13
39		0.05	−0.48	0.15	−0.60	−0.31
40		−0.84	−0.62	−2.63	−0.85	−1.37
41		−0.46	−0.40	−0.27	−0.49	−0.39
42		−1.47	−0.81	−2.52	−1.59	−1.64
43		−0.55	−0.34	−0.05	−0.74	−0.37

(continued)

Table 8.12 (continued)

	−lgLD$_{50}$(rats), mmol/kg				
Structure	Observed	Predicted model **XVI**	Predicted model **XVII**	Predicted model **XVIII**	Predicted model **XIX**	Consensus model **XX**
44		−0.64	−0.62	−4.08	−0.91	−1.87
45		−0.57	−0.75	−0.96	−0.47	−0.73
46		−0.85	−0.92	−0.75	−0.54	−0.74
47		−0.57	−0.27	−0.65	−0.79	−0.57
48		−0.72	−0.19	−0.65	−1.06	−0.63
49		0.01	0.02	−0.17	−0.19	−0.11
50		0.47	0.68	0.44	0.57	0.56
51		−0.29	−0.08	0.43	−0.25	0.03
52		0.46	0.48	0.44	0.51	0.48
53		−0.27	−0.08	0.22	−0.25	−0.04
54		0.37	0.35	0.55	0.13	0.34
55		0.02	−0.05	0.27	0.26	0.16
56		−0.44	−0.35	−0.57	−0.42	−0.45
57		−0.42	−0.36	−0.36	0.56	−0.06
58		0.26	0.52	0.04	1.01	0.52
59		0.23	0.71	0.04	1.08	0.61
60		−0.46	−0.53	−0.57	−0.47	−0.52
61		0.22	0.33	0.37	0.36	0.35
62		−0.65	−0.39	0.23	−0.60	−0.26
63		0.17	0.21	0.09	0.23	0.18
64		0.29	0.41	0.04	0.34	0.26
65		−0.17	−0.46	0.13	−0.54	−0.29
66		0.49	0.08	0.27	0.22	0.19
67		−0.30	−0.49	−0.45	−0.28	−0.41
68		−0.34	−0.22	−0.25	−0.40	−0.29
69		−0.20	−0.09	−0.32	−0.19	−0.20

Reprinted from Kuz'min et al. [39]. With kind permission of © Springer (2008)

Note: Training set molecules have been marked by bold font

[a]This molecule has been used for model **XVII** test set

[b]This molecule has been used for model **XVIII** test set

[c]This molecule has been used for model **XIX** test set

Depending on their physicochemical characteristics [45–47, 108] (see above), the atoms were divided into seven groups corresponding to:

1. Partial charge: $A \leq -0.1 < B \leq -0.05 < C \leq -0.01 < D \leq 0.01 < E \leq 0.05 < F \leq 0.1 < G$
2. Lipophilicity: $A \leq -1 < B \leq -0.5 < C \leq -0.1 < D \leq 0.1 < E \leq 0.5 < F \leq 1 < G$
3. Refraction: $A \leq 2 < B \leq 3 < C \leq 4 < D \leq 6 < E \leq 9 < F \leq 12 < G$
4. Electronegativity: $A \leq 1.5 < B \leq 2 < C \leq 2.5 < D \leq 3 < E \leq 3.5 < F$
5. van der Waals attraction potential: $A \leq 249 < B \leq 447 < C \leq 645 < D \leq 844 < E \leq 1042 < F \leq 1240 < G$
6. van der Waals repulsion potential: $A \leq 68882 < B \leq 130603 < C \leq 192324 < D \leq 254045 < E \leq 315766 < F \leq 377487 < G$

As mentioned above, the 1D QSAR analysis was carried out as the preliminary step of this study. The satisfactory two latent variables model ($R^2 = 0.82$; $Q^2 = 0.72$) was obtained using the PLS method with preliminary filtration of structural descriptors (*vide supra*) for all 28 molecules, indicating that the presence of certain combinations of atoms in the molecule substantially determines its toxicity. More detailed analysis of information obtained (Table 8.11) allowed for observation of the trends described below.

The increase in the presence of nitrogen and/or oxygen atoms (N, O, OH_2 fragments) in the molecule is important to the toxicity increase. Because the nitrogen atoms in the training set used belong only to the nitro group and oxygen could additionally be included in hydroxyl groups, one can conclude that these groups are essential factors in toxicity, i.e., increasing of the number of nitro and hydroxyl groups in the compound leads to the toxicity rise. On the other hand, the accumulation of nitrogen atoms (C_3HN_3 fragments) and, hence, nitro groups in nitroaromatic molecule decreases toxicity, i.e., the insertion of the third nitro group (N_3 means exclusively three nitro groups) into the aromatic ring interferes with the toxicity of the compounds under investigation. Summarizing the opposite effects of the mentioned fragments on toxicity, one can conclude that the toxicity of trinitroaromatics is not higher than the toxicity of dinitroaromatics. Such results again indicate the nonadditive character of the simplex approach. In the molecules investigated, an increase in the number of carbon atoms (C_4 and C_6Cl fragments) was associated with a decrease in toxicity. Introduction of alkyl, specifically methyl and chlorine alkyl (e.g., CH_2Cl) substituents, leads to a decrease in toxicity, whereas introduction of fluorine atoms into the benzene ring (H_2F and CH_2F fragments) results in an increase of toxicity.

As expected, expansion to the 2D level of molecular structure representation allows development of much more accurate QSAR models. The models obtained satisfy all the requirements of QSAR Setubal Principles [85]. They have high statistical indexes: adequacy-of-fit, robustness, and predictivity ($R^2 = 0.96$–0.98; $Q^2 = 0.84$–0.93; $R^2_{test} = 0.89 - 0.92$). Interestingly, the training set decrease, due to the detachment of six molecules and their insertion into the test set, did not appreciably worsen the statistical characteristics of models **XVII–XIX** ($R^2 = 0.96$; $Q^2 = 0.84$–0.93; $R^2_{test} = 0.89 - 0.92$). The consensus model **XX** (averaged by models **XVI–XIX**) (for model **XX**: $R^2 = 0.97$) prediction quality decreased only insignificantly in comparison to model **XVI** (for model **XVI**: $R^2 = 0.98$; $Q^2 = 0.91$) (all 28 molecules included).

Thus, taking into account the high statistical characteristics of the 2D QSAR models obtained, their extensions to the models of the next levels of HiT QSAR technology were considered inexpedient. Therefore, the second part of the study involved application of the best model to the other set of nitrobenzene derivatives having a similar chemical structure. The considered set of compounds that includes different combinations of substituents in an aromatic ring is presented in Fig. 8.4 and Table 8.12. All of these compounds are nitroaromatics, i.e., belong to the same chemical class. The whole set of substituents used for their design is represented in the initial training set. Toxicity values for 41 structures from the new set of

compounds (29–69) were predicted. Later, their link to domain applicability was estimated via model **XVI**. As expected, almost all of the investigated molecules, except compounds 58 and 59, located inside the space of structural features fall into the domain applicability [106]. Most likely, this is caused by poor representation of trinitroaromatics in initial training set (only two compounds 24 and 27 are included). On the other hand, there is only one fluorine-containing compound (dinitroaromatic 23) in the training set, and a lack of prediction reliability for monofluoro mononitroaromatic compounds 67–69 can be expected. In reality, the compounds in this study are situated inside model DA, i.e., they have been predicted reliably. It can be easily explained by the advantages described above of the SiRMS model which uses various types of atom's differentiations in simplexes. This allows one to reveal and apply more common characteristics of new compounds related to the test compounds than one can conclude just by comparing their structural formulas.

Based on the results obtained in the framework of model **XVI**, new information can be obtained as to nitroaromatic toxicity. Assuming reliable data on oral rat toxicity of 69 related nitroaromatic compounds, some trends in the dependencies of toxicity on the structure of nitroaromatic molecules can be analyzed. In practically all considered cases, as follows from Fig. 8.5a, an aromatic ring with nitro group(s) contributes positively to toxicity, even though this contribution varies widely, depending on the nature and number of other substituents. Clearly, the contribution range is wider for the work set than for the training set. The increase in toxicity is noticeable during the transition from mononitrobenzene derivatives to dinitrobenzene ones. A subsequent transition to substituted trinitrobenzenes does not appreciably result in the increase of toxicity (compounds 58 and 59 were not considered in this case). This corresponds quite well to the information obtained at the preliminary stage (1D QSAR model).

More extended analysis of aromatic ring substituents' influence on oral rat toxicity is illustrated in Fig. 8.5b. It can be concluded that nitro, hydroxyl, carboxyl groups, and fluorine promote an increase in toxicity, corresponding well to results of the 1D QSAR analysis. Both potential donors (substituents of the first group species: OH, F) and potential acceptors (substituents of the second group species: NO_2, COOH) contribute positively to toxicity. Methyl and chloromethyl groups slightly decrease activity. Chlorine, as a substituent to an aromatic ring, reveals an ambiguous influence on toxicity.

In considering toxicity changes within the separate groups of substituted mono-, di-, and trinitrobenzenes (Fig. 8.6a–c), it is evident from Fig. 8.6a, that methyl and chloromethyl derivatives of nitrobenzene are less toxic than unsubstituted nitrobenzene, whereas insertion of chlorine, hydroxyl, or fluorine into nitrobenzene promotes toxicity. There are no simple trends for the influence of isomerism on the toxicity of nitrobenzene derivatives. However, in most cases, *meta*-isomers are more toxic, and *para*-isomers are less toxic. In addition, for substituted 1,3-dinitrobenzenes (Fig. 8.6b), the influence of isomerism (A, B, C isomers) is more noticeable than in the previous case. Also, in most cases, C isomers are less and A isomers are more toxic. The tendency toward toxicity increase in the series CH_3, Cl, OH, and F is also predicted. Similarly, insertion of chlorine, fluorine, or hydroxyl in
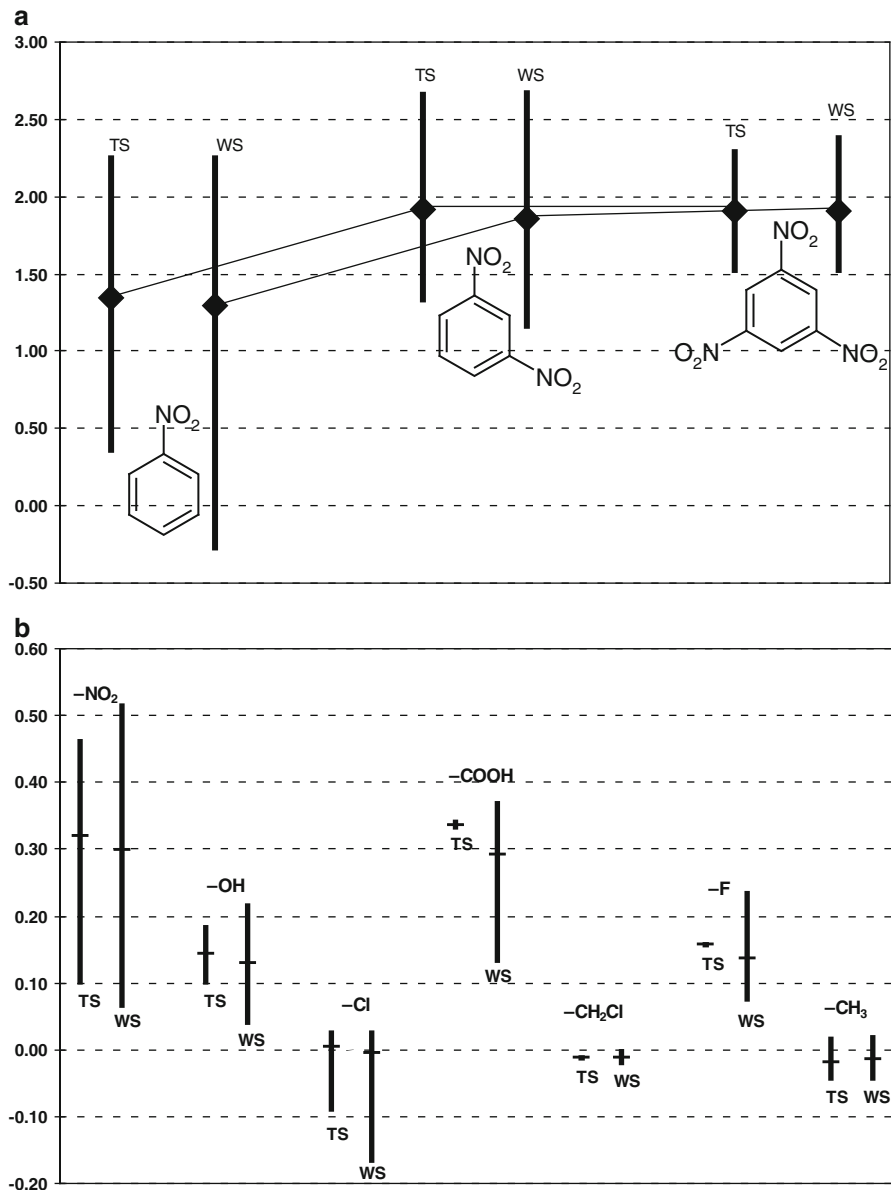
Fig. 8.5 Molecular fragment contributions D($-$lgLD$_{50}$) to toxicity change: (**a**) nitroaromatic fragments; (**b**) substituents in benzene ring (*ts* training set, *ws* work set) (Reprinted from Kuz'min et al. [39]. With kind permission of © Springer 2008)
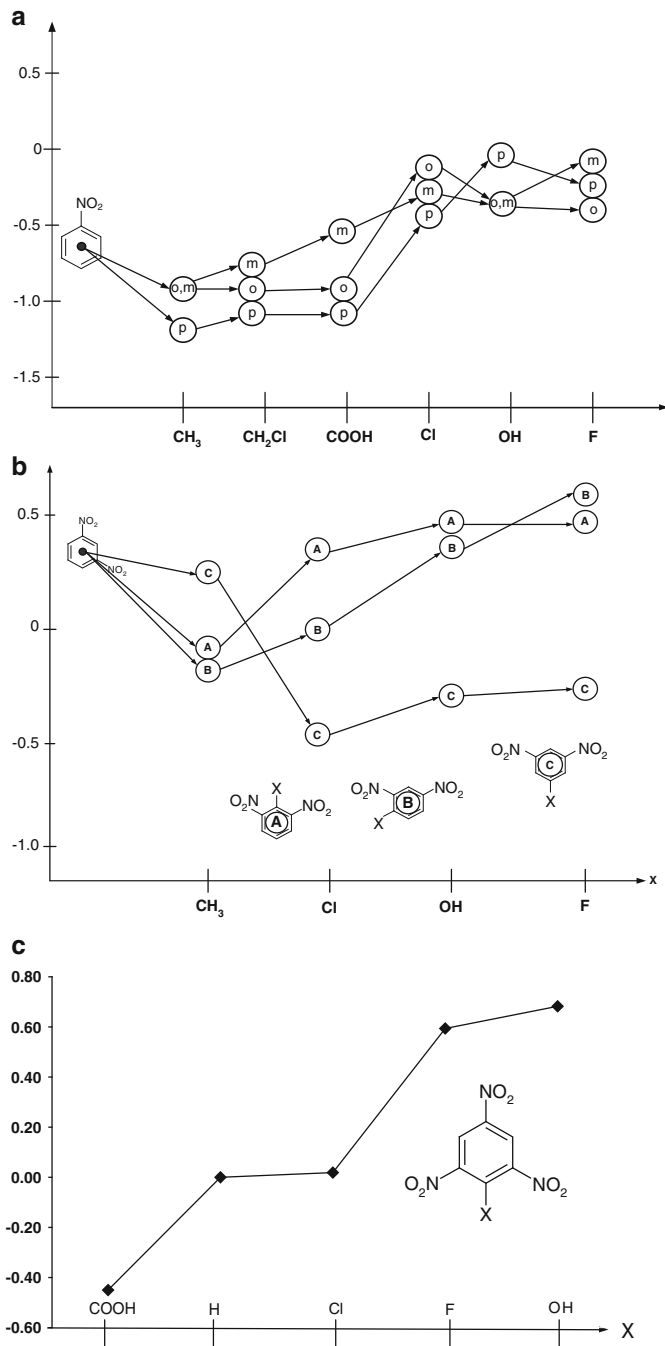
Fig. 8.6 Toxicity change for isomers (o *ortho*, m *meta*, p *para*) of monosubstituted: (**a**) nitrobenzene; (**b**) dinitrobenzene; (**c**) trinitrobenzene (Reprinted from Kuz'min et al. [39]. With kind permission of © Springer 2008)
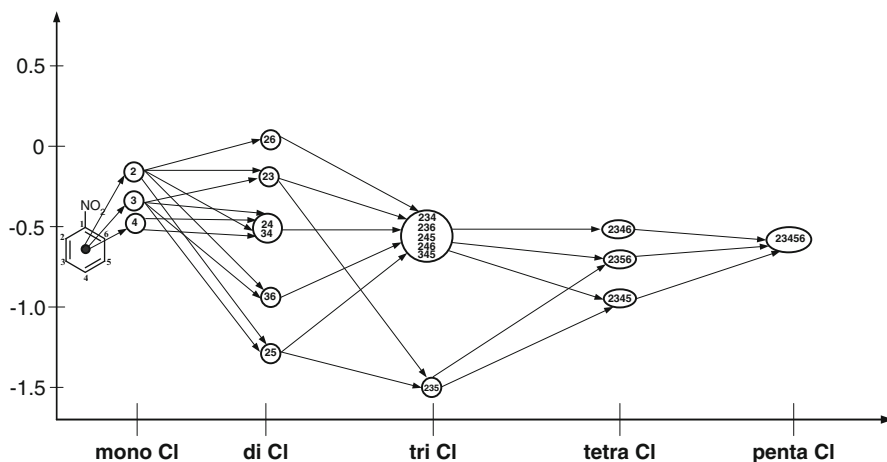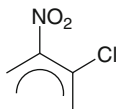
Fig. 8.7 Evolution of nitrobenzene chloroderivative toxicity change (*digits in circles* are the corresponding positions of substituents in benzene ring) (Reprinted from Kuz'min et al. [39]. With kind permission of © Springer 2008)
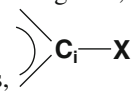
1,3,5-trinitrobenzene increases toxicity (Fig. 8.6c). As noted before, information for compounds 58 and 59 is not sufficiently reliable. At the same time, 2,4,6-trinitrobenzoic acid is less toxic than the other species from the given group of compounds.

Since the chlorine derivatives are more comprehensively represented in the initial work set and since, as mentioned above, they deserve more careful study, we have carried out a more detailed analysis of their influence on toxicity. "Evolution" of toxicity changes for this group of compounds is represented in Fig. 8.7. The largest toxicity changes are observed for nitrobenzene dichloro derivatives. An addition of new substituents (new chlorine atoms) decreases such changes. Presumably, the accumulation of chlorine atoms in the benzene ring results in cancellation of their influence on toxicity. Both the most toxic chlorine substituted nitrobenzenes and the least toxic ones contain the chlorine atom in the *ortho* position relatively to the nitro group. We expect that the fragment is a "toxicophore" and the other substituents (atoms of chlorine) are "modulators" that may increase or decrease toxicity.
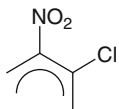
Finalizing the analysis of chlorine substituents, we developed another way to describe the influence of chlorine atoms on toxicity values of chlorine derivatives of mono nitrobenzene (compounds 3, 9, 37, 39, 42). In Fig. 8.8, the toxicity of each molecule is presented as six separate contributions, where C_i—*i*th
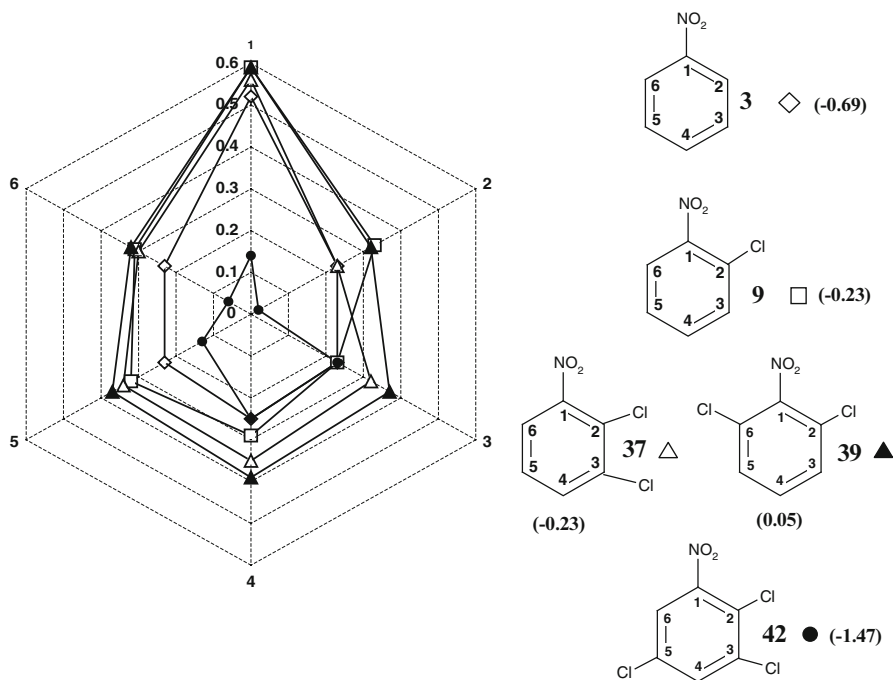
Fig. 8.8 The analysis of structural fragment influence on toxicity for some chlorosubstituted nitrobenzenes (compound number marked by *bold*; *digits in brackets* are the toxicity values) (Reprinted from Kuz'min et al. [39]. With kind permission of © Springer 2008)

($i = 1$–6) C atom on benzene ring and X—corresponds to substituent (H, Cl, NO_2). We analyzed the influence on the toxicity the sequential insertion of substituents into the benzene ring. We found that insertion of a chlorine atom in the *ortho* position relative to the nitro group (compound 9) leads to a toxicity increase in comparison with nitrobenzene (compound 3). This effect is not limited only to the chlorine atom. Actually, the contributions to toxicity of all other atoms are amplified (except C–H bond in *ortho* position to the C–Cl bond, Fig. 8.8). An insertion of another chlorine atom in the *ortho* position to the previous one (compound 37) has only a small effect on toxicity. Although the new C–Cl bond (position 3) increases the toxicity of a molecule, the contributions of the nitro group and of other C–Cl fragment (position 2) have been diminished. The influence of C–H bonds in positions 5 and 6 has virtually no effect on toxicity. The C–H bond in position 4 slightly increases toxicity. Thus, in spite of the redistribution of influence on toxicity between different fragments of molecule 37 (Fig. 8.8), the toxicity of this whole compound hardly changes compared to compound 9.

The situation is completely different (Fig. 8.8) for the other isomer (compound 39). Substitution of the hydrogen atom by chlorine in position 6 has practically no effect on this fragment's contribution to toxicity as well as to the toxicity of the

nitro group in comparison with the compound 9. However, the contributions of C–H bonds in positions 3–5 substantially increases toxicity. The last factor determines the increase in toxicity for compound 39.

A dramatic change in toxicity was predicted for compound 42. Substitution of hydrogen by chlorine in position 5 of molecule 37 results in substantial lowering of toxicity. It is interesting that this result has the effect of diminishing contributions to the toxicity of all analyzed fragments (see Fig. 8.8). The influence on toxicity change of the C–Cl bond in position 2 is especially noticeable. It is interesting that this fragment is situated in *para* position to the new, additional chlorine atom. Thus, it is possible to assume an important role for the chlorine atom as the substituent of the first species (electron-donating) and its polar influence on the aromatic system. Since we do not have any conclusive proofs about the mechanism of chlorinated nitro compounds action, one can conclude that the nitro groups making the halogen more susceptible to SNAr reactions or the halogens are facilitating the reduction of the nitro groups. Both of the mentioned mechanisms are probable. Thus, the toxicity of all of considered compounds has been substantially affected by interference of the substituents.

Summarizing, the obtained results indicate that the influence of substituents in the benzene ring on toxicity is considerably nonadditive (see Fig. 8.8). In addition, the presented toxicity trends do not follow the simple donor acceptor rules known in organic chemistry (substituent polar influence is discussed below).

As follows from our study, the 1,3-dinitrobenzene derivatives containing a fluorine or hydroxyl group (compounds 50, 52, and 66) are the most toxic. Except for benzene and toluene, which do not possess nitro groups, the least toxic compounds are methyl derivatives of nitrobenzene (compounds 5, 33–35) and chlorine derivatives of nitrobenzene (compounds 17 and 42) that contain the

following fragment .

As shown earlier [40, 41, 109], it is possible within the framework of the SiRMS approach to estimate the relative influence of different physical and chemical factors on toxicity change and to divide the total toxicity into contributions based on electrostatic, hydrophobic, and van der Waals interactions of toxicants with the proper biological target. The results of the application of this technique suggest that all three factors contribute to toxicity in approximately equal amounts: electrostatic 34%, hydrophobic 33%, and van der Waals 33%. It can also be concluded that the hydrophobic characteristics of nitroaromatics regulate their transport function (delivery to the biological target). Charge distribution in toxicants (electrostatic characteristics) likely determines the degree of its interaction with a biological target as well as the stability of the reaction species (ion and/or radical). Finally, van der Waals forces can be an important factor of toxicant–target interaction.

Interestingly, in spite of substituent polar effects undoubtedly being important, their influence does not follow well-known rules of classical organic chemistry since we did not find meaningful Hammett σ and σ^+ constants—toxicity value dependences ($R = 0.06-0.28$) for the training set and its parts.

8.6   Conclusion

This chapter reveals that application of simplex representation of molecular structure methodology in conjunction with multiple linear regression (MLR) and random forest (RF) statistical methods represents a powerful tool that is able to effectively predict physical, chemical, and biological properties of nitrocompounds. The following analysis of nitrocompounds properties has been performed:

Adequate "structure–aqueous solubility" 2D QSPR models were developed for a diverse set of organic molecules and successfully validated with an external test set. Better predictions were obtained when the random forest model was used. The influence of selected molecular fragments on aqueous solubility of compounds of military interest has also been studied. Relationships were highlighted that relate the number of nitrogen atoms in an aromatic ring, the ability for a molecular fragment to participate in hydrogen bonding and lipophilicity to aqueous solubility.

Accurate "structure–$\text{Log}K_{\text{ow}}$" 2D QSPR model based on simplex representation of molecular structure approach and random forest statistical model has been developed for a set of 10,973 organic compounds and successfully validated with two external test sets. The developed model predicts the $\text{Log}K_{\text{ow}}$ values with the accuracy of the best modern models. Using this model, the $\text{Log}K_{\text{ow}}$ values of 29 military important compounds with unknown experimental data have been predicted.

For the first time, 1D models on the base of SiRMS were used as separate and independent tools for development of QSAR analysis. The comprehensive analysis of toxicity changes as a function of substituent's position and characteristics was carried out. Among contributions analyzed are electrostatic, hydrophobic, and van der Waals interactions of toxicants with the biological targets. It was found that in most cases, insertion of fluorine and hydroxyl groups into nitroaromatics increases toxicity, whereas insertion of a methyl group has the opposite effect. The influence of chlorine on toxicity is ambiguous. Insertion of chlorine in *ortho* position relative to the nitro group leads to substantial increase in toxicity, whereas the second chlorine atom (in *para* position to the first one) results in considerable decrease in toxicity. It was shown that the mutual influence of substituents in the benzene ring is substantially nonadditive and plays a crucial role in their toxicity. The influence of different substituents on toxicity can be mediated via different C–H fragments of the aromatic ring. The correspondence between observed and predicted toxicity values by obtained 1D and 2D models is good. The developed single models were summarized in the most adequate consensus model that allows improving accuracy of toxicity prediction and shows its ability to be used as a virtual screening tool.

Army Corps of Engineers by the USAERDC. Permission was granted by the Chief of Engineers to publish this information. The findings of this report are not to be construed as an official Department of the Army position unless so designated by other authorized documents.

References

1. Bradbury SP, Russom CL, Ankley GT, Schultz TW, Walker JD (2003) Environ Toxicol Chem 22:1789–1798
2. Cronin MT, Dearden JC, Walker JD, Worth AP (2003) Environ Toxicol Chem 22:1829–1843
3. Cronin MT, Jaworska JS, Walker JD, Comber MH, Watts CD, Worth AP (2003) Environ Health Perspect 111:1391–1401
4. Cronin MT, Walker JD, Jaworska JS, Comber MH, Watts CD, Worth AP (2003) Environ Health Perspect 111:1376–1390
5. Dearden JC (2003) J Comput Aided Mol Des 17:119–127
6. Eriksson L, Jaworska J, Worth AP, Cronin MT, McDowell RM, Gramatica P (2003) Environ Health Perspect 111:1361–1375
7. Fang H, Tong WD, Welsh WJ, Sheehan DM (2003) J Mol Struct (THEOCHEM) 622:113–125
8. Patlewicz G, Rodford R, Walker JD (2003) Environ Toxicol Chem 22:1885–1893
9. McKinney JD, Richard A, Waller C, Newman MC, Gerberick F (2000) Toxicol Sci 56:8–17
10. Siraki AG, Chevaldina T, Moridani MY, O'Brien PJ (2004) Curr Opin Drug Discov Devel 7:118–125
11. Hansch C, Maloney PP, Fujita T, Muir RM (1962) Nature 194:178
12. Contrera JF, Matthews EJ, Kruhlak NL, Benz RD (2004) Regul Toxicol Pharmacol 40:185–206
13. Lessigiarska I, Cronin MT, Worth AP, Dearden JC, Netzeva TI (2004) SAR QSAR Environ Res 15:169–190
14. Walker JD, Carlsen L, Hulzebos E, Simon-Hettich B (2002) SAR QSAR Environ Res 13:607–616
15. Walker JD, Jaworska J, Comber MH, Schultz TW, Dearden JC (2003) Environ Toxicol Chem 22:1653–1665
16. Russom CL, Breton RL, Walker JD, Bradbury SP (2003) Environ Toxicol Chem 22:1810–1821
17. Gorb L, Hill FC, Kholod Y, Muratov EN, Kuz'min VE, Leszczynski J (2012) Progress in predictions of environmentally important, physico-chemical properties of energetic materials: applications of quantum-chemical calculations. In: Leszczynski J, Shukla MK (eds) Practical aspects of computational chemistry II. Springer, Heidelberg
18. Kriek E (1979) Aromatic amines and related compounds as carcinogenic hazards to man. In: Emmelot P, Kriek E (eds) Environmental carcinogenesis. Elsevier, Amsterdam, pp 143–164
19. Won WD, di Salvo LH, Ng J (1976) Appl Environ Microbiol 31:576
20. Slater EC (1962) Comp Biochem Physiol 4:281
21. Donlon BA, Razo-Flores E, Field JA, Lettinga G (1995) Appl Environ Microbiol 61:3889
22. Lipnick RL (1995) In: Rand GM (ed) Aquatic toxicology. Taylor & Francis, London, pp 609–655
23. Escher B, Schwarzenbach RP (2002) Aquat Sci 64:20
24. Patai S (1982) The chemistry of amino, nitroso, and nitro compounds and their derivatives. Wiley, New York
25. Feuer H, Nielsen AT (1990) Nitro compounds: recent advances in synthesis and chemistry. VCH Publishing, New York, p 636
26. Neilson AH, Allard A-S (2008) Environmental degradation and transformation of organic chemicals. CRC, Boca Raton, p 710

27. Talmage SS, Opresko DM, Maxwell CJ, Welsh CJE, Cretella FM, Reno PH, Daniel FB (1999) Rev Environ Contam Toxicol 161:1–156
28. Rickert DE (1984) Toxicity of nitroaromatic compounds. Hemisphere Publishing Corp, Bristol, p 295
29. Robidoux PY, Svendsen C, Caumartin J, Hawari J, Ampleman G, Thiboutot S, Weeks JM, Sunahara GI (2000) Environ Toxicol Chem 19(7):1764
30. Katritzky AR, Oliferenko P, Oliferenko A, Lomaka A, Karelson M (2003) J Phys Org Chem 16:811
31. Agrawal WK, Khadikar PV (2001) Bioorg Med Chem 9:3035
32. Cronin MTD, Schultz TW (2001) Chem Res Toxicol 14:1284
33. Cronin MTD, Gregory BW, Schultz TW (1998) Chem Res Toxicol 11:902
34. Kuz'min VE, Artemenko AG, Muratov EN, Polischuk PG, Ognichenko LN, Liahovsky AV, Hromov AI, Varlamova EV (2009) In: Puzyn T, Cronin M, Leszczynski J (eds) Recent advances in QSAR studies. Springer, New York. doi:10.1007/978-1-4020-9783-6_5
35. Artemenko AG, Muratov EN, Kuz'min VE, Kovdienko NA, Hromov AI, Makarov VA, Riabova OB, Wutzler P, Schmidtke M (2007) J Antimicrob Chemother. doi:10.1093/jac/dkm172
36. Kuz'min VE, Artemenko AG, Muratov EN, Volineckaya IL, Makarov VA, Riabova OB, Wutzler P, Schmidtke M (2007) J Med Chem 50:4205
37. Muratov EN, Artemenko AG, Kuz'min VE, Lozitsky VP, Fedchuk AS, Lozitska RN, Boschenko YA, Gridina TL (2005) Antiviral Res 65(3):62
38. Kuz'min VE, Artemenko AG, Polischuk PG, Muratov EN, Hromov AI (2005) J Mol Mod 11:457
39. Kuz'min VE, Artemenko AG, Muratov EN (2008) J Comput Aided Mol Des 22. doi:10.1007/s10822-008-9179-6
40. Kuz'min VE, Artemenko AG, Lozitska RN, Fedtchouk AS, Lozitsky VP, Muratov EN, Mescheriakov AK (2005) SAR QSAR Environ Res 16:219
41. Kuz'min VE, Artemenko AG, Lozitsky VP, Muratov EN, Fedtchouk AS, Dyachenko NS, Nosach LN, Gridina TL, Shitikova LI, Mudrik LM, Mescheriakov AK, Chelombitko VA, Zheltvay AI, Vanden Eynde J-J (2002) Acta Biochim Pol 49:157
42. Muratov E, Artemenko A, Kuz'min V, Konup I, Konup L, Kotlyar S, Kamalov G, Fedtchuk A, Mykhaylovska N (2006) Clin Microbiol Infect 12(Suppl 4):1558
43. Zhang S, Golbraikh A, Oloff S, Kohn H, Tropsha A (2006) J Chem Inf Model 46:1984
44. Kuz'min VE (1995) About homo- and heterochirality of dissymmetrical tetrahedrons (chiral simplexes). Stereochemical tunneling. Zh Strucur Khim 36:873–878 (in Russian)
45. Jolly WL, Perry WB (1973) J Am Chem Soc 95:5442–5450
46. Wang R, Fu Y, Lai L (1997) J Chem Inf Comp Sci 37:615
47. Ioffe BV (1983) Chemistry refractometric methods. Himiya, Leningrad, p 352
48. Kuz'min VE, Muratov EN, Artemenko AG, Gorb L, Qasim M, Leszczynski J (2008) Chemosphere 72:1373
49. Seel M, Turner DB, Wilett P (1999) HQSAR – a highly predictive QSAR technique based on molecular holograms. QSAR 18:245–252
50. Baurin N, Mozziconacci JC, Arnoult E et al (2004) J Chem Inf Model 44:276–285
51. Lindgren F, Geladi P, Rännar S, Wold S (1994) J Chemometr 8:349
52. Kubinyi H (1996) J Chemometr 10:119
53. Hasegawa K, Miyashita Y, Funatsu K (1997) J Chem Inf Comput Sci 37:306
54. Carhart RE, Smith DH, Venkataraghavan R (1995) J Chem Inf Comput Sci 25:64
55. Kuz'min VE, Artemenko AG, Kovdienko NA, Tetko IV, Livingstone DJ (2000) J Mol Model 6:517
56. Jaworska J, Nikolova-Jeliazkova N, Aldenberg T (2005) Altern Lab Anim 33:445
57. Breiman L (2001) Mach Learn 45(1):5
58. Breiman L, Friedman JH, Olshen RA, Stone CJ (1984) Classification and regression trees. Wadsworth, Belmont, CA, republished by CRC Press, p 368
59. Dearden JC (2006) Drug Dis 1(1):31

60. Valvani SC, Yalkowsky SH, Roseman TJ (1981) J Pharm Sci 70:502
61. Lyman WJ, Reehl WF, Rosenblatt DH (1982) Solubility in water, Handbook of chemical property estimation methods. McGraw-Hill, New York. 2(1):2–52
62. Chastrette M, Rajzmann M, Chanon M, Purcell KF (1985) J Am Chem Soc 107:1
63. Kamlet MJ, Doherty RM, Abraham MH, Carr PW, Doherty RF, Taft RW (1987) J Phys Chem 91:1996
64. Yalkowsky SH, Banerjee S (1992) Aqueous solubility: methods of estimation for organic compounds. Marcel Dekker, New York
65. Bergstrom CAS, Strafford M, Lazorova L, Avdeef A, Luthman K, Artursson P (2003) J Med Chem 46:558
66. Bergstrom CAS, Wassvik CM, Norinder U, Luthman K, Artursson P (2004) J Chem Inf Comput Sci 44:1477
67. Wegner JK, Zell A (2003) J Chem Inf Comput Sci 43:1077
68. Sun H (2004) J Chem Inf Comput Sci 44:748
69. Raevsky OA, Raevskaja OE, Schaper K-E (2004) QSAR Comb Sci 23:327
70. Catana C, Gao H, Orrenius C, Stouten PFW (2005) J Chem Inf Model 45:170–176
71. Wang Y-L, Hu Y-D, Wu L-Y, An W-Z (2006) Int J Mol Sci 7:47
72. Jain N, Yang G, Machatha SG, Yalkowsky SH (2006) Int J Pharm 319:169–171
73. Lu G-N, Dang Z, Tao X-Q, Yang C, Yi X-Y (2008) QSAR Comb Sci 27:618
74. Yang G-Y, Yu J, Wang Z-Y, Zeng X-L, Xue-Hai Ju (2007) QSAR Comb Sci 26:352
75. Wang J, Krudy G, Hou T, Holland G, Xu XX (2007) J Chem Inf Model 47:1395
76. Wang J, Hou T, Xu X (2009) J Chem Inf Model 49:571
77. Ghasemi J, Saaidpour S (2007) Chem Pharm Bull 55:669
78. Tomida D, Nishino T, Yokoyama C (2007) Jpn J Thermophys Prop 21:19
79. Palmer DS, O'Boyle NM, Glen RC, Mitchell JBO (2007) J Chem Inf Model 47:150
80. Yalkowsky SH, He Y (2003) Handbook of aqueous solubility data. CRC Press, Boca Raton
81. Kovdienko NA, Polishchuk PG, Muratov EN, Artemenko AG, Kuz'min VE, Gorb L, Hill F, Leszczynski J (2010) Mol Inf 29:394
82. Ferste E, Renz B (1979) Methoden der Korrelations und Regressionanalyse. Die Wirtschaft, Berlin
83. Hansch C, Quinlan JE, Lawrence GL (1968) J Org Chem 33(1):347
84. Abraham MH, Le J (1999) J Pharm Sci 88:868
85. Joint meeting of the chemicals committee and the working party on chemicals, pesticides and biotechnology (2004) OECD series on testing and assessment: The report from the expert group on (Quantitative) Structure-Activity Relationships [(Q)SARs] on the principles for the validation of (Q)SARs. OECD. Paris. ENV/JM/MONO(2004)24, v.49:206
86. Wang R, Gao Y, Lai L (2000) Perspect Drug Discov 19:47
87. Leo AJ (1993) Chem Rev 93:1281
88. Tetko IV, Tanchuk VY, Villa AEP (2001) J Chem Inf Comput Sci 41(5):1407–1421. http://www.vcclab.org/lab/alogps
89. Niemi GJ, Basak SC, Veith GD, Grunwald G (1992) Environ Toxicol Chem 11:893
90. Makino M (1998) Chemosphere 37:13
91. Petrauskas AA, Kolovanov EA (2000) Perspect Drug Discov 19:99
92. Meylan W, Howard PH (2000) Perspect Drug Discov 19:67
93. Gaillard P, Carrupt PA, Testa B, Boudon AJ (1994) J Comput Aided Mol Des 8:83
94. Klopman G, Li J, Wang S, Dimayuga M (1994) J Chem Inf Comput Sci 34:752
95. Viswanadhan VN, Ghose AK, Wendoloski J (2000) Perspect Drug Discov 19:85
96. Convard T, Dubost JP, Solleu HI, Kummer E (1994) Quant Struct-Act Rel 13:34
97. Suzuki T, Kudo Y (1990) J Comput Aided Mol Des 4:155
98. Muratov EN, Kuz'min VE, Artemenko AG, Kovdienko NA, Gorb L, Hill F, Leszczynski J (2010) Chemosphere 79:887
99. Syracuse Research Corporation (1994) Physical/chemical property database (PHYSPROP). SRC Environmental Science Center, Syracuse
100. Advanced Chemistry Development, Inc. (ACD/Labs). http://www.acdlab.com

101. Tropsha A, Gramatica P, Gombar VK (2003) QSAR Comb Sci 22:69
102. Tropsha A, Golbraikh A (2007) Curr Pharm Des 13:3494
103. Muratov EN, Artemenko AG, Varlamova EV, Polischuk PG, Lozitsky VP, Fedtchuk AS, Lozitska RN, Gridina TL, Koroleva LS, Sil'nikov VN, Galabov AS, Makarov VA, Riabova OB, Wutzler P, Schmidtke M, Kuz'min VE (2010) Future Med Chem 2:1205
104. Tropsha A (2010) Mol Inf 29:476
105. Isayev O, Rasulev B, Gorb L, Leszczynski J (2006) Mol Divers 10:233
106. Kuz'min VE, Muratov EN, Artemenko AG, Gorb L, Qasim M, Leszczynski J (2008) J Comput Aided Mol Des 22:747
107. Gramatica P (2004) Evaluation of different statistical approaches for the validation of Quantitative Structure –Activity Relationships. ECVAM, Ispra, p 177 p
108. Rappe AK, Casewit CJ, Colwell KS, Goddart WA, Skiff WM (1992) J Am Chem Soc 114:10024
109. Kuz'min VE, Artemenko AG, Muratov EN, Lozitsky VP, Fedchuk AS, Lozitska RN, Boschenko YA, Gridina TL (2005) Antiviral Res 65(3):A70–A71

Chapter 9
Progress in Predictions of Environmentally Important Physicochemical Properties of Energetic Materials: Applications of Quantum-Chemical Calculations

Leonid Gorb, Frances C. Hill, Yana Kholod, Eugeniy N. Muratov, Victor E. Kuz'min, and Jerzy Leszczynski

Abstract The review describes the advances of quantum-chemically based approximations (namely, COSMO-RS) in the prediction of several environmentally important physicochemical properties of energetic materials: vapor pressure, Henry's law constants, water solubility, and octanol–water partition coefficients. It includes introduction, the section that briefly discusses COSMO-RS – the most popular quantum-chemistry-based statistical thermodynamics approximation, and the references on similar quantum-chemical approaches. Since the solubility, probably, plays the most important role in many environmental characteristics of energetic materials, the major section of the review describes the current status of the quantum-chemically based predictions of this property. Also, the description of a modeling of salinity effects is discussed. Then subsequent few sections review the current advancements of the calculations of other environmentally important physical properties of energetic compounds.

It is concluded that the combination of continuum model of solvent with statistical thermodynamics (what in fact represents the approximations of the COSMO-RS

L. Gorb
Badger Technical Services, LLC, Vicksburg, MS, USA

F.C. Hill • J. Leszczynski
Environmental Laboratory, US Army ERDC, Vicksburg, MS 39180, USA
e-mail: Frances.C.Hill@usace.army.mil; jerzy@icnanotox.org

Y. Kholod • J. Leszczynski (✉)
Interdisciplinary Center for Nanotoxicity, Department of Chemistry and Biochemistry, Jackson State University, P.O. Box 17910, 1325 Lynch Street, Jackson, MS 39217, USA
e-mail: yana@icnanotox.org; jerzy@icnanotox.org

E.N. Muratov • V.E. Kuz'min
Laboratory of Theoretical Chemistry, Department of Molecular Structure, A.V. Bogatsky Physical-Chemical Institute National Academy of Sciences of Ukraine, Lustdorfskaya Doroga 86, Odessa 65080, Ukraine
e-mail: murik@email.unc.edu; theorchem@gmail.com

type) is a quite accurate prediction tool that on one hand avoids empirically based QSPR approximations, and on another hand, allows not to use such computationally demanding techniques as molecular dynamics and Monte Carlo approaches.

9.1   Introduction

Energetic materials include the following classes of compounds:

1. Classical organic explosives, such as TNT (2,4-trinitrotoluene), RDX (hexahydro-1,3,5-triazine), HMX (octahydro-1,3,5,7,-tetranitro-1,3,5,7-tetrazocine)
2. Insensitive organic explosives such as N-methyl-4-nitroaniline (MNA) and 2,4-dinitroanisole (DNAn) and 1,3,5-triamino-2,4,6-trinitrobenzene (TATB)
3. Thermite systems consisting of separate fuels and oxidizers. They are used in primers, main charges, propellants, pyrotechnic mixtures, or as reactive materials.

Production and handling of energetic materials generate large quantities of contaminated wastewater. Therefore, it is very important to understand the environmental behavior of these potential toxic hazards, which is primarily controlled by the change of the physicochemical properties of the compound. Thus, accurate determination of their physicochemical properties is critical to developing valid environmental models and impact assessments.

Among the most important physicochemical properties relating to the environmental behavior of energetic materials are four key characteristics: aqueous solubility (S_w), octanol–water partition coefficient (K_{OW}), Henry's law constant (K_H), and vapor pressure (P_v). These parameters are also used extensively in medicinal chemistry (pharmacokinetics, drug design, and anesthesiology), chromatography, and pesticide chemistry.

Aqueous solubility is defined as the equilibrium distribution of a solute between water and solute phases at a given temperature and pressure. Because S_w represents the maximum solute concentration possible at equilibrium, it can also serve as a limiting factor in concentration-dependent processes. Inorganic salts, present in large amounts in the environment, greatly influence the mass transfer equilibrium of organic compounds between different phases. The aqueous solubility of organic compounds usually decreases in the presence of inorganic salts. This is defined as the salting-out effect. Salting-out offers several practical applications that could be used to modify the physical behavior of the solution, separate the components of a system, and improve the sensitivity of analytical techniques.

The octanol–water partition coefficient represents the ratio of the concentration of a solute in octanol and water at equilibrium and a specified temperature. Octanol is an organic solvent that is used as a surrogate for natural organic matter. This partition coefficient is utilized in many environmental studies to determine the fate of chemicals in the environment. Prediction of the extent of bioaccumulation

of a contaminant in fish provides an example of the application of the partition coefficient in ecological ventures. It is assumed that the molecular speciation of the solute is the same in both solvents, and that the solutions are sufficiently dilute.

The distribution equilibrium of a compound between the water phase and the gas phase is characterized by the Henry's law constant. This distribution is equal to the ratio of concentration of the species in air and water in equilibrium. The Henry's law is very important in environmental studies and chemical analyses: it controls the driving force of the mass transfer of the compound between water and air. In many industrial, toxicological, and environmental processes, the Henry's law constant and its dependency on temperature play an important role in modeling the exchange of semi-volatile chemicals between gaseous and aqueous phases.

And, finally, vapor pressure or, more accurately, the pressure of vapor of a compound at the equilibrium with its pure condensed phase controls the distribution of pure substances between its surface and the air. Therefore, the four key characteristics: solubility, octanol–water partition coefficient, Henry's law constant, and vapor pressure quantify the extent of a chemical's partitions between solid–liquid, liquid–liquid, air–water, and air–solid, respectively.

Physical properties of some energetic materials such as trinitrotoluene (TNT), cyclotri-ethylenetrinitramine (RDX), and cyclotetramethylene-tetramitramine (HMX), have been studied extensively, and numerous physical property data are available for these compounds. For TNT, octanol–water partition coefficients, Henry's law constants, vapor pressures, and aqueous solubility have all been determined experimentally by a number of groups [1–4]. Vapor pressures have also been determined for RDX and HMX [5]. The solubility of CL-20 was reported by Karakaya et al. [6]. However, in cases where multiple data sets exist, every now and then significant differences are being observed between some of the data sets. For example, reported values of the aqueous solubility for TNT may vary by as much as a factor of 2 [7]. The cases of new synthesized energetic materials are even more critical, since very often those experimentally measured physical property data are not yet published. The same applies also to environmentally important physical properties of numerous products of their natural decomposition – very often they are not measured yet.

The lack of consistent physical properties and the critical need for such data that may be used to provide some prediction of the environmental fate of a particular compound drive the development of methodologies for the prediction of relevant physicochemical properties. The most common of these methods is Quantitative Structure Property Relationship (QSPR) [8]. There are numerous variants of QSPR (for application of QSRP techniques to predict solubility and lipophilicity of energetic compounds see our review in this book [9]), but in essence, a large number of "descriptors" is fitted to reproduce a specific physical property (vapor pressure, log K_{OW}, etc.) for molecules in the "training set." Training sets may contain anywhere from a few hundred to tens of thousands of molecules and, in general, the larger the training set, the better the predictive capability and accuracy of the applied approach. Overall, most QSPRs do an excellent job of predicting physical properties for molecules with similar molecular structure as those in the

training set. However, for molecules that differ significantly from those used in the development of the QSPR, which applies to many energetic materials, there is a concern that the predictions of QSPR may not be representative of experimental data [10, 11]. Therefore, approaches other than QSAR/QSPR methodologies are needed that will yield reliable predictions in the absence of experimental data. In fact, such a methodology exists and has a long history of successful development and applications [12]. It is called ab initio quantum chemistry and is based on application of physical, quantum-mechanical laws to molecular systems. This technique virtually does not require any additional information, except the data on a molecular (crystal) structure. The outcome of the corresponding calculations is any physical property that could be represented by a quantum-mechanical operator.

Below, we will present the short description of such ab initio techniques that are specifically applicable for the evaluation of environmentally important physical properties. Particularly, we will discuss their current status related to the predictions of the most important physical properties of energetic materials. However, in reality, those techniques are not limited only to predictions of such properties, and in addition, they are able to calculate any property which is dependent on the difference in Gibbs free energies, or chemical potentials in two different phases.

The review is organized in the following way. The next section briefly describes the most popular quantum-chemistry-based statistical thermodynamics approximation that is denoted as COSMO-RS. The references to similar quantum-chemical approximations are also provided. Since the solubility probably plays the most important role for the considered phenomena, the next section reveals the current advances in the quantum-chemical-based predictions of this property. This section also discusses a modeling of salinity effects. Then subsequent few sections review the current status in the calculations of other environmentally important physical properties of energetic materials. Also, since, there are just a few publications related to the prediction of physical and chemical properties of energetic materials, we complete the review by presenting the works on the predictions of physical properties for possible environmental contaminants others than the energetic materials.

9.2 COSMO-RS and Other Quantum-Chemical Approximations

COSMO-RS (COSMO for Real Solvents) is a quantum-chemistry-based statistical thermodynamics approximation for the verification and prediction of thermodynamic properties of liquids, liquid mixtures, and dissolved solids. The details of COSMO-RS are described in a number of publications (see, e.g., [13–15]). Below we will follow the COSMO-RS description which is presented in [16, 17].

The approximation involves two steps. The first one is based on a quantum-chemical continuum model of solvent called COSMO (conductor-like screening

model) [15]. In a COSMO calculation, the solute is placed inside a molecular-shaped cavity and the surrounding solvent is described by a conducting continuum. Instead of using the exact dielectric boundary condition that is typical for most PCM-type models [18], COSMO in general applies a scaled-conductor boundary condition. The COSMO algorithm is implemented in quantum-chemical self-consistent field procedures in many quantum-chemistry programs [19, 20].

The first step of COSMO-RS approximation has two levels of accuracy. At the high level (also called BP-TZVP level), the geometry optimization is performed using the DFT method at the BVP86/TZVP level. This level is recommended for the accurate calculations of small number of compounds. The level called BP-SVP-AM1 uses the optimization at the semiempirical AM1 level, followed by single-point calculations at the BVP86/SVP level. This approach is recommended for screening of hundreds or even thousands of compounds. In practice, a commercially available COSMOTherm program [21] is accompanied by databases collecting the pre-calculated information for thousands of compounds at each level of accuracy. Thus, very often the quantum-chemical calculations are not needed and one could start predictions right from the second step.

The second step of the COSMO-RS approximation [15] uses optimized geometries, energies, and surface-screening charge densities as the input for application of statistical thermodynamics. COSMO-RS treats the solvent S as an ensemble of pair-wise interacting surface segments. The interaction energies of the surface pairs are defined in terms of the screening charge densities and the respective surface segments. For the COSMO-RS statistical thermodynamics, it is sufficient to consider histograms of the screening charge densities, the so-called σ-profiles $\rho^x(\sigma)$, which give the relative amount of surface with polarity σ for a molecule X. From the molecular σ-profiles, the σ-profiles of pure or mixed solvents S can be easily derived as mole fraction weighted sum of the σ-profiles of its compounds in combination with a surface normalization:

$$\rho_s(\sigma) = \frac{\sum_i x_i \rho^{x_i}(\sigma)}{\sum_i x_i A^{x_i}} \tag{9.1}$$

COSMO-RS treats electrostatic, hydrogen-bonding, and van der Waals interactions by effective approximate expressions. Electrostatics (E_{misfit}) and hydrogen bonding (E_{HB}) are described as functions of the screening charges of two interacting surface segments σ and σ' or σ_{acceptor} and σ_{donor} if the segments belong to hydrogen bond donor or acceptor atom. The less-specific van der Waals (E_{vdW}) interactions are taken into account in a slightly more approximate way – the resulting expression for E_{vdW} does not depend on a σ.

The COSMO-RS methodology operates by means of pseudo-chemical potentials of liquid or mixed liquids. The pseudo-chemical potential is calculated as follows:

$$\mu_s^x = \mu_{\text{C,S}}^x + \int \rho^x(\sigma)\mu_s(\sigma)\,d\sigma \tag{9.2}$$

where

$$\mu_s(\sigma) = \frac{RT}{\alpha_{\text{eff}}} \ln \left[\int \rho_s(\sigma') \exp \left(\frac{1}{RT} (\alpha_{\text{eff}} \mu_s(\sigma') - E_{\text{misfit}}(\sigma, \sigma') - E_{\text{HB}}(\sigma, \sigma')) \right) d\sigma \right]$$

(9.3)

and $\mu_{C,S}^x$ is a special combinatorial term that takes into account size and shape differences of the molecules in the system.

With Eq. 9.2, one is able to calculate the chemical potential of all compounds of an arbitrary mixture at a given temperature. Subsequently, a wide variety of thermodynamic properties can be derived. Below we present the expressions that allow calculating the properties discussed in the review.

Vapor pressure:

$$P_i^{\text{vapor}} = X_i \exp[(\mu^{\text{solv}} - \mu^{\text{gas}})/RT]$$

(9.4)

Henry's Law constants:

$$k_H = 1/V_{\text{solv}} X_i \exp[(\mu^{\text{gas}} - \mu^{\text{solv}})/RT]$$

(9.5)

Octanol–water partition coefficients:

$$\log(P) = \log[\exp((\mu_{\text{oct}} - \mu_{\text{water}})/RT)V_1/V_2]$$

(9.6)

Water solubility:

$$\log(X_S) = [\mu_{\text{self}} - \mu_{\text{solv}}]/RT \ln(10)$$

(9.7)

Currently, COSMO-RS is the most popular among quantum-chemically based techniques devoted to obtaining Gibbs free-energy-dependent properties. Another approximation that is denoted as COSMO-SAC is [22] quite similar; however, it uses different expressions to estimate electrostatic, hydrogen-bonding, and van der Waals interactions and also different values for empirical parameters. In addition, some estimates have been published based on an application of continuum SM5 solvation model [23].

9.3 Environmentally Important Physical Properties of Energetic Materials

9.3.1 Solubility

Since most of the energetic materials are solids, Eq. 9.7 is not valid for this group of compounds. It should be replaced by the following expression:

$$\log(X_\mathrm{S}) = [\mu_\mathrm{self}^0 - \mu_\mathrm{solv}^0 - \Delta G'_\mathrm{fus}]/RT \ln(10), \quad \text{where} \quad \Delta G'_\mathrm{fus} = \begin{cases} 0 & \Delta G_\mathrm{fus} \leq 0 \\ \Delta G_\mathrm{fus} & \Delta G_\mathrm{fus} > 0 \end{cases}$$

$$(9.8)$$

where ΔG_fus represents Gibbs free energy of fusion. According to definition, ΔG_fus should have positive value for a solid at a given temperature. Since for liquids ΔG_fus is negative by definition, Eq. 9.8 reduces to Eq. 9.7 for liquid solute.

Therefore, in case of solids, in addition to the calculations of chemical potentials μ_self^0 and μ_solv^0 that are evaluated at the COSMO level, one needs to obtain the value of ΔG_fus, which the COSMO-RS approach suggests to estimate in one of the following two ways:

The first one is to estimate it using the QSPR equation which is preloaded inside of COSMOThermX [24] graphical interface. An application of such technique has been described by Quasim et al. [25]. In this study, the values of solubility calculated at the BP-TZVP and BP-SVP-AM1 levels have been compared with the experimental ones. The results are displayed in Table 9.1. One can see that the predicted solubility values for liquid compounds (NB, 2-NT, and 3-NT) at both the SVP and TZVP levels are in very close agreement with the experimental values (ca. 0.1 LU error). This is in accord with the reported accuracy for the COSMO-RS method for liquids (0.3 LU) [28]. However, the accuracy decreases considerably in the case of solid energetic materials. Although for some solids the predicted water solubility values are in good agreement with the experimental values, the errors for prediction of solubilities for other substances, in particular, RDX, HMX, and CL-20, are quite large: 1.6–2.5 LU. As a result, the mean absolute error (MAE) at the SVP level is equal to 0.82 LU, and at the TZVP level it is equal to 0.61 LU. The MAE values obtained at both levels are beyond the limitations of the intrinsic error of the COSMO-RS method for solids, reported as 0.5 LU [26]. A higher degree of accuracy was expected for predictions at the TZVP level since this approach is based on the higher and more accurate level of theory.

In order to determine the possible reasons for such disagreements, the terms of Eqs. 9.7 and 9.8 have been analyzed in detail. All the components of Eq. 9.7 for the liquid compounds at experimental measurement temperature and the components of Eq. 9.8 for solids are given in Table 9.2. Since most compounds of interest are solids under given temperatures the authors [25] have paid special attention to the values of ΔG_fus, which are obtained statistically in the COSMO-RS theory. Analysis of the data presented in Table 9.2 suggests that the difference $\mu_\mathrm{self}^0 - \mu_\mathrm{solv}^0$ is negative. This corroborates the meaning of these terms according to Eqs. 9.7 and 9.8, since COSMO-RS is designed for predictions of solubility of rather low soluble solutes [26]. The difference $\mu_\mathrm{self}^0 - \mu_\mathrm{solv}^0$ is negative for low-soluble compounds, when energy of the compound in pure state is lower than in solution. Therefore, the only functional parameter is represented by the difference between μ_self^0 and μ_solv^0. Consequently, this difference is displayed in Table 9.2, instead of individual values of standard chemical potentials.

ΔG_fus parameter is not applicable for liquid compounds; accordingly, this value is not estimated by the COSMO-RS procedure for liquid solute, and solubility

Table 9.1 Comparison of the water solubilities (S_W) computed using the COSMO-RS approach and available experimentally measured water solubility values

Compound		COSMO-RS S_W, log (mg/L)[a]		Errors		Exp. S_W, log (mg/L)[b]	Temp (°C)
		SVP	TZVP	SVP	TZVP		
Solids							
1	TNB	1.79	2.12	0.65	0.32	2.44	15
2	1,2-DNB	2.33	2.83	0.21	0.71	2.12	25
3	1,3-DNB	2.76	2.88	0.03	0.15	2.73	25
4	1,4-DNB	2.47	2.86	0.63	1.02	1.84	25
5	2,4,6-TNT	1.50	1.79	0.56	0.27	2.06	23
6	2,4-DNT	2.50	2.55	0.07	0.12	2.43	22
7	2,6-DNT	2.62	2.65	0.32	0.35	2.30	25
8	3,4-DNT	2.33	2.42	0.33	0.42	2.00	25
9	4-NT	2.98	2.94	0.33	0.29	2.65	30
10	4-Am-26-DNT	3.79	4.03	0.7	0.94	3.09	25
11	2,4,6-TNAN	1.73	1.71	0.57	0.59	2.30	15
12	2,4-DNAN	2.79	2.61	0.6	0.42	2.19	15
13	RDX	3.54	3.74	1.79	1.99	1.75	25
14	HMX	2.42	3.72	1.77	3.07	0.65	25
15	CL-20	1.80	2.99	1.24	2.43	0.56	25
16	Tetryl	1.84	1.84	0.03	0.03	1.87	25
17	1,4-DNsB	3.40	3.57	0.06	0.11	3.46	25
18	NsB	3.45	3.74	0.12	0.41	3.33	25
19	2,3,4-TNT	2.07	2.06	0.05	0.06	2.12	25
20	2,4,5-TNT	1.71	2.04	0.48	0.15	2.19	25
21	2,3-DNT	2.57	2.38	0.23	0.04	2.34	25
22	2,5-DNT	2.44	2.54	0.1	0.2	2.34	25
23	2-Am-46-DNT	3.53	3.80	0.44	0.71	3.09	25
24	3,5-DNAN	2.01	2.22	0.47	0.26	2.48	25
	MAE[c]	0.85	0.63				
Liquids							
25	NB	3.28	3.21	0.04	0.11	3.32	25
26	2-NT	3.05	2.95	0.24	0.14	2.81	30
27	3-NT	2.87	2.83	0.17	0.13	2.70	30
	MAE[c]	0.15	0.13				

Reprinted from Kholod et al. [34]. With kind permission of © The American Chemical Society (2009)

[a]All COSMO-RS calculations were performed at the temperature of experimental measurements
[b]References for experimental solubility values: CL-20 [6], all other compounds [27]
[c]Mean absolute error

values are computed according to Eq. 9.7. However, in the case of solid compounds, the COSMO-RS estimated values of ΔG_{fus} are surprisingly negative. This finding contradicts the meaning of the ΔG_{fus} term, which has a positive value for solids, interpreted as the energy necessary to break intermolecular bonds in a crystal lattice. A careful check of the values of this parameter for organic non-electrolyte compounds of different classes reveals that ΔG_{fus} values are always positive.

Table 9.2 Difference of the standard chemical potentials and free energies of fusion (ΔG_{fus}) computed using the COSMO-RS approach and the water solubility (S_W) values calculated using these terms according to Eq. 9.7 for liquid and Eq. 9.8 for solid solute

		SVP			TZVP		
	Compound	$\mu_{self} - \mu_{solv}$, kcal/mol	ΔG_{fus}, kcal/mol	S_W log(X)	$\mu_{self} - \mu_{solv}$, kcal/mol	ΔG_{fus}, kcal/mol	S_W log(X)
Solids							
1	TNB	−6.96	−1.42	−5.28	−6.54	−1.84	−4.95
2	1,2-DNB	−6.34	−0.75	−4.64	−5.65	−1.08	−4.14
3	1,3-DNB	−5.75	−0.58	−4.21	−5.58	−1.01	−4.09
4	1,4-DNB	−6.14	−0.68	−4.50	−5.6	−1.02	−4.10
5	2,4,6-TNT	−7.29	−1.45	−5.38	−6.9	−1.95	−5.09
6	2,4-DNT	−6.08	−0.53	−4.50	−6.02	−1.03	−4.46
7	2,6-DNT	−5.99	−0.56	−4.39	−5.94	−1.08	−4.36
8	3,4-DNT	−6.38	−0.68	−4.68	−6.26	−1.15	−4.59
9	4-NT	−5.41	−0.10	−3.90	−5.47	−0.35	−3.94
10	4-Am-26-DNT	−4.43	−0.04	−3.25	−4.1	−0.40	−3.01
11	2,4,6-TNAN	−7.37	−1.53	−5.40	−7.14	−1.90	−5.42
12	2,4-DNAN	−5.8	−0.55	−4.25	−5.84	−1.13	−4.43
13	RDX	−4.84	−0.96	−3.55	−4.57	−1.64	−3.35
14	HMX	−6.55	−1.37	−4.80	−4.77	−1.94	−3.49
15	CL-20	−7.61	−2.60	−5.58	−6	−2.77	−4.39
16	Tetryl	−8.2	−2.25	−6.01	−7.31	−2.70	−5.36
17	1,4-DNsB	−4.75	−0.09	−3.48	−4.52	−0.33	−3.31
18	NsB	−4.28	0.25	−3.33	−3.96	0.18	−3.03
19	2,3,4-TNT	−6.87	−1.30	−5.03	−6.88	−1.77	−5.04
20	2,4,5-TNT	−7.35	−1.45	−5.39	−6.9	−1.94	−5.06
21	2,3-DNT	−6.06	−0.58	−4.44	−6.31	−1.09	−4.62
22	2,5-DNT	−6.23	−0.61	−4.56	−6.09	−1.08	−4.46
23	2-Am-46-DNT	−4.79	−0.17	−3.51	−4.42	−0.47	−3.24
24	3,5-DNAN	−6.86	−0.88	−5.03	−6.58	−1.30	−4.82
Liquids							
25	NB	−4.86	−	−3.56	−4.95	−	−3.63
26	2-NT	−5.32	−	−3.83	−5.46	−	−3.93
27	3-NT	−5.56	−	−4.01	−5.62	−	−4.05

Therefore, one has to conclude that the QSPR equation used in the original COSMO-RS method for predictions of ΔG_{fus} is inadequate for the considered class of nitro-compounds. In addition, one might also assume that the large error observed for nitramines occurs because those compounds should have higher ΔG_{fus} than nitroaromatic compounds. Neglecting this issue causes inaccuracy. In order to increase the accuracy of the predictions of the solubility values of nitro-compounds, and to extend the application of the COSMO-RS method for various species including military important compounds, the QSPR procedure of ΔG_{fus} estimation has been modified as described in the next section.

Table 9.3 Basic statistical parameters of selected SiRMS QSPR models

	R^2	Q^2	S(ws)	S(cv)	A	D	M
SVP	0.86	0.78	0.43	0.55	2	28	132
TZVP	0.87	0.82	0.52	0.62	2	46	132

R^2 determination coefficient, Q^2 cross-validation determination coefficient, S(ws) standard error of prediction for the work set, S(cv) standard error of prediction for the work set in cross-validation terms, A number of PLS latent variables, D number of descriptors, M number of molecules in the training set

For alternative ΔG_{fus} estimation, simplex representation of molecular structure (SiRMS) QSPR approach developed by Kuz'min and coworkers [28] has been used. The principal physical basis of SiRMS in the application to ΔG_{fus} is established on the hypothesis that the ΔG_{fus} parameter is mainly determined not by the whole molecule but by a combination of its structural parts, for example, substituents [28]. This requires development of specific structural parameters. For this purpose, bounded and unbounded simplex descriptors of fixed composition and topology (2D level) were generated. Simplexes were differentiated by atom nature (element and type), partial charge, lipophilicity, refraction, and their ability to be a donor or acceptor in H bonding. Statistical models have been obtained by the partial least squares or projections on latent structures (PLS) method. An application of SiRMS in combination with PLS allows determining such fragments (simplexes) and their combinations that are important for ΔG_{fus} estimation. Each molecule is represented by a unified set of simplexes and can be explicitly retrieved from this set.

QSPR procedures require that a training set is constructed for evaluation of the property of interest. In the considered study, free energy of fusion (ΔG_{fus}) values for the training set $\{x_{\text{exp}}\}$ were estimated. This set was composed of 150 common organic and drug compounds that are solid at 25°C. Initially, this data set was proposed by Duffy and Jorgensen [29] and then used by Klamt et al. [26] for obtaining a regression equation for ΔG_{fus} estimation in the COSMO-RS approach for solid solutes. The σ-profiles of these compounds implemented in the COSMOtherm database were used for computation of the solubility values in COSMO-RS at both the SVP and TZVP levels. Since all the compounds of the $\{x_{\text{exp}}\}$ set are solids at 25°C, all of the corresponding ΔG_{fus}^* values are constrained to be positive. Thus, all the compounds of the training set with negative ΔG_{fus}^* values were excluded. Then a data set $\{x_{\text{exp}}\}$ of 125 remaining compounds and seven additionally included nitro-species (2-NT, 3-NT, 4-NT, 2,4-DNT, 2,6-DNT, RDX, and 5-nitro-1,10-phenanthroline) were used to create the training work set for ΔG_{fus} estimation.

Starting from this step, the QSPR protocol proposed in [26] was changed. Thus, instead of applying the fitting equation with predetermined descriptors, the SiRMS QSAR approach [28] was used for prediction of ΔG_{fus} values. Basic statistical parameters that characterize the quality of 2D PLS models for the SVP and TZVP levels are presented in Table 9.3.

Table 9.4 Statistical parameters for the external validation set prediction by the considered SiRMS QSPR models

	R^2_{test}	Q^2_{test}	$S(\text{ts})$
COSMO-RS/SVP, original	0.49	0.67	1.05
COSMO-RS/SVP, modified	0.46	0.51	1.29
COSMO-RS/TZVP, original	0.44	0.62	1.13
COSMO-RS/TZVP, modified	0.66	0.71	0.99

R^2_{test} squared correlation coefficient for external test set, Q^2_{test} determination coefficient for external test set, $S(\text{ts})$ standard error of a prediction for external test set

As follows from the analysis of the data collected in Table 9.3 one has succeeded in developing QSPR equations of near the same quality for the SVP and TZVP levels that are both robust and well-constrained.

In order to validate the predictive ability of the proposed models, the ΔG_{fus} and solubility values have been applied to 53 drugs and pesticides collected from the literature (see Ref. [25] for the details), and five nitro-compounds: TNB, TNT, 4-Am-2,6-DNT, CL-20, and HMX. The modified solubility values for this set of compounds were calculated according to Eq. 9.8. The statistical parameters of the developed models are presented in Table 9.4.

The analysis of data in Table 9.4 shows that the modified COSMO-RS/TZVP model can provide quite accurate predictions.

The next step of the verification of the modified model was to estimate the Gibbs free energies of fusion for nitro-compounds listed in Table 9.1. To obtain a correct statistical picture of the influence of the modification on the solubility predictions, 4-NT, 2,4-DNT, 2,6-DNT, and RDX were excluded from consideration at this point, since, as mentioned above, these compounds were the constituents of the training set for the QSPR model development. In view of the fact that the QSPR model was developed to estimate the ΔG_{fus} values at 25°C, adjustments had to be made for TNB, 2,4,6-TNT, 2,4,6-TNAN, and 2,4-DNAN to estimate their ΔG_{fus} at the temperatures of experimental measurements that have been carried out at temperatures different from the 25°C reference.

As shown in [30] and then applied in [31], the solubility can be estimated as

$$\ln(\gamma_s x_s) = \frac{\Delta H_{\text{fus}}}{RT}\left(1 - \frac{T}{T_{\text{melt}}}\right) \tag{9.9}$$

where γ_s represents the activity coefficient, ΔH_{fus} is the enthalpy change for melting the solute, T_{melt} – melting point temperature. In the case of ideal solubility $\gamma_s = 1$, and the solubility is determined only by the intermolecular forces in solid solute crystal that are characterized by the free energy of fusion. Thus, the Eq. 9.4 can be rewritten for ΔG_{fus}:

$$\Delta G_{\text{fus}}(T) = -\Delta H_{\text{fus}}\left(1 - \frac{T}{T_{\text{melt}}}\right) \tag{9.10}$$

Using Eq. 9.10, the ΔG_{fus} at 25°C (298 K) obtained using the proposed QSPR model can be adjusted for temperature T if the melting point temperature T_{melt} is known:

$$\Delta G_{\text{fus}}^T = \Delta G_{\text{fus}}^{298} \left(\frac{T_{\text{melt}} - T}{T_{\text{melt}} - 298} \right) \qquad (9.11)$$

The ΔG_{fus} values for TNB, 2,4,6-TNT, 2,4,6-TNAN, and 2,4-DNAN were adjusted depending on the temperature of the experiment according to Eq. 9.11. Melting point temperatures were taken from the PhysProp database [27].

Based on the ΔG_{fus} values and standard chemical potentials calculated with new QSPR model combined with the COSMO-RS approach, the new water solubility values for solids, according to Eq. 9.8 have been calculated. In addition, the prediction of the solubility values of these chemicals using the US Environmental Protection Agency recommended EPI Suite [32] and SPARC [33] predictive tools have been performed. All the results are collected in Table 9.5. As seen from the data in Table 9.5, all the ΔG_{fus} values estimated by the developed QSPR model are positive; that is, in agreement with the physical meaning of this parameter.

For comparison of accuracy, the MAEs have been calculated for the predictions made for the 21 nitro-compounds. They are displayed in Table 9.5 for all models used. One may see that the accuracy of the COSMO-RS technique with the modified QSPR procedure is higher than the accuracy of solubility predictions by the EPI [32] and SPARC [33] techniques. Similar to the original COSMO-RS model, in EPI and SPARC the highest errors are observed for nitramines. The errors of the solubility values computed by the modified COSMO-RS approach for both the SVP and TZVP levels are now within the limits of the COSMO-RS method for solid solute. The errors for all compounds under study are quite low. The MAE for the solubility values calculated with the modified procedure for ΔG_{fus} decreased by 0.40 LU when compared to the original COSMO-RS method at the SVP level. In the case of the TZVP level, the predictions for all compounds have improved, and the MAE decreased by 0.16 LU, compared with the original model.

The comparison of the results obtained for the current set of compounds at both levels shows that SVP as well as TZVP approaches yield quite accurate results. This allows using of faster, SVP level for calculation of water solubilities of large sets of compounds. However, as statistical results in Table 9.4 show, the reliability of SVP model is lower, that TZVP (it means that in some cases SVP can result in higher errors), so if computational resources allow, one recommends application of the TZVP level as more reliable.

It is apparent that the modified approach provides an efficient tool to compute solubility. The results of its application to prediction room temperature solubility values for 23 nitro-compounds have been revealed in a recent publication [34].

Another method to apply Eq. 9.8, which is recommended by COSMO-RS developers, is to use Eq. 9.10 to obtain ΔG_{fus} values. This option has been chosen in [31, 35] to evaluate the accuracy of the COSMO-RS theory for the prediction of the aqueous solubility of nitro-compounds in freshwater (deionized) at various temperatures. For verification, the authors used the experimental data of Luning

Table 9.5 The free energies of fusion (ΔG_{fus}) estimated on the base of SiRSM equations and corresponding water solubility values (S_w) computed at SVP and TZVP levels along with available EPI and SPARC data

| | Compound | SVP[a] | | | TZVP[a] | | | S_w, log (mg/L) | | | |
| | | | | | | | | EPI[b] | | | |
		ΔG_{fus} (kcal/mol)	S_w, log (mg/L)	Error	ΔG_{fus} (kcal/mol)	S_w, log (mg/L)	Error	Frag	K_{OW}	SPARC[a]	Exp
1	TNB	0.35	1.71	0.73	0.66	1.80	0.64	2.38	3.18	2.96	2.44
2	1,2-DNB	0.32	2.10	0.02	0.69	2.32	0.2	2.67	2.96	3.17	2.12
3	1,3-DNB	0.19	2.61	0.12	0.55	2.47	0.26	2.67	3.14	3.35	2.73
4	1,4-DNB	0.19	2.33	0.49	0.45	2.54	0.7	2.67	3.16	2.93	1.84
5	2,4,6-TNT	0.37	1.27	0.79	0.69	1.31	0.75	1.88	2.74	2.32	2.06
6	3,4-DNT	0.36	2.07	0.07	0.76	1.86	0.14	2.18	2.56	2.96	2.00
7	4-Am-26-DNT	0.72	3.26	0.17	0.82	3.43	0.34	2.50	3.09	2.27	3.09
8	2,4,6-TNAN	0.49	1.37	0.93	1.01	1.15	1.15	2.11	2.72	2.22	2.30
9	2,4-DNAN	0.31	2.56	0.37	0.90	2.10	0.09	2.41	2.80	2.43	2.19
10	HMX	2.76	0.39	0.26	3.03	1.50	0.85	6.00	3.97	0.67	0.65
11	CL-20	2.21	0.18	0.38	3.77	0.23	0.33	6.00	2.95	−5.73	0.56
12	Tetryl	0.56	0.78	1.09	1.34	0.86	1.01	2.48	2.76	1.06	1.87
13	1,4-DNsB	0.38	3.12	0.34	0.16	3.45	0.01	2.04	3.46	6.13	3.46
14	NsB	0.48	3.28	0.05	0.41	3.57	0.24	2.60	3.33	4.47	3.33
15	2,3,4-TNT	0.36	1.81	0.31	0.64	1.59	0.53	1.88	2.41	2.08	2.12
16	2,4,5-TNT	0.36	1.45	0.74	0.97	1.33	0.86	1.88	2.41	2.44	2.19
17	2,3-DNT	0.36	2.30	0.04	0.76	1.82	0.52	2.18	2.48	2.69	2.34
18	2,5-DNT	0.23	2.27	0.07	0.52	2.16	0.18	2.18	2.48	3.04	2.34
19	2-Am-46-DNT	0.72	3.00	0.09	0.82	3.20	0.11	2.50	3.09	2.06	3.09
20	3,5-DNAN	0.27	1.81	0.67	0.13	2.13	0.35	2.41	2.80	2.33	2.48
	MAE (original)[c]		0.79			0.62		0.90	0.66	0.95	
	MAE (modified)[c]		0.39			0.46					

[a] All COSMO-RS and SPARC calculations are at the temperature of experimental measurements indicated in Table 9.2

[b] All EPI calculations are at 25°C, because it is the only available option. frag – S_w values calculated from fragments; K_{OW} – S_w values calculated from octanol–water partition coefficients (K_{OW}s are theoretically estimated in EPI as well)

[c] Mean absolute errors for original and modified COSMO-RS models. MAE for the original and modified COSMO-RS at both SVP and TZVP levels were recalculated at this step for the set of twenty compounds collected in the current table in purpose of correct comparison of predictive ability of original and modified COSMO-RS models

Prak and O'Sullivan [36, 37] as well as the earlier data from different sources (see, [31, 35] for details). Data are available for nitrobenzene (NB), 1,3,5-trinitrobenzene (1,3,5-TNB), 2-nitrotoluene (2-NT), 3-nitrotoluene (3-NT), 4-nitrotoluene (4-NT), 2,4-dinitrotoluene (2,4-DNT), 2,6-dinitrotoluene (2,6-DNT), 2,3-dinitrotoluene (2,3-DNT), 3,4-dinitrotoluene (3,4-DNT), 2,4,6-trinitrotoluene (2,4,6-TNT), MNA (n-methyl-p-nitroaniline), NTO (3-nitro-1,2,4-triazole-5on), and TATB (1,3,5-triamino-2,4,6-trinitro-benzene).

Since the trends and accuracy in solubility prediction is virtually the same in both publications, we will typically discuss the results obtained in [35]. The theoretically predicted values plotted versus experimental data are depicted in Fig. 9.1.

As follows from the values of MAE presented in Fig. 9.1, the relatively low accuracy obtained for TNB and TNT molecules is due to the challenges encountered in representing solvation using a continuum model for compounds with very small dipole moments [38]. A more detailed analysis of the data suggests that predicted values for compounds with lower melting points (2-NT and 4-NT) are slightly overestimated, while predicted values for the solutes with higher melting points are lower than corresponding experimental data. There are also two exceptions: 3-NT shows underestimated solubility values at low temperatures, and overestimated ones at higher temperatures. The possible reason for this phenomenon may be the phase transition occurring at 16°C (melting point). Because of this transition, different equations for aqueous solubility (for liquid or solid solute) are applied that may lead to higher errors in computations. Another exception is NB, which, despite having a low melting temperature, reveals underestimated predicted solubility compared to the experimentally measured one.

The general ability and flexibility of the COSMO-RS methodology to predict temperature-dependent trends for aqueous solubility of the compounds is adequate to allow an additional modification necessary to be able to predict another parameter that describes solute in solvent. The original model was amended by introducing the influence of salinity (from the COSMO-RS methodology point of view, this means the inclusion in thermodynamic treatment of the additional σ-profiles corresponding to electrolyte ions). Based on this modification, the solubility of the ten nitro-compounds in saline water has been studied and compared with the experimental data by Luning Prak and O'Sullivan. Salinity was varied from 25% to 100%, corresponding to salt content variation from 8.8 to 33.1 g NaCl/kg water.

The COSMO-RS approach has been tested for several electrolytes (NaCl, KCl, and NaBr). The test revealed that the difference in predicted salting-out effects was insignificant for those salts at the considered range of salt concentrations. Therefore, the discussed modeling was performed for the case when only NaCl was present. This is also in line with the data presented in the Table 9.1, suggesting significant predominance of the Cl^- and Na^+ ions in seawater. Thus, we believe that the applied approximation is reasonable for this study. The corresponding plots of cross-dependences of aqueous solubility on temperature and salt types are represented in Fig. 9.2.

Figure 9.2 demonstrates the decrease of aqueous solubilities for all compounds with an increase of salt concentration. The computed solubility decreases faster
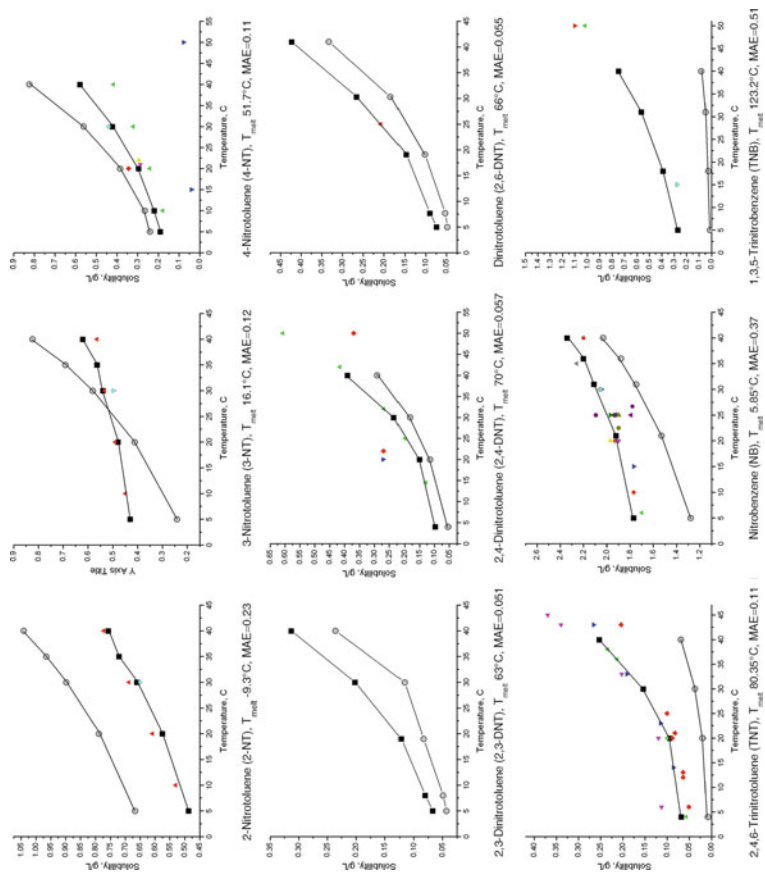
Fig. 9.1 Theoretically predicted (*gray circles*) versus experimentally measured by Prak and O'Sullivan [34, 35] (*black squares*) and earlier experimental data on aqueous solubilities of nine nitro-compounds at various temperatures. Mean absolute errors (*MAE, g/L*) of theoretical predictions are shown for each compound (Reprinted from Kholod et al. [35]. With kind permission of © Elsevier 2011)
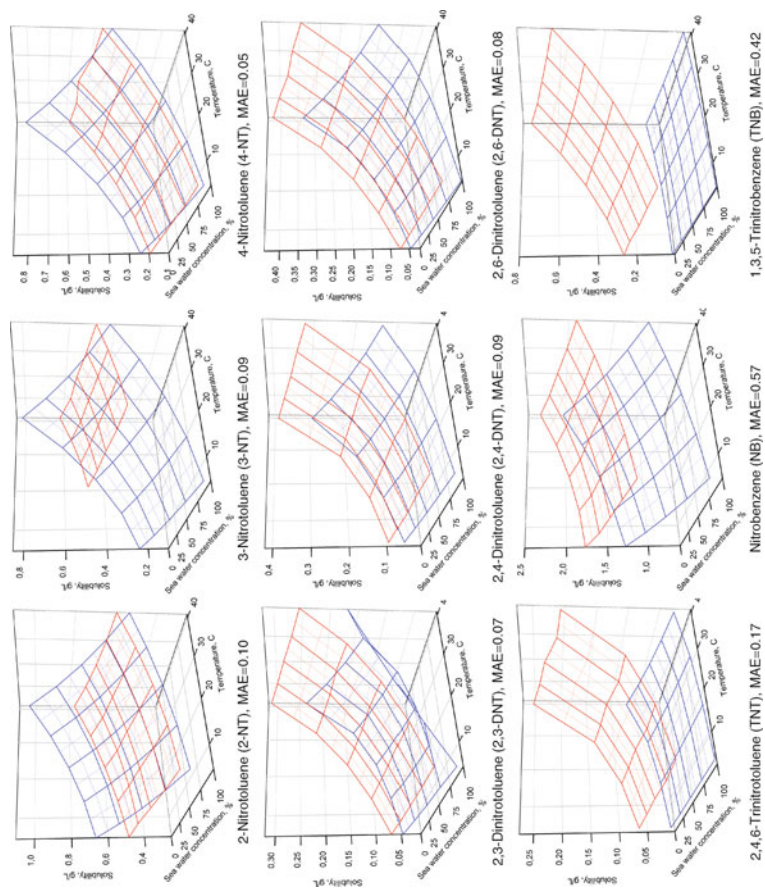
Fig. 9.2 Theoretically predicted (*blue*) versus experimentally measured by Prak and O'Sullivan [34, 35] (*red*) aqueous solubilities of nine nitro-compounds at various temperatures and concentration of seawater. Mean absolute errors (*MAE*, g/L) of theoretical predictions are shown for each compound (Reprinted from Kholod et al. [35]. With kind permission of © Elsevier 2011)

with salt addition for mononitrotoluenes and nitrobenzene, as compared with experimental values, causing surface intersections for nitrotoluenes. Unfortunately, the solubility in seawater was not measured for 3-NT at a full range of temperatures, so the theoretical/experimental comparison is incomplete for this compound. Also, the solubility in 25% seawater was not measured for 2,4-DNT, and TNT, so we interpolated these data in the displayed figures based on the corresponding values at seawater concentration equal to 0% and 50%. One can conclude that the accuracy of theoretical predictions is quite high for mono and dinitrotoluenes, while it is comparatively lower for NB, TNB, and TNT. High numerical values of MAE for NB are caused by its higher solubility as well as faster decrease of solubility in the presence of salts. Such behavior is observed for other solutes with low melting points (mononitrotoluenes), as mentioned above. The reason for higher MAE for TNB and TNT has been discussed in the previous section.

Based on theoretically predicted aqueous solubilities in pure water and saline water, the salting-out K'_s parameters for nine nitro-compounds were calculated using the Setschenow equation:

$$\text{Log}\left(\frac{S_w}{S}\right) = K'_s I \tag{9.12}$$

and then compared to the experimental data by Luning Prak and O'Sullivan.

The results obtained are presented in Table 9.6. One may see that all calculated values for K'_s are overestimated. Such trend indicates that theory predicts faster decrease of water solubility with an increase of salt concentration than is found in nature. We hypothesize that this systematic error is caused partially by the model simplification of the complex nature of the seawater electrolyte mixture, as well as difficulties to simulate the behavior of ions in water solution using COSMO-RS theory. Nevertheless, two important characteristics of the salting-out process for nitro-compounds are reproduced correctly: the values of K'_s are positive (this reflects the solubility decrease with increase of NaCl concentration) and the values of the salting-out parameters are constants, which corresponds to the physical meaning of K'_s in the Setschenow equation and agrees with the available experimental data. Therefore, one concludes that qualitative estimation of salting-out coefficients is feasible at the COSMO-RS level using NaCl as the main component of marine water.

As the next step, the 19 nitro-compounds, including nitroaromatics, nitramines, and their derivatives, which are commonly used by military and industry as explosives, propellants, and their degradation products were chosen to predict their aqueous solubility values (see Ref. [35] for details). Analysis of the results presented in [35] demonstrates that the aqueous solubility increases when temperature rises, and it decreases in the presence of electrolytes. Among the 19 explosives under study, BCHMX, CPX, and tetragen are the most soluble. Decagen, TATB, and CL-20 are the least soluble. Nitrotoluenes and nitroanisoles have moderate solubility. Taking into account the structural features, it can be concluded, as expected, that the more polar compounds are more soluble. Qualitatively, analyzing

Table 9.6 Theoretical and experimental salting-out parameters (K'_s) of nitro-compounds at different temperatures

Temp (°C)	K'_s L·mol^{-1}		Temp (°C)	K'_s L·mol^{-1}		Temp (°C)	K'_s L·mol^{-1}	
	Calc	Exp		Calc	Exp		Calc	Exp
2-Nitrotoluene			*3-Nitrotoluene*			*4-Nitrotoluene*		
5	0.42	0.15	5	0.42		5	0.42	0.15
21	0.43	0.15	21	0.42	0.14	8	0.42	0.16
31	0.43	0.14	31	0.43	0.14	19	0.42	0.15
36	0.43	0.14	36	0.43	0.13	30	0.42	0.13
41	0.43	0.14	41	0.43	0.14	41	0.43	0.14
Average	0.43	0.14	Average	0.42	0.14	Average	0.42	0.15
MAE	0.29		MAE	0.28		MAE	0.27	
2,3-Dinitrotoluene			*2,4-Dinitrotoluene*			*2,6-Dinitrotoluene*		
5	0.48	0.14	4	0.46	0.13	5	0.46	0.11
7	0.49	0.14	20	0.47	0.1	7	0.46	0.12
19	0.49	0.12	30	0.48	0.1	19	0.47	0.11
30	0.25	0.12	40	0.48	0.12	30	0.47	0.13
41	0.49	0.13				41	0.47	0.12
Average	0.44	0.13	Average	0.47	0.11	Average	0.47	0.12
MAE	0.31		MAE	0.36		MAE	0.35	
Trinitrotoluene			*Nitrobenzene*			*Trinitrobenzene*		
4	0.55	0.11	5	0.37	0.13	5	0.52	0.08
20	0.55	0.09	21	0.38	0.12	7	0.52	
30	0.55	0.15	31	0.38	0.12	19	0.52	0.1
40	0.56	0.14	36	0.38	0.12	30	0.52	0.09
			41	0.38	0.12	41	0.53	0.09
Average	0.55	0.12	Average	0.38	0.12	Average	0.52	0.09
MAE	0.43		MAE	0.26		MAE	0.43	

Reprinted from Kholod et al. [35]. With kind permission of © Elsevier (2011)
MAE mean absolute error

the salting-out coefficients, one can assume that the solubility of decagen and CL-20 decreases rapidly in the presence of electrolytes, as compared with other explosives under study.

9.3.2 Vapor Pressure

Physical properties such as vapor pressure, Henry's law constants, and octanol–water partition coefficient have been discussed in publications devoted to selected energetic materials [25, 39]. The purpose of such studies was twofold. First, they have been performed to compare the quality of predictions obtained by using the COSMO-RS technique with the QSPR program recommended by the Environmental Protection Agency for similar predictions – the EPI SuiteTM package [32]. Second, certain trends in changes of vapor pressure, air–water Henry's law con-

stants, and octanol–water partition coefficients during environmental degradation of TNT have been studied. To carry out such investigations, the authors [25] designed two hypothetic degradation pathways that are displayed in Scheme 9.1. The first pathway is based on numerous experimental data that suggest that degradation of TNT in soil proceeds as a series of reduction steps producing a wide diversity of intermediate compounds, and finally results in animoderivatives [40, 41]. The second pathway originates from the fact that TNT has as impurities various nitro-compounds that are the products of toluene nitration. Therefore, mono- and dinitro-substituted intermediates can contaminate soils and water bodies as wastes of toluene nitration processes [42]. The obtained results are collected in Table 9.7 and analyzed below.

Based on the calculations performed, it was revealed that the data of statistical treatment suggest a slightly better fit in the case of application of the EPI Suite™ package in comparison with the COSMO-RS results. However, the correlation coefficients are high enough in both cases, and the standard deviations as well as MUE are quite small. Since lower VP corresponds to less volatilizing substances, it was assumed that the COSMO-RS approach predicts a slight decrease of volatility over the degradation pathway, resulting in formation of 2,4,6AmT and a significant increase of volatility over the second transformation pathway, presented in Scheme 9.1. The data of the EPI Suite™ reveal approximately the same volatility for all substances involved in the first transformation pathway, and for the second pathway, a similar tendency as shown in the COSMO-RS predictions.

9.3.3 Henry's Law Constants

The data on air–water Henry's law constants (HLC) presented in Table 9.7 show insignificantly better fitting of the COSMO-RS predictions as compared with the predictions of the EPI SuiteTM package. However, an important disadvantage of the EPI SuiteTM data is that this program does not distinguish the structures of isomers. For example, it predicts the same HLC for 2-NT and 4-NT; 2,4-DNT and 2,6-DNT; 2,4-AmNT and 2,6-AmNT species. In contrast, the COSMO-RS predicts nonidentical HLC values. Furthermore, COSMO-RS predicts qualitatively correct relative order of air–water Henry's law constants if compared with the experimental data. The same applies for the case of vapor pressure, as well as for octanol–water partition coefficients (as shown below). Both COSMO-RS and EPI SuiteTM [32] data show a decrease in volatility from aqueous solutions over the degradation pathway, resulting in 2,4,6-AmT formation. The single discrepancy in this data set represents the prediction of the absolute value for the final product (2,4,6-AmT). COSMO-RS predicts c.a. 4 orders of magnitude larger HLC than the EPI SuiteTM [32]. However, both approaches reveal a significant increase of HLC for the second pathway.

Table 9.7 Comparison of vapor pressures, Henry's law constants, and octanol–water partition coefficients calculated with the COSMO-RS approach, EPI™ suite and available experimental values for nitro- and amino-derivatives of toluene

Compound	Vapor pressure, log(kPa)			Henry's law constant, Log(atm·m³·mol⁻¹)			Octanol–water partition coefficient, Log(K_{OW})		
	COSMO-RS	EPI	Exp	COSMO-RS	EPI	Exp	COSMO-RS	EPI	Exp
TNT	−4.85	−5.64	−5.97	−6.89	−9.44	−7.68	2.76[a]	1.99	1.6
2-AmDNT	−9.03	−5.85	–	−12.77	−10.49	–	1.88	1.84	1.84
4-AmDNT	−6.22	−4.97	−5.85	−10.22	−10.49	−10.49	1.75	1.84	1.84
2,4-AmNT	−6.77	−5.44	–	−11.64	−11.53	–	0.45	0.55	–
2,6-AmNT	−6.89	−5.44	–	−11.67	−11.53	–	0.52	0.55	–
2,4,6AmT	−6.11	−4.98	–	−8.14	−12.58	–	−0.93	−0.76	–
2,4DNT	−3.62	−4.02	−4.71	−6.20	−7.03	−7.27	2.32	2.18	1.98
2,6DNT	−3.42	−3.97	−4.12	−6.08	−7.03	−6.13	2.21	2.18	2.1
2NT	−1.68	−1.80	−1.60	−4.68	−4.63	−4.90	2.11	2.36	2.3
4NT	−1.97	−2.44	−1.66	−4.96	−4.63	−5.25	2.15	2.36	2.37
T	0.52	0.50	0.58	−2.39	−2.23	−2.18	2.39	2.54	2.73
R	0.967	0.983	–	0.988	0.961	–	0.701	0.902	–
D	0.69	0.49	–	0.44	0.79	–	0.25	0.17	–
MUE	0.533	0.444	–	0.414	0.548	–	0.311	0.116	–

Reprinted from Qasim et al. [25]. With kind permission of © Elsevier (2007)

[a]This value was excluded from the correlation to obtained statistical values presented in Table 9.7
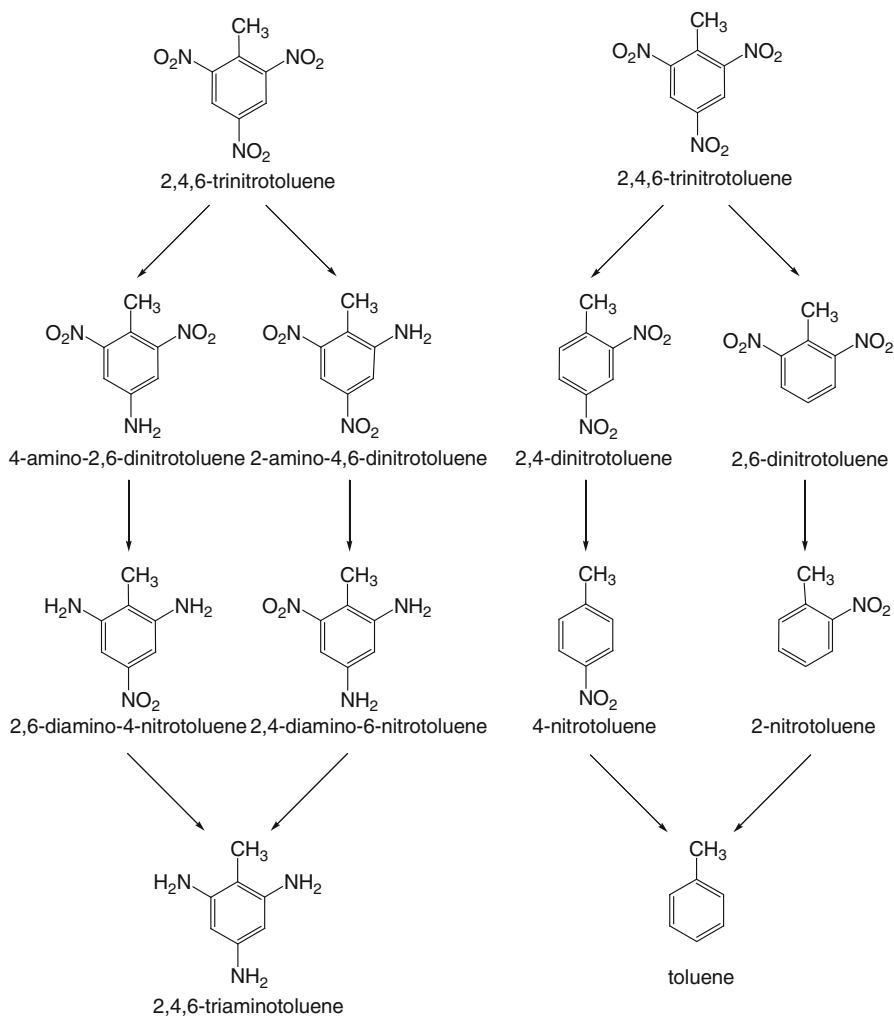
Scheme 9.1 Two hypothetic degradation pathways for 2,4,6-TNT

9.3.4 Octanol–Water Partition Coefficients

Table 9.7 shows that the accuracy of K_{OW} predictions at the COSMO-RS level is lower if compared to the other considered properties. The most probable reason for this behavior is a quite inaccurate prediction of K_{OW} for the TNT molecule itself. However, the quality of the other COSMO-RS predictions of K_{OW} is also lower than the accuracy of the results obtained by the EPI SuiteTM [32]. Nevertheless, both programs predict a very clear tendency in the decrease of K_{OW} during the first degradation pathway, including preferable solubility of 2,4,6-AmT in water. This is

in contrast to all other species considered for this pathway that are preferably soluble in octanol. Furthermore, both methods predict similar octanol–water distribution for the second degradation pathway.

9.4   Other Environmentally Relevant Applications

Here we would like to briefly review other relevant publications that apply quantum-chemically based techniques to prediction of the properties of possible environmental contaminants.

A number of organic solvents (alcohols, amines, and carbo- and heterocycles) have been studied at the COSMO-SAC level [43]. The absolute average deviations of 0.03 vapor-phase mole fraction has been found between experimentally measured and COSMO-RS results. Two publications [44, 45] are devoted to COSMO-RS application to predict pressure composition in diethyl sulfide/n-heptane (2,2,4-trimethylpentane) and thiophene n-hexane (1-hexene) mixtures. A behavior of vapor pressure was also studied in C4-hydrocarbons/2-propanone systems [46] and for chlorobenzenes and chlorophenols [47] at the COSMO-RS level. Slight underestimation of the predicted total pressure has been revealed. And finally, the data and mean unsigned errors for the prediction of vapor pressure at the SM5 level of 156 molecules representing diverse classes of organic compounds are also available [23].

A prediction of Henry's law constants has been mostly related to benzene derivatives. Among them are polycyclic aromatic hydrocarbons [48–50] treated at the COSMO-RS level, biphenyl congeners [44] investigated at the COSMO-SAC level and hydrocarbon–alcohol systems [45]. The advantage of these studies is not just the evaluation of Henry's law constant at a certain temperature but also predicting of the temperature-dependent values. Overall, the estimations are accurate within the order of magnitude of the calculated parameter.

There are two types of studies related to the prediction of octanol–water partition coefficients. The first group [16, 48, 51, 52] has dealt with only limited amount of compounds. Such limitations prevent performing reliable statistical treatment of obtained results. The second group [53, 54] reports investigations of thousands of compounds that cover most of the classes of organic molecules. The general conclusions of these studies mostly agree with the result obtained during the $\log K_{OW}$ prediction for energetic compounds. For instance, the correlation coefficient between experimental and predicted values of $\log K_{OW}$ obtained in [49] during the study of 4,155 organic compounds equal to 0.76 is quite close to the one which is obtained for the energetic materials and displayed in the Table 9.7.

Finally, among the solubility predictions we would like, first of all, to highlight the pioneering contribution of Klamt et al. [26] who initiated broad application of COSMO-RS methodology to forecast this parameter for possible contaminants. Also very valuable are the results presented by Oleszek-Kudlak et al. [55] where

COSMO-RS approach has been applied for the temperature-dependent solubility and salinity of chlorobenzenes. Among recent contributions one should acknowledge quite accurate prediction of Gibbs hydration energy of 55 pesticides and drugs presented by Klamt et al. in [56, 57].

9.5 Conclusions

It is generally accepted that the current advances of quantum chemistry allow providing results of experimental accuracy for molecular and ionic species having close electronic shell and located in the gas phase. There are, however, areas where computational approaches do not provide accurate predictions. In this chapter, we have reviewed the application of quantum chemically based continuum model of solvent in conjunction with statistical thermodynamics treatment of pair-wise interaction in a liquid phase. The focus was on predictions of environmentally important physicochemical properties of energetic materials dissolved in water. In spite of limited amount of applications related just to energetic materials dissolved in water, we have revealed that the combination of continuum model of solvent with statistical thermodynamics represents a quite accurate prediction tool. Such approach avoids empirically based QSPR approximations and restricts applications of computationally demanding techniques such as molecular dynamics and Monte Carlo methods.

Like any other model, the abovementioned approximations have advantages and limitations. In these regards, we would like to refer to the opinion of Dr. Andreas Klamt, who is instrumental in the development of the most popular COSMO-RS technique. Among the most fundamental limitation of COSMO-RS, Klamt highlights the following [15]:

1. Inability to handle dynamic properties such as viscosity and diffusion coefficients. At present, this approach is also unable to predict structural properties such as density of a liquid. Thus, COSMO-RS cannot give a complete picture of liquid-phase thermodynamics.
2. COSMO-RS has severe problems with a few, but important, solvents and solutes, for example, secondary and tertiary amine systems, dimethyl sulfoxide (DMSO), or dimethylformamide (DMF) and dimethylacetamide (DMA). While for the amines the problem might be at least qualitatively understood, and some ideas for systematic correction have been developed, the bad performance of COSMO-RS for solvents such as DMSO, DMF, and DMA is still not understood.

On the other hand, there are several clear perspectives for future improvements and extensions of COSMO-RS. Among them, first of all, are the applications of higher correlated ab initio methods such as coupled cluster calculations at affordable computational cost. Also, quantum-chemical calculation of local polarizability and development of suitable descriptors for dispersion forces should provide additional

information about the strength of local surface interactions and can be used to improve the various surface interaction functionals. At the other end, the quantum-chemical COSMO calculations for larger biomolecules and enzymes, which have just become available at reasonable computational costs, are opening a wide area of application of the basic COSMO-RS concepts to study problems of biological and medicinal chemistry, for example, the calculations of drug binding to receptors. Therefore, we are just at the initial stages, and much development and improvement can be expected in the coming years.

References

1. Sangster J (1997) Octanol-water partition coefficients: fundamental and physical chemistry. Wiley, New York
2. Lenchitz C, Velicky RW (1970) J Chem Eng Data 15:401–403
3. Leggett DC (1977) J Chromatogr A 133:83–90
4. Pella PA (1977) J Chem Thermodyn 9:301–305
5. Cundall RB, Palmer TF, Wood CEC (1978) J Chem Soc Farad T 1 74:1339–1345
6. Karakaya P, Sidhoum M, Christodoulatos C, Nicolich S, Balas W (2005) J Hazard Mater 120:183–191
7. Ro KS, Venugopal A, Adrian DD, Constant D, Qaisi K, Valsaraj KT, Thibodeaux LJ, Roy D (1996) J Chem Eng Data 41:758–761
8. Hansch C, Leo A (eds) (1995) Exploring QSAR: fundamentals and applications in chemistry and biology, vol 1. An American Chemical Society Publication, Washington, DC
9. Ognichenko LN, Kuz'min VE, Gorb L, Muratov EN, Artemenko AG, Kovdienko NA, Hill FC, Leszczynski J (2012) In: Leszczynski J, Shukla MK (eds) Practical aspects of computational chemistry II. Springer, Berlin
10. Doweyko AM (2004) J Comput Aided Mol Des 18:587–596
11. Hughes LD, Palmer DS, Nigsch F, Mitchell JBO (2008) J Chem Inf Model 48:220–232
12. Schleyer PvR (ed) (1998) Encyclopedia of computational chemistry. Wiley & Sons, Chichester, New York, Weinheim, Brishbane, Singapore, Toronto
13. Klamt A (1995) J Phys Chem 99:2224–2235
14. Kholod Y, Okovytyy S, Kuramshina G, Qasim M, Gorb L, Leszczynski J (2007) J Mol Struc 843:14–25
15. Klamt A (2005) COSMO-RS: from quantum chemistry to fluid phase thermodynamics and drug design. Elsevier Science
16. Klamt A, Eckert F, Diedenhofen M (2009) Fluid Phase Equilibr 285:15–18
17. Diedenhofen M, Klamt A (2010) Fluid Phase Equilibr 294:31–38
18. Cammi R (1998) J Chem Phys 109:3185–3196
19. Schafer A, Klamt A, Sattel D, Lohrenz JCW, Eckert F (2000) Phys Chem Chem Phys 2: 2187–2193

20. Tanpipat N, Klamt A, Clausen I, Andzelm J (1999) Abstr Pap Am Chem Soc 217:U671
21. Diedenhofen M, Klamt A (2010) Fluid Phase Equilib 294:31–38
22. Lin ST, Sandler SI (2002) Ind Eng Chem Res 41:899–913
23. Winget P, Hawkins GD, Cramer CJ, Truhlar DG (2000) J Phys Chem B 104:4726–4734
24. COSMOThermX is commertial software of COSMOlogic GmbH & Co. http://www.cosmologic.de/index.php
25. Qasim M, Kholod Y, Gorb L, Magers D, Honea P, Leszczynski J (2007) Chemosphere 69:1144–1150
26. Klamt A, Eckert F, Hornig M, Beck ME, Burger T (2002) J Comput Chem 23:275–281
27. On line Interactive PhysProp Database. http://www.srcinc.com/what-we-do/product.aspx?id=133
28. Kuz'min V, Artemenko A, Muratov E (2008) J Comput Aided Mol Des 22:403–421
29. Duffy EM, Jorgensen WL (2000) J Am Chem Soc 122:2878–2888
30. Klopman G, Zhu H (2001) J Chem Inf Comput Sci 41:439–445
31. Toghiani RK, Toghiani H, Maloney SW, Boddu VM (2008) Fluid Phase Equilibr 264:86–92
32. US EPA (2011) Estimation Programs Interface Suite™ for Microsoft® Windows, v 4.10. United States Environmental Protection Agency, Washington, DC, USA. http://www.epa.gov/opptintr/exposure/pubs/episuite.htm
33. Hilal SH, Carreira LA, Karickhoff SW (2003) QSAR & Combinatorial Science 22:565–574
34. Kholod YA, Muratov EN, Gorb LG, Hill FC, Artemenko AG, Kuzmin VE, Qasim M, Leszczynski J (2009) Environ Sci Technol 43:9208–9215
35. Kholod YA, Gryn'ova G, Gorb L, Hill FC, Leszczynski J (2011) Chemosphere 83:287–294
36. Luning Prak DJ, O'Sullivan DW (2011) J Chem Eng Data 56:2630–2633
37. Luning Prak DJ, O'Sullivan DW (2009) J Chem Eng Data 54:1231–1235
38. Rivail J-L, Rinaldi D (1976) Chem Phys 18:233–242
39. Boddu V, Render P (eds) (2010) In: Energetic materials. Thermophysical Properties, Predictions, and Experimental Measurements. CRS Press, Taylor & Fransis Group, Boca raton, London, New York
40. Schmelling DC, Gray KA, Kamat PV (1996) Environ Sci Technol 30:2547–2555
41. Li MZ, Comfort DS, Shea JP (1997) Destruction of 2,4,6-trinitrotoluene by Fenton oxidation. American Society of Agronomy, Madison. ETATS-UNIS
42. Suen WC, Spain JC (1993) J. Bacteriol 175:1831–1837
43. Lin S-T, Sandler SI (2001) Ind Eng Chem Res 41:899–913
44. Sapei E, Zaytseva A, Uusi-Kyyny P, Keskinen KI, Aittamaa J (2006) J Chem Eng Data 52:192–198
45. Sapei E, Zaytseva A, Uusi-Kyyny P, Keskinen KI, Aittamaa J (2006) J Chem Eng Data 51:2203–2208
46. Pasanen M, Zaytseva A, Uusi-Kyyny P, Pokki JP, Pakkanen M, Aittamaa J (2006) J Chem Eng Data 51:554–561
47. Verevkin SP, Emel'yanenko VN (2007) J Chem Eng Data 52:499–510
48. Schroder B, Santos LMNBF, Rocha MAA, Oliveira MB, Marrucho IM, Coutinho JAP (2010) Chemosphere 79:821–829
49. Phillips KL, Sandler SI, Greene RW, Di Toro DM (2008) Environ Sci Technol 42:8412–8418
50. Franke R, Hannebauer B, Jung S (2010) Chem Eng Technol 33:251–257
51. Buggert M, Cadena C, Mokrushina L, Smirnova I, Maginn EJ, Arlt W (2009) Chem Eng Technol 32:977–986
52. Boda A, Musharaf Ali S, Shenoi MRK (2010) Fluid Phase Equilibr 288:111–120
53. Wittekindt C, Goss K-U (2009) Chemosphere 76:460–464
54. Wittekindt C, Klamt A (2009) QSAR Comb Sci 28:874–877
55. Oleszek-Kudlak S, Grabda M, Shibata E, Eckert F, Nakamura T (2005) Environ Toxicol Chem 24:1368–1375
56. Klamt A, Eckert F, Diedenhofen M (2009) J Phys Chem B 113:4508–4510
57. Klamt A, Diedenhofen M (2010) J Comput Aided Mol Des 24:357–360

Chapter 10
State-of-the-Art Calculations of the 3d Transition-Metal Dimers: Mn_2 and Sc_2

Ilya G. Kaplan and Ulises Miranda

Abstract The problem of calculation of the electronic structure of transition-metal clusters (even dimers) still presents a challenge for computational chemistry. The reason is that the expansion of the ground state wave function on electronic configurations does not contain a principal configuration and a large number of reference configurations must be treated equally. Thus the multireference (MR) approaches are, in general, mandatory.

According to our studies of Mn_2 by the MRCISD(+Q)/aug-cc-pVQZ and ACPF approaches, the ground state is the singlet, $X^1\Sigma_g^+$, with the binding energy $D_e = 1.7$ kcal/mol (0.07 eV) and $R_e = 3.6$ Å. It was proved that the binding in the Mn_2 dimer is of the van der Waals type. The calculation of Sc_2 at the MRCISD(+Q)/cc-pV5Z level, showed that its ground state corresponds to a quintet, $^5\Sigma_u^-$, in agreement with experiment and previous precise calculations. The triplet $^3\Sigma_u^-$ state is located about 1.1 kcal/mol above. The ground state, $X^5\Sigma_u^-$, of the Sc_2 dimer was calculated by the MRCISD(+Q) method at the complete basis set (CBS) limit. This is the first MRCISD(+Q) calculation of $3d$ transition-metal clusters at the CBS limit. From the Mulliken population analysis and comparison with atomic energies follows that in the ground state Sc_2 dissociates on one Sc in the ground state and the other in the second excited quartet state, ^4F_u. The spectroscopic parameters of the ground potential curve, obtained by the Dunham analysis at the valence MRCISD(+Q)/CBS level, are: $R_e = 5.20$ bohr, $D_e = 50.37$ kcal/mol, and $\omega_e = 234.5$ cm^{-1}. The obtained value for the harmonic frequency agrees very well with the experimental one, $\omega_e = 239.9$ cm^{-1}. The Sc_2 dimer is stabilized by the covalent bonding on the hybrid atomic orbitals.

I.G. Kaplan (✉) • U. Miranda
Instituto de Investigaciones en Materiales, Universidad Nacional Autónoma de México, Apdo. Postal 70-360, 04510 México D.F., Mexico
e-mail: kaplan@iim.unam.mx; ulimirandone@gmail.com

10.1 Introduction

The $3d$ transition-metal clusters had attracted and still attract a wide attention both experimentally and theoretically [1, 2]. This great interest is associated with their important catalytic and magnetic properties. For instance, manganese systems are characterized by very unusual magnetic behavior depending on their environment [3, 4]. Solid Mn, known as α-Mn, is antiferromagnetic and has a very complex lattice structure with 54 atoms per unit cell, while the dilute "solutions" of Mn in Cu behave like spin glasses [5]. The unusual magnetic behavior of Mn systems appears as well in the nanoscale range in the case of Mn clusters [6–8]. The electron spin resonance (ESR) studies of Mn_2 and Mn_5 in rare-gas matrices, revealed that Mn_2 has an antiferromagnetic ground state with $S = 0$, whereas Mn_5 has a ferromagnetic ground state with all spins parallel and $S = 25/2$ [6]. Both theoretical and experimental studies of $3d$ transition-metal clusters are needed for the determination and comprehension of their magnetic properties; they should enhance our understanding of catalysis and chemical bonding.

In Table 10.1 we systematized the experimental data for $3d$ transition-metal homoatomic dimers presented in review [2]. As follows from Table 10.1, the total spin S in the ground state of the dimer corresponds, besides the singlet state, also triplet and higher spin states; e.g. $S = 2$ for Sc_2 and Co_2, and $S = 3$ for Fe_2. This stems from the fact that the $3d$ atoms, except Sc and Cu, have the ground state with $S \geq 1$. For finding the multiplicity of the dimer ground state in the theoretical calculations, one should study all states with possible values of S. For instance, the Mn atom has in the ground state $S = 5/2$. Therefore, the dimer Mn_2 can be in six spin states with $S = 0 - 5$.

Usually the dissociation energy, D_e, is not measured directly; its values are extracted from experimental data basing on some models. This is the reason that for most of dimers, the values of dissociation energy are widely scattered (see Table 10.1); they are different in different experimental studies. For instance, for the

Table 10.1 Experimental data reported for the dimers of the first row transition-metal atoms

Dimer	Ground state	R_e (Å)	D_e (eV)	ω_e (cm^{-1})
Sc_2	$^5\Sigma_u^-$	–	0.79–1.65	239.9
Ti_2	$^3\Delta_g$	1.9422	1.40	407.9
V_2	$^3\Sigma_g^-$	1.77	2.75–3.27	529.5–537.5
Cr_2	$^1\Sigma_g^+$	1.6788	1.443–1.53	302.0–480.6
Mn_2	$^1\Sigma_g^+$	3.4	0.02–0.82	76.4–124.69
Fe_2	$^7\Delta_u$	2.02	0.78–1.75	299.6
Co_2	$^5\Delta_g \big/ \, ^5\Sigma_g^+$	2.56	1.32–1.72	162–296.8
Ni_2	$O_g^+ \left(^3\Sigma_g^- + \, ^1\Sigma_g^+ \right)$	2.15–2.207	2.03–2.068	192–329
Cu_2	$^1\Sigma_g^+$	2.22–2.41	1.90–2.1	260–266.46

Mn_2 dimer the reported values of D_e are in the region from 0.02 eV [9] to 0.56 eV [10]. Thus, they may not be considered as the reference data and computational studies become crucial.

It is worthwhile to mention that ab initio calculations of $3d$-clusters (even dimers) are still a challenge to theorists. The main reason is that they cannot be treated by single-reference approaches, on which the modern standard methods: configuration interaction (CI), coupled cluster (CC), and Møller–Plesset perturbation theory (MPPT) are based.

As was shown in 1980 [11, 12], a reliable potential curve for the ground state of the Cr_2 dimer can be obtained only by multireference (MR) methods (see next section). Bauschlicher [13] demonstrated that in the case of Mn_2, the ground state wave function found at the complete active space (CASSCF) level, has a pronounced multireference character. In its configuration expansion

$$\Psi^{\text{CASSCF}} = c_0 \Psi \left(K_0^{\text{SCF}} \right) + \sum_i c_i \Psi \left(K_i \right) \tag{10.1}$$

the Hartree–Fock configuration appears with the coefficient $c_0 = 0.08$, while among other configurations, more than 130 configurations have coefficients $c_i > 0.05$. Thus, instead of one base configuration in the CI procedure, a large number of reference configurations must be treated equally.

In the next section, we shortly describe the ideas of main multireference methods, in consequent sections we discuss the problems and results of calculations of the dimers Mn_2 and Sc_2.

10.2   Configuration Interaction Methods

All modern effective quantum chemical methods are based on the *Hartree–Fock* (HF), or *self-consistent field* (SCF), method; see Ref. [14], Appendix 3. The HF method is a one-electron approximation; each electron is described by its own one-electron wave function (orbital) $\varphi_m(\mathbf{r})$ and is located on an one-electron level ε_m. The ground state in the restricted HF (RHF) method has the double filled orbital configuration

$$K_0 : \varphi_1^2 \varphi_2^2 \cdots \varphi_{\frac{N}{2}}^2. \tag{10.2}$$

It is the closed-shell configuration corresponding to the total spin $S = 0$. In real systems of interacting electrons, electrons lose their individuality. The movement of each electron is correlated with other electrons. This corresponds to an additional energy: the *electron correlation energy*. The simplest way to go beyond HF (or to take into account the electron correlation) is to apply the variational function as a linear combination of different orbital configurations constructed from the HF configuration K_0, Eq. 10.2, by transferring electrons from occupied to nonoccupied (virtual) orbitals.

In the approach designated as the *direct configuration interaction* (CI) method, the variational function is represented as a linear combination of antisymmetric functions (Slater's determinants):

$$\Psi^{\mathrm{CI}} = A_0 \Psi^{\mathrm{HF}}(K_0) + \sum_{n,e} A_n^e \Psi\left((K_0)_n^e\right) + \sum_{n,e} \sum_{m,i} A_{nm}^{ei} \Psi\left((K_0)_{nm}^{ei}\right) + \cdots \quad (10.3)$$

where the coefficients A_i are parameters found by minimizing the variational function; $(K_0)_n^e$ is a singly excited configuration, in which an electron occupying orbital n is excited to the virtual orbital e; $(K_0)_{nm}^{ei}$ is a doubly excited configuration with two electrons excited to virtual orbitals e and i from the occupied orbitals n and m, respectively. Expansion (10.3) may include triply, quadruply, and so on excited configurations. The calculation becomes more accurate as the number of configurations involved in the expansion increases. In the full CI (FCI) method, all the configurations, which can be built up at the given basis, are taken into account. For a very large basis set, the FCI method is, in principle, almost exact; although, practically, it cannot be realized.

A more precise approach is the synthesis of the FCI and SCF (HF) method. It is called *multiconfiguration self-consistent field* (MCSCF) method. In this method, the coefficients A_j in the CI expansion

$$\Psi^{\mathrm{MCSCF}} = \sum_{j=1}^{k} A_j \Psi\left(K_j\right) \quad (10.4)$$

and c_q in the orbital expansion of the HF orbitals $\varphi_m(\mathbf{r})$ on a basis set $\{\chi_q\}$ of size v,

$$\varphi_m(\mathbf{r}) = \sum_{q=1}^{v} c_{mq} \chi_q \quad (10.5)$$

are varied simultaneously. There are kv^2 unknown coefficients. The configurations $\Psi\left(K_j\right)$ in the linear expansion (10.4) are selected from some physicochemical considerations. At the same number of configurations, the MCSCF, evidently, is more precise than the direct CI because the orbitals in all configurations are optimized. The MCSCF method was elaborated for two-atom molecules by Das and Wahl [15] and by Veillard and Clementi [16] for many-atom molecules. Further improvements [17–19] have led to a wide use of the MCSCF method in the calculations of molecular systems.

A useful modification of MCSCF is the *complete active space* SCF (CASSCF) method. In the CASSCF approach, the orbitals are divided on *active* and *inactive* (usually the inner-shell orbitals). Then, a FCI treatment is performed at the MCSCF level with the variational function

$$\Psi^{\mathrm{CASSCF}} = \sum_{j} A_j \Psi\left(K_j\right) = c_0 \Psi\left(K_0^{\mathrm{SCF}}\right) + \sum_{i} c_i \Psi\left(K_i\right) \quad (10.6)$$

where in K_i only the electrons occupying the active orbitals participate in CI. Again, it is worthwhile to stress that CASSCF is more precise than FCI with frozen core, because it is performed at the MCSCF level. At present, very effective procedures for CASSCF codes have been developed [20, 21]. They allow one to use a large complete active space and can carry out computations with more than 10^5 state configuration functions.

Usually, the HF configuration, K_0^{SCF}, is a dominant one in the CASSCF expansion and the standard programs can be employed. However, in transition-metal clusters this is not the case. As we discuss in Sect. 10.1, for many 3d-clusters the dominant configuration in the CASSCF expansion cannot be selected. For these systems, reliable potential energy surface can be obtained only by the so-called *multireference methods*.

In the widely applied *multireference* CISD (MRCISD) method, the first stage corresponds to the CASSCF calculation. Then, the configurations with coefficients c_i in the expansion (10.6) larger than some certain value, usually $c_i \geq 0.05$, are used as reference configurations for the direct CISD calculation. Let us assume there are p reference configurations. Then, the variational function is presented as a linear combination of singly and doubly excited configurations for each of the reference configurations:

$$\Psi^{\mathrm{MRCISD}} = \sum_{r=1}^{p} \left\{ A_r \Psi (K_r) + \sum_{n,e} (A_r)_n^e \, \Psi \left((K_r)_n^e\right) + \sum_{n,e} \sum_{m,i} (A_r)_{nm}^{ei} \, \Psi \left((K_r)_{nm}^{ei}\right) \right\}.$$

$$(10.7)$$

The modern codes allow one to perform MRCISD calculations with more than 10^9 configurations. Although, it is important to mention that MRCISD and ordinary CISD as well, have a drawback, namely, the *size-inconsistency error* [22–24]: the precision depends on the number of electrons involved in CI. The size inconsistency error is considerably reduced, if the quadruple excited configurations are taken into account. The simplest way of doing it, is to use the so-called *Davidson (+Q) correction*. This correction does not require the quadruple CI calculations,

$$\Delta E_Q = \left(1 - c_0^2\right) \left(E^{\mathrm{CISD}} - E^{\mathrm{SCF}}\right) \tag{10.8}$$

where c_0 is the coefficient corresponding to the SCF configuration in the CISD calculation. The expression (10.8) was derived for the single reference CI approach [22, 23]. The (+Q) correction for the multireference approach was developed by Werner and Knowles; see Ref. [25].

Often, the large-scale MRCISD(+Q) calculations still contain significant size-inconsistency error and for more precise results it is necessary to apply MR methods, which are free of the size-inconsistency error. One of such methods is the multireference average coupled pair functional (ACPF) method [24, 26]. We will discuss the results of its application in the section devoted to Mn₂ calculations.

10.3 Manganese Dimer

10.3.1 Literature Survey

The ab initio calculations performed up-to-date [27–37] demonstrated that Mn_2 presents a great challenge to theorists. Only in 2008, six papers of theoretical studies of the Mn_2 were published; this is a clear indication of the problems and interest that this molecule represents.

The first ab initio calculation of Mn_2 was carried out by Nesbet [27] at the Hartree–Fock approximation using the Heisenberg exchange Hamiltonian

$$H = -J\mathbf{S}_a\mathbf{S}_b \tag{10.9}$$

with eigenenergy

$$E(S) = \frac{J}{2}\left[S(S+1) - s(s+1)\right] \tag{10.10}$$

where $\mathbf{S}_a$ and $\mathbf{S}_b$ are the spin operators of two atoms, S is the total spin of the dimer, s is the atomic spin, and J is the exchange coupling constant. From Eq. 10.10, the so-called Landé interval rule follows,

$$\Delta_{S,S-1} = E(S) - E(S-1) = -JS, \tag{10.11}$$

the difference between adjacent spin states is proportional to the value of the total spin with J as a coefficient of proportionality. In ESR experiments, it was found $J = -9 \pm 3$ cm^{-1} [6]; ultraviolet and Raman spectroscopy gave a near value $J = -10 \pm 0.6$ cm^{-1} [9]. Nesbet found the antiferromagnetic ground state with $J = -4.1$ cm^{-1}, $R_e = 2.88$ Å and $D_e = 0.79$ eV [27].

The first calculation beyond the Hartree–Fock approximation was performed only after 40 years [28]. The reasons for such long delay were quite essential. Similar to the case of the Cr_2 dimer [11, 12], a reliable potential curve for Mn_2 cannot be obtained by the standard single-reference approach. As we discussed in Sect. 10.1, for study of the Mn_2 potential curve it is necessary to use multireference methods treating a large number of reference configurations equally.

Wang and Chen [28] used the Møller–Plessett perturbation theory at the II order, constructed on the reference configurations found in the CASSCF calculation (CASPT2). They obtained the potential curves for all spins, $S = 0 - 5$. The ground state corresponds to $S = 0$ and has a binding energy $D_e = 0.12$ eV at $R_e = 3.64$ Å. The equilibrium distance increases with the S value to $R_e = 3.79$ Å for $S = 5$. The binding energy changes very little from 0.12 eV for $S = 0$ to 0.10 eV for $S = 5$. According to Wang and Chen [28], the exchange interaction energies $E(S)$ deviates significantly from the Landé interval rule, Eq. 10.11. It should be noted that the potential curves calculated in Ref. [28] were presented in a relatively narrow distance range and their spatial symmetry was not assigned.

Next multireference calculation of Mn_2 was published by Yamamoto et al. [29]. The authors used the second-order multiconfiguration quasidegenerate perturbation theory (MCQDPT2) developed by Nakano [37]. They considered only states with the minimum and maximum total spin: $S = 0$, $^1\Sigma_g^+$ state, and $S = 5$, $^{11}\Sigma_u^+$ and $^{11}\Pi_u$ states; the $^1\Sigma_g^+$ state was found as the ground state with $R_e = 3.29$ Å and $D_e = 0.14$ eV.

In their study, Negodaev et al. [30] performed CASPT2 calculations with the basis set $[6s5p4d3f2g1h]$ for the six lowest Σ states of Mn_2 correlating to $Mn(^6S) + Mn(^6S)$, from singlet to undecet. It was found that D_e decreases monotonically from 0.28 to 0.24 eV as we go from $^1\Sigma_g^+$ to $^{11}\Sigma_u^+$ state. The results of study [30] cannot be considered as reliable, after the basis set superposition error (BSSE) correction, these values reduced to 0.14 and 0.12, respectively, and this must not be because a relatively large basis set was employed.

Buchachenko [31] performed restricted coupled cluster (RCCSD(T)) calculations on the maximum spin state of the Mn_2, namely $^{11}\Sigma_u^+$ at the CBS limit. This state has single-reference character, which allows to use such method and this approach can be considered as the best calculations of this state. The results obtained by Buchachenko are: $R_e \approx 3.69$ Å and $D_e \approx 540$ cm^{-1} (=0.0667 eV).

Camacho et al. [32], using second-order multireference perturbation theory (MRPT2), studied the ground state of Mn_2, the $^1\Sigma_g^+$ state, with a sequence of eight different active spaces. In their calculations, the authors confirmed the multireference character of the ground state and showed how crucial is the stage of choosing the active space for multiconfigurational calculations.

Another study based on perturbation theory, was by Angeli et al. [33]. The authors used CASSCF followed by the multireference n-electron valence state perturbation theory (NEVPT) [38, 39] calculations on the singlet states $^1\Sigma_g^+$ y $^1\Delta_g$, and on the undecet states $^{11}\Sigma_{g/u}^+$ and $^{11}\Delta_{g/u}$, obtaining $^1\Sigma_g^+$ as the ground state. Mon et al. [34] also employed a PT-based multireference method; it was the same method as employed by Yamamoto et al. [29]. In fact, they studied the same states reported in Ref. [29], $^1\Sigma_g^+$, $^{11}\Sigma_u^+$ and $^{11}\Pi_u$. Although, Mo et al. [34] employed a relativistic model core potential, $spds$MCP (a MCP with a $3s3p3d4s$ GTF basis set developed for the first-row transition-metal atoms) [40], and reproduced the results obtained by Yamamoto et al. [29]. Thus, they showed that MCP can be an alternative to all-electron calculations for studying transition-metal clusters.

Tzeli et al. [35], on the other hand, performed CASSCF/MRCI (including the Davidson correction $(+Q)$) calculations with the Dunning-type basis set aug-cc-pVQZ of Balabanov and Peterson [41] taken from the Pacific Northwest National Laboratory website [42]. The lack of size consistency in these calculations (even the Davidson correction was not enough to reduce the error) made mandatory to use of a method free of this problem, so we employed the ACPF method [24, 26]. The six lowest states of Mn_2 correlating to $Mn(^6S) + Mn(^6S)$: $^1\Sigma_g^+$, $^3\Sigma_u^+$, $^5\Sigma_g^+$, $^7\Sigma_u^+$, $^9\Sigma_g^+$, and $^1\Sigma_g^+$ and six undecet states correlating to $Mn(^6S) + Mn(^6D)$: $^{11}\Pi_u$, $^{11}\Sigma_g^+$, $^{11}\Delta_g$, $^{11}\Delta_u$, $^{11}\Sigma_u^+(2)$ and $^{11}\Pi_g$ were studied; we will discuss the results for the lowest states in Sect. 10.3.3.

In 2009, Buchachenko et al. [36] also studied the Mn_2 molecular states correlating to the $Mn(^6S) + Mn(^6S)$. The results obtained in their study are in good agreement with those obtained by Tzeli et al. [35], see discussion below. An important aspect assessed in the paper of Buchachenko et al. [36] is related to the analysis of the multireference perturbation theory. The authors compared the results obtained at CASPTn, $n = 2$, 3, with three different sets of active spaces, with the results obtained by the MRCISD(+Q) and RCCSD(T) methods. It was found that perturbative methods seriously overestimate the binding energy and the splitting between different molecular states due to a poor convergence of the perturbation theory expansion. Concerning the active space selection, the authors noted that nonclosed active spaces may artificially influence the multireference calculations leading to wrong results.

The majority of Mn_2 calculations were performed by the DFT method [43–57], they represented in Table 10.2. The results obtained by different groups considerably differ from one another. The bond lengths and the dissociation energy strongly depend on the functional used. For instance, the three functionals, LSDA, BPW91, and B3LYP, used in Ref. [46], gave $R_e = 1.62$, 2.50, and 3.55 Å and $D_e = 1.54$, 0.91, and 0.06 eV, respectively. Most of DFT calculations predict the ferromagnetic ground state with $S = 5$, although in several DFT studies the antiferromagnetic singlet ground state was obtained and in one the triplet ground state was predicted.

As a whole, the DFT results are quite contradictive. The problems with spin in the density functional theory were analyzed by one of the author in Refs. [58, 59], where a group-theoretical proof (theorem) was given that the electron density of an arbitrary N-electron system is invariant with respect to the total spin S. Hence, the conventional Kohn–Sham equations have the same form for all values of S and cannot distinguish the states with different values of the total spin. Analysis of the existing DFT procedures, developed up-to-date for the calculation of spin-multiplet structure [59], revealed that they modify only the expression for the exchange energy and use correlation functionals (if used) not corresponding to the total spin S of the state. The data of DFT calculations presented in Table 10.2 confirmed the theoretical conclusions made in Refs. [58, 59].

It should be mentioned that in spite of an incorrect form of the correlation functional, the spin-multiplet procedures developed can produce for some systems quite reasonable multiplet energies due to not essential dependence of calculated multiplet structure on the correlation energy or a successful projection procedure. Probably, this takes place in the case of Sc_2, see below. However, the considered procedures are unsafe, their predictive value will be always doubtful.

In the following sections, we describe the methodology of our calculations [35] and discuss the results obtained for the dimer states correlating to $Mn(^6S) + Mn(^6S)$.

10.3.2 Methodology

The basis sets employed were the Dunning-type basis sets developed by Balabanov and Peterson [41], which are available at the Pacific National Northwest Laboratory

Table 10.2 Results of the DFT calculations on the ground state of Mn$_2$

References	Method	S = 0		S = 5		Ground state $\Delta E(S = 5, S = 0)$ (eV)
		R_o (Å)	D_e (eV)	R_o (Å)	D_e (eV)	
[43]	LSDA	–	–	2.66 ($^{11}\Pi_u$) 2.70 ($^{11}\Sigma_u^+$)	1.25 1.25	S = 5
[44]	LSDA	2.52 ($^1\Sigma_g^+$)	0.86	–	–	S = 0
[45]	LSDA	3.4	0.7	–	–	S = 0
[46]	LSDA, BPW91, B3LYP			1.62–3.55	1.54–0.06	S = 5
[48]	PW86, PBE96	Unbound		2.60	0.99	S = 5
[49]	PBE96	Unbound		2.62	0.63	S = 5
[50]	BOP, B3LYP, B-null, PW91	Unbound		Unbound		–
[51]	B3LYP, B3P86, BHLYP, BLYP, BP86, LSDA	1.61–1.70 ($^1\Sigma_g^+$)	–	3.3–3.5 ($^{11}\Sigma_u^+$) 2.61–2.66 ($^{11}\Pi_u$)	– –	Undetermined
[52]	BPW91, PW91PW91, BLYP, BP86, BPBE, PBEPBE	2.68 ($^1\Sigma_g^+$)	0.45	2.61–2.65 ($^{11}\Pi_u$)	1.15–0.65	S = 5 ($^{11}\Pi_u$) $\Delta E = 0.60$
[53]	PAW	1.66	1.35	2.53	1.29	S = 1 ($^3\Sigma_u^-$)
[54]	PBE96	2.70	–	2.60	0.98	S = 5 $\Delta E = 0.44$
[55]	PAW – PBE96	2.61	–	2.58	1.04	S = 5 $\Delta E = 0.61$
[56]	B3LYP + conversion original scheme [57]	3.62	0.04	–	–	S = 0 $\Delta E = 0.004$

website [42]. Namely, for the Mn_2 computations the aug-cc-pVQZ basis set was used. This basis set comprises ($23s19p12d4f3g2h$) spherical functions, which were contracted to [$9s8p6d4f3g2h$] and was designed for studying van der Waals-type molecules [41]. The optimization of the reference wave functions was performed at the CASSCF level. To construct the corresponding wave functions, the active electrons belong to the $3d$ atomic orbitals (10 electrons) and the selected active space included only the corresponding $3d$ orbitals (10 active orbitals). Due to the multireference character of the Mn_2 molecular states, the dynamic correlation energy (see Sect. 10.4.2.1) was computed by means of MRCISD(+Q) approach. For these calculations, the unoptimized $4s$ orbitals were included. This procedure was followed to make the calculations feasible, because, if the $4s$ atomic orbitals were included for optimization of the wave function, with the consecutive configuration interaction expansion, the computing time would be extremely long.

The maximum spin state, $^{11}\Sigma_u^+$ has a dominant configuration (the Hartree–Fock one) and thus, it can be treated by a single-reference method; in this case, the restricted coupled cluster method with single, double and noniterative triple excitations, RCCSD(T), was used.

The relativistic effects were estimated only for the state with maximum spin, $^{11}\Sigma_u^+$, via the second-order Douglas–Kroll–Hess approach [60], which was corrected in Ref. [61]. The BSSE was evaluated by the counterpoise method [62–64].

Because of the number of electrons involved in the binding (10 active electrons), the MRCISD calculations for the Mn_2 have a large size-inconsistency error; it was reduced using the quadruple Davidson correction (+Q). Nevertheless, this was not enough to reasonably reduce it; therefore we also employed the ACPF [24, 26] method. All calculations were performed with the MOLPRO [65] suite of codes.

10.3.3 Results and Discussion

10.3.3.1 Six Lowest Molecular States

By means of the methodology described above, it was possible to obtain the potential-energy curves for six quasidegenerate molecular states dissociating on the two ground-state Mn atoms $^6S(4s^23d^5)$. As can be seen in Table 10.3, there is a remarkable difference between the MRCISD, (+Q) and ACPF energies. The size-inconsistency error is considerably large, even taking into account the Davidson correction. For instance, for all six molecular states presented in Table 10.3, the dissociation energy, D_e, calculated at the ACPF level is almost twice larger than at the MRCISD level. The Davidson correction (+Q) improves the MRCISD result, but still the difference with the ACPF value is not small, about 20–50 cm^{-1}. Nonetheless, at all approximations, the $^1\Sigma_g^+$ state is the lowest one, indicating that in all cases (even with the size-consistency drawback) this is the ground state of Mn_2 (see Figs. 10.1 and 10.2). As we mentioned above, for the state with the maximum spin the single-reference method can be applied. As follows from the Table 10.3,

Table 10.3 Absolute energies E (hartree), equilibrium distances R_e (Å), binding energies D_e and D_0 (cm^{-1}), and harmonic frequencies ω_e (cm^{-1}) for the six states of Mn₂ correlating to Mn(^{6}S) + Mn(^{6}S) and obtained at the different levels of theory [35]

State	Method	$-E$	R_e	D_e	D_e (BSSE)	ω_e
$X^1\Sigma_g^+$	MRCI	2299.995299	4.128	238.2	218	24.3
	MRCI + Q	2300.024239	3.795	426.4	397	36
	ACPF	2300.028386	3.644	474.3	440	42
$^3\Sigma_u^+$	MRCI	2299.995297	4.130	238.2	218	24.4
	MRCI + Q	2300.024228	3.800	424.5	395	36
	ACPF	2300.028359	3.652	469.0	436	40
$^5\Sigma_g^+$	MRCI	2299.995294	4.132	237.5	217	24.6
	MRCI + Q	2300.024207	3.809	419.4	392	34
	ACPF	2300.028308	3.669	458.5	425	41
$^7\Sigma_u^+$	MRCI	2299.995290	4.135	236.8	217	24.4
	MRCI + Q	2300.024179	3.822	413.4	385	35
	ACPF	2300.028239	3.693	441.2	412	39
$^9\Sigma_g^+$	MRCI	2299.995287	4.138	236.1	216	24.5
	MRCI + Q	2300.024147	3.838	406.1	378	35
	ACPF	2300.028158	3.723	426.4	395	38
$^{11}\Sigma_u^+$	MRCI	2299.995291	4.137	237.1	216	24.8
	MRCI + Q	2300.024136	3.836	403.6	375	37
	ACPF	2300.028136	3.737	420.4	390	38
	RCCSD(T)	2300.034432	3.700	529.2	494	41.8

Reprinted with permission from Tzeli et al. [35]. Copyright (2008), American Institute of Physics

the RCCSD(T) method gives a best result, even in comparison with ACPF. The latter is also size consistent, but it takes into account only singly and doubly excited configurations, while in the RCCSD(T) approach the configurations with higher excitations are also allowed.

Equilibrium distance, R_e, increases with the total spin, ranging from 3.644 Å (for the state with $S = 0$) to 3.737 Å (for the state with $S = 5$). A qualitative explanation of this trend is the following. A higher value of S means there are more electrons with parallel spin; this creates a certain repulsion between the atoms and leads to larger values of R_e. On the other hand, the dissociation energies range from $D_e = 474$ cm^{-1} (for the singlet state) to 420 cm^{-1} (for the undecet), because the interaction between the two atoms is weaker if the number of electrons with parallel spin is increased. The relativistic corrections made for the $^{11}\Sigma_u^+$ state diminish 22 cm^{-1} from D_e but do not modify R_e; the final RCCSD(T) results for the highest spin state are $D_e = 529.2$ cm^{-1} and $R_e = 3.7$ Å, respectively. Basis set superposition errors are lower than 0.03 kcal/mol for the ground state and 0.07–0.14 kcal/mol for the highest spin state. The harmonic frequency obtained for the ground state is $\omega_e = 42$ cm^{-1}, while the experimental values are 68.1 cm^{-1} [66] and 59 cm^{-1} [67].

The results obtained by Buchachenko et al. [36] for the same molecular states referred to in this section follow the same pattern described above. At the
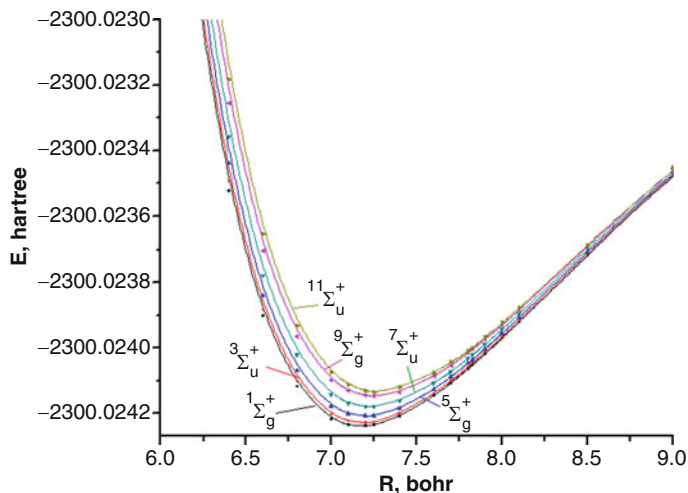
Fig. 10.1 MRCI(+Q)/aug-cc-pVQZ potential energy curves of the six lowest molecular states of Mn_2 correlating to the $Mn(^6S) + Mn(^6S)$ dissociation limit. The *inset* is an amplification of the points around the minimum reproducing the energy curves for the molecular states with different total spin [35] (Reprinted with permission from Tzeli et al. [35]. Copyright (2008), American Institute of Physics)
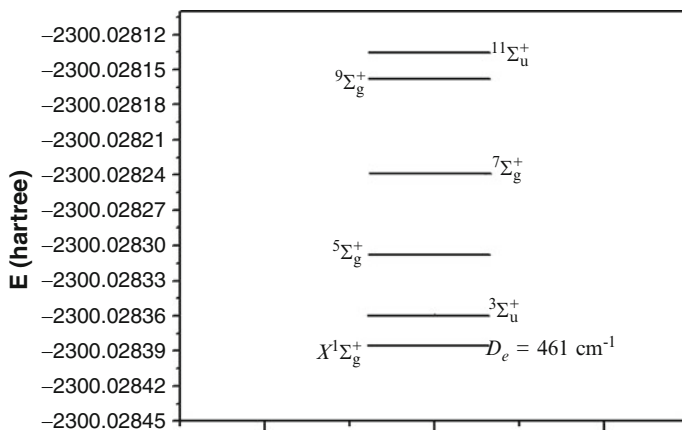
Fig. 10.2 The energy levels for the six lowest molecular states correlating to $Mn(^6S) + Mn(^6S)$ Mn_2 at the ACPF level of theory [35] (Reprinted with permission from Tzeli et al. [35]. Copyright (2008), American Institute of Physics)

MRCISD(+Q) level of theory, the values of R_e in Ref. [36] range from 3.823 Å for the singlet state, to 3.853 Å for the undecet state; the values of D_e range 394 cm^{-1} for the state with $S = 0$–369.8 cm^{-1} for the state with maximum spin.

Table 10.4 Interaction energies at the HF and MRCI levels and the correlation energy for the maximum spin state of Mn_2, $^{11}\Sigma_u^+$ [35]

R, a_0	E_{int}^{SCF}	E_{int}^{MRCI}	E_{corr}^{MRCI}
15.000	0.00054690	−0.03901648	−0.03956338
10.000	0.14513419	−0.36567965	−0.51081384
9.000	0.37583429	−0.53256949	−0.90840378
8.000	0.95578855	−0.67108737	−1.62687592
7.900	1.05015275	−0.67570212	−1.72585487
7.875	1.07523294	−0.67635420	−1.75158714
7.850	1.10094640	−0.67678057	−1.77772697
7.825	1.12730568	−0.67697494	−1.80428062
7.818	1.13480479	−0.67698619	−1.81179098
7.800	1.15432958	−0.67692478	−1.83125436
7.500	1.53840130	−0.65248414	−2.19088544
7.000	2.52568915	−0.44665731	−2.97234646
6.000	7.51255839	1.93384122	−5.57871717
5.100	22.57105408	12.79749999	−9.77355409
4.000	117.53076973	75.38111384	−42.14965589
3.600	168.65155285	120.97560305	−47.67594980

Reprinted with permission from Tzeli et al. [35]. Copyright (2008), American Institute of Physics

10.3.3.2 Correlation Energy and Magnetic Properties

As the Mn atom has a relatively small nuclear charge (Z = 25), it can be treated nonrelativistically. Let us stress that only in a nonrelativistic approach the total spin is a good quantum number. Within this approximation, the total wave function can be written as a linear combination of many-electron spin functions and many-electron coordinate wave functions with an appropriate permutation symmetry [68]. The energy depends on the total spin S due to the dependence on S of the coordinate wave function permutation symmetry. As was shown by Kaplan and Rodimova [69], it is only the exchange terms that depend on the symmetry of the state and, as consequence, on the spin, and this dependence is proportional to the orbital overlap integrals. In this way, the smaller the overlap is, the smaller dependence on S. It is important to note that the mean radius of the 3d and 4s atomic orbitals is 1.13 a_0 and 3.38 a_0 [70], respectively. These values indicate that the 3d orbitals are deeply inside the 4s orbitals, which leads to a very small 3d–3d atomic-orbital overlap. As a consequence, our results indicate that the dependence of energy on S is very small.

In Table 10.4 the interaction energies at the HF and MRCI levels and the correlation energy for the $^{11}\Sigma_u^+$ state are presented. The E_{corr} was determined according to Löwdin's definition [71],

$$E_{corr}^{MRCI} = E^{MRCI} - E^{HF}. \tag{10.12}$$

At the HF level, the potential curve has no minimum, it is repulsive. This can be explained if we take into account that the HF energy can be divided into direct electrostatic, exchange and induction contributions [14]. Given that the ground

Table 10.5 Energy differences $\Delta_{S,\,S-1}$ in Mn_2 calculated at the ACPF level [35]

S (estado)	R_e (Å)	$\Delta_{S,\,S-1}$ (cm^{-1})	$\Delta_{S,\,S-1}/S = -J$
$0\left(X^1\Sigma_g^+\right)$	3.64		
$1\left(^3\Sigma_u^+\right)$	3.65	5.93	5.93
$2\left(^5\Sigma_g^+\right)$	3.67	11.19	5.60
$3\left(^7\Sigma_u^+\right)$	3.69	15.14	5.05
$4\left(^9\Sigma_g^+\right)$	3.72	17.78	4.44
$5\left(^{11}\Sigma_u^+(1)\right)$	3.74	4.83	1.04

Reprinted with permission from Tzeli et al. [35]. Copyright (2008), American Institute of Physics

state of the Mn atom has spherical symmetry, ^6S, it has no electrostatic multipole moments and the electrostatic and induction interactions in Mn_2 have a pure overlap origin, which causes their short-range character. The exchange interactions between the closed inner shells and $4s^2$ as well are repulsive. Since the overlap between the atomic $3d$ orbitals is very small (see discussion above), and causes a small $3d$-electron exchange interaction, the latter cannot change the total exchange repulsion. The result is that Mn_2 is unstable at the HF approximation.

It is the electron correlation forces that stabilize the molecule; they coincide with dispersion forces at large distances [14, 72]. At intermediate distances, the pure dispersion forces cannot be defined without including exchange effects. In the $^{11}\Sigma_u^+$ state, at equilibrium distance (Table 10.4), $R_e = 4.137$ Å (7.818 a_0), the attractive correlation energy is about 1.6 times larger than the exchange repulsion and provides the stability of Mn_2. At ACPF level, the electron correlation contribution is even larger. Thus, the only factor of the Mn_2 stability is the electron correlation energy with the dispersion energy being the only attractive factor since the exchange forces are repulsive. Therefore, the Mn_2 dimer can be safely attributed to the van der Waals type molecules.

Using the Landé interval rule, Eq. (10.11), the exchange coupling constant was obtained from the energy differences between the adjacent spin states. The energy differences $\Delta_{S,S-1}$ and the corresponding values of the constant J, calculated at the ACPF level, are presented in Table 10.5. It can be seen that the results for $S = 1$–3 follow the Landé interval rule; but for S $= 4$ and, specially, for $S = 5$ the Landé rule is violated.

The average value of J over all spin states is $\bar{J} = -4.41$ cm^{-1}, which is in a good agreement with the value reported by Nesbet [27], $\bar{J} = -4.13$ cm^{-1}. In the ESR [6] experiments, only the levels up to $S = 3$ were occupied; by averaging J over the states with spin $S = 1$–3, the value for $\bar{J} = -5.53$ cm^{-1}, which is in agreement with the reported experimental value for the same states, $\bar{J} = -9 \pm 3$ cm^{-1} [6].

10.3.4 Conclusions

1. Although the MRCISD wave functions employed for Mn_2 include many millions of configuration state functions, the size-consistency error is rather large, even

taking into account the Davidson correction ($+$Q). For this reason, it is necessary to be very careful at analyzing the results obtained with this method for molecules with a considerably large number of valence electrons.

2. The results obtained with the ACPF approach are most reliable in comparison with MRCISD and MRCISD ($+$Q). Although, to study the single-reference state $^{11}\Sigma_u^+$, the RCCSD(T) method is better and the results obtained for this state with the mentioned single-reference method are the best.

3. From the reported mean radius of the atomic 3d and 4s orbitals [70], it can be concluded that the overlap of atomic 3d orbitals is practically negligible. The small D_e values, the correlation energy, and the analysis of the results indicate that the Mn$_2$ is a van der Waals type molecule, that is, it has a physical binding.

4. The value of the exchange coupling constant presented and discussed in the previous section, $J = -5.53$ cm^{-1}, is in good agreement with those obtained in the experimental studies [6], $\bar{J} = -9 + -3$ cm^{-1}.

10.4   Scandium Dimer

10.4.1   Literature Survey

Scandium clusters have attracted less attention than manganese clusters; nevertheless, a great number of theoretical [43, 51–53, 73–88] and experimental [9, 89–91] studies of scandium clusters are published. It is worthwhile to mention that fullerenes encapsulating Sc$_n$, $n = 2,3$ were also studied [92, 93]. Wang et al. [92] generated soot containing Sc$_2$@C$_{66}$; they also prepared other metallofullerenes [94, 95].

As well as Mn$_2$, the Sc$_2$ dimer is also a challenging molecule. In spite of only one electron in the 3d shell of Sc, the scandium dimer presents a complex computational problem. On the one hand, Sc$_2$ cannot be precisely treated by a single reference approach; on the other hand, the existence of a large number of degenerate and quasi-degenerate terms makes the calculation of Sc$_2$ potential curves extremely complicated.

The ground state of Sc is ^{2}D$_g$(4$s^2$3d), with the first three excited states ^{4}F$_g$(4s3d^2), ^{2}F$_g$(4s3d^2), and ^{4}F$_u$(4s3d4p), which are located 1.43, 1.85, and 1.96 eV above [96]. The relatively small excitation energy makes quite probable the existence of several asymptotic dissociation limits for lowest potential curves; the symmetric Sc(^{2}D$_g$) + Sc(^{2}D$_g$) and the three asymmetric: Sc(^{2}D$_g$) + Sc*(^{4}F$_g$), Sc(^{2}D$_g$) + Sc*(^{2}F$_g$), and Sc(^{2}D$_g$) + Sc*(^{4}F$_u$). In the second and fourth limits the maximum total spin of the dimer is $S = 2$. Thus, for these asymptotes the Sc$_2$ dimer can possess $S = 0$, 1, and 2. The total number of the lowest terms having these four dissociation limits is very high and equals 270. In Table 10.6 we represent the 160 possible triplet and quintet terms arising in the second and fourth dissociation limits.

Table 10.6 Molecular states stemming from the interaction of one Sc atom in the ground ^2D_g state and one Sc atom in the excited ^4F state

Sc(3d4s^2; ^{2}D) + a Sc*(3d^{2}4s; ^{4}F$_g$)		Sc(3d4s^2; ^{2}D) + z Sc*(3d4s4p; ^{4}F$_u$)	
Triplets	Quintets	Triplets	Quintets
$^3\Sigma_g^+(2),^3\Sigma_u^+(2)$	$^5\Sigma_g^+(2),^5\Sigma_u^+(2)$	$^3\Sigma_g^+(3),^3\Sigma_u^+(3)$	$^5\Sigma_g^+(3),^5\Sigma_u^+(3)$
$^3\Sigma_g^-(3),^3\Sigma_u^-(3)$	$^5\Sigma_g^-(3),^5\Sigma_u^-(3)$	$^3\Sigma_g^-(2),^3\Sigma_u^-(2)$	$^5\Sigma_g^-(2),^5\Sigma_u^-(2)$
$^3\Pi_g(5),^3\Pi_u(5)$	$^5\Pi_g(5),^5\Pi_u(5)$	$^3\Pi_g(5),^3\Pi_u(5)$	$^5\Pi_g(5),^5\Pi_u(5)$
$^3\Delta_g(4),^3\Delta_u(4)$	$^5\Delta_g(4),^5\Delta_u(4)$	$^3\Delta_g(4),^3\Delta_u(4)$	$^5\Delta_g(4),^5\Delta_u(4)$
$^3\Phi_g(3),^3\Phi_u(3)$	$^5\Phi_g(3),^5\Phi_u(3)$	$^3\Phi_g(3),^3\Phi_u(3)$	$^5\Phi_g(3),^5\Phi_u(3)$
$^3\Gamma_g(2),^3\Gamma_u(2)$	$^5\Gamma_g(2),^5\Gamma_u(2)$	$^3\Gamma_g(2),^3\Gamma_u(2)$	$^5\Gamma_g(2),^5\Gamma_u(2)$
$^3H_g,^3H_u$	$^5H_g,^5H_u$	$^3H_g,^3H_u$	$^5H_g,^5H_u$

In the ESR experiments by Knight et al. [88], the ground state of Sc$_2$ was assigned as $^5\Sigma_u^-$. Let us stress that it was not obtained in a direct measurement. Processing their experimental data, the authors [88] made some assumptions. Several years before, the quintet ground state, $^5\Sigma_u^-$, was predicted in the DFT calculations by Harris and Jones [43]. They employed a rough (but the best at that time) local spin density approximation (LSDA). So, it is surprising that Harris and Jones were able to predict by their method such exotic ground state, corresponding to an asymmetric dissociation. However, they mentioned that the triplet state, $^3\Sigma_u^-$, can also be a candidate for the ground state.

In one of the first precise ab initio studies of Sc$_2$ by Walch and Bauschlicher [79] on the basis of the complete active space CASSCF/CISD calculations, it was demonstrated that the triplet states $^3\Sigma_g^-$ and $^3\Sigma_u^-$ are above the quintet $^5\Sigma_u^-$ state by about 0.04–0.05 eV. The authors [79] came to the conclusion that the term $^5\Sigma_u^-$ corresponds to the ground state and supported this conclusion by an analysis of the bonding in the Sc dimer. The reported dissociation energy was $D_e = 0.44$ eV, in respect to the $^2D + ^2D$ dissociation limit.

It is interesting to mention that in all published, to the best of our knowledge, DFT calculations of Sc$_2$ [43, 51–53, 73–76], the quintet state, $^5\Sigma_u^-$, was claimed as the ground state. This consensus is in sharp contrast with the DFT calculations of other transition-metal dimers; e.g., for Mn$_2$ the DFT results are quite conflicting; see discussion in the previous section. It should be noted that only in limited DFT studies different spin states of Sc$_2$ were studied; in most published DFT calculations only $^5\Sigma_u^-$ state was selected and authors studied the dependence of the obtained results on the functionals used.

As discussed for the manganese dimer (see Sect. 10.3.4), the predictive value of DFT calculations of transition-metal clusters is always doubtful because of the multiconfigurational character of the transition-metal clusters and the problems arising in DFT when the value of S is not 0 [58, 59]. Similar to the case of other transition-metal dimers, precise computational results for Sc$_2$ can be obtained only by ab initio multireference methods with large basis sets.

Till recent time the most precise ab initio calculations of Sc$_2$ were performed by Åkeby et al. [81] using a multireference treatment at the ACPF level. In regards to

the dissociation limit (^{2}D +^{4}F), they obtained D_e (ACPF,v) = 1.888 eV (without the core correlation). After including the core correlations and the first-order relativistic correction, the dissociation energy increased, D_e (ACPF, v + 3p, rel.) = 2.118 eV. The experimentally measured dissociation energy must be defined in respect to the lowest asymptotic limit ^{2}D +^{2}D. After all corrections, including the corrections on the experimental atomic excitation energy, the authors [81] obtained D_e = 0.77 eV. The final results reported for other spectroscopic constants are the following: R_e = 5.051 a_0 and ω_e = 197 cm^{-1}.

Several years after the publications of Åkeby et al. [81, 82], Sc$_2$ was studied by Suzuki et al. [83] at the MRCISD (+Q) level. Their results are comparable to those obtained by Åkeby et al. [81], namely, D_e = 0.59 eV (corrected to the ^{2}D +^{2}D dissociation limit), R_e = 5.17 a_0 and ω_e = 224 cm^{-1}. After these publications it became widely accepted that the ground state of Sc$_2$ is the quintet state.

In 2008 Matxain et al. [84] revised the problem of the Sc$_2$ ground state. They stressed that only the $^5\Sigma_u^-$ state had been studied at a high level [81, 83], whereas the triplet terms were calculated in Ref. [82] using a not sufficiently precise CASSCF approach. Matxain et al. [84], applying the quantum diffusion Monte Carlo (DMC) method, have calculated at the same level of theory ten low-lying states of the scandium dimer, including the $^5\Sigma_u^-$ and $^3\Sigma_u$ states (the upper index in the Σ state was not specified). According to their calculations, the $^3\Sigma_u$ state is more stable than the $^5\Sigma_u^-$ state by 0.17 eV. The authors [84] claimed that the correct ground state of scandium dimer is the $^3\Sigma_u$ state, but not the $^5\Sigma_u^-$ state, as was accepted in all previous investigations.

However, the calculations by Matxain et al. [84] did not have a sufficient level of accuracy to be reliable; they were less precise than the previous calculations by Åkeby et al. [81] and by Suzuki et al. [83]. The authors [84] used a relatively small basis set and checked the DMC results comparing it with CASPT2 calculation (the latter is taken as a final criteria). However, as we discuss in Sect. 10.4, the CASPT2 method is very sensitive to the choice of the active space and the use of non-closed active space can lead to large errors. Exactly that took place in the calculations of Matxain et al. [84], as was noted by the authors in Erratum [97]. It is also worthwhile to mention that the CASPT2 and MRMP2 methods suffer from the intruder state problem [98]. A change of the shift parameter in the intruder state removal techniques can lead to a change of the order of states, as was demonstrated in Ref. [98] just for Sc$_2$. Thus, the conclusion of Matxain et al. [84] had to be verified in more precise calculations. This has been done in the recent publications [85, 86].

In the study by Kalemos et al. [85], precise MRCISD(+Q)/cc-pVQZ calculations were carried out for the two competitive terms $^5\Sigma_u^-$ and $^3\Sigma_u^-$. It was established that the quintet state, $^5\Sigma_u^-$, is really the ground state and the triplet state, $^3\Sigma_u^-$, is located just 1 kcal/mol (0.04 eV) above. These results were qualitatively confirmed in the study by Camacho et al. [86] where the NEVPT method was employed. The authors found that the triplet state, $^3\Sigma_u^-$, is located about 0.10 eV above the ground state, the $^5\Sigma_u^-$ state.

Recently, Kaplan and Miranda [87, 88] performed a detailed study of the nature of binding in the ground state of the Sc_2 dimer using MRCISD(+Q) method at the complete basis set (CBS) limit. A special attention was paid to study the dissociation limit. For the possibility to obtain the two Sc atoms in different states, we used the C_{2v} symmetry restriction (in all previous studies of Sc_2 the D_{2h} symmetry group was used). We showed that the dimer Sc_2 dissociates on one Sc in its ground state and the other in the second excited quartet state ^4F_u ($4s^1 3d^1 4p^1$). The results [87, 88] will be discussed in detail in the following subsections.

10.4.2 Methodology

10.4.2.1 Computational Method

The wave functions were optimized by means of the CASSCF method, Sect. 10.2; the active space was defined by the $3d$, $4s$ and $4p$ orbitals, making a set of 18 active orbitals and 6 active electrons, 3 from the atomic valence shells of each atom. As was discuss in Sect. 10.4.1, the ground state of the scandium dimer, $^5\Sigma_u^-$, stems from the interaction between one ground state Sc atom and other in an excited state, therefore the calculations were done under C_{2v} symmetry constraints. The C_{2v} calculation is much more time consuming than D_{2h} one, but it allows to obtain the two Sc atoms in different states at the dissociation limit. Although, because of the identity of Sc atoms, the average electron configurations of both Sc atoms should be the same, see Eq. 10.21.

The final results were obtained by the multireference internally contracted MR-CISD method [99, 100]. The size-inconsistency error was corrected only through the Davidson (+Q) approach, since this error in the case of Sc_2 is small. According to our results, see Table 10.7, the quadruple Davidson corrections lead to small changes; e.g., the difference in D_e is about 0.04 eV.

For the cc-pV5Z basis set, the number the reference wave functions was approximately 34,000, their corresponding valence MRCI expansions contain about 1.65×10^8 configuration functions (CF), which are internally contracted to 6.7×10^6 CFs according to procedure described in Refs. [99, 100]. The Dunning-type basis sets [41], presented in the Pacific Northwest National Laboratory basis set website [42] was employed. The relativistic corrections were obtained by means of the Douglas–Kroll–Hess approach in the second order scheme [60, 61] with the relativistic basis set cc-pV5Z-DK [41]. For all calculations the MOLPRO 2009 suite of programs [101] was used.

The energy obtained at the MRCI level includes some additional electron correlation energy, in comparison with the CASSCF energy,

$$E^{MRCI} = E^{CAS} + E^{dc} \tag{10.13}$$

This energy is named the *external* or *dynamical correlation energy* [102, 103]; it arises from the non-specific instantaneous correlation motion of electrons and was introduced by Oktay Sinanoĝlu [104, 105].

Sinanoĝlu and coworkers [104–106] showed that the correlation energy can be roughly divided into two types: dynamical correlations, which are transferable from system to system, and non-dynamical correlations, which are not. Usually non-dynamical correlations are responsible for a correct description of the dissociation products and in some papers are named *left-right correlation* [107]. Sinanoĝlu stressed that a good example of the transferable correlation energy is the closed $1s^2$ shell for the first-row atoms. At that time the MRCI approach was not created. Brown and Truhlar [103] divided the dynamical correlations into core and valence contributions. The latter corresponds to the dynamical correlation energy defined by Eq. 10.13.

10.4.2.2 Complete Basis Set Limit

To study the dependence of calculation results on the basis set size and finding the complete basis set (CBS) limit, we performed calculations with three basis sets, cc-pVXZ with $X = 3$, 4, and 5. The largest basis set, cc-pV5Z, is constructed with $[28s20p12d4f3g2h1i]$ functions, which are contracted to $[9s8p6d4f3g2h1i]$, and comprises 306 Gaussian functions. The basis set cc-pVQZ is made with $[22s18p11d3f2g1h]$ functions contracted to $[8s7p5d3f2g1h]$ and comprises 208 Gaussian functions; and the cc-pVTZ basis set is formed by $[20s16p8d2f1g]$ functions contracted to $[7s6p4d2f1g]$ and comprises 136 Gaussian functions.

After the development by Dunning [108] of the correlation-consistent cc-pVXZ basis sets, it was recognized that the sequence of results obtained with different XZ can allow an extrapolation to the CBS limit [109–111]. Calculation of E_X with different values of X makes possible to find the CBS limit, E_∞, using some analytical function of X connecting E_X and E_∞. At present, several asymptotic formulae for finding the CBS limit at the HF, CASSCF, and MRCI levels have been developed, see Ref. [102] and references therein.

We applied the procedure for obtaining the CBS limit at the MRCI level suggested by Varandas [102]. It is based on the presentation of E^{MRCI} as two terms, Eq. (10.12), and finding the CBS limit for each term separately.

For energy at the CASSCF level we used the Karton–Martin [112] extrapolation formula, which is based on the work by Jensen [113]. The equation employed is

$$E_X^{CAS} = E_\infty^{CAS} + A(X + 1)e^{-b\sqrt{X}} \tag{10.14}$$

in which A and b are parameters found after solving equations and E_∞^{CAS} is the quantity sought for. Inserting in Eq. 10.14 the energy E_X^{CAS} calculated for $X = 3$, 4, and 5, we obtain three equations for three unknowns: A, b, and E_∞^{CAS}, which can be precisely solved,

$$E_3^{CAS} = E_\infty^{CAS} + 4A \exp\left(-b\sqrt{3}\right),$$

$$E_4^{CAS} = E_\infty^{CAS} + 5A \exp\left(-2b\right),$$

$$E_5^{CAS} = E_\infty^{CAS} + 6A \exp\left(-b\sqrt{5}\right). \tag{10.15}$$

If we subtract E_4^{CAS} from E_3^{CAS} denoting the result as k_{34}, and then subtract E_5^{CAS} from E_4^{CAS} denoting this result $b/45$, and divide k_{34} on k_{45}, we obtain the equation

$$\frac{k_{34}}{k_{45}} = \frac{4e^{-b\sqrt{3}} - 5e^{-2b}}{5e^{-2b} - 6e^{-b\sqrt{5}}}, \tag{10.16}$$

from which we can find parameter b by trial and error method. It should be mentioned that in the original work by Karton–Martin [112] the parameter b was optimized on a great number of simple molecules with light atoms. They recommended $b = 9$. Since our dimer is formed of $3d$ transition-metal atoms, we put b as a free parameter. We found that $b = 5.925$ gives better results than $b = 9$. At this point we could determine the value of parameter A through the equation

$$A = \frac{k_{34}}{4e^{-b\sqrt{3}} - 5e^{-2b}} = \frac{k_{45}}{5e^{-2b} - 6e^{-b\sqrt{5}}}. \tag{10.17}$$

The constants k_{34} and k_{45} have different values, so according to Eq. 10.17, the parameter A has two values. Although, they are very close, and for the CBS limit of the CAS energy we obtained $E_X^{CAS} = -1519.533960$ hartree

The CBS limit for the dynamical correlation energy, E_∞^{dc}, was found using the Varandas USTE scheme [102]. The employed equation has the following form:

$$E_X^{dc} = E_\infty^{dc} + \frac{A_3}{(X - 3/8)^3}\left[1 + \frac{1}{(X - 3/8)^2}\left(\frac{a}{A_3} + cA_3^{1/4}\right)\right] \tag{10.18}$$

where a and c are fixed numerical coefficients and A_3 is a parameter that has to be found. Thus Eq. 10.18 has only two unknowns, E_∞^{dc} and A_3. They were found using a code based on the least-squares method. The best results were obtained for the basis set pair with the highest XZ, $X = 4$ and 5, which produces two equations:

$$E_4^{cor} = E_\infty^{cor} + \frac{A_3}{(4 + \alpha)^3}\left[1 + \frac{1}{(4 + \alpha)^2}\left(\frac{A_5^0}{A_3} - cA_3^{1/4}\right)\right] \tag{10.19}$$

$$E_5^{cor} = E_\infty^{cor} + \frac{A_3}{(5 + \alpha)^3}\left[1 + \frac{1}{(5 + \alpha)^2}\left(\frac{A_5^0}{A_3} - cA_3^{1/4}\right)\right] \tag{10.20}$$

The obtained CBS value for the dynamical correlation energy was $E_\infty^{cor} = -0.040620$ hartree.

Table 10.7 The dependence of the equilibrium distance, R_e (a_0), total energy, E (hartree), dissociation energy, D_e (eV), and the harmonic frequency, ω_e (cm^{-1}) on the basis set cc-pVXZ and the CBS limit for Sc_2 in the ground state $^5\Sigma_u^-$ [87, 88]

Basis	MRCI				MRCI(+Q)			
set	R_e	E	D_e	ω_e	R_e	E	D_e	ω_e
TZ	5.202	−1519.567779	2.073	222.6	5.214	−1519.569566	2.111	223.6
QZ	5.195	−1519.570613	2.107	224.5	5.206	−1519.572522	2.150	224.8
5Z	5.193	−1519.571661	2.122	226.3	5.204	−1519.573631	2.166	229.2
CBS					5.200	−1519.574560	2.183	234.5

10.4.3   Results and Discussion

10.4.3.1   Calculations at the Complete Basis Set Limit

The dependence of obtained results on the basis set is presented in Table 10.7. The CBS limit data are also included. The CBS limit was obtained using the basis sets cc-pVXZ, with $X = 3$, 4, and 5, by the procedure described in Sect. 10.4.2.2. The final CBS results at the MRCISD(+Q) level were obtained as a sum of the CBS estimations of E_∞^{CAS} and E_∞^{dc}; see Sect. 10.4.2.2. We calculated the harmonic part of the ground state potential curve for all three basis sets with $X = 3$, 4, and 5 and also at the CBS limit and found its spectroscopic parameters using Dunham analysis [114]. According to Table 10.7, the larger is the basis set, the stronger is the bonding. The dissociation energy D_e at the CBS limit is equal to 2.183 eV (50.30 kcal/mol). The obtained equilibrium distance R_e at the MRCISD(+Q)/CBS level is equal to $R_e = 5.200$ a_0 (2.752 Å). The account of the $3s3p$ correlation effects does not change D_e, which is natural, but reduced R_e on 0.2 a_0 [85]. Thus, the corrected value is R_e should be 5.0 a_0 (2.65 Å). The harmonic frequency ω_e at the MRCISD(+Q)/CBS level, is equal to 234.5 cm^{-1}, which is in an excellent agreement with the experimental value 239.9 cm^{-1} [90].

The relativistic calculations using cc-pV5Z-DK basis set do not modify the equilibrium distance. As for the dissociation energy, the difference in D_e in comparison with the value obtained with the nonrelativistic cc-pV5Z basis set is very small; at the CASSCF level it equals 0.36 kcal/mol and at the MRCISD(+Q) it is only 0.07 kcal/mol, see Table 10.8. The change of the harmonic frequency, ω_e, is also small; at the CASSCF level it equals 6.8 cm^{-1} and at the MRCISD(+Q) level it is reduced up to 0.1 cm^{-1}.

The potential energy curves of Sc_2 in the ground state $^5\Sigma_u^-$, calculated at the CASSCF, MRCISD, and MRCISD(+Q) levels with the largest basis set cc-pV5Z, are represented in Fig. 10.3. The last two curves almost coincide (in the hartree scale). This fact and the data in Table 10.7 for the equilibrium distance indicate that in the case of Sc_2 the size-inconsistency error is small, in contrast with the Mn_2 dimer case [35]. Thus, the MRCISD(+Q) approach can be considered as a quite satisfactory approximation for the study of the Sc_2 dimer.

Table 10.8 Comparison of the dissociation energy, D_e, and harmonic frequency, ω_e, for the Sc_2 ground state potential curves calculated at the scalar relativistic level with cc-pV5Z-DK basis set and the nonrelativistic MRCISD(+Q) level with the basis set cc-pV5Z; energies are in eV (kcal/mol), frequencies are in cm^{-1} [87, 88]

Basis set	CASSCF		MRCISD		MRCISD(+Q)	
	D_e	ω_e	D_e	ω_e	D_e	ω_e
5Z	1.563 (36.01)	217.1	2.122 (48.90)	226.3	2.166 (49.91)	229.2
5Z-DK	1.578 (36.37)	223.9	2.127 (49.01)	229.0	2.169 (49.98)	229.1
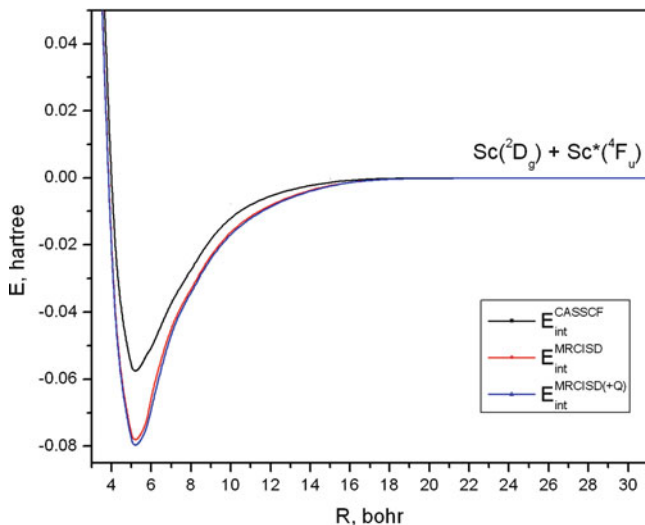
Fig. 10.3 Potential energy curves for the ground state of Sc_2 at the CASSCF, MRCISD, and MRCISD (+Q) levels calculated with cc-pV5Z basis set [87, 88]

10.4.3.2 Dissociation Limit

The determination of the dissociation limit of the Sc_2 ground state potential curve is a rather delicate problem. From the experiment [89] and precise calculations, see discussion in Sect. 10.4.1, it follows that the Sc_2 ground state corresponds to the $^5\Sigma_u^-$ term, which can be obtained only if one of Sc is created in an excited quartet state. In this case the total spin S of Sc_2 can be equal 2. But according to Table 10.6, the quintet term $^5\Sigma_u^-$ can have the two dissociation limits: $Sc(^2D_g) + Sc^*(^4F_g)$ and $Sc(^2D_g) + Sc^*(^4F_u)$. In both limits Sc_2 dissociates on one Sc in the ground state and another in an excited state. With the usually applied D_{2h} symmetry restrictions one cannot distinguish Sc atoms because of the inversion symmetry. For the possibility to obtain two Sc in different state we employed the C_{2v} symmetry restrictions.

In Table 10.9 the Mulliken atomic valence orbital populations at the equilibrium, R_e, and dissociation limit, $R = 50\ a_0$, distances are represented. At the

Table 10.9 Mulliken population in Sc_2 at the equilibrium and dissociation limit distances at different levels of theory [88]

(a) MRCISD

R_e: $4s^{1.22}3d^{1.29}4p^{0.46}$: $4s^{1.22}3d_{z^2}^{0.49}3d_{x^2-y^2}^{0.01}3d_{xz}^{0.39}3d_{yz}^{0.39}3d_{xy}^{0.01}4p_z^{0.22}4p_x^{0.12}4p_y^{0.12}$

$R = 50a_0$: Sc $(4s^23d^1)$: $4s^{1.82}3d_{z^2}^{0.01}3d_{x^2-y^2}^{0.00}3d_{xz}^{0.01}3d_{yz}^{0.01}3d_{xy}^{0.98}4p_z^{0.05}4p_x^{0.05}4p_y^{0.05}$

Sc $(4s^13d^14p^1)$: $4s^{0.95}3d_{z^2}^{0.02}3d_{x^2-y^2}^{0.99}3d_{xz}^{0.01}3d_{yz}^{0.01}3d_{xy}^{0.00}4p_z^{0.98}4p_x^{0.01}4p_y^{0.01}$

(b) CASSCF

R_e: $4s^{1.22}3d^{1.26}4p^{0.47}$: $4s^{1.22}3d_{z^2}^{0.48}3d_{x^2-y^2}^{0.01}3d_{xz}^{0.38}3d_{yz}^{0.38}3d_{xy}^{0.01}4p_z^{0.23}4p_x^{0.12}4p_y^{0.12}$

$R = 50a_0$:Sc $(4s^23d^1)$: $4s^{1.82}3d_{z^2}^{0.00}3d_{x^2-y^2}^{0.50}3d_{xz}^{0.00}3d_{yz}^{0.00}3d_{xy}^{0.49}4p_z^{0.06}4p_x^{0.05}4p_y^{0.05}$

Sc $(4s^13d^14p^1)$: $4s^{0.96}3d_{z^2}^{0.02}3d_{x^2-y^2}^{0.50}3d_{xz}^{0.01}3d_{yz}^{0.01}3d_{xy}^{0.50}4p_z^{0.98}4p_x^{0.01}4p_y^{0.01}$

MRCISD(+Q) level, Sc_2 dissociates on one Sc in the ground state, Sc $(4s^23d^1$; $^2D_g)$, and another in the second excited quartet state, Sc^* $(4s^13d^14p^1$; $^4F_u)$. The same dissociation limit is obtained at the CASSCF level.

Hence, from the Mulliken population it follows that the ground state potential energy curve of Sc_2 has the $Sc(^2D_g) + Sc^*(^4F_u)$ dissociation limit. On the other hand, both Sc atoms are identical and each of them can be excited. So, at the dissociation limit the wave function of the dimer must be a linear combination of the wave function, in which one Sc atom is in the ground state and another Sc atom is in an excited state, and the wave function describing the opposite possibility:

$$\Psi(Sc_2, R \to \infty) = \frac{1}{\sqrt{2}}\left[\Psi_0(Sc_a)\Psi_n(Sc_b^*) + \Psi_n(Sc_a^*)\Psi_0(Sc_b)\right] \quad (10.21)$$

This reflects the quantum-mechanical indistinguishability of identical atoms. As a result, both Sc atoms have an equal population: $4s^{1.5} 3d^1 4p^{0.5}$.

The dissociation on one of the atoms in the second excited quartet state seems quite unusual. For the verification of this result we have compared the dimer energy at $R = 50$ bohr with the sum of atomic energies for different quartet states calculated at the same level of theory. As follows from Table 10.10, the energy of Sc_2 at $R = 50$ bohr corresponds to the sum of energies $Sc(^2D_g) + Sc^*(^4F_u)$. The dissociation level $Sc(^2D_g) + Sc^*(^4F_g)$ is located 0.0141 hartree (or 8.82 kcal/mol) below, which is much larger than the calculation error. At the CASSCF level we cannot arrive to definite conclusions using the atomic energy calculations.

Thus, Sc_2 dissociates with one of atoms in the ^4F_u excited state. But, after about 10^{-8}s, the atom in the ^4F_u state undergoes a radiative transition (fluorescence) to the level ^4F_g with $E_{ph} = 0.529$ eV $= 1.279 \times 10^{14}$ Hz. The excited state ^4F_g is metastable and loses its energy by phosphorescence for time about $10^{-3}–10^{-6}$s, with emitting quant $E_{ph} = 1.427$ eV $= 3.45 \times 10^{14}$ Hz. Thus, the dissociation of Sc_2 should be followed by the chemiluminiscence in the infrared region that can be experimentally detected.

We would like to note that in the recent study [85] of $^5\Sigma_u^-$ state with the D_{2h} symmetry restriction, the $Sc(^2D_g) + Sc^*(^4F_u)$ dissociation limit was obtained.

Table 10.10 Comparison of the dissociation limit energy of Sc_2 in the ground state and energies of the Sc atom in the ground and excited states calculated with the basis set cc-pV5Z at different levels of theory; energies are in hartree, Δ is in kcal/mol [88]

	CASSCF	MRCISD	MRCISD + Q
$Sc_2(R = 50a_0)$	-1519.476420	-1519.493675	-1519.494029
$Sc(^2D_g) + Sc^*(^4F_g)$	-1519.465245	-1519.498898	-1519.508093
$Sc(^2D_g) + Sc^{**}(^4F_u)$	-1519.467668	-1519.493072	-1519.494483
$\Delta\,(^4F_g)^a$	7.01	3.27	8.82
$\Delta\,(^4F_u)^b$	5.5	0.38	0.28

$^a\Delta\,(^4F_g) = Sc_2(R = 50a_0) - [Sc(^2D_g) + Sc^*(^4F_g)]$
$^b\Delta\,(^4F_u)^b = Sc_2(R = 50a_0) - [Sc(^2D_g) + Sc^{**}(^4F_u)]$

Table 10.11 CBS D_e values with relativistic corrections for two dissociation limits; energies are in eV (kcal/mol) [88]

Method	D_e $^2D_g + {}^4F_u$	D_e $^2D_g + {}^2D_g$
CASSCF	1.58 (36.40)	$-0.196\,(-4.52)$
MRCISD(+Q)	2.186 (50.37)	0.433 (9.98)

Nevertheless, it was rejected as a wrong asymptote and the creation of one of Sc in ^4F_g state was postulated. Camacho et al. [86], basing on an almost negligible $4p$ population obtained in their studies, also made conclusion that at the dissociation limit Sc does not appear in the ^4F_u state. But from the population of excited orbitals at the equilibrium distance it may not be done any conclusions about the population at the dissociation limit. The interatomic interactions at the equilibrium distance can populate excited orbitals, although this does not prevent atoms to dissociate in their ground states. Just this takes place in the case of the alkaline-earth dimers [72].

Thus, a more detailed analysis demonstrates that the conclusions about the dissociation limit of the Sc_2 ground state potential curve made in Refs. [85, 86] were not properly substantiated.

The values of the dissociation energy, D_e, obtained at the CBS limit and corrected on the scalar relativistic effects are presented in Table 10.11. For obtaining D_e at the symmetric dissociation limit $Sc(^2D_g) + Sc(^2D_g)$, the calculated atomic excitation energy $E\,[Sc^*(^4F_u)] - E\,[Sc(^2D_g)]$ was subtracted from D_e obtained in the dissociation limit $Sc(^2D_g) + Sc^*(^4F_u)$. At the CASSCF level a negative value of D_e for the symmetric dissociation limit was obtained. This is connected with a lack of precision for calculating the atomic excited states at this level.

10.4.3.3 Nature of Bonding

According to our results, at the dissociation limit one of the Sc atoms is formed in the second excited quartet state (it has the populated $4p$-shell). When atoms are approaching, the atomic orbital population is redistributed between atoms.

At the equilibrium distance both atoms have the same orbital population. As follows from Table 10.9, the MRCISD orbital population on each atom is equal to $4s^{1.22}3d^{1.29}4p^{0.46}$. Thus, at the equilibrium distance the $4p$ orbital is populated by equal parts on each Sc, $4p^{0.46}$, and a part of the $4s$ electron density is transferred to $3d$ orbitals. On the other hand, as we discussed above, at the dissociation limit each Sc in average has the equal $4p^{0.5}$ population.

The main references configurations obtained in our CASSCF calculations are the following:

$$\left|^5\Sigma_u^-\right\rangle = 0.826 \left|4s\sigma^2 4s\sigma^1 3d_{z^2}\sigma^1 3d_{xz}\pi_x^1 3d_{yz}\pi_y^1\right\rangle$$

$$- 0.237 \left|4s\sigma^2 4s\sigma^1 4p_z\sigma^1 3d_{xz}\pi_x^1 4p_y\pi_y^1\right\rangle$$

$$- 0.237 \left|4s\sigma^2 4s\sigma^1 4p_z\sigma^1 4p_x\pi_x^1 3d_{yz}\pi_y^1\right\rangle \qquad (10.22)$$

In their early study of Sc$_2$, Walch and Bauschlicher [79] analyzed only the dominant configuration, which does not contain the $4p$ orbitals. They did not consider the participation of the $4p$-orbitals in bonding and stressed the important role of the one-electron $3d\pi$ bonds. But if we take into account that the mean radius of $3d$ shell is $\langle r_{3d}\rangle = 1.68$ bohr [70], which is much smaller than the equilibrium distance $R_e = 5.2$ bohr, it becomes evident that the $3d$ overlap integrals are very small and in reality the one-electron $3d$-bonds do not contribute to the bonding. It is also worthwhile to mention that the $4s$ shell has a much larger mean radius, $\langle r_{4s}\rangle = 3.96$ bohr [70] and $\langle r_{4s}\rangle / \langle r_{3d}\rangle = 2.36$, meaning that $3d$ electrons are deeply inside the $4s$ electron shell.

The second and third configurations in expansion (10.22) contain molecular orbitals built of $4p$ atomic orbitals. So, the $4p$ orbitals are involved in the bonding process. The latter also follows from the Mulliken population at the equilibrium distance: $4s^{1.22}3d^{1.29}4p^{0.46}$. This population is favorable for the atomic hybridization [115]. The hybridized orbitals enhance the overlap in the bond region increasing the strength of the bond. The most probable is the creation of three hybrid orbitals on each Sc:

$$h_1 = a_1 4s + a_2 4p_z,$$
$$h_2 = b_1 3d_{xz} + b_2 4p_x,$$
$$h_3 = c_1 3d_{yz} + c_2 4p_y. \qquad (10.23)$$

It can be concluded that the dimer is stabilized by the formation of one two-electron $h_1\sigma_g$-bond and two one-electron $h_2\pi_{xu}$- and $h_3\pi_{yu}$-bonds. These hybridized orbitals should make the bonds stronger. Thus, in the Sc$_2$ dimer there is a covalent chemical bonding in contrast with the Mn$_2$ dimer [35].

10.4.4   Conclusions

1. In our studies of Sc_2 [87, 88], the CBS limit at the MRCISD(+Q) level was
   obtained for the transition-metal clusters for the first time. The calculations
   under the C_{2v} symmetry restrictions allow one to obtain the Sc atoms at the
   dissociation limit in different states. Namely, it has been demonstrated that
   the ground state potential curve, $^5\Sigma_u^-$, has the asymptotic dissociation limit
   $Sc(^2D_g) + Sc^*(^4F_u)$ with one of the Sc atoms in the second excited quartet
   state. The CBS dissociation energy in the ground state is equal to 2.183 eV
   (50.30 kcal/mol) and in respect to the thermodynamically stable dissociation
   limit with both Sc atoms in their ground states it is equal to 9.93 kcal/mol.
   The harmonic frequency $\omega_e = 234.5$ cm^{-1} is in an excellent agreement with the
   experimental value 239.9 cm^{-1} [90].
2. The dissociation of Sc_2 is followed by chemiluminescence that can be detected
   experimentally; see Sect. 10.4.3.2.
3. In all $3d$ transition-metal atoms, the $3d$-shell has a small mean radius and is
   located deeply inside the $4s$-shell. The unpaired $3d$-electrons densities practically
   are not overlapped, so the $3d$ electrons directly not involved in the bonding. The
   atoms with the closed valence $4s$-shell should be bound by the weak van der
   Waals dispersion forces; but the Sc_2 dimer is an exception from this rule. At
   the equilibrium distance a strong atom-atom interaction populates the $4p$ atomic
   orbitals, adds $0.29e$ on $3d$ orbitals and makes the closed $4s$ shell partly open. This
   favors the atomic hybridization, in which the $3d$ orbitals are also involved. The
   dimer is stabilized by the formation of one two-electron $(4s4p_z)\sigma_g$ bond and two
   one-electron bonds: $(3d_{xz}4p_x)\pi_{xu}$ and $(3d_{yz}4p_y)\pi_{yu}$. As a result, the Sc_2 dimer
   has a chemical covalent bonding.
4. Final remark about multireference perturbation theory methods. As follows from
   the analysis of the multireference perturbation theory methods, the selection of
   the active space has to be carried out very carefully to avoid large errors [36]. The
   perturbation multireference methods often give an artificial stabilization and can
   create a wrong order of states; they suffer also from the intruder-state problem
   [98]. It should be noted that the NEVPT method can give the zero electron
   population for orbitals that are populated in calculations by other more precise
   methods; see Sect. 10.4.3.2.

References

1. Morse MD (1986) Chem Rev 86:1049
2. Lombardi JR, Davis B (2002) Chem Rev 102:2431
3. Demangeat C, Parbelas JC (2002) Rep Prog Phys 65:1679
4. Dagotto E (2003) The physics of manganites and related compounds, vol 136, Solid-state
   science. Springer, Berlin
5. Chu D, Kenning CG, Orbach R (1994) Phys Rev Lett 72:3270

6. Baumann CA, Van Zee RJ, Bhat SV, Weltner W Jr (1983) J Chem Phys 78:190
7. Cheeseman M, Van Zee RJ, Flanagan HL, Weltner W Jr (1990) J Chem Phys 92:1553
8. Knickelbein MB (2004) Phys Rev B 70:014424
9. Haslett TL, Moskovits M, Weitzman AL (1989) J Mol Spectrosc 135:259
10. Terasaki A, Minemoto S, Kondow T (2002) J Chem Phys 117:7520
11. Walch S, Bauschlicher CW Jr, Roos BO (1983) Chem Phys Lett 103:175
12. Das GP, Jaffe RL (1984) Chem Phys Lett 109:206
13. Bauschlicher CW Jr (1989) Chem Phys Lett 156:95
14. Kaplan IG (2006) Intermolecular interactions: physical picture, computational methods and model potentials. Wiley, Chichester
15. Das G, Wahl AC (1966) J Chem Phys 44:87
16. Veirllad A, Clementi E (1967) Theor Chim Acta 7:133
17. Werner H-J (1987) Adv Chem Phys 69:1
18. Shepard R (1987) Adv Chem Phys 69:63
19. Roos BO (1987) Adv Chem Phys 69:399
20. Werner H-J, Knowles PJ (1985) J Chem Phys 82:5053
21. Knowles PJ, Werner H-J (1985) Chem Phys Lett 115:259
22. Langhoff SR, Davidson ER (1974) Int J Quantum Chem 8:61
23. Davidson ER, Silver DW (1977) Chem Phys Lett 52:403
24. Gdanitz RJ, Ahlrichs R (1988) Chem Phys Lett 143:413
25. MOLPRO 2010.1, a package of ab initio programs written by Werner H-J, Knowles PJ, Lindh R, Manby FR, M. Schütz, Celani P, Korona T, Mitrushenkov A, Rauhut G, Adler TB, Amos RD, Bernhardsson A, Berning A, Cooper DL, Deegan MJO, Dobbyn AJ, Eckert F, Goll E, Hampel C, Hetzer G, Hrenar T, Knizia G, Köppl C, Liu Y, Lloyd AW, Mata RA, May AJ, McNicholas SJ, Meyer W, Mura ME, Nicklaß A, Palmieri P, Pflüger K, Pitzer R, Reiher M, Schumann U, Stoll H, Stone AJ, Tarroni R, Thorsteinsson T, M. Wang, A. Wolf
26. Werner H-J, Knowles PJ (1990) Theor Chim Acta 78:175
27. Nesbet RK (1964) Phys Rev 135:A460
28. Wang B, Chen Z (2004) Chem Phys Lett 387:395
29. Yamamoto S, Tatewaki H, Moriyama H, Nakano H (2006) J Chem Phys 124:124302
30. Negodaev I, de Graaf C, Caballol R (2008) Chem Phys Lett 458:290
31. Buchachenko AA (2008) Chem Phys Lett 459:73
32. Camacho C, Yamamoto S, Witek HA (2008) Phys Chem Chem Phys 10:5128
33. Angeli C, Cavallini A, Cimiraglia R (2008) J Chem Phys 128:244317
34. Mon MS, Mori H, Miyoshi E (2008) Chem Phys Lett 462:23
35. Tzeli D, Miranda U, Kaplan IG, Mavridis A (2008) J Chem Phys 129:154310
36. Buchachenko AA, Chałasiński G, Szczęśniak MM (2010) J Chem Phys 132:024312
37. Nakano H (1993) J Chem Phys 99:7983
38. Angeli C, Cimiraglia R, Evangelisti S, Leininger T, Malrieu J-P (2001) J Chem Phys 114:10252
39. Angeli C, Pastore M, Cimiraglia R (2007) Theor Chem Acc 117:743
40. Osanai Y, Mon MS, Noro T, Mori H, Miyoshi E (2008) Chem Phys Lett 452:210
41. Balabanov NB, Peterson KA (2005) J Chem Phys 123:064107
42. https://bse.pnl.gov/bse/portal
43. Harris J, Jones RO (1979) J Chem Phys 70:830
44. Salahub DR, Baykara NA (1985) Surf Sci 156:605
45. Fujima N, Yamaguchi T (1995) J Phys Soc Jpn 64:1251
46. Nayak SK, Jena P (1998) Chem Phys Lett 289:473
47. Nayak SK, Rao BK, Jena P (1998) J Phys Condens Mat 10:10863
48. Pederson MK, Reuse FA, Khanna SN (1998) Phys Rev B 58:5632
49. Desmarais N, Reuse FA, Khanna SN (2000) J Chem Phys 112:5576
50. Yanagisawa S, Tsuneda T, Hirao K (2000) J Chem Phys 112:545
51. Barden CJ, Rienstra-Kiracofe CC, Schaefer HF III (2000) J Chem Phys 113:690
52. Gutsev GL, Bauschlicher CW Jr (2003) J Phys Chem A 107:4755

53. Valiev M, Bylaska EJ, Weare JH (2003) J Chem Phys 119:5955
54. Bobadova-Parvanova P, Jackson KA, Srinivas S, Horoi M (2005) J Chem Phys 122:014310
55. Kabir M, Mookerjee A, Kanhere DJ (2006) Phys Rev B 73:224439
56. Jellinek J, Acioli PH, García-Rodeja J, Zheng W, Thomas OC, Bowen KH Jr (2006) Phys Rev B 74:153401
57. Jellinek J, Acioli PH (2003) J Chem Phys 118:7783
58. Kaplan IG (2007) J Mol Struct 838:39
59. Kaplan IG (2007) Int J Quantum Chem 107:2595
60. Douglas M, Kroll NM (1974) Ann Phys (NY) 82:89
61. Jansen G, Hess BA (1989) Phys Rev A 39:6016
62. Jansen HB, Ros P (1969) Chem Phys Lett 3:140
63. Boys SF, Bernardi F (1970) Mol Phys 19:553
64. Liu B, Mclean AD (1973) J Chem Phys 59:4557
65. Werner H-J, Knowles PJ, Lindh R, Manby FR, Schütz M, Celani P, Korona T, Mitrushenkov A, Rauhut G, Adler TB, Amos RD, Bernhardsson A, Berning A, Cooper DL, Deegan MJO, Dobbyn AJ, Eckert F, Goll E, Hampel C, Hetzer G, Hrenar T, Knizia G, Köppl C, Liu Y, Lloyd AW, Mata RA, May AJ, McNicholas SJ, Meyer W, Mura ME, Nicklaß A, Palmieri P, Pflüger K, Pitzer R, Reiher M, Schumann U, Stoll H, Stone AJ, Tarroni R, Thorsteinsson T, Wang M, Wolf A (2006) MOLPRO 2006.1, a package of *ab initio* programs
66. Kirkwood AK, Bier KD, Tompson JK, Haslett TL, Huber AS, Moskovits M (1991) J Phys Chem 95:2644
67. Bier KD, Haslett TL, Kirkwood AK, Moskovits M (1988) J Chem Phys 89:6
68. Kaplan IG (1975) Symmetry of many-electron systems. Academic, New York
69. Kaplan IG, Rodimova OB (1973) Int J Quantum Chem 7:1203
70. Bunge CF, Barrientos JA, Bunge A (1993) Atomic Data Nucl Data Tables 53:113
71. Löwdin P-O (1959) Adv Chem Phys 2:207
72. Kaplan IG, Roszak S, Leszczynski J (2000) J Chem Phys 113:6245
73. Pápai I, Castro M (1997) Chem Phys Lett 267:551
74. Gutsev GL, Jena P, Rao BK, Khanna SN (2001) J Chem Phys 114:10738
75. Furche F, Perdew JP (2006) J Chem Phys 124:044103
76. Zhao Y, Truhlar DG (2006) J Chem Phys 124:224105
77. Das G (1982) Chem Phys Lett 86:482
78. Walch SP, Bauschlicher CW Jr (1983) Chem Phys Lett 94:290
79. Walch SP, Bauschlicher CW Jr (1983) J Chem Phys 79:3590
80. Jeung GH (1986) Chem Phys Lett 125:407
81. Åkeby H, Peterson LGM, Siegbahn PEM (1992) J Chem Phys 97:1850
82. Åkeby H, Peterson LGM (1993) J Mol Spectrosc 159:17
83. Suzuki Y, Asai S, Kobayashi K, Noro T, Sasaki F, Tatewaki H (1997) Chem Phys Lett 268:213
84. Matxain JL, Rezabal E, Lopez X, Ugalde JM, Gagliardi L (2008) J Chem Phys 128:194315
85. Kalemos A, Kaplan IG, Mavridis A (2010) J Chem Phys 132:024309
86. Camacho C, Cimiraglia R, Witek HA (2010) J Chem Phys 132:244306
87. Kaplan IG, Miranda U (2011) AIP Advances 1:022108
88. Miranda U, Kaplan IG (2011) Eur Phys J D. doi:DOI: 10.1140/epjd/e2010-10607-y
89. Knight LB, Van Zee JR, Weltner W (1983) Chem Phys Lett 94:296
90. Moskovits M, Di Lella DP, Limm W (1984) J Chem Phys 80:626
91. Knight LB, McKinley AJ, Babb RM, Hill DW, Morse MD (1993) J Chem Phys 99:7376
92. Wang C-R, Kai T, Tomiyama T, Yoshida T, Kobayashi Y, Nishibori E, Takata M, Sakata M, Shinohara H (2000) Nature 408:426
93. Stevenson S, Fowler PW, Heine T, Duchamp JC, Rice G, Glass T, Harich K, Hajdu E, Bible R, Dorn HC (2000) Nature 408:427
94. Shinohara H, Sato H, Ohkohchi M, Ando Y, Kodama T, Shida T, Kato T, Saito Y (1992) Nature 357:52
95. Yannoni CS, Hoinkis M, de Vries MS, Bethune DS, Salem JR, Crowder MS, Johnson RD (1992) Science 256:1191

96. Ralchenko Y, Kramida AE, Reader J, NIST ASD Team (2008) NIST atomic spectra database (version 3.1.5), Online. Available http://physics.nist.gov/asd3 (Aug 14 2009). National Institute of Standards and Technology, Gaithersburg
97. Matxain JL, Rezabal E, Lopez X, Ugalde JM, Gagliardi L (2008) J Chem Phys 132:139901
98. Camacho C, Cimiraglia R, Witek HA (2010) Phys Chem Chem Phys 12:5058
99. Werner H-J, Knowles PJ (1988) J Chem Phys 89:5803
100. Knowles PJ, Werner H-J (1988) Chem Phys Lett 145:514
101. Werner H-J, Knowles PJ, Lindh R, Manby FR, Schütz M, Celani P, Korona T, Mitrushenkov A, Rauhut G, Adler TB, Amos RD, Bernhardsson A, Berning A, Cooper DL, Deegan MJO, Dobbyn AJ, Eckert F, Goll E, Hampel C, Hetzer G, Hrenar T, Knizia G, Köppl C, Liu Y, Lloyd AW, Mata RA, May AJ, McNicholas SJ, Meyer W, Mura ME, Nicklaß A, Palmieri P, Pflüger K, Pitzer R, Reiher M, Schumann U, Stoll H, Stone AJ, Tarroni R, Thorsteinsson T, Wang M, Wolf A (2009) MOLPRO 2009.1, a package of *ab initio* programs
102. Varandas AJC (2007) J Chem Phys 126:244105
103. Brown FR, Truhlar DG (1985) Chem Phys Lett 117:307
104. Hollister C, Sinanôĝlu O (1966) J Am Chem Soc 88:13
105. Őksűz I, Sinanôĝlu O (1969) Phys Rev 181:42
106. Sinanôĝlu O, Brueckner KA (1970) Three approaches to electron correlation in atoms, Chapter 5, Yale University Press, New Haven, CT
107. Becke AD (2003) J Chem Phys 119:2972
108. Dunning TH Jr (1989) J Chem Phys 90:1007
109. Feller D (1992) J Chem Phys 96:6104
110. Xantheas SS, Dunning TH Jr (1993) J Phys Chem 97:18
111. Feller D, Sordo JA (2000) J Chem Phys 113:485
112. Karton A, Martin JML (2006) Theor Chem Acc 115:330
113. Jensen F (2005) Theor Chem Acc 113:267
114. Dunham JL (1932) Phys Rev 41:721
115. McWeeny R (1979) Coulson's valence, 3rd edn. Oxford University Press, Oxford

Chapter 11
Theoretical Study of σ-Bond Activation Reactions and Catalytic Reactions by Transition Metal Complexes

Shigeyoshi Sakaki

Abstract This chapter reports mini-review of theoretical and computational studies of σ-bond activation reactions by transition metal complexes. Because the σ-bond activation reaction through oxidative addition has been theoretically investigated well for long, I wish to focus on the different types of σ-bond activation reactions here. One good example is the C–H σ-bond activation of benzene and methane by Pd(II)–formate complex. The σ-bond activation of methane by Ti(IV)-imido complex is another good example. Their theoretical and computational studies clearly indicate that these reactions are typical heterolytic σ-bond activation without any change of metal oxidation state. The orbital interaction diagram is completely different between the heterolytic σ-bond activation and the oxidative addition reactions; in the heterolytic σ-bond cleavage, the mixing of the C–H σ-bonding orbital into the bonding overlap between the C–H σ^*-antibonding and the M–X bonding orbitals plays crucial roles. Theoretical study of oxidative addition to the M–L moiety, which is a new type of σ-bond activation, is also discussed based on theoretical study and recent experimental report. In this reaction, not only metal center but also organic ligand participates in the σ-bond activation reaction like the heterolytic σ-bond activation. However, the metal oxidation state increases by 2 in a formal sense like the usual oxidative addition, which is different from the heterolytic σ-bond activation. The heterolytic σ-bond activation is involved in many catalytic reactions. One of such good examples is Ru-catalyzed hydrogenation of CO_2 to formic acid, in which the H–H bond cleavage with the Ru-(η^1-OCOH) moiety is involved as a key step. This reaction is essentially the same as the C–H σ-bond activation of benzene with the Pd-(η^1-OCOH) moiety. Another example is Pd-catalyzed cross-coupling reaction in which transmetallation is involved as a key step. This transmetallation is understood to be the heterolytic σ-bond

S. Sakaki (✉)
Fukui Institute for Fundamental Chemistry, Kyoto University, Nishihiraki-cho, Takano, Sakyo-ku, Kyoto 606-8103, Japan
e-mail: sakaki.shigeyoshi.47e@st; kyoto-u.ac.jp

activation. I wish to discuss how to accelerate this reaction based on theoretical and computational studies. Recently reported direct-cross coupling reaction occurs via heterolytic C–H σ-bond activation reaction, which is also discussed based on theoretical study.

11.1 Introduction

Theoretical studies of transition metal complexes and their reactions are of considerable importance nowadays [1, 2], because theoretical knowledge is indispensable to understand well the varieties of geometry, bonding nature, and reaction behavior of transition metal complexes. Actually, the number of theoretical/computational studies of organometallic compounds and their reactions is steeply increasing after 1995 [2]. In addition, theoretical/computational studies have been providing many important results on the catalytic reactions by transition metal complexes. All these are because new knowledge and new explanation are often requested for understanding well the various experimental findings of organometallic compounds and also because the experimental knowledge on the catalytic reactions is limited, in general. For instance, it is not easy to elucidate what is active species, what kind of intermediate exists, and what is rate-determining step, because the catalytic reaction rapidly occurs with low concentration of catalyst. In this regard, many theoretical/computational studies of catalytic reactions have been reported, so far. Also, theoretical/computational studies have been carried out on such common elementary steps as σ-bond activation, insertion reaction, β–H abstraction reaction, and so on, because many catalytic cycles consist of those common elementary steps. I wish to present a catalytic cycle of Pd-catalyzed cross-coupling reaction as a good example; [3] as shown in Scheme 11.1, the first step is the oxidative addition of organic halide, the second step is transmetallation, and the last step is reductive elimination. In the first and second steps, a σ-bond is broken and in the last step a σ-bond is formed, which is the reverse of the σ-bond activation. This means that the catalytic cycle of Pd-catalyzed cross-coupling reaction consists only of σ-bond activation reaction. In other words, theoretical/computational knowledge of such σ-bond activation reaction is indispensable to understand well the cross-coupling reaction and to make further development of this type of reaction.

The σ-bond activation is interesting not only from the viewpoint of catalytic chemistry and organometallic chemistry [4–12] but also from the viewpoint of theoretical/computational chemistry [13–16] as follows. The σ-bond has occupied MOs at low energies and unoccupied MOs at high energies, in general. This means that the reactivity of the σ-bond is not high. Moreover, the σ-bond does not interact well with the transition metal complex unlike olefin, acetylene, and CO, which have π, π*, and lone pair orbitals useful for the interaction with the transition metal center. Thus, it is of considerable interest how the inert σ-bond is activated by the

Scheme 11.1 General catalytic cycle of Pd-catalyzed cross-coupling reaction

Reductive Elimination   PdL$_2$

R1-R2   Oxidative Addition

R1-X

R1   Transmetallation   R1
| |
L–Pd—R2   ←——   L–Pd—X
| |
L   R2-M   L
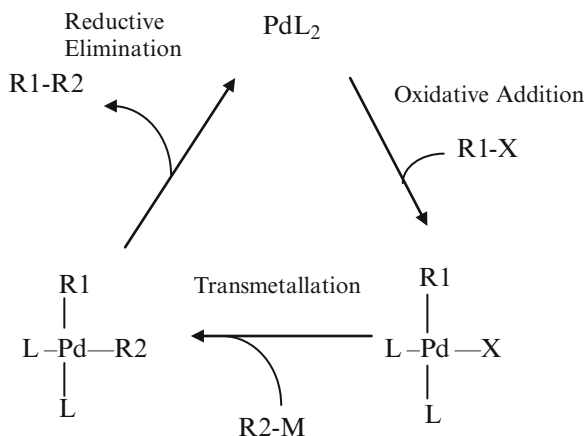
transition metal complex. Considering the interest and importance of the σ-bond activation, I wish to concentrate here on the σ-bond activation reaction.

In my understanding, the σ-bond activation reactions are classified into two main categories; [2, 13, 16] one is the σ-bond activation by metal center only, as shown in Eq. 11.1, and the other is the σ-bond activation by metal–ligand moiety, as shown in Eqs. 11.2 and 11.3.

$$ML_n + R1 - R2 \rightarrow M(R1)(R2)L_n \tag{11.1}$$

$$MXL_n + R1 - R2 \rightarrow M(R1)L_n + R2 - X \tag{11.2}$$

$$M(L')L_n + R1 - R2 \rightarrow M(L' - R1)(R2)L_n \tag{11.3}$$
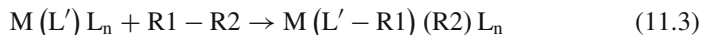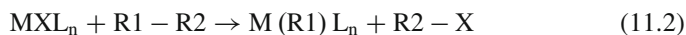
$$R1, R2 = H, alkyl, or aromatic group$$

In the reaction of Eq. 11.1, the metal oxidation state increases by 2 in a formal sense, as is well-known, because alkyl, vinyl, hydride, etc. bound with metal are considered to be anion. This is the reason why Eq. 11.1 is called oxidative addition. This reaction occurs either in a concerted manner or in a step-wise manner including nucleophilic attack of a metal ion followed by anion coordination with metal center. In the last two decades, many theoretical studies have been carried out about the σ-bond activation reaction by the oxidative addition reaction [1, 2, 13–16]. Nowadays, we have deep and correct theoretical knowledge of the oxidative addition reaction. Besides the oxidative addition, however, various σ-bond activation reactions are observed in the experimental field. In those reactions, the activation is performed with metal–ligand (M–L) moiety. In other words, these are understood in terms of ligand-assisted σ-bond activation. This is also understood as metathesis. This is further classified into two categories—one is σ-bond activation without change of metal oxidation state (Eq. 11.2). Equation 11.2 occurs when an

Scheme 11.2 Orbital
interaction diagram for
oxidative addition

A-B σ*

dπ

A   B

L   L

A   B

A-B σ

L   L

A-B
+
M

A   B

M

L   L

L   L
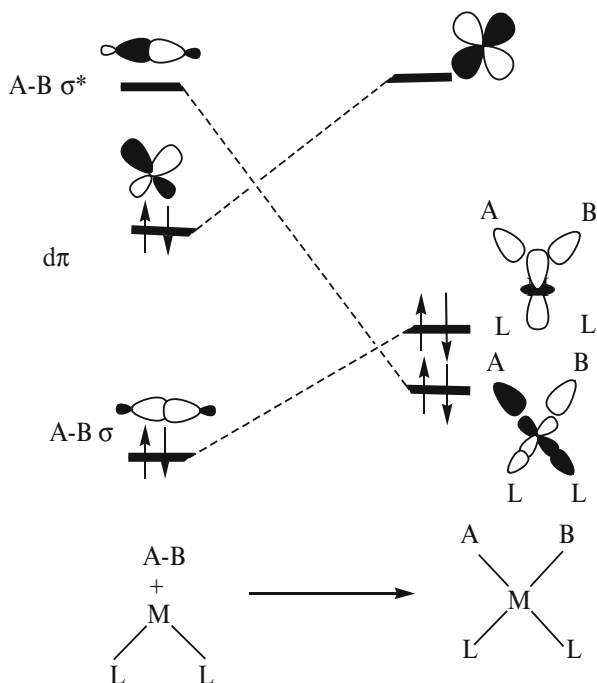
X anion ligand participates in the σ-bond activation. In this reaction, R1 becomes
negatively charged because it is bound with the metal center in the product, while R2
becomes positively charged because it is bound with the anion X. In other words, the
R1–R2 bond is cleaved in a heterolytic manner and the metal oxidation state does
not change at all. The other example is Eq. 11.3, in which the σ-bond activation
is achieved by the M–L moiety like Eq. 11.2; whereas the metal oxidation state
increases by 2. This reaction is possible when L′ is either alkyne or alkene: In
Eq. 11.3, the alkene (or alkyne) moiety is converted to alkyl (or vinyl) group by the
reaction with R1. These alkyl and vinyl groups are considered to be anion because
they are bound with the metal center. Also, R2 is considered to be anion because
R2 is bound with the metal center. Thus, the metal oxidation state increases by 2
in this reaction. In other words, this reaction is understood to be oxidative addition
to the M–L moiety. The reports of this reaction have been very limited, but several
interesting examples were reported, as will be discussed below.

As mentioned above, the oxidative addition has been theoretically investigated
for a long time [1, 2, 13–16]. For instance, the orbital interaction in the oxidative
addition reaction was discussed previously [17], as shown in Scheme 11.2. Appar-
ently, the doubly occupied d-orbital interacts with the antibonding σ*-MO of the
σ-bond to induce the charge-transfer (CT), which leads to the σ-bond breaking and
the formations of M–R1 and M–R2 bonds. As a result of this CT, the metal oxidation
state increases by 2, which is the origin of the name "oxidative addition." From this

scheme, one can understand that the driving force arises from energy stabilization induced by the change of the doubly occupied d-orbital to the M–R1 and M–R2 bonding orbitals. This means that the low-valent transition metal complex can perform this reaction because such transition metal complex has d-orbitals at high energies.

To avoid the overlap with previous theoretical reviews of oxidative addition [2, 13–16], I will discuss here the theoretical studies of ligand-assisted σ-bond activation such as heterolytic σ-bond activation (Eq. 11.2) and the oxidative addition to the M–L moiety (Eq. 11.3). Both have not been theoretically discussed well. Our purposes here are to present detailed computational results about these σ-bond activation reactions, provide fundamental understanding, and propose theoretical prediction. Then, we wish to present theoretical studies of several interesting catalytic reactions including σ-bond activation process as a key elementary step.

11.2   Heterolytic σ-Bond Activation Reaction

11.2.1   Geometry and Energy Changes in the Reaction

In this section, we wish to discuss the reaction of Eq. 11.2. The C–H σ-bond activation of methane by Pt(II) complex (Eq. 11.4) is considered to be a key step of the Shilov reaction [18]. This reaction was theoretically investigated by Siegbahn group by DFT method with B3LYP functional, where microsolvation was considered by adding one or two H_2O molecules to quantum mechanical (QM) calculations and also where bulk solvation effects were taken into consideration with PCM method [19].

$$CH_4 + PtCl_2(H_2O)_2 \rightarrow PtCl(CH_3)(H_2O)_2 + HCl \tag{11.4}$$

The activation barrier was evaluated to be 20.5 kcal/mol. This barrier is moderate, considering that the very strong C–H bond is cleaved. In this reaction, the oxidation state of Pt does not change at all, because the Pt is coordinated with two anion ligands such as Cl and CH_3 in the product. This indicates that the Pt oxidation state does not change but it is still +2. The CH_3 group is bound with the Pt center, indicating that the CH_3 is considered to be an anion. The H atom is bound with the Cl anion, indicating that the H is a proton. Thus, this reaction belongs to the above-mentioned category of Eq. 11.2 and the C–H bond is cleaved in a heterolytic manner. However, the C–H bond is not polarized very much in the transition state.

Fujiwara-Moritani reaction (Eq. 11.5) is another important example including heterolytic σ-bond activation by palladium(II) acetate complex [20]. This reaction is

$$C_6H_6 + H_2C = CHR \xrightarrow{\text{Pd(OAc)}_2} C_6H_5 - CH = CHR \tag{11.5}$$

C=C double bond insertion
and β-H abstraction

C-H Activation

$$
\text{R1} \quad \text{R2}
$$

$$
\text{C=C}
$$

$$
\text{H} \quad \text{R3}
$$

Ar-H

$$
\text{R1} \quad \text{R2}
$$

$$
\text{C=C}
$$

Pd(OAc)2 $\longrightarrow$ Ar— Pd(OAc) $\longrightarrow$

$$
\text{Ar} \quad \text{R3}
$$

AcOH

[O]/HOAc
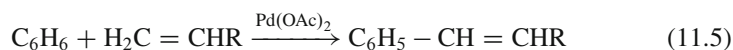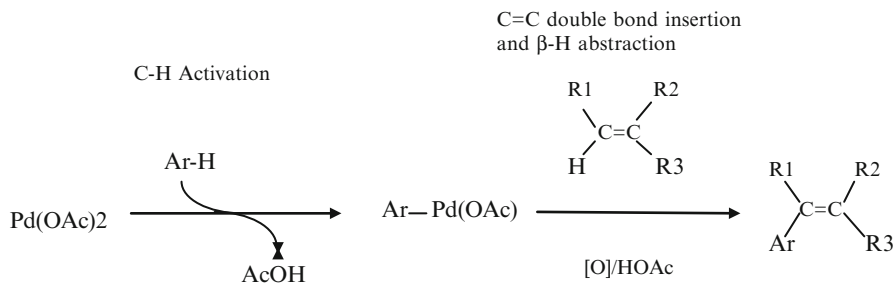
Scheme 11.3 Fujiwara-Moritani reaction [20]

understood to occur through the C–H σ-bond activation of aromatic compound forming Pd(II)-aromatic group, alkene insertion into the Pd(II)-aromatic group, and β–H abstraction reaction (Scheme 11.3). This is the first report of the C–H σ-bond activation, in my knowledge. Although this is a very old reaction, several interesting synthetic reactions have been reported as revival of this reaction recently [21–25]. Sakaki and his coworkers theoretically investigated the C–H σ-bond activation of benzene by palladium(II) formate complex $Pd(\eta^2\text{-}O_2CH)_2$ which was employed as a model of palladium(II) acetate complex $Pd(\eta^2\text{-}O_2CCH_3)_2$ [26]. They employed the DFT method for geometry optimization and the DFT, MP2–MP4, and CCSD(T) methods for evaluation of energy changes. This reaction occurs through palladium(II) benzene complex as intermediate to afford palladium(II) phenyl formate complex and formic acid, as shown in Fig. 11.1. In the first transition state (**TS1a**), one of the formate O atoms is dissociating from the Pd center to afford an unsaturated coordinating site on the Pd center. Simultaneously, benzene is approaching the Pd center. In the intermediate (**I1**), one of format ligands completely changes to the η^1-O coordinating formate and benzene coordinates with the Pd center through the CT from its π-orbital to the d-orbital of Pd, which is clearly shown by population changes, as will be discussed below. In the second transition state (**TS1b**), the Ph group is changing the direction of its sp^2 orbital toward the Pd center and the H atom is moving from the Ph group toward the O atom of the η^1-formate. In the product (**P1**), the Ph group is bound with the Pd center and the H atom is bound with the formate to afford formic acid. The formic acid coordinates with the Pd center, which is clearly shown by the short Pd-O distance. This reaction occurs with moderate activation barrier and considerably large exothermicity, as shown in Table 11.1. Several important results should be noted in Table 11.1 from the viewpoint of computational chemistry: (1) The CCSD(T) and MP4(SDQ) present similar BE, Ea, and ΔE values. (2) These BE, Ea, and ΔE values moderately fluctuate around MP2 and MP3 but converge when going to CCSD(T) from MP3, indicating that the CCSD(T) and MP4 present reliable BE, Ea, and ΔE values. (3) The DFT method with B3LYP functional presents somewhat smaller Ea value, although the DFT(B3LYP)-calculated ΔE value is less negative than the CCSD(T)-calculated value. Because these calculations were performed previously, the M06 and other new functionals were not used. It is
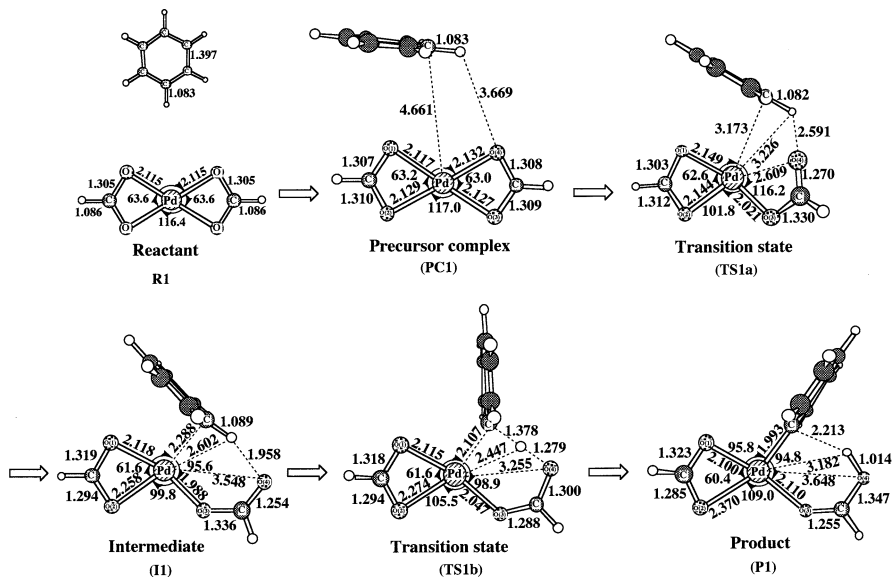
Fig. 11.1 Geometry changes in C–H σ-bond activation of benzene by Pd(η²-O₂CH)₂. The DFT method was employed with B3LYP functional. Bond distance in angstrom and bond angle in degree (Reproduced from Ref. [26]. With kind permission of © The American Chemical Society 2000)

Table 11.1 Activation barrier (Ea)ᵃ and reaction energy (ΔE)ᵇ of the C–H σ-bond activations of benzene and methane by Pd(η²-O₂CH)₂ and Pt analogue (kcal/mol)

	Benzene			Methane		
	BE	Ea	ΔE	BE	Ea	ΔE
(A) C–H activation of benzene and methane by Pd(η²-O₂CH)₂						
DFT(B3LYP)	−0.3	9.9	−12.4	−0.6	13.9	−4.9
MP2	−0.9	11.5	−20.4	−1.3	17.5	−12.8
MP3	−0.4	15.8	−20.4	−1.2	19.8	−12.8
MP4(DQ)	−0.4	16.3	−19.5	−1.2	21.1	−12.0
MP4(SDQ)	−0.7	15.7	−17.2	−1.3	21.5	−8.3
CCSD(T)	−1.9	14.1	−17.5	−1.5	20.5	−24.7
(B) C–H activation of benzene and methane by Pt(η²-O₂CH)₂						
DFT(B3LYP)	−0.4	10.7	−19.3	−0.8	11.3	−10.5
MP4(SDQ)	−1.9	20.9	−24.1	−2.6	17.3	−13.3
CCSD(T)	−2.5	20.0	−24.7	−3.0	17.7	−12.6

ᵃThe energy difference between transition state and intermediate (or precursor complex)

ᵇThe energy difference between product and the sum of reactant

interesting to apply these new functionals to this kind of reaction to check the reliability. The important results from the viewpoint of organometallic chemistry are summarized below. (4) The C–H σ-bond activation by the palladium(II) formate complex Pd(η²-O₂CH)₂ occurs with moderate Ea value and considerably negative ΔE value (considerably large exothermicity), although the oxidative additions of

(A) $Pd(\eta^2\text{-}O_2CH)_2 + C_6H_6$ → $Pd(C_6H_5)(\eta^2\text{-}O_2CH)(HCOOH)$

    Bond Breaking   **Bond Formation**

    D(C-H) = 109.0   **D(Pd-Ph) = 51.0**

    D(Pd-O)=23.2[a)]   **D(O-H) = 114.4**

    a)   The Pd-O bond energy was defined as an energy difference
    between $Pd(\eta^2\text{-}O_2CH)_2$ and $Pd(\eta^2\text{-}O_2CH)(\eta^1\text{-}O_2CH)$.

(B) $Pd(PH_3)_2 + C_6H_6$ →   **$Pd(H)(C_6H_5)(PH_3)$**
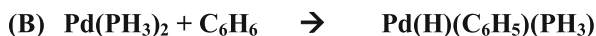
    Bond Breaking   **Bond Formation**

    D(C-H) =109.0   **D(Pd-Ph)=51.0**

                                 D(Pd-H)=49.5

Scheme 11.4 Bond energies (in kcal/mol) related to heterolytic σ-bond activation by $Pd(\eta^2\text{-}O_2CH)_2$ and oxidative addition to $Pd(PH_3)_2$

methane and benzene to palladium(0) complex $Pd(PH_3)_2$ need much larger Ea value with considerably large endothermicity; Ea is 35.1 and 28.9 kcal/mol for reactions of methane and benzene, respectively; and ΔE is 31.0 and 24.6 kcal/mol for those of methane and benzene, where the CCSD(T)-calculated values are presented. (5) The palladium(II) complex is more reactive than the platinum(II) complex for the C–H σ-bond activation of benzene, although the exothermicity is larger in the platinum(II) complex than in the palladium(II) complex. And, (6) for the C–H σ-bond activation of methane, the platinum(II) complex is more reactive than the palladium(II) complex.

The above results (5) and (6) are useful for experimentalists who want to apply transition metal complex to C–H activation. Actually, the palladium(II) complex was used for the reaction including the C–H activation of aromatic compounds [20–25]; but platinum(II) complex was used for the Shilov reaction [18] and the conversion reaction of methane to methnol [27]. Actually, the C–H σ-bond activation of methane with platinum(II) complex was theoretically investigated with the DFT method, in which the heterolytic C–H σ-bond activation was found to occur [28]. Because some debate has been presented about the C–H σ-bond activation by platinum(II) complexes, we will discuss the C–H σ-bond activation by platinum(II) complexes below.

Here, we wish to discuss the reason why the C–H σ-bond activation is easily performed by the palladium(II) complex, $Pd(\eta^1\text{-}O_2CH)_2$, but with much difficulty by the palladium(0) complex, $Pd(PH_3)_2$ [26]. The reason is easily understood in terms of bond energy. As shown in Scheme 11.4, the C–H bond of benzene is broken in both C–H σ-bond activations by palladium(II) and palladium(0) complexes. In the oxidative addition to $Pd(PH_3)_2$, any other bond is not broken in the reactant,

and the Pd–H and Pd–Ph bonds are formed in the product. In the C–H σ-bond activation by $Pd(\eta^1\text{-}O_2CH)_2$, on the other hand, both the C–H bond and the Pd–O coordinate bond should be broken in the reactant; note that the η^2-coordinating formate must change to the η^1-coordinating form to afford a coordination site for benzene (or methane). This is unfavorable compared with the oxidative addition to $Pd(PH_3)_2$. However, a very strong O–H bond is formed in the product, which overcomes well the energy destabilization by the Pd–O bond breaking. It should be noted that the Pd–H bond is formed by the oxidative addition but it is not strong enough; it is much weaker than the O–H bond which is formed by the C–H activation by the palladium(II) complex. The other important factor is that the Pd–O bond to be broken in the reaction is not very much strong. This is because the Pd–O bond breaking occurs by the conversion of the $Pd(\eta^2\text{-}O_2CH)$ bond to the $Pd(\eta^1\text{-}O_2CH)$ bond with a moderate energy destabilization; in other words, one Pd–O bond breaking of the $Pd(\eta^2\text{-}O_2CH)$ moiety is compensated by the strengthening of another remaining Pd–O bond. As a result, the oxidative addition to the palladium(0) complex is significantly endothermic but the C–H σ-bond activation by the palladium(II) complex is exothermic. Thus, it should be concluded that the formation of the strong O–H bond is one of the important driving forces of this C–H σ-bond activation by $Pd(\eta^2\text{-}O_2CH)_2$. This is very important to understand the heterolytic σ-bond activation reaction. We wish to emphasize that this conclusion is also useful to present prediction about transmetallation, which I will describe below.

Similar C–H σ-bond activations of methane and benzene were reported experimentally with Ti(IV)-imide complex, $(Me_3SiO)_2Ti{=}NSiMe_3$, which is considered

$$(Me_3SiO)_2Ti{=}NSiMe_3 + R - H \rightarrow (Me_3SiO)_2Ti\,(R)\,(NHSiMe_3)$$

$$R{=}CH_3 \text{ or } C_6H_5 \tag{11.6}$$
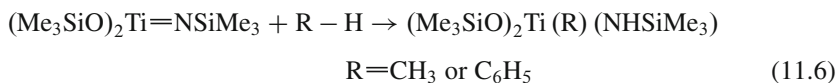
to involve a Ti=N double bond in a formal sense [29, 30]; see Eq. 11.6. Similar C–H σ-bond activations have been reported experimentally for different metals [31–33]. Many reports of these experimental works suggest that this type of C–H σ-bond activation is important in organometallic chemistry. The C–H σ-bond activation with the Ti=N bond and Ti=C bond have been theoretically investigated by Cundari and his coworkers [34, 35]. Recently, the σ-bond activation reaction of methane by $(Me_3SiO)_2Ti{=}NSiMe_3$ was theoretically investigated with the DFT, MP2 to MP4(SDQ), and CCSD(T) methods, in a comparison with the oxidative addition of methane to $Pt(PH_3)_2$ [36]. As shown in Fig. 11.2, methane approaches the Ti–N bond to form a methane complex. In this methane complex, the C–H bond of methane is moderately elongated like the C–H bond of the system including agostic interaction. In the transition state, the methyl group is approaching the Ti center, changing its direction toward the Ti center. The H atom of methane is moving from the methyl group toward the N atom of the imido ligand, and its position is almost intermediate between the C of methane and the N atom. This location of the H atom is essentially the same as that of the transition state of
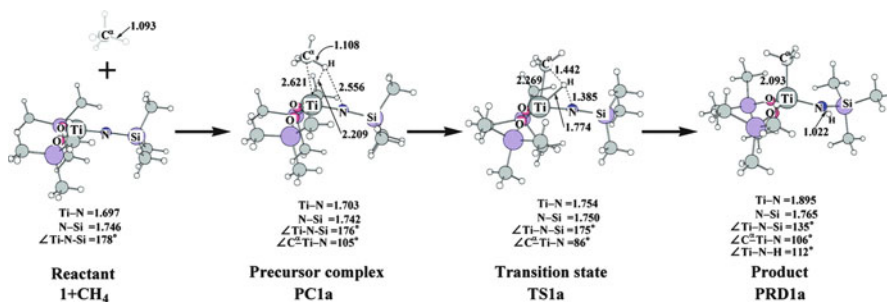
Fig. 11.2 DFT-optimized geometry changes in C–H σ-bond activation of methane by $(Me_3SiO)_2Ti=NSiMe_3$ (Reproduced from Ref. [36]. With kind permission of © The American Chemical Society 2007)

Table 11.2 Binding energy (BE), activation barrier (Ea), and reaction energy (ΔE) of the C–H σ-bond activation reaction of methane by $(Me_3SiO)_2Ti(=NSiMe_3)$ and its model complex $(H_3SiO)_2Ti(=NHSiH_3)$

	BE	Ea	ΔE
(A) Reaction by $(Me_3SiO)_2Ti(=NSiMe_3)$ leading to $(Me_3SiO)_2Ti(CH_3)[N(H)(SiMe_3)]$			
MP2	−9.8	17.6	−16.5
MP3	−7.1	12.7	−36.5
MP4(DQ)	−7.8	18.0	−25.3
MP4(SDQ)	−9.4	21.5	−16.5
DFT	−4.5	14.6	−22.7
(B) Reaction by $(H_3SiO)_2Ti(=NSiH_3)$ leading to $(H_3SiO)_2Ti(CH_3)[N(H)(SiMe_3)]$			
MP2	−9.6	18.7	−14.9
MP3	−7.0	12.9	−35.4
MP4(DQ)	−7.8	18.7	−24.2
MP4(SDQ)	9.4	22.8	−14.8
CCSD(T)	−9.0	17.0	−22.7
DFT	−5.5	15.5	−22.6
(C) Reverse regioselective reaction leading to $(Me_3SiO)_2Ti(H)[N(CH_3)(SiMe_3)]$			
DFT	−4.2	60.4	−1.2

the C–H σ-bond activation of benzene by the palladium(II) η^2-formate complex; see Fig. 11.1. The product is a four-coordinate Ti(IV) complex in which the Ti–CH$_3$ and the N–H bonds are formed. The energy changes are evaluated with a real complex $(Me_3SiO)_2Ti=NSiMe_3$ and a model complex $(H_3SiO)_2Ti=NSiH_3$, as shown in Table 11.2. In these two systems, the Möller-Plesset perturbation theory and CCSD(T) method present similar BE value, which corresponds to a stabilization energy of the methane complex. However, the DFT method with B3LYP functional presents smaller BE value. Similar underestimation of the binding energy is often observed in methane and benzene complexes [26] and even in olefin complexes [37], when B3LYP and similar functionals were employed. This weak point of B3LYP and similar functionals may be solved with the use of M06-series functionals,
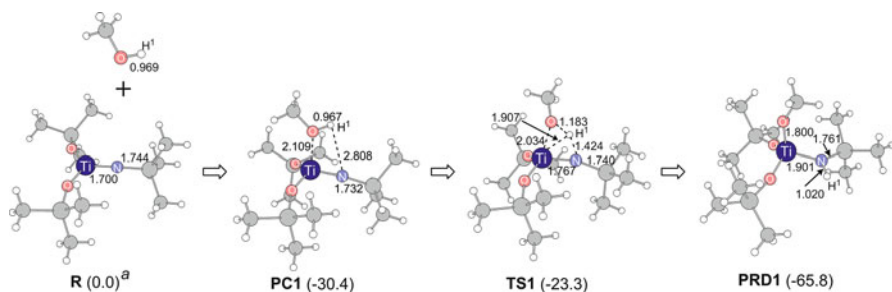
Fig. 11.3 Geometry and energy changes in the O–H s-bond activation of methanol by $(H_3SiO)_2Ti=N-SiMe_3$. In *parentheses* are energy changes calculated by the DFT(B3LYP) method (Reproduced from Ref. [40]. With kind permission of © Canadian Chemical Society 2005)

proposed by Truhlar and his colleagues [38]. The Ea value moderately fluctuates when moving from MP2 to MP4(SDQ) and CCSD(T), while the ΔE value considerably fluctuates. This unsuccessful results by MP2 to MP4(SDQ) are in contrast with the successful results by MP2 to MP4(SDQ) in the case of the C–H σ-bond activation by the palladium(II) formate complex. It is also noted that the Ea value fluctuates much less than the ΔE value. This result is a little bit unexpected, because the transition state contains a lot of electron correlation effects, in general. However, this result can be understood in terms of the presence of instability of Hartree-Fock wavefunction in the reactant Ti-imido complex. Because the transition state still contains the similar electronic structure to that of the reactant, the Ea moderately fluctuates. In the product, the ΔE value much fluctuates when moving to CCSD(T) from MP2 because the electronic structure of the product is much different from that of the reactant. On the other hand, the CCSD(T) and DFT with B3LYP functional present similar Ea and ΔE values. In the 3d transition metal complex, we must be careful because of the instability of Hartree-Fock wavefunction in many cases [39]. In both of CCSD(T) and DFT-calculated energy changes, the Ea value is moderate and the ΔE value is considerably negative, indicating that the C–H activation of methane easily occurs with the Ti=N double bond.

The σ-bond activation reactions between this Ti complex and such various substrates as methanol, NH_3, silane (SiH_4), and methysilane (CH_3-SiH_3) [40] were theoretically investigated. Note that the N–H σ-bond activation is challenging. In fact, it had not been succeeded for long. This is probably because the stable adduct of ammonia is formed before the N–H activation. But, it was very recently succeeded by the Hartwig group [41]. The geometry changes of the O–H σ-bond activation reaction are shown in Fig. 11.3 as an example. Methanol approaches the Ti center to form a methanol complex as a precursor complex. In the transition state, the H atom is moving from the O atom toward the N atom. However, the O–H distance (1.183 Å) is moderately elongated but the N–H distance is still long (1.424 Å), indicating that this transition state is slightly more reactant-like than that of the C–H activation of methane. In the product, the methoxide coordinates with the Ti

Table 11.3 Energy changes of the N–H, O–H, Si–H and Si–C σ-bond activation reactions by $(Me_3SiO)_2Ti=N-SiMe_3$

	BE	Ea	E
N–H	−31.4	19.0	−45.0
O–H	−30.4	7.1	−65.8
Si–H	−6.8	2.6	−32.5
Si–C	−8.1	19.1	−33.9
C–H	−4.5	14.6	−22.7

The DFT(B3LYP) method was employed

Table 11.4 Bond energies[a] relating to the C–H, O–H, N–H, Si–H, and Si–C σ-bond activation reactions by $(Me_3SiO)_2Ti=N-SiMe_3$

	DFT(B3LYP)	MP2	MP3	MP4(DQ)	MP4(SDQ)	CCSD(T)
Ti–H	65.4	69.9	62.0	64.4	70.1	67.5
Ti–SiH$_3$	45.9	59.4	47.4	49.0	55.9	54.2
Ti–OCH$_3$	108.7	130.5	105.6	109.5	119.5	116.8
Ti–CH$_3$	68.4	83.0	69.0	69.3	75.2	74.5
N–H	115.9	116.9	114.0	114.2	114.2	114.5
N–SiH$_3$	104.6	114.4	107.9	107.5	107.8	108.4
N–CH$_3$	100.3	108.4	101.0	100.4	100.8	102.1
C–H	118.4	114.5	115.0	114.9	115.1	115.5
Si–H	94.8	90.6	92.9	93.2	93.3	93.4
O–H	107.2	111.0	106.5	107.1	107.0	107.3
Si–C	96.1	99.0	96.7	95.6	95.9	96.5

[a]In kcal/mol unit

center and the H atom is bound with the N atom to form an amino group. The energy changes calculated with the DFT(B3LYP) method are listed in Table 11.3. Interesting results are found in this table. The BE value is very large in the N–H σ-bond activation of NH_3 and in the O–H σ-bond activation of methanol. These are because NH_3 and methanol strongly coordinate with the Ti center through their lone pair orbitals. This feature is completely different from those of other substrates such as methane and silane in which the BE values are not large because those substrates do not have lone pair orbital. The Ea value increases in the order Si–H < O–H < C–H and the ΔE value increases in the order C–H < Si–H < O–H. In these reactions, the N–H and Ti–X (X $=$ CH_3, SiH_3, or OCH_3) bonds are produced. Thus, the ΔE value is determined by the energy difference between the X–H and Ti–X bond energies. We evaluated these bond energies, as shown in Table 11.4. Fortunately, these bond energies moderately fluctuate around MP2 and MP3, but the convergence is observed when moving to the CCSD(T). In the case of the methanol reaction, the strong O–H bond should be broken. But the C–H bond is stronger than the O–H bond and the Ti–OCH$_3$ bond is much stronger than the Ti–CH$_3$ bond (Table 11.4), which leads to the large exothermicity of the O–H σ-bond activation, as shown in Table 11.3. Because of this large exothermicity, the transition state becomes reactant-like compared to that of the C–H σ-bond activation, and also, the
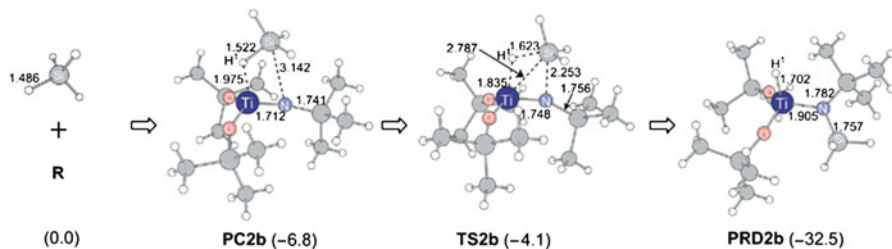
Fig. 11.4 Geometry changes in the C–H σ-bond activation of methane by $(H_3SiO)_2Ti=N–SiMe_3$ yielding a different product $(H_3SiO)_2Ti(H)[NH(SiMe_3)]$ (Reproduced from Ref. [36]. With kind permission of © The American Chemical Society 2007)

Ea value is moderate in spite of the large BE value. It is noted that the Si–H σ-bond activation occurs with the smallest Ea value. This is because the BE value is small and the Si–H bond is the weakest. However, the ΔE value is the smallest, because the Ti–SiH$_3$ bond is the weakest. These results indicate that the Ea and ΔE values depend on BE, Ti–R, and N–H bond energies. Thus, the BE and the Ti–R and R–H bond energies are useful to present prediction of the reactivity of this reaction.

In the C–H σ-bond activation reaction, there is another possibility that the $(H_3SiO)_2Ti(H)[N(CH_3)(SiMe_3)]$ is formed as a product (Eq. 11.7) in which not the

$$(H_3SiO)_2Ti=NSiH_3 + CH_4 \rightarrow (H_3SiO)_2Ti\,(H)\,[N\,(SiH_3)\,(CH_3)] \qquad (11.7)$$

Ti–CH$_3$ and N–H bonds but the Ti–H and N–CH$_3$ bonds are formed. This product was not reported experimentally. This regioselectivity was theoretically investigated [36], as shown in Fig. 11.4. Methane approaches the Ti center in a different orientation from that depicted in Fig. 11.2. In the transition state, the CH$_3$ group moves toward the N atom by changing its direction. The C–H distance is much more elongated than in the transition state of the normal C–H σ-bond activation. However, the C–N distance is still long. Consistent with these geometrical features of the transition state, the Ea value is considerably large, being 60.4 kcal/mol, where the DFT(B3LYP)-calculated value is presented. The ΔE value is also very small, −1.2 kcal/mol. The small ΔE value is interpreted well in terms of bond energies in Table 11.4; the Ti–H bond is weaker than the Ti–CH$_3$ bond and the N–CH$_3$ bond is weaker than the N–H bond. Ziegler et al. previously investigated the bond energy and found that the Ti–CH$_3$ bond is weaker than the Ti–H bond [42]. However, the difference in Ea between the normal and reverse regioselective C–H σ-bond activations is much larger than the difference in ΔE. This means that not only the bond energy but also some other factor is responsible for the large Ea value of this reverse regioselective C–H σ-bond activation. The orbital interaction is also responsible for the difference in Ea, which will be discussed below.

Fig. 11.5 Population
changes in the C–H bond
activations of benzene by
$M(\eta^2\text{-}O_2CH)_2$ (M = Pd or
Pt). A *positive value*
represents an increase in
population (vice versa). *Solid
lines* represent population
change for M = Pd, and
dotted lines represent
population changes for
M = Pt (Reproduced from
Ref. [26]. With kind
permission of © The
American Chemical Society
2000)
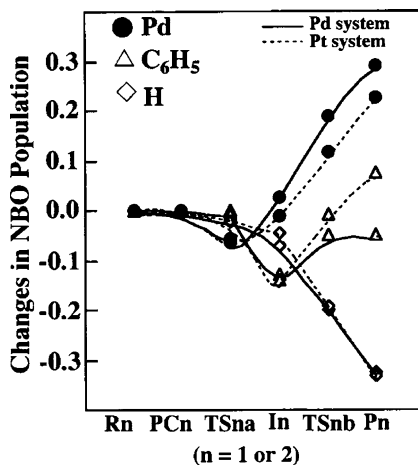
11.2.2 Population Changes and Electronic Process of the Heterolytic σ-Bond Activation

Population changes by the reaction of Eq. 11.5 are shown in Fig. 11.5 [26]. From these population changes, we can easily understand why this reaction is called heterolytic σ-bond activation reaction, as follows: When moving from the reactant to the benzene complex, the electron population of benzene somewhat decreases. This population change clearly indicates that the CT occurs from benzene to the Pd(II) center in the benzene complex. When moving from the Pd(II)-benzene complex to the transition state (**TSnb**) including the C–H σ-bond cleavage, the electron population of the Ph group considerably increases but the H atomic population considerably decreases. These results clearly show that the C–H σ-bond cleavage occurs in a heterolytic manner. It is noted that the Pd atomic population increases in the reaction. This population increase of the Pd center is consistent with the experimental proposal that this reaction is understood to be an electrophilic attack of the Pd(II) center to benzene.

The similar population changes are observed in the C–H σ-bond activation of methane by the $Ti(IV) = N(SiR_3)$ bond, as shown in Fig. 11.6 [36]. In the methane complex, the electron population of methane (the sum of H and CH_3 electron populations) moderately decreases and the Ti atomic population moderately increases. This is similar to the Pd(II)-benzene complex. The C–H bonding orbital participates in the interaction, which is essentially the same as that of the agostic interaction. When moving from the precursor complex to the transition state, the electron population of the CH_3 group substantially increases and the H atomic population substantially decreases, like the electron populations of the Ph and H groups of the benzene C–H σ-bond activation (Fig. 11.5). Simultaneously, the Ti atomic population considerably increases, but then, it somewhat decreases when moving to the product from the transition state. This change is different from that of

Fig. 11.6 Population
changes by C–H σ-bond
activations by
$(H_3SiO)_2Ti=N–SiMe_3$ and
$Pt(PH_3)_2$ (Reproduced from
Ref. [36]. With kind
permission of © The
American Chemical Society
2007)
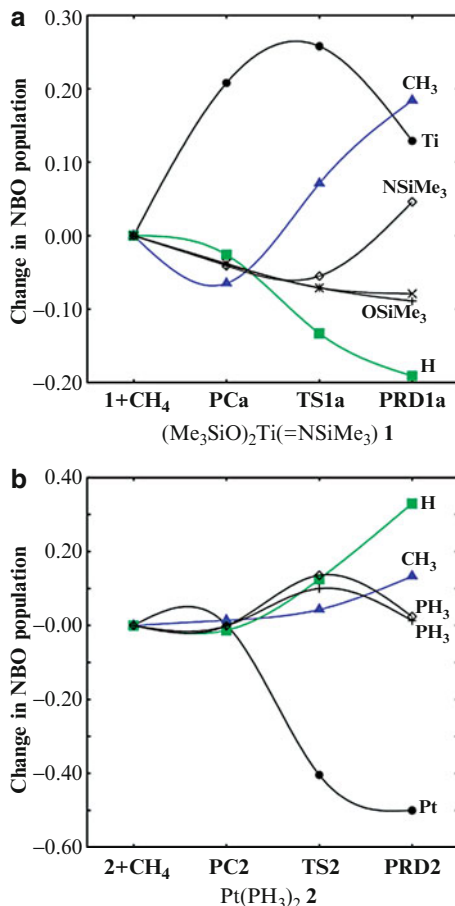
the Pd atomic population; the Pd atomic population never decreases when moving from the transition state to the final product. The origin of this decrease is not clear at this moment, but it is likely that the Ti center wants to become positively charged to strengthen the electrostatic interaction of the Ti(IV) center with the R and $NH(SiMe_3)$ ligands. In spite of this unexpected Ti population change at the final stage, it is concluded that the essential features of this reaction are the significantly large increase in the CH_3 electron population and the significantly large decrease in the H atomic population. These features are common in this type of heterolytic σ-bond activation reaction. Because it is unlikely that methane easily undergoes the electrophilic attack of Pd and Ti centers, we believe that this type of reaction should be understood not to be the electrophilic attack of the metal center but to be the heterolytic σ-bond activation.

It is noted here that these population changes are completely different from those of the oxidative addition to the Pt(0) complex, as compared in Fig. 11.6 [36]. In the oxidative addition to $Pt(PH_3)_2$, both electron populations of Ph and H groups
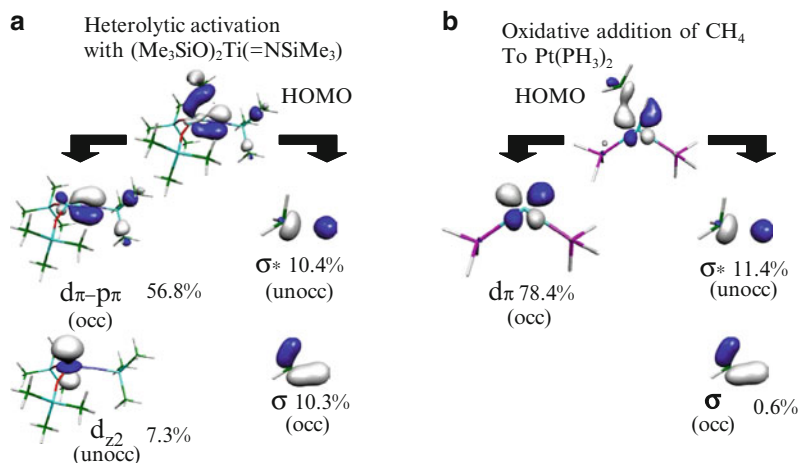
Scheme 11.5 Orbital components in the important MO of the transition state of the σ-bond activation (This figure is reproduced from Ref. [36]. Under permission of ACS)

considerably increase and the Pt atomic population considerably decreases, as shown in Fig. 11.6b. These features are consistent with our understanding that the Pt oxidation state increases in the reaction. These population changes can be understood by the orbital interaction. The important orbital interaction was previously discussed by Tastumi, Hoffmann, and their coworkers [17]. However, the theoretical evidence has not been presented well. In the heterolytic σ-bond activation, the electronic process is not clearly understood; for instance, we do not know the reasons why and how one moiety of substrate becomes positively charged and another moiety becomes negatively charged in the reaction. The orbital interaction diagram must be very much different from that of the oxidative addition reaction. However, such orbital interaction diagram has not been reported at all. This means that the next issue to be theoretically studied is to present the clear evidence of the orbital interaction diagram in the oxidative addition and to present a clear orbital interaction diagram that plays important roles in the heterolytic σ-bond activation.

We wish to discuss the orbital interaction diagram that is important in the oxidative addition and the heterolytic σ-bond activation. The important molecular orbital (MO) is shown at the top of Scheme 11.5 [36]. This MO was investigated with the linear combination of molecular orbitals (LCMO) of fragments—the MO of the total system A–B can be represented with the LCMO of fragments A and B [43–45].

$$\psi_i \, (\mathrm{AB}) = \sum_m C_{im}^{\mathrm{A}} \varphi_m \, (\mathrm{A}) + \sum_n C_{in}^{\mathrm{B}} \varphi_n \, (\mathrm{B}) \qquad (11.8)$$

where $\psi_i \, (\mathrm{AB})$ is the i-th MO of the system AB, $\varphi_m(\mathrm{A})$ is the m-th MO of the fragment A, and C_{im}^{A} is expansion coefficient of $\varphi_m(\mathrm{A})$. Here, we separate the

a Orbital mixing of C-H σ-bonding
and σ*-antibonding orbitals

b Charge transfer from C-H
σ-bonding orbital to empty
Ti dz2

c Orbital diagram
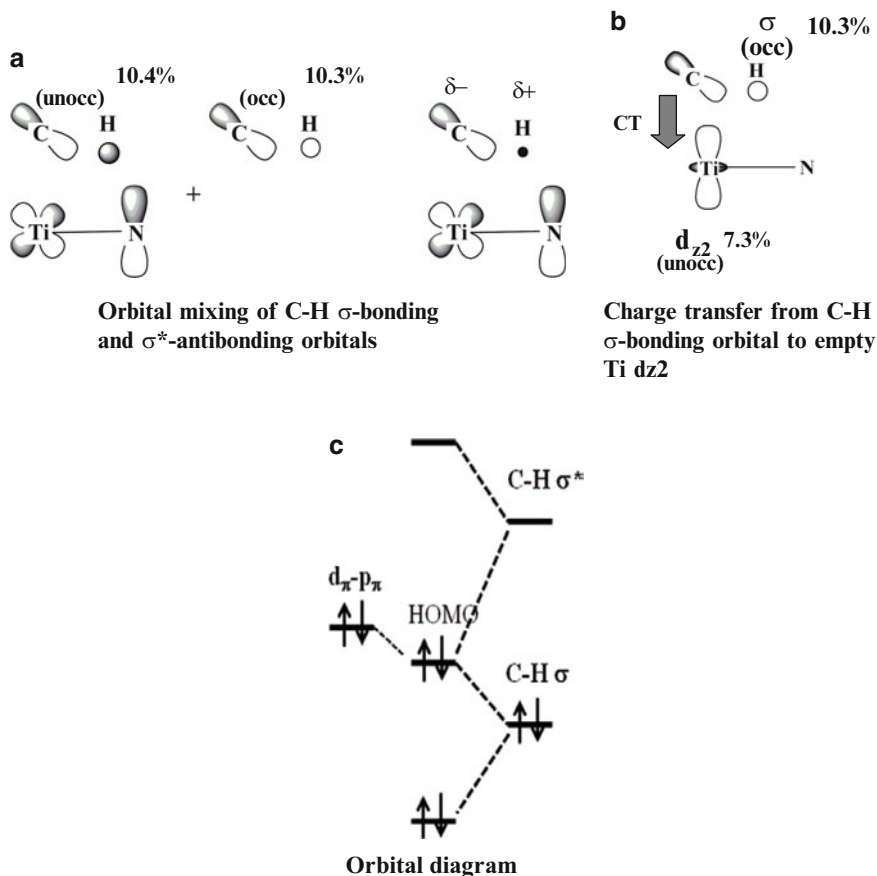
Scheme 11.6 Important orbital mixings in heterolytic σ-bond activation (Reprinted from Ref. [36]. With kind permission of © The American Chemical Society 2007)

reaction system into methane and the Ti-imido complex to represent what MOs of methane and the Ti-imido complex participate in the MO of the total reaction system [36]. As shown in Scheme 11.5a, the HOMO in the transition state mainly consists of the Ti–N d_π-p_π bonding orbital into which the C–H σ*-antibonding orbital mixes in a bonding way with the p_π of the N atom, but the C–H σ-bonding orbital mixes in an antibonding way. Also, the Ti d_{z2} orbital mixes with the C–H σ-bonding orbital in a bonding way. The mixing of the σ-bonding orbital into the σ*-antibonding orbital in this MO increases the component of the methyl sp^3 orbital but decreases the component of the H 1s orbital, as shown in Scheme 11.6a. As a result, the H atom becomes positively charged and the methyl group becomes negatively charged. The empty d_{z2} orbital of Ti interacts with the enlarged sp^3 orbital of the methyl group to form CT interaction; see Scheme 11.6b. This CT stabilizes the negatively charged methyl group and also leads to the formation of the Ti–CH$_3$

bond. Thus, the characteristic feature of the heterolytic σ-bond activation arises from the orbital mixing of the C–H σ-bonding orbital into the C–H σ*-antibonding orbital. This mixing is induced by the presences of the empty Ti d_{z^2} orbital and the polarized Ti–N d_{π}-p_{π} bonding orbital in which the N p_{π} orbital is much larger than the Ti d_{π} orbital.

In the oxidative addition to Pt(PH$_3$)$_2$, on the other hand, the important MO mainly consists of the Pt d_{π} orbital into which the C–H σ*-antibonding orbital mixes in a bonding way, as shown in Scheme 11.5b [36]. It is noted that the C–H σ-bonding orbital little participates in this MO. These features clearly indicate that the CT from the occupied d orbital of the Pt to the empty σ*-antibonding orbital of the C–H bond plays important roles in the oxidative addition to the low-valent transition metal complex. This is a theoretical support to the orbital interaction discussed previously [17].

The reason why this type of orbital mixing occurs in the heterolytic σ-bond activation is easily understood in terms of the first order orbital interaction, as shown in Scheme 11.6c. The Ti–N d_{π}-p_{π} bonding orbital interacts with the C–H σ*-orbital to form bonding overlap, because the C–H σ*-orbital exists at higher energy than the Ti–N d_{π}-p_{π} orbital. However, the C–H σ-bonding orbital interacts with the d_{π}-p_{π} bonding orbital in an antibonding way because this σ-bonding orbital exists at much lower energy than the d_{π}-p_{π} orbital. This type of three-orbital interaction is often found in the reactions and compounds by transition metal elements.

In summary, the σ-bond activation by Eq. 11.2 is clearly understood in terms of heterolytic σ-bond cleavage and its important driving force is the formation of the strong R1–X bond. The LCMO analysis clearly disclosed that the mixing of the C–H σ-bonding orbital into the C–H σ*-antibonding orbital plays important roles in the heterolytic σ-bond activation, unlike the oxidative addition.

Here, we wish to return to the regioselectivity in the heterolytic σ-bond activation reaction of methane by (H$_3$SiO)$_2$Ti=NSiH$_3$ in which the product is a titanium(IV) hydride (methysilylamino) complex, (H$_3$SiO)$_2$Ti(H)[N(SiH$_3$)(CH$_3$)] (Eq. 11.7) [36]. In this reverse regioselective reaction, the activation barrier becomes larger and the reaction energy becomes much less negative, as compared in Table 11.2, indicating that this reverse regioselective reaction is unfavorable both kinetically and thermodynamically. As discussed above, the thermodynamical result is easily interpreted in terms of bond energies. The kinetic factor should be discussed in terms of the interaction at the transition state. Actually, the orbital overlap is less favorable in the reverse regioselective reaction than in the normal regioselective reaction. In the reverse regioselective reaction, the H 1s orbital must overlap with the Ti d_{z^2} orbital and the sp^3 orbital of the methyl group must overlap with the N p_{π} orbital. In both of the normal and reverse regioselective reactions, the methane approaches the Ti–N moiety with the H atom in the lead. Because the Ti–N d_{π}-p_{π} bonding orbital largely consists of the p_{π} orbital of the N atom and moderately of the Ti d_{π} orbital, the H 1s orbital can form larger overlap with the N p_{π} orbital in the normal regioselective reaction but much less overlap with the Ti d_{π} orbital in the reverse regioselective reaction, as schematically shown in Scheme 11.7 [36]. As a result, the transition state becomes more unstable in the reverse regioselective reaction than in the normal regioselective reaction.

a   **b**

Normal regioselective reaction   **Reverse regioselective reaction**
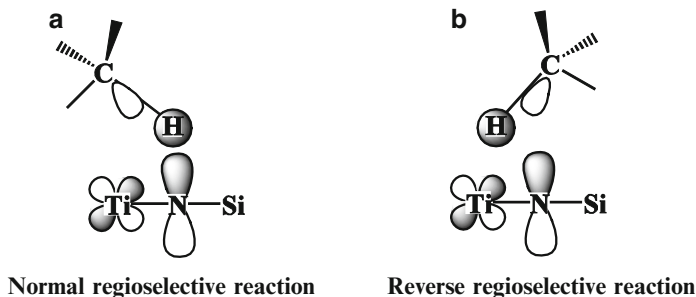
Scheme 11.7 Schematic features of orbital overlap between the C–H σ^*-antibonding MO and the d_π-p_π bonding MO of the Ti-NSiMe$_3$ bond
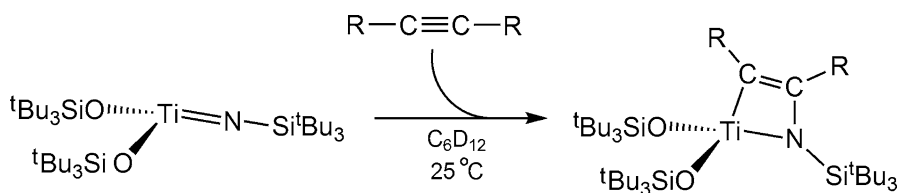
Scheme 11.8 The 2+2 coupling reaction between the Ti≡N double bond and the C≡C triple bond of alkyne (Reprinted from Ref. [52]. With kind permission of © The American Chemical Society 2010)

11.2.3 Similarity of the Heterolytic σ-Bond Activation to the Completely Different 2 + 2 Coupling Reaction

Interestingly, the Ti(IV)-imido complex (H$_3$SiO)$_2$Ti=NSiMe$_3$ undergoes the 2 + 2 coupling reaction with alkyne [46], as shown in Scheme 11.8. The similar coupling reactions were reported for the several M=N multiple bonds [47, 48]. Also, the similar reaction between M = alkylidene double bond and the C=C double bond of alkene is considered to be an important elementary process in the closing metathesis [49] and cross metathesis [50, 51]. These reactions are considered to be 2 + 2 coupling reaction between the M–X double bond and the C–C double or triple bond. As it is well-known, the 2 + 2 coupling reaction of organic molecules is forbidden in the Woodward-Hoffmann rule. However, these reactions occur easily without irradiation of light. To understand the reason, we theoretically investigated here the reaction of Scheme 11.8 with DFT, CCSD(T), and MRMP2 methods [52]. In the thermal 2 + 2 coupling reaction, we need to consider two electron configurations at the transition state, at least; as shown in Scheme 11.9, the configuration **1** is a main contributor in the reactant but the configuration **2** recently is a main configurator in the product. Thus, both must be considered at the transition state. This is the reason why we employed MRMP2 here. The geometry changes are shown in Fig. 11.7 and the energy changes are shown in Fig. 11.8. In

Scheme 11.9 Orbital
diagram of 2+2 coupling
reaction
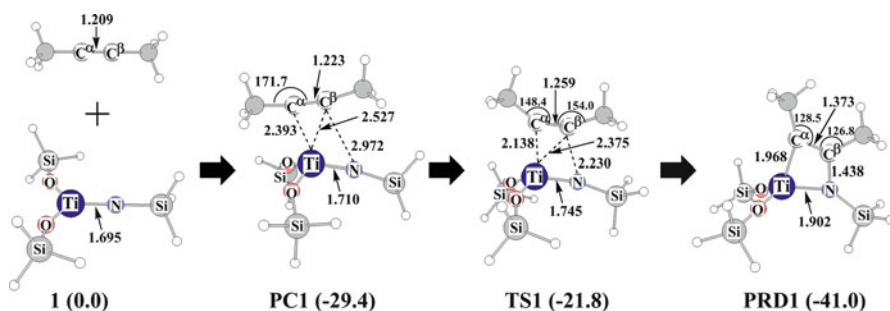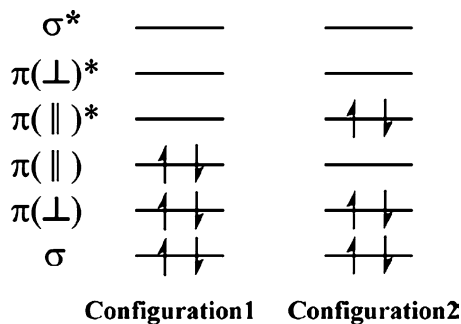
Fig. 11.7 Geometry changes by the $2+2$ coupling reaction between (H3SiO)2Ti-NSiMe3 and 2-butyene (Reproduced from Ref. [52]. With kind permission of © The American Chemical Society 2010)
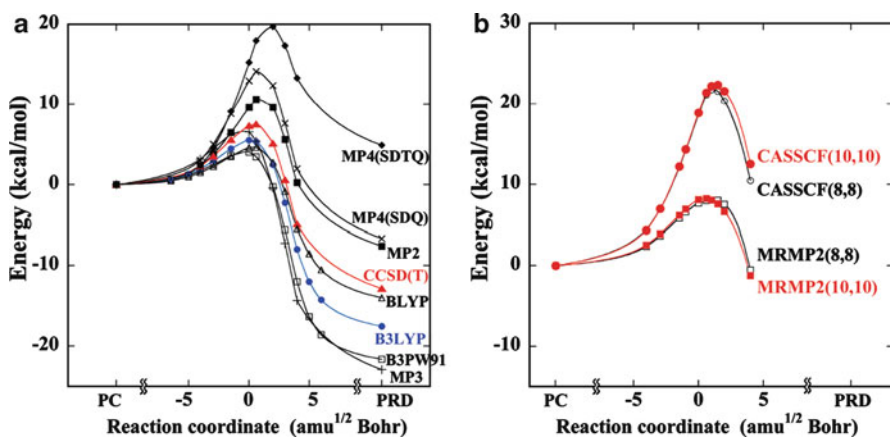
Fig. 11.8 Energy changes calculated by DFT, MP2 to MP4(SDTQ), CCSD(T), CASSCF and MRMP2 methods for the $2+2$ coupling reaction of $(Me_3SiO)_2Ti=NSiMe_3$ with 2-butyne (Reproduced from Ref. [52]. With kind permission of © The American Chemical Society 2010)

Fig. 11.9 Population changes in the 2 + 2 coupling reaction between $(H_3SiO)_2Ti=NSiMe_3$ and 2-butyene (Reproduced from Ref. [52]. With kind permission of © The American Chemical Society 2010)
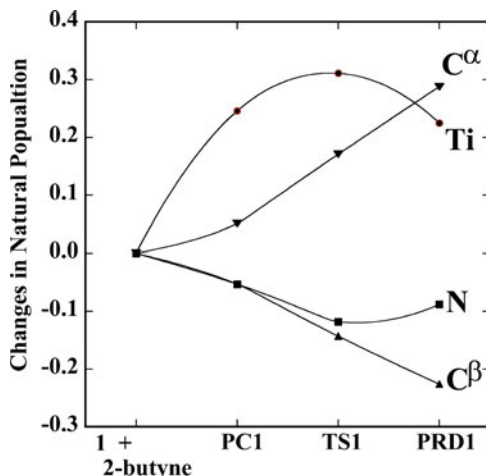
the precursor complex, 2-butyne coordinates with the Ti center like usual alkyne complex, although the Ti–C distances are a little bit longer than the expected value. In the transition state, the Ti–C^α distance becomes shorter and the N–C^β distance (2.230 Å) is still considerably longer than that of the product. The Ti–N distance is moderately elongated, but it is still considerably shorter than that of the product. These geometrical features indicate that the transition state is rather reactant-like. The energy changes considerably fluctuate when going from MP2 to MP4(SDTQ), as shown in Fig. 11.8a, like the energy changes in the C–H σ-bond activation by $(H_3SiO)_2Ti=NSiH_3$. However, the CCSD(T) and DFT methods present similar energy changes. The CASSCF(8,8) and CASSCF(10,10) methods present similar energy changes to each other, and also, the MRMP2(8,8) and MRMP2(10,10) present similar energy changes to each other, indicating that the active space (8,8) is reasonable. The MRMP2 presents much smaller energy barrier than the CASSCF. This means that the dynamical correlation is important. Interestingly, the MRMP2, CCSD(T), and DFT methods present similar energy changes. From these results, it is concluded that the static correlation is not very much important in this reaction; in other words, it is not necessary to consider the two reference configurations shown in Scheme 11.9 even at the transition state.

As shown in Fig. 11.9, the C^α atomic population considerably increases but the C^β atomic population considerably decreases when moving from the precursor alkyne complex to the product. The Ti atomic population considerably increases when moving to the transition state but then moderately decreases when moving from the transition state to the product. It should be noted that all these population changes are almost the same as those of the C–H σ-bond activation by $(H_3SiO)_2Ti=NSiMe_3$, as clearly compared in Figs. 11.6a and 11.9. In the 2 + 2 coupling reaction, the orbital mixing occurs, as shown in Scheme 11.10, in which the d_π-p_π bonding MO of $(H_3SiO)_2Ti=NSiMe_3$ undergoes an antibonding mixing of the π MO of 2-butyne because the π MO exists at a lower energy than the d_π-p_π
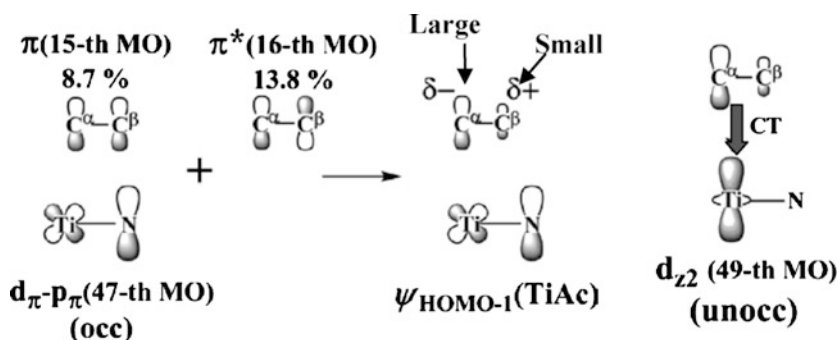
Scheme 11.10 Results of LCMO analysis and Orbital Mixing (Reprinted from Ref. [52]. With kind permission of © The American Chemical Society 2010)

bonding MO. Into this antibonding overlap, the π^* MO of 2-butyne mixes in a bonding way with the d_π-p_π bonding MO because the π^* MO exists at a higher energy than the d_π-p_π bonding MO. This mixing increases the p orbital contribution of the C^α atom but decreases that of the C^β atom, as shown in Scheme 11.10. These orbital mixings are essentially the same as those of Scheme 11.6, which was found in the heterolytic C–H σ-bond activation by $(H_3SiO)_2Ti=NSiMe_3$.

It is of considerable interest to elucidate the reason why the same orbital mixings occur in both the heterolytic C–H σ-bond activation and the $2 + 2$ coupling reactions. In both the d_π-p_π bonding, MO of $(H_3SiO)_2Ti=NSiMe_3$ plays important roles. Because the p_π orbital of the N atom is much larger than the d_π orbital of the Ti center in this MO, the π MO of 2-butyne induces an antibonding mixing with the p orbital of the N atom and the π^* MO of 2-butyne induces a bonding mixing with the p orbital of the N atom. This means that this polarized MO causes asymmetrical mixings of π and π^* MOs of 2-butyne into the d_π-p_π bonding MO of $(H_3SiO)_2Ti=NSiMe_3$; in other words, the polarized d_π-p_π MO breaks the forbidden character of the $2 + 2$ coupling reaction. At the same time, this polarized d_π-p_π MO induces the orbital mixings that increase the C^α p orbital component and decrease the C^β p orbital component in the HOMO of the system of $(H_3SiO)_2Ti=NSiMe_3 + 2$-butyne. In the C–H σ-bond activation, methane approaches the Ti=N moiety with the H atom in a lead. In this geometry, the C–H σ-bonding MO induces an antibonding mixing with the p orbital of the N atom, and also the C–H σ^*-antibonding MO induces a bonding mixing with the p orbital of the N atom. These orbital mixings induce the characteristic population changes in the heterolytic σ-bond activation. In both reactions, the presence of the polarized d_π-p_π bonding MO in $(H_3SiO)_2Ti=NSiMe_3$ induces the similar population changes and breaks the symmetry forbidden feature in the $2 + 2$ coupling reaction. It is concluded that the polarized d_π-p_π bonding MO in $(H_3SiO)_2Ti=NSiMe_3$ plays crucial roles in these two different reactions.

Fig 11.10 Relation between the O–H bond energy and Ea value for C–H dissociation (Reproduced from Ref. [55]. Under permission of © The American Institute of Physics 2008)
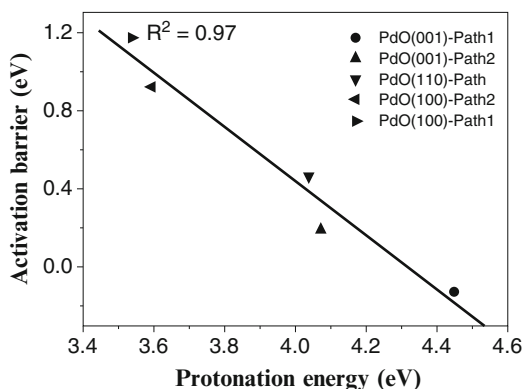
11.2.4   Other Theoretical Studies of Heterolytic C–H σ-Bond Activation and Similar Reactions

Heterolytic σ-bond activations have been found in other reaction systems. For instance, the C–H σ-bond activation of alkane by metal oxide is also understood to be the heterolytic σ-bond activation [53, 54]. This reaction has been theoretically investigated in relation to selective oxidation of alkane, model reactions of metal oxide surface, and model of biological oxidation by metal enzymes in many cases. There are three plausible reaction courses; one is concerted mechanism, the second is radical mechanism, and the last is oxygen-insertion mechanism. In the reaction of

$$FeO^+ + C_6H_6 \rightarrow Fe + C_6H_5 - OH \qquad (11.9)$$
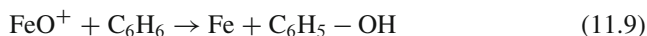
benzene with FeO^+ to phenol (Eq. 11.9), the theoretical study reported that the concerted mechanism is the most favorable [53d]. The relation between activation barrier and O–H bond energy was clearly shown by the DFT study in the reaction between methane and metal oxide; see Fig. 11.10 [55]. The similar relation between reaction energy and activation barrier was found in the C–H σ-bond activation by various d^0 metal oxide bearing tetrahedral coordination structure, indicating that the formation of the O–H bond is important for this reaction [56]. These results deeply relate to the discussion of the driving force in the heterolytic C–H σ-bond activation by $Pd(\eta^2\text{-}O_2CH)_2$ [26].

Metal oxide has several spin states in many cases. Actually, many works reported that the spin crossing occurs in the reaction [53]. This means that the spin states must be carefully investigated in these reactions. We need to consider carefully the electron correlation effects in these reactions because these effects are different in different spin states. Also, it is well-known that the DFT functional including a lot of Hartree-Fock exchange tends to overestimate the stability of high spin state.

Thus, the energy changes along the spin crossing must be carefully investigated with post–Hartree-Fock method and with various functionals in the case of DFT calculation.

The σ-bond activation by metal oxide is certainly a reasonable model of the activation reaction by solid metal oxide bearing both M=O double bond and bridging O atom such as M–O–M. DFT study of methane activation by Mo_3O_9 clearly shows that the terminal M=O is more reactive than the bridging O atom [57].

The N–H σ-bond activation of ammonia with FeO^+ and VO^+ was theoretically investigated with the DFT method [58]. The same reaction with MO^+ (M = Sc to Zn) was experimentally and theoretically investigated [59]. In these reactions, the first step is the formation of ammonia adduct (Eq. 11.10) and then the reaction occurs in several reaction channels; one is dehydration, which leads to $[M(NH)]^+$ and H_2O (Eq. 11.11); the second is hydrogen atom abstraction, which leads to $[M(OH)]^+$ and NH_2 (Eq. 11.12); and the third is oxygen atom transfer from M to N, which leads to hydroxylamine (Eq. 11.13).

$$[MO]^+ + NH_3 \rightarrow [MO\,(NH_3)]^+ \tag{11.10}$$

$$[MO\,(NH_3)]^+ \rightarrow [M\,(NH)]^+ + H_2O \tag{11.11}$$

$$[MO\,(NH_3)]^+ \rightarrow [M\,(OH)]^+ + NH_2 \tag{11.12}$$

$$[MO\,(NH_3)]^+ \rightarrow M^+ + NH_2OH \text{ or } M + [NH_2OH]^+ \tag{11.13}$$
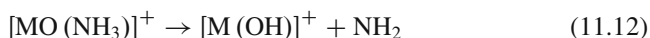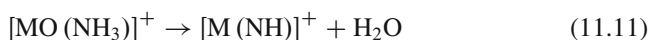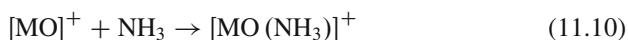
Interestingly, the first and the second channels (Eqs. 11.11 and 11.12) are possible depending on the metal, but the last channel (Eq. 11.13) is less possible. The first and the second channels become exothermic at Cr and Mn when going from Sc to Zn. The third channel (Eq. 11.13) becomes feasible for Ni to Zn. The exothermicity of Eq. 11.11 increases when moving from Sc to Zn, while the exothermicity of Eq. 11.12 is the largest at Mn but decreases when moving from Mn to Zn [59]. These results were discussed based on bond energy and ionization potential. The N–H σ-bond activations with Ti-imido complex and Ta-imido amido surface complex were also theoretically investigated [60]. In the latter reaction, the Ta center does not directly interact with either H or NH_2 group. The N–H activation can occur when excess ammonia molecules exist. Such ammonia molecules accelerate the H atom transfer from ammonia to amido or imido ligand. In other words, many ammonia molecules play a role to accelerate proton-transfer in this gas phase reaction like solvent molecules. This suggests that the N–H σ-bond activation is expected to be accelerated by polar solvent.

Many Cp_2ML type complexes (M = Zr, Lanthanide) perform heterolytic σ-bond activation reactions, as theoretically reported by Eisenstein and her coworkers [61]. In this section, we will use the term "metathesis" instead of "heterolytic σ-bond

$$Cp_2Ln - H + D - D \rightarrow Cp_2Ln - D + H - H \tag{11.14}$$
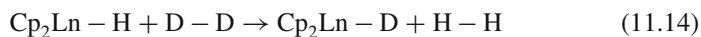
Scheme 11.11 Two possibilities of transition state (This figure is reproduced from Ref. [61c]. Under permission of RCS)

1   **2**
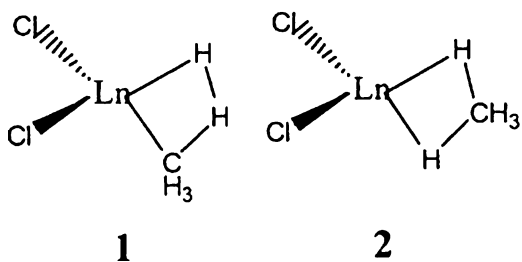
activation" because these authors used the term metathesis. In the H–H σ-bond

$$Cl_2Ln - H + EH_3 - H \rightarrow Cl_2Ln - EH_3 + H - H \qquad (11.15a)$$

$$Cl_2Ln - H^* + EH_3 - H \rightarrow Cl_2Ln - H + H^* - EH_3 \qquad (11.15b)$$

$$Cl_2Ln - EH_3{}^* + EH_3 - H \rightarrow Cl_2Ln - EH_3 + H - EH_3{}^*$$
$$(E = C \text{ or } Si) \qquad (11.15c)$$
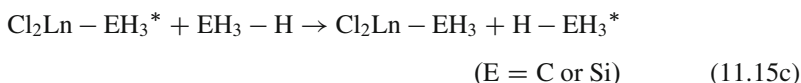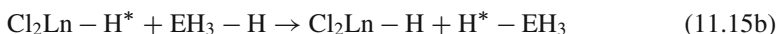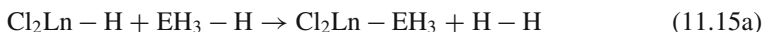
activations, the H/D exchange occurs easily with moderate activation energy [61a]. The transition state is four-center, as expected. In the C–H σ-bond activation, [61c] there are three possible reactions such as Eq. 11.15a, 11.15b, and 11.15c, where Cp was replaced by Cl to decrease computational costs. The energy changes are well-reproduced by this replacement. The transition states for Eq. 11.15a and 11.15c are energetically accessible. However, that exists for Eq. 11.15b at very high energy, indicating that this reaction is difficult. These results agree with the experimental results. These transition states are represented to be 4c–4el metathesis. In Eq. 11.15a, there are two possible transition states; see Scheme 11.11. The transition state **1** is more favorable than the transition state **2**. In this transition state **1**, the proton-like H atom is moving from anionic CH_3 to anionic H(hydride) ligand; in other words, heterolytic C–H σ-bond cleavage occurs in this transition state. The Si–H σ-bond activation easily occurs but the reaction behavior is different from that of the C–H σ–bond activation [61]. In this reaction, the transition state **2** is more favorable than the transition state **1** unlike in the C–H σ-bond activation, which was discussed in terms of hypervalency of the Si center. The other factors to be considered may be steric effect and the $Si^{\delta+} - H^{\delta-}$ polarization. The H/H scrambling occurs very easily with very small barrier. Although the activation barrier is very large, Eq. 11.15b is thermodynamically more favorable than Eq. 11.15a. The Ln–H, Ln–SiH$_3$, H–H, and Si–H bond energies must be investigated to understand the reason. The reaction of Eq. 11.15c is methyl-exchange. This reaction was also theoretically investigated for M = Sc, Y, and lanthanides [61f]. The activation enthalpy is 16–18 kcal/mol, which is much larger than that of the H exchange, as expected. The transition state is symmetrical, as shown in Fig. 11.11a. In this transition state, the H atom is moving from one CH_3 group to another CH_3 group, where the H atom is positively charged and two CH_3 groups are negatively charged. This type of polarization is often observed in heterolytic σ-bond activation.The

a
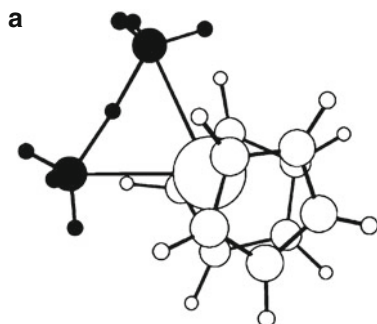
The reaction between Cp*$_2$M-CH$_3$
and CH$_4$

b

10 (0)   **11** (1)

12 (0)   **13** (1)
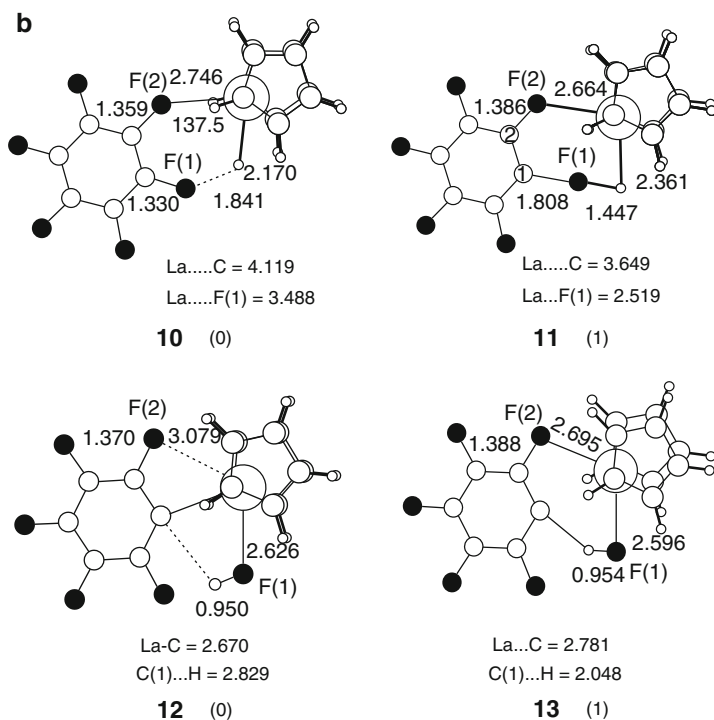
The reaction Cp'$_2$CeH and C$_6$F$_6$

Fig. 11.11 Transition states of methyl exchange in the reactions between Cp$_2$*M–CH$_3$ (**a**) and CH$_4$ and between Cp'$_2$CeH and C$_6$F$_6$ (**b**) (Reproduced from Ref. [61f and 61d]. With kind permission of © The American Chemical Society and Royal Chemical Society 2004 and 2006)

similar complex, [(1,3,4-Me$_3$C)$_3$C$_5$H$_2$]$_2$CeH, performs the C–F and similar C–X (X = other halogen) σ-bond activations. This reaction was theoretically investigated by Eisenstein and coworkers [61d]. This reaction is interesting because the very strong C–F bond is activated. Of course, the activation barrier (38.6 kcal/mol)

is higher than that of the methyl transfer, as expected, but it is not very large. Actually, this reaction is experimentally observed [61d, j]. The transition state for the C–F and C–X bond cleavages is interesting [61d, j]. As shown in Fig. 11.11b, perfluorobenzene C_6F_6 approaches the Ce center to form a precursor complex **10** in which one F atom interacts with the Ce center but another F atom interacts with the H ligand. In the transition state **11**, one F atom is moving to the H ligand from the C atom of perfluorobenzene. In the intermediate $Cp'_2Ce(C_6F_5)(HF)$ **12**, the Ce–C_6F_5 bond and HF molecule are formed, where HF interacts with the Ce center through the F atom. In the second transition state **13**, a new C–H bond formation is in progress and the C_6F_5 moiety is dissociating from the Ce center. The transition state **11** is quite different from that of metathesis. But, it is understood to be six-center associative interchange. This is certainly similar to the transition state of the heterolytic C–H σ-bond activation of benzene by $Pd(\eta^2\text{-}O_2CH)_2$. The polarization of the C–F bond and the H atomic charge are interesting in **10** and **11**. In **10**, the C–F bond to be broken is polarized as $C^{(+0.31)}$–$F^{(-0.29)}$ and the H ligand has −0.64 e, because it is a hydride, where numbers are NBO charges. But, **11** (transition state) shows the polarization of $C^{(0.0)}$–$F^{(-0.51)}$ and the H atomic charge of −0.11 e. This is because the F atom approaches the negatively charged $H^{(-0.64)}$ ligand to form HF; i.e., the H (hydride) ligand changes to proton and the C–F covalent bond changes to the H–F highly polarized bond. The C–F bond activation of perfluorinated olefins was also theoretically investigated recently.[61n]

Theoretical studies of hydrogenase showed that the H–H σ-bond activation occurs in a heterolytic manner [62]. From these results, we expect that the heterolytic σ-bond activation plays important roles in many catalytic reactions, including metalloenzyme reactions.

At the end of this section, I wish to mention some ambiguous situation on the question; which of the oxidative addition and the heterolytic C–H σ-bond activation more favorably occurs in Pt(II) complex? As discussed in Sect. 11.2.1, Siegbahn et al. reported that the heterolytic C–H σ-bond activation of methane occurs with $PtCl_2(H_2O)_2$. However, Hush and his coworkers theoretically investigated the C–H σ-bond activation of methane by *cis*-platin, *cis*-$PtCl_2(NH_3)_2$, and its trans-isomer [63]. They found that the oxidative addition and metathesis are comparable in *cis*-platin; but, the oxidative addition is more feasible than the metathesis in *trans*-platin. Also, they concluded that the oxidative addition occurs more feasibly to $[Pt(NH_3)_2(OSO_3H)_2]$ or $[Pt(NH_3)_2(OSO_3H)(H_2SO_4)]^+$ in the conversion of methane to methanol catalyzed by Pt(II) complex in sulfuric acid. The similar oxidative addition of methane to a Pt(II) complex $[PtCl_4]^{2-}$ was theoretically investigated by Ziegler and coworker to clearly shed light on the Shilov reaction [64]. They concluded that (1) the substitution of H_2O ligand for methane is a rate-determining step, (2) both dissociative and associative mechanisms are comparable, and (3) the oxidative addition of the C–H bond to the Pt(II) center occurs in the Pt(II)-methane complex. In my opinion, the comparison between dissociative and associative substitutions is not easy in solution because it is difficult to evaluate translation entropy in solution [2]. Important conclusion here is that not heterolytic activation but oxidative addition easily occurs even in the case of Pt(II) complexes. Borden and his coworkers theoretically investigated reductive elimination of methane from

Pt(II) and Pt(IV) complexes with DFT and CCSD(T) methods [65]. Although their discussion was focused on the question whether ligand dissociation occurs or not, prior to reductive elimination, it was clearly shown that the reductive elimination of methane from $PtCl(H)(CH_3)(PH_3)_2$ is considerably exothermic. Recently, Schwarz and coworkers theoretically investigated the C–H σ-bond activation by [M(bipy-H)]$^+$ and [M(imine)R]$^+$ (M = Ni, Pd, or Pt; R = CH$_3$) with the DFT method [66]. When the substrates are benzene and toluene, the $C(sp^2)$–H bond activation occurs via metathesis for M = Ni and Pd [66c, d]. But, the oxidative addition and metathesis are comparable for M = Pt. In the $C(sp^3)$–H σ-bond activation of methane and benzylic position in toluene, the oxidative addition more favorably occurs than the metathesis. When the CH$_3$ ligand is substituted for Cl, the heterolytic C–H σ-bond activations of benzene and methane become endothermic for M = Ni, Pd, or Pt. Only benzylic C–H bond activation of toluene is exothermic in all these complexes. These results clearly indicate that the reactivity significantly depends on the ligand, and maybe, the bond energy is an important factor for the metathesis; because the H–Cl bond is much weaker than the C–H bond, the heterolytic σ-bond activation becomes difficult when CH$_3$ is substituted for Cl. Recently, Ess, Goddard, and Periana carefully investigated C–H σ-bond activation of methane by various metal complexes and discussed the reaction in terms of electrophilic, ambiphilic, and nucleophilic properties of transition state [67]. Although the nucleophilic C–H σ-bond activation corresponds to the oxidative addition in many cases, it is not the same here. Here, the nucleophilic C–H activation means that the CT occurs from the metal complex to the C–H bond. In the late transition metal complexes with high oxidation state, the electrophilic activation is favorable, which means that metathesis occurs favorably. The nucleophilic activation is more favorable in the early transition metal complexes such as Sc, and also in middle transition metal complexes such as Ir, Rh, and Ru. These results suggest that ligand effects, d orbital energy, and d electron number must be carefully considered in the discussion of the C–H σ-bond activation.

There are many issues to be theoretically investigated in the C–H σ-bond activation by transition metal complexes. There remains one of the important factors to be investigated theoretically. It is the solvation effect—the σ-bond to be broken is polarized in the transition state of heterolytic σ-bond activation. The product is also polarized. These features mean that solvation effects are considerably large and should be taken into consideration in theoretical study.

11.3 Oxidative Addition to M–L Moiety

11.3.1 Theoretical Examples of Oxidative Addition to M–L Moiety

Examples of this type of σ-bond activation have been limited, to our knowledge. One is the B–SR σ-bond activation with $Pd(PR_3)_2(C_2H_2)$, as shown in Eq. 11.16.

This reaction was investigated as one part of thioboration of acetylene by Musaev, Morokuma, and their coworker [68]. Through this reaction, the B–SR single bond is

$$Pd(PR_3)_2(C_2H_2) + (HO)_2B - SR \rightarrow Pd(SR)[CH_2CH_2B(OH)_2](PR_3)_2 \quad (11.16)$$
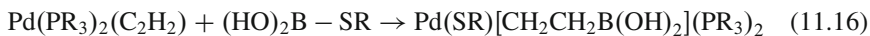
cleaved. Then, the SR group is bound with the Pd center, and the boryl group is bound with the C atom of acetylene. Thus, acetylene converts to the vinyl group in the product through this reaction. As discussed in Introduction, the vinyl group bound with the metal center is considered to be an anion. The boryl group is also considered to be an anion because it is bound with the Pd center. Thus, the oxidation state of the Pd center increases by 2 in this reaction in a formal sense. This reaction is, therefore, understood to be the oxidative addition of the B–SR bond to the Pd(0)-alkyne moiety.

In the case of the platinum analogue, not this type of oxidative addition but the usual oxidative addition to the metal center occurs in general [69, 70].

$$Pt(PR_3)_2 + (HO)_2B - B(OH)_2 \rightarrow Pt[B(OH)_2]_2(PR_3)_2 \quad (11.17)$$
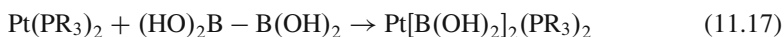
The difference between the platinum(0) and palladium(0) complexes is easily interpreted in terms of the d orbital energy level. As is well-known, the d orbitals of the palladium atom exist at lower energies than those of the platinum atom. As a result, the oxidative addition to the palladium center is difficult. But, the oxidative addition to the Pd(0)-alkyne moiety can occur probably because the formation of the C–B bond with acetylene provides enough energy gain. Although this discussion was not presented in the original paper, we believe that this is plausible and reasonable explanation for the oxidative addition of the B–SR bond to the Pd(0)-alkyne moiety.

The next example is found in our theoretical study of the hydrosilylation of ethylene by Cp_2Zr complex [71]. In the usual reaction mechanism of metal-catalyzed hydrosilylation, olefin is inserted into the metal-hydride or metal-silyl bond, as shown in Scheme 11.12 [72]. The reaction mechanism including the former insertion is called Chalk-Harrod mechanism, and that including the latter insertion is called modified Chalk-Harrod mechanism. In these two reaction mechanisms, the oxidative addition and reductive elimination are involved as key elementary steps. The Pt-catalyzed hydrosilylation occurs through the Chalk-Harrod mechanism, while the Rh-catalyzed hydrosilylation occurs through the modified Chalk-Harrod mechanism. We clarified the reasons previously [72, 73]. On the one hand, the different reaction between Cp_2Zr(olefin) with silane was experimentally proposed, as shown in Scheme 11.13 [74, 75], while on the other hand, direct evidence has not been presented. In this mechanism, the new reaction of Eq. 11.18a was involved.

$$Cp_2Zr\,(C_2H_4) + H - SiH_3 \rightarrow Cp_2Zr\,(H)\,(CH_2CH_2SiH_3) \quad (11.18a)$$
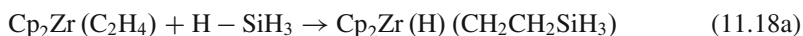
This type of reaction can be understood to be the σ-bond activation of the Si–H bond by the metal-olefin moiety, because the Zr-silyl and C-silyl bonds are
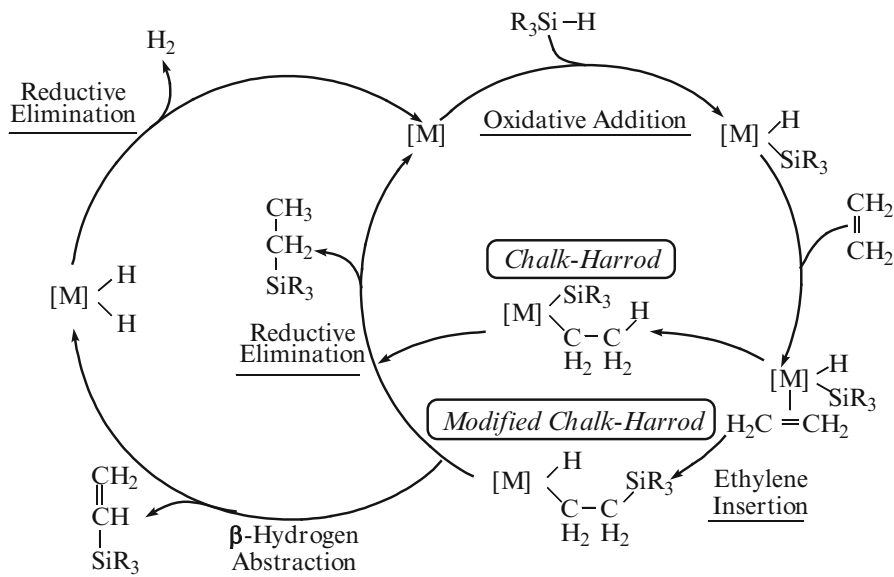
Scheme 11.12 Metal-catalyzed hydrosilylation of orefine, Chalk-Harrod mechanism and modified Chalk-Harrod mechanism
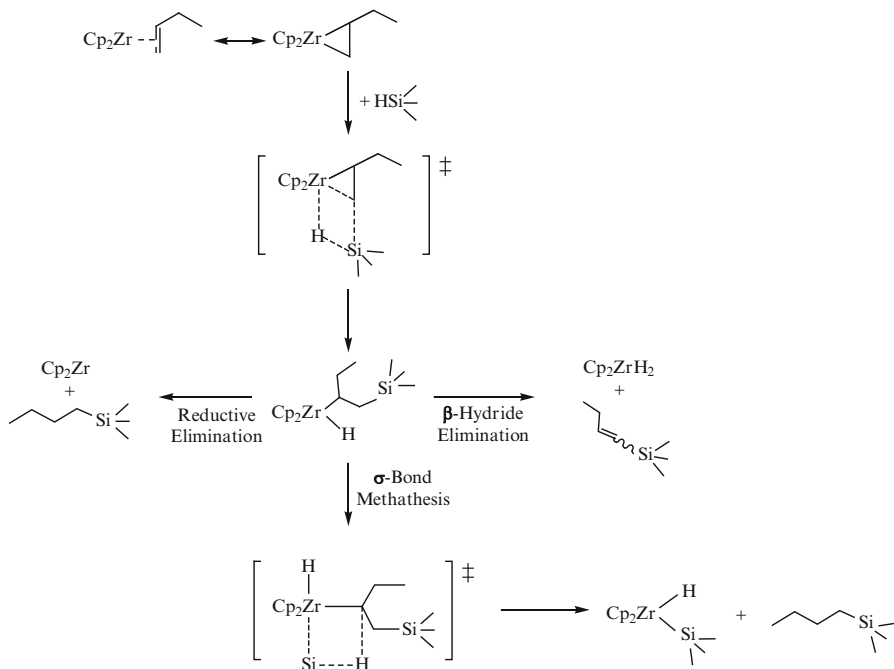
Scheme 11.13 New reaction scheme between Zr-alkene complex and silane (Reproduced from Ref. [75]. With kind permission of © The American Chemical Society 1992)
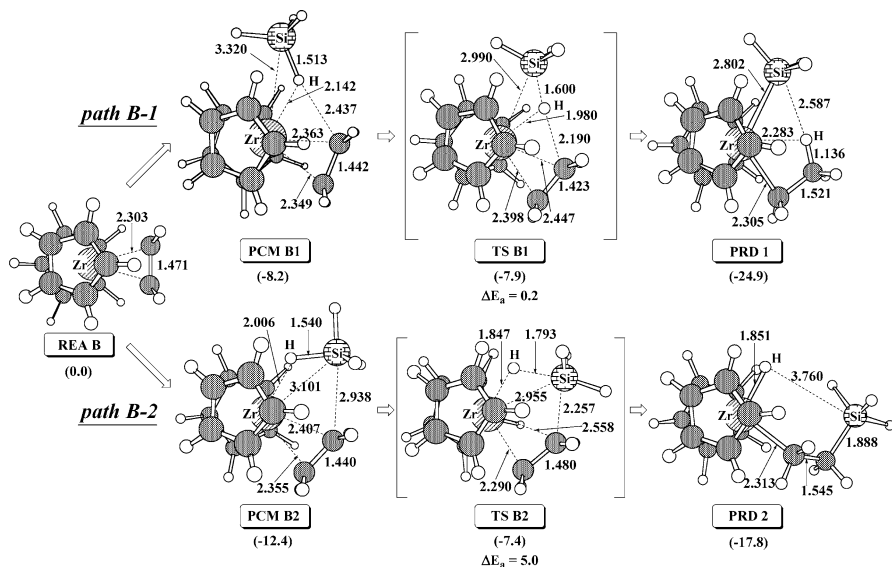
Fig. 11.12 Geometry changes in the reaction of silane and Cp₂Zr(ethylene) (Reproduced from Ref. [71b]. With kind permission of © The American Chemical Society 2004)

formed concomitantly with the Si–H σ-bond breaking as given in Eq. 11.3. This reaction was theoretically investigated with the DFT method. As shown in Fig. 11.12 [71], silane approaches the Zr-(alkene) moiety. In the transition state, the Si center seems to take a five-coordinate trigonal bipyramidal structure, suggesting that the Si center takes hypervalency. Although only Cp₂Zr(H)(CH₂CH₂SiH₃) was proposed as an intermediate in the experimental work, the computational study indicated that another product Cp₂Zr(SiH₃)(CH₂CH₃) was formed with similar or even smaller activation barrier.

$$Cp_2Zr\,(C_2H_4) + H - SiH_3 \rightarrow Cp_2Zr\,(SiH_3)\,(CH_2CH_3) \qquad (11.18b)$$
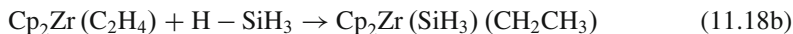
The energy changes were calculated by the DFT method with B3LYP functional and the MP2 to MP4(SDQ) methods. As shown in Table 11.5, both reactions easily occur with small activation barriers and considerably large exothermicities. It is noted that the DFT method with B3LYP functional presents small stabilization energy of the precursor silane complex, Cp₂Zr(C₂H₄)(H–SiH₃). This type of underestimation of the stabilization energy of the reactant complex is often observed when we employed B3LYP and similar hybrid functionals, as mentioned above. The activation barrier (Ea) and reaction energy (ΔE) moderately fluctuate around the MP2 and MP3 but seem to converge when moving to MP4(SDQ). These results indicate that the MP4(SDQ) method presents reliable Ea and ΔE values. On the other hand, the DFT(B3LYP) presents much smaller Ea and ΔE values.

Table 11.5 Energy changes (in kcal/mol) in the reaction between SiH_4 and $Cp_2Zr(C_2H_4)$

Product	$Cp_2Zr(C_2H_5)(SiH_3)$			$Cp_2Zr(H)(C_2H_5\text{-}SiH_3)$		
	BE	Ea	DE	BE	Ea	DE
DFT(B3LYP)	−8.2	0.3	−24.9	−12.4	5.0	−17.8
MP2	−19.9	1.8	−36.4	−25.4	5.3	−24.2
MP3	−15.3	1.4	−32.5	−19.4	6.5	−24.4
MP4(DQ)	−15.8	1.2	−33.3	−20.0	6.3	−24.4
MP4(SDQ)	−16.6	0.8	−35.9	−21.2	4.9	−26.0

Transition state leading to
$Cp_2Zr(C_2H_5)(SiH_3)$

Transition state leading to
$Cp_2Zr(H)(C_2H_5SiH_3)$
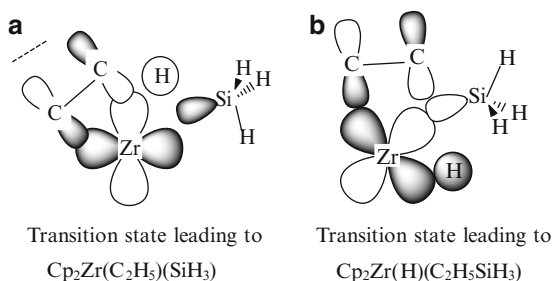
Scheme 11.14 HOMO of Transition state of the reaction between $Cp_2Zr(C_2H_4)$ and SiH_4. (**a**) Transition state leading to $Cp_2Zr(C_2H_5)(SiH_3)$; (**b**) transition state leading to $Cp_2Zr(H)(C_2H_5SiH_3)$ (Reproduced from Ref. [36]. With kind permission of © The American Chemical Society (2007))

In several experimental works, the Zr–C bond was discussed to be strong and the metallacyclopropane is involved in Cp_2Zr(olefin). In such case, the Zr center is considered to takes +IV oxidation state. However, it is unlikely to consider that the olefin moiety becomes dianion. If we think it is unlikely, the Zr center in Cp_2Zr(olefin) is considered to take +II oxidation state. In these reactions, Eq. 11.18a and 18b, the oxidation state of the Zr center increases by 2 because the product possesses one hydride and one alkyl groups (or one alkyl and one silyl groups), which are considered to be anion. In other words, these reactions are understood to be oxidative addition to the M–L moiety.

It is of considerable interest to clarify the orbital interaction, which plays important roles in these reactions. Reasonable orbital interaction schemes were proposed in the theoretical study, as shown in Scheme 11.14. The Si–H σ^*-antibonding MO overlaps well with the d_π-π^* bonding MO between the Zr d_π orbital and C_2H_4 π^* MO in a bonding way in both reactions 11.18a and 11.18b. This type of interaction becomes possible because a very good overlap is formed between the Zr d_π orbital and C_2H_4 π^* MO. Such good overlap is formed because the Zr d_π orbital exists at high energy.

a

The reaction of Cr(0)-silabenzene complex with water

b
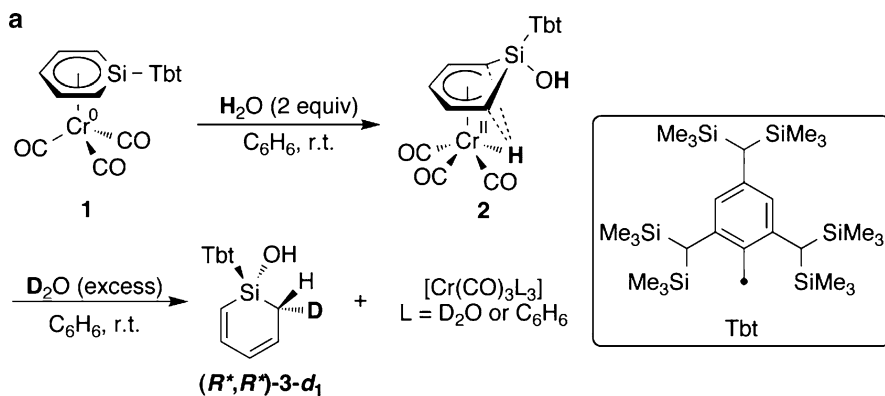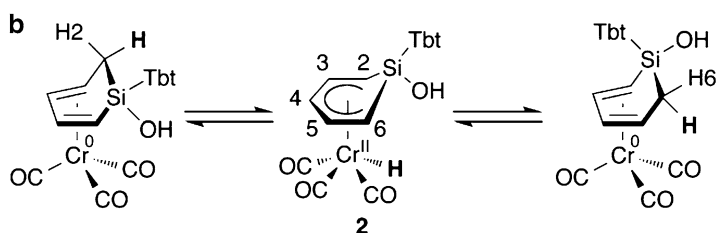
Flexible feature of the product

Scheme 11.15 O–H σ-bond activation with Cr(0)-silabenzene complex. (**a**) The reaction of Cr(0) silabenzene complex with water; (**b**) flexible feature of the product (This figure is reproduced from Ref. [76a] under permission of CSJ

11.3.2   Experimental Evidence of Oxidative Addition of σ-Bond to M–L Moiety

Recently, Tokitoh and his coworkers experimentally reported this type of oxidative addition to the M–L moiety in their Cr(0)-η^6-silabenzene complex, as shown in Scheme 11.15a [76]. In this reaction, the Cr-silabenzene moiety reacts with the O–H bond to induce the O–H σ-bond cleavage to form the Cr–H and Si–OH bonds. In the product, the Cr oxidation state is +2 because the H ligand is considered to be an anion and the C$_5$SiH$_5$Tbp-OH moiety is also considered to be an anion. Further, the H atom transfer from the Cr center to one of the carbon atoms of silabenzene was reported, as shown in Scheme 11.15b, in which the Cr center becomes 0 oxidation state. This indicates that the Cr oxidation state is flexible. It is likely that the important driving force of this reaction is the formation of the strong Si–OH bond. It is interesting to apply this complex to the X–H σ-bond activation where X represents electronegative group.

Although the examples of this type of σ-bond activation via oxidative addition to M–L moiety have been limited so far, I believe that this type of σ-bond activation would be found in many transition metal complexes in future.

11.4 Catalytic Reactions Involving Heterolytic σ-Bond Activation

The heterolytic σ-bond activation is involved as key elementary step in many catalytic reactions. One of the good examples is Ru-catalyzed hydrogenation of carbon dioxide [77]. We theoretically investigated all possible reaction courses of this reaction, as shown in Scheme 11.16 and found that this reaction occurs through CO_2 insertion into the Ru–H bond to form a η^1-formate intermediate and subsequent six-center σ-bond metathesis with dihydrogen molecule in the absence of water molecule [78]. The four-center transition state for the metathesis is much more unstable than the six-center transition state. The other possible reaction course is reductive elimination between the H and formate ligands because one H ligand still coordinates with the Ru center after the CO_2 insertion. However, the three-center transition state of reductive elimination is more unstable than the four-center σ-bond metathesis and the five-center transition state of the reductive elimination is more unstable than the six-center transition state of σ-bond metathesis. This six-center σ-bond metathesis of dihydrogen molecule is essentially the same as the heterolytic σ-bond activation of the C–H σ-bond of benzene with $Pd(\eta^2\text{-}O_2CH)$, as shown in Fig. 11.13. In this transition state, the H atom is moving from the Ru center to the O atom of carbon dioxide. This transition state structure comes from the presence of lone pair orbital on the O atom of formate, as shown in Scheme 11.17. In the four-center transition state, one O atom that interacts with the M center must start
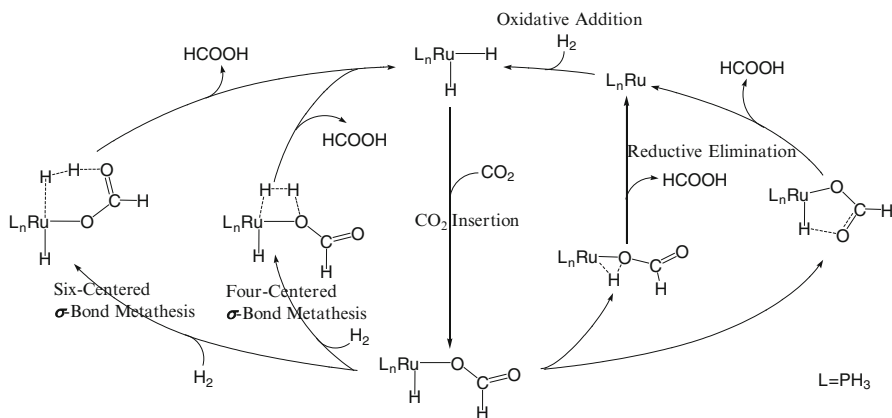
Scheme 11.16 Possible reaction courses of Ru-catalyzed hydrogenation of CO_2 to formic acid
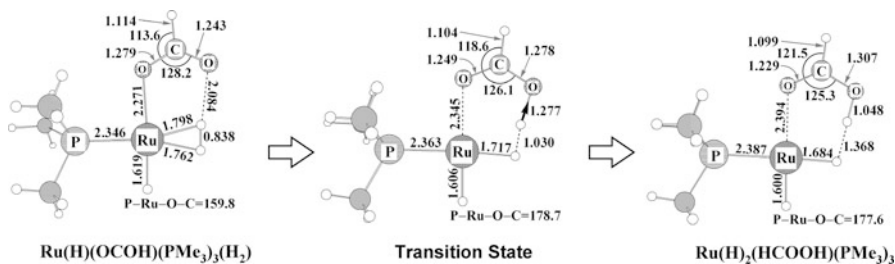
Fig. 11.13 DFT-optimized geometry changes by the metathesis of $Ru(H)(\eta^1\text{-OCOH})(PMe_3)_3$ with the dihydrogen molecule (two PMe_3 ligands in *front* of and *behind* the Ru center are omitted in all the figures to show clearly the geometry changes by the reaction). Bond lengths are in angstrom and bond angles are in degree. *Arrow in transition state* represents geometry changes involved in each imaginary frequency (Reproduced from Ref. [78]b. With kind permission of © The American Chemical Society 2005)
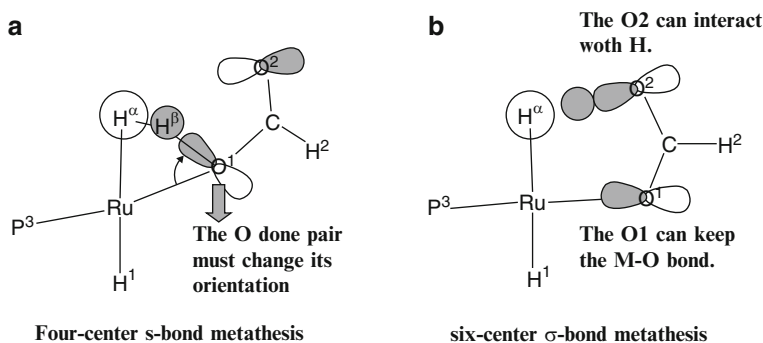
Scheme 11.17 Bi-dentate bonding nature of η^1-formate. (**a**) Four-center σ-bond metathesis; (**b**) six-center σ-bond metathesis (Reproduced from Ref. [78]a. With kind permission of © The American Chemical Society (2000))

to interact with polarized dihydrogen molecule (see Scheme 11.17a). In the six-center transition state, one O atom of the formate interacts with metal center using one lone pair and the remaining O atom can interact with polarized dihydrogen molecule, as shown in Scheme 11.17b. Thus, the M-(η^1-OCOH) moiety performs the six-center heterolytic σ-bond activation without large energy loss. This situation is more favorable than that of the four-center transition state because the O atom interacting with the metal center must interact with one of H atoms of dihydrogen molecule in the four-center transition state, as shown in Scheme 11.17a. However, the four-center metathesis was theoretically reported to occur in the reaction of Rh(I)-(η^1-OCOH) complex and dihydrogen molecule [79].

Because the main purpose of Ref. [78] was to clarify the reaction mechanism, no discussion was presented on the reason why the six-center heterolytic σ-bond activation is more favorable here than the reductive elimination. However, the
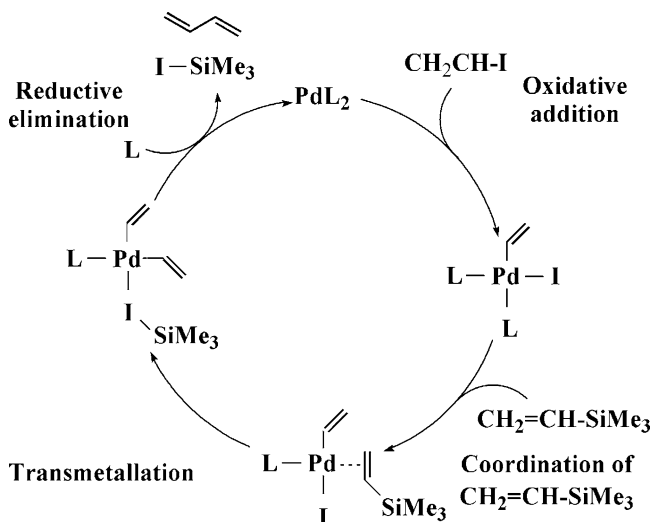
Scheme 11.18 Reaction mechanism of the Hiyama Cross-Coupling Reaction

heterolytic σ-bond activation of dihydrogen molecule with the M-(η^1-OCOH) moiety was compared with the reductive elimination in other theoretical work [80]. It was concluded that the heterolytic σ-bond activation of dihydrogen molecule occurs easier than the reductive elimination when the M–H bond is strong. This means that the reductive elimination does not occur in such cases because the strong M–H bond must be broken in the reductive elimination. In other words, the relative strengths of M–H and O–H bond energies determine the reaction course on which of heterolytic σ-bond activation and reductive elimination occurs as the product releasing step in the catalytic cycle.

Another good example is the Pd-catalyzed cross-coupling reaction such as the Suzuki-Miyaura cross-coupling reaction, Pd-catalyzed borylation of iodobenzene with diborane [81], and the Hiyama cross-coupling reaction (Pd-catalyzed cross-coupling reaction between vinyliodide and vinylsilane) [82]. In this type of reaction, transmetallation is involved as key elementary step. We theoretically investigated Pd-catalyzed borylation of iodobenzene with diborane [83] and the Hiyama cross-coupling reaction [84] and reported that the transmetallation is understood to be heterolytic σ-bond activation [83, 84]. Here, we wish to focus on the theoretical study of the Hiyama cross-coupling reaction, because this reaction is interestingly accelerated very much by addition of fluoride anion to the reaction solution.

This catalytic reaction is believed to occur via oxidative addition of vinyliodide to Pd(0) complex to afford Pd(II)-vinyl complex, transmetallation from vinylsilane to Pd(II)-vinyl complex, and reductive elimination of conjugate diene, as shown in Scheme 11.18. We evaluated the energy changes along these elementary steps in the absence of fluoride anion, as shown in Fig. 11.14. Apparently, the transmetallation needs significantly large activation barrier. This large activation barrier indicates
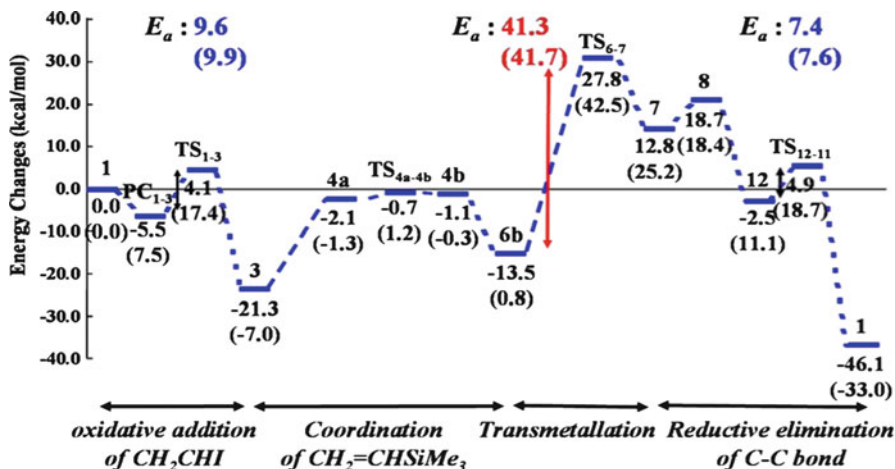
Fig. 11.14 The energy changes by whole catalytic cycle of Pd-catalyzed cross-coupling reaction of vinyliodide and vinylsilane in the absence of fluoride anion. The DFT method was employed. In *parentheses* are free energy (Reproduced from Ref. [84]. With kind permission of © The American Chemical Society 2008)
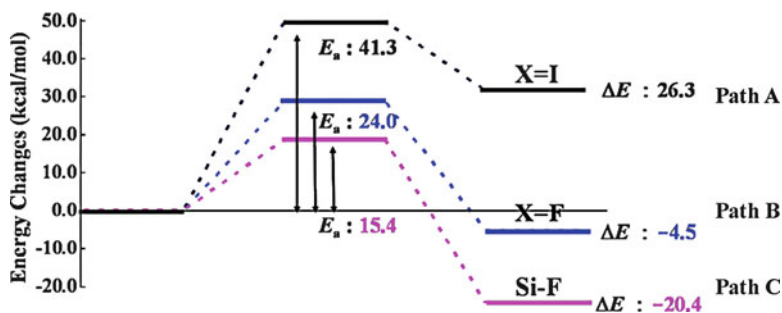
Scheme 11.19 Comparison of energetic in the transmetallation among the Pd(II)-iodide complex, Pd(II)-fluoride complex, and the nucleophilic attack of fluoride from the outside of vinylsilane

that the cross-coupling reaction is difficult in the absence of fluoride anion. When the iodide ligand is substituted for the fluoride ligand, the transmetallation occurs in $Pd(CH=CH_2)F(PMe_3)$. The activation barrier (24.3 kcal/mol) is moderate and the reaction becomes exothermic (6.4 kcal/mol); see Path *B* in Scheme 11.19, in comparison with the transmetallation of $Pd(CH=CH_2)I(PMe_3)$ (Path *A* in Scheme 11.19). Another possibility is that the fluoride anion attacks the Si center to induce the transfer of the vinyl group to the Pd(II) center, which is called Path *C* (Scheme 11.19). This is a little bit different σ-bond activation, which we summarized in Introduction. In this σ-bond activation, the third species participates in the reaction to activate the σ-bond. As shown in Fig. 11.15, the fluoride anion is

$$Pd-C^2= 2.424$$
$$C^2-Si = 1.911$$
$$Si-F = 3.243$$

$$Pd-C^2= 2.239$$
$$C^2-Si = 2.424$$
$$Si-F = 1.795$$

$$Pd-C^2= 2.048$$
$$Si-F = 1.632$$
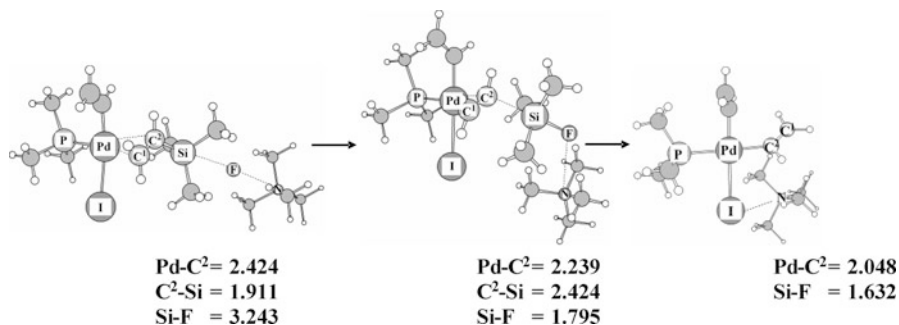
Fig. 11.15 Transmetallation of $Pd(CH=CH_2)I(PMe_3)$ with vinylsilane $(CH_2=CH)(SiMe_3)$ induced by nucleophilic attack of fluoride to the Si center (Reproduced from Ref. [84]. With kind permission of © The American Chemical Society 2008)

approaching the Si center from the opposite side of the Pd center. Interestingly, the $SiMe_3$ moiety becomes almost planar and the vinyl group is moving from the Si center to the Pd(II) center in the transition state. These reaction features are essentially the same as those of S_N2 substitution reaction. The activation barrier becomes very small and the reaction becomes considerably exothermic (Scheme 11.19). It is worth elucidating why the significantly large difference is observed among Paths *A*, *B*, and *C*. In the reaction of $Pd(CH_2=CH)I(PMe_3)$ with $(CH_2=CH)SiMe_3$ (Path *A*), the Pd–I bond changes to the Pd–$(ISiMe_3)$ coordinate bond and the Si–vinyl bond is broken, while the Si–I covalent bond is formed. In the reaction of $Pd(CH_2=CH)F(PMe_3)$ with $(CH_2=CH)SiMe_3$ (Path *B*), the Pd–F bond changes to Pd–$(FSiMe_3)$ coordinate bond and the Si–vinyl bond is broken, while the Si–F covalent bond is formed. Although the Pd–F bond is stronger than the Pd–I bond, the Si–F bond is much stronger than the Si–I bond. As a result, the transmetallation of $Pd(CH=CH_2)F(PMe_3)$ occurs easier than that of $Pd(CH=CH_2)I(PMe_3)$. In the reaction of $Pd(CH=CH_2)I(PMe_3) + [NMe_4]F$ with $(CH_2=CH)SiMe_3$ (Path *C*), the Si–vinyl bond is broken and the Si–F covalent bond is formed, while the Pd–I bond does not change at all. Because the strong Si–F bond is formed without any change of the Pd–I coordinate bond, Path *C* is the best.

$$\Delta E_{cov} = \sqrt{(\varepsilon_A - \varepsilon_B)^2 + 4\beta^2} \qquad (11.19a)$$

$$\Delta E_{cov}^{approx} = |\varepsilon_A - \varepsilon_B| + \frac{\beta^2}{|\varepsilon_A - \varepsilon_B|} \qquad (11.19b)$$

Considering the above results, it is concluded that the acceleration by addition of fluoride anion arises from the formation of the strong Si–F bond. This is essentially the same as the C–H σ-bond activation of benzene by Pd(II) formate complex in which the formation of the strong O–H bond is the driving force. The next issue is to clarify the reason why the Si–F bond is much stronger than the Si–I bond. The reason is easily found, as follows. Based on simple Hückel MO theory, the covalent
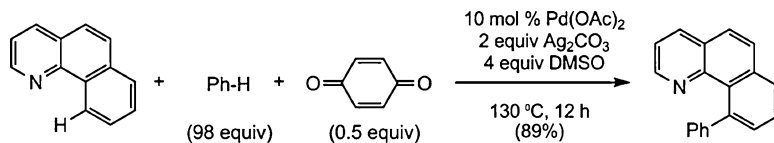
Scheme 11.20 Direct-cross coupling reaction catalyzed by Pd(II) (This figure is reproduced from Ref. [23]. Under kind permission of © American Chemical Society 2007)

bond energy is approximately represented by Eqs. 11.19a and 11.19b [84, 85], where ε_A and ε_B are valence orbital energies of A and B, respectively, and β is resonance integral. Equation 11.19b is derived from Eq. 11.19a, when $|\varepsilon_A - \varepsilon_B|$ is much larger than $|\beta|$. From these equations, one can easily expect that the covalent bond energy increases as the orbital energy difference increases. The valence orbital energy is calculated to be –9.1 eV for $SiMe_3$, –11.9 eV for iodine, and –14.4 eV for fluorine. Although these are Kohn-Sham orbital energies calculated by the DFT method with B3LYP functional, the Hartree-Fock orbital energy presents the same trend. Thus, the Si–F bond is much stronger than the Si–I bond because the difference in energy between valence orbitals of·$SiMe_3$ and fluorine is much larger than that between·$SiMe_3$ and iodine. Because the valence orbital of $SiMe_3$ exists at high energy, use of electronegative X group leads to formation of strong Si–X bond, which is crucial for the acceleration of the transmetallation.

In the Pd-catalyzed borylation of iodobenzene with diborane, we found that the transmetallation occurs via heterolytic σ-bond activation of the B–B bond and that the electronegative group accelerates the transmetallation like the Hiyama cross-coupling reaction [83].

We wish to report one more theoretical studies of catalytic reaction including heterolytic C–H σ-bond activation [86]. Recently, direct cross-coupling reaction between two aromatic compounds by Pd(II) complex was reported, as shown in Scheme 11.20 [23]. This reaction occurs only when benzoquinone is added to reaction solution. Theoretical study was carried out with DFT and ONIOM(CCSD(T):DFT) methods. The first step is the C–H σ-bond activation of 10-phenylbenzo[h]quinoline by Pd(η^2-$O_2CMe)_2$, like the C–H activation of benzene by Pd(η^2-$O_2CH)_2$. The geometry changes are essentially the same as those of the activation by Pd(η^2-$O_2CH)_2$, as shown in Fig. 11.16a. The next step is coordination of benzoquinone. Then, the second C–H activation of benzene occurs by the remaining acetate on the Pd center, as shown in Fig. 11.16b. The final step is reductive elimination of C–C bond. Benzoquinone plays a role to accelerate the reductive elimination, not the C–H activation. We believe that the combination of metal and acetate or similar ligand is useful for this type of synthetic reaction. It should be noted that the C–H σ-bond activation of aromatic compound by the Pd(η^2-O_2CMe) moiety is very important in this type of catalytic synthesis.

In summary, the heterolytic σ-bond activation plays crucial roles in catalytic reactions by transition metal complex. The transmetallation involved in cross-coupling reaction is understood in terms of heterolytic σ-bond activation. One of
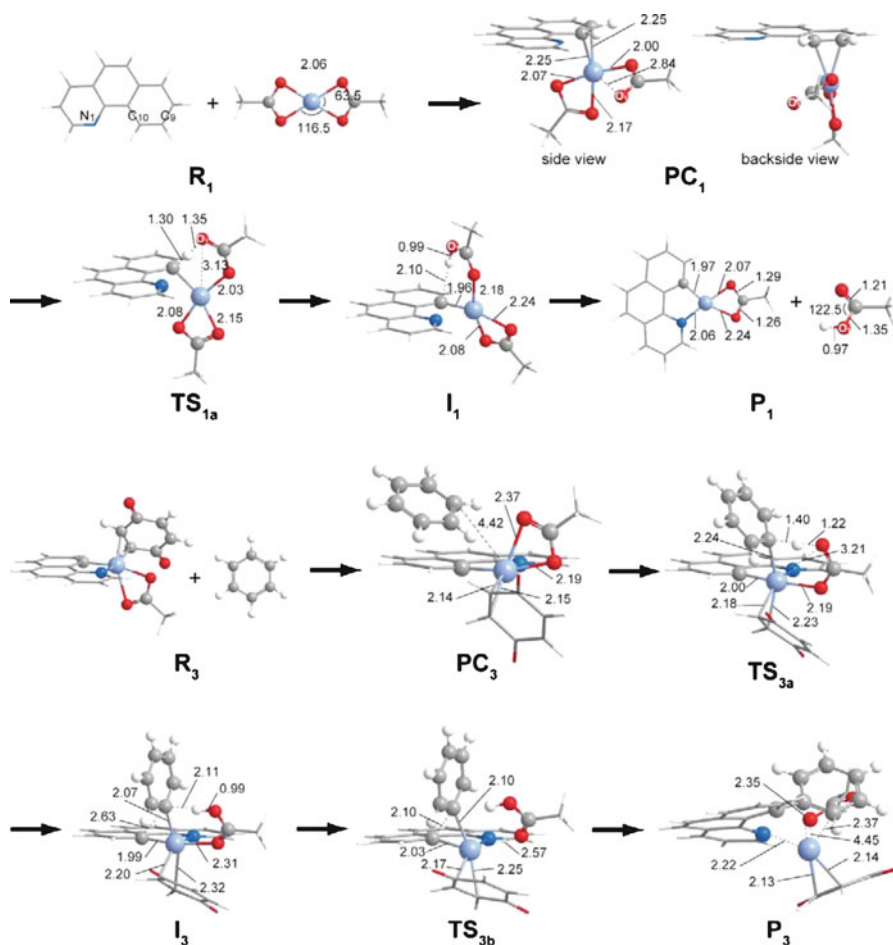
Fig. 11.16 Geometry changes in C–H activation of aromatic compound by $Pd(\eta^2\text{-}O_2CMe)_2$ (Reproduced from Ref. [86]. With kind permission of © The Royal Society of Chemistry 2010)

the most important results here is that the formation of polarized bond such as Si–F bond is the driving force of the heterolytic σ-bond activation. This is one of the important factors in the heterolytic σ-bond activation. Considering this driving force, we wish to present theoretical proposal that the use of electronegative group accelerates the transmetallation, because the boryl and silyl groups often used in the transmetallation are electropositive. Because the C–H σ-bond activation of aromatic compounds with the Pd(II)-acetate easily occurs, this reaction can be utilized for many synthetic reactions. We expect that the combination between metal and anionic ligand would increase the application of this type of activation reaction.

11.5 Future Perspectives

Apparently, the σ-bond activation and its reverse reaction (the σ-bond formation) by transition metal complex are involved as the key elementary steps in many catalytic reactions. This is because the bond breaking followed by the C–C bond formation or C–X bond formation (X = functional group) is involved as important process in many catalytic reactions. In this regard, the correct knowledge of σ-bond activation reaction is crucial for further development of organometallic reactions and catalytic reactions by transition metal complexes. Thus, we believe that theoretical inspection to the σ-bond activation is necessary for further development of catalytic reaction. In fundamental chemistry, of course, theoretical study of σ-bond activation is of considerable interest, because the interaction between transition metal and σ-bond is not clear and not obvious.

In my understanding, the oxidative addition has been investigated well by many theoreticians. We believe that fundamental knowledge and the essence of the heterolytic σ-bond activation have been clearly presented here. On the other hand, the oxidative addition to the M–L moiety has not been theoretically and experimentally investigated well. This type of reaction must be theoretically investigated well in the near future. In this reaction, the metal oxidation state increases by 2 by the conversion of neutral ligand to anion ligand. We need to clarify the driving force and important orbital interactions in this type of reaction. Also, the C–H activation by radical species is important in the chemistry of transition metal complexes. Such σ-bond activation has not been investigated well theoretically. The σ-bond activation by metal oxide must be carefully investigated with post–Hartree-Fock method. In this reaction, spin state changes several cases. The relative stabilities of various spin states depend on functional of the DFT method, and also, electron correlation effects depend on spin state.

Theoretical chemistry must provide experimentalists with correct understanding, fundamental knowledge, and correct prediction. What transition metal system is useful for the σ-bond activation and the catalytic reaction including the σ-bond activation? If theoretician can present clear answer to such question, the chemistry of transition metal complexes can be made further development.

References

1. Recent reviews: (a) Morokuma K, Musaev J (eds) (2008) Computational modeling for homogeneous and enzymatic catalysis, Wiley-VCH, Weinheim; (b) Maseras F, Lledós A (eds) (2002) Computational modeling of homogeneous catalysis. Kluwer Academic, Drodrecht; (c) Dedieu A (1999) Top Organomet Chem 4:69; (d) Torrent M, Sola M, Frenking G (2000) Chem Rev 100:433

2. Sakaki S, Ohnishi Yy, Sato H (2010) Chem Rec 10:49
3. (a) Miyaura N, Suzuki A (1995) Chem Rev 95:2457; (b) Suzuki A (1999) J Organomet Chem 576:147; (c) Miyaura N (2008) Bull Chem Soc Jpn 81:1535; (d) Miyaura N (2002) Cross-coupling reactions. Topics in current chemistry series, vol 219. Springer, New York, p 111
4. Recent reviews for C–H σ-bond activation: (a) Crabtree RH (1985) Chem Rev 85:245; (b) Crabtree RH (1995) Chem Rev 95:987; (c) Crabtree RH (2004) J Organomet Chem 689:4083; (d) Crabtree RH (2001) (trans: Dalton) J Chem Soc 2437
5. Arndtsen BA, Bergman RG, Mobley TA, Peterson TH (1995) Acc Chem Res 28:154
6. Jones WD (1999) Top Organomet Chem 3:9
7. Sen A (1999) Top Organomet Chem 3:81
8. Labingerand JA, Bercaw JE (2002) Nature 417:507
9. Shilov AE, Shul'pin GB (1997) Chem Rev 97:2879
10. Colby DA, Bergman RG, Ellman JA (2010) Chem Rev 110:624
11. Gunay A, Theopold KH (2010) Chem Rev 110:1060
12. Lyons TW, Sanford MS (2010) Chem Rev 110:1147
13. (a) Sakaki S (2005) Topics in organometallic chemistry, vol 12. In: Frenking G (ed) Theoretical aspects of transition metal catalysis. Springer, Berlin, p 31; (b) Sakaki S (2003) Bull Korean Chem Soc 24:829
14. Niu SQ, Hall MB (2000) Chem Rev 100:353
15. Dedieu A (2000) Chem Rev 100:543
16. Balcels D, Clot E, Eisenstein O (2010) Chem Rev 110:749
17. Tatsumi K, Hoffmann R, Yamamoto A, Still JK (1981) Bull Chem Soc Jpn 54:1857
18. Shilov AE (1984) Activation of saturated hydrocarbons by transition metal complexes. D. Riedel, Dordrecht
19. Siegbahn PEM, Crabtree RH (1996) J Am Chem Soc 118:4442
20. (a) Moritani I, Fujiwara Y (1967) Tetrahedron Lett 1119; (b) Fujiwara Y, Takagi K, Taniguchi Y (1006) Synlett 591, and references therein
21. Ackermann L (2011) Chem Rev 111:1315
22. Beccalli EM, Broggini G, Martinelli M, Sottocornola S (2007) Chem Rev 107:5318
23. (a) Hull KL, Sanford MS (2007) J Am Chem Soc 129:11904; (b) Lyons TW, Hull KL, Sanford MS (2011) J Am Chem Soc 133:4455
24. Chen X, Li JJ, Hao XS, Goodhue CE, Yu JQ (2006) J Am Chem Soc 128:78
25. Wu J, Cui X, Chen L, Jiang G, Wu Y (2009) J Am Chem Soc 131:13888
26. Biswas B, Sugimoto M, Sakaki S (2000) Organometallics 19:3985
27. Periana RA, Taube DJ, Gamble S, Taube S, Satoh T, Fujii H (1998) Science 280:560
28. (a) Kua J, Xu X, Periana RA, Goddard WA III (2002) Organometallics 21:511; (b) Xu X, Kua J, Periana RA, Goddard WA III (2003) Organometallics 22:2057
29. Cummins CC, Schaller CP, Van Duyne GD, Wolczanski PT, Chan EA-W, Hoffmann R (1991) J Am Chem Soc 113:2985
30. Bailey BC, Fan H, Baum EW, Huffman JC, Baik M-H, Mindiola DJ (2005) J Am Chem Soc 127:16016
31. (a) Schaller CP, Cummins CC, Wolczanski PT (1996) J Am Chem Soc 118:591; (b) Schaller CP, Bonanno JB, Wolczanski PT (1994) J Am Chem Soc 116:4133; (c) Schaller CP, Wolczanski PT (1993) Inorg Chem 32:131; (d) Schafer DF II, Wolczanski PT (1998) J Am Chem Soc 120:4881
32. de With J, Horton AD (1993) Angew Chem Int Ed Engl 32:903–905
33. Hoyt HM, Bergman RG (2007) Angew Chem Int Ed Engl 46:5580
34. (a) Cundari TR (1992) J Am Chem Soc 114:10557; (b) Cundari TR (1993) Organometallics 12:1998; (c) Cundari TR (1993) Organometallics 12:4971; (d) Cundari TR (1994) J Am Chem Soc 116:340; (e) Benson MT, Cundari TR, Moody EW (1995) J Organomet Chem 504:1; (f) Cundari TR, Matsunaga N, Moody EW (1996) J Phys Chem 100:6475; (g) Cundari TR, Klinchkman TR, Wolczanski PT (2002) J Am Chem Soc 124:1481
35. (a) Cundari TR (2000) Chem Rev 100:807; (b) Cundari TR, Gordon MS (1991) J Am Chem Soc 113:5231; (c) Cundari TR, Gordon MS (1992) J Am Chem Soc 114:539; (d) Cundari TR

(1992) J Am Chem Soc 114:7879; (e) Cundari TR (1992) J Am Chem Soc 114:10557; (f) Cundari TR (1993) Organometallics 12:1998

36. Ochi N, Nakao Y, Sato H, Sakaki S (2007) J Am Chem Soc 129:8615
37. (a) Kameno Y, Ikeda A, Nakao Y, Sato, H, Sakaki S (2005) J Phys Chem A 109:8055; (b) Ikeda A, Nakao Y, Sato H, Sakaki S (2007) J Phys Chem A 111:7124–7132; (c) Ikeda A, Kameno Y, Nakao Y, Sato H, Sakaki S (2007) J Organomet Chem 692:299–306
38. Zhao Y, Truhlar DG (2008) Acc Chem Res 41:157
39. Ohnishi YY, Nakao Y, Sato H, Sakaki S (2007) J Phys Chem A 111:7915
40. Ochi N, Nakao Y, Sato H, Sakaki S (2009) Can J Chem 87:1415
41. (a) Zhao J, Goldman AS, Hartwig JF (2005) Science 307:1080; (b) Kanzelberger M, Zhang X, Emge TJ, Goldman AS, Zhao J, Incarvito C, Hartwig JF (2003) J Am Chem Soc 125:13644
42. (a) Ziegler T, Tschinke V, Becke A (1987) J Am Chem Soc 109:1351; (b) Ziegler T, Cheng W, Baerend ET, Ravenek W (1988) Inorg Chem 27:3458; (c) Ziegler T, Tschinke V, Versluis L (1988) Polyhedron 7:1625
43. Baba H, Suzuki S, Takemura T (1969) J Chem Phys 50:2078
44. Kato S, Yamabe S, Fukui K (1974) J Chem Phys 60:572
45. Frenking G (1995) J Phys Chem 99:9352
46. Bennett JL, Wolczanski PT (1997) J Am Chem Soc 119:1
47. (a) Walsh PJ, Baranger AM, Bergman RG (1992) J Am Chem Soc 114:1708; (b) Poise JL, Anderson RA, Bergman RG (1998) J Am Chem Soc 120:13405; (c) Anderson LL, Schmidt JAR, Arnold J, Bergman RG (2006) Organometallics 25:3394
48. Vujkovic N, Ward BD, Maisse-Francois A, Wadepohl H, Mountford P, Gade LH (2007) Organometallics 26:5522
49. (a) Fu GC, Grubbs RH (1992) J Am Chem Soc 114:5426; (b) Fu GC, Grubbs RH (1992) J Am Chem Soc 114:7324; (c) Fu GC, Grubbs RH (1993) J Am Chem Soc 115:3800; (d) Fujimura O, Fu GC, Grubbs RH (1994) J Org Chem 59:4029; (e) Grubbs RH, Miller SJ, Fu GC (1995) Acc Chem Res 28:446, and references therein
50. Crowe WE, Zhang ZJ (1993) J Am Chem Soc 115:10998
51. (a) Schlund R, Schrock RR, Crowe WE (1989) J Am Chem Soc 111:8004; (b) Schrock RR, Murdzek JS, Bazan GC, Robbins J, DiMare M, O'Regan M (1992) J Am Chem Soc 112:3875
52. Ochi N, Nakao Y, Sato H, Sakaki S (2010) J Phys Chem A 114:659–665
53. (a) Yoshizawa K, Shiota Y, Yamabe T (1998) J Am Chem Soc 120:564; (b) Yoshizawa K, Shiota Y, Yamabe T (1998) Organometallics 17:2825; (c) Yoshizawa K, Shiota Y, Yamabe T (1999) J Am Chem Soc 121:147; (d) Shiota Y, Suzuki K, Yoshizawa K (2005) Organometallics 24:3532
54. (a) Böhme DK, Schwarz H (2005) Angew Chem Int Ed Engl 44:2336; (b) Dietl N, Schlangen M, Schwartz H (2011) Chem-A Eur J 17:1783; (c) Bozˇovic´ A, Feil S, Koyanagi GK, Viggiano AA, Zhang X, Schlangen M, Schwarz H, Bohme DK (2010) Chem Euro J 16:11605–11610
55. Li HY, Guo YL, Guo Y, Lu GZ (2008) J Chem Phys 128:051101
56. Fu G, Chen ZN, Xu X, Wan HL (2008) J Phys Chem A 112:717
57. Fu G, Xu X, Lu X, Wan H (2005) J Am Chem Soc 127:3989
58. Chiodo S, Kondakova O, Michelini MC, Russo N, Sicilia E (2003) Inorg Chem 42:8773
59. Kretschmer R, Zhang X, Schlangen M, Schwarz H (2011) Chem Euro J 17:3886
60. (a) Goure E, Avenier P, Solans-Monfort X, Veyre L, Baudouin A, Kaya Y, Taoufik M, Basset JM, Eisenstein O, Quadrelli OA (2011) New J Chem 35:1011; (b) Avenier P, Solans-Monfort X, Veyre L, Renili F, Basset JM, Eisenstein O, Taoufik M, Quadrelli EA (2009) Top Catal 52:1482
61. See also references cited in ref. 12. (a) Maron L, Eisenstein O (2001) J Am Chem Soc 123:1036; (b) Perrin L, Maron L, Eisenstein O (2002) Inorg Chem 41:4355; (c) Maron L, Perrin L, Eisenstein O (2002) J Chem Soc Dalton Trans 534; (d) Clot E, Megret C, Kraft BM, Eisenstein O, Jones WD (2004) J Am Chem Soc 126:5647; (e) Maron L, Werkema EL, Perrin L, Eisenstein O, Andersen RA (2005) J Am Chem Soc 127:279; (f) Barros N, Eisenstein O, Maron L (2006) Dalton Trans 3052; (g) Perrin L, Eisenstein O, Maron L (2007) New J Chem 31:549; (h) Werkema EL, Andersen RA, Yahia A, Maron L, Eisenstein O

(2009) Organometallics 28:3173; (i) Perrin L, Maron L, Eisenstein O, Tilley TD (2009) Organometallics 28:3767; (j) Werkema EL, Andersen RA, Maron L, Eisenstein O (2010) Dalton Trans 39:6648; (k) Guihaume J, Raynaud C, Eisenstein O, Perrin L, Maron L, Tilley TD (2010) Angew Chem Int Ed Engl 49:1816; (l) Werkema EL, Andersen RA, Maron L, Eisenstein O (2010) Dalton Trans 39:6648; (m) Werkema EL, Yahia A, Maron L, Eisenstein O, Andersen RA (2010) Organometallics 29:5103; (n) Kraft BM, Clot E, Eisenstein O, Brennessel WW, Jones WD (2010) Fluor Chem 131:1122

62. (a) Siegbahn PEM, Blomberg MRA, Pavlov MWN, Crabtree RH (2001) J Biol Inorg Chem 6:460; (b) Siegbahn PEM (2007) Chem Rev 107:4414
63. Mylvaganam K, Bacskay GB, Hush NS (2000) J Am Chem Soc 122:2041
64. Zhu H, Ziegler T (2006) J Organomet Chem 691:4486
65. (a) Bartlett KL, Goldberg KI, Borden WT (2000) J Am Chem Soc 122:1456; (b) Bartlett KL, Goldberg KI, Borden WT (2001) Organometallics 20:2669–2678
66. (a) Butschke B, Schlangen M, Schroder D, Schwarz H (2008) Chem Eur J 14:11050; (b) Butschke B, Schlangen M, Schroder D, Schwarz H (2008) Helv Chim Acta 91:1902–1915; (c) Butschke B, Schroder D, Schwarz H (2009) Organometallics 28:4340; (d) Butschke B, Schwarz H (2011) Organometallics 30:1588
67. Ess DH, Goddard WA III, Periana RA (2010) Organometallics 29:6459
68. Cui Q, Musaev DG, Morokuma K (1998) Organometallics 17:1383
69. Cui Q, Musaev DG, Morokuma K (1998) Organometallics 17:742
70. Sakaki S, Kai S, Sugimoto M (1999) Organometallics 18:4825–4837
71. (a) Sakaki S, Takayama T, Sugimoto M (2001) Chem Lett 1222–1223; (b) Sakaki S, Takayama T, Sumimoto M, Sugimoto M (2004) J Am Chem Soc 126:3332–3348
72. (a) Sakaki S, Ogawa M, Musashi Y, Arai T (1994) J Am Chem Soc 116:7258–726; (b) Sakaki S, Mizoe N, Sugimoto M (1998) Organometallics 17: 2510–2523; (c) Sakaki S, Mizoe N, Musashi Y, Sugimoto M (1999) J Mol Struct (Theochem) 461–462:533–546
73. Sakaki S, Sumimoto M, Fukuhara M, Sugimoto M, Fujimoto F, Matsuzaki M (2002) Organometallics 21:3788–3802
74. Takahashi T, Hasegawa M, Suzuki N, Saburi M, Rousset CJ, Fanwick PE, Negishi E-I (1991) J Am Chem Soc 113:8564
75. Corey JY, Zhu X-H (1992) Organometallics 11:672
76. (a) Tanabe Y, Mizuhata Y, Tokitoh N (2008) Chem Lett 37:724–725; (b) Tanabe Y, Mizuhata Y, Tokitoh N (2010) Pure Appl Chem 82:879–890
77. (a) Jessop PG, Ikariya T, Noyori R (1994) Nature 368:231; (b) Jessop PG, Hsiano Y, Ikariya T, Noyori R (1994) J Am Chem Soc 116:8851; (c) Jessop PG, Ikariya T, Noyori R (1996) J Am Chem Soc 118:344
78. (a) Musashi Y, Sakaki S (2000) J Am Chem Soc 122:3867; (b) Ohnishi Y-y, Matsunaga T, Nakao Y, Sato H, Sakaki S (2005) J Am Chem Soc 127:4021; (c) Ohnishi Y-y, Nakao Y, Sato H, Sakaki S (2006) Organometallics 25:3352
79. (a) Hutschka F, Dedieu A, Eichberger M, Fornikca R, Reitner W (1997) J Am Chem Soc 119:4432; (b) Hutschka F, Dedieu A (1997) J Chem Soc Dalton Trans 1899
80. Musashi Y, Sakaki S (2002) J Am Chem Soc 124:7588
81. (a) Ishiyama T, Murata M, Miyaura N (1995) J Org Chem 60:7508; (b) Ishiyama T, Ahiko T, Miyaura N (1996) Tetrahedron Lett 6889; (c) Ishiyama T, Itoh Y, Kitano T, Miyaura N (1997) Tetrahedron Lett 3447; (d) Ahiko T, Ishiyama T, Miyaura N (1997) Chem Lett 811
82. Hiyama T (2002) J Organomet Chem 653:58
83. Sumimoto M, Iwane N, Takahama T, Sakaki S (2004) J Am Chem Soc 126:10457
84. Sugiyama A, Ohnishi Y-y, Nakaoka M, Nakao Y, Sato H, Sakaki S, Nakao Y, Hiyama T (2008) J Am Chem Soc 130: 12975
85. (a) Sakaki S, Biswas B, Sugimoto M (1998) Organometallics 17:1278; (b) Sakakai S, Kai S, Sugimoto M (1999) Organometallics 18:4825; (c) Sakaki S, Biswas B, Musashi Y, Sugimoto M (2000) J Organomet Chem 611:288
86. Ishikawa A, Nakao Y, Sato H, Sakaki S (2010) Dalton Trans 39:3279

Chapter 12
Application of Quantum-Chemical Techniques to Model Environmental Mercury Depletion Reactions

Devashis Majumdar, Szczepan Roszak, and Jerzy Leszczynski

Abstract Modeling of atmospheric/environmental mercury depletion reactions are finding increasing importance as it is an effective tool to understand the origin of increased mercury level in the environment over the period of the last two decades. Quantum-chemical methods could play an important role in such modeling. In the present review, we have introduced the applications of various quantum-chemical techniques to investigate the kinetics and thermodynamic properties of such reactions. These approaches involve high-level structural analysis techniques (quantum-chemical) to analyze the structural properties of various reactive ingredients. The results obtained through such computations are used to generate desired kinetic and thermodynamic properties. Their relevance in modeling various mercury depletion reactions are discussed by comparison with the available experiments.

Abbreviations

AMDE	Atmospheric mercury depletion event
APES	Analytical potential energy surface
BFR	Brominated flame retardant
CBS	Complete basis set
CCSD	Coupled-cluster calculations involving single and double excitations

---

D. Majumdar • J. Leszczynski (✉)
Department of Chemistry and Biochemistry, Jackson State University, Jackson, MS 39217, USA
e-mail: devashis@icnanotox.org; jerzy@icnanotox.org

S. Roszak
Institute of Physical and Theoretical Chemistry, Wroclaw University of Technology, Wybrzeze Wyspianskiego 27, 50-370 Wroclaw, Poland
e-mail: szczepan.roszak@pwr.wroc.pl

CCSD(T)	Coupled-cluster calculations including triple excitations
CPCM	Polarized continuum model with conductor-like screening reaction field
CVT	Canonical variational transition (state theory)
CVTST	Canonical variational transition state theory
DFT	Density functional theory
GEM	Gaseous elemental mercury
Hg(p)	Mercury associated with particulate matter
ICVT	Improved canonical variational transition (state theory)
ME	Master Equation
MECCA	Module Efficiently Calculating the Chemistry of the Atmosphere
MP2	Møller-Plesset second-order perturbation (theory)
MR-CI	Multireference configuration interaction
PES	Potential energy surface
PFOA	Perfluorooctanoic acid
PFOS	Perfluorooctane Sulfonate
PHg	Particle-bound mercury
POP	Persistent organic pollutant
QCT	Quasi-classical trajectory
RGM	Reactive gaseous mercury
RRKM	Rice-Ramsberger-Kassel-Marcus (theory)
SO	Spin orbit
TS	Transition state
TST	Transition state theory
VTST	Variational transition state theory
μVT	Microcanonical variational transition (state theory)

12.1 Introduction

Mercury contamination in the environment is of serious environmental concern because of the highly toxic nature of the contaminants (produced through reactions with mercury). Local, regional, and long-distance transport and dispersion of atmospheric mercury from anthropogenic sources have been attributed to deposition patterns [1–4]. Mercury is present in coal and municipal solid wastes. In the atmosphere, mercury exists in three different forms: elemental mercury vapor, Hg^0; gaseous divalent compounds, Hg(II); and mercury associated with particulate matter, Hg(p). Mercury is released into the atmosphere from both natural and anthropogenic sources [1–4]. It is estimated that globally up to 70% of current Hg emissions into the atmosphere are of anthropogenic origin [5]. Natural sources, including the oceans, volcanic activity, and crusted out-gassing emit predominantly elemental mercury. The main anthropogenic sources of mercury to the atmosphere, such as fossil fuel combustion (coal and oil), waste incineration, nonferrous metal,

iron, steel, and cement production release either Hg^0 or reactive gaseous mercury (RGM) and particle-bound mercury (PHg) [1–5]. RGM shows correlations with temperature, solar radiation, and O_3 and SO_2 concentrations suggesting seasonal trends similar to those observed for other regional air pollutants [6, 7].

Mercury is relatively inert toward oxidation and, therefore, mainly present in the atmosphere as elemental Hg [8]. Its global background concentration range is 1–2 ng m^{-3}. In the atmosphere, mercury is transported and transformed into a variety of mercury species with different properties. The fate of atmospheric mercury depends on its physical properties and oxidation state. The lifetime of atmospheric mercury is about 1–2 years. Some fraction of the elemental mercury is oxidized in ambient air and clouds to form ionic compounds of Hg(II). The natural lifetime of the oxidized form of mercury, that is, Hg(II), is much shorter. These species are highly water soluble (at least five orders of magnitude more than Hg^0) and their water solubility strongly supports removal processes and increases deposition rates from the atmosphere [1–5, 9, 10]. Detailed atmospheric dispersion modeling using fine-scale models, accurate emission inventory data, ambient monitoring network, and model validation helps to understand the mercury dispersion patterns.

Quantum-chemical techniques play an important role in modeling atmospheric mercury reactions. The main objective of these approaches is to focus on the thermodynamic characteristics of these reactions, which in turn could lead to the understanding of the kinetics of the reactions involved. These results are useful to monitor the validity of the proposed mercury deposition models in the atmosphere. In the present review, we will discuss various quantum-chemical applications concerning modeling of atmospheric mercury deposition reactions with an initial brief résumé of the important experimental findings and related models in these contexts.

12.2   Various Types of Atmospheric Mercury Deposition

In this section we will discuss various kinds of mercury pollutions. It is beyond the scope of the present review to go for a detailed account of these phenomena. Such details and related experiments are available in recent reviews [6, 7, 9, 10]. We will present a brief account of the various kinds of mercury contaminations and the related mercury cycle (modeling such phenomena). The model would be based on halide formations as they are the most well-known contaminants studied through both experimental and theoretical techniques.

Mercury pollution occurs through various kinds of contaminations and could be broadly classified as environmental and polar region pollutions, atmospheric contamination, pollution through worldwide anthropogenic mercury sources, and contamination of mercury in snow and air, and snow and ice interactions. Mercury behaves exceptionally in the environment due to its volatility, its potential to be

methylated, and its ability to accumulate in aquatic food webs. The three most important species of Hg known to occur in the environment are as follows [11]:

(a) Elemental mercury (Hg) [Hg^0 or Hg(0)], which has a high vapor pressure and a relatively low solubility in water. Of the Hg species found in the atmosphere, Hg(0) is the most stable and dominant and is subject to undergo long-range transport.

(b) Divalent inorganic mercury [Hg^{2+} or Hg(II)], which is thought to be the dominant form in wet deposition, is more soluble in water than Hg(0) and has a strong affinity for many inorganic and organic ligands, especially those containing sulfur.

(c) Methyl mercury [CH_3Hg^+ or MeHg], which is toxic and is strongly bio-accumulated by living organisms.

12.2.1 Polar Region Contamination

Polar ecosystems are generally considered to be the last pristine environments on earth as they are relatively unaffected by human activities. There are four major pollutant groups (listed below) that are well known to migrate to high latitudes. Three have been recognized for more than a decade, while the fourth group, a new and emerging group of organic contaminants, is of growing concern. This last group is concerned with four aspects, namely, acidifying gases (SO_x) from Eurasian smelters and industry [12]; heavy metals, including Hg, from fossil fuel combustion, industry, and mining [13]; classical persistent organic pollutants (POPs) including pesticides and polychlorinated biphenyls [14]; and (d) emerging POPs, such as brominated flame retardants (BFRs) and polyfluorinated compounds (PFOA, PFOS) [15, 16]. These contaminants are of concern because most of them bio-magnify through the marine food chain to elevated levels, which may create adverse physiological effects [17–19].

12.2.2 Atmospheric Contamination

The residence time of gaseous elemental mercury (GEM) in the atmosphere is quite long (about 1 year) [11], which is thus sufficient to allow for homogeneous mixing, at least within the hemisphere of origin. Since anthropogenic sources of Hg emissions into the atmosphere are primarily located in the northern hemisphere, a concentration gradient between the two hemispheres should be expected. Indeed, the global background concentration (the average sea-level atmospheric concentration of Hg(0) at remote sites) is generally 1.5–1.7 ng m^{-3} in the northern hemisphere and 1.1–1.3 ng m^{-3} in the southern hemisphere [20–23]. The lifetime of Hg in the atmosphere also depends on its chemical form. GEM can be transported globally,

while oxidized forms of Hg are more reactive and travel much shorter distances before they are scavenged or deposited. Temporal variations in deposition can result from changes in Hg emission rates, changes in local and regional sources (e.g., NO_x and SO_2), and from changes in climate (e.g., changes in precipitation amounts, air temperature, sea ice coverage) [24]. An increase of O_3 concentrations and aerosol loadings will also impact the atmospheric residence time and deposition fluxes of elemental and oxidized mercury [25].

The most prevalent species of Hg in the atmosphere include GEM [or Hg(0)], oxidized RGM (consisting of Hg(II) or Hg(I) compounds), and particle-bound Hg(II or I) mercury (PHg). The reactive forms of Hg (e.g., RGM and some PHg) have short lifetimes in the atmosphere and are deposited from the atmosphere close to emission sources. However, the existence of reactive Hg in a particular air sample does not necessarily imply the existence of a local emission source but can be the result of atmospheric chemical reactions involving GEM transported from distant sources [25–27].

12.2.3 Anthropogenic Contamination

The onset of major industrial activities has altered the global Hg cycle via the anthropogenic transfer of large quantities of Hg from deep geological stores to the earth's surface and atmosphere [20, 28, 29]. Slemr et al. [21] reconstructed the worldwide trend of atmospheric Hg concentrations and suggested that Hg concentrations in the global atmosphere have increased since the first measurements in 1977 to a maximum in the 1980s, subsequently decreased to a minimum in 1996, and then remained at a constant level of about 1.7 ng m^{-3}, in the northern hemisphere, until 2001. However, this assessment and analysis includes several significant assumptions and an alternative hypothesis has been proposed that suggests that the total gaseous Hg concentration in the northern hemisphere remained virtually unchanged since 1977 [25]. The change in the oxidation potential of the atmosphere over the past several decades [30] may partially account for the discrepancy between measurement trends of atmospheric Hg (either constant or decreasing) and Hg emission inventories (increasing: Lindberg et al. [25]). Further, Lindberg et al. [25] concluded that reductions in anthropogenic inputs will not produce a linear decrease in Hg deposition, especially at remote locations that are dominated by the global pool.

12.2.4 Mercury Contamination in Snow and Air

Mercury can be deposited onto snow surfaces through both wet and dry deposition. Dry deposition in the polar regions mainly corresponds with the deposition of RGM formed during atmospheric mercury depletion events (AMDEs) [31–34]. Mercury

in snow is mainly found in its oxidized form (e.g., Hg(II)) with concentrations that can range from a few up to hundreds of ng/L [32, 34–39]. AMDEs can lead to increased Hg concentrations in the surface snow [31, 32, 40]; however, it has also been observed that within 24 h after deposition of Hg from the atmosphere, a fraction is reemitted as GEM back to the atmosphere [31, 41]. Polar snowpacks themselves have been investigated for their role as a chemical reactor that leads to the formation of active oxidants/reductants [42]. Hence, it appears that snow packs can act both as a sink and a source of Hg to the atmosphere depending on the environmental conditions (e.g., temperature, irradiation, presence of water layers around snow grains) and the chemical composition of the snow (e.g., presence of halogens, organic substances) [34, 41, 43].

There is much discussion about the fate of the deposited Hg to polar snowpacks through AMDEs during and after snow melt. The reduction and subsequent reemission of a fraction of Hg from the snowpack is largely believed to occur through photochemical processes [34]. King and Simpson [44] have shown that solar irradiation can effectively penetrate the first few centimeters of the snowpack, possibly leading to photoreduction of Hg complexes contained therein. The interaction of microbes within the surface grains of the snowpack and the Hg contained therein is also of interest during this critical period [45].

12.2.5   Models of Atmospheric Mercury Pollution

Various kinds of mercury pollution models are available at present to understand the long-ranged atmospheric transport of Hg. These models are based on year-long monitoring of Hg in the atmosphere and studies on the kinetics of the formation of various contaminants (mostly chlorides and bromides). The depletion of GEM is thought to be due to conversion into reactive gas-phase mercury (RGM) and into particulate mercury. An anti-correlation between measured GEM and the concentration of particulate mercury was found during AMDEs. The chemical reactions causing the AMDEs [32, 46–48] are probably similar to those driving the ozone depletion events [49–51], and the oxidation of GEM by reactive halogen species like Br atoms and BrO radicals is considered to be a key process of mercury depletion [33, 48, 52, 53].

Reactive bromine species can be generated from sea salt aerosols and in the course of sea ice formation, when concentrated salt solutions (brine) are separated from ice. It often forms frost flowers, when an open lead of seawater begins to freeze. These are dendritic vapor-deposited ice crystals that suck up brine from the freezing ice [54–56] and can serve as sites of halogen activation and sources of sea salt aerosols [51]. Recently, Sander et al. [57] used the MECCA (Module Efficiently Calculating the Chemistry of the Atmosphere) box model to study the role of carbonate precipitation in freezing seawater for the generation of reactive bromine.

Table 12.1 Comparison of mercury models with halogen chemistry

Br	Cl	Aqueous phase	Mass transfer	Region	References
−	+	+	Dynamic (k_{mt})	Northern hemisphere	[58]
−	+	+	Equilibrium	Northern hemisphere	[59]
−	+	+	Dynamic (k_{mt})	Global	[60]
+	+	−	−	Polar	[61]
+	+	−	−	Northern hemisphere	[53]
−	+	Dilute droplets	Equilibrium	Unspecified	[2]
−	+	Dilute droplets	Equilibrium	Unspecified	[62]
−	+	Dilute droplets	Dynamic (k_{mt})	Unspecified	[63]
+	+	Aerosol	Dynamic (k_{mt})	Remote marine boundary Layer	[64]
+	+	Aerosol	Dynamic (k_{mt})	Mediterranean	[65]
+	+	Aerosol	Dynamic (k_{mt})	Marine boundary layer	[66]
+	+	Aerosol	Dynamic (k_{mt})	Mediterranean	[67]
+	+	Aerosol	Dynamic (k_{mt})	Polar	[68]
+	+	Aerosol	Dynamic (k_{mt})	Urban	[69]
+	+	Aerosol	Dynamic (k_{mt})	Polar	[10]

Reproduced from Xie et al. [10]. With kind permission of © Copernicus Publications and the European Geosciences Union (2008 and the corresponding author (Z-Q Xie))

Other model studies of atmospheric mercury chemistry are listed in Table 12.1. These models have been commonly used to investigate the long-range transport of mercury. All of these models have their positive sides as well as shortcomings. Several of these models used, for example, chemical reactions of Hg species related to SO_2 and chlorine but they do not consider bromine chemistry, while the others used measured rate constants for the reaction of Hg with Br but did not consider aqueous-phase species. A detailed discussion in this context is available in [10]. Xie and coworkers [10] have recently presented a model to study the oxidized species in both gas and aqueous phases (including bromine chemistry) with a fully coupled gas/aqueous chemistry mechanism. This is shown in Fig. 12.1 and is based on the atmospheric chemistry box model MECCA by Sander et al. [57]. It describes the release of halogens from sea salt aerosols under conditions of the polar boundary layer at 82°N with a fully pH-dependent aqueous-phase chemistry mechanism. Here, mercury chemistry has been added to the polar MECCA model. The release process of reactive halogens and the reactions with mercury and ozone in both aerosol and gas phase are shown in this model (Fig. 12.1). Dry deposition had been switched off in the model because under the conditions of the model calculations, there were enough aerosol surfaces available so that uptake of RGM to aerosols dominates over dry deposition. MECCA only simulates locally occurring chemistry; advection of an air mass already depleted in GEM and RGM cannot be modeled.

With this background of experimental models of atmospheric mercury chemistry, we will now discuss various quantum-chemical approaches to study such reaction in both gas phases as well as in aqueous medium. Potential reactions of Hg in the atmosphere have recently been summarized by Steffen et al. [9], and theoretical
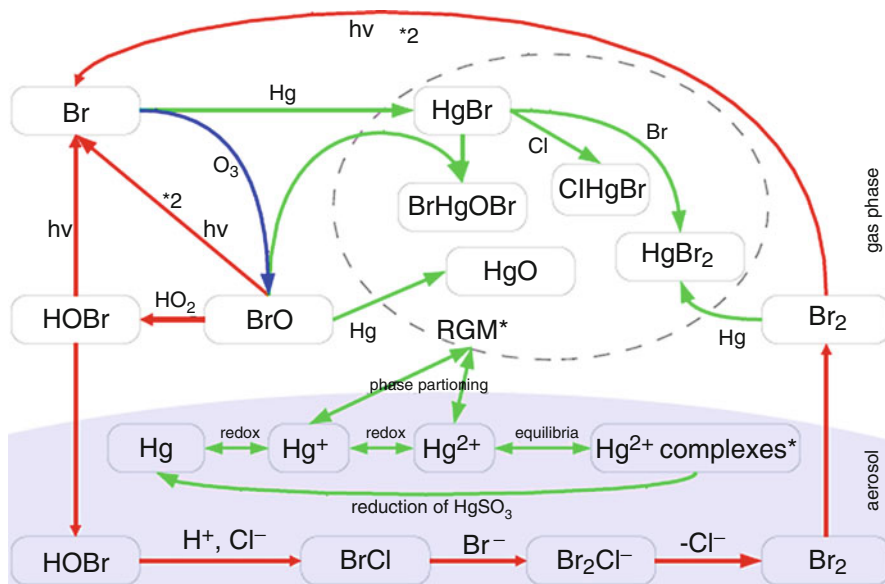
Fig. 12.1 Simplified halogen and mercury chemistry. Bromine chemistry is shown with *red arrows*, Hg chemistry in *green*, and ozone destruction in *blue*. "RGM*" refers to all gas-phase species in our model that contain mercury, except for elemental Hg. Hg^{2+} complexes* refers to $HgSO_3$, $Hg(SO_3)_2^{-2}$, $Hg(OH)_2$, $HgOHCl$, $HgCl^+$, $HgCl_2$, $HgCl_3^-$, $HgCl_4^{2-}$, $HgBr^+$, $HgBr_2$, $HgBr_3^-$, and $HgBr_4^{2-}$ (Reproduced from Xie et al. [10] with kind permission of Copernicus Publications and the European Geosciences Union 2008 and the corresponding author, Z-Q Xie)

studies of these reactions are important as they are the building blocks of the available atmospheric models of mercury transportations. We will not explicitly present these reactions in the present review. They would be compared with the computed results whenever needed. Readers are referred to [6, 7, 9, 10] (and references in Table 12.1) for a complete account of such reactions (i.e., kinetics, equilibrium constants, etc.).

12.3 Quantum-Chemical Modeling of Atmospheric Mercury Reactions

The atmospheric mercury reactions mainly involve the reactions of elemental mercury with halogen atoms. The other two classes of such reactions involve formation of mercury-halogen compounds in radical and ionic (due to solvation effect) forms. These last two varieties follow the reaction paths with starting reactants in radical/ionic forms also. Such investigations need extensive knowledge of the electronic properties of the individual reaction components together with the thermodynamic properties of these specific reactions. The electronic structures of

various mercury halides have been extensively studied in the gas phase using state-of-the-art quantum-chemical techniques at various levels of sophistication. These approaches include density functional theory (DFT), coupled-cluster calculations involving double and triple excitations (CCSD and CCSD(T)), and multireference configuration interaction (MR-CI) calculations including explicit relativistic corrections [70–75]. The structures of the mercury halides analyzed are mostly HgX, HgX^+, HgX_2, HgX_3^-, $HgX_3^\bullet$, HgX_4^{2-}, and $HgX_4^{2\bullet}$ (X = Cl, Br, I). While HgX, HgX^+, and HgX_2 are linear, HgX_3^- ($HgX_3^\bullet$), HgX_4^{2-} ($HgX_4^{2\bullet}$) are respectively triangular and pyramidal in their ground states. Several oxygen derivatives of mercury halides (e.g., HgClO, HgBrO), and the compound HgBrCl with linear structures have also been investigated in this context [76–80]. These structural information and the dissociation properties of the respective compounds are used to explore the kinetics of various mercury reactions (involving halide formations) [48, 76, 81, 82]. These kinetics results could be compared with experiments to verify the proposed reaction mechanisms, and the results are important to design various models of atmospheric mercury transformations. There are several other reactions which also contribute to mercury speciation in the atmosphere. They are not fully explored through quantum chemical techniques. A brief résumé of such studies would be provided at the end of the section.

12.3.1 Reactions of Mercury with Halogens: Kinetics Studies Using Collision Theory

The mercury-halogen reactions are treated as recombination reactions with the formation of HgX and HgX_2 (X = Cl, Br, and I). Khalizov and coworkers [76] studied HgX formation reactions using collision theory models and compared their results with the Canonical Variational Transition State Theory (CVTST). They used the following sequence of elementary steps to compute the rate constants:

$$Hg + X \rightleftharpoons HgX^* \tag{12.1}$$

$$HgX + M \rightarrow HgX + M \tag{12.2}$$

The first step (reaction 12.1) accounts for the formation of the diatomic molecule HgX^* from the separated atomic reactants. This molecule is primarily formed in an unbound excited vibrational state and may either be stabilized by a collision with a molecule of the bath gas (M) or dissociate back to the atomic reactants. If the pressure is high, the deactivation mechanism (reaction 12.2) is extremely fast and the overall rate constant for recombination equals the rate constant for the first step. Conversely, if the bath gas pressure is low, the collisional deactivation mechanism may play an important role.
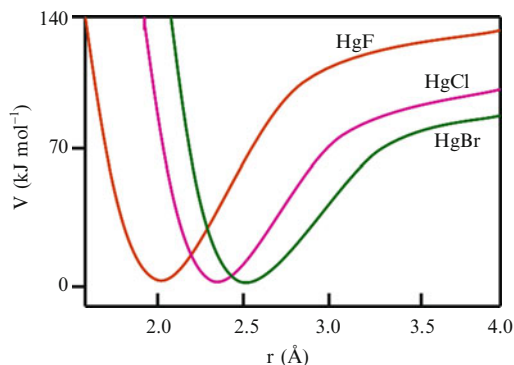
Fig. 12.2 Schematic representation of the HgF (D_e =136.65 kJ mol^{-1}, b = 2.429 Å^{-1}, r_e = 1.992 Å), HgCl (D_e = 96.45 kJ mol^{-1}, b = 2.206 Å^{-1}, r_e = 2.349 Å) and HgBr (D_e = 61.62 kJ mol^{-1}, b = 2.447 Å^{-1}, r_e = 2.498 Å) energy potentials. The computed parameters (D_e, b, and r_e) were obtained by fitting Morse function to the *ab initio* data (at the CCSD(T) level of theory) together with the application of the spin-orbit correction to the dissociation energy (D_e). Refer to the text (and ref. 76 for the original fitted energy curves) for the details regarding these parameters

The Morse function was used in the collision theory and CVTST [83] calculations to describe the Hg-X interaction potential. The function parameters were obtained by fitting Eq. 12.3 to the Hg-X energies at different separations calculated at the CCSD(T) level of theory [76]:

$$V(r) = D_e\{1 - \exp(-\beta(r - r_e))\}^2 \tag{12.3}$$

where D_e is the dissociation energy (kJ mol^{-1}), r_e is the equilibrium bond distance (Å), and parameter β is (Å^{-1}). These parameters are computed by fitting the HgX (X = Cl, Br, I) potential energy curves with Morse potential (as shown Fig. 12.2). Explicit spin-orbit (SO) coupling corrections to the energy is needed for each point (from at least intermediate separation) of the potential energy surface for these gas-phase reactions. Indeed, upon complete dissociation, the HgX radical in $^2\Sigma^+$ ground electronic state, is transformed into atoms Hg ($^1S_0$) and X ($^2P_{3/2}$). The SO contribution to the interaction potential due to the Hg–X complex changes from zero at equilibrium (since ground state of HgX ($^2\Sigma^+$) is nondegenerate) [84] to −1.61, −3.52, or −14.70 kJ mol^{-1} for halogen atoms at infinite separation form. Around the equilibrium geometry at $|r-r_e| < 0.5$ Å the Hg . . . X collision complex resembles the HgX moiety rather than the separate atoms Hg and X. Thus, only the energies at moderate separations were used in the fitting procedure when it was safe to assume that the $^2\Sigma^+$ electronic state for the Hg . . . X complex is preserved and the SO effect is zero. At the same time, the dissociation energies of HgX were corrected for the SO coupling due to halogen atoms.

The idea of using the Morse function for the calculation of rate constants is based on the very premises of collision theory that defines transition state (TS) at a given energy E with respect to the bottom of the reactant channel by the position of the top of the centrifugal barrier [85, 86]. This effective potential barrier, created by an exact

compensation of the centrifugal repulsive force and the attractive interaction force is characterized by its position along the reaction coordinate ($r^{\neq}$), and the maximum value of the angular momentum (L_{max}) compatible with the energy through the two following conditions:

$$
\begin{cases}
V(r^{\neq}, L_{max}) = \dfrac{L_{max}^2}{2\mu r^{\neq}} + V(r^{\neq}) = E \\
\left. \dfrac{\partial V(r, L_{max})}{\partial r} \right|_{r^{\neq}} = 0
\end{cases}
\tag{12.4}
$$

where μ is the diatomic molecule reduced mass, r is the interatomic distance, and $V(r)$ is the potential describing the interaction between the two atoms. L_{max} is related to the capture cross section $\sigma(E)$ through the relation.

$$
\sigma(E) = \frac{\pi L_{max}^2}{2\mu E}
\tag{12.5}
$$

The high-pressure limit canonical rate constant is recovered by averaging the energy-resolved capture cross section over the relative kinetic energy distribution at a given temperature T,

$$
k_{\infty}(T) = \frac{1}{k_B T} \left(\frac{8}{\pi \mu k_B T} \right)^{1/2} \int_0^{\infty} E \sigma(E) e^{-k_B T} \, dE
\tag{12.6}
$$

where k_B is the Boltzmann constant.

The calculation of the CVTST rate constant primarily involves the computation of the equilibrium constant K_{eq} and the high-pressure limit for the rate of unimolecular decomposition $k^{CVT}(T)$. The rate constant for recombination is then evaluated. The rate constant $k^{CVT}(T)$ is calculated at a fixed temperature by minimizing the generalized rate constant, $k^{GT}(T, r)$, with respect to r, which defines the dividing surface [83].

The vibrationally excited diatomic molecule, HgX*, is supposed to be stabilized if it collides with a bath gas molecule during its lifetime (according to the deactivation step of reaction 12.2). At given energy E and angular momentum L, this lifetime is approximated by one period of vibration, which is defined by [81]

$$
\tau(E, L) = 2 \int_{r^-}^{r^{\neq}} \left\{ \frac{2}{\mu} \left(E - \frac{L^2}{2\mu r^2} - V(r) \right) \right\}^{-1/2} dr
\tag{12.7}
$$

where $r^{\neq}$ is the position of the transition TS (see Eq. 12.4) and r^- is determined by the integrand condition of existence. The range between $r^{\neq}$ and r^- defines arbitrarily the configuration domain for which HgX* is considered as a stabilized molecular entity. For $r > r^{\neq}$, Hg and X are considered as separated atoms. The average lifetime for a given energy E is then given by

$$
\tau(E) = \frac{1}{L_{max}} \int_0^{L_{max}} \tau(E, L) \, dL
\tag{12.8}
$$

The capture cross section (σ_{de} (E)) is computed from the knowledge of deactivation probability $P(E)$ ($= Z\tau$ (E)) and collision frequency (Z) of HgX* with the bath gas molecules (N_2 and O_2) using relation (12.9).

$$\sigma_{de}(E) = \pi \frac{L_{max}^2}{2\mu E} P(E) \tag{12.9}$$

The corresponding pressure-dependent thermal rate constant $k_P(T)$ is computed from Eq. 12.6 by replacing $\sigma(E)$ with $\sigma_{de}(E)$. The readers should refer to [76] for details regarding the necessary parameterization to compute the rate constants.

The computed rate constants through collision theory are represented below (M stands for *molecule* in all of the rate equations in this review):

$$\begin{cases} \text{Hg} + \text{F} \rightarrow \text{HgF} & k_p(1 \text{ atm}, T) = 0.92 \times 10^{-12} \exp\left(\frac{206.81}{T}\right) \text{cm}^3\text{M}^{-1}\text{s}^{-1} \\ \text{Hg} + \text{Cl} \rightarrow \text{HgCl} & k_p(1 \text{ atm}, T) = 1.38 \times 10^{-12} \exp\left(\frac{208.02}{T}\right) \text{cm}^3\text{M}^{-1}\text{s}^{-1} \\ \text{Hg} + \text{Br} \rightarrow \text{HgBr} & k_p(1 \text{ atm}, T) = 1.01 \times 10^{-12} \exp\left(\frac{209.03}{T}\right) \text{cm}^3\text{M}^{-1}\text{s}^{-1} \end{cases}$$
$$\tag{12.10}$$

The computed rate constants show that the reactions of Hg with atomic halogens are considerably fast and it is very likely that they (with the exception of the reaction with atomic fluorine whose concentration in the troposphere is negligibly low) may contribute to the chemistry of mercury in the gas phase. Assuming Cl and Br steady-state concentrations to be 10^4 and 10^7 atom cm^{-3} [87, 88], the estimated lifetime of Hg due to its depletion reactions with chlorine and bromine atoms was found to be almost 2 years and half a day, respectively. Hence, despite the faster rate coefficient of the Cl-atom-initiated reaction of mercury, the concentration of chlorine atoms is far too low to play a significant role. Atomic bromine, however, is present in a high enough concentration to completely destroy mercury within a short period of time, as observed in the Arctic.

12.3.2 Oxidation of Hg^0 to HgBr$_2$ and Related Reactions: Kinetics Study Using RRKM Theory

The oxidation of elemental mercury (Hg^0) to the divalent gaseous mercuric bromide (HgBr$_2$) has been proposed to account for the removal of Hg^0 during depletion events in the springtime Arctic. The mechanism of this process was explored by Goodsite and coworkers using density functional level of theories [48]. Rice-Ramsberger-Kassel-Marcus (RRKM) theory, together with ab initio quantum calculations were used to estimate the recombination rate coefficients of Hg with Br, I, and O, the thermal dissociation rate coefficient of HgBr, and the recombination rate coefficients of HgBr with Br, I, OH, and O_2.

Several mechanisms have been proposed to explain the oxidation of GEM to RGM [32, 46]. These include the reactions between Hg^0 and halogen oxides or halogen atoms to produce HgO, $HgBr_2$, and $HgCl_2$:

$$Br(Cl) + O_3 \rightarrow BrO(ClO) + O_2 \tag{12.11}$$

$$BrO(ClO) + Hg \rightarrow HgO + Br(Cl) \tag{12.12}$$

$$Hg + Br(Cl) \rightarrow HgBr(HgCl) \rightarrow\rightarrow HgBr_2(HgCl_2) \tag{12.13}$$
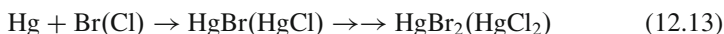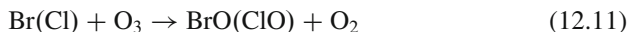
The possible role of oxidants such as OH, HO_2, $O(^1D$ and $^3P)$, and NO_3 that are associated with high levels of NO resulting from photodenitrification processes in the snowpack [38] were also included in such studies. Goodsite and coworkers [48] considered the following mechanism for producing HgBrY:

$$Hg + Br(+ M) \rightarrow HgBr(M = third\ body) \tag{12.14a}$$

$$HgBr(+ M) \rightarrow Hg + Br \tag{12.14b}$$

$$HgBr + Y(+ M) \rightarrow HgBrY(Y = Br, I, OH, O_2\ etc.) \tag{12.15}$$
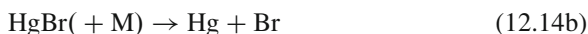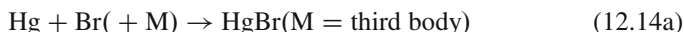
The structures of the relevant compounds were determined using DFT level of theories. The mercury bromides are linear structures, while HgOH ($^2A'$), HgBrOH ($^1A'$), and $HgBrO_2$ (^2A) are angular in their ground states. The details of such analysis are available in the literature [48]. A recombination reaction is considered to proceed via the following mechanism (exemplified by reaction 12.14a with atomic Br):

$$Hg + Br \rightarrow HgBr^* \tag{12.14c}$$

$$HgBr^* \rightarrow Hg + Br \tag{12.14d}$$

$$HgBr^* + M \rightarrow HgBr + M(M = N_2) \tag{12.14e}$$
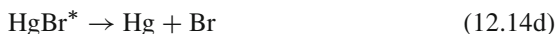
where $HgBr^*$ denotes that the nascent HgBr formed in reaction 12.14c has sufficient internal energy to dissociate back to the reactants (reaction 12.14d). This mechanism is quite common to study diatomic molecule formation reaction (in gas phase) using collision theory and similar to the approach described in Sect. 12.3.2. The only difference is that Master Equation (ME) formalism is invoked here to compute rate equations using RRKM theory. In this approach, the energy of the adduct HgBr is first divided into a contiguous set of grains (width 30 cm^{-1}), each containing a bundle of rovibrational states of average energy, E_i. Each grain was then assigned a microcanonical rate coefficient for dissociation, k_{-i}. The ME describes the time-evolution of the grain populations and can be represented as

$$\frac{d}{dt}\rho_i(t) = \omega \sum_j P_{ij}\rho_j(t) - \omega\rho_i(t) - k_{-i}\rho_i(t) + R_i \tag{12.16}$$

where R_i is the rate of population of HgBr (E_i) via reaction 12.14c, ω is the frequency of collisions between HgBr* and N_2, and P_{ij} is the probability of transfer of HgBr from grain j to grain i on collision with N_2. The individual P_{ij}s were estimated using the exponential down model [89]. The average energy for downward transitions ($i < j$), $\langle\Delta E\rangle_{\text{down}}$, was set to be 400 cm^{-1} for N_2 [89] and assumed to be independent of temperature. The parameters ω and ε/k, which describe the intermolecular potential between HgBr and N_2 from which ω is calculated, were set to typical values of 4 Å and 400 K, respectively [90]. For upward transitions where $j > i$, P_{ij} was calculated by a detailed balance. An absorbing boundary was set at 24 kJ mol^{-1} below the energy of the reactants to simulate irreversible stabilization of HgBr via reaction 12.14e. This ensures that collisional energization from the boundary to the threshold becomes highly improbable. The rate of population of grain i, R_i, is given by detailed balance between reactions 12.14c and 12.14d:

$$R_i = k_{\text{rec},\infty} [\text{Hg}] [\text{Br}] \eta_i \qquad (12.17)$$

where $k_{\text{rec},\infty}$ is the limiting high-pressure association rate coefficient (reaction 12.14c) and

$$\eta_i = \frac{k_{-i} f_i}{\sum_i k_{-i} f_i} \qquad (12.18)$$

f_i is the equilibrium Boltzmann distribution of HgBr (E_i).

The microcanonical rate coefficients for dissociation of HgBr determined through Inverse Laplace transformation [91], which links $k_{-i}(E_i)$ directly to $k_{\text{rec},\infty}$, is given by

$$k_{-i} = \frac{A^\infty (2\pi\mu)^{3/2}}{N(E_i)\Gamma(1.5)h^3} \int_0^{E_1 - E^\infty - b_e} N_p(x)[(E_i - E^\infty - b_e) - x]^{1/2} dx \qquad (12.19)$$

The occurrence of A^∞ and E^∞ terms in Eq. 12.19 is due to their relation with $k_{\text{rec},\infty}$ through Arrhenius equation of the form $A^\infty \exp(-E^\infty/RT)$. Assuming that collisions between Hg and Br are governed by the long-range attractive dispersion force, the parameters A^∞ and E^∞ were found to be 1.67×10^{-10} cm^3 mol^{-1} s^{-1} and -423 J mol^{-1}, respectively [48], for the dissociation of HgBr. $N(E_i)$ is the density of states of HgBr at energy E_i and is calculated using a combination of the Beyer-Swinehart algorithm for the vibrational modes (including a correction for anharmonicity) and a classical densities of states treatment for the rotational modes. $N_p(E_i)$ is the convoluted density of states of Hg and Br; b_e is the Hg–Br bond energy; μ is the reduced mass of Hg and Br; and Γ ($\bullet$) is the gamma function. The ME was expressed in matrix form and then solved to yield k_6, the bimolecular recombination rate constant (of reaction 12.14a) at a specified pressure and temperature. The dissociation rate coefficient, k_{-6}, was calculated by detailed balance with k_6. The parameterizations and the fuller details of such calculations are described in [48] and [91]. The calculated rate constants at 1 atm pressure ($T = 180$–400 K) for the reactions (12.14a) to (12.15) are

$$\text{Hg} + \text{Br} \rightarrow \text{HgBr}, \quad k_6 = 1.1 \times 10^{-12} \left(\frac{T}{298 \text{ K}} \right)^{-2.37} \text{cm}^3 \text{ M}^{-1} \text{ s}^{-1}$$

$$\text{HgBr} \rightarrow \text{Hg} + \text{Br}, \quad k_{-6} = 1.2 \times 10^{10} \exp \left(-\frac{8357}{T} \right) \text{s}^{-1}$$

$$\text{HgBr} + \text{Br} \rightarrow \text{HgBr}_2, \quad k_7 = 2.5 \times 10^{-10} \left(\frac{T}{298 \text{ K}} \right)^{-0.57} \text{cm}^3 \text{ M}^{-1} \text{ s}^{-1}$$
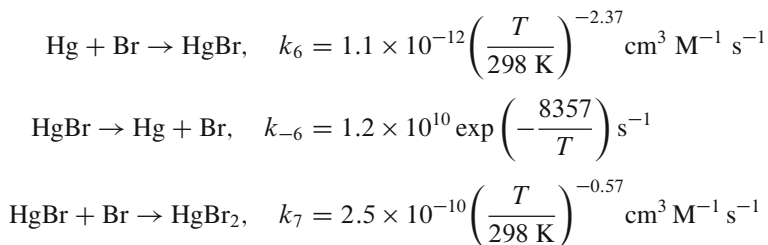
Reaction 12.15 is close to the high-pressure limit at 1 atm. Since Hg–I and Hg–OH bonds ($D_0 = 46.3$ and 39.4 kJ mol^{-1}, respectively) are only slightly less strongly bound than HgBr ($D_0 = 63.8 \text{ kJ mol}^{-1}$) [48], the rate coefficients for these reactions are very similar to k_7, essentially at their high-pressure limits. The products HgBr$_2$, HgBrI, and HgBrOH are extremely stable against thermal dissociation at temperatures below 400 K. For the recombination reactions of Hg with I and OH, and the dissociation of HgI and HgOH, application of RRKM theory yields (pressure = 1 atm N$_2$; $T = 180$–400 K) [48]

$$\text{Hg} + \text{I} \rightarrow \text{HgI}, \quad k = 4.0 \times 10^{-13} \left(\frac{T}{298 \text{ K}} \right)^{-2.38} \text{cm}^3 \text{ M}^{-1} \text{ s}^{-1}$$

$$\text{Hg} + \text{OH} \rightarrow \text{HgOH}, \quad k = 3.2 \times 10^{-13} \left(\frac{T}{298 \text{ K}} \right)^{-3.06} \text{cm}^3 \text{ M}^{-1} \text{ s}^{-1}$$

$$\text{HgI} \rightarrow \text{Hg} + \text{I}, \quad k = 3.0 \times 10^{9} \exp \left(\frac{-3742}{T} \right) \text{s}^{-1}$$

$$\text{HgOH} \rightarrow \text{Hg} + \text{OH}, \quad k = 2.7 \times 10^{9} \exp \left(\frac{-4061}{T} \right) \text{s}^{-1}$$
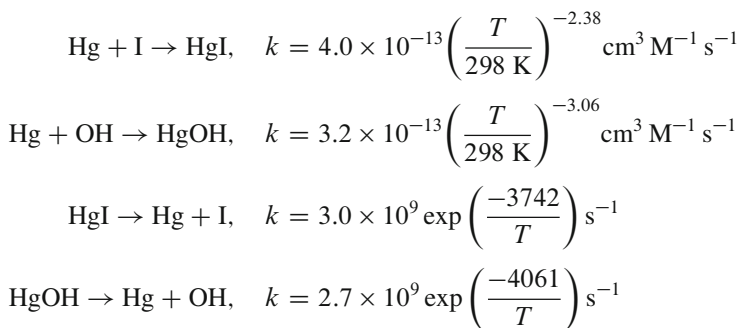
The temperature dependencies of these reactions are illustrated in Fig. 12.3. It demonstrates several important points with respect to the oxidation of Hg. First, the recombination of Hg with Br or I is surprisingly fast for an atom-atom recombination. This is attributed to the high density of rovibrational states arising from the low vibrational frequency and small rotational constant of HgBr or HgI [48]. The theoretical estimate of k_6 for HgBr is about a factor of 3 lower than the recent experimental measurement [46]. In fact, the experimental value could be matched with the calculated bond energy of HgBr ($D_0 = 63.8 \text{ kJ mol}^{-1}$) [48], if it is increased to over 100 kJ mol^{-1}, that is, about 30 kJ mol^{-1} higher (~36 kJ mol$^-$ higher than the calculated value) than the current experimental measurement of $74.9 \pm 4 \text{ kJ mol}^{-1}$ [92, 93]. However, the recent experimental estimate of k_6 refers to a relative rate measurement that required several significant correction factors [46], and Ariya and coworkers had similar inaccuracy in the estimation of rate constant of HgBr recombination reaction in the gas phase (Sect. 12.3.1 and [76]). The computed rate constants, of course, have some practical consequences. In the first place, relative rates of several such reactions could be compared without
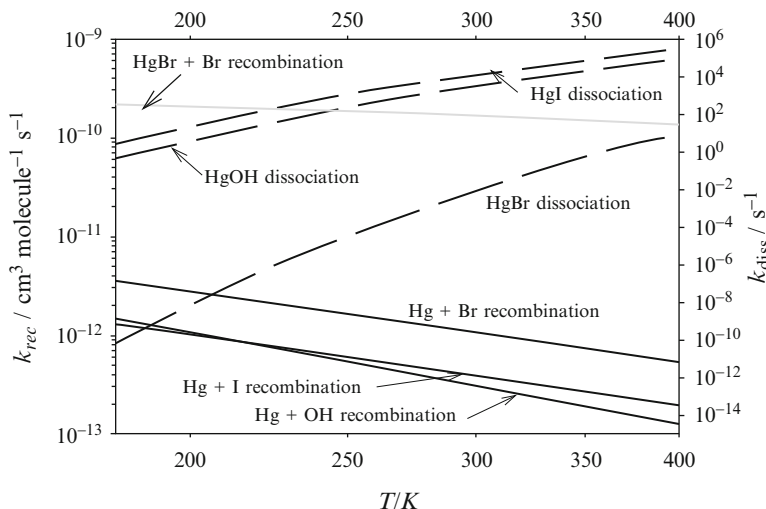
Fig. 12.3 Rate coefficients calculated using RRKM theory, plotted as a function of temperature in Kelvin (T/K) for the recombination of Hg with Br, I, and OH and of HgBr with Br (*solid lines*, *left-hand ordinate*); and for the thermal dissociation of HgBr, HgI, and HgOH (*broken lines*, *right-hand ordinate*) (Reproduced from Goodsite et al. [48]. With kind permission of The American Chemical Society 2004)

much error. It could be shown further, that the lifetime to convert Hg^0 to Hg (II) depends on the rate at which HgBr (and other HgX compounds) decomposes (reaction (12.14b)). The rate constant, k_{-6}, is obtained by detailed balance with k_6 so that the lifetime of Hg^0 is not very dependent on the choice of k_6. In the case of reaction 12.15, the addition of the second bromine to HgBr is predicted to be a very fast reaction, proceeding close to the high-pressure limit (essentially the collision number) at atmospheric pressure.

Two important points that emerge from Fig. 12.3 are the relatively slower rate constants of I and OH recombination reactions (with Hg) and very slow thermal dissociation of HgBr ($\sim 10^6$ times) with respect to HgI and HgOH (below 300 K). These two factors are dependent on the relative binding energies of the respective compounds and it could be concluded that Hg^0 is oxidized to Hg (II) by recombination with HgBr.

There is also a competition between further addition of Br to form $HgBr_2$, or thermal decomposition of HgBr. The addition of I to HgBr may also be significant in some marine locations; however, the OH concentration in the clean marine boundary layer (typically less than $106 \, cm^{-3}$) is probably too low for OH addition to HgBr to be significant. The addition of O_2 to form $HgBrO_2$ will not be an important process because this peroxy radical is so weakly bound ($D_0 = 30 \, kJ \, mol^{-1}$) [79] that it will dissociate rapidly even at Arctic temperatures.

The lifetime (τ) of Hg^0 against conversion to $HgBr_2$ has further been computed to check the availability range of Hg in the atmosphere against bromine concentration

Fig. 12.4 Contour plot of the lifetime in hours for Hg^0 oxidation to $HgBr_2$, plotted as a function of Br in parts per trillion and temperature in Kelvin (Reproduced from Goodsite et al. [48]. With kind permission of © The American Chemical Society 2004)
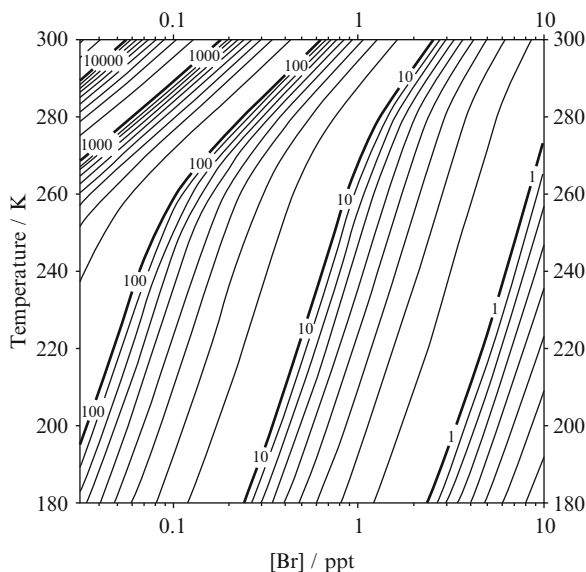
([Br]) (Eq. 12.20) [48]. The computation is an upper bound of τ as other factors affecting the removal of Hg^0 were not considered during this computation.

$$\tau = \frac{k_{-6} + k_7\,[Br]}{k_6 k_7 [Br]^2} \tag{12.20}$$

The plot of τ against [Br] showed (Fig. 12.4) that around 230–260 K and low [Br] (~0.2 ppt), the Hg depletion period is 35–60 h (hours). With higher [Br] (6.0 ppt), τ is only 0.7–1.5 h. A typically observed 10.0 h τ of Hg would correspond to 0.7 ppm bromine concentration [79]. It was further observed that with higher temperature (>280 K) other side reactions (e.g., formation of BrO, reactions with atomic I and OH) become competitive, since [Br] drops to ~0.1 ppt. Such a situation increases τ of Hg to >4,000 h (Fig. 12.4) and it is in accord with the observed global lifetime of Hg (more than 1 year) [94–96]. Since HgBr photodissociation rate is significant in the troposphere, this lifetime might increase even more.

12.3.3 Use of Analytical Potential Energy Surface (APES) to Compute Kinetics of Mercury Recombination Reactions with Bromine

Bromine-mercury reactions are considered to be the most important mercury depletion event. In the last two sections we have discussed the strategy used to compute various mercury depletion reactions through collision theory and RRKM

Fig. 12.5 Notation of coordinates for $HgBr_2$ used in sampling and fitting the PES (Reproduced from Benjamin et al. [81]. With kind permission of © The American Chemical Society 2005)
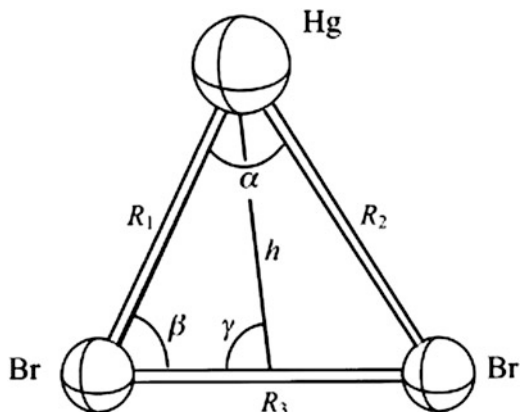
theory (through ME formalism). Balbanov and coworkers constructed a global potential energy surface (PES) for the $^1A'$ ground state of $HgBr_2$ in order to determine the rate constants for atmospherically important reactions involving mercury and bromine [81]. Their strategy was based on the calculations using quasi-classical trajectory (QCT) and variational transition state theory (VTST). A detailed discussion of the techniques used is beyond the scope of the present review. We will discuss the salient features of this approach with results of kinetics analysis. Interested readers are referred to the original articles [81].

The basic idea behind the generation of the analytical potential energy surface of $HgBr_2$ was to divide the surface into three regions corresponding to the abstraction reaction $HgBr + Br \rightarrow Hg + Br_2$, insertion reaction $Hg + Br_2 \rightarrow HgBr_2$, and recombination reaction $Br + HgBr \rightarrow HgBr_2$. Each of these sections was sampled by a regular three-dimensional grid in its natural internal coordinates. These internal coordinates (R_1, R_2, R_3, h, α, β, and γ) are defined in Fig. 12.5. The surfaces of the different reactions are sampled into grids of several configurations (more than 1,200 grid points are generated for each reaction through various choices of internal coordinates). The energies at each point were constructed through SO corrections on MR-CI energies (including Davidson's correction [97]) with complete basis set (CBS) extrapolation [98]. The data of regular grids for the recombination, abstraction, and insertion reaction regions were first decomposed using the general many-body expansion [99] (Eq. 12.21).

$$\tilde{V}(R_1, R_2, R_3) = V^{(1)} + V_{HBr}^{(2)}(R_1) + V_{HgBr}^{(2)}(R_2) + V_{BrBr}^{(2)}(R_3) + V^{(3)}(R_1, R_2, R_3)$$

$$(12.21)$$

These individual $V^{(i)}$ terms are interpolated via various one-dimensional ($V^{(2)}$), and multidimensional ($V^{(3)}$) techniques and these fitted potentials are used to generate the final global $HgBr_2$ potential energy surface. A detailed discussion of such procedures is available in the original publications [79, 81].

The thermal rate constants of the reactions $HgBr + Br \rightarrow$ products were computed with the help of the analytical potentials and the compute $HgBr_2$ transition state. This transition state has an angular geometry (r (Hg–Br) = 2.85 Å; and θ (Br–Hg–Br) = 55.7°) with a high barrier (27.2 kcal mol^{-1}). QCT method was used to compute the thermal rate constants ($k(T)$) using Eq. 12.22:

$$k(T) = \sum_{v,j} k^{vj}(T) \frac{(2j + 1) \exp\left\{-E_{vj}/k_B T\right\}}{Q_{vr}(T)} \qquad (12.22)$$

where Q_{vr} is the rovibrational partition function; E_{vj} is the HgBr rovibrational energy for the vibrational and rotational quantum numbers v and j, and $k^{vj}(T)$ is the reaction rates for each (v, j) rovibrational energy level. E_{vj} and $k^{vj}(T)$ terms are computed with the help of the calculated analytical two-body HgBr potential (with standard rovibrational energy expression) and the knowledge of reaction cross section (as discussed earlier in Sect. 12.3.1). The details are available in [77]. We will present only the relevant rate constants computed using this technique. Several other rate constant calculation techniques, which include canonical (CVT), improved canonical (ICVT), microcanonical (μVT) variational transition state theory [83], were also used to compare the rate constants through QCT technique. The computed rate constants are presented below ($T = 298$ K, Eq. 12.18) [81]. The bimolecular rate constants A–E are expressed in cm^3 M^{-1} s^{-1}, and the unimolecular rate constants for the reaction F and G are expressed in s^{-1}. The thermal rate constant for the insertion reaction C is very small. The transition state corresponds to a geometry (r(Hg–Br) = 2.857 Å; θ (Br–Hg–Br) = 56.6°) close to that predicted through APES (discussed earlier). In the case of abstraction reaction A and recombination reaction B, ICVT predicts collinear geometries for the transition states (A: r (Hg–Br) = 2.56 Å, r (Br–Br) = 3.80 Å; B: r_1 (Hg–Br) = 2.54 Å, r_2 (Hg–Br) = 4.57 Å) in contrast to the angular geometry of the transition state predicted through APES

A. $HgBr + Br \rightarrow Hg + Br_2$ 3.89×10^{-11}(QCT); 6.15×10^{-11}(CVT); 5.30×10^{-11}(ICVT); 4.52×10^{-11}(μVT)

B. $HgBr + Br \rightarrow HgBr_2$ 2.98×10^{-11}(QCT); 1.27×10^{-10}(CVT); 1.22×10^{-10}(ICVT); 1.05×10^{-10}(μVT)

C. $Hg + Br_2 \rightarrow HgBr_2$ $\cdots$(QCT)2.76×10^{-31}(CVT); 2.76×10^{-31} (CVT); 2.74×10^{-31}(μVT)

D. $BrHg + Br \rightarrow Br + HgBr$ 3.97×10^{-11}(QCT)

E. $Hg + Br_2 \rightarrow HgBr + Br$ 3.4×10^{-31}(QCT); 5.4×10^{-31}(CVT); 4.6×10^{-31}(ICVT); 3.9×10^{-31}(μVT)

F. $HgBr_2 \rightarrow HgBr + Br$ 5.5×10^{-39}(QCT); 2.4×10^{-38}(CVT); 2.3×10^{-38}(ICVT); 2.0×10^{-38}(μVT)

G. $HgBr_2 \rightarrow Hg + Br_2$ $\cdots$(QCT); 5.90×10^{-39}(CVT); 5.90×10^{-39}(ICVT); 5.80×10^{-39}(μVT)   (12.23)

The computed rate constant for the reaction B in QCT technique is ten times faster than the experimental rate constant [46, 52]. The predicted rate constant in the other three methods is even faster (40 times). The computed rate constant by Goodsite and coworkers [48], in this respect, is more reasonable, although done at much lower level of theory. The insertion reaction C is also predicted to be much faster at the VTST level of theories (with respect to the experiment (9.0×10^{-17} cm^3 M^{-1} s^{-1}) [46]). The rest of the reactions represent different reaction channels, but their computed rates cannot be verified because of the lack of experimental data.

There are several explanations for the observed discrepancies, and most probable explanation could be the experimental conditions of such experiments [81]. Theoretical calculations also have their shortcoming in accounting for the proper thermodynamics of such reactions, which plays an important role in accounting for the more sensitive reaction parameter, that is, rate constants. The accuracy level of thermochemical calculations in such reactions will be discussed in the latter section of this review.

12.3.4 Kinetics of Mercury Oxidation by Chlorine Through Simple Transition State Theory (TST)

Coal combustion flue gases are usually accompanied by the oxidation of particulate mercury by HCl, Cl$_2$, or HOCl. The role of these species may be minimal for mercury oxidation in the atmospheric condition, but their role is critical in understanding the speciation of mercury in the quench zone of the flue gases. Such oxidation reactions are represented in the following reactions (12.24–12.26):

$$Hg + HCl \underset{k_{-1}}{\overset{k_1}{\rightleftharpoons}} HgCl + H \tag{12.24}$$

$$Hg + Cl_2 \underset{k_{-2}}{\overset{k_2}{\rightleftharpoons}} HgCl + Cl \tag{12.25}$$

$$Hg + HOCl \underset{k_{-3}}{\overset{k_3}{\rightleftharpoons}} HgCl + OH \tag{12.26}$$
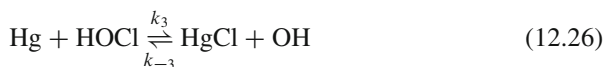
The experimental equilibrium constants data of the reactions (12.1) and (12.2) are available in the temperature range 298.15–2,000 K, and thus theoretical studies were carried out using transition state theory (TST) to explore the kinetics of such reactions [82], so that the behavior of such reactions could be understood properly at varying range of temperatures. The structural analysis of the reactants and products were carried out using DFT calculations with relativistic basis set of mercury. Triple-ζ quality basis sets were used for other elements [82]. The structural characteristics of the transition states were determined from the extensive potential energy surface of the individual reactions. The detailed methodology and structural analysis are available in the original manuscript [82].

The computations of the reaction rates of (both forward and backward reactions) involve the use of transition state theory (Eq. 12.27) [100], with Wigner's tunneling correction (Eq. 12.28) [101]. The final rate constant is expressed as the product of $k(T)$ and k_T.

$$k(T) = \frac{k_B T}{h} \frac{Q_{TS}}{\Pi Q_i} \exp\left(-E_a / RT\right) \tag{12.27}$$

$$k_T = 1 + \frac{1}{24}\left[\frac{hc\nu}{k_B T}\right]^2 \tag{12.28}$$

In the right-hand side of the equations, k_B is Boltzmann's constant, h is Plank's constant, T is temperature, E_a is activation barrier, R is the ideal gas constant, and Q terms are the partition functions of the transition state (Q_{TS}) and reaction species. The properties of the computed rate constants (in terms of Arrhenius expressions) for reactions (12.24)–(12.26) (for both forward and reverse reactions) are discussed below. These rate constants were computed in the temperature range of 298.15–2,000 K at an interval of 300 K.

Reaction (12.24):

$$k_1 = 1.93 \times 10^{13} \exp\left(-\frac{93.3}{RT}\right) \ (cm^3/M/s)$$

$$k_{-1} = 2.55 \times 10^{12} \exp\left(-\frac{13.8}{RT}\right) (cm^3/M/s)$$

(Transition state (TS) geometry: r(Hg–Cl): 2.55 Å; r(Cl–H): 2.70 Å; θ(Hg–Cl–H): 180.0°)

Reaction (12.25):

$$k_2 = 6.15 \times 10^{13} \exp\left(-\frac{43.3}{RT}\right) \ (cm^3/M/s)$$

$$k_{-2} = 7.23 \times 10^{12} \exp\left(-\frac{11.8}{RT}\right) (cm^3/M/s)$$

(TS geometry: r(Hg–Cl): 2.55 Å; r(Cl–Cl): 3.45 Å; θ(Hg–Cl–Cl): 180.0°)

Reaction (12.26):

$$k_3 = 3.06 \times 10^{13} \exp\left(-\frac{36.6}{RT}\right) \ (cm^3/M/s)$$

$$k_{-3} = 6.87 \times 10^{11} \exp\left(-\frac{6.2}{RT}\right) (cm^3/M/s)$$

(TS geometry: r(HO–Cl): 2.50 Å; r(Cl–Hg): 2.51 Å; θ(O–Cl–Hg): 180.0°; θ(H–O–Cl): 180.0°)

The forward activation energies (93.3 kcal mol^{-1}) used in the rate constant equations of reaction (12.24) deviated by no more than ~3 kcal mol^{-1} with respect to the experiment at each temperature, while for the reverse reaction (E_a =13.8 kcal mol^{-1}) the deviation was ~2.5 kcal mol^{-1} [82]. The highest
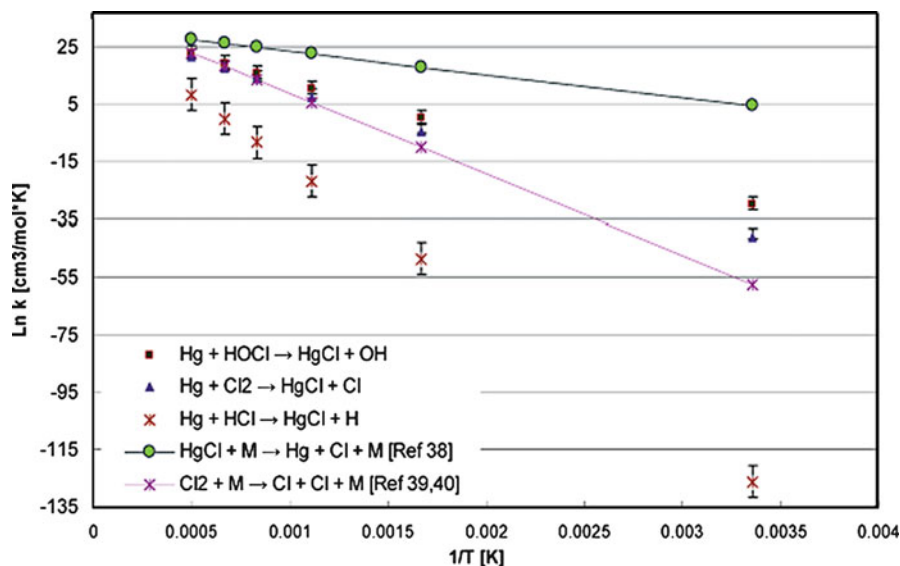
Fig. 12.6 Comparison of forward rate constants as a function of temperature (Reproduced from Wilcox [82]. With kind permission of © The American Chemical Society 2009)

deviations were found at the lower temperatures examined, suggesting that the deviation from the developed model will increase as temperature decreases. In the case of reaction (12.25) the computed barrier height deviated ∼1.7 kcal mol^{-1} for the forward reaction and ∼1.9 kcal mol^{-1} for the reverse reaction within the specified temperature range, while deviations are ∼1.8 and ∼6.2 kcal mol^{-} for the forward and reverse reactions (of reaction (12.26)) [82]. The maximum deviation in both of the cases is at higher temperature (2,000 K).

A comparison of rate constants (Fig. 12.6) over the entire temperature range of 298.15–2,000 K shows that, in general, oxidation involving HOCl is faster than that of Cl_2, which is faster than that of HCl. However, oxidation via HOCl and Cl_2 compete with one another at high temperatures. The rate expressions for two additional reactions are also plotted in Fig. 12.6, that is, $HgCl + M \rightleftharpoons Hg + Cl + M$ [102] and $Cl_2 + M \rightleftharpoons 2Cl + M$ [103]. Within each of these unimolecular reactions, M is the collision partner or gas bath, which does not participate chemically in the reactions, but is taken into account within the pressure-dependent kinetic predictions using RRKM theory. The depletion of HgCl as temperature decreases is faster than the three HgCl formation reactions, while it is comparable to the formation reactions involving HOCl and Cl_2 at high temperatures. The dissociation reaction of Cl_2 to chlorine radicals is comparable to the formation reactions involving HOCl and Cl_2 at high temperatures, but is slower at low temperatures, which ensures the presence of chlorine radicals at high temperatures. Due to the higher concentration of chlorine present in the flue gases compared to elemental mercury, the generation of chlorine radicals and the presence of Cl_2 should be expected throughout the quenching

zone. This would imply that the oxidation reactions involving Cl and Cl_2 should be dominant over the others and the oxidation involving HOCl will occur, provided its concentration is available in sufficient quantity.

12.3.5 Thermochemical Approaches (Using Quantum Chemical Methods) on the Mercury Speciation Reactions

Thermochemical studies on various atmospheric mercury depletion reactions are quite important in understanding the nature of such reactions in both gas phase and in aqueous medium. Shepler and coworkers [80] investigated the reactions of Hg with IX (X = I, Br, Cl, and O) using high-level quantum chemical calculations involving CCSD(T) method (with CBS extrapolation) including relativistic corrections. The objective was to generate relatively accurate heat of reaction (ΔH) (with respect to the experimental data), which could be used to interpret the thermodynamic properties of such reactions. They inferred [80] that the reactions HgI + X/HgX + I → HgIX are strongly exothermic. The results could be considered quite reliable as the authors have reproduced the ΔH within 1 kcal mol^{-1} (with respect to the experimental data) for several of such reactions. Shepler and coworkers [84] also computed the thermodynamic properties of several microsolvated mercury halide species using Møller-Plesset second-order perturbation (MP2) theory [104] and DFT [70] techniques (with CBS extrapolation [98]). They found that the presence of water favors the formation of oxidized mercury halide species. This is an important observation and led to the further investigation of the thermodynamic characteristics of various radical [105] and ionic forms [106] of mercury halide reactions, as they have important contribution to mercury depletion reactions in the polar regions and in upper atmospheric conditions.

12.3.5.1 Thermochemistry of Elemental Mercury Reactions with Halogen Radicals and Anions

Maron and coworkers [105] have computed the thermochemical characteristics of GEM with halogen radicals and/or anions to explain mercury depletion events (ADMEs) that lead to significant deposition of Hg^{2+} in snow and ice surfaces in the polar region. It was generally known that deposition of GEM onto environmental surfaces occurs following the oxidation by ozone and hydroxyl radicals [107]. In recent times, halogen radicals, especially bromine and bromine oxides have been suspected to be the main chemical oxidants in the polar atmosphere in spring, when ADMEs occur [32, 108]. During ADME, Hg^0 is rapidly transformed into water-soluble and reactive species of Hg (gaseous Hg^{II} complexes and/or Hg^{II} bound to particles) leading to a massive deposition of divalent Hg onto environmental

surfaces such as snowpacks, sea ice, and open ocean. Part of the deposited Hg is reemitted back into the atmosphere after reduction of Hg^{II} complexes in the snow, which is likely to be light-initiated [41].

Thermochemical analysis (through quantum chemical methods) of such mercury depletion reactions needs rigorous structural analysis of the reactive species (radicals or ions) at the primary stage. These structural aspects were studied by Maron and coworkers using density functional techniques [105]. They found that the radicals of mercury (e.g., $HgX_3^{\bullet}$ and $HgX_4^{2\bullet}$ − usually open-shell doublets and triplets) possess distorted geometry with respect to their anionic counterparts [105]. The Gibbs free energy changes (ΔG, kcal mol^{-1}) were monitored for the following reactions (reactions 12.29–12.33) using the computed structural information of the reactive ingredients [105]:

$$Hg + 2X^{\bullet} \rightarrow HgX_2 \qquad (12.29); \Delta G = -82.3, -66.7, -51.9 \quad (\text{for X} = \text{Cl, Br, I})$$

$$Hg + 3X^{\bullet} \rightarrow HgX_3^{\bullet} \qquad (12.30); \Delta G = -87.4, -72.3, -59.0 \quad (\text{for X} = \text{Cl, Br, I})$$

$$Hg + 4X^{\bullet} \rightarrow HgX_4^{2\bullet} \qquad (12.31); \Delta G = -87.4, -74.0, -61.0 \quad (\text{for X} = \text{Cl, Br, I})$$

$$Hg + 2X^{\bullet} + X^{-} \rightarrow HgX_3^{-} \qquad (12.32); \Delta G = -122.7, -105.1, -88.2 \quad (\text{for X} = \text{Cl, Br, I})$$

$$Hg + 2X^{\bullet} + 2X^{-} \rightarrow HgX_4^{2-} \qquad (12.33); \Delta G = -72.1, -54.7, -38.8 \quad (\text{for X} = \text{Cl, Br, I})$$
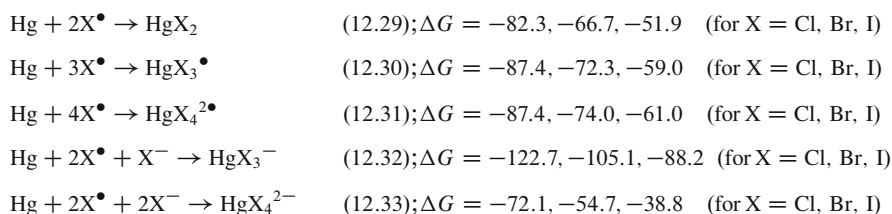
The computed ΔG values show that the coordination of two radicals to the mercury center is highly favorable in the gas phase for all halogens. Interestingly, the coordination of the third and fourth halogen radical is also found to be thermodynamically favorable, leading to stable structures. Moreover, it appears that these two extra coordinations (leading to $HgX_3^{\bullet}$ and $HgX_4^{2\bullet}$) are calculated to be only slightly exergonic with respect to the two first ones (formation of HgX_2) so that these radical species could act as a halogen free-radical source. The ΔG values further show that the formation of HgX_3^{-} is highly favorable in the gas phase for all halogens. On the other hand, the formation of the tetrahedral HgX_4^{2-} is predicted to be unfavorable. This is explained by the repulsion between the ten d electrons of the mercury and the valence electrons of the four halogen ligands (eight electrons). This repulsion is greater for mercury than for other atoms of Group 12, since due to relativistic effects the 5d shell is close in energy to the 6s and 6p shells used for making the bonds with the ligands.

By comparing the formation energies of the radical and anionic forms of HgX_3 it appears that the anionic structure is more stable than the radical one. The stability of such a complex was already reported in the literature [109]. On the other hand, it is noteworthy that the radical form of HgX_4 is more likely than its anionic counterpart. The results further show the importance HgX_3^{-} (especially $HgCl_3^{-}$) in the solution chemistry of Hg.

Another alternative for the creation or destruction of GEM without light is that a redox reaction can occur in solution. The redox potentials of the couples HgX_2/Hg for X = Cl, Br, and I were computed through Nernst law [105]. These redox potentials were found to be 0.52 V for Cl, 0.48 V for Br, and 0.04 V for I. Thus, based on the knowledge of the composition of snowpacks, it is possible to
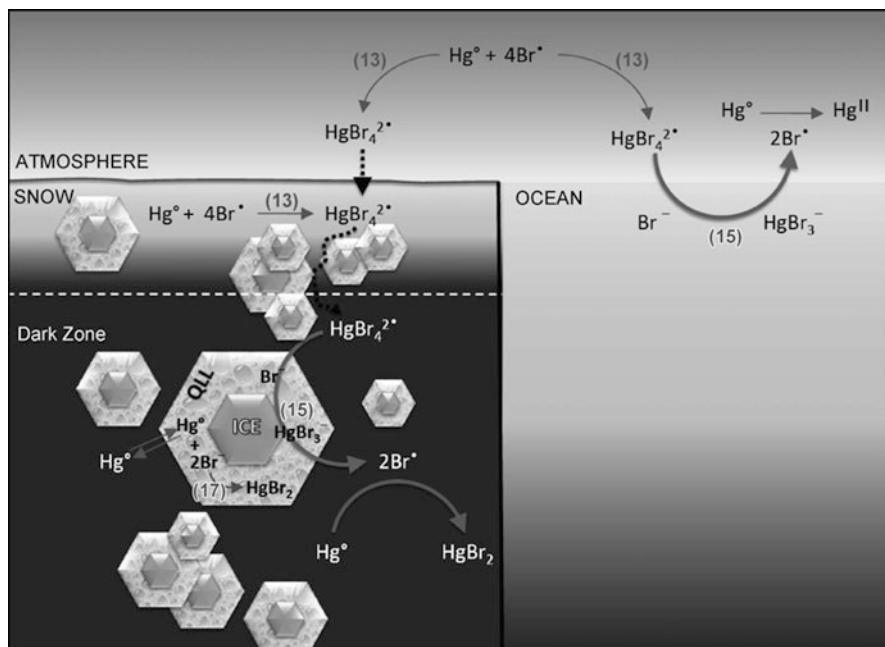
Fig. 12.7 A schematic view of some oxidation pathways of gaseous elemental mercury (GEM, Hg^0) in polar regions, based on the reactions defined in Eqs. 12.34 and 12.36 ($n = 4$). (These reactions are marked as 13 and 15 in the figure. An additional reaction 17 (defined in [105]) is also used to design the reaction cycle) (Reproduced from Maron et al. [105]. With kind permission of © Wiley−VCH 2008)

predict either the formation or the destruction of GEM. These redox potentials are therefore an interesting tool to predict the possible reactions in solution, even though they do not deal with the kinetics.

Based on the thermochemistry of the reactions 12.29–12.33, results of redox behavior of the HgX_2/Hg couple, and the previously discussed collisional kinetics studies by Goodsite and coworkers (Ref. [48], Sect. 12.3.3), the following reactions schemes could be proposed for catalytic cycle of mercury destruction:

$$Hg + nX^\bullet \rightarrow HgX_n^{(n-2)\bullet} \quad \text{for } n = 3, 4 \tag{12.34}$$

$$HgX_n^{(n-2)\bullet} + (Hg^\bullet \text{or collision}) \rightarrow HgX_2 + (n-2)X^\bullet \tag{12.35}$$

$$HgX_n^{(n-2)\bullet} + X^- \rightarrow HgX_3^- + (n-2)X^\bullet \tag{12.36}$$
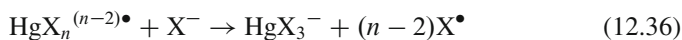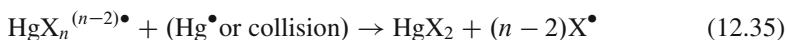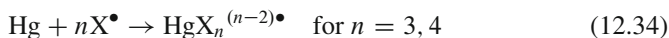
The last reaction could occur when gas/solution interface is present. These ideas lead to propose an oxidation cycle pathways of GEM in the polar region (Fig. 12.7). The pathways are depicted for reactions involving Br atoms. They could be expanded and written similarly for the chlorine atoms [105].

12.3.5.2 Thermochemistry of Mercuric Ion with Halide and Pseudohalides in Aqueous Medium

It has been discussed in Sect. 12.3.5.1 how the stability and solubility of mercury in various forms strongly influence the rate of its removal from the atmosphere through wet deposition. Most of the atmospheric mercury (ca 98%) exists in the gas-phase in elemental (Hg^0) form, and in the last few sections various experimental and theoretical approaches have been discussed, which lead to the understanding of the behavior of Hg^0 toward atmospheric oxidizing agents (mostly halides and halogen oxides). Significant concentration of mercury is also found in cloud droplets, and this exceeds the solubility of normal $Hg_{(aq)}^0$ by almost three orders of magnitude [7, 110]. This finding led to the conclusion that, unlike in the gas phase, the mercury in the atmospheric water exists mostly as soluble mercuric ion ($Hg_{(aq)}^{2+}$) and the reactivity of such solvated mercuric ion has also significant role in the atmospheric speciation of mercury.

The ionic composition of the droplets or aerosols makes a difference to the quantity of $Hg_{(aq)}^{2+}$, which can be feasibly associated with the particles [7]. Modeling studies showed that because of the greater number of potential complexes between $Hg_{(aq)}^{2+}$ and $Cl_{(aq)}^-$ (and other halides), compared to $OH_{(aq)}^-$ or $SO_3^{2-}{}_{(aq)}$, higher concentration of $Hg_{(aq)}^{2+}$ (by a factor of 100) could be found in droplets with high halide concentrations [7]. The reactivity of mercuric ion toward different halide ions was explored through electronic structure calculations combined with the thermochemistry (Gibbs potential, ΔG°_{aq}) of such reactions in aqueous medium using CCSD [71] level of theories [106]. A reasonable estimation of these thermochemical quantities is important as they could be subsequently used to compute the kinetics of several such reactions in aqueous medium.

The following mercury compounds were studied: HgX^+, HgX_2, HgX_3^-, HgX_4^{2-} (X = Cl, Br, I, CN, and SCN). Pseudohalides (CN^-, and SCN^-) were also added in the studies, as they also form known mercury compounds in the environment with thermochemical characteristics comparable to those of halides [111]. The molecular structures were fully optimized in the gas phase using CCSD techniques and these structures were all verified using the available experimental results. For few larger systems, the structures were optimized at the MP2 level. The information of the gas-phase structures were used to generate structures of these species in aqueous medium (through geometry optimization) at the CCSD/MP2 level using a polarized continuum model with conductor-like screening reaction field (CPCM) [112, 113]. The full details of structure analysis are available in the original article [106].

The reactions considered for the thermochemical studies could be written in the following way:

$$HgX_n{}^q(aq) + X^-(aq) \rightarrow HgX_n{}^{q-1}(aq) \tag{12.37}$$
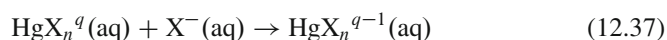
where q represents charge of the species $HgX_n{}^q$ ($n = 0$–4), depending on the number of X (n) attached to it. The Gibbs free energies computed for the gas phase and the

Table 12.2 Calculated ΔG°_{aq} (kcal mol^{-1}) for the various HgX$_n^m$ (X = Cl, Br, I, CN, SCN) formation reactions due to vertical and equilibrium solvation of the respective solutes in aqueous medium at the CCSD/CPCM level of theories (unless otherwise mentioned)[a,b]

Reactions	ΔG°_{aq}		
	Vertical	Equilibrium	Expt.[d]
$Hg_{(aq)}^{++} + Cl_{(aq)}^{-} \rightarrow HgCl_{(aq)}^{+}$	−14.17	−17.63	−9.22
$HgCl_{(aq)}^{+} + Cl_{(aq)}^{-} \rightarrow HgCl_{2(aq)}$	−15.58	−16.95	−8.73
$HgCl_{2(aq)} + Cl_{(aq)}^{-} \rightarrow HgCl_3^{-}{}_{(aq)}$	1.21	2.24	−1.13
$HgCl_3^{-}{}_{(aq)} + Cl_{(aq)}^{-} \rightarrow HgCl_4^{2-}{}_{(aq)}$	3.11	5.68	−1.52
$Hg_{(aq)}^{++} + 4Cl_{(aq)}^{-} \rightarrow HgCl_4^{2-}{}_{(aq)}$	−25.44	−26.69	−20.61
$Hg_{(aq)}^{++} + Br_{(aq)}^{-} \rightarrow HgBr_{(aq)}^{+}$	−10.38	−12.60	−12.33
$HgBr_{(aq)}^{+} + Br_{(aq)}^{-} \rightarrow HgBr_{2(aq)}$	−8.84	−9.95	−11.45
$HgBr_{2(aq)} + Br_{(aq)}^{-} \rightarrow HgBr_3^{-}{}_{(aq)}$	5.83	3.67	−2.97
$HgBr_3^{-}{}_{(aq)} + Br_{(aq)}^{-} \rightarrow HgBr_4^{2-}{}_{(aq)}$	6.06	10.10	−1.80
$Hg_{(aq)}^{++} + 4Br_{(aq)}^{-} \rightarrow HgBr_4^{2-}{}_{(aq)}$	−7.04	−8.78	−8.78
$Hg_{(aq)}^{++} + I_{(aq)}^{-} \rightarrow HgI_{(aq)}^{+}$	−12.86	−13.93	−17.46
$HgI_{(aq)}^{+} + I_{(aq)}^{-} \rightarrow HgI_{2(aq)}$	−7.77	−9.83	−15.16
$HgI_{2(aq)} + I_{(aq)}^{-} \rightarrow HgI_3^{-}{}_{(aq)}$	5.71	4.85	−5.17
$HgI_3^{-}{}_{(aq)} + I_{(aq)}^{-} \rightarrow HgI_4^{2-}{}_{(aq)}$	7.53	9.34	−2.78
$Hg_{(aq)}^{++} + 4I_{(aq)}^{-} \rightarrow HgI_4^{2-}{}_{(aq)}$	−7.39	−9.67	−40.57
$Hg_{(aq)}^{++} + CN_{(aq)}^{-} \rightarrow HgCN_{(aq)}^{+}$	−26.24	−26.69	−17.46
$HgCN_{(aq)}^{+} + CN_{(aq)}^{-} \rightarrow Hg(CN)_{2(aq)}$	−25.21	−25.46	−15.16
$Hg(CN)_{2(aq)} + CN_{(aq)}^{-} \rightarrow Hg(CN)_3^{-}{}_{(aq)}$	3.88	2.62	−5.17
$Hg(CN)_3^{-}{}_{(aq)} + CN_{(aq)}^{-} \rightarrow Hg(CN)_4^{2-}{}_{(aq)}$	0.61[c]	0.72[c]	−4.09
$Hg_{(aq)}^{++} + 4CN_{(aq)}^{-} \rightarrow Hg(CN)_4^{2-}{}_{(aq)}$	−63.96	−66.25	−56.29
$Hg_{(aq)}^{++} + SCN_{(aq)}^{-} \rightarrow HgSCN_{(aq)}^{+}$	−12.88	−13.63	−23.59
$HgSCN_{(aq)}^{+} + SCN_{(aq)}^{-} \rightarrow Hg(SCN)_{2(aq)}$	−7.85	−10.46	−23.50
$Hg(SCN)_{2(aq)} + SCN_{(aq)}^{-} \rightarrow Hg(SCN)_3^{-}{}_{(aq)}$	3.93[c]	3.20[c]	−5.10
$Hg(SCN)_3^{-}{}_{(aq)} + SCN_{(aq)}^{-} \rightarrow Hg(SCN)_4^{2-}{}_{(aq)}$	2.18[c]	1.41[c]	−2.52
$Hg_{(aq)}^{++} + 4SCN_{(aq)}^{-} \rightarrow Hg(SCN)_4^{2-}{}_{(aq)}$	−25.44[c]	−26.21[c]	−29.59

Experimental data are also added for comparison, Reprinted from Majumdar et al. [106]. With kind permission of © Elsevier (2010)

[a]The ΔG°_{aq} is calculated using Eq. 12.38

[b]The parameters for calculation of ΔG°_{aq} is available in the supplementary section of [106]

[c]Computed at the MP2/CPCM level

[d]Ref. [111, 114]

solvated species were used to estimate the ΔG°_{aq} of the reaction using the relation (12.38) (obtained through thermodynamic cycle) [106].

$$\Delta G^\circ_{aq} = (\Delta G^\circ_g + \Delta G^\circ_{s3}) - (\Delta G^\circ_{s1} + \Delta G^\circ_{s2}) \qquad (12.38)$$

Here ΔG°_{si} ($i = 1$–3) are the corresponding ΔG°_{sol} (Gibbs free energy of solvation) of HgX$_n^q$, X$^-$, and HgX$_n^{q-1}$, respectively and ΔG°_g is the Gibbs free energy change for the gas-phase reaction. The various reactions studied for the formation of the mercuric compounds HgX$_n^q$ are shown in Table 12.2 together with the

corresponding ΔG°_{aq} values. Both vertical and equilibrium solvation conditions were considered and the available thermodynamic data (experimental) from the literature [111, 114] were included for comparison. It is to be noted from the ΔG°_{aq} that while the behaviors of cyanides are very different from rest of the halides, the thiocyanate reactions are very close to those of iodides.

The results (Table 12.2) show that although the calculated values are quite close to ΔG_{aq}° from the literature, there are large deviations in a few cases. Two possible sources of error are feasible in such calculations. The first source of error lies in the inaccuracy of the calculated ΔG°_s of cations and anions (ΔG°_{s1} and ΔG°_{s2}). The results from most of the continuum solvation calculations [115, 119] on various cations and anions are usually close to the data of Marcus [120] (the so-called absolute ΔG°) and reliability of the computed values could be checked by fitting them with those of the absolute ΔG°. It has been found that the computed values on various divalent cations and monovalent anions (using similar level of theory used for mercury compounds) fit linearly with the data of Marcus [120] quite well [106]. But the more serious problem lies in obtaining the reliable absolute ΔG° of mercury halides, cyanides, and thiocyanates through Marcus's scale (because of the lack of sufficient thermodynamic data in this respect). If it is assumed that whatever might be the scale of reference, the ultimate value of ΔG°_{aq} for the formation of such compounds are the same (since it generates equilibrium constant K of such reactions), the most practical approach in the present situation would be to fit the computed ΔG°_{aq} with respect to those of standard thermodynamic data (Table 12.2). Figure 12.8 shows that the computed ΔG°_{aq}, using both vertical and equilibrium solvation of the solutes, fits linearly with those of the standard data. The recalculated ΔG°_{eq} in most of the cases is within ~ 2 kcal mol^{-1} of the experimental data. The results might not produce accurate kinetics of such reactions, but it could be a good starting point to study the qualitative features related to the kinetics of such processes.

12.3.6   Mercury Depletion Involving Other Oxidizing Agents

Apart from halides and halogen oxides, several other oxidizing agents also play important role in atmospheric mercury depletions. These are mostly O_3, atmospheric OH radical, H_2O_2, and SO_3. Both gas-phase and aqueous-phase rate constants as well as the equilibrium constants of such reactions are experimentally known. These are represented below with references (within square brackets).

Gas-phase reactions:

$Hg + O_3 \rightarrow HgO + O_2$; $k = 8.43 \times 10^{-17} \times \exp(-1407 K/T) \, cm^3 M^{-1} s^{-1}$ [121]

$Hg + OH \rightarrow HgO + H$; $k = 3.55 \times 10^{-14} \times \exp(294 \, K/T) \, cm^3 M^{-1} s^{-1}$ [122]

$Hg + H_2O_2 \rightarrow HgO + H_2O$; $k = 8.5 \times 10^{-14} cm^3 M^{-1} s^{-1}$ [123]
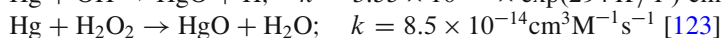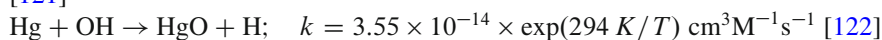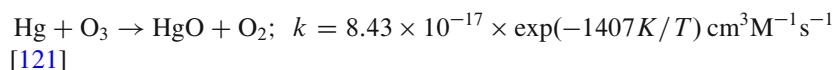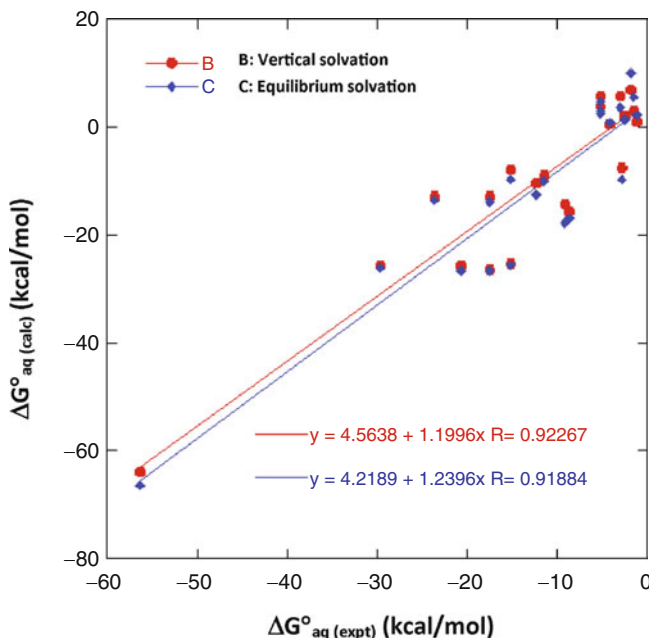
Fig. 12.8 Correlation of the experimental and calculated ΔG°_{aq} of the various HgX^+, HgX_2, HgX_3^-, and HgX_4^{2-} (X = Cl, Br, I, CN, and SCN) complexes. The data are available in Table 12.2. Three of the calculated values (i.e., HgI_4^{2-}, $HgBr_4^{2-}$, and $Hg(SCN)_2$), which are quite off from the experiment (see Table 12.2) are not included in the correlation (Reproduced from Majumdar et al. [106]. With permission of © Elsevier 2010)

Aqueous-phase reactions:

$Hg + O_3 \rightarrow HgO + O_2;\quad k = 4.7 \times 10^7 M^{-1}s^{-1}$ [124]
$HgO + H^+ \rightarrow Hg^{2+} + OH^-;\quad k = 1.0 \times 10^{10}\ M^{-1}s^{-1}$ [63]
$Hg + OH \rightarrow Hg^{2+} + OH^-;\quad k = 2.0 \times 10^9 M^{-1}s^{-1}$ [125]
$Hg^+ + OH \rightarrow Hg^{2+} + OH^-;\quad k = 1.0 \times 10^{10} M^{-1}s^{-1}$ [125]
$HgSO_3 + [H_2O] \rightarrow Hg + HSO_4^- + H^+; k = 0.011 s^{-1}$ [69]
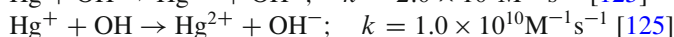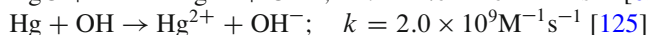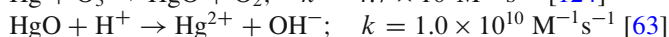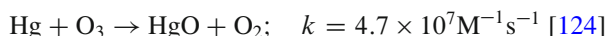
Aqueous-phase equilibria:

$Hg^{2+} + OH^- \rightleftharpoons HgOH^+;\quad K = 4.0 \times 10^{-10} M^{-1}$ [114]
$HgOH^+ + OH^- \rightleftharpoons Hg(OH)_2;\quad K = 1.58 \times 10^{-11} M^{-1}$ [114]
$Hg^{2+} + SO_3^{2-} \rightleftharpoons HgSO_3;\quad K = 2.0 \times 10^{13} M^{-1}$ [126]
$HgSO_3 + SO_3^{2-} \rightleftharpoons Hg(SO_3)_2^{2-};\quad K = 1.0 \times 10^{10} M^{-1}$ [126]
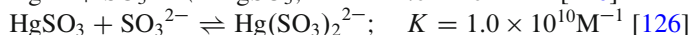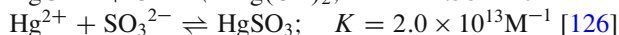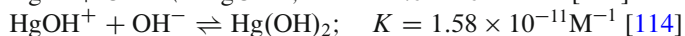
The reactions involving $HO_2^{\bullet}$ and/or $O_2^{\bullet-}$ are not included in this class of reactions as they were found to be quite unlikely from one-electron reduction potential measurements [110]. These reactions are quite important in atmospheric mercury depletion reactions and generation of Hg^{2+} ions in the atmosphere in aqueous condition for further recombination reactions. Important quantum chemical

approaches have not yet been carried out for such reactions. They are included here because of their importance in future studies on more accurate Hg-depletion reaction modeling.

12.3.7   Concluding Remarks

The present review is primarily motivated by the need to introduce the usefulness of quantum-chemical methods to study the kinetics and thermochemical characteristics of various environmental mercury depletion reactions. After a brief survey of the various models of mercury depletion processes, the available reaction kinetics involving such reactions are discussed in details. The reactions investigated are mostly based on collisional process, as it is considered to be the most likely reaction feature in the upper atmospheric region. Elemental forms of mercury and halogen, halogen oxides, and OH radical (as oxidants) are involved in such reactions. The methods of computation of such kinetics are discussed in details and the results are compared with experiments. The mercury depletion can also occur through gas-snow interfaces, inside snowpacks or in purely solvated conditions. Thermochemical studies can lead to detailed understanding of such processes and they are discussed in detail in the latter part of the review (Sects. 12.3.4 and 12.3.5). Mercury depletion reactions involving other oxidants (e.g., O_3, OH, H_2O_2) have been discussed in the last section (Sect. 12.3.6). Proper quantum chemical treatments are not explored yet in such cases. It is to be observed that the rate constants as well as Gibbs free energy change (ΔG^0) are very sensitive to the theoretical approaches employed and even with the use of very high level quantum-chemical approaches, the experimental results are not reproduced properly (within 1 kcal mol^{-1}). Several reasons are there for such disparity and they have been addressed in this review. On the other hand, as we have discussed, these methods could be employed to almost all kinds of reactions with sufficient accuracy to model such mercury depletion reactions in the environment. This is the most important advantage of the use of quantum-chemical techniques in the evaluation of such processes.

References

1. Chrristensen JH, Brandt J, Frohn LM, Skov H (2004) Modeling of mercury in the arctic with Danish Eulerian Hemispheric model. Atmos Chem Phys 4:2251–2257
2. Pan L, Carmichael GR (2005) A two-phase box model to study mercury atmospheric mechanism. Environ Chem 2:205–214

3. Lohman K, Seigneur C, Edgerton E, Jansen J (2006) Modeling mercury in power plant plumes. Environ Sci Technol 40:3848–3854

4. Peleg M, Matveev V, Tas E, Luria M, Valente RJ, Obrist D (2007) Mercury depletion events in the troposphere in mid-latitudes at the dead sea Israel. Environ Sci Technol 41:7280–7285

5. Pirrone N, Cinnirella S, Feng X, Finkelman RB, Friedli HR, Leaner J, Mason R, Mukherjee AB, Stracher GB, Streets DG, Telmer K (2010) Global mercury emissions to the atmosphere from anthropogenic and natural sources. Atmos Chem Phys 10:5951–5964

6. Ariya PA, Peterson KA (2005) Chemical transformation of gaseous elemental mercury in the atmosphere. In: Pirrone N, Mahaffey KR (eds) Dynamics of mercury pollution on regional and global scales: atmospheric processes and human exposures around the world. Springer, New York, pp 261–291

7. Hedgecock IM, Pirrone N (2005) Modelling chemical and physical process of Hg compounds in the marine boundary layer. In: Pirrone N, Mahaffey KR (eds) Dynamics of mercury pollution on regional and global scales: atmospheric processes and human exposures around the world. Springer, New York, pp 295–317

8. Mason RP, Fitzgerald WF, Morel FM (1994) The biogeochemical cycling of elemental mercury: anthropogenic influences. Geochim Cosmochim Acta 58:3191–3198

9. Steffen A, Douglas T, Amyot M, Ariya P, Aspmo K, Berg T, Bottenheim J, Brooks S, Cobbett F, Dastoor A, Dommergue A, Ebinhaus R, Ferrari C, Gardfeldt K, Goodsite ME, Lean D, Poulain AJ, Scherz C, Skov H, Sommar J, Temme C (2008) A synthesis of atmospheric mercury depletion event chemistry in the atmosphere and snow. Atmos Chem Phys 8:1445–1482

10. Xie Z-Q, Sander R, Pöschl U, Slemr F (2008) Simulation of atmospheric mercury depletion events (AMDEs) during polar springtime using MECCA box model. Atmos Chem Phys 8:7165–7180

11. Schroeder WH, Munthe J (1995) Atmospheric mercury – an overview. Atmos Environ 32:809–822

12. Barrie LA, Olson MP, Oikawa KK (1989) The flux of anthropogenic sulphur into the Arctic from mid-latitudes in 1979/80. Atmos Environ 23:2505–2512

13. Akeredolu F, Barrie LA, Olson MP, Oikawa KK, Pacyna JM (1994) The flux of anthropogenic trace metals into the Arctic from the mid-latitudes in 1979/80. Atmos Environ 28:1557–1572

14. Muir DCG, Wageman R, Hargrave BT, Thomas DJ, Peakall DB, Norstrom RJ (1992) Arctic marine ecosystem contamination. Sci Total Environ 122:75–134

15. Giesy JP, Kannan K (2001) Global distribution of perfluorooctane sulfonate in wildlife. Environ Sci Technol 35:1339–1342

16. Smithwick M, Mabury SA, Solomon KR, Sonne C, Martin JW, Born EW, Dietz R, Derocher AE, Letcher RJ, Evans TJ, Gabrielsen GW, Nagy J, Stirling I, Taylor MK, Muir DCG (2005) Circumpolar study of perfluoroalkyl contaminants in polar bears (ursus maritimus). Environ Sci Technol 39:5517–5523

17. Dewailly E, Ayotte P, Bruneau S, Laliberte C, Muir DCG, Norstrom RJ (1991) Innuit exposure to organochlorines through the aquatic food chain in arctic Quebec. Environ Health Perspect 101:618–620

18. Bacon CE, Jarman WM, Cossa DP (1992) Organochlorine and polychlorinated biphenyl levels in pinniped milk from the arctic, the Antarctic California and Australia. Chemosphere 24:779–791

19. Bossi R, Riger FF, Dietz R (2005) Temporal and spatial trends of perfluorinated compounds in ringed seals (Phoca hispids) from Greenland. Environ Sci Technol 39:7416–7422

20. Ebinghaus R, Jennings SG, Schroeder WH, Berg T, Donaghy T, Ferrara R, Guentzel J, Kenny D, Kock HH, Kvietkus K, Landing W, Mazzolai B, Mühleck T, Munthe J, Prestbo EM, Schneeberger D, Slemr F, Sommar J, Urba A, Wallschläger D, Xiao Z (1999) International field intercomparison measurements of atmospheric mercury species at Mace Head, Ireland. Atmos Environ 33:3063–3073

21. Slemr F, Brunke E, Ebinghaus R, Temme C, Munthe J, Wängberg I, Schroeder WH, Steffen A, Berg T (2003) Worldwide trend of atmospheric mercury since 1977. Geophys Res Lett 30:23–1–23–4

22. Temme C, Ebinghaus R, Einax JW, Steffen A, Schroeder WH (2004) Application of time series analysis on long-time data sets of atmospheric mercury concentrations at two different sites. Anal Bioanal Chem 380:493–501
23. Kock HH, Bieber E, Ebinghaus R, Spain TG, Thees B (2005) Comparison of long-term trends and seasonal variations of atmospheric mercury concentrations at the two European coastal monitoring stations Mace Head, Ireland and Zingst, Germany. Atmos Environ 39:7549–7556
24. Macdonald RW, Harner T, Fyfe J (2005) Recent climate change in the Arctic and its impact on contaminant pathways and interpretation of temporal trend data. Sci Total Environ 342:5–86
25. Lindberg S, Bullock R, Ebinghaus R, Engstrom DR, Feng X, Fitzgerald WF, Pirrone N, Prestbo E, Seigneur C (2007) A synthesis of progress and uncertainties in attributing the sources of mercury in deposition. Ambio 36:19–32
26. Gauchard PA, Aspmo K, Temme C, Steffen A, Ferrari CP, Berg T, Ström J, Kaleschke L, Dommergue A, Bahlmann E, Magand O, Planchon F, Ebinghaus R, Banic C, Nagorski S, Baussand P, Boutron CF (2005) Study of the origin of atmospheric mercury depletion events recorded in Ny-Ålesund, Svalbard, spring 2003. Atmos Environ 39:7620–7632
27. Bottenheim J, Chan HM (2006) A trajectory study into the origin of spring time Arctic boundary layer ozone depletion. J Geophys Res 111:D19301. doi:10.1029/2006JD007055
28. Ferrara R (1999) Mercury mines in Europe: assessment of emissions and natural contamination. In: Ebinghaus R, Turner RR, Lacerda D, Vasiliev O, Salomons W (eds) Mercury contaminated sites-characterization, risk assessment and remediation. Springer, New York, pp 51–72
29. Shotyk W, Goodsite ME, Roos-Barraclough F, Givelet N, Le Roux G, Weiss D, Cheburkin AK, Knudsen K, Heinemeier J, van der Knaap WO, Norton SA, Lohse C (2005) Accumulation rates and predominant atmospheric sources of natural and anthropogenic Hg and Pb on the Faroe Islands. Geochim Cosmochim Acta 69:1–17
30. Schimel J (2000) News and views; global change: rice, microbes and methane. Nature 403:375–377
31. Lu JY, Schroeder WH, Barrie LA, Steffen A, Welch HE, Martin K, Lockhart L, Hunt RV, Boila G, Richter A (2001) Magnification of atmospheric mercury deposition to polar regions in springtime: the link to tropospheric ozone depletion chemistry. Geophys Res Lett 28:3219–3222
32. Lindberg SE, Brooks S, Lin C-J, Scott KJ, Landis MS, Stevens RK, Goodsite M, Richter A (2002) Dynamic oxidation of gaseous mercury in the Arctic troposphere at polar sunrise. Environ Sci Technol 36:1245–1256
33. Ariya P, Dastoor A, Amyot M, Schroeder W, Barrie L, Anlauf K, Raofie F, Ryzhkov A, Davignon D, Lalonde J, Steffen A (2004) The arctic: a sink for mercury. Tellus B 56:397–403
34. Lalonde JD, Poulain AJ, Amyot M (2002) The role of mercury redox reactions in snow on snow-to-air mercury transfer. Environ Sci Technol 36:174–178
35. Steffen A, Schroeder WH, Bottenheim J, Narayan J, Fuentes JD (2002) Atmospheric mercury concentrations: measurements and profiles near snow and ice surfaces in the Canadian Arctic during Alert 2000. Atmos Environ 36:2653–2661
36. Berg T, Sekkesæter S, Steinnes E, Valdal AK, Wibetoe G (2003) Springtime depletion of mercury in the European Arctic as observed at Svalbard. Sci Total Environ 304:43–51
37. Ferrari CP, Dommergue A, Boutron CF (2004) Profiles of mercury in the snow pack at Station Nord, Greenland shortly after polar sunrise. Geophys Res Lett 31:L03401. doi:10.1029/2003GL018961
38. Ferrari CP, Gauchard PA, Dommergue A, Magand O, Nagorski S, Boutron CF, Temme C, Bahlmann E, Ebinghaus R, Steffen A, Banic C, Aspmo K, Berg T, Planchon F, Barbante C (2005) Snow to air exchange of mercury in an Arctic seasonal snow pack in Ny-Alesund, Svalbard. Atmos Environ 39:7633–7645
39. Lahoutifard N, Poissant L, Scott SL (2006) Scavenging of gaseous mercury by acidic snow at Kuujjuarapik, Northern Qu´ebec. Sci Total Environ 355:118–126
40. Brooks SB, Saiz-Lopez A, Skov H, Lindberg SE, Plane JMC, Goodsite MEG (2006) The mass balance of mercury in the springtime arctic environment. Geophys Res Lett 33:L13812. doi:10.1029/2005GL025525

41. Dommergue A, Ferrari CP, Poissant L, Gauchard P-A, Boutron CF (2003) Chemical and photochemical processes at the origin of the diurnal cycle of gaseous mercury within the snowpack at Kuujjuarapik, Qu´ebec. Environ Sci Technol 37:3289–3297
42. Domine F, Shepson PB (2002) Air-snow interactions and atmospheric chemistry. Science 297:1506–1510
43. Fain X, Ferrari CP, Gauchard P-A, Magand O, Boutron CF (2006) Fast depletion of elemental gaseous mercury in the kongsvegen Glaciersnowpack in Svalbard. Geophys Res Lett 33:L06826. doi:10.1029/2005GL025223
44. King MD, Simpson WR (2001) Extinction of UV radiation in arctic snow at alert, Canada (82°N). J Geophys Res 106:12499–12507
45. Amato P, Hennebelle R, Magand O, Sancelme M, Delort A-M, Barbante C, Boutron CF, Ferrari C (2007) Bacterial characterization of the snow cover in Svalbard, Spitzberg. FEMS Microbiol Ecol 59:255–264
46. Ariya PA, Khalizov A, Gidas A (2002) Reactions of gaseous mercury with atomic and molecular halogens: kinetics, product studies, and atmospheric implications. J Phys Chem A 106:7310–7320
47. Calvert JG, Lindberg SE (2004) The potential influences of iodine-containing compounds on the chemistry of the troposphere in the polar spring. II. Mercury depletion. Atmos Environ 38:5105–5116
48. Goodsite M, Plane JMC, Skov H (2004) A theoretical study of the oxidation of Hg^0 to $HgBr_2$ in the troposphere. Environ Sci Technol 38:1772–1776
49. Bottenheim JW, Gallant AG, Brice KA (1986) Measurements of NO_y species and O_3 at 82°N latitude. Geophys Res Lett 13:113–116
50. Barrie LA, Bottenheim JW, Schnell RC, Crutzen PJ, Rasmussen RA (1988) Ozone destruction and photochemical reactions at polar sunrise in the lower Arctic atmosphere. Nature 334:138–141
51. Simpson WR, von Glasow R, Riedel K, Anderson P, Ariya P, Bottenheim J, Burrows J, Carpenter LJ, Frieß U, Goodsite ME, Heard D, Hutterli M, Jacobi H-W, Kaleschke L, Neff B, Plane J, Platt U, Richter A, Roscoe H, Sander R, Shepson P, Sodeau J, Steffen A, Wagner T, Wolff E (2007) Halogens and their role in polar boundary-layer ozone depletion. Atmos Chem Phys 7:4375–4418
52. Calvert JG, Lindberg SE (2004) Potential influence of iodine-containing compounds on the chemistry of the troposphere in the polar spring. I. Ozone depletion. Atmos Environ 38:5087–5104
53. Skov H, Christensen JH, Goodsite ME, Heidam NZ, Jensen B, Wåhlin P, Geernaert G (2004) Fate of elemental mercury in the Arctic during atmospheric mercury depletion episodes and the load of atmospheric mercury to the Arctic. Environ Sci Technol 38:2373–2382
54. Perovich DK, Richter-Menge JA (1994) Surface characteristics of lead ice. J Geophys Res 99C:16341–16350
55. Rankin AM, Wolff EW, Martin S (2002) Frost flowers: implications for tropospheric chemistry and ice core interpretation. J Geophys Res 107:4683. doi:10.1029/2002JD002492
56. Canosa-Mas CE, King MD, Lopez R, Percival CJ, Wayne RP, Shallcross DE, Pyle JA, Daele V (1996) Is the reaction between $CH_3(O)O_2$ and NO_3 important in the night-time troposphere? J Chem Soc Faraday Trans 92:2211–2222
57. Sander R, Burrows J, Kaleschke L (2006) Carbonate precipitation in brine – a potential trigger for tropospheric ozone depletion events. Atmos Chem Phys 6:4653–4658
58. Christensen JH, Brandt J, Frohn LM, Skov H (2004) Modelling of mercury in the Arctic with the Danish Eulerian Hemispheric Model. Atmos Chem Phys 4:2251–2257
59. Travnikov O (2005) Contribution of the intercontinental atmospheric transport to mercury pollution in the Northern Hemisphere. Atmos Environ 39:7541–7548
60. Dastoor AP, Larocque Y (2004) Global circulation of atmospheric mercury: a modeling study. Atmos Environ 38:147–161
61. Calvert JG, Lindberg SE (2003) A modeling study of the mechanism of the halogen-ozone-mercury homogeneous reactions in the troposphere during the polar spring. Atmos Environ 37:4467–4481

62. Seigneur C, Wrobel J, Constantinou E (1994) A chemical kinetic mechanism for atmospheric inorganic mercury. Environ Sci Technol 28:1589–1597
63. Pleijel K, Munthe J (1995) Modelling the atmospheric mercury cycle – chemistry in fog droplets. Atmos Environ 29:1441–1457
64. Hedgecock IM, Pirrone N (2001) Mercury and photochemistry in the marine boundary layer-modelling studies suggest the in situ production of reactive gas phase mercury. Atmos Environ 35:3055–3062
65. Hedgecock IM, Pirrone N, Sprovieri F, Pesenti E (2003) Reactive gaseous mercury in the marine boundary layer: modeling and experimental evidence of its formation in the Mediterranean region. Atmos Environ 37:S41–S49
66. Hedgecock IM, Pirrone N (2004) Chasing quicksilver: modeling the atmospheric lifetime of $Hg^0(g)$ in the marine boundary layer at various latitudes. Environ Sci Technol 38:69–76
67. Hedgecock IM, Trunfio GA, Pirrone N, Sprovieri F (2005) Mercury chemistry in the MBL: Mediterranean case and sensitivity studies using the AMCOTS (atmospheric mercury chemistry over the sea) model. Atmos Environ 39:7217–7230
68. Hedgecock IM, Pirrone N, Sprovieri F (2008) Chasing quicksilver northward: mercury chemistry in the Arctic troposphere. Environ Chem 5:131–134
69. van Loon L, Mader E, Scott SL (2000) Reduction of the aqueous mercuric ion by sulfite: UV spectrum of $HgSO_3$ and its intramolecular redox reaction. J Phys Chem A 104:1621–1626
70. Parr RG, Yang W (1994) Density-functional theory of atoms and molecules. Oxford University Press, New York
71. Scuseria GE, Janssen CL, Schaefer HF III (1989) An efficient reformulation of the closed-shell coupled cluster single and double excitation (CCSD) equations. J Chem Phys 89:7382–7387
72. Pople JA, Head-Gordon M, Raghavachari K (1987) Quadratic configuration interaction − a general technique for determining electron correlation energies. J Chem Phys 87:5968–5975
73. Knowles PJ, Werner H-J (1988) An efficient method for the evaluation of coupling coefficients in configuration interaction calculations. Chem Phys Lett 145:514–522
74. Werner H-J, Knowles PJ (1988) An efficient internally contracted multiconfiguration-reference configuration interaction method. J Chem Phys 89:5803–5814
75. Pitzer RM, Winter NW (1988) Electronic structure methods for heavy-atom molecules. J Phys Chem 92:3061–3063
76. Khalizov AF, Viswanathan B, Larregaray P, Ariya A (2003) A theoretical study of reactions of Hg with halogens: atmospheric implications. J Phys Chem A 107:6360–6365
77. Balabanov NB, Peterson KA (2003) Mercury and reactive halogens: the thermochemistry of Hg + {Cl2, Br2, BrCl, ClO, and BrO}. J Phys Chem A 107:7465–7470
78. Tossell JA (2003) Calculation of the energetics for oxidation of gas-phase elemental Hg by Br and BrO. J Phys Chem A 107:7804–7808
79. Balabanov NB, Peterson KA (2003) A systematic ab initio study of the structure and vibrational spectroscopy of $HgCl_2$, $HgBr_2$, and HgBrCl. J Chem Phys 119:12271–12278
80. Shepler BC, Balabanov NB, Peterson KA (2005) Ab initio thermochemistry involving heavy atoms: an investigation of the reactions Hg + IX (X = I, Br, Cl, O). J Phys Chem A 109:10363–10372
81. Balabanov NB, Shepler BC, Peterson KA (2005) Accurate global potential energy surface and reaction dynamics for the ground state of $HgBr_2$. J Phys Chem A 109:8765–8773
82. Wilcox J (2009) A kinetic investigation of high-temperature mercury oxidation by chlorine. J Phys Chem A 113:6633–6639
83. Fernandez-Ramos A, Ellingson BA, Garrett BC, Truhlar DG (2007) Variational transition state theory with multidimensional tunneling. Rev Comput Chem 23:125–232
84. Shepler BC, Wright AD, Balabanov NB, Peterson KA (2007) Aqueous microsolvation of mercury halide species. J Phys Chem A 111:11342–11349
85. Levine RD, Bernstein RB (1987) Molecular reaction dynamics and/chemical reactivity. Oxford University Press, Oxford
86. Light JC (1964) Phase-space theory of chemical kinetics. J Chem Phys 40:3221–3229

87. Ariya PA, Jobson BT, Sander R, Niki H, Harris GW, Hopper JF, Anlauf KG (1998) Measurements of C_2–C_7 hydrocarbons during the polar sunrise experiment 1994: further evidence for halogen chemistry in the troposphere. J Geophys Res 103:13169–13180

88. Jobson BT, Niki H, Yokouchi Y, Bottenheim J, Hopper F, Leaitch R (1994) Measurements of C2–C6 hydrocarbons during the polar sunrise 1992 experiment: evidence for Cl atom and Br atom chemistry. J Geophys Res 99:25355–25368

89. Gilbert RG, Smith SC (1990) Theory of unimolecular and recombination reactions. Blackwell, Oxford

90. Herzberg G (1950) Molecular spectra and molecular structure, volume 1: spectra of diatomic molecules. Van Nostrand Reinhold, New York

91. De Avillez Pereira R, Baulch DL, Pilling MJ, Robertson SH, Zeng G (1997) Temperature and pressure dependence of the multichannel rate coefficients for the CH3 + OH system. J Phys Chem 101:9681–9690

92. Jordan KJ, Bascal HA, Lipson RH, Melchior M (1993) The $B^2\Sigma^+ \leftarrow X^2\Sigma^+$ transition of HgI. J Mol Spectrosc 159:144–155

93. Lide DR (ed) (1997) Handbook of Physics and Chemistry, 78th edn. CRC Press, Boca Raton

94. Slemr F, Schuster G, Seiler W (1985) Distribution, speciation and budget of atmospheric mercury. J Atmos Chem 3:407–434

95. Schroeder WH, Jackson RA (1987) Environmental measurements with an atmospheric mercury monitor having speciation capabilities. Chemosphere 16:183–199

96. Lamborg CH, Fitzgerald W, O'Donnell J, Torgersen T (2002) A non-steady-state compartmental model of global-scale mercury biogeochemistry with interhemispheric atmospheric gradients. Geochim Cosmochim Acta 66:1105–1118

97. Langhoff SR, Davidson ER (1974) Configuration interaction calculations on the nitrogen molecule. Int J Quantum Chem 8:61–72

98. Nyden MR, Petersson GA (1981) Complete basis set correlation energies. I. The asymptotic convergence of pair natural orbital expansions. J Chem Phys 75:1843–1862

99. Murrell JN, Carter S (1984) Approximate single-valued representations of multivalued potential energy surfaces. J Phys Chem 88:4887

100. Eyring H (1935) The activated complex in chemical reactions. J Chem Phys 3:107–115

101. Wigner E (1932) On the penetration of potential energy barriers in chemical reactions. Z Phys Chem Abt B 19:203–216

102. Wilcox J, Marsden DCJ, Blowers P (2004) Evaluation of basis sets and theoretical methods for estimating rate constants of mercury oxidation reactions involving chlorine. Fuel Process Technol 85:391–400

103. Huybrechts G, Narmon M, Van Mele B (1996) The pyrolysis of CCl4 and C_2Cl6 in the gas phase. Mechanistic modeling by thermodynamic and kinetic parameter estimation. Int J Chem Kinet 28:27–36

104. Møller C, Plesset MS (1934) Note on an approximation treatment for many-electron systems. Phys Rev 46:0618–0622

105. Maron L, Dommergue A, Ferrari C, Delacour-Larose M, Faïn X (2008) How elemental mercury reacts in the presence of halogen radicals and/or halogen anions: a DFT investigation. Chem Eur J 14:8322–8329

106. Majumdar D, Roszak S, Leszczynski J (2011) Probing the structures and thermodynamic characteristics of the environment polluting mercuric halides, cyanides and thiocyanates. Chem Phys Lett 501:308–314

107. Lin CJ, Pehkonen SO (1999) The chemistry of atmospheric mercury: a review. Atmos Environ 33:2067–2079

108. Schroeder WH, Anlauf KG, Barrie LA, Lu JY, Steffen A, Schneeberger DR, Berg T (1998) Arctic springtime depletion of mercury. Nature 394:331–332

109. Zhang H (2006) Photochemical redox reactions of mercury. In: Atwood DA (ed) Recent developments in mercury science — structure and bonding, vol 120. Springer, Berlin/Heidelberg, pp 37–79

110. Gardfeldt K, Jonsson M (2003) Is bimolecular reduction of Hg(II) complexes possible in aqueous systems of environmental importance. J Phys Chem A 107:4478–4482

111. Helper LG, Olofsson G (1975) Mercury: thermodynamic properties, chemical equilibria, and standard potentials. Chem Rev 75:585–602

112. Barone V, Cossi M (1998) Quantum calculation of molecular energies and energy gradients in solution by a conductor solvent model. J Phys Chem A 102:1995–2001

113. Cossi M, Rega N, Scalmani G, Barone V (2003) Energies, structures, and electronic properties of molecules in solution with the C-PCM solvation model. J Comput Chem 24:669–681

114. Wagman DD, Evans WH, Parker VB, Schumm RH, Halow IH, Baily SM, Churney KL, Nuttall RL (1982) The NBS tables of chemical thermodynamic properties. Selected values for inorganic and C_1 and C_2 organic substances in SI units. J Phys Chem 11(Ref. Data Suppl. 2): 2-1–2-391

115. Pliego JR Jr, Riveros JM (2000) New values for the absolute solvation free energy of univalent ions in aqueous solution. Chem Phys Lett 332:597–602

116. Pliego JR Jr, Riveros JM (2001) Th cluster − continuum model for the calculation of solvation free energy of ionic species. J Phys Chem A 105:7241–7247

117. Asthagiri D, Pratt LR, Paulaitis ME, Rempe SB (2004) Hydration structure and free energy of biomolecularly specific aqueous dications, including Zn2+ and first transition row metals. J Am Chem Soc 126:1285

118. Kelly P, Cramer CJ, Truhlar DG (2005) SM6: a density functional theory continuum solvation model for calculating aqueous solvation free energies of neutrals, ions, and solute-water clusters. J Chem Theory Comput 1:1133–1152

119. Bryantsev VS, Diallo MS, Goddard WA III (2008) Calculation of solvation free energies of charged solutes using mixed cluster/continuum models. J Phys Chem B 112:9709–9719

120. Marcus Y (1985) Ion solvation. Wiley, New York

121. Pal B, Ariya PA (2004) Studies of ozone initiated reactions of gaseous mercury: kinetics, product studies, and atmospheric implications. Phys Chem Chem Phys 6:572–579

122. Pal B, Ariya PA (2004) Gas-phase HO-initiated reactions of elemental mercury: kinetics, product studies, and atmospheric implications. Environ Sci Technol 38:5555–5566

123. Tokos JJS, Hall B, Calhoun JA, Prestbo EM (1998) Homogeneous gas-phase reaction of Hg^0 with H_2O_2, O_3, CH_3I, and $(CH_3)_2 S$: implications for atmospheric Hg cycling. Atmos Environ 32:823–827

124. Munthe J (1992) The aqueous oxidation of elemental mercury by ozone. Atmos Environ 26A:1461–1468

125. Lin C-J, Pehkonen SO (1997) Aqueous free radical chemistry of mercury in the presence of iron oxides and ambient aerosol. Atmos Environ 31:4125–4137

126. van Loon LL, Mader EA, Scott SL (2001) Sulfite stabilization and reduction of the aqueous mercuric ion: kinetic determination of sequential formation constants. J Phys Chem A 105:3190–3195

Chapter 13
Computational Perspectives on Organolithium Carbenoids

B. Ramu Ramachandran and Lawrence M. Pratt

Abstract Lithium carbenoids are extremely useful reagents in synthetic organic chemistry and have been widely used for generating various reactive intermediates needed for chemical synthesis with high yield under relatively mild conditions. The mechanisms of their reactions are typically quite complex and often strongly influenced by aggregation state, solvent effects, relative stabilities of diastereomers and constitutional isomers, formation of pre-reactive complexes, and Lewis acid catalysis, in addition to factors under the control of the experimentalist, such as reagent preparation, concentration, and temperature. Computational studies are indispensable for understanding the role played by the former factors in the reactions and to gain insights into the impact of the latter on the former. In this chapter, we discuss some themes that have emerged and the insights gained from more than a decade of computational investigations. We focus on two types of organolithium reagents: halomethyllithiums and oxiranyllithiums. They appear to represent contradictory paradigms in certain aspects. In the context of these molecules, we also report on recent studies of the performance of a collection of density functional approximations for reproducing the geometries and energetics predicted by correlated wave function methods.

B.R. Ramachandran (✉)
College of Engineering & Science, Louisiana Tech University, Ruston, LA 71272, USA
e-mail: ramu@latech.edu

L.M. Pratt
Department of Chemistry, Fisk University, Nashville, TN 37208, USA
e-mail: lpratt@fisk.edu

13.1 Introduction

Lithium carbenoids are important reagents in synthetic organic chemistry. The widespread use of organometallic carbenoid species for synthesizing cyclopropane rings has a long history dating back at least to the 1958 report by Simmons and Smith (using the "Simmons-Smith" or SS reagent IZnCH$_2$I) [1], which was followed up by a more detailed report in 1959 [2]. Halomethyllithiums (X-CH$_2$-Li; X = F, Cl. Br, I) are exceptionally well-suited for inserting the methylene group into a double bond in a stereospecific manner under extremely mild conditions. In addition to halomethyllithiums, carbene-like reactivity has been observed in 1-halo-1-lithioalkenes and α-lithioethers, particularly oxiranyllithium compounds. Reports of experimental studies indicate that Li–CH$_2$–X (X = halogen) are more reactive than Li–CH$_2$–O–R, where R = H, or some other group (as in lithium oxiranes) [3–5]. As carbene-like species, lithium carbenoids undergo a variety of single- and double-bond insertion reactions. Nucleophilic reactions of related oxiranyllithium carbenoids are also known [6–9].

The chemistry of organolithium compounds in general, and carbenoid species in particular, is quite complex because of their tendency to form aggregates in solution. The reactivity and the thermochemistry often depend sensitively on the aggregation state and solvation effects [10, 11]. The precise nature of the reactive species is difficult to characterize experimentally and, therefore, computational investigations are necessary to further our understanding. However, computational investigations of organolithium chemistry also present many challenges. Semiempirical methods are poorly parameterized for lithium compounds [12]. Electron correlation effects appear to be quite important in the intermolecular interactions in these species, which means that relatively high levels of theory are necessary. Ethereal solvents like tetrahydrofuran (THF) bind quite strongly as ligands to the lithium atoms, forming a "supermolecule" consisting of the organolithium molecule and its first solvation sphere [13, 14]. Steric and electronic effects of the coordinated ligands are important in determining the aggregation state and reactivity, and the steric effects introduced by the solvent ligands cannot be adequately represented by continuum solvation models.

In this chapter, we discuss the general themes that have emerged and the insights gained from more than a decade of computational investigations of organolithium carbenoids. We focus on two types of organolithium reagents: halomethyllithiums and oxiranyllithiums. In the context of these molecules, we also report on recent studies of the performance of a collection of density functional approximations for reproducing the geometries and energetics predicted by computationally much more expensive correlated wave function methods.

The following aspects of computational organolithium chemistry are addressed in the subsequent subsections of this chapter.

- Relative stability of aggregated states, and the role of solvents in determining relative stabilities

- Influence of aggregation states on reactivities
- Formation of pre-reactive complexes and the implications for "naïve" evaluation of reaction barriers
- The choice of DFT functionals, especially for modeling aggregation states and solvation states

Unless explicitly specified, the computational results discussed below were obtained with the split valence polarized basis set 6-31 + G(d) which, we have found, offers an acceptable compromise between a reasonably complete description of the various types of interactions present and computational effort. Various recent versions of Gaussian were used in our work: Gaussian 98 [15] in some of the earliest work described, and Gaussian 03 [16] and Gaussian 09 [17] in the more recent work. Our strategy for locating transition states has been to start with a "reasonable" geometry as input and then use the opt = TS option in Gaussian with an initial calculation of force constants, at a low level of theory, typically Hartree-Fock (HF). If this attempt failed, we employed the QST2 or QST3 algorithms [18, 19] to locate the transition states. Once a saddle point geometry is identified (with one imaginary frequency), then that geometry is used as input for post-HF methods such as second-order Møller-Plesset perturbation theory (MP2), coupled-cluster theory [CCSD(T)] as well as Kohn-Sham Density Functional Theory (DFT). Intrinsic reaction coordinate (IRC) calculations were performed using the algorithms of Gonzalez and Schlegel [20] as implemented in Gaussian 03 and Gaussian 09.

Special care is taken to ensure consistent handling of standard states [21, 22]. Specifically, a correction term $RT\ln(c°RT/P°)$ must be added per mole of each species in the reaction under consideration, which represents the change in free energy involved in compressing the system from standard pressure $P°$ (or a concentration of $P°/RT$) used in gas-phase calculations to the standard concentration of $c° = 1$ mol/L commonly used for solutions. This term is numerically equal to $+0.91$ kcal/mol at 173.15 K and $+1.89$ kcal/mol at 298.15 K. While it cancels from both sides when the net change in the number of moles due to reaction $\Delta n = 0$, it is a non-negligible correction in cases where $\Delta n \neq 0$.

Solvent effects in coordinating solvents, in this case THF, were modeled by placing explicit solvent ligands on the lithium atoms. Yet another correction is required for cases where a THF ligand dissociates, as in

$$\text{RLi} \cdot n\text{THF} \rightleftarrows \text{RLi} \cdot m\text{THF} + (n - m)\,\text{THF}$$
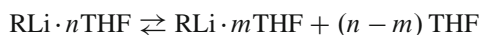
for which

$$\Delta G° = -RT \ln \frac{[\text{RLi} \cdot m\text{THF}]}{[\text{RLi} \cdot n\text{THF}]} - (n - m)\,RT \ln \frac{[\text{THF}]}{c°}. \qquad (13.1)$$

Since the concentration of pure THF is different from the standard concentration $c°$, it needs to be evaluated from its molar volume at the temperature and pressure under consideration. This is most conveniently done using the empirical expression

provided by Govender et al. [23]. This approach to modeling solvation effects on organolithium compounds has been used in other studies [22–29], and has been found to give results in agreement with available experimental results.

13.2 Relative Stability of Aggregated States and the Role of Solvents in Determining Relative Stabilities

The tendency of organolithium compounds to form aggregates was mentioned earlier. A review by Gossage et al. provides a well-referenced discussion of this aspect [30]. It is well-known that n-butyllithium, a very commonly employed organolithium reagent, exists as a hexamer in solid state. This aggregation state persists at least to some extent in nonpolar solutions. In polar solvents, especially those that coordinate to the lithium (such as ethers), it has been suggested that smaller aggregates are more common [31]. In such media, the solvent molecules co-ordinate quite strongly with lithium as has been established by NMR spectroscopy, kinetics, and X-ray crystallography [32–34]. Because of this, the steric effects of the first solvation shell needs to be explicitly included in computational treatments [11, 28, 35]. In lithium carbenoids and carbanions, the Li atom acquires a rather high partial positive charge. Aggregation appears to be primarily driven by the long-range noncovalent interactions induced by such charge concentration.

Halomethyllithium carbenoids readily form dimers and tetramers in the gas phase. Our previous work suggested that the dominant reactive species in halomethyllithium carbenoids are dimers or tetramers in the gas phase and noncoordinating solvents [36, 37]. Many mixed aggregates are also quite stable relative to the monomers [29]. Table 13.1 summarizes the dimerization energies of halomethyllithium carbenoids with respect to the monomer. Two constitutional isomers of the dimers were identified in our previous work [37]. These are labeled **6**

Table 13.1 Gas-phase dimerization and tetramerization free energies at 173.15 K, ΔG° (kcal/mol), for halomethyllithiums ($LiCH_3X$; X = F, Cl, Br), which form two types of dimers labeled **6** and **7**

	$\Delta G^\circ{}_{\text{B3LYP}}$	$\Delta G^\circ{}_{\text{MP2}}$	$\Delta G^\circ{}_{\text{MP2// B3LYP}}$
$2\,LiCH_3X \rightarrow \mathbf{6}$			
X = F	−38.65	−40.25	−40.29
X = Cl	−31.69	−37.44	−38.01
X = Br	−32.17	−36.17	−36.50
$2\,LiCH_3X \rightarrow \mathbf{7}$			
X = F	−38.21	−39.48	−39.46
X = Cl	−29.53	−35.51	−35.84
X = Br	−31.43	−35.61	−35.93
$2\,\mathbf{6} \rightarrow (LiCH_3X)_4$			
X = F	−19.59	−23.58	−23.83
X = Cl	−16.70	−29.37	−29.69
X = Br	−28.02	−39.99	−40.12

Table 13.2 Gas-phase dimerization and tetramerization free energies ΔG° (kcal/mol) at 298.15 K for oxiranyllithiums (CH_2–(O)–CH–Li), which form two diastereomeric dimers (RR, RS) and three diastereomeric tetramers (RRRR, RRRS, and RRSS)

	ΔG°_{B3LYP}	ΔG°_{M062X}	$\Delta G^\circ_{MP2//B3LYP}$	$\Delta G^\circ_{MP2//M06\text{-}2X}$
2 $CH_2 - (O) - CH - Li \rightarrow$ Dimer				
RR	−39.12	−42.39	−41.21	−41.16
RS	−39.22	−42.49	−41.27	−41.28
Dimer $\rightarrow$ Tetramer				
RRRR	−10.02	−22.85	−19.03	−17.71
RRRS	−9.92	−22.91	−18.74	−18.87
RRSS	−9.25	−19.61	−17.74	−14.52

and **7** in our numbering scheme, which is presented in a later section of this chapter. Table 13.1 also presents the tetramerization energy of dimer **6** with respect to the dimer.

For halomethyllithiums, the dimerization free energies are found to be substantial. Although gas-phase results are shown, the standard state correction mentioned above makes aggregation even more favorable in nonpolar solvents by increasing the free energy of the "reactants" relative to the "products" by $RT\ln(c^\circ RT/P^\circ)$, as noted earlier. There are differences of 1–6 kcal/mol in the ΔG° values predicted by B3LYP [38] and MP2 for halomethyllithiums but both sets of predictions are qualitatively in agreement. Also, the MP2 energies calculated at B3LYP geometries (MP2//B3LYP) are in excellent agreement with the MP2 results, indicating that both methods predict very similar geometries. It is immediately obvious that halomethyl carbenoids, even in moderate concentrations in such environments, are overwhelmingly tetrameric (perhaps even higher aggregation states).

Oxiranyllithiums also readily form aggregates in the gas phase and nonpolar solvents [39], as shown in Table 13.2. There are two diastereomers of the dimer, labeled RR and RS, and the tetramer can exist in three possible forms: RRRR, RRRS, and RRSS. In the case of the tetramer, substantial differences are observed between the predictions of B3LYP and M06-2X [40] but both methods predict that the tetramers are more stable than the dimers. The MP2 energies calculated at the DFT geometries are more consistent with each other, suggesting that both B3LYP and M06-2X yield equilibrium geometries that are very similar. The three tetrameric diastereomers are of comparable stability, and their relative concentrations in a nonpolar solvent can be calculated from the free energy changes in Table 13.2 after imposing the standard state correction factor of $RT\ln(c^\circ RT/P^\circ)$. This analysis is shown in Table 13.3 for B3LYP and MP2//B3LYP based on an assumed total concentration of 1 M Li^+. The concentrations of RRRR, RRRS, and RRSS add up to 0.250 in both cases. Since each tetramer contains 4 Li atoms, this accounts for nearly all of the Li^+ present, leaving only trace amounts ($\leq 10^{-4}$ M) of dimeric species in the solution.

Therefore, in nonpolar solvents, the dominant species present are the larger aggregates. We will see below that the situation could change rather drastically

Table 13.3 Relative equilibrium concentrations (in mol L^{-1}) of dimeric and tetrameric oxiranyllithium species in the gas phase resulting from a total 1.0 mol L^{-1} of Li (in whatever form)

Isomer	B3LYP	MP2//B3LYP
RRRR	0.126	0.168
RRRS	0.090	0.063
RRSS	0.034	0.019

Table 13.4 THF-phase dimerization and dimer de-solvation free energies at 173.15 K, $\Delta G°$ (kcal/mol), for halomethyllithiums (LiCH$_3$X; X = F, Cl, Br), which form two types of dimers labeled **6** and **7**

	$\Delta G°_{\text{B3LYP}}$	$\Delta G°_{\text{MP2}}$	$\Delta G°_{\text{MP2//B3LYP}}$
2 LiCH$_3$X · 2THF → **6** · 4THF			
X = F	−11.78	−25.01	−21.60
X = Cl	−1.82	−22.26	−15.03
X = Br	−13.68	−29.53	−27.63
2 LiCH$_3$X · 2THF → **7** · 4THF			
X = F	−9.73	−23.24	−19.71
X = Cl	−0.32	−20.71	−17.22
X = Br	−11.60	−30.95	−29.57
2 **6** · 4THF → (LiCH$_3$X)$_4$ · 4THF + 4THF			
X = F	−10.75	11.40	6.75
X = Cl	−5.70	10.03	−2.57
X = Br	−6.70	1.76	−0.42
6 · 4THF → **6** · 3THF + THF			
X = F	−2.21	8.46	5.86
X = Cl	−5.08	10.29	3.17
X = Br	1.05	11.32	11.51
7 · 4THF → **7** · 3THF + THF			
X = F	−3.77	7.58	6.63
X = Cl	−3.28	11.43	7.42
X = Br	−0.04	10.49	10.57

in ethereal solvents that coordinate tightly to the Li. In later sections of this chapter, we will also see that aggregation states have profound influences on the formation of pre-reactive complexes and on reaction barrier heights, with some direct linkages between the two. Thus, computational chemistry appears to be able to make recommendations as to the type of solvents to be used in reagent preparation for various synthesis experiments with organolithium compounds.

While nonpolar solvents like hexane or cyclohexane are widely used, organolithium reactions are often studied in polar solvents like tetrahydrofuran (THF). Such solvents coordinate strongly to the lithium atoms and influence the relative stability of the aggregates and their reactivities. As an example, consider the dimerization and tetramerization energies of halomethyllithium carbenoids in THF, shown in Table 13.4. We see that the formation of tetrasolvated dimers from

disolvated monomers is highly favorable. Unlike Table 13.1, however, there are significant differences between the ΔG° values predicted by B3LYP and MP2, and also between those from MP2 and MP2//B3LYP. In such cases, the MP2 energies were lower than MP2//B3LYP, suggesting that the B3LYP equilibrium structure was significantly different from those found by MP2 [37].

The performance of B3LYP relative to MP2 in the formation of THF-solvated tetramers is even more problematic and deserves discussion. For steric reasons, it appears unlikely that the primary solvation sphere of the tetramer will contain more than one THF coordinated to each lithium, an assumption supported by X-ray structures of other tetrameric organolithium species [41]. So, the formation of the THF-solvated tetramer can be envisioned as

$$2(\text{LiCH}_2\text{X})_2 \cdot 4\text{THF} \rightarrow (\text{LiCH}_2\text{X})_4 \cdot 4\text{THF} + 4\text{THF} \qquad (13.2)$$
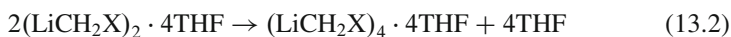
Table 13.4 shows that B3LYP predicts that Eq. 13.2 is thermodynamically favorable while MP2 calculations indicate that they are unfavorable. As shown in [37], these differences in ΔG° can be traced to large discrepancies between MP2 and MP2//B3LYP energies for the solvated dimers, implying that the geometries found by B3LYP are significantly different from those obtained by MP2. These energy differences get magnified by a factor of 2 in Eq. 13.2. The energy differences $E_{\text{MP2//MP2}} - E_{\text{MP2//B3LYP}}$ for the solvated tetramers for X = F, Cl, and Br are, respectively, -7.11, -9.04, and -4.68 kcal/mol. The combined differences in absolute energies are sufficient to account for the large differences between the MP2 and MP2//B3LYP results tabulated in Table 13.11. As one would expect from Table 13.1, the differences $E_{\text{MP2//MP2}} - E_{\text{MP2//B3LYP}}$ for the gas-phase tetramers are quite small, ranging from -0.16 kcal/mol for X = F to -1.42 kcal/mol for X = Cl.

Therefore, in the sections that follow, we will base conclusions about THF-solvated halomethyllithium dimers and tetramers on MP2 results. Further comments about the performance of B3LYP for these cases are postponed until later in this chapter, where we shall discuss the relative performance of DFT functionals.

Examining once again the MP2 results for solvated tetramer formation in Table 13.4 we see that, in sharp contrast to the dimerization and tetramerization energies in Table 13.1, the formation of the THF-coordinated tetramers are not thermodynamically favored, although in the case X = Br, appreciable tetramer concentrations can be expected to coexist with the dimers in a THF solution. The reason for the dominance of dimers in THF solution, in sharp contrast to the situation in nonpolar solvents, is obviously the steric effects introduced by the tight coordination of the ethereal oxygens to the lithium atoms.

The aggregation states of oxiranyllithiums in THF have also been examined. In Table 13.5, we present the free energy changes for the formation of THF-solvated dimers from solvated monomers. Not surprisingly, all methods predict that THF coordination to the lithium atoms up to 2 THF ligands per lithium in the monomer is thermodynamically favorable. However, significant differences between the predictions of B3LYP and MP2//B3LYP are in evidence, while there are much smaller differences between M06-2X and MP2//M06-2X. This trend is

Table 13.5 Free energies of formation of THF-solvated oxiranyllithium dimers from monomers (kcal/mol)

Process	$\Delta G^{\circ}_{\text{B3LYP}}$	$\Delta G^{\circ}_{\text{M062X}}$	$\Delta G^{\circ}_{\text{MP2//B3LYP}}$	$\Delta G^{\circ}_{\text{MP2//M06-2X}}$
R + 2THF → R·2THF	−17.79	−21.08	−24.85	−21.04
2R·2THF → RR·2THF + 2THF	−16.97	−15.19	−11.29	−13.85
2R·2THF → RS·2THF + 2THF	−16.52	−15.00	−10.88	−13.58
RR·2THF + 2THF → RR·4THF	7.21	−6.91	−10.88	−11.26
RS·2THF + 2THF → RS·4THF	6.39	−7.73	−11.60	−13.20

Table 13.6 Tetramerization free energies of THF-solvated oxiranyllithium (kcal/mol)

Process	$\Delta G^{\circ}_{\text{B3LYP}}$	$\Delta G^{\circ}_{\text{M062X}}$	$\Delta G^{\circ}_{\text{MP2//B3LYP}}$	$\Delta G^{\circ}_{\text{MP2//M06-2X}}$
2RR·2THF → RRRR·4THF	7.21	−15.47	−16.01	−21.37
2RR·2THF → RRSS·4THF	7.04	−13.70	−15.10	−21.25
RR·2THF + RS·2THF → RRRS·4THF	6.59	−14.08	−15.51	−21.52
2RR·4THF → RRRR·4THF + 4THF	−7.22	−1.66	5.74	1.15
2RR·4THF → RRSS·4THF + 4THF	−7.61	−1.56	5.83	−0.38
RR·4THF + RS·4THF → RRRS·4THF + 4THF	−7.01	0.74	6.96	2.94

exacerbated in the case of the formation of disolvated dimers. The formation of tetrasolvated dimers are predicted to be thermodynamically unfavorable by B3LYP but are favored by other methods listed.

The thermodynamics of THF-solvated tetramer formation is even more problematic, as shown in Table 13.6. Formation of tetrasolvated tetramers from disolvated dimers is found to be unfavorable by B3LYP but is predicted to be favorable by the other methods employed, including MP2//B3LYP. The formation of tetrasolvated tetramers from tetrasolvated dimers, including the ejection of 4 moles of pure solvent, which requires the additional standard state correction using Eq. 13.1, is predicted to be favorable by B3LYP, unfavorable by MP2//B3LYP, and marginally favorable or unfavorable (within the probable margin of error in these calculations) by M06-2X and MP2//M06-2X. Our experiences with THF-solvated halomethyl-lithiums suggest that B3LYP geometries and energetics for THF-solvated species might be problematic. Also, for the last three entries of Table 13.6, the average of $|\Delta G_{\text{B3LYP}} - \Delta G_{\text{MP2//B3LYP}}|$ is 13.5 kcal/mol, whereas the average of $|\Delta G_{\text{M06-2X}} - \Delta G_{\text{MP2//M06-2X}}|$ is only 2.1 kcal/mol. Therefore, we draw conclusions using the MP2//M06-2X results in this case. This suggests that (a) tetrasolvated dimers are readily formed in THF-solution of oxiranyllithiums, and (b) tetrasolvated tetramers may coexist with them in comparable or smaller amounts. Full optimization of these large molecules with MP2 proved to be beyond the capabilities of the computational resource available to us.

The marginal relative stability of tetrasolvated species of oxiranyllithiums compared to the dimers can be attributed to be the steric effects introduced by the

relatively bulky THF ligands. In the case of halomethyllithiums, the steric effects made tetrasolvated tetramers less stable compared to the dimers. It is clear that continuum solvation models will not be able to account for the relative stabilities of solvated dimers and tetramers observed in these cases (see Table 12 of [37] and the associated discussion). Explicitly including solvent molecules in the calculations (13 atoms per THF) significantly increases the computational effort, especially the MP2 structure optimizations of the "floppy" molecules that one is forced to deal with. This is, in fact, a major computational challenge in the study of organolithium species. The larger aggregates that form the dominant species in a reagent solution are not only of interest from an energetic and thermodynamic point of view but also, as we shall discuss in the following subsection of this chapter, they also exhibit considerably different reactivities in some cases and can play decisive roles in determining the reaction mechanism.

13.3 Influence of Aggregation States on Reactivities

We now come to one of the main themes of this chapter, namely the role of aggregation and solvation states in the reactivity of organolithium reagents. The influence of aggregation states in determining reaction pathways was recently and powerfully illustrated in the case of the cylopropanation reactions of halomethyllithiums, which could be viewed as the lithium analogue of the SS reaction:

$$H_2C = CH_2 + Li - CH_2 - X \rightarrow cyclopropane + LiX$$
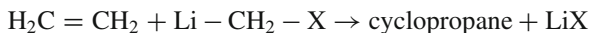
On the basis of the stereospecificity of the reaction and other experimental observations, Simmons and Smith proposed a direct, or concerted, addition of CH_2 to the double bond as the mechanism. A two-step mechanism involving carbometalation of the alkene, resulting in $X-(CH_2)_3-M$ (where X is the halogen and M the metal) as intermediate, was proposed by Hoberg in 1962 [42]. Although Burger and Huisgen in 1970 [43] ruled out this mechanism for $X = Cl$ and $M = Li$ on the basis of the stereospecificity of the reaction, the collection of available experimental evidence is not conclusive. For example, Stiasny and Hoffmann [44] studied intramolecular cyclopropanation reactions using bromolithium carbenoids and observed that the direct mechanism appears to have the lowest activation energy, proceeding quite readily even at extremely low temperatures ($-110°C$). However, they also concluded that Lewis-acid-assisted carbolithiation leading to cyclopropanation (the two-step mechanism) was competitive at higher temperatures ($-20°C$ or higher). The possibility of free carbenes (rather than lithiocarbenoids) being responsible for the reaction has been ruled out by the complete absence of hydrocarbon isomerization products in these experiments.

One of the first computational studies of the reactions considered here Eq. 13.2 appear to be that of Nakamura et al. [45] who briefly examined the case of Li-CH$_2$-Cl for comparison while conducting a study of the Zn-based SS reactions. Based on the B3LYP/6-31G(d) reaction barrier heights of gas-phase (or nonpolar solvent)

reactions involving monomeric carbenoid species, Nakamura et al. concluded that no preference existed between the two pathways for the case of Li (in contrast, the SS reaction with the organozinc reagent showed a clear preference for the concerted mechanism). Hermann et al. studied the concerted pathway only, in a study of the influence of leaving groups (X = F, Cl, Br, I, and OH) [46]. The first computational study to consider the influence of aggregates and explicit solvation on this reaction is that of Ke, Zhao, and Phillips (KZP) [47], in which the cases of X = F and OH were studied at the B3LYP/6-311 G(d,p) level of theory. That paper is part of a long series of outstanding computational investigations of metalocarbenoid-mediated cyclopropanation reactions from Phillips and coworkers [47–52], which includes a careful reinterpretation of the experimental observations of Stiasni and Hoffman. The work of KZP in [47] was followed by the study of Pratt, Ramachandran, and coworkers [37] (for X = F, Cl, Br), which confirmed many of the conclusions of KZP and also reported some novel aspects of these reactions.

Prior to the work of KZP, computational studies of monomeric reactants suggested that cyclopropanation using halomethyllithium carbenoids proceed either by a direct insertion into the alkene C-C bond as shown in Eq. 13.3, or by a multistep process in which a 3-halo-1-propyllithium intermediate is first formed as shown in Eq. 13.4.

$$H_2C = CH_2 + Li - CH_2 - X \rightarrow TS\mathbf{1} \rightarrow cyclopropane + LiX \qquad (13.3)$$

$$H_2C = CH_2 + Li - CH_2 - X \rightarrow complex\ \mathbf{2'} \rightarrow TS\ \mathbf{2} \rightarrow Li - (CH_2)_3 - X \qquad (13.4)$$
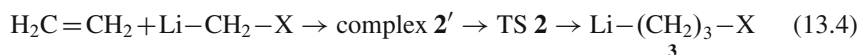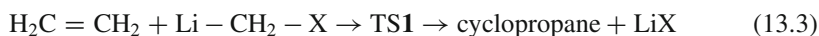
The intermediate could then undergo a syn- or anti-elimination of the lithium halide to form cyclopropane:

$$Li - (CH_2)_3 - X \rightarrow [TS\ \mathbf{4}\ (anti)\ or\ \mathbf{5}\ (syn)] \rightarrow cyclopropane + LiX. \qquad (13.5)$$
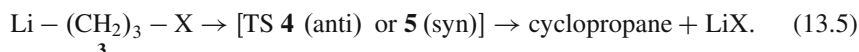
These reaction pathways, including the formation of the pre-reactive complex $\mathbf{2'}$, were confirmed by IRC calculations at the MP2 level of theory in the gas phase by us in [37].

Reactions of the dimeric species are analogous to Eqs. 13.3 and 13.4. Pratt and coworkers have identified two distinct constitutional isomers for the dimeric species [53], denoted as $\mathbf{6}$ and $\mathbf{7}$, with structures shown below.

$$H_2C = CH_2 + \underset{\mathbf{6}\ or\ \mathbf{7}}{(Li - CH_2 - X)_2} \rightarrow \underset{TS\ \mathbf{8}\ or\ TS\ \mathbf{9}}{[TS\ structure]}$$

$$\rightarrow cyclopropane + LiX + Li - CH_2 - X \qquad (13.6)$$

$$H_2C = CH_2 + \underset{\mathbf{6}\ or\ \mathbf{7}}{(Li - CH_2 - X)_2} \rightarrow complex\ \mathbf{10'}\ or\ \mathbf{11'}$$

$$\rightarrow \underset{TS\ \mathbf{10}\ or\ TS\ \mathbf{11}}{[TS\ structure]} \rightarrow Li - (CH_2)_3 - X + Li - CH_2 - X; \qquad (13.7)$$
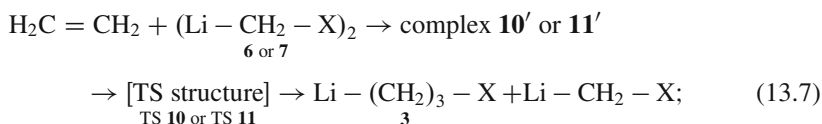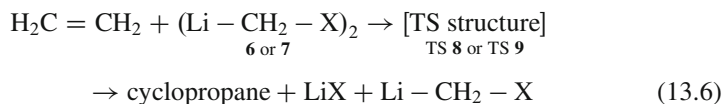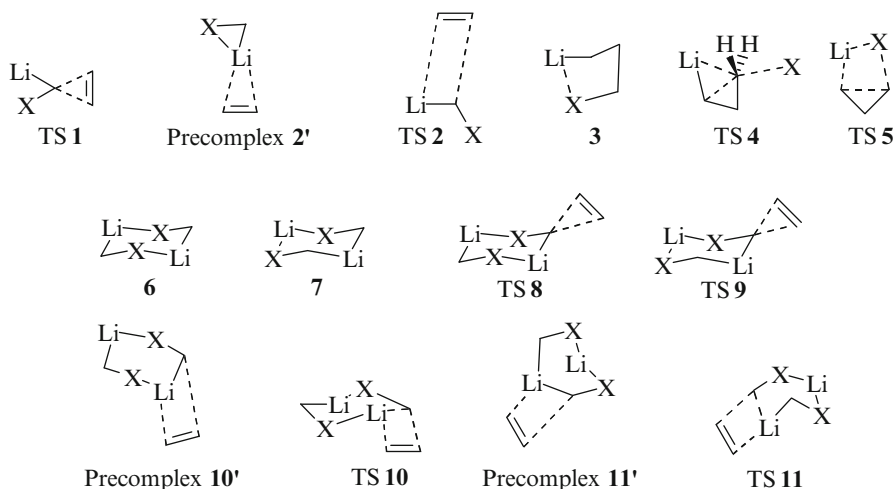
As in the case of the monomers, the existence of the pre-reactive complexes in Eq. 13.7 was verified by IRC calculations at the MP2 level [37]. The structural formulae of the important monomeric and dimeric species studied for the case of ethylene are summarized above.

We have also verified [37] that the reactions of lithium carbenoids with 2,3-dimethyl-2-butene (DMB) proceed through similar mechanisms and involve similar intermediate and transition state structures, thus establishing the generality of the observations and conclusions to be presented below.

The remainder of this subsection is organized as follows. In Sect. 13.1.3.1, we discuss the reactions of monomeric and dimeric halomethlylithiums with ethylene in the gas phase. The reactions of the monomers and dimers in THF medium are discussed in Sect. 13.1.3.2. The reaction of gas-phase tetramers is the subject of Sect. 13.1.3.3. The formation of substituted cyclopropane rings is examined in Sect. 13.1.3.4 by considering the reactions of halomethyllithium monomers and dimers with 2,3-dimethyl-2-butene. The reactions of monomeric and aggregated oxiranyllithiums with ethylene are discussed in Sect. 13.1.3.5. Finally, in Sect. 13.1.3.6, we present the calculations of reaction rate constants and the estimation of Arrhenius activation energies for these reactions using the Eyring equation.

13.3.1 Reactions of Halomethyllithiums with Ethylene in Gas Phase or Nonpolar Solvents

In Table 13.7, we tabulate the free energy of activation $\Delta G^{\ddagger}$ at $-100°C$ (173.15 K) with respect to reactants for the concerted and stepwise pathways of the monomer (Eqs. 13.3 and 13.4), the concerted and stepwise reactions of the two dimers (Eqs. 13.6 and 13.7), and those of the tetramer formed from two units of dimer **6**, all in the gas phase. With the correction factor for standard states, described above,

Table 13.7 Reaction barriers $\Delta G^\ddagger$ (kcal/mol) for the methylene transfer (direct) and carbolithiation (stepwise) pathways of halomethyllithium monomers, dimers Eqs. 13.3–13.7 and tetramers in the gas phase at 173.15 K

	$\Delta G^\ddagger_{\text{B3LYP}}$	$\Delta G^\ddagger_{\text{MP2}}$	$\Delta G^\ddagger_{\text{MP2//B3LYP}}$
$H_2C = CH_2 + Li - CH_2 - X \rightarrow$ TS **1** Eq. 13.3			
X = F	11.44	12.80	12.84
X = Cl	10.49	13.42	12.96
X = Br	10.49	11.67	11.56
$H_2C = CH_2 + Li - CH_2 - X \rightarrow$ TS **2** Eq. 13.4			
X = F	9.38	12.34	12.20
X = Cl	12.14	11.97	11.66
X = Br	11.72	12.14	12.03
TS **4**(anti), relative to $H_2C = CH_2 + LiCH_3X$ Eq. 13.5			
X = F	24.85	19.92	19.69
X = Cl	15.88	15.38	15.04
X = Br	15.43	11.14	10.82
TS **5**(syn), relative to $H_2C = CH_2 + LiCH_3X$ Eq. 13.5			
X = F	5.52	8.09	8.54
X = Cl	10.16	14.89	14.63
X = Br	10.65	14.11	14.33
$H_2C = CH_2 + $ **6** $\rightarrow$ TS **8** Eq. 13.6			
X = F	11.44	11.60	11.49
X = Cl	13.69	14.83	16.51
X = Br	11.18	12.59	12.62
$H_2C = CH_2 + $ **7** $\rightarrow$ TS **9** Eq. 13.6			
X = F	10.59	10.43	10.29
X = Cl	9.80	12.23	11.74
X = Br	13.93	10.55	10.47
$H_2C = CH_2 + $ **6** $\rightarrow$ TS **10** Eq. 13.7			
X = F	27.42	29.21	29.21
X = Cl	29.24	30.54	33.71
X = Br	24.04	23.73	24.32
$H_2C = CH_2 + $ **7** $\rightarrow$ TS **11** Eq. 13.7			
X = F	23.81	25.26	25.19
X = Cl	23.78	24.29	27.20
X = Br	21.66	21.33	21.97

these results can be considered valid for nonpolar solvents as well. The effect of this correction will be to lower all $\Delta G^\ddagger$ values in Table 13.7 uniformly by 0.91 kcal/mol at 173.15 K.

As already noted, the monomers appear to show no preference between the two pathways. However, the reaction barriers for the stepwise reaction of the dimers are higher than those for the direct pathway by more than a factor of 2, indicating a clear preference for the former, especially at the low temperatures in which these reactions are typically carried out. We have already seen in Table 13.1 that in nonpolar solvents, the tetrameric form dominates. Toward the bottom of Table 13.7, we show the reaction barriers for the concerted and stepwise reactions of the tetramer formed from two units of dimer **6**. The $\Delta G^\ddagger$ for the concerted reactions of the tetrameric species are even lower than those for the dimers, while
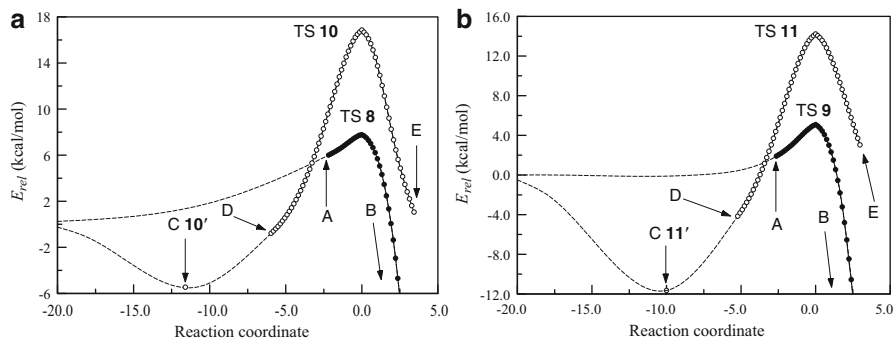
Fig. 13.1 The MP2/6-31 + G(d) IRC in (amu)$^{1/2}$ bohr for the concerted and stepwise reactions of gas-phase dimers of LiCH$_2$Br. All energies are relative to the asymptotic reactants H$_2$C=CH$_2$ + LiCH$_2$Br. (**a**) IRCs of dimer **6**. The point B is at an energy of −13.8 kcal/mol, at reaction coordinate value of 2.97. (**b**) IRCs of dimer **7**. The point B is at an energy of −15.2 kcal/mol, at reaction coordinate value of 2.69. The significance of the *dashed lines* is the same as in Fig. 13.1. The zero of the energy axis represents the reactants at infinite separation (Reproduced from Pratt et al. [37]. With kind permission of © The Chemical Society of Japan 2009)

the tetrameric $\Delta G^{\ddagger}$ for the stepwise reactions are even higher. These results are consistent with the B3LYP/6-311 G(d,p) of KZP. The conclusion we can draw is that the preferred reaction pathways and indeed the reactivity of cyclopropanation reactions of halomethyllithiums depend sensitively on the aggregation states of the reactants. Given that halomethyllithiums in nonpolar media are overwhelmingly in the aggregated state (Table 13.1), the data presented in Table 13.7 establishes that the cyclopropanation reactions of halomethyllithiums with alkenes proceed by the direct mechanism in nonpolar solvents.

We have examined the reactions of 2,3-dimethylbutene with the halomethyllithiums and found that the same pattern in $\Delta G^{\ddagger}$ for the concerted and stepwise reactions are observed for the monomers and dimers. Thus, it appears that the formation of substituted cyclopropane rings is also more facile with aggregated Li-CH$_2$-X species.

The MP2/6-31 + G(d) level IRCs for the concerted and stepwise reactions of the gas-phase dimers **6** and **7** are presented in Fig. 13.1, for the case of X = Br. The solid symbols connected by the solid line represent the IRC of the concerted mechanism Eq. 13.6. The point A represents the farthest point along the IRC for which structures could be converged, starting from the transition states TS **8** or **9** and proceeding toward the reactants. The empty symbols connected by the solid line represents the IRC for the first step of the stepwise mechanism Eq. 13.7, and the point D represents the minimum value of the IRC for which structures could be converged, starting from TS **10** or **11** and proceeding toward the reactants. The nature of this IRC suggested that pre-reactive complexes are being formed in both cases. The optimized structure of these complexes are represented by the point C, which is
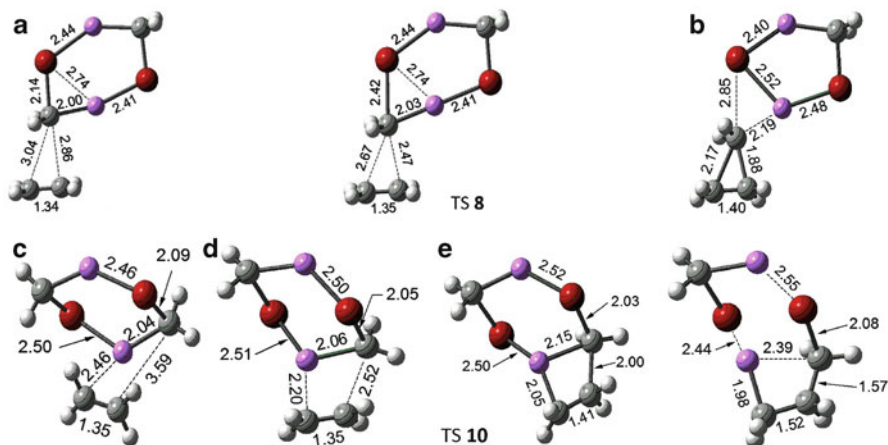
Fig. 13.2 The structures corresponding to the labeled points on the IRCs of dimer **6** shown in Fig. 13.5 for LiCH$_2$X, X = Br. The corresponding structures for X = F and Cl are similar. Bond lengths shown are in Angstroms (Adapted from Pratt et al. [37]. With kind permission of © The Chemical Society of Japan 2009)

placed schematically on the IRC (i.e., the value of the reaction coordinate for this point is guided only by the physically reasonable expectation that the IRC should smoothly connect the point D to the reactants while passing through C). Spline interpolations connecting these calculated points to the asymptotic reactants in a physically reasonable manner are shown as dashed lines. The molecular structures corresponding to the labeled points for dimer **6** are shown in Fig. 13.2. We have examined and confirmed that the IRCs and structures for the cases X = F and Cl are qualitatively similar. The structures at the labeled points along the IRC for dimer **7** are given in Fig. 7 of [37].

The IRCs plotted in Fig. 13.1 clearly show that in the case of dimeric halomethyl-lithiums, the concerted pathway is overwhelmingly preferred to the stepwise reaction pathway. In contrast, the IRCs for the direct and stepwise reactions of the monomeric halomethyllithiums [37] show no such preference. In those cases also, the IRCs provided strong indications that pre-reactive complexes were formed in the case of the stepwise pathway, but not in the concerted pathway. From the structures shown in Fig. 13.2 and those given in [37] for the monomers, it appears that the reaction pathway is determined by the relative orientations of the reactants during the initial approach. If the methylene group approaches the double bond first, the concerted pathway is followed. On the other hand, if the Li atom approaches the π-cloud of the ethylene double bond, the pre-reactive complexes are formed, which puts the reactants on the stepwise reaction pathway. This would have an inhibitory effect on the net reaction rate because, given the high reaction barriers for the stepwise reaction pathway, the reaction cannot proceed unless the pre-reactive complexes dissociate and reorient so as to follow the direct pathway.

13.3.2 Reactions of Halomethyllithiums in THF with Ethylene

The primary solvation shell of lithium carbenoids in THF appears to consist of two THF ligands strongly bound to each Li. Steric factors inhibit the coordination by additional solvent molecules. The bis-THF-solvated carbenoid monomers were found to undergo similar reactions to those in the gas phase. The direct insertion is initiated by the interaction of the methylene group with the alkene double bond, leading to TS **1**·2THF.

Comparisons between the calculations of KZP [47] and our own [37] reveal some interesting differences in the structure and solvation states in dimethylether (DME) versus THF. Unlike the gas-phase carbometalation reactions and the calculations of KZP with coordinated DME ligands, we were unable to identify a pre-reactive complex for the bis-THF-solvated monomers. An intermediate similar to the gas-phase pre-reactive complex **2′** in Fig. 13.1 was found for the monosolvated case:

$$H_2C = CH_2 + LiCH_2Cl \cdot 1THF \rightarrow \textbf{2}' \cdot 1THF\,(X = Cl)\,;$$
$$\Delta U^{\circ}_{0,B3LYP} = -2.90\,\text{kcal/mol} \tag{13.8}$$
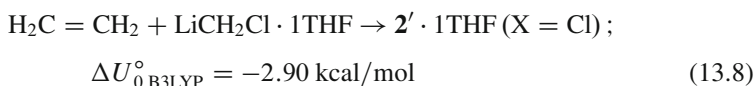
However, relative to ethylene and LiCH$_2$Cl·2THF, the formation of the monosolvated complex is energetically unfavorable:

$$H_2C = CH_2 + LiCH_2X \cdot 2THF \rightarrow \textbf{2}' \cdot 1THF\,(X = Cl) + THF;$$
$$\Delta U^{\circ}_{0,B3LYP} = 8.55\,\text{kcal/mol} \tag{13.9}$$
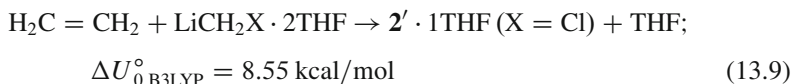
The formation of the pre-reactive complex is also unfavorable on the basis of free energy change, which is found to be $\Delta G^{\circ} = +4.13$ kcal/mol for Eq. 13.8 and $+9.90$ kcal/mol for Eq. 13.9 at the B3LYP/6-31 + G(d) level.

KZP report a weakly bound ($\Delta U^{\circ}_{B3LYP/6-311+G(d,p)} = -1.4$ kcal/mol) complex between LiCH$_2$F·2DME and ethylene, but the alkene is more than 5 Å away from the solvated species (Fig. 4 of [47]). We searched for, but could not find, a similar complex for LiCH$_2$X·2THF at the DFT or MP2 levels of theory. It appears that the more rigid structure of the THF ligands and their stronger interaction with the Li atom introduces greater steric and energetic constraints that are not present in the DME solvent. In spite of the absence of a stable pre-reactive complex in the case of the bis-THF-solvated monomers, the stepwise addition appears to follow the essential stages of the gas-phase reaction, including the formation of the four-membered TS **2**·2THF leading to the intermediate **3**·2THF.

The B3LYP, MP2, and MP2//B3LYP free energy changes associated with the concerted and stepwise insertions (through TS **1**·2THF and TS **2**·2THF, respectively) and the formation of the intermediate **3**·2THF are summarized in Table 13.8.

Comparison of the MP2 and MP2//B3LYP results in Tables 13.7 and 13.8 show that, with the exception of X = Br, solvation has no significant effect on the $\Delta G^{\ddagger}$ for direct insertion while solvation increases the barrier heights for the stepwise reaction by 3–7 kcal/mol. (The difference in the $\Delta G^{\ddagger}$ of TS **2** and TS **2**·2THF is much larger

Table 13.8 The free energy differences (kcal/mol) at 173.15 K for the cyclopropanation reactions of $H_2C=CH_2$ and $LiCH_3X.2THF$ in THF solvent

	$\Delta G^{\circ}_{\text{B3LYP}}$	$\Delta G^{\circ}_{\text{MP2}}$	$\Delta G^{\circ}_{\text{MP2//B3LYP}}$
$H_2C=CH_2 + LiCH_3X \cdot 2THF \rightarrow \textbf{TS1} \cdot \sqrt{2}$ 2THF Eq. 13.3			
X = F	13.30	12.73	13.27
X = Cl	12.91	13.26	13.10
X = Br	10.26	8.45	8.42
$H_2C=CH_2 + LiCH_3X \cdot 2THF \rightarrow \textbf{TS2} \cdot$ 2THF Eq. 13.4			
X = F	18.58	16.80	15.38
X = Cl	23.05	17.85	18.45
X = Br	21.30	15.90	17.27
$H_2C=CH_2 + LiCH_3X \cdot 2THF \rightarrow \textbf{3} \cdot$ 2THF Eq. 13.4			
X = F	−12.46	−19.15	−18.59
X = Cl	−4.09	−13.39	−12.70
X = Br	−4.75	−13.30	−12.68
$H_2C=CH_2 + LiCH_3X \cdot 2THF \rightarrow$ Cyclopropane $+ LiX \cdot 2THF$			
X = F	−59.40	−66.00	−66.89
X = Cl	−58.62	−64.31	−65.65
X = Br	−55.76	−64.13	−64.61
TS $\textbf{4} \cdot$ 2THF (anti), relative to $H_2C=CH_2 + LiCH_3X \cdot 2THF$ Eq. 13.5			
X = F	13.67	7.37	7.05
X = Cl	6.76	4.83	4.79
X = Br	6.33	0.87	0.24
TS $\textbf{5} \cdot$ 2THF (syn), relative to $H_2C=CH_2 + LiCH_3X \cdot 2THF$ Eq. 13.5			
X = F	13.77	13.77	14.25
X = Cl	18.34	19.33	20.77
X = Br	16.13	15.95	16.76

at the B3LYP level of theory, ranging from 9 to 11 kcal/mol.) Unlike the gas phase, the concerted mechanism is preferred over the stepwise reaction of monomers when explicit THF solvation is considered. These observations are consistent with the trends in the energy barriers reported by KZP (Table 1 of [1]) for the case of two coordinated dimethylether (DME) solvent molecules.

The effect of THF solvation on the second step in the stepwise mechanism, namely, the elimination of the lithium halide through syn or anti pathways, also appears to be quite significant as shown in Table 13.8. When compared to the gas phase (Table 13.7), THF solvation appears to uniformly lower the energy of TS **4**·2THF for anti-elimination relative to the reactants while raising the energy of the transition state TS **5**·2THF for syn elimination. This is likely a result of increased stability of the separated ions X^- and Li^+ in the presence of a strongly coordinating polar solvent, while the direct formation of LiX from TS **5** is more favorable in the gas phase. The structures of TS **4**·2THF and TS **5**·2THF are shown in Fig. 13.3.

Another aspect of Table 13.8 deserves comment, namely, the rather large differences in the B3LYP and MP2 energy differences in the formation of TS
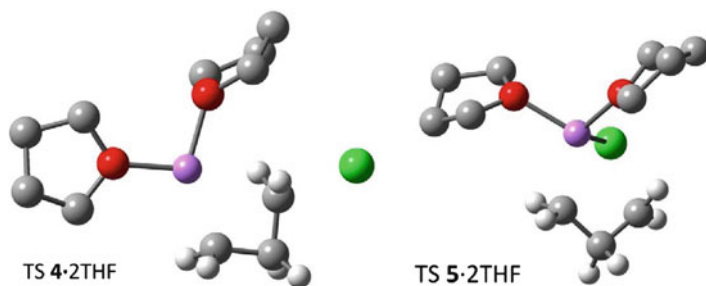
Fig. 13.3 MP2 optimized geometries of THF-solvated TS structures **4** and **5** for anti and syn eliminations, respectively, of LiX from the intermediate **3**. Structures are shown for X = Cl

2·2THF and **3**·2THF (Table 13.5), and the energy of TS **4**·2THF relative to the reactants (Table 13.6). In these cases, the MP2 and MP2//B3LYP results are reasonably close, indicating that the B3LYP geometries are close to those found by MP2, but the B3LYP functional yields a rather different energy. This is quite different from the situation with the dimerization energies reported in Table 13.4. In that case, it appears that the B3LYP geometries themselves were quite different from those predicted by MP2. As noted in connection with the discussion surrounding Table 13.4, later in this chapter, we will examine the relative performances of various DFT functionals in predicting the equilibrium geometries and relative energies compared to the correlated wave function method represented by MP2.

As mentioned above, we also examined the reactions of monosolvated monomers in the case of X = Cl at the B3LYP/6-31 + G(d) level, including IRC calculations of reaction paths. Except for the discovery of the pre-reactive complex for the stepwise reaction (See Eq. 13.7), the results were qualitatively similar to those reported by KZP for X = F in DME, and the gas-phase results reported above, in this work. Since the monosolvated monomers are unstable relative to the disolvated species (see Eq. 13.9), they are not discussed further.

The dimeric halomethyllithium carbenoids exist largely as the tetrasolvates in THF solution (Table 13.4). However, dissociation to the trisolvated forms is reasonably facile:

$$2 \, LiCH_2X \cdot 2THF \rightarrow (LiCH_2X)_2 \cdot 4THF \tag{13.10}$$

$$(LiCH_2X)_2 \cdot 4THF \rightarrow (LiCH_2X)_2 \cdot 3THF + THF \tag{13.11}$$
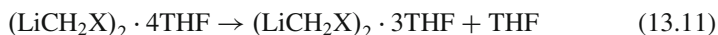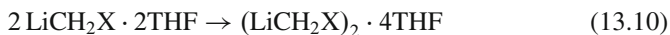
Several attempts were made to locate a TS structure for the concerted insertion reaction of the tetrasolvated dimer with ethylene, but steric constraints proved to be too hard to overcome. KZP reported tetrasolvated dimeric TS structures in DME solvent [47], which points to yet another difference in the cyclopropanation reactions of LiCH_2X in DME and THF. As mentioned earlier, it is possible that the more rigid structure of the THF ring and its stronger binding to the Li atom introduce steric effects not present in the case of more flexible ethereal solvent molecules.
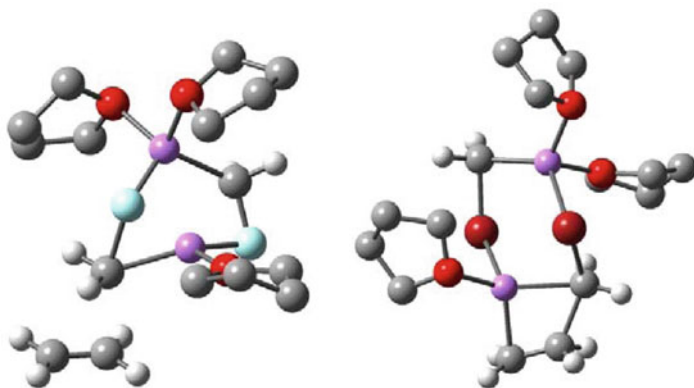
Fig. 13.4 Transition state structures for the concerted and stepwise reactions of **6**·3THF (TS **8**·3THF and **TS10**·3THF, respectively). Structures shown for X = F for TS **8**·3THF (*left*) and X = Br for **TS10**·3THF (*right*)

Table 13.9 The MP2 reaction barriers $\Delta G^{\ddagger}$ and free energy change ΔG° for the formation of the THF-solvated intermediate **3**·2THF (kcal/mol) at 173.15 K for the cyclopropanation reactions of $H_2C{=}CH_2$ and halomethyllithium dimers in THF solvent *relative to the tetrasolvated reactants*

| | 3·2THF from | | | | 3·2THF from | |
	TS8·3THF	6·4THF	TS9·3THF	TS10·3THF	7·4THF	TS11·3THF
X = F	17.85	5.86	17.21	32.68	5.00	31.69
X = Cl	19.02	8.87	21.27	36.46	8.23	30.83
X = Br	13.87	16.23	16.64	29.59	18.56	30.43

TS structures were successfully located for the reaction of the trisolvated form. In keeping with the numbering scheme already adopted, the transition states are labeled TS **8**·3THF and TS **9**·3THF for the concerted and stepwise reactions of **6**, respectively, and TS **10**·3THF and TS **11**·3THF, respectively, for the analogous reactions of **7**. The structures of TS **8**·3THF and TS **10**·3THF are shown in Fig. 13.4. Table 13.9 summarizes the MP2 free energy changes associated with the reactions.

The results tabulated in Table 13.9 show that, compared to the case of the gas-phase dimers (Table 13.7), the barriers are significantly higher for both the concerted and stepwise mechanisms. For example, the MP2 $\Delta G^{\ddagger}$ for TS **8** (X = F) for the gas-phase dimer **6** is 11.60 kcal/mol compared to 17.85 kcal/mol in THF. The barriers for the stepwise reaction also increase for this species, from 29.21 kcal/mol in the gas phase to 32.68 kcal/mol in THF. This trend appears to be absent in DME solvent. Another significant difference between the behavior of gas-phase and THF-solvated dimers is that the formation of intermediate 3·2THF according to

$$H_2C = CH_2 + (Li - CH_2 - X)_2 \cdot 4THF$$

$$\rightarrow \underset{\textbf{3·2THF}}{Li - (CH_2)_3 - X \cdot 2THF} + Li - CH_2 - X \cdot 2THF \qquad (13.12)$$
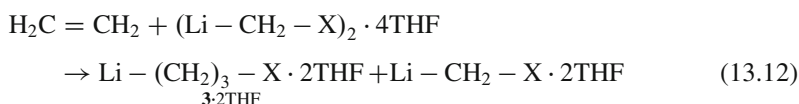
Table 13.10 Reaction barriers $\Delta G^{\ddagger}$ (kcal/mol) for the methylene transfer (direct) and carbolithiation (stepwise) pathways of halomethyllithium tetramers and tetramers in the gas phase Eqs. 13.14 and 13.15 at 173.15 K

	$\Delta G^{\ddagger}_{B3LYP}$	$\Delta G^{\ddagger}_{MP2}$	$\Delta G^{\ddagger}_{MP2//B3LYP}$
$H_2C = CH_2 + (Li - CH_2 - X)_4 \to$ TS **12** (concerted)			
X = F	8.07	7.11	7.24
X = Cl	14.74	16.57	16.89
X = Br	8.82	8.14	8.32
$H_2C = CH_2 + (Li - CH_2 - X)_4 \to$ TS **13** (stepwise)			
X = F	36.23	37.06	37.23
X = Cl	34.26	35.47	35.77
X = Br	32.82	32.24	32.25

is thermodynamically unfavorable at 173.15 K, as shown in Table 13.9. Therefore, in addition to the higher barriers, the stepwise mechanism may be frustrated in THF by the relative instability of the required reactive intermediate. KZP did not study the carbometalation pathway for the DME-solvated dimer and, therefore, a comparison of the behavior in DME for this pathway cannot be made.

13.3.3 Reactions of Halomethyllithiums Tetramers with Ethylene

The formation of the tetramer from the dimer is highly favored in the gas phase (Table 13.4). Since dimers are much more stable than the monomers, we examine the formation of tetramers from the dimers, taking dimer **6** as a representative.

$$2\,(LiCH_2X)_2 \to (LiCH_2X)_4 \qquad (13.13)$$
$$\underset{\mathbf{6}}{}$$
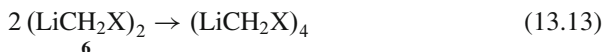
The relevant $\Delta G°$ data are summarized in Table 13.4. Note that tetramerization is even more favorable in nonpolar solvents, in which case each free energy change shown will further decrease by $2 \times 0.91 = 1.82$ kcal/mol at 173.15 K (see the paragraph above Eq. 13.6). Table 13.10 shows the $\Delta G^{\ddagger}$ for the concerted and stepwise reactions of the gas-phase tetramer, proceeding through TS **12** and TS **13**, respectively:

$$H_2C = CH_2 + (LiCHX)_4 \to \text{TS } \mathbf{12} \text{ (concerted mechanism)} \qquad (13.14)$$
$$H_2C = CH_2 + (LiCH_2X)_4 \to \text{TS } \mathbf{13} \text{ (stepwise mechanism)} \qquad (13.15)$$
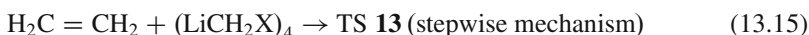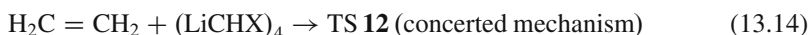
The MP2 structures for the tetramer, TS **12**, and TS **13** are given in Fig. 13.5. The structure of TS **12** in the vicinity of the alkene double bond and the methylene group being inserted into it are comparable to TS **1** and TS **8**, and the transition state for the stepwise insertion, TS **13**, also has the four-membered structure similar to the analogous reactions of the monomer and dimer **6** (Fig. 13.2, TS **8** and **10**).
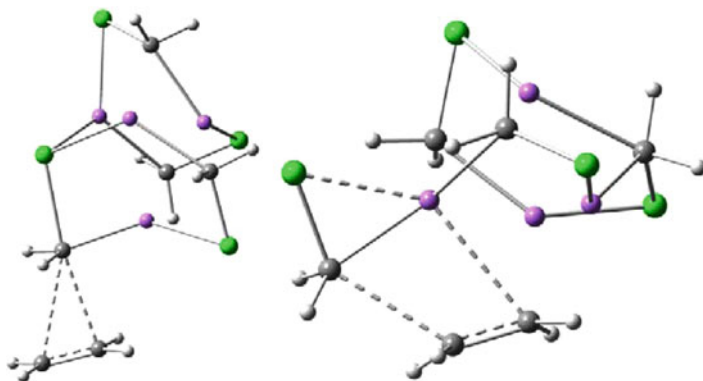
Fig. 13.5 The MP2/6-31 + G(d) structures for the transition state for the concerted (TS **12**; *left*) and stepwise (TS **13**; *right*) reactions for the case X = Cl

Table 13.10 suggests that as the size of the halomethyllithium aggregates increases, the reaction barrier $\Delta G^{\ddagger}$ for the concerted reaction goes down. For the case of X = F, the MP2 free energy barriers are 12.80 kcal/mol for the monomer (Table 13.7), 11.60 for dimer **6** (Table 13.7), and 7.11 for the tetramer (Table 13.10). At the same time, the barriers for the stepwise pathway increases with aggregate size: 12.34, 29.21, and 37.06 kcal/mol, respectively for the monomer, dimer **6**, and tetramer of X = F. Similar trend for 0 K energy barrier heights $\Delta U^{\ddagger}$ was reported by KZP (7.8, 5.9, and 4.9 kcal/mol, respectively, for the concerted reaction of the monomer, dimer, and tetramer for X = F; 4.3,22.6, and 30.8 kcal/mol for the stepwise reaction) based on B3LYP/6-311 G(*d,p*) calculations. Our own B3LYP/6-31 + G(*d*) results for $\Delta U^{\ddagger}$ (see [37]) for the concerted and stepwise pathways for X = F, of 4.53 and 30.94 kcal/mol, respectively, compare well with the 4.9 and 30.8 kcal/mol reported by KZP (Fig. 3c of [47]) for the same processes.

Since it seems that the dominant species of LiCH$_2$X in THF solution is likely to be the dimer (based on the MP2 results in Table 13.4), and also because of the computational difficulties associated with treating large systems at MP2 level of theory (72 atoms for the tetrasolvated tetramer), we did not examine the barrier heights for the reactions of the tetrasolvated tetramer with ethylene.

13.3.4 Reactions of Halomethyllithiums with Dimethylbutene

In [37] we also studied the reactions of (LiCH$_2$X)$_2$ with 2,3-dimethyl-2-butene, (CH$_3$)$_2$C=C(CH$_3$)$_2$, abbreviated as DMB for convenience. These studies served to confirm that the general conclusions drawn above for the cyclopropanation of ethylene with halomethyllithiums could be generalized to longer chain alkenes also.
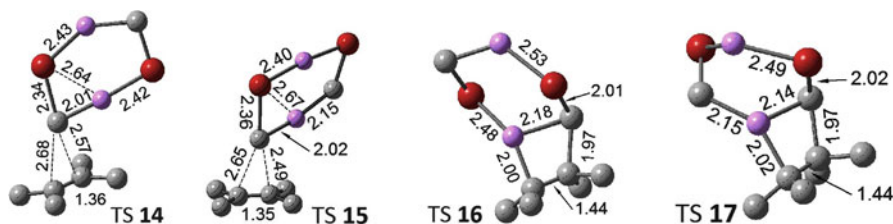
Fig. 13.6 The MP2/6-31 + G(d) transition states for the concerted reactions of dimer **6** (TS **14**) and dimer **7** (TS **15**), and those for the stepwise reactions (TS **16** for dimer **6**, and TS **17** for dimer **7**) with 2,3-dimethylbutene for the case X = Br. Hydrogens are not shown for clarity (Adapted from Pratt et al. [37]. With kind permission of © The Chemical Society of Japan 2009)

It was also discovered that the formation of pre-reactive complexes in this case could serve to make the reactions essentially barrier free with respect to the reactants.

The transition state structures for the direct (TS **14**, **15**) and stepwise pathways (TS **16**, **17**) shown in Fig. 13.6 are structurally similar to TS **8**, **9**, **10**, and **11** for analogous reactions of the cyclopropanation of ethyelene. As in the case of ethylene, we were able to identify relatively stable pre-reactive complexes in which one of the Li atoms of the dimer interacted strongly with the alkene double bond. The relative free energies at 173.15 K and standard pressure, $\Delta G°$, for the processes studied are summarized in Table 13.11. The analogous results for ethylene are given in Table 13.4. It is clear from Table 13.11 that the concerted mechanism is clearly preferred over the stepwise pathway for cyclopropanation of dimethylbutene at all levels of theory examined. The barriers for the concerted pathway are generally lower than those for ethylene (compare to TS **8** and TS **9** in Table 13.7), especially in the case of dimer **7**, while those for the stepwise pathway are higher, indicating an even stronger preference for the direct pathway compared to that of ethylene.

IRC calculations for the reactions of halomethyllithiums with DMB revealed the presence of pre-reactive complexes for both the concerted and stepwise pathways – an important difference from the reaction with ethylene. The classical (or Born-Oppenheimer) energy barriers with respect to the reactants $\Delta E^{\ddagger}$ for the concerted reactions of the dimer **7** (LiCH$_2$X)$_2$, X = Cl and Br with DMB are actually *negative* (−1.62 and −1.19 kcal/mol at MP2 and MP2//B3LYP levels of calculation) with respect to the reactants, as shown in Fig. 13.7. The reason, as explained in [37], appears to be that the electrostatic interactions between the halomethyllithiums and the DMB double bond are quite strong, stabilizing the activated complex. Of course, the addition of vibrational zero point energies and thermal corrections yield the positive, but low, free energies of activation tabulated in Table 13.11.

These considerations suggest that the concerted mechanism for cyclopropanation using halomethyllithium aggregates should become increasingly facile under extremely mild conditions in the cases of larger alkenes than ethylene. An equally important conclusion is that the formation of stable pre-reactive complexes along the reaction pathway can lead to very low free energies of activation for reactions. It seems highly likely that the tendency of organolithium reagents to yield nearly complete reactions at extremely low temperatures may be associated with this aspect.

Table 13.11 The ΔG° at 173.15 K for the reactions of the gas-phase dimers **6** and **7** (in kcal/mol) with 2,3-dimethyl-2-butene

	$\Delta G_{\textbf{B3LYP}}$	$\Delta G_{\textbf{MP2}}$	$\Delta G_{\textbf{MP2// B3LYP}}$
Concerted : $Me_2C = CMe_2 + \textbf{6} \rightarrow$ TS **14**			
X = F	12.14	8.80	9.19
X = Cl	13.67	9.67	12.27
X = Br	13.32	9.52	10.06
Stepwise : $Me_2C = CMe_2 + \textbf{6} \rightarrow$ Pre − reactivecomplex (**16′**)			
X = F	−1.23	−6.78	−6.16
X = Cl	0.21	−7.43	−6.61
X = Br	−2.51	−10.46	−9.36
Stepwise : $Me_2C = CMe_2 + \textbf{6} \rightarrow$ TS **16**			
X = F	40.31	34.32	35.15
X = Cl	46.89	37.10	38.38
X = Br	38.43	29.15	30.16
Concerted : $Me_2C = CMe_2 + \textbf{7} \rightarrow$ **TS15**			
X = F	11.07	7.21	7.45
X = Cl	9.87	7.50	7.51
X = Br	8.90	4.59	5.08
Stepwise : $Me_2C = CMe_2 + \textbf{7} \rightarrow$ Pre − reactivecomplex (**17′**)			
X = F	−0.66	−6.45	−5.96
X = Cl	−1.42	−9.11	−8.12
X = Br	−2.69	−10.51	−10.28
Stepwise : $Me_2C = CMe_2 + \textbf{7} \rightarrow$ TS **17**			
X = F	39.66	33.97	34.60
X = Cl	41.43	32.10	33.45
X = Br	36.07	26.86	28.20

13.3.5 Cyclopropanation Reactions of Oxiranyllithiums with Ethylene

As noted in the Introduction, oxiranyllithiums, which are lithioethers, are also used for introducing a methylene group into a double bond, creating cyclopropane derivatives. We have studied this system extensively, using a large number of correlated wave function and density-based methods [54]. Figure 13.8 shows the monomeric reagent as well as the transition states, and products for the monomeric and dimeric oxiranyllithium reacting with ethylene.

Table 13.12 summarizes the free energy of activation $\Delta G^{\ddagger}$ for the cyclopropanation reactions of oxiranullithium monomer, the two dimers, and the three tetramers in nonpolar medium, and the monomer and dimers in THF solution. In this case, as part of the investigation mentioned earlier [54], we have also calculated the energetics using the M06-2X [40] and MP2//M06-2X methods.

Table 13.12 suggests that, in contrast to halomethyllithiums, the reaction barriers for cyclopropanation of alkenes using oxiranyllithiums appear to be generally
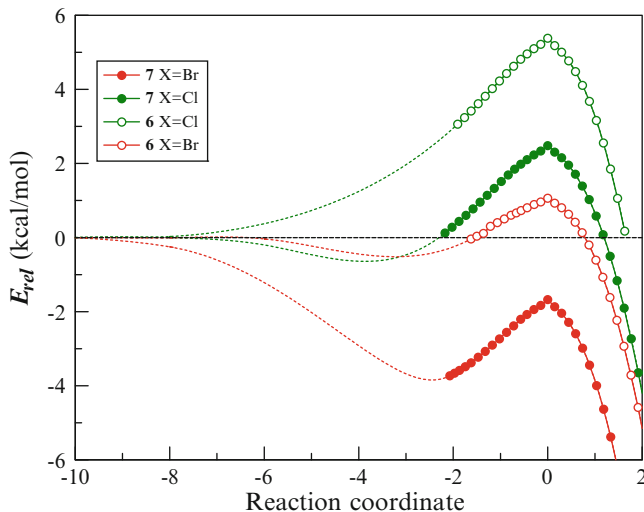
Fig. 13.7 MP2/6-31 + G(d) IRCs in (amu)$^{1/2}$ bohr for dimers **6** and **7** for X = Cl and Br reacting with dimethylbutene along the concerted reaction path. The symbols connected by *solid lines* indicate the extent to which IRC calculations could be converged. The *dashed lines* are "physically reasonable" spline interpolations constrained to reach zero energy at −10. The zero of the energy axis represents the reactants at infinite separation (Adapted from Pratt et al. [37]. With kind permission of © The Chemical Society of Japan 2009)
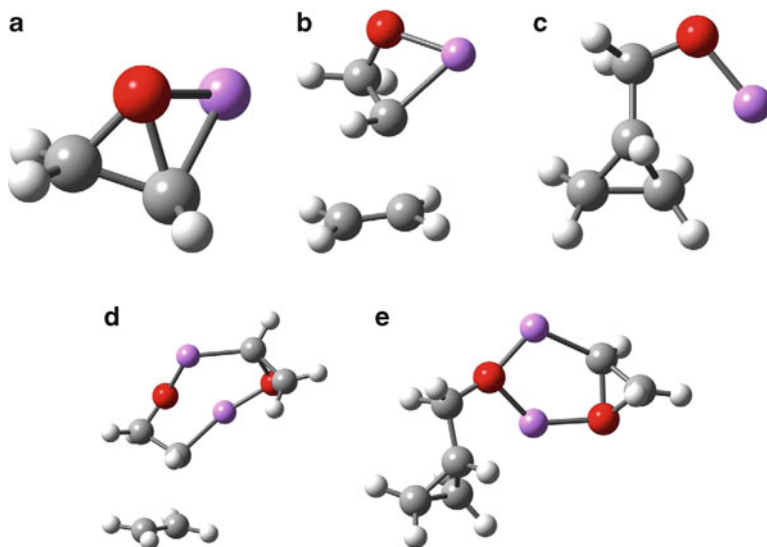
Fig. 13.8 Equilibrium structures of (**a**) oxyranillithium monomer, (**b**) the transition state for the monomer reacting with ethylene, (**c**) the product of the reaction of monomeric oxiranyllithium with ethylene, (**d**) the transition state for dimeric oxiranyllithium reacting with ethylene, and (**e**) the corresponding product

Table 13.12 The $\Delta G^{\ddagger}$ for the reactions of oxiranyllithiums with ethylene

	ΔG_{B3LYP}	$\Delta G_{\text{M06-2X}}$	$\Delta G_{\text{MP2//B3LYP}}$	$\Delta G_{\text{MP2//M06-2X}}$
Nonpolar solvent				
R	18.32	21.45	20.44	19.88
RR	18.51	21.87	19.78	19.65
RS	18.88	22.09	20.36	20.20
RRRR	14.53	15.44	17.28	16.34
RRRS	13.37	16.90	13.60	15.13
RRSS	10.29	14.33	2.53	−0.23
THF solution				
R·2THF	20.10	21.77	20.40	17.89
RR·2THF	20.48	22.91	21.46	19.35
RR·4THF	21.41	24.16	20.64	20.67
RS·2THF	19.26	21.46	20.14	17.85
RS·4THF	21.95	24.49	21.90	21.78

insensitive to aggregation states or solvation states at least for the dimers. The free energies of activation for the monomer and the dimer are practically the same. While the $\Delta G^{\ddagger}$ for the tetramers are lower than those of the monomers or dimers, the barrier height with respect to reactants is still quite considerable, except in the very puzzling case of the MP2//B3LYP and MP2//M06-2X results for the RRSS isomer. We have not been able to understand the reason for this discrepancy.

13.3.6   Reaction Rates and Arrhenius Activation Energies

We now calculate and compare the temperature dependence of the second-order rate constants for the most facile reaction pathways for halomethyl lithium carbenoids and oxiranyllithiums. We assume that the free energy of activation is approximately temperature independent within the range 100–300 K, so that the rate constants over the temperature range of interest can be calculated using the Eyring equation as

$$k(T) = \left(\frac{k_{\text{B}}T}{hc^{\circ}}\right) e^{-\Delta G^{\ddagger}/(RT)}, \tag{13.16}$$

where k_{B} is the Boltzmann constant, c° is the standard concentration (mol L^{-1} for our present application) and $\Delta G^{\ddagger}$ is the free energy of activation including the corrections for condensed phase and involvement of solvent molecules as outlined in the Introduction.

The $\Delta G^{\ddagger}$ for the reactions of specific aggregates presented thus far (Tables 13.7, 13.9, 13.10, and 13.11) were always calculated relative to the reactants for the species under consideration. For example, we reported the $\Delta G^{\ddagger}$ for monomers with respect to the monomeric species and ethylene, and the $\Delta G^{\ddagger}$ for the dimers were

Table 13.13 Arrhenius activation energies E_a for the cyclopropanation reactions of halomethlylithium carbenoids (LiCH$_2$X) and oxiranyllithium (LiOx) with ethylene

	Nonpolar solvent			THF microsolvation	
	Monomer	Dimer	Tetramer	Monomer	Dimer
LiCH$_2$F[a]	22.83	12.10	3.91	13.03	8.86
LiCH$_2$Cl[a]	23.90	15.19	8.67	12.60	9.45
LiCH$_2$Br[a]	25.37	15.77	4.43	12.01	7.88
LiOx[b]	28.50	18.04	9.06	16.06	13.44

In the case of the former, only the low energy concerted pathway is considered

[a]MP2/6-31 + G(d)

[b]M06-2X/6-31 + G(d)

reported relative to the dimers and ethylene. This was sufficient to reveal that the direct pathway is more favorable than the stepwise pathway for cyclopropanation except for the monomers. However, the question of practical importance to the experimentalist has to do with the reactivity of the dominant species in a given mixture of reagents. For example, we conclude from our discussion so far that halomethyllithiums in a nonpolar solvent would be in a tetrameric (or higher) aggregation state. Oxiranyllithium solutions are also dominated by tetrameric (or higher) aggregates in nonpolar solvents. In THF, however, it seems likely that dimers are the more favorable aggregation state for both types of reagents. Therefore, in order to understand the competition between reactive species, we compute the reaction rate constants for each species *relative to the most stable species in that solution*. So, in the case of fluoromethyllithium carbenoid in the gas phase, at the MP2 level of theory, we get $\Delta G^{\ddagger} = 7.11$ kcal/mol for the tetramer (Table 13.10), $11.60 + 0.50 \times 23.58 = 23.39$ kcal/mol for the dimer, where 23.58 is the free energy change required to form two moles of dimer **6** from the tetramer (Table 13.1), and $12.80 + 0.50 \times 23.58 + 0.50 \times 40.25 = 44.72$ kcal/mol for the monomer, where 40.25 kcal/mol is the free energy change required to form two moles of the monomer from the dimer (Table 13.1). The standard state corrections mentioned earlier are then applied to these gas-phase free energies of activations to get the $\Delta G^{\ddagger}$ in nonpolar solvents. The *relative* free energies of activation for the oxiranyllithium species were also calculated in the same fashion, using M06-2X results, relative to the tetramer in nonpolar media, and the dimer in THF.

The rate constants calculated from Eq. 13.16 using the $\Delta G^{\ddagger}$ thus obtained over the temperature range of 100–300 K are subjected to the standard linear regression analysis to get the Arrhenius activation energies E_a. The results of this analysis are tabulated in Table 13.13. The calculated rate constants for the dominant forms of bromomethyllithium and oxyranillithium reacting with ethylene in nonpolar (tetramers) and THF (dimers) solvents are shown in Fig. 13.9. This figure and Table 13.13 suggests that the most efficient cyclopropanation of ethylene under extremely mild conditions is through halomethyllithiums, particularly the fluoro and bromo analogues, in a nonpolar solvent.
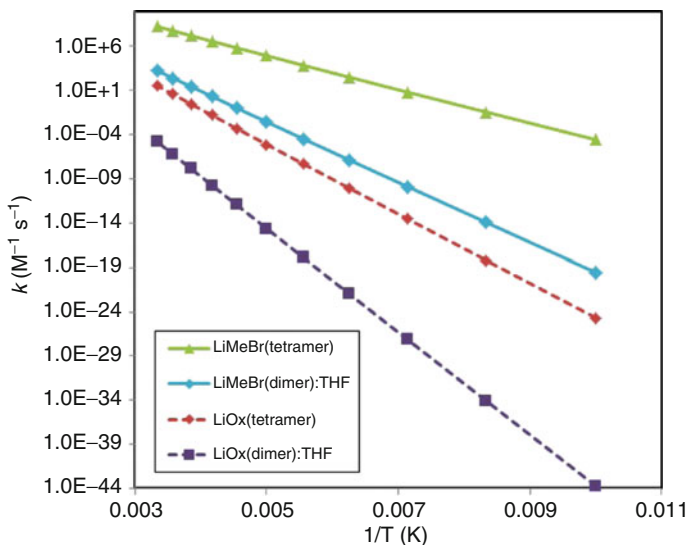
Fig. 13.9 Reaction rate constants for the reactions of bromomethyllithium species and oxiranyl-lithium species reacting with ethylene, as a function of temperature. *Green*: LiCH$_2$Br tetramer (nonpolar solvent), *Blue*: LiCH$_2$Br dimer (THF solvent), *Red*: oxiranyllithium tetramer (nonpolar solvent), and *Purple*: oxiranyllithium dimer (THF solvent)

13.4 Density Functional Theory in Computational Organolithium Chemistry

We now describe a research direction motivated by some of the results obtained during the investigation of cyclopropanation reactions using halomethyllithium carbenoids. To set the stage, let us revisit the dimerization and tetramerization energetics summarized in Table 13.4 and other Tables presented and discussed above. In the previous section, we commented on the large differences between the B3LYP and MP2 free energy changes for dimerization, and the *qualitative* differences between the $\Delta G°$ predicted by the two methods for tetramerization of both halomethyllithium carbenoids and oxiranyllithiums. In the case of tetramerization, the MP2//B3LYP results are also qualitatively different from MP2 results in a couple of instances. Such discrepancies suggest that the energy differences and the equilibrium geometries obtained from the B3LYP functional were at odds with those calculated by MP2. These suggestions were confirmed for fluoromethyllithium carbenoids by comparisons of structures and energetics, as described in detail in [37]. This apparent failure of the most popular DFT functional in chemistry [55] was the starting point for the investigations described below.

It is beyond dispute now that the Kohn-Sham density functional theory [55, 56] has delivered many functionals that achieve comparable accuracy in atomization energies, ionization potentials, electron affinities, thermochemistry, and reaction

barriers as correlated wave function methods at comparable or lesser computational cost [57]. Their performances have been tested using quite extensive databases incorporating experimental data and high-level ab initio calculations, such as the Gaussian training sets [58], the Minnesota databases of the Truhlar group [59], and the Weizmann 1–4 databases [60–64], and, indeed, some of them have been parameterized using subsets of such data sets.

However, organolithium compounds are conspicuously missing from these databases. Clearly, the scarcity of experimental thermochemical data is one good reason for their exclusion. A second and equally important reason is that it is nearly impossible to compute high-level ab initio (i.e., WFT methods that systematically account for dynamical correlation used with large, polarized basis sets) data for the dominant reactive species in the reactions of organolithum compounds and their transition states, because of the need to consider rather large aggregates of molecules. In a recent paper [65], we examined the performance of 13 modern DFT functionals, when used with a double-zeta quality polarized basis set, in predicting the geometries and energetics relevant for the reactions discussed in the previous section, that is, the cyclopropanation reactions of halomethyllithium carbenoids (Li–CH$_2$–X; X = F, Cl, Br) with ethylene. The goal of this study was to examine how well various DFT functionals reproduced the geometries and energy differences predicted by the highest level correlated wave function method that could be practically applied to all the molecules and transition states considered.

It was observed earlier that among the WFT methods that systematically include dynamic correlation energy, only the MP2 with a modest basis set is practical for routine study of organolithium aggregates, especially when solvated by strongly coordinating ethereal solvents. However, MP2 geometry optimizations and frequency calculations for large molecules also require considerable computational resources (computing time, memory, disk). DFT functionals tend to be far less demanding computationally but, as the example of B3LYP mentioned above shows, their reliability remains to be systematically studied in the context of organolithium species. The forces responsible for aggregation and coordination to ethereal solvents are due to nonbonded interactions driven by electron polarization. Moreover, in all aggregates, the lithium is "hypervalent" in the sense that it strongly interacts with more than one atom. Such interactions, in other contexts, have been found to be challenging for many DFT functionals.

Our investigation of the relative performance of DFT functionals in the context of cyclopropanation reactions of halomethyllithium carbenoids [65] used a database of 84 molecules, out of which 33 include coordinated THF-solvent molecules, 45 gas-phase reactions of (LiCH$_2$X)$_n$; X = F, Cl, Br, n = 1 or 2, and 33 reactions of (LiCH$_2$X)$_n$·mTHF; m = 0, 2, 3, or 4. The data used for performance evaluation include MP2 single-point energies at DFT-optimized geometries ($E_{MP2//DFT}$), the reaction energies ΔE (the difference in the Born-Oppenheimer energies of the products and reactants), and the barrier heights $\Delta E^{\ddagger}$, the difference in energy between the saddle points and the reactants. The test set includes 36 transition states, 24 in the gas phase and 12 in THF solution. The gas-phase test set includes nine pre-reactive complexes that display long-range, nonbonded interactions between the Li

atom and the ethylene double bond. The organolithium species in the condensed phase have strong coordination between the Li and the oxygen atoms of THF as well as the interactions with ethylene.

In [65] we describe the calculations that were used to establish a practical benchmark against which the performance of the DFT methods could be evaluated. Essentially, this amounted to an evaluation of MP2/6-31 + G(d) structures and energies against higher-level wave function methods. First, the MP2/6-31 + G(d) equilibrium structural parameters for 13 small molecules [LiCH$_2$F, LiCH$_2$Cl, LiCH$_2$Br, TS **1** (F, Cl, Br), TS **2** (F, Cl, Br), LiCl, ethylene, cyclopropane, and THF] were compared against QCISD/6-311 G(d,p) geometries. Next, the MP2/6-31 + G(d)// QCISD/6-311 G(d,p) energies were compared against MP2/6-31 + G(d) energies. The average difference between MP2/6-31 + G(d)// QCISD/6-311 G(d,p) and MP2/6-31 + G(d) energies over the test set of molecules was only 0.17 kcal/mol, the average difference in bond lengths, 0.014 Å, average difference in bond angles, 0.71°, and average difference in dihedrals, 1.52°. These comparisons served to establish that MP2/6-31 + G(d) geometries can be used as the standard against which DFT geometries can be evaluated.

A benchmark for the energy differences between reactants and products and reactants and transition states were also established. In this case, we examined the reaction energies ΔE and the barrier heights $\Delta E^{\ddagger}$ for the eight reactions of (LiMeCl)$_2$ with ethylene at the MP2/6-31 + G(d), MP2/6-311 + G(2df,2p), and CCSD(T)/6-31 + G(d) levels of theory, where all the molecular and transition state geometries are optimized at the MP2/6-31 + G(d) level. These reactions were selected because they incorporate various types of interactions that are typical in organolithium chemistry, such as those responsible for the formation of dimers, pre-reactive complexes, and transition states. These calculations helped us establish a benchmark for *relative* energies, that is, ΔE values, using the relationship

$$\Delta E_{\text{benchmark}} = \Delta E_{\text{MP2/6−311+G(2df,2p)//6−31+G(d)}}$$
$$+ \left[\Delta E_{\text{CCSD(T)/6−31+G(d)}} - \Delta E_{\text{MP2/6−31+G(d)}} \right] \quad (13.17)$$

which is similar in spirit to the strategy reported by Zhao and Truhlar in generating benchmarks for evaluating various methods [66–68]. Comparison of the benchmark reaction energetics for eight candidate reactions against those calculated from MP2/6-31 + G(d) results showed that the average absolute difference is 1.98 kcal/mol, most of which can be attributed to two reactions in which cyclopropane and LiCl are formed. Excluding these two reactions, the average absolute difference decreases to 0.97 kcal/mol, just below the "chemical accuracy" goal of ± 1 kcal/mol. Therefore, we adopt $\Delta E_{\text{MP2/6–31+G(d)}}$ as a compromise yardstick against which the performance of various DFT "model chemistries" (see below) may be evaluated.

A more recent investigation, reported here for the first time, examined the cyclopropanation reactions of oxiranyllithiums with ethylene. In this case, we limited ourselves to five DFT functionals but included single-point

CCSD(T)/6-31 + G(d) calculations for the gas-phase molecules as another method against which to compare the DFT results. Further discussion of these calculations is provided in a later subsection.

13.4.1   *Jacob's Ladder and DFT Functionals*

The "Jacob's ladder" analogy of Perdew [69, 70] is very useful for classifying the nature and sophistication of density functionals. The first rung of the ladder is occupied by local spin density functionals that are generally quite useful in solid-state physics but typically lead to large errors for small molecules. The second rung consists of the generalized gradient approximation (GGA) functionals. Of these, we examine PW91PW91 [71], mPWPW91 [72], and PBEPBE [73]. For the remainder of this chapter, we shall abbreviate the first and last functionals as PW91 and PBE, respectively. The third rung is occupied by the so-called meta-GGA (m-GGA) functionals that incorporate orbital kinetic energy density. We consider TPSSTPSS [74] (abbreviated hereafter as TPSS) and M06-L [75] in this category. The fourth rung belongs to the hybrid or hyper GGAs (h-GGA) which introduce nonlocal effects by mixing in exact Hartree-Fock-type exchange, and hybrid meta-GGAs (h-m-GGA) or hyper-GGAs, which, in addition to exact exchange, also incorporate the kinetic energy density of meta-GGAs. In the fourth rung, we consider the h-GGAs B3LYP [38, 76, 77] B3PW91 [71, 76], mPW1LYP [72, 77], mPW1PW91 [71, 72], and PBE1PBE [78]; and the h-m-GGAs BMK [79], M06 [40], and M06-2X [40]. The hybrid PBE1PBE has been referred to as PBE0 to emphasize the nonempirical determination of the fraction of exact exchange in the functional (i.e., that it is a hybrid with zero empirical parameters), and we will abbreviate it as PBE0 hereafter.

Except for the benchmark calculations related to Eq. 13.17), each of the 13 functionals named above were used with the 6-31 + G(d) basis set, which is the largest polarized double-zeta basis with diffuse functions that is *practical* for geometry optimizations and MP2 calculations with the largest molecules studied. The benchmark calculations helped establish that this basis achieves excellent convergence in geometry and reasonable convergence in reaction energetics at the MP2 level of theory. In addition to the DFT/6-31 + G(d) model chemistries, we also considered MP2 single-point energy calculations at the DFT/6-31 + G(d) optimized geometries, leading to the two-step model chemistry MP2/6-31 + G(d)//DFT/6-31 + G(d).

13.4.2   *Molecules and Methods*

Our test set includes 84 molecules, out of which 33 are coordinated to THF-solvent molecules. Using these molecules as reactants, intermediates, transition states, or products, we consider 45 gas-phase reactions and 33 reactions of THF-solvated

molecules. Structural representations of the different types of gas-phase molecules in our test set are shown in Sect. 13.1.3. In both gas phase and THF, each type of molecule is present with X = F, Cl, and Br. In THF, each lithium atom is coordinated to two THF molecules except in transition states **8–11,** which, as we have already seen, are trisolvated. Three molecules included in our test set (ethylene, THF, and the lithium halides LiX) are not shown.

The MP2//DFT energies serve two purposes in our work: first, the agreement between the MP2//DFT and MP2 energies is one measure of the agreement between the optimized geometries predicted by the DFT method and MP2; second, the MP2//DFT approach, which involves only a single MP2 energy calculation, is practical even for aggregated and solvated systems of up to ∼70–90 atoms and so, we wish to assess the performance of these model chemistries as tools for the routine study of organolithium chemistry. We assess the ability of each DFT functional to yield geometries close to those predicted by MP2 by examining $\delta E_{\text{DFT}} = |E_{\text{MP2//DFT}} - E_{\text{MP2}}|$. The performance of the DFT functionals in reproducing *relative energies* in the gas phase is analyzed using reaction energies ΔE, and barrier heights $\Delta E^{\ddagger}$. We define quantities $\delta \Delta E_{\text{DFT}} = |\Delta E_{\text{DFT}} - \Delta E_{\text{MP2}}|$, and $\delta \Delta E_{\text{MP2//DFT}} = |\Delta E_{\text{MP2//DFT}} - \Delta E_{\text{MP2}}|$ for this purpose.

13.4.3   Results for Halomethyllithium Carbenoids

Having established that MP2/6-31 + G(d) yields accurate geometries compared to the benchmark QCISD/6-311 G(d,p) results, the first question we tried to answer in this study was "which functional yields optimized geometries closest to those predicted by MP2?" The quantity $\delta \Delta E_{\text{DFT}}$ defined above serves as a useful metric in this investigation. In Table 13.14, we summarize the results of this analysis. The "best" functionals for gas-phase, for THF-solvated, and overall are identified in boldface. Most of the DFT functionals reproduce MP2 geometries fairly well in the gas phase, but THF coordination proves to be challenging for most of them. The average error of B3LYP for predicting THF-solvated geometries is twice as larger than that of M06-2X, the functional with the lowest error. The superior performance of PBE0 in the gas phase and overall has to be noted.

Turning now to reaction energetics, we use quantities $\delta \Delta E_{\text{DFT}} = |\Delta E_{\text{DFT}} - \Delta E_{\text{MP2}}|$, and $\delta \Delta E_{\text{MP2//DFT}} = |\Delta E_{\text{MP2//DFT}} - \Delta E_{\text{MP2}}|$ defined earlier. The test set now consists of 45 gas-phase cases (24 transition states and 21 reaction energies) and 33 THF-solvated cases (12 transition states and 21 reaction energies), so that the overall test set consists of 78 cases (36 transition states and 42 reaction energies). The results of our analysis are presented in Table 13.15. The poor performance of B3LYP noted earlier in the context of dimerization and tetramerization of THF-solvated halomethyllithium carbenoids can be seen reflected in these results. We eliminated the BMK functional from consideration except for the gas phase because the functional could not obtain converged transition state structures for **TS 8–12** in THF. It may seem surprising that a functional designed for kinetics would have such

Table 13.14 The average of $\delta E_{DFT} = |E_{MP2//DFT} - E_{MP2}|$ in kcal/mol over the test set derived from the study of cyclopropanation reactions of halomethyllithium carbenoids

Functional	Type	Gas phase (51)	THF-phase (33)	Overall (84)
PW91	GGA	0.95	2.44	1.61
mPW91	GGA	0.99	3.60	2.12
PBE	GGA	0.86	2.87	1.74
TPSS	m-GGA	0.86	3.19	1.88
M06-L	m-GGA	0.69	2.19	1.35
B3PW91	h-GGA	0.39	2.57	1.37
B3LYP	h-GGA	0.75	3.66	1.98
mPW1PW91	h-GGA	0.44	2.24	1.23
mPW1LYP	h-GGA	0.64	2.31	1.37
PBE0	h-GGA	**0.33**	1.79	**0.96**
BMK	h-m-GGA	0.63	2.50	1.26
M06	h-m-GGA	0.64	1.91	1.20
M06-2X	h-m-GGA	0.57	**1.85**	1.14

The functionals are arranged according to the rungs of the Jacob's ladder

difficulties. However, in determining the percentage of exact exchange in the BMK functional, Boese and Martin relied on single-point energies calculated at transition state geometries obtained using high-level correlated WFT methods. Therefore, it is possible that the ability of the functional to converge to saddle point geometries, especially in challenging cases, may not have been evaluated.

From this analysis, it appears that the most practical approach to study the reaction energetics of organolithium compounds is to perform geometry optimizations using M06-2X or PBE0, followed by MP2 single-point energy evaluations. This point is driven home by Fig. 13.10, redrawn from [65], which presents the average of the errors $\langle \delta \Delta E_{DFT} \rangle$ and $\langle \delta \Delta E_{MP2//DFT} \rangle$ for each rung of the Jacob's ladder, and also the $\langle \delta \Delta E_{DFT} \rangle$ and $\langle \delta \Delta E_{MP2//DFT} \rangle$ for the best functionals in each rung. The best functionals in each rung of the ladder outperform the average by significant margins. The curves representing the two-step model chemistries MP2//DFT show that the performance depends only weakly on the sophistication of the DFT functional used for geometry optimization. However, the steady downward trend of these lines is an indication that the increasing sophistication of the functionals have indeed translated into increased accuracy in geometry prediction.

We invite the reader to examine [65] for a more detailed description of the analysis.

13.4.4 Performance of DFT for Oxiranyllithiums

In the case of oxiranyllithiums, we examined the reaction free energies $\Delta G°$ and free energies of activation $\Delta G^{\ddagger}$ for a smaller set of reactions, but we added higher-level

Table 13.15 The average of the absolute deviation in reaction energies $\delta \Delta E_{DFT} = |\Delta E_{/DFT} - \Delta E_{MP2}|$ and $\delta \Delta E_{MP2//DFT} = |\Delta E_{MP2//DFT} - \Delta E_{MP2}|$ in kcal/mol over 42 gas phase, 33 THF-phase, and the overall average over the 75 reactions

Functional	Type	Gas phase (45) $\delta \Delta E_{DFT} = |\Delta E_{/DFT} - \Delta E_{MP2}|$	THF-phase (33)	Overall	Gas phase (45) $\delta \Delta E_{MP2//DFT} = |\Delta E_{MP2//DFT} - \Delta E_{MP2}|$	THF-phase (33)	Overall
PW91	GGA	5.75	6.18	5.93	0.75	0.86	0.80
mPW91	GGA	5.51	6.79	6.05	0.79	1.38	1.04
PBE	GGA	5.33	6.02	5.62	0.58	1.14	0.81
TPSS	m-GGA	5.55	6.67	6.02	0.70	1.37	0.98
M06-L	m-GGA	3.21	3.21	3.21	0.43	0.91	0.63
B3PW91	h-GGA	3.20	6.44	4.57	0.30	1.32	0.73
B3LYP	h-GGA	4.28	7.73	5.74	0.52	1.97	1.13
mPW1PW91	h-GGA	2.86	5.47	3.97	0.33	1.07	0.64
mPW1LYP	h-GGA	4.11	6.74	5.22	0.36	1.26	0.74
PBE0	h-GGA	2.79	4.91	3.69	0.18	1.02	0.54
BMK	h-m-GGA	2.86	–	–	0.37	–	–
M06	h-m-GGA	3.12	3.23	3.17	0.43	1.11	0.72
M06-2X	h-m-GGA	2.46	2.48	2.47	0.35	0.67	0.48

Fig. 13.10 The average of the $\langle\delta\Delta E_{\text{DFT}}\rangle$ (*blue*) and $\langle\delta\Delta E_{\text{MP2//DFT}}\rangle$ (*red*) for functionals at each rung of the Jacob's ladder, and the $\langle\delta\Delta E_{\text{DFT}}\rangle$ (*green*) and $\langle\delta\Delta E_{\text{MP2//DFT}}\rangle$ (*purple*) for the best functionals at each rung, for the set of reaction energies and barrier heights for $(\text{LiCH}_2\text{X})_n$ + ethylene; $n = 1,2$; X = F, Cl, Br, in gas phase and THF solvent (Adapted from Ramachandran et al. [65]. With kind permission of © The American Chemical Society 2010)

correlated wave function methods as standards against which the DFT and two-step model chemistries based on DFT methods could be evaluated for the gas-phase molecules.

The functionals chosen for study in this case are M06L in the third rung, the h-GGAs B3LYP and PBE0 as well as the m-h-GGAs M06 and M062X in the fourth rung. The two-step model chemistries used for energetics are MP2//DFT, CCSD(T)//DFT, and also CCSD(T)//MP2, all employing the $6\text{-}31 + \text{G}(d)$ basis set. Five gas-phase reaction barriers and reaction energies for the monomeric and dimeric oxiranyllithium reacting with ethylene were considered. In the case of the THF-solvated species, the CCSD(T) calculations proved to be impractical even for dimeric species with 4 coordinated THF molecules, and therefore, we restricted the wave function methods to MP2//DFT.

Table 13.16 summarizes the mean absolute errors $\delta\Delta E_{\text{DFT}}$ [re-defined in the case of CCSD(T) calculations] as well as $\delta\Delta E_{\text{MP2}}$ and $\delta\Delta E_{\text{CCSD(T)//MP2}}$, in kcal/mol, evaluated against various standards, which are given in the column headings. The test set consists of ten data points, five each of $\Delta G°$ and $\Delta G^\ddagger$, representing reactions of the monomer and two types of dimers (each in the RR and RS steroisomeric forms) with ethylene. In this case, it is appropriate to consider the "horizontal" averages, that is, average errors for a given method as measured against the

Table 13.16 Analysis of the model chemistries DFT/6-31 + G(d) and MP2//DFT/6-31 + G(d) for the gas phase (or nonpolar media) cyclopropanation reactions of oxiranyllithium with ethylene, against selected standards given as column headings

	CC//MP2	MP2	CC//M062X	MP2//M062X	H-<Avg>	H-σ
M06L	2.29	2.45	1.43	2.94	2.28	0.63
B3LYP	1.73	4.53	2.29	5.02	3.39	1.63
PBE0	3.20	1.08	2.62	0.95	**1.96**	1.12
M06	3.56	1.79	2.70	1.81	2.46	0.84
M062X	3.68	1.02	3.25	1.56	2.38	1.29
MP2//M06L	3.15	0.67	2.62	0.33	1.69	1.40
MP2//B3LYP	3.08	0.44	2.65	0.38	**1.64**	1.43
MP2//PBE0	2.86	0.97	2.27	0.59	**1.67**	1.07
MP2//M06	3.25	0.89	2.68	0.45	1.82	1.36
MP2//M062X	3.36	0.69	2.86	–	2.30	1.42
V-<Avg>	3.10	1.34	2.66	1.39		
V-σ	0.57	1.25	0.29	1.57		

The mean absolute errors are in kcal/mol. The horizontal average for each row, H-<Avg>, and standard deviation, H-σ, as well as the vertical average, V-<Avg>, for each column and standard deviation V-σ, are shown

various standards, and the standard deviation in them. From the work presented in the previous section, it appears that M06-2X predicts geometries very close to that obtained by MP2, and, therefore, we also included the two-step model chemistry CCSD(T)//M06-2X and MP2//M06-2X in the standards against which the performance of other methods are evaluated.

The top half of Table 13.16 evaluates the performance of various DFT functionals against the "standards," while the bottom half is devoted to two-step model chemistries MP2//DFT. In the top half of Table 13.16, PBE0 emerges as a superior functional among the DFT functionals based on $\delta\Delta E_{DFT}$. Among the two-step model chemistries, B3LYP emerges as the winner, with PBE0 as a close second. Note that in Table 13.15, PBE0 had the lowest $\langle\delta\Delta E_{MP2//DFT}\rangle$ for gas-phase reactions. In the case of halomethyllithiums (gas phase $\delta\Delta E_{DFT}$ in Table 13.15), PBE0 was among the best DFT functionals for reproducing MP2 energy differences (the best in that case being M06-2X) while B3LYP's performance was not particularly impressive. Tables 13.15 and 13.16 suggest that PBE0 may be a superior general purpose GGA for geometry optimizations of clusters of organolithium reactive species, transition states, and products in the gas phase.

In the case of the reactions of the THF-solvated oxiranyllithium species, we adopted MP2//M06-2X and MP2//PBE0 and M06-2X itself as the standards against which energetics are compared. Our test set consists of ten data points, five each of ΔG° and $\Delta G^\ddagger$, representing reactions of the monomer and two stereoisomers (RR and RS) of one type of dimer with ethylene. We considered the reactions of disolvated (one THF per Li) and tetrasolvated (two THF per Li) dimers.

Table 13.17 summarizes the results of this analysis. Among the DFT functionals, M06-2X does a superior job of reproducing energy differences, and the improvement gained by going to the two-step MP2//M06-2X is rather modest. Once again,

Table 13.17 Analysis of the model chemistries DFT/6-31 + G(d) and MP2//DFT/6-31 + G(d) for the THF-phase cyclopropanation reactions of oxiranyllithium with ethylene, against selected standards given as column headings

	MP2//M062X	MP2//PBE0	M062X	H-\<Avg\>	H-σ
B3LYP	3.78	4.00	3.97	3.92	0.12
M06	2.90	2.79	3.65	3.11	0.47
M06L	3.18	3.17	3.90	3.42	0.42
M062X	1.13	1.42	–	**1.27**	0.20
PBE0	2.32	1.78	2.66	2.25	0.44
MP2//B3LYP	1.40	0.96	0.94	**1.10**	0.26
MP2//M06	1.78	1.88	1.95	1.87	0.08
MP2//M06L	1.32	1.26	2.12	1.57	0.48
MP2//M062X	–	0.99	1.13	**1.06**	0.10
MP2//PBE0	0.99	–	1.42	1.20	0.30
V-\<Avg\>	2.09	2.03	2.42		
V-σ	1.00	1.06	1.19		

The mean absolute errors are in kcal/mol. The horizontal average for each row, H-\<Avg\>, and standard deviation, H-σ, as well as the vertical average, V-\<Avg\>, for each column and standard deviation V-σ, are shown

MP2//B3LYP emerges as a strong contender among two-step model chemistries, contrary to our experience with the THF-solvated halomethyllithiums (Table 13.15) where B3LYP predicted geometries for solvated dimers that were at considerable variance in structure and energy from those predicted by MP2 as well as other DFT functionals.

This work is currently in progress and a more complete analysis is expected to appear elsewhere in the near future [54].

13.5 Summary and Conclusions

The most important insights gained in the past decade through computational research on the reactions of lithium carbenoids is the clear establishment of the role of aggregation states in determining the reactivity. There are two ways in which aggregation states have manifested their importance in the case of organolithium carbenoids. The first is in determining the preferred reaction pathway where more than one is possible. The monomeric forms of halomethyllithium carbenoids used for cyclopropanation of alkenes show a mild preference for the stepwise (carbometalation) pathway while experimental evidence, at least in the case of intermolecular reactions, was in favor of the concerted (methylene transfer) pathway. This, coupled with the fact that the Simmons-Smith reagent ($IZnCH_2I$) [45] and $ISmCH_2I$, investigated computationally by Zhao, Wang, and Phillips [50], show clear preference for the concerted pathway in monomeric form itself, is clearly the reason that the case of lithium carbenoids remained unsettled for so many years. Recent advances in computational technology and resources made it possible to

study the reactions of dimeric and tetrameric species [37, 47] at reasonable levels of theory, and this revealed that the aggregated forms, which are dominant species in any reaction mixture, clearly prefer the concerted pathway.

A second way in which aggregation states influence reactivity in the preferred pathway itself is the observed lowering of free energy of activation, $\Delta G^{\ddagger}$, and the consequent lowering of the Arrhenius activation energy, E_a, of both halomethyllithium carbenoids and oxiranyllithiums as the aggregates get larger. Table 13.13 shows that the activation energy of both fluoromethyllithium carbenoid and bromomethyllithium carbenoid reacting with ethylene, relative to the dominant reactive species in solution, decreases by a factor of 6 from the monomeric form to the dominant tetrameric form in nonpolar media. The effect of aggregation is less dramatic in the case of cyclopropanation with oxiranyllithium, but Table 13.13 shows that the activation energy still decreases by a factor of 3 from the monomer to the tetramer in nonpolar solvents.

The importance of the steric effects introduced by the strong coordination of ethereal solvents like dimethyl ether (DME) or THF to the lithium atom has been well-recognized for a number of years, even though the computational resources needed to handle large solvated aggregates at high levels of theory using correlated wave function methods remain barely within reach.

Explicit inclusion of the primary solvation shell in geometry optimizations and free energy calculations reveal the dependence of the aggregation state on the solvent. In the case of halomethyllithium carbenoids, the preferred aggregation state in nonpolar media is tetrameric (or larger) while strongly solvated dimers appear to be the dominant species in THF solution. The case of oxiranyllithium is less clear-cut from our computations: tetramers are clearly dominant in nonpolar solution and may coexist with appreciable concentrations of dimers in THF. The decreased preference for larger aggregates with larger numbers of THF solvent molecules is clearly a steric phenomenon.

The strength of solvent coordination also affects reactivity. In the case of tetra-solvated dimeric halomethyllithiums, we discovered [37] that partial de-solvation to the trisolvated form was necessary in order for the cyclopropanation reaction, whether by the concerted or stepwise pathway, to proceed. However, the less polar DME solvent, considered by Ke et al. [47], appears to be less susceptible to this type of steric interference: they were able to find methylene transfer transition states for tetrasolvated species in DME.

Comparison of our recent work on cyclopropanation with halomethyllithiums [37] with that of Ke et al. [47] revealed another type of solvent influence on the reaction path itself. Ke et al. observed the formation of moderately stable pre-reactive complexes for both the concerted and stepwise pathways in DME. These pre-reactive complexes could potentially decrease the relative energy all along the reaction path and could, in extreme cases, result in a negative reaction barrier relative to the reactants, as shown in Fig. 13.7 in the case of DMB reacting with bromomethyllithium carbenoids. The discovery of pre-reactive complexes in the concerted pathway for DMB suggests that the reaction barriers for cyclopropanation of longer chain or other substituted alkenes could also be extremely low or even nonexistent, relative to the reactants.

A conclusion of practical importance that can be drawn from these calculations is that stereoselective insertion of a methylene group into an alkene can be achieved with nearly 100% yield under extremely mild conditions by using halomethyl-lithium carbenoids as reagents and a nonpolar solvent as the reaction medium. The reactive species in such reactions are likely to be tetramers or higher aggregates of the carbenoids.

The discussion so far makes it clear that the ability to perform high-level computations on large, solvated aggregates of molecules is an absolute necessity for fruitful work in the area of organolithium chemistry. Second-order perturbation theory (MP2), when used with a modest polarized basis set such as the $6\text{-}31 + G(d)$, is viable for geometry optimizations of aggregates up to ~ 80 atoms, provided a very large amount of memory and scratch disk are available. Even then, frequency calculations with analytical second derivatives on such molecules are, of course, extremely difficult. DFT functionals (or, as some people prefer, density functional approximations, or DFAs) are the most obvious and computationally preferred alternatives. It was noted in Sect. 13.4 that the training sets used in the development of existing functionals do not include a single organolithium molecule. This fact, coupled with the observation that B3LYP appeared to predict physically counterintuitive thermodynamics for THF-solvated halomethyllithium carbenoids, led us to investigate the overall performance of several popular DFAs against the test set provided by our earlier investigations.

The happy conclusion from these studies is that modern fourth-rung DFT functionals, especially PBE0 and M06-2X, appear to do a very good job of predicting geometries, even for the difficult cases of THF-solvated aggregates. The purely local, and computationally less expensive M06-L also does very well overall in predicting optimized geometries, when compared to those obtained from well-established correlated wave function methods. These methods do less well in the calculation of *energy differences*, needed for reaction energetics and thermodynamics. However, MP2//DFT, especially with any of the three functionals mentioned above, is a practical, and by all current observations, accurate approach to studying large aggregates of organolithium compounds.

References

1. Simmons HE, Smith RD (1958) J Am Chem Soc 80:5323
2. Simmons HE, Smith RD (1959) J Am Chem Soc 81:4256
3. Schöllkopf U, Eisert M (1963) Liebigs Ann Chem 664:78

4. Bosold F, Zulauf P, Marsh M, Harms K, Lohrenz J, Boche G (1991) Angew Chem Int Ed Engl 30:1455
5. Boche G, Opel A, Marsh M, Harms K, Haller F, Lohrenz J, Thiimmler C, Koch W (1992) Chem Ber 125:2265
6. Satoh T (1996) Chem Rev 96:3303
7. Capriati V, Degennaro L, Favia R, Florio S, Luisi R (2002) Org Lett 4
8. Wiedemann SH, Ramirez A, Collum DB (2003) J Am Chem Soc 125:15893
9. Hodgson DM, Reynolds NJ, Coote SJ (2004) Org Lett 6:4187
10. Campos PJ, Sampedro D, Rodriguez MA (1998) Organometallics 17:5390
11. Pratt LM, Ramachandran B, Xidos JD, Cramer CJ, Truhlar DG (2002) J Org Chem 67:7607
12. Pratt LM, Khan IM (1995) J Comput Chem 16:1067
13. Romesberg FE, Collum DB (1992) J Am Chem Soc 114:2112
14. Rutherford JL, Collum DB (2001) J Am Chem Soc 123:199
15. Frisch MJ, Trucks GW, Schlegel HB, Scuseria GE, Robb MA, Cheeseman JR, Zakrzewski VG, Montgomery JA Jr, Stratmann RE, Burant JC, Dapprich S, Millam JM, Daniels AD, Kudin KN, Strain MC, Farkas O, Tomasi J, Barone V, Cossi M, Cammi R, Mennucci B, Pomelli C, Adamo C, Clifford S, Ochterski J, Petersson GA, Ayala PY, Cui Q, Morokuma K, Salvador P, Dannenberg JJ, Malick DK, Rabuck AD, Raghavachari K, Foresman JB, Cioslowski J, Ortiz JV, Baboul AG, Stefanov BB, Liu G, Liashenko A, Piskorz P, Komaromi I, Gomperts R, Martin RL, Fox DJ, Keith T, Al-Laham MA, Peng CY, Nanayakkara A, Challacombe M, Gill PMW, Johnson B, Chen W, Wong MW, Andres JL, Gonzalez C, Head-Gordon M, Replogle ES, Pople JA (1998) Gaussian 98. Gaussian, Inc, Pittsburgh
16. Frisch MJ, Trucks GW, Schlegel HB, Scuseria GE, Robb MA, Cheeseman JR, Montgomery JA Jr, Vreven T, Kudin KN, Burant JC, Millam JM, Iyengar SS, Tomasi J, Barone V, Mennucci B, Cossi M, Scalmani G, Rega N, Petersson GA, Nakatsuji H, Hada M, Ehara M, Toyota K, Fukuda R, Hasegawa J, Ishida M, Nakajima T, Honda Y, Kitao O, Nakai H, Klene M, Li X, Knox JE, Hratchian HP, Cross JB, Bakken V, Adamo C, Jaramillo J, Gomperts R, Stratmann RE, Yazyev O, Austin AJ, Cammi R, Pomelli C, Ochterski JW, Ayala PY, Morokuma K, Voth GA, Salvador P, Dannenberg JJ, Zakrzewski VG, Dapprich S, Daniels AD, Strain MC, Farkas O, Malick DK, Rabuck AD, Raghavachari K, Foresman JB, Ortiz JV, Cui Q, Baboul AG, Clifford S, Cioslowski J, Stefanov BB, Liu G, Liashenko A, Piskorz P, Komaromi I, Martin RL, Fox DJ, Keith T, Al-Laham MA, Peng CY, Nanayakkara A, Challacombe M, Gill PMW, Johnson B, Chen W, Wong MW, Gonzalez C, Pople JA (2003) Gaussian 03. Gaussian, Inc, Wallingford
17. Frisch MJ, Trucks GW, Schlegel HB, Scuseria GE, Robb MA, Cheeseman JR, Scalmani G, Barone V, Mennucci B, Petersson GA, Nakatsuji H, Caricato M, Li X, Hratchian HP, Izmaylov AF, Bloino J, Zheng G, Sonnenberg JL, Hada M, Ehara M, Toyota K, Fukuda R, Hasegawa J, Ishida M, Nakajima T, Honda Y, Kitao O, Nakai H, Vreven T, Montgomery JA Jr, Peralta JE, Ogliaro F, Bearpark M, Heyd JJ, Brothers E, Kudin KN, Staroverov VN, Kobayashi R, Normand J, Raghavachari K, Rendell A, Burant JC, Iyengar SS, Tomasi J, Cossi M, Rega N, Millam JM, Klene M, Knox JE, Cross JB, Bakken V, Adamo C, Jaramillo J, Gomperts R, Stratmann RE, Yazyev O, Austin AJ, Cammi R, Pomelli C, Ochterski JW, Martin RL, Morokuma K, Zakrzewski VG, Voth GA, Salvador P, Dannenberg JJ, Dapprich S, Daniels AD, Farkas O, Foresman JB, Ortiz JV, Cioslowski J, Fox DJ (2009) Gaussian 09, Revision B.1. Gaussian, Inc, Wallingford
18. Peng C, Schlegel HB (1993) Israel J Chem 33:449
19. Peng C, Ayala PY, Schlegel HB, Frisch MJ (1996) J Comput Chem 17:49
20. Gonzalez C, Schlegel HB (1989) J Chem Phys 90:2154; (1990) J Phys Chem 94:5523
21. Thompson JD, Cramer CJ, Truhlar DG (2003) J Chem Phys 119:1661
22. Pratt LM, Nguyen NV, Ramachandran B (2005) J Org Chem 70:4279
23. Govender UP, Letcher TM, Garg SK, Ahluwalia JC (1996) J Chem Eng Data 41:147
24. Pratt LM, Streitwieser A (2003) J Org Chem 68:2830
25. Pratt LM, Mogali S, Glinton K (2003) J Org Chem 68:6484

26. Pratt LM, Mu R (2004) J Org Chem 69:7519
27. Pratt LM (2005) Bull Chem Soc Jpn 78:890
28. Pratt LM, Nguyen NV, Le LT (2005) J Org Chem 70:2294
29. Pratt LM, Nguyen NV (2006) J Phys Chem A 110:687
30. Gossage RA, Jastrzebski JTBH, van Koten G (2005) Angew Chem Int Ed Engl 44:1448
31. Kottke T, Stalke D (1993) Angew Chem Int Ed Engl 32:580
32. Fraenkel G, Chow A, Winchester WR (1990) J Am Chem Soc 112:2582
33. Fraenkel G, Duncan JH, Wang J (1999) J Am Chem Soc 121:432
34. Fraenkel G, Duncan JH, Martin K, Wang J (1999) J Am Chem Soc 121:10538
35. Sun X, Collum DB (2000) J Am Chem Soc 122:2452; (2000) J Am Chem Soc 122:2459
36. Pratt LM, Phan-Tran DH, Tran PTT, Nguyen NV (2007) Bull Chem Soc Jpn 80:1587
37. Pratt LM, Tran PTT, Nguyen NV, Ramachandran B (2009) Bull Chem Soc Jpn 82:1107
38. Stephens PJ, Devlin FJ, Chabalowski CF, Frisch MJ (1994) J Phys Chem A 98:11623
39. Pratt LM, Ramachandran B (2005) J Org Chem 70:7238
40. Zhao Y, Truhlar DG (2008) Theor Chem Acc 120:215; (2008) Acc Chem Res 41:157
41. Amstutz R, Schweizer WB, Seebach D, Dunitz JD (1981) Helv Chim Acta 64:2617
42. Hoberg H (1962) Liebigs Ann Chem 656:1
43. Burger U, Huisgen R (1970) Tetrahedron Lett 11:3049
44. Stiasny HC, Hoffmann RW (1995) Chem Eur J 1:619
45. Nakamura M, Hirai A, Nakamura E (2003) J Am Chem Soc 125:2341
46. Hermann H, Lohrenz JC, Kuhn A, Boche G (2000) Tetrahedron 56:4109
47. Ke Z, Zhao C, Phillips DL (2007) J Org Chem 72:848
48. Zhao CY, Wang DQ, Phillips DL (2002) J Am Chem Soc 124:12903
49. Wang DQ, Phillips DL, Fang WH (2002) Organometallics 21:5901
50. Zhao CY, Wang DQ, Phillips DL (2003) J Am Chem Soc 125:15200
51. Zhao CY, Wang DQ, Phillips DL (2004) J Org Chem 69:5512
52. Ke Z, Zhou Y, Gao H, Zhao CY, Phillips DL (2007) Chem Eur J 13:6724
53. Pratt LM, Merry S, Nguyen SC, Quan P, Thanh BT (2006) Tetrahedron 62:10821
54. Pratt LM, Mai BK, Ramachandran B (to be submitted for publication)
55. Sousa SF, Fernandes PA, Ramos MJJ (2007) J Phys Chem A 111:10439
56. Kümmel S, Kronik L (2008) Rev Mod Phys 80:3
57. Zheng J, Zhao Y, Truhlar DG (2009) J Chem Theory Comput 5:808
58. Curtiss LA, Raghavachari K, Redfern PC, Pople JA (1997) J Chem Phys 106:1063; Curtiss LA, Redfern PC, Raghavachari K, Pople JA (1998) J Chem Phys 109:42; Curtiss LA, Raghavachari K, Redfern PC, Pople JA (2000) J Chem Phys 112:7374; Curtiss LA, Redfern PC, Raghavachari K, Pople JA (2001) J Chem Phys 114:108
59. Lynch BJ, Truhlar DG (2003) J Phys Chem A 107:3898; (2003) J Phys Chem A 107:8996; (2004) erratum 108:1460
60. Martin JML, de Oliviera GJ (1999) J Chem Phys 111:1843
61. Martin JML (2001) In: Cioslowski J (ed) Quantum mechanical prediction of thermochemical data. Kluwer, Dordrecht, p 31
62. Prathiban S, Martin JML (2001) J Chem Phys 114:6014
63. Boese AD, Oren M, Atasoylu O, Martin JML, Kállay M, Gauss J (2004) J Chem Phys 120:4129
64. Kraton A, Rabinovich E, Martin JML, Ruscic B (2006) J Chem Phys 125:144108
65. Ramachandran B, Kharidehal P, Pratt LM, Voit S, Okeke FN, Ewan M (2010) J Phys Chem A 114:8423
66. Zhao Y, Tishchenko O, Truhlar DG (2005) J Phys Chem B 109:19046
67. Zhao Y, Truhlar DG (2006) J Phys Chem A 109:10478
68. Zhao Y, Ng HT, Hanson E (2009) J Chem Theory Comput 5:2726
69. Perdew JP, Schmidt K (2002) In: Van Doren V, Van Alsenoy C, Geerlings P (eds) Density functional theory and its application to materials. AIP Press, Melville
70. Perdew JP, Ruzsinszky A, Constantin LA, Sun J, Csonka GIJ (2009) J Chem Theory Comput 5:902

71. Perdew JP (1991) In: Ziesche P, Eschig H (eds) Proceedings of the 21st annual symposium on the electronic structure of solids, '91; Akademie Verlag: Berlin, p 11; Perdew JP, Wang Y (1992) Phys Rev B 45:13244
72. Adamo C, Barone VJ (1998) J Chem Phys 108:664
73. Perdew JP, Burke K, Ernzerhof M (1996) Phys Rev Lett 77:3865; (1997) Phys Rev Lett 78:1396(E)
74. Tao J, Perdew JP, Staroverov VN, Scuseria GE (2003) Phys Rev Lett 91:146401
75. Zhao Y, Truhlar DG (2006) J Chem Phys 125:194101
76. Becke AD (1993) J Chem Phys 98:5648
77. Lee C, Yang W, Parr RG (1988) Phys Rev B 37:785
78. Perdew JP, Ernzerhof M, Burke K (1996) J Chem Phys 105:9982
79. Boese AD, Martin JML (2004) J Chem Phys 121:3405

Chapter 14
Potential Path of DNA Damage: Electron Attachment–Induced DNA Single-Strand Breaks

Jiande Gu, Jing Wang, and Jerzy Leszczynski

Abstract The theoretical study of the electron attachment to DNA reveals the possible mechanism of one of the possible paths of damages in DNA single strands – the low energy electron induced strand breaks. This mechanism includes the formation of an electronically stable radical anion at the nascent stage, and the bond breaking at the C–O σ-bonds at the subsequent steps. In the gas phase, the strand break in the pyrimidine diphosphates is dominated by the $C_{3'}$–$O_{3'}$σ-bond cleavage pathway. Moreover, due to the low electron affinities of the purine diphosphates and the low vertical electron detachment energies of the corresponding radical anions, the bond breaks is unlikely to occur in the gas phase. However, the existence of the polarizable surroundings appreciably changes the scenarios. The comparatively high electron affinities of the 3′,5′-dGDP and the vertical detachment energy of 3′,5′-dGDP$^{·-}$ ensure the formation of the electronically stable radical anion. Furthermore, the surrounding-solute interactions greatly reduce the activation barriers of the C–O bond cleavage, which facilitates the $C_{5'}$–$O_{5'}$ or $C_{3'}$–$O_{3'}$ bond ruptures at the guanosine site in DNA dominating the damages in aqueous solutions.

J. Gu (✉)
Drug Design & Discovery Center, State Key Laboratory of Drug Research,
Shanghai Institute of Materia Medica, Shanghai Institutes for Biological Sciences, CAS,
Shanghai 201203, P.R., China

J. Gu • J. Wang • J. Leszczynski (✉)
Interdisciplinary Nanotoxicity Center, Department of Chemistry and Biochemistry,
Jackson State University, P.O. Box 17910, 1325 Lynch Street, Jackson, MS 39217, USA
e-mail: jiande@icnanotox.org; jingw@icnanotox.org; jerzy@icnanotox.org

14.1   Introduction

Electron attachment to DNA and RNA fragments is one of the important factors that lead to the understanding of the mechanism of a specific class of chemical reactions of DNA and RNA [1–5]. This process has been found to play the key roles in biochemical transformations related to DNA damage and repair [1, 6–12], charge transfer along DNA [13–17], and the initiation of reactions leading to mutation [16, 18]. Comprehension of the complex details of the electron attachment to DNA and RNA requires close interactions among various biological and chemical disciplines. This has been only feasible during the last 20 years. Due to improvements in both experimental techniques and theoretical methods, the investigations of the electron attachment to DNA, RNA, and their subunits have been greatly advanced since 1990. Gradually, the physical picture of the electron attachment to DNA and RNA starts to appear. The results of both experimental and theoretical investigations of different DNA models have indicated that the electron attachment, especially low energy electron (LEE) attachment, play a vital role in the nascent stage of DNA radiolysis and may induce strand breaks in DNA via dissociative electron attachment [1, 4, 9–12, 19–34]. Traditionally, it was believed that the electron attachment to DNA or RNA is of less significance in aqueous solutions. This is due to the fact that electrons are solvated by water molecules and result in creation of OH^- radicals [35]. However, contrary to the previous believes, recent developments of the experiments on the reductive DNA damage induced by dissociative electron transfer reactions suggest the great importance of the electron attachment-induced DNA bond breaks in aqueous solutions [35–37].

Various experiments have provided strong evidence that low energy electrons may cause σ-bond breaks in DNA and RNA single strands or their components [9–12]. Nevertheless, the mechanisms of these important chemical reactions are less clear and have not been studied in details by experimental techniques. A comprehensive understanding of such mechanisms is one of the key steps toward governing the effects of ionizing radiation at a molecular level. In this aspect, along with experimental studies, theoretical investigations at sophisticated levels of theory based upon different DNA and RNA models have been started to uncover the veil that shades the long kept secrets of the mechanisms of the processes of the LEE induced DNA and RNA damages [1, 4–6, 20, 23–27, 30–32, 34, 38, 39].

The progress in theoretical investigations has been possible due to improvements in hardware and more sophisticated software that becomes available to scientific community. The important first step for such studies was the selection of the theory level that could provide accurate information along with the efficient utilization of computational resources. Although the second order perturbation theory (MP2) has been wildly used to study the DNA subunits, this method may not be suitable for the gas-phase investigation of the electron attachment. The negative values predicted at the MP2 level of theory for electron affinity of the pyrimidine nucleotides in the gas phase [23–25] are inconsistent with experimental results on DNA [40] and RNA [19] fragments and higher-level theoretical investigations. Both experiments

and accurate theoretical investigations indicate unambiguously the positive electron affinities for the pyrimidine bases, the pyrimidine nucleosides, and the pyrimidine nucleotides in the gas phase [3, 27, 41, 42]. On the other hand, the development of a comprehensive density functional theory (DFT) bracketing technique [43] reveals the adiabatic electron affinity (EA_{ad}) values for the DNA and RNA bases consisting well with the experimental data [40, 42]. With the reliably calibrated B3LYP/DZP++ approach, accurate calculations of the electron affinities of the 2′-deoxyribonucleosides have been accomplished [3, 44]. These theoretical predictions of the electron affinities of the 2′-deoxyribonucleosides have been confirmed by the recent experiment [45]. In accord with previous successful applications, the B3LYP/DZP++ method was used in the studies of the mechanisms of the LEE-induced DNA and RNA damages.

14.2 Location of the Excess Electron in the Radical Anions of Nucleotides

Although early experimental and theoretical studies suggested that electron attachment might occur at the phosphate group [20, 33], more sophisticated investigations reveal that the electron is captured at the base sites [1, 4, 22, 24, 27, 32, 34]. Based on the density functional theory studies of the sugar-phosphate-sugar (S-P-S) model, Li, Sevilla, and Sanche [20] proposed that the near 0 eV electron may be captured first by the phosphate group, forming a phosphate-centered radical anion. More detailed study suggested that the excess electron is trapped in the dipolar field of two OH groups in the sugar phosphate backbone [46]. The subsequent $C_{3'}$–$O_{3'}$ or $C_{5'}$–$O_{5'}$ σ-bond breaking was estimated to have an energy barrier of approximately 10 kcal/mol. In addition, the other theoretical studies have been performed [24], which suggested that electrons with kinetic energies near 0 eV cannot directly attach to the phosphate units at a significant rate. The small values of electron affinity (−0.003; 0.033 eV [20]) of the evaluated S-P-S model seem to suggest that, instead of the phosphate group in DNA species, low energy electrons might be trapped in the pyrimidine bases. The electron affinities of near 0 eV were detected for those bases in experiments [40] while 0.03 eV (cytosine) ∼0.2 eV (thymidine) values were revealed by calculations at the B3LYP/DZP++ level of theory [42]. More direct evidence for the location of the unpaired electron in the radical anions is given by the DFT study of the electron attachment to the nucleotide 2′-deoxycytidine-3′-monophosphate (3′-dCMP) [41]. In this study, both nucleobase-centered radical anion and phosphate-bounded radical anion (Fig. 14.1) have been located. The adiabatic electron affinity (EA_{ad}) of the formation of the base-centered radical anion of 3′-dCMP is predicted to be 0.44 eV, while the EA_{ad} of the formation of the phosphate-centered one is −0.14 eV (Table 14.1). Since the total energy for the phosphate-centered radical anion is higher than the predicted value for neutral species, this anion is unlikely to be the intermediate when interacting with low

Base attached 3'-dCMP·⁻   Phosphate attached 3'-dCMP·⁻
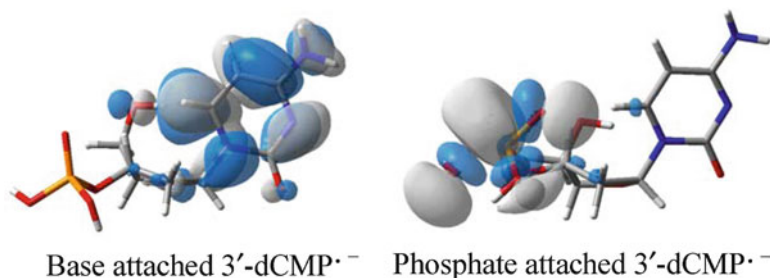
Fig. 14.1 The singly occupied molecular orbitals (SOMOs) of the two different 3'-dCMP radical anions (Reproduced with permission from Ref. [41], Copyright (2006), American Chemical Society)

Table 14.1 Electron attachment energies for 3'-dCMP (in eV). Values with zero-point vibrational corrections are given in parentheses

	EA_{ad}	VEA^a	VDE^b
Gas phase			
3'-dCMP → Base Attached 3'dCMP·⁻	0.33 (−0.44)	0.15	1.28
3'-dCMP → Phosphate Attached 3'dCMP·⁻	−0.20 (−0.14)	—^{c}	2.63
S-P-S → S-P-S·⁻	−0.003; 0.033^d		
PCM^e			
3'-dCMP → Base 3'-dCMP·⁻	2.18	1.72	2.97
3'-dCMP → Phosphate 3'-dCMP·⁻	1.20	—^{c}	4.04
S-P-S → S-P-S·⁻	0.88^d		

^{a}VEA = E(neutral) – E(anion), with the energies evaluated based on the optimized neutral structures
^{b}VDE = E(neutral) – E(anion), with the energies taken from the optimized anion structures
^{c}The anionic phosphate attached 3'-dCMP·⁻ collapses to the more stable base attached 3'-dCMP·⁻
^{d}Reference [20]
^{e}PCM model, using water as solvent with $\varepsilon = 78$

energy electrons. Moreover, the vertical electron affinity (VEA) value of 0.15 eV for 3'-dCMP suggests that the formation of the phosphate-centered radical anion of 3'-dCMP is less possible.

To make computational studies more relevant for the biomolecules, one also needs to consider the effect of the polar surroundings on the investigated phenomena. It was predicted that the inclusion of the effects of the polarizable medium stabilizes the radical anions significantly [5]. However, it does not increase the possibility of the formation of the phosphate-attached 3'-dCMP·⁻. The EA_{ad} of the phosphate-centered radical anion (1.20 eV) is significantly smaller than the EA_{ad} (2.18 eV) and the VEA (1.72 eV) of the base-centered 3'-dCMP·⁻ in the polarizable continuum model (PCM) [47] calculations. The singly occupied molecular orbital
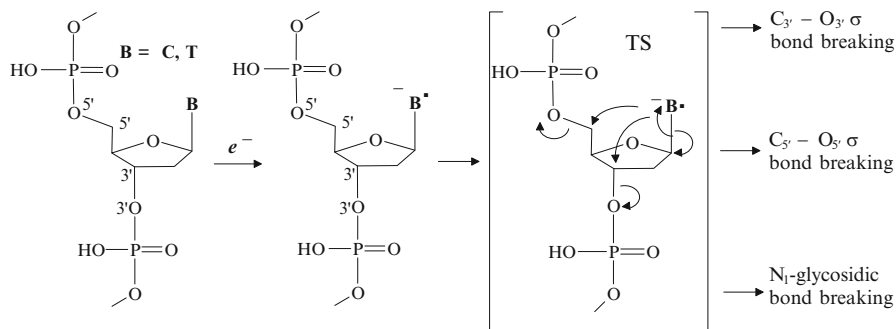
Scheme 14.1 The possible mechanism of the LEE induced DNA single-strand breaks at pyrimidine sites

(SOMO, Fig. 14.1) of the 3′-dCMP radical anion (base attached 3′-dCMP$^-$) demonstrates that the excess electron resides on the π* orbital of the base.

Based on the above arguments, one can assume the following possible mechanism of the LEE induced DNA single-strand breaks. At the nascent stage, the excess electron resides on the π* orbital of nucleobase in the radical anion, forming an electronically stable radical anion. Redistribution of the excess electron accompanied by the thermo movement of the atoms in the molecule subsequently leads to bond breaking at either C–O σ bonds or N-glycosidic bond (Scheme 14.1).

It should be mentioned that, based on the studies of different models (2′-deoxycytidine-3′-monophosphate and 2′-deoxythymidine-3′-monophosphate molecule) [23–26], Simons suggested that only in an aqueous solution the very low energy electrons can attach to the π* orbitals of the DNA bases and then undergo $C_{3'}$–$O_{3'}$ bond cleavage [23–26, 30].

14.3   Electron Attachment–Induced DNA Single-Strand Breaks at the Pyrimidine Sites

Since big fragments of DNA are too large to be studied using ab initio methods, one needs to consider smaller models that are able to capture most molecular characteristics vital for the investigated phenomena. The electron attachment to the nucleotides of pyrimidines has been studied based on various models. The most sophisticated models are the 2′-deoxycytidine-3′,5′-diphosphate (3′,5′-dCDP) and 2′-deoxythymidine-3′,5′-diphosphate (3′,5′-dTDP) [39]. Such models allow simultaneously examining both $C_{5'}$–$O_{5'}$ and $C_{3'}$–$O_{3'}$ bond cleavages and N-glycosidic bond rupture processes. Other models include the corresponding nucleosides (dC and dT) [27, 32] and the nucleoside monophosphates (3′-dCMP, 3′-dTMP, 5′-dCMP, and 5′-dTMP) [1, 4]. Scheme 14.2 depicts the structures of these models. The EA$_{ad}$ of 0.27 eV for 3′,5′-dCDP and 0.35 eV for 3′,5′-dTDP facilitate the formation of
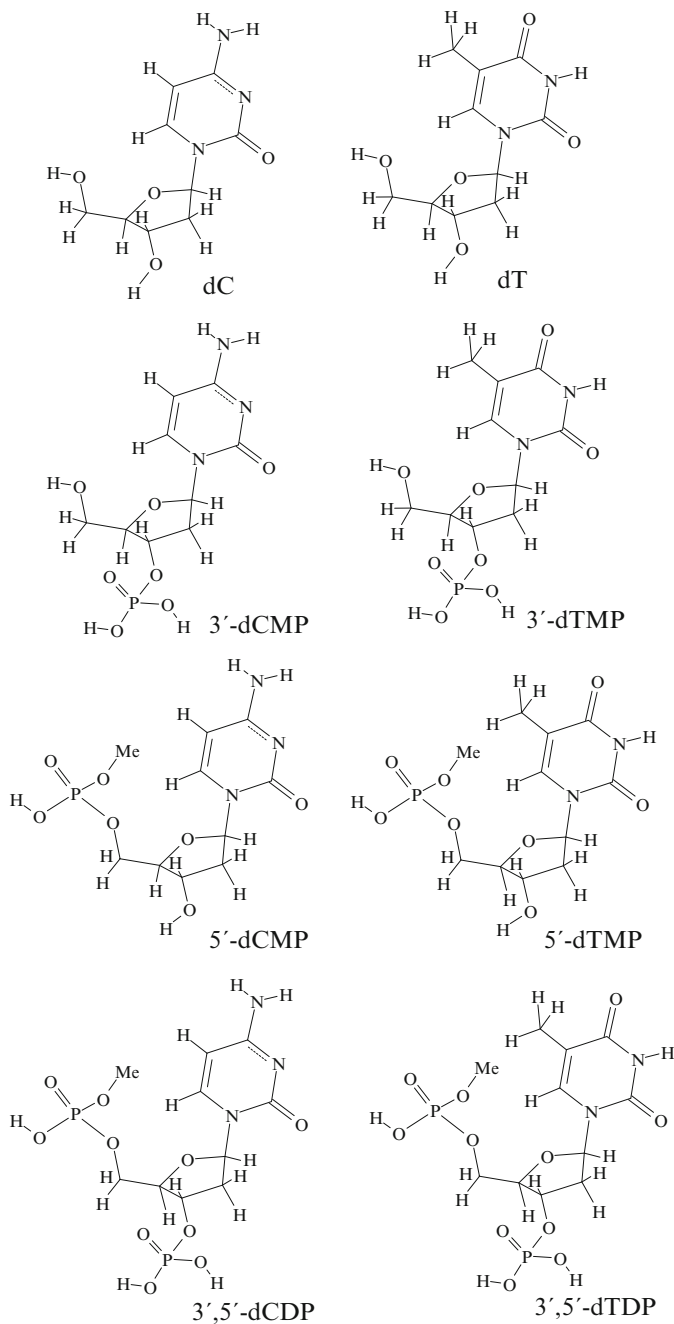
Scheme 14.2 The structures of the nucleosides and nucleotides of pyrimidines applied in the studies of the electron attachment to the DNA single strands

Table 14.2 Electron attachment and detachment energies (in eV). Numbers within the parentheses are the zero-point vibrational energy corrected

Process	EA_{ad}	VEA^a	VDE^b
$3',5'$-dCDP $\rightarrow 3',5'$-dCDP$^{\cdot-}$ gas-phase	0.27 (0.44)^c	0.03^c	0.71^c
$3',5'$-dTDP $\rightarrow 3',5'$-dTDP$^{\cdot-}$ gas-phase	0.35 (0.52)^c	0.17^c	0.67^c
$3',5'$-dCDP $\rightarrow 3',5'$-dCDP$^{\cdot-}$ PCM model	1.99^c	1.45	2.22
$3',5'$-dTDP $\rightarrow 3',5'$-dTDP$^{\cdot-}$ PCM model	1.98^c	1.57	2.17

^{a}VAE = E(neutral) – E(anion); the energies are evaluated using the optimized neutral structures
^{b}VDE = E(neutral) – E(anion); the energies are evaluated using the optimized anion structures
^{c}Reference [5]

the corresponding radical anions [5]. Meanwhile, the large values of the vertical detachment energy (VDE) for these two radical anions (0.71 eV for $3',5'$-dCDP$^{\cdot-}$ and 0.67 eV for $3',5'$-dTDP$^{\cdot-}$) ensure that, in the gas phase, electron detachment will not compete with the subsequent reactions with the activation energy barrier less than 16.37 kcal/mol (0.71 eV) for $3',5'$-dCDP$^{\cdot-}$ and 15.45 kcal/mol (0.67 eV) for $3',5'$-dTDP$^{\cdot-}$ (see Table 14.2).

Once again, there is a need to evaluate investigated processes in the polar environment. Solvent effects remarkably increase the electron capturing ability of the nucleoside diphosphates. The EA_{ad}s are 1.99 eV and 1.98 eV for $3',5'$-dCDP$^{\cdot-}$ and $3',5'$-dTDP$^{\cdot-}$, respectively, in the PCM calculation. Moreover, the increased VDE of $3',5'$-dCDP$^{\cdot-}$ (2.22 eV) and $3',5'$-dCTP$^{\cdot-}$ (2.17 eV) due to the solvent interactions suggests that in aqueous solution the reactions with energy barrier less than 50 kcal/mol might undergo without any electron detachment from this radical anion.

14.3.1 Activation Energies of the $C_{5'}$–$O_{5'}$ σ Bond Breaking

The transition state structures for the $C_{5'}$–$O_{5'}$ σ bond cleavage process of the $3',5'$-dCDP$^{\cdot-}$ and $3',5'$-dTDP$^{\cdot-}$ have been characterized by the elongated $C_{5'}$–$O_{5'}$ atomic distance of 1.777 Å (1.769 Å) for cytidine (thymidine) and by the analysis of normal mode corresponding to the imaginary vibrational frequency (Figs. 14.2 and 14.3). The activation energy of the $C_{5'}$–$O_{5'}$ σ-bond cleavage process has been predicted to be 14.17 kcal/mol for $3',5'$-dCDP$^{\cdot-}$ and 13.37 kcal/mol for $3',5'$-dTDP^{-} (Table 14.3, without the zero point energy correction, ZPE). These values are very close to the activation energy needed for the $C_{5'}$–$O_{5'}$ σ-bond breaking in small models $5'$-dCMP$^{\cdot-}$ (14.27 kcal/mol) and in $5'$-dTMP$^{\cdot-}$ (13.84 kcal/mol) [1]. Table 14.3 also lists the ZPE corrected activation energy barriers and the corresponding free energy differences at 298 K.

The solvent effects increase the $C_{5'}$–$O_{5'}$ σ-bond breaking energy barrier dramatically. The energy barriers predicted using the PCM model are 18.73 kcal/mol for
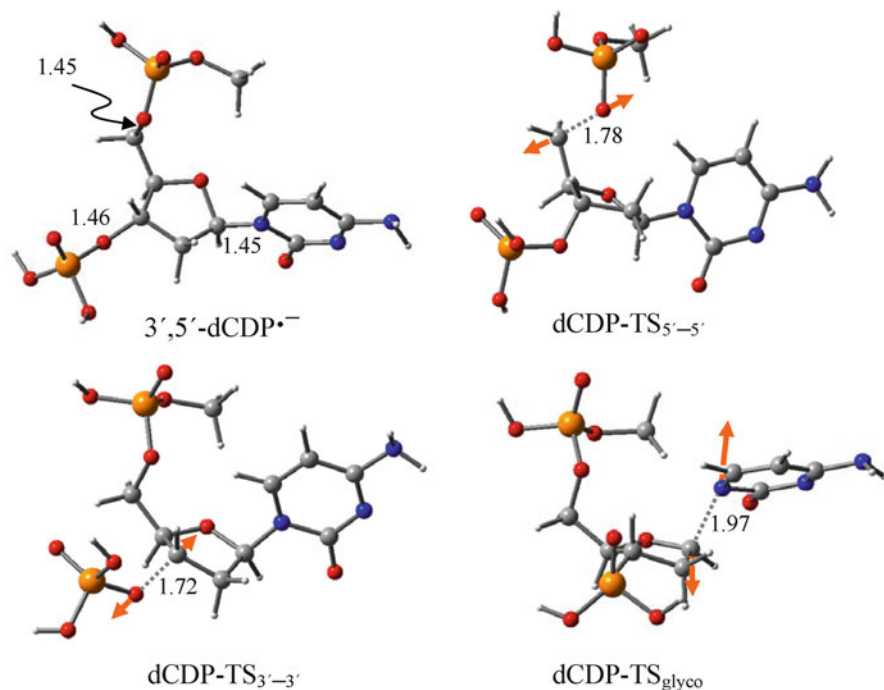
Fig. 14.2 The optimized structures of the radical anion of 2′-deoxycytidine-3′,5′-diphosphate (3′,5′-dCDP⁻) and the transition state structures related to: $C_{5'}$–$O_{5'}$ bond breaking (dCDT-TS$_{5'-5'}$), $C_{3'}$–$O_{3'}$ bond breaking (dCDT-TS$_{3'-3'}$), and N-glycosidic bond breaking (dCDT-TSglyco). Atomic distances are in Å. *Orange arrows* in the transition states represent the single imaginary frequency related vibration mode. Color representations: *red* – oxygen, *gray* – carbon, *blue* – nitrogen, *orange* – phosphorous, and *white* – hydrogen (Reproduced with permission from Ref. [39], Copyright (2010) Oxford University Press)

3′,5′-dCDP⁻ and 18.76 kcal/mol for 3′,5′-dTDP⁻ (Table 14.3). This noticeable increase of the energy barriers is close to that found for the pyrimidine monophosphate models (17.97 kcal/mol for 5′-dCMP⁻ and 17.86 kcal/mol for 5′-dTMP⁻) in the presence of polarizable medium [1].

14.3.2 Activation Energies of the $C_{3'}$–$O_{3'}$ σ-Bond Breaking

The transition states for $C_{3'}$–$O_{3'}$ σ-bond cleavage process in the radical anion of 3′,5′-dCDP and 3′,5′-dTDP are characterized by the elongated $C_{3'}$–$O_{3'}$ atomic distance (1.738 Å) and the normal mode corresponding to the imaginary vibrational frequency. The activation energy of the $C_{3'}$–$O_{3'}$ σ-bond breaking has been predicted to be 6.02 and 6.37 kcal/mol for the radical anions (Table 14.3, without ZPE). This energy barrier is similar to that report based on the 3′-dCMP and 3′-dTMP models
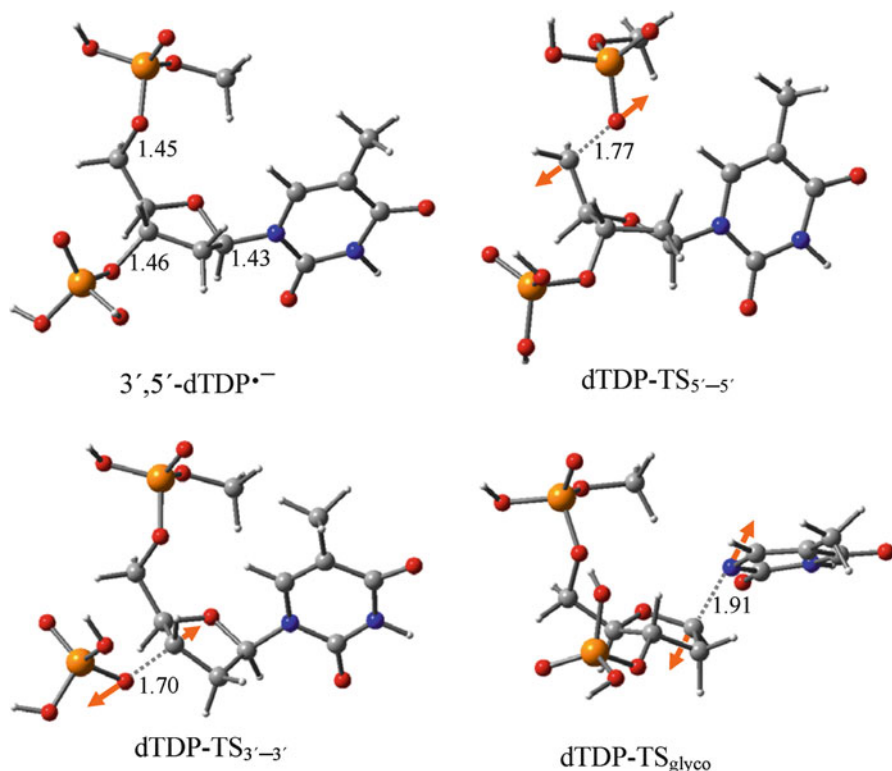
Fig. 14.3 The optimized structures of the bond-broken products: $C_{5'}-O_{5'}$ bond broken (dCDP-$P_{5'-5'}$ and dTDP-$P_{5'-5'}$), $C_{3'}-O_{3'}$ bond broken (dCDP-$P_{3'-3'}$ and dTDP-$P_{3'-3'}$), and N-glycosidic bond broken (dCDP-P_{glyco} and dTDP-P_{glyco}) (Reproduced with permission from Ref [39], Copyright (2010), Oxford University Press)

(6.17 kcal/mol for the former and 7.06 kcal/mol for the latter) at the same level of theory [4]. The presence of the phosphate group at the 5′-position slightly decreases the $C_{3'}-O_{3'}$ σ bond breaking energy barrier. This low energy barrier in the $C_{3'}-O_{3'}$ σ-bond breaking process has been suggested to have the SN2-like mechanism.

The solvent effects increase the energy barrier of the $C_{3'}-O_{3'}$ σ-bond rupture. The corresponding energy barrier in the PCM model is high, up to 13.36 kcal/mol and 14.18 kcal/mol for 3′,5′-dCDP$^{\cdot-}$ and 3′,5′-dTDP$^{\cdot-}$, respectively (Table 14.3). As comparison, the energy barrier amounts to 12.82 kcal/mol for 3′-dCMP$^{\cdot-}$ and 13.83 kcal/mol for 3′-dTMP$^{\cdot-}$ in the PCM model computations [4]. It should be noted that these high activation energy barrier calculations based on the PCM model are close to that for the $C_{5'}-O_{5'}$ σ-bond breaking process in the gas phase. Therefore, SN2-like mechanism observed in the gas phase for the $C_{3'}-O_{3'}$ σ-bond breaking reaction is blocked by the solvent-solute interactions.

Table 14.3 The relative energies of the transition states of bond break pathways in gas phase (kcal/mol)

Bond breaking	ΔE_{TS}[a]	ΔE_{TS}(PCM)[b]	ΔE_{TS}^{0} [c]	ΔG_{TS}^{0} [d]
3′,5′-dCDP·⁻				
$C_{5'}$–$O_{5'}$ bond	14.17 (14.27[e])	18.73 (17.97[e])	12.31 (12.52[e])	13.53 (12.75[e])
$C_{3'}$–$O_{3'}$ bond	6.03 (6.17[f])	13.36 (12.82[f])	5.23 (4.68[f])	7.60 (4.54[f])
N-glycosidic bond	26.21 (21.6[g])	26.34	24.95 (20.4[g])	26.57 (21.2[g])
3′,5′-dTDP·⁻				
$C_{5'}$–$O_{5'}$ bond	13.39 (13.84[e])	18.76 (17.86[e])	11.59 (11.91[e])	11.49 (11.82[e])
$C_{3'}$–$O_{3'}$ bond	6.04 (7.06[f])	14.18 (13.73[f])	5.66 (5.29[f])	6.92 (4.42[f])
N-glycosidic bond	19.19 (18.9[g])	28.77	18.79 (17.6[g])	21.10 (18.0[g])

[a] ΔE_{TS} = E(Transition state) – E(Radical anion)
[b] ΔE_{TS} (PCM), using PCM model with $\varepsilon = 78.39$
[c] With the zero point energy (ZPE) correction
[d] Free energy at $T = 298$ K
[e] Reference [1], using 2′-deoxypyrimidine-5′ monophosphate as the model
[f] Reference [4], using 2′-deoxypyrimidine-3′ monophosphate as the model
[g] Reference [27], using 2′-deoxypyrimidine nucleoside as the model

14.3.3 Activation Energies of the N-Glycosidic Bond Breaking

The transition state for N-glycosidic bond breaking of the radical anion has been located and characterized by the elongated $C_{1'}$–N_1 atomic distance (1.873 Å for 3′,5′-dCDP and 1.873 Å for 3′,5′-dTDP) and the corresponding normal mode representing the $C_{1'}$–N_1 σ-bond breaking. The activation energy of the $C_{1'}$–N_1 glycosidic bond breaking has been predicted to be 26.21 kcal/mol (Table 14.3) for 3′,5′-dCDP·⁻, about 4.61 kcal/mol higher than that found for the nucleoside model. An important feature in the glycosidic bond breaking structure representing transition state of cytidine is the existence of a strong H-bonding interaction between the proton at the $O_{5'}$ and the N_1 atom (the $H(O_{5'}) \cdots N_1$ distance is 1.78 Å in dC·⁻). However, because of the phosphorylation at the $O_{5'}$ position in 3′,5′-dCDP·⁻, this H-bonding pattern is absent in the corresponding transition state. Therefore, this energy barrier increase is not unexpected. Similarly, in spite of the intramolecular H-bonding between the $O_{5'}$ atom and the proton of the 3′-phosphate, the activation energy for the N-glycosidic bond breaking in 3′,5′-dTDP·⁻ is also higher than that in the corresponding nucleoside (19.20 kcal/mol vs. 18.9 kcal/mol) [27, 32]. The predicted activation energy barrier increases for the N-glycosidic bond dissociation due to the presence of the adjoining phosphate groups that parallels the recent experimental observation [48]. It has been detected that while the LEE induced base release percentage amounts to 16.5 in the oligomer TpT, it is reduced to 0.5 in the oligonucleotide pTpTp [48].

   Similar to the discussed C–O σ-bond rupture, the solvent effects raise the energy barrier of the N-glycosidic bond breaking. It amounts to 28.77 kcal/mol for 3′,5′-dTDP·⁻ in the PCM model simulated aqueous solutions. This substantial increase in the energy barrier due to the solvent-solute interactions is in accordance with the largely reduced dipole moment of the corresponding transition state (17.7 Debye

Table 14.4 The relative energies of the bond broken products (kcal/mol)

Bond breaking process	ΔE^a	$\Delta E_{PCM}^{\ b}$
3′,5′-dCDP·⁻		
$\quad$ C$_{5'}$–O$_{5'}$ bond	−22.00	−16.99
$\quad$ C$_{3'}$–O$_{3'}$ bond	−41.97	−27.92
$\quad$ N-glycosidic bond	−0.03	11.12
3′,5′-dTDP·⁻		
$\quad$ C$_{5'}$–O$_{5'}$ bond	−32.89	−18.98
$\quad$ C$_{3'}$–O$_{3'}$ bond	−43.09	−27.72
$\quad$ N-glycosidic bond	−7.67	6.57

$^a \Delta E = E$(Bond broken product) – E(Radical anion)
$^b \Delta E_{PCM} = E$(Bond broken product) – E(Radical anion); using PCM model with $\varepsilon = 78.39$

vs. 22.8 Debye for the optimized radical anion) in aqueous solutions. On the other hand, the solvent-solute interactions only slightly increase the activation energy of the N-glycosidic bond rupture in 3′,5′-dCDP·⁻ (26.34 kcal/mol). Correspondingly, the dipole moments of the local minimum structure and the transition state of 3′,5′-dCDP·⁻ are very similar (17.9 Debye vs. 17.0 Debye).

14.3.4 Products of the C–O σ-Bonds and N-Glycosidic Bond Breaking

Both C$_{3'}$–O$_{3'}$ and C$_{5'}$–O$_{5'}$ σ-bond ruptures lead to the energetically stable complexes consisting of a phosphate anion and a corresponding carbon-centered neutral radical. In the case of the C$_{5'}$–O$_{5'}$ σ-bond breaking these products are 22.0 kcal/mol and 32.9 kcal/mol more stable than 3′,5′-dCDP·⁻ and 3′,5′-dTDP·⁻, respectively (Table 14.4). Meanwhile, the energies of the C$_{3'}$–O$_{3'}$ σ-bond broken products are 42.0 kcal/mol and 43.1 kcal/mol lower than those of the corresponding reactants, 3′,5′-dCDP·⁻ and 3′,5′-dTDP·⁻, respectively [39].

Interestingly, the energy release during the N$_1$–C$_{1'}$ bond breaking process is less significant as compared to that during the C–O σ-bond rupture. N-glycosidic bond broken product of cytidine diphosphate (P$_{dCglyco}$) in the gas phase has the total energy almost the same as that of 3′,5′-dCDP·⁻. This bond-ruptured complex contains a dehydrogenated cytosine anion and a P-S-P neutral radical in the gas phase. In parallel, the complex formed by the N-glycosidic bond breaking of 3′,5′-dTDP·⁻ (P$_{dTglyco}$) is about 7.67 kcal/mol more stable than 3′,5′-dTDP·⁻ [39].

In general, solvent effects increase the energy of the bond broken products of the pyrimidine diphosphate complexes. The polarizable medium decreases stability of the N-glycosidic bond broken products considerable. The total electronic energy of the product of the N-glycosidic bond breaking of 3′,5′-dCDP·⁻ (P$_{dCglyco}$) is 11.12 kcal/mol higher than that of 3′,5′-dCDP·⁻. Meanwhile, the PCM model calculations reveal that the total energy of the N-glycosidic bond breaking of 3′,5′-dTDP·⁻ (P$_{dTglyco}$) is 6.57 kcal/mol higher than that of 3′,5′-dTDP·⁻. Both in the gas phase and in the presence of the polarizable medium, the C$_{3'}$–O$_{3'}$ bond breaking

process has the highest driving force among the three bond breaking pathways considered in this study. The reaction pathway through the $C_{3'}$–$O_{3'}$ bond breaking is the most thermodynamically favorable. Meanwhile, relatively higher energies of the N-glycosidic bond broken products suggest that the pathway through N_1–$C_{1'}$ bond rupture is not thermodynamically preferred [39].

14.3.5 Reaction Pathways of the LEE-Induced DNA Single Strands

In the gas phase, the glycosidic bond breaking process requires activation energy as high as 19.19 kcal/mol. Therefore, base release should be excluded based on the mechanisms proposed above. The energy barrier for the $C_{3'}$–$O_{3'}$ σ-bond cleavage process ($\sim$6.0 kcal/mol for both cytidine and thymidine) suggests that this reaction pathway is the most favorable as compared to the other possible pathways. On the other hand, the relatively low activation energy barrier ($\sim$14 kcal/mol) for the $C_{5'}$–$O_{5'}$ σ-bond cleavage process indicates that this pathway could be possible, especially when the incident electrons have relatively high energy (a few electron volts). However, as the energy of the incident electrons decrease, the possibility of the reactions through the $C_{5'}$–$O_{5'}$ σ-bond cleavage pathway is expected to decrease. Therefore, the strand breaks caused by the attachment with near-zero energy electrons is dominated by the $C_{3'}$–$O_{3'}$ σ-bond cleavage pathway for the isolated nucleotides [1, 4, 39].

An application of the PCM model to describe the solvent effects excludes accounting for contributions of potentially vital processes as proton transfer or charge transfer that might proceed exist between solute and solvent. On account of such an assumption, solvent effects greatly increase the activation energies of either C–O σ-bond cleavage processes or the N-glycosidic bond breaking process. Within the solvated model, the predicted activation energy barriers of 26–28 kcal/mol for the N-glycosidic bond breaking process eliminate possibility of the observable reactions occurring based on this pathway. It is important to note that the activation energy barrier of the $C_{3'}$–$O_{3'}$ σ-bond cleavage process rises to 13.4 kcal/mol in the PCM calculations, which is about 5 kcal/mol lower than that for the $C_{5'}$–$O_{5'}$ σ-bond cleavage process (18.76 kcal/mol). In comparison with the gas phase, the importance of the $C_{5'}$–$O_{5'}$ σ-bond cleavage process (vs. the $C_{3'}$–$O_{3'}$ σ-bond cleavage process) increases under the solvated condition. However, the $C_{3'}$–$O_{3'}$ σ-bond cleavage pathway still dominates the LEE induced DNA single strands in the presence of the polarizable surroundings. The energy profiles along the reaction pathways depicted in Figs. 14.4 and 14.5 clearly reveal that the products of the $C_{3'}$–$O_{3'}$ σ-bond cleavage are favored both kinetically and thermodynamically. Nevertheless, we want to emphasize again that since the activation energy barriers predicted in the polarizable surroundings are in general higher than those in the gas phase, the LEE-induced DNA single strands breaking in the polarizable medium should be less important than the corresponding phenomenon in the gas phase.
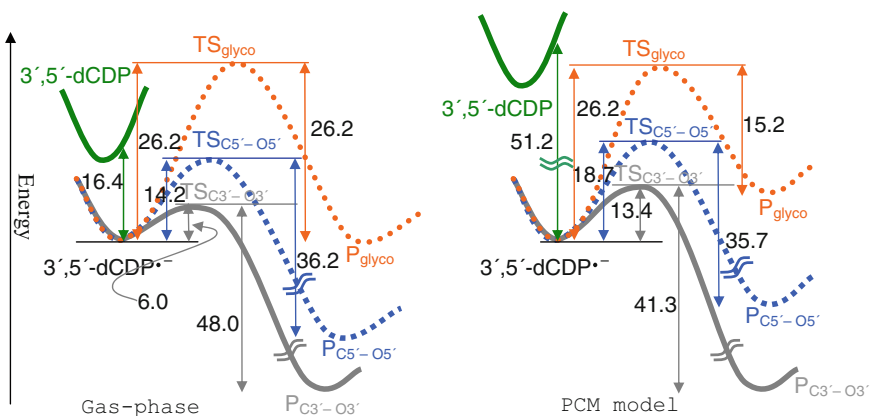
Fig. 14.4 The energy profile of the $C_{5'}-O_{5'}$, $C_{3'}-O_{3'}$, and N-glycosidic bond breaking process for $3',5'$-dCDP$^{\bullet-}$ in the gas-phase and in aqueous solutions (Reproduced with permission from Ref. [39], Copyright (2010), Oxford University Press)
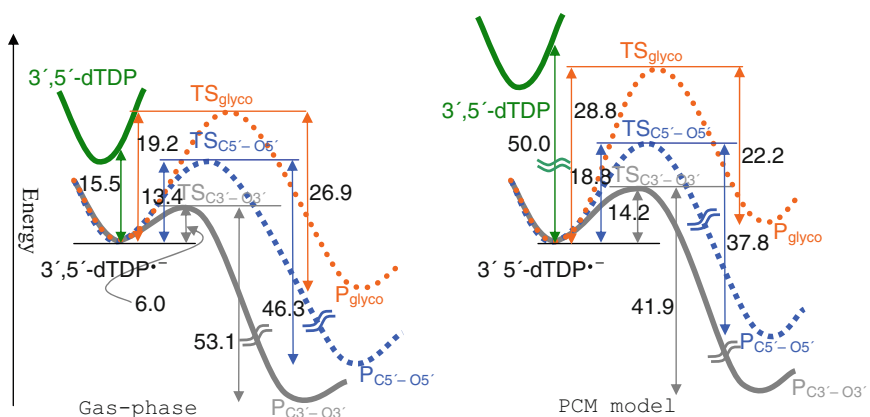
Fig. 14.5 The energy profile of the $C_{5'}-O_{5'}$, $C_{3'}-O_{3'}$, and N-glycosidic bond breaking process for $3',5'$-dTDP$^{\bullet-}$ in the gas phase and in aqueous solutions (Reproduced with permission from Ref. [39], Copyright (2010), Oxford University Press)

14.4 Electron Attachment Induced DNA Single-Strand Breaks at the Adenine Site

The electron attachment and detachment energies of $2'$-deoxyadenosine-$3',5'$-diphosphate ($3',5'$-dADP) are summarized as follows: the adiabatic electron affinity (EA$_{ad}$) of $3',5'$-dADP is 0.22 eV, the vertical attachment energy is 0.02 eV, and the vertical detachment energy (VDE) of the corresponding $3',5'$-dADP$^{\bullet-}$ radical anion is 0.26 eV [5]. It should be noted that in the gas phase, electron attachment to

Table 14.5 Electron attachment and detachment energies (in eV)

Process	EA_{ad}	VEA^a	VDE^b
$3',5'$-dADP $\rightarrow$ $3',5'$-dADP$^{\cdot-}$ gas-phase	0.10 (0.22)[c]	0.04[c]	0.26[c]
$3',5'$-dADP $\rightarrow$ $3',5'$-dADP$^{\cdot-}$ PCM model	1.59[c]	1.37	1.59

[a] $VAE = E(neutral) - E(anion)$; the energies are evaluated using the optimized neutral structures

[b] $VDE = E(neutral) - E(anion)$; the energies are evaluated using the optimized anion structures

[c] Reference [5]

$3',5'$-dADP leads to the formation of a valence anion in which the excess electron partially locates on the base and partially resides on the phosphate group [5]. However, it still can initiate the bond breakings in the radical anion of $3',5'$-dADP.

An interaction with the polarizable surroundings (represented by water as a solvent) remarkably improves the electron capture ability of $3',5'$-dADP ($EA_{ad} = 1.59$ eV and $VEA = 1.37$ eV in the PCM model). Moreover, due to the solvent interactions, the VDE of $3',5'$-dADP– increases up to 1.59 eV. This large VDE value implies that in the presence of the polarizable surroundings, the reactions with energy barriers less than 23 kcal/mol might occur before the electron detachment for this radical anion [49] (Table 14.5).

14.4.1 Activation Energies of the $C_{5'}$–$O_{5'}$ σ Bond Breaking Process in the Radical Anion of $3',5'$-dADP

The $C_{5'}$–$O_{5'}$ bond length in the transition state corresponding to the $C_{5'}$–$O_{5'}$ σ-bond association for the radical anions of $3',5'$-dADP is elongated. $C_{5'}$–$O_{5'}$ bond distance of 1.714 Å is predicted as well as the normal mode corresponding to the imaginary vibrational frequency. These data confirm that the above transition state is associated with the $C_{5'}$–$O_{5'}$ σ-bond breaking process (Fig. 14.6). The activation energy of the $C_{5'}$–$O_{5'}$ σ-bond cleavage process has been predicted to be 9.99 kcal/mol (Table 14.6, without the zero point energy correction, ZPE). As a comparison, the activation energy predicted for the $C_{5'}$–$O_{5'}$ σ-bond breaking is higher in $3',5'$-dCDP$^{\cdot-}$ (13.37 kcal/mol) and in $3',5'$-dTDP$^{\cdot-}$ (14.17 kcal/mol) [39].

The effects of the polarizable medium raises the $C_{5'}$–$O_{5'}$ σ-bond breaking energy barrier dramatically (22.54 kcal/mol with the PCM model prediction, Table 14.6) in $3',5'$-dADP$^{\cdot-}$. This substantial increase complements the cases of pyrimidine nucleotides in which the effects of the polarizable surroundings raise the $C_{5'}$–$O_{5'}$ σ-bond breaking energy barrier up to 18.73 kcal/mol for $3',5'$-dCDP$^{\cdot-}$ and to 18.76 kcal/mol for $3',5'$-dTDP$^{\cdot-}$ [39].
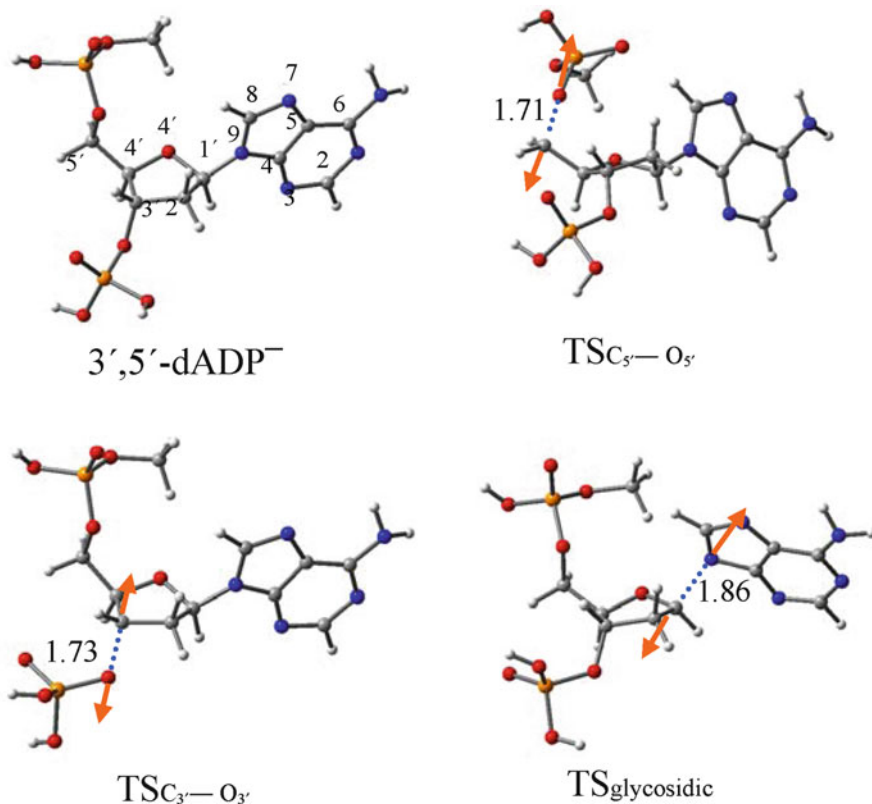
Fig. 14.6 The optimized structures of the radical anion of 2′-deoxyguanosine-3′,5′-diphosphate (3′,5′-dADP$^{·-}$) and the transition state structures of the C$_{5'}$–O$_{5'}$ bond breaking (TSC$_{5'}$–O$_{5'}$), C$_{3'}$–O$_{3'}$ bond breaking (TSC$_{3'}$–O$_{3'}$), and N-glycosidic bond breaking (TSglycosidic). Atomic distances are in Å. *Orange arrows* in the transition states represent the vibration mode related to single imaginary frequency [49]. (Reproduced with permission from Ref. [49], Copyright (2011), American Chemical Society)

Table 14.6 The relative energies of transition states responsible for bond breaks in 3′,5′-dADP$^{·-}$ (kcal/mol)

Bond breaking process	ΔE_{TS}[a]	ΔE_{TS}(PCM)[b]	ΔE_{TS}^0[c]	ΔG_{TS}^0[d]
C$_{5'}$–O$_{5'}$ bond	9.99	22.54	9.32	11.06
C$_{3'}$–O$_{3'}$ bond	8.94	13.22	7.07	7.33
N-glycosidic bond	21.29 (20.3[e])	20.91	19.99	20.99

[a] $\Delta E_{TS} = E$(Transition state) – E(Radical anion)
[b] ΔE_{TS} (PCM) = E(Transition state) – E(Radical anion); using PCM model with $\varepsilon = 78$
[c] With the zero point energy (ZPE) correction
[d] Free energy at $T = 298$ K
[e] Reference [32], using 2′-deoxyadenosine as the model

14.4.2   Activation Energies of the $C_{3'}$–$O_{3'}$ σ Bond Breaking Process in the Radical Anion of 3′,5′-dADP

The transition state for $C_{3'}$–$O_{3'}$ σ-bond cleavage process in the radical anion of 3′,5′-dADP has been located and related to the single imaginary vibrational frequency. The elongated $C_{3'}$–$O_{3'}$ bond distance (1.733 Å) and the normal mode corresponding to the imaginary vibrational frequency characterize the $C_{3'}$–$O_{3'}$ σ-bond breaking process. The activation energy of the $C_{3'}$–$O_{3'}$ σ-bond breaking process has been predicted to be 8.94 kcal/mol (Table 14.6). As a comparison, the activation energy needed for the $C_{3'}$–$O_{3'}$ σ-bond breaking in pyrimidine nucleotides is lower in 3′,5′-dCDP⁻ (6.2 kcal/mol) and in 3′,5′-dCDP⁻ (7.1 kcal/mol) [18], owing to the SN2-like reaction mechanism.

Similar to the process of the $C_{5'}$–$O_{5'}$ σ-bond rupture, the effects of the polarizable surroundings increase significantly the energy barrier of the $C_{3'}$–$O_{3'}$ σ-bond rupture in 3′,5′-dADP⁻ (13.22 kcal/mol with the PCM model prediction).

14.4.3   Activation Energies of the N-Glycosidic Bond Breaking Process in the Radical Anion of 3′,5′-dADP

The transition state for N-glycosidic bond breaking of the radical anion of 3′,5′-dADP has been located and characterized by the elongated $C_{1'}$–N_9 atomic distance (1.861 Å). The activation energy of the $C_{1'}$–N_9 glycosidic bond breaking has been predicted to be 21.29 kcal/mol (Table 14.6, without ZPE). Based on the nucleoside model, this bond rupture energy barrier is predicted to be 20.3 kcal/mol [13]. The existence of the neighboring phosphates on the ribose moiety slightly increases the energy barrier. Moreover, this energy barrier is also close to that reported in the previous studies on the LEE induced glycosidic bond cleavage in pyrimidine nucleosides, in which the activation energy was predicted to be 18.9–21.6 kcal/mol for the C–N bond break [27, 32].

In contrast to the C–O σ-bond rupture process, the polarizable surroundings barely influences the energy barrier of the N-glycosidic bond breaking (20.91 kcal/mol for 3′,5′-dADP⁻ in the presence of the polarizable surroundings).

14.4.4   Products of the C–O σ-Bonds and N-Glycosidic Bond Breaking Processes of the Radical Anion of 3′,5′-dADP

Both $C_{3'}$–$O_{3'}$ and $C_{5'}$–$O_{5'}$ σ-bonds rupture lead to the energetically stable complexes consisting of a phosphate anion and a corresponding carbon-centered neutral radical. In the former case, the $C_{5'}$–$O_{5'}$ σ-bond broken product is by 54.09 kcal/mol more stable than 3′,5′-dADP⁻ (Table 14.7). Meanwhile, the energy of the $C_{3'}$–$O_{3'}$

Table 14.7 The relative energies of the bond broken products (kcal/mol)

Bond breaking process	ΔE^{a}	$\Delta E_{PCM}{}^{b}$
$C_{5'}$–$O_{5'}$ bond	−54.09	−38.13
$C_{3'}$–$O_{3'}$ bond	−45.25	−36.22
N-glycosidic bond	−9.36	−0.89

[a] $\Delta E = E$(Bond broken product) − E(Radical anion)
[b] $\Delta E_{PCM} = E$(Bond broken product) − E(Radical anion); using PCM model with $\varepsilon = 78$

σ-bond broken product is 45.25 kcal/mol lower than that of 3′,5′-dADP$^{\cdot-}$. However, solvent effects destabilize these products by about 16 kcal/mol (9 kcal/mol for the $C_{3'}$–$O_{3'}$ σ-bond broken product).

N-glycosidic bond broken product in the gas phase is about 9.36 kcal/mol lower than 3′,5′-dADP$^{\cdot-}$. In the gas phase, this complex contains a deprotonated adenine anion and a ribose-centered P-S-P radical. In the presence of the polarizable surroundings, this N-glycosidic bond broken product is significantly destabilized by the surrounding-solute interactions. The total energy of this complex is only about 0.89 kcal/mol lower than that of 3′,5′-dADP$^{\cdot-}$.

14.4.5   Reaction Pathways of the LEE-Induced DNA Single Strands at Adenine Site

The low energy electron-induced single-strand bond breaking in the adenine-rich DNA might take place in the same way as the corresponding process proceeds in the pyrimidines: the electrons partly bound to the base group, forming an adenine-centered radical anion of the nucleotide. Subsequently, this radical anion undergoes the C–O bond or glycosidic bond breaking and yield corresponding radical fragments and anions.

In the gas phase, the glycosidic bond breaking requires activation energy as high as 21.28 kcal/mol. Therefore, the DNA base release should be excluded based on the energy consideration. The energy barrier for the $C_{3'}$–$O_{3'}$ σ-bond cleavage process (8.94 kcal/mol) is close to that of $C_{5'}$–$O_{5'}$ σ-bond cleavage (9.99 kcal/mol). Both pathways seem to be compatible. However, relatively small electron vertical detachment energy (VDE = 0.26 eV, or 6.00 kcal/mol) of the corresponding radical anion 3′,5′-dADP$^{\cdot-}$ suggests that electron detachment should dominate in the gas phase. Therefore, the LEE attachment is unlikely to directly induce the strand breaks at the adenine site in the DNA single strands.

In PCM approximation, the effects of the polarizable surroundings not only greatly increase the activation energies of the C–O σ-bond cleavage processes (13.22 kcal/mol for $C_{3'}$–$O_{3'}$ σ-bond rupture and 22.54 kcal/mol for $C_{5'}$–$O_{5'}$σ-bond rupture) but also significantly increase the electron vertical detachment energy (VDE = 1.59 eV, or 36.69 kcal/mol) of 3′,5′-dADP$^{\cdot-}$. Consequently, $C_{3'}$–$O_{3'}$ σ-bond rupture is expected to be able to take place for the adenine-centered radical anion in
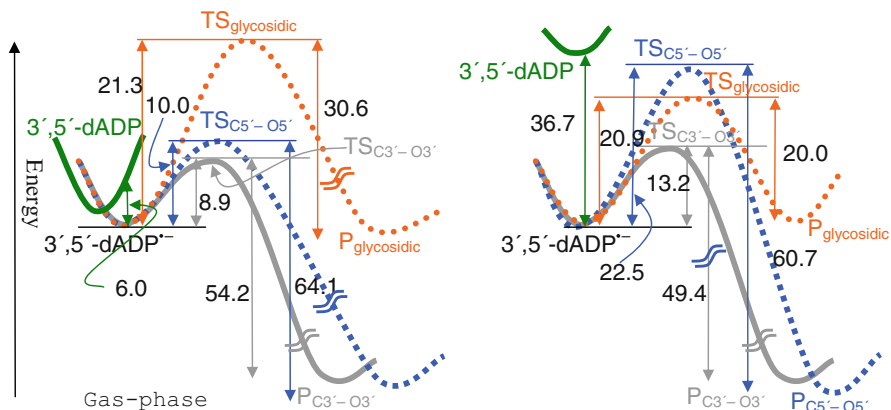
Fig. 14.7 The energy profile of the $C_{5'}-O_{5'}$, $C_{3'}-O_{3'}$, and N-glycosidic bond breaking process of $3',5'$-dADP·⁻ in the gas-phase and in the presence of the polarizable surroundings [49] (Reproduced with permission from Ref. [49], Copyright (2011), American Chemical Society)

the presence of polarizable medium. Considering that the presence of the polarizable surroundings hardly changes the activation energy barrier of N-glycosidic bond breaking, the $C_{3'}-O_{3'}$ σ-bond cleavage processes should dominate the LEE induced DNA single strand dissociation in the adenine-rich DNA (Fig. 14.7).

14.5 Electron Attachment Induced DNA Single-Strand Breaks at the Guanine Site [38]

The study of the electron attachment to $2'$-deoxyguanosine-$3',5'$-diphosphate ($3',5'$-dGDP) reveals that the EA_{ad} of $3',5'$-dGDP reaches 0.36 eV and the vertical detachment energy (VDE) of the corresponding radical anion ($3',5'$-dGDP·⁻) amounts to 0.32 eV. This suggests that such radical anion is able to endure the reactions with the activation energy barrier less than 7.37 kcal/mol (0.32 eV) in the gas phase. Unlike in pyrimidine bases, electron attachment to $3',5'$-dGDP does not lead to the formation of base-center valence radical anion. However, the electron affinities of $3',5'$-dGDP suggest that in the gas phase it is possible to form a dipole-bound radical anion that would represent the local minimum on the potential energy surface. This dipole-bound state of the radical anion might serve as the precursor of the electron attchment induced bond breakings.

Again, one needs to know how this process is carried out in the polar environment. The influence of the polarizable surroundings remarkably improves the ability of $3',5'$-dGDP to capture an electron (EA_{ad} amounts to 0.95 eV in aqueous solution). Moreover, due to the solvent interactions, the increased VDE of $3',5'$-dGDP·⁻ (1.01 eV) suggests that in the presence of the polarizable surroundings, the reactions with energy barrier of less than 23 kcal/mol might occur before the electron detachment for this radical anion (Table 14.8).

Table 14.8 Electron attachment and detachment energies of $3',5'$-dGDP (in eV)

Process	EA_{ad}	VEA^a	VDE^b
$3',5'$-dGDP $\rightarrow$ $3',5'$-dGDP$^-$ gas-phase	0.24 (0.36)^c	0.14^c	0.32^c
$3',5'$-dGDP $\rightarrow$ $3',5'$-dGDP$^-$ PCM model	0.95^c		1.01

^{a}VAE $= E$(neutral) – E(anion); the energies are evaluated using the optimized neutral structures
^{b}VDE $= E$(neutral) – E(anion); the energies are evaluated using the optimized anion structures
^{c}Reference [5]

14.5.1   *Activation Energies of the C₅′–O₅′ σ-Bond Breaking Process in 3′,5′-dGDP·⁻*

The transition state for the radical anions of $3',5'$-dGDP is characterized by the existence of a single imaginary vibrational frequency (848i cm^{-1}). The $C_{5'}$–$O_{5'}$ σ-bond breaking can be traced through the elongated $C_{5'}$–$O_{5'}$ atomic distance of 1.776 Å and by the normal mode corresponding to the imaginary vibrational frequency (Fig. 14.8). The activation energy of the $C_{5'}$–$O_{5'}$ σ-bond cleavage process has been predicted to be 12.97 kcal/mol (Table 14.9, without ZPE) [38]. As a comparison, the activation energy needed for the $C_{5'}$–$O_{5'}$ σ-bond breaking for $3',5'$-dADP·⁻ is 9.9 kcal/mol. The $C_{5'}$–$O_{5'}$ σ-bond is weak in the purine sites of DNA [38].

The effects of the polarizable surroundings are vital for this process – they lower the $C_{5'}$–$O_{5'}$ σ-bond breaking energy barrier dramatically (1.06 kcal/mol with the PCM model prediction, Table 14.9) in $3',5'$-dGDP·⁻. This substantial decrease of the energy barrier is mainly due to the large dipole moment (19.8 Debye) induced by the solvent-solute interaction at the transition state corresponding to the $C_{5'}$–$O_{5'}$ σ-bond rupture. On the contrary, the effects of the polarizable surroundings raise the $C_{5'}$–$O_{5'}$ σ-bond breaking energy barrier for the other nucleotides significantly (18.73 kcal/mol for $3',5'$-dCDP·⁻, 18.76 kcal/mol for $3',5'$-dTDP·⁻, and 22.54 kcal/mol for $3',5'$-dADP·⁻).

14.5.2   *Activation Energies of the C₃′–O₃′ σ Bond Breaking Process in 3′,5′-dGDP·⁻*

In order to evaluate the activation barriers one needs to obtain detailed information about transition state relates to such barriers. The transition state for $C_{3'}$–$O_{3'}$ σ-bond cleavage process in the radical anion of $3',5'$-dGDP is characterized by the elongated $C_{3'}$–$O_{3'}$ atomic distance (1.738 Å). The activation energy of the $C_{3'}$–$O_{3'}$ σ-bond breaking has been predicted to be 11.23 kcal/mol (Table 14.9, without ZPE) [38]. Similar energy barrier is reported based on the $3'$-dGMP model (10.28 kcal/mol) at the same level of theory by Schyman et al. [50]. The presence of the phosphate group slightly increases the $C_{3'}$–$O_{3'}$ σ-bond breaking energy barrier. As a comparison, the activation energy needed for the $C_{3'}$–$O_{3'}$ σ-bond breaking in pyrimidine nucleotides is lower, owing to the SN2-like reaction mechanism.
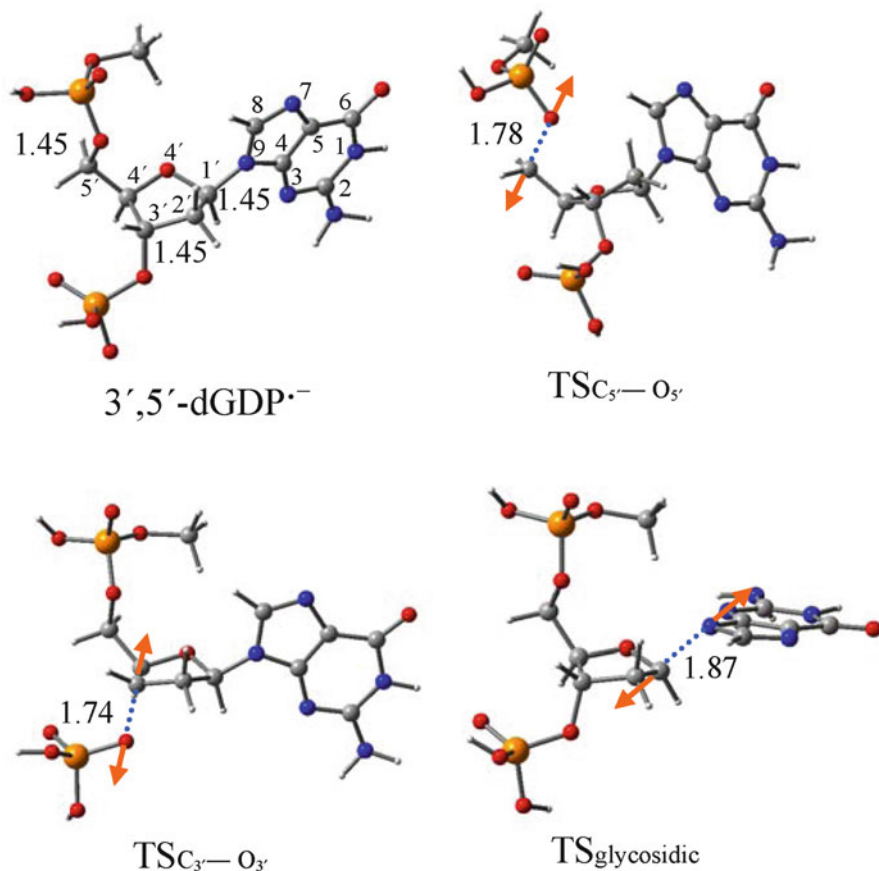
Fig. 14.8 The optimized structures of the radical anion of 3′,5′-dGDP·⁻ and the transition state structures of the C₅′–O₅′ bond breaking (TSC₅′–O₅′), C₃′–O₃′ bond breaking (TSC₃′–O₃′), and N-glycosidic bond breaking (TSglycosidic). Atomic distances are in Å. *Orange arrows* in the transition states represent vibration mode related to the single imaginary frequency (Reproduced with permission from Ref. [38], Copyright (2010), John Wiley & Sons)

Table 14.9 The relative energies of transition states of bond breaks in 3′,5′-dGDP·⁻ (kcal/mol)

Bond breaking process	ΔE_{TS} [a]	ΔE_{TS}(PCM) [b]	ΔE_{TS}^0 [c]	ΔG_{TS}^0 [d]
C₅′–O₅′ bond	12.97	1.06	11.06	10.40
C₃′–O₃′ bond	11.23 (10.28[e])	3.56 (5.25[e])	9.25 (8.56[e])	8.59
N-glycosidic bond	24.08	9.99	21.64	21.05

[a] $\Delta E_{TS} = E$(Transition state) – E(Radical anion)
[b] ΔE_{TS} (PCM) = E(Transition state) – E(Radical anion); using PCM model with $\varepsilon = 78$
[c] With the zero point energy (ZPE) correction
[d] Free energy at $T = 298$ K
[e] Reference [50], using 2′-deoxyguanosine-3′ monophosphate as the model

The effects of the polarizable surroundings decrease significantly the energy barrier of the $C_{3'}-O_{3'}$ σ-bond rupture in 3′,5′-dGDP$^{•-}$ (3.56 kcal/mol with the PCM model prediction) [38]. This effect can also be seen in the 3′-dGMP model (5.25 kcal/mol) [50]. The dipole moment (8.9 Debye) induced by the solvent-solute interaction in the transition state corresponding to the $C_{3'}-O_{3'}$ σ-bond rupture is only half of that revealed for the transition state structure related to the $C_{5'}-O_{5'}$ σ-bond breaking. Therefore, the effect of the polar surroundings on the activation energy barrier is more profound in the $C_{5'}-O_{5'}$ σ-bond breaking process.

14.5.3 Activation Energies of the N-Glycosidic Bond Breaking Process in 3′,5′-dGDP$^{•-}$

The transition state for N-glycosidic bond breaking of the radical anion of 3′,5′-dGDP has been located and characterized by the elongated $C_{1'}-N_9$ atomic distance (1.873 Å). This is further confirmed by the existence of single imaginary vibrational frequency of 576i cm^{-1} and the corresponding normal mode representing the $C_{1'}-N_9$ σ-bond breaking. The activation energy of the $C_{1'}-N_9$ glycosidic bond breaking has been predicted to be 24.08 kcal/mol (Table 14.9, without ZPE) [38]. This energy barrier is noticeable higher than that reported in the previous studies on the LEE-induced glycosidic bond cleavage in pyrimidine nucleosides, in which the activation energy was predicted to be 18.9–21.6 kcal/mol for the C–N bond break [38].

Similarly to the C–O σ-bond rupture, the effects of the surroundings lower the energy barrier of the N-glycosidic bond breaking down to 9.99 kcal/mol for 3′,5′-dGDP$^{•-}$ in the presence of the polarizable environment. This substantial decrease in the energy barrier due to the surrounding-solute interactions is in accordance with the large dipole moment of the corresponding transition state (18.7 Debye) revealed in the PCM model calculation.

14.5.4 Products of the C–O σ-Bonds and N-Glycosidic Bond Breaking Processes of the Radical Anion of 3′,5′-dGDP

Both $C_{3'}-O_{3'}$ and $C_{5'}-O_{5'}$ σ-bonds rupture lead to the energetically stable complexes consisting of a phosphate anion and a corresponding carbon-centered neutral radical. In the former case, the $C_{5'}-O_{5'}$ σ-bond broken product is by 30.13 kcal/mol more stable than 3′,5′-dGDP$^{•-}$ (Table 14.10). Meanwhile the energy of the $C_{3'}-O_{3'}$ σ-bond broken product is 24.42 kcal/mol lower than that of 3′,5′-dGDP$^{•-}$ [38]. Interestingly, the formation of a H-bond between the phosphate groups in the $C_{5'}-O_{5'}$ σ-bond broken product is the reason for this energy difference between these two C–O σ-type bond broken products. In addition, the solvent effects further stabilize these products by about 10 kcal/mol (16 kcal/mol for the $C_{3'}-O_{3'}$ σ-bond broken product) [38].

Table 14.10 The relative energies of the bond broken products of $3',5'$-dGDP$^{\cdot-}$ (kcal/mol)

Bond breaking process	ΔE^{a}	$\Delta E_{PCM}{}^{b}$
$C_{5'}$–$O_{5'}$ bond	−30.13	−40.70
$C_{3'}$–$O_{3'}$ bond	−24.42	−40.16
N-glycosidic bond	−1.26	−20.13

[a] $\Delta E = E$(Bond broken product) – E(Radical anion)
[b] $\Delta E_{PCM} = E$(Bond broken product) – E(Radical anion); using PCM model with $\varepsilon = 78$

N-glycosidic bond broken product in the gas phase is only by about 1.3 kcal/mol lower than $3',5'$-dGDP$^{\cdot-}$. In the gas phase this complex contains a dehydrogenated guanine neutral radical and a P-S-P anion. However, in the presence of the polarizable surroundings, this N-glycosidic bond broken product is significantly stabilized by the surrounding-solute interactions. The total energy of this complex is about 20 kcal/mol lower than that of $3',5'$-dGDP$^{\cdot-}$ [38].

14.5.5 Reaction Pathways of the LEE-Induced DNA Single Strands at the Guanine Site

The mechanism of the low energy electron-induced single-strand bond breaking in the guanine-rich DNA is proposed as follows: The electrons partly bound to the phosphate group in adjacent to the guanine in DNA oligomers, forming a phosphate-centered radical anion of the nucleotide. Subsequently, this radical anion undergoes the C–O bond or glycosidic bond breaking and yields corresponding radical fragments and anions.

In the gas phase, the glycosidic bond breaking requires activation energy as high as 24.08 kcal/mol. Therefore, base release should be excluded based on the energy consideration. The energy barrier for the $C_{3'}$–$O_{3'}$ σ-bond cleavage process (11.23 kcal/mol) is close to that of $C_{5'}$–$O_{5'}$ σ-bond cleavage process (12.97 kcal/mol) [38]. Both pathways seem to be compatible. However, relatively small electron VDE (VDE = 0.32 eV, or 7.37 kcal/mol) of the corresponding radical anion $3',5'$-dGDP$^{\cdot-}$ suggests that electron detachment should dominate in the gas phase. Therefore, the LEE attachment is unlikely to directly induce the strand breaks at the guanine site in the DNA single strands.

In order to evaluate the effect of polar environment on the studied phenomena, the PCM model was employed. Its limitations imply that one cannot directly account for the effects of proton transfer or charge transfer between solute and solvent. In this approximation, the effects of the polarizable surroundings not only greatly decrease the activation energies of the C–O σ-bond cleavage processes (1.06 to 3.56 kcal/mol) but also significantly increase the electron VDE (VDE = 1.01 eV, or 23.29 kcal/mol) of $3',5'$-dGDP$^{\cdot-}$ [38]. Consequently, C–O σ-bond cleavage processes are easy to carry out. Although the presence of the polarizable surroundings also lowers the
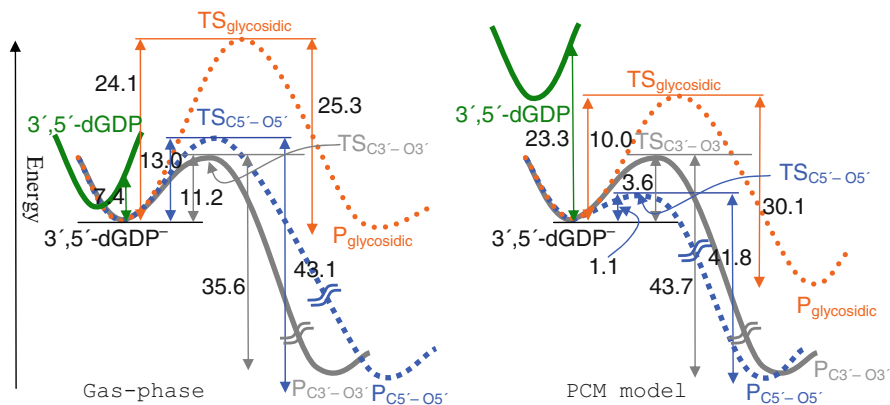
Fig. 14.9 The energy profile of the $C_{5'}-O_{5'}$, $C_{3'}-O_{3'}$, and N-glycosidic bond breaking process of $3',5'$-dGDP$^-$ in the gas phase and in the presence of the polarizable surroundings (Reproduced with permission from Ref. [38], Copyright (2010), John Wiley & Sons)

activation energy barrier of N-glycosidic bond breaking down to 9.99 kcal/mol, this process is expected to be suppressed by the C–O σ-bond cleavage processes (Fig. 14.9).

LEE-induced bond breaks experiment on the oligonucleotide tetramer CGTA in the thin solid films reported the ratio of 29:11:0 for the bond breaks of $C_{5'}-O_{5'}$, $C_{3'}-O_{3'}$, and N-glycosidic bonds [28]. This ratio clearly follows the theoretical sequence of the bond breaking reaction pathways in aqueous solutions. In the experiment the oligonucleotide CGTA was in the thin solid films [28]. The consistency between experimental and theoretical data related to the reaction pathway ratio suggests that the influence of the surroundings in the thin solid film on the LEE-induced DNA damages is similar to the effects of the polarizable surroundings described by the PCM model.

14.6 Comparison with the Experimental Results

For cytidine, the experiments of LEE-induced bond breaks of oligonucleotide tetramer GCAT in the thin solid films revealed the ratio of 5:11 for the bond breaks of $C_{5'}-O_{5'}$ to the bond breaks of $C_{3'}-O_{3'}$ (at the site of cytidine) induced by the incident electrons with the energy of 15 eV. This ratio decreases to 3:8 (10 eV) and 4:21 (6 eV) as the energy of the incident electrons diminishes [28]. Therefore, one should expect that the ratio of the bond breaks of $C_{5'}-O_{5'}$ against that of $C_{3'}-O_{3'}$ induced by the near-zero electron attachment will be even smaller. On the other hand, the fraction of the cytosine base release is negligible. This ratio observed in the experiments clearly follows our theoretical sequence of the bond breaking reaction pathways either in solvent or in the gas phase.

For thymidine, the experiment of LEE-induced bond breaks of oligonucleotide trimer TTT (TpTpT) [48] in the solid films yields the ratio of 2.5:2.9 for the bond breaks of $C_{5'}$–$O_{5'}$ to the bond breaks of $C_{3'}$–$O_{3'}$ with the relatively high energy incident electrons (11 eV). This ratio is also qualitatively consistent with the theoretical predictions.

Considering that the oligonucleotide GCAT is in the thin solid films in the experiment [28], the influence of the surroundings in the thin solid film on the LEE-induced DNA damages is greater than that revealed by the gas phase simulations; however, the outcome is lesser than suggested by the solvent effects evaluated by the PCM model. The consistency between the theoretical prediction and the experimental observation related to the reaction pathway ratio provides strong supportive evidence for the base-centered radical anion mechanism of the low energy electron-induced single-strand bond breaking around the pyrimidine sites of the DNA single strands, mentioned above.

Recent experiments demonstrated that guanosine is one of the vulnerable sites in DNA in aqueous solutions under the bombardment of low energy electrons [35–37]. In the presence of the polarizable surroundings, the significant increase in the electron affinities of the $3',5'$-dGDP and in vertical detachment energy of $3',5'$-dGDP$^{\cdot-}$ ensure the formation of the electronically stable radical anion. Furthermore, the surrounding-solute interactions greatly reduce the activation barriers of the C–O bond cleavage to approximately 1.1–3.6 kcal/mol [38]. These low energy barriers ensure either $C_{5'}$–$O_{5'}$ or $C_{3'}$–$O_{3'}$ bond rupture to take place at the guanosine site in DNA single strands. The activation energies of these C–O bond cleavages indicate that $C_{5'}$–$O_{5'}$ bond breaking is superior over that of $C_{3'}$–$O_{3'}$ involving process.

14.7   Summary

One of the possible mechanisms for the low energy electron-induced single-strand breaking in DNA might involve the electron's attachment to the pyrimidine DNA bases and the formation of the base-centered radical anions of the nucleotides in the first step. Subsequently, these electronically stable radical anions are capable of undergoing either C–O or glycosidic bond breaking, producing the neutral ribose radical fragments and the corresponding phosphoric anions or base anions. The results of the theoretical studies, along with the findings of the earlier investigations indicate that this mechanism is able to elucidate the recent experimental observations on the LEE induced damages in DNA single strands.

For the pyrimidine diphosphates, the strand breaks caused by the attachment of near-zero energy electrons is dominated by the $C_{3'}$–$O_{3'}$ σ-bond cleavage pathway in the gas phase. The relatively high activation energy barrier for the glycosidic bond breaking suggests that based on the base-centered radical anion mechanism, LEE attachment is unlikely to directly induce the base release at the pyrimidine sites in the DNA single strands. Moreover, due to the low electron affinities of the purine diphosphates and the low VED energies of the corresponding radical anions, the

bond breaks during the low energy electron attachment to DNA single strands is unlikely to occur at the purine sites in the gas-phase.

However, the existence of the polarizable surroundings appreciably changes the scenarios. In the presence of polarizable surroundings, the interactions between the nucleotides and the polarizable medium increase the activation barriers to 13–14 kcal/mol for the $C_{3'}$–$O_{3'}$ bond cleavage and to 18–19 kcal/mol for the $C_{5'}$–$O_{5'}$ bond cleavage, respectively. These relatively high energy barriers suggest that only $C_{3'}$–$O_{3'}$ bond rupture takes place in a reasonable rate at the pyrimidine sites in DNA single strands. On the other hand, the comparatively high electron affinities of the 3′,5′-dGDP and in vertical detachment energy of 3′,5′-dGDP$^-$ ensure the formation of the electronically stable radical anion. Furthermore, the surrounding-solute interactions greatly reduce the activation barriers of the C–O bond cleavage to approximately 1–4 kcal/mol. These low energy barriers ensure either $C_{5'}$–$O_{5'}$ or $C_{3'}$–$O_{3'}$ bond rupture to take place at the guanosine site in DNA single strands significantly. In addition, the activation energies of these C–O bond cleavages indicate that $C_{5'}$–$O_{5'}$ bond breaking is superior over that of $C_{3'}$–$O_{3'}$.

It should be emphasized that the PCM model only accounts for the effects of the polarizable surroundings. However, there are other important factors governing characteristics of solvated species in aqueous solutions such as microsolvation and proton transfer between solvent and solute, which are not accounted for in the PCM calculations. In addition to the effects of the polarizable surroundings (which increase the activation energy barriers for C–O σ-bonds and glycosidic bond cleavage), microhydration and proton transfer between water molecules and the radical anions would further stabilize the reactants by reducing the excessive negative charge of the radical anions. Therefore, electron-induced DNA single-strand bond breaking might have different scenarios in aqueous solutions, as concluded in the experimental studies [51].

References

1. Bao X, Wang J, Gu J, Leszczynski J (2006) Proc Natl Acad Sci USA 103:5658–5663
2. Ray SG, Daube SS, Naaman RJ (2005) Proc Natl Acad Sci USA 102:15–19
3. Richardson NA, Gu J, Wang S, Xie Y, Schaefer HF (2004) J Am Chem Soc 126:4404–4411
4. Gu J, Wang J, Leszczynski J (2006) J Am Chem Soc 128:9322–9323
5. Gu J, Xie Y, Schaefer HF (2007) Nucleic Acid Res 35:5165–5172
6. Becker D, Sevilla MD (1993) The chemical consequences of radiation damage to DNA. In: Lett J (ed) Advances in radiation biology, vol 17. Academic, New York, pp 121–180
7. Kelley SO, Barton JK (1999) Science 283:375–381
8. Ratner M (1999) Nature 397:480–481

 9. Boudaiffa B, Cloutier P, Hunting D, Huels MA, Sanche L (2000) Science 287:1658–1659
10. Pan X, Cloutier P, Hunting D, Sanche L (2003) Phys Rev Lett 90:208102
11. Caron LG, Sanche L (2003) Phys Rev Lett 91:113201
12. Zheng Y, Cloutier P, Hunting D, Wagner JR, Sanche L (2004) J Am Chem Soc 126:1002–1003
13. Hall DB, Holmlin RE, Barton JK (1996) Nature 382:731–735
14. Steenken S (1997) Biol Chem 378:1293–1297
15. Taubes G (1997) Science 275:1420–1421
16. Berlin YA, Burin AL, Ratner MA (2001) J Am Chem Soc 123:260–268
17. Beljonne D, Pourtois G, Ratner MA, Bredas JL (2003) J Am Chem Soc 125:14510–14517
18. Huels MA, Hahndorf I, Illenberger E, Sanche L (1998) J Chem Phys 108:1309–1312
19. Hanel G, Gstir B, Denifl S, Scheier P, Probst M, Farizon B, Farizon M, Illenberger E, Mark TD (2003) Phys Rev Lett 90:188104–1–188104–4
20. Li X, Sevilla MD, Sanche L (2003) J Am Chem Soc 125:13668–13669
21. Huels MA, Boudaiffa B, Cloutier P, Hunting D, Sanche L (2003) J Am Chem Soc 125: 4467–4477
22. Abdoul-Carime H, Gohlke S, Fischbach E, Scheike J, Illenberger E (2004) Chem Phys Lett 387:267–270
23. Barrios R, Skurski P, Simons J (2002) J Phys Chem B 106:7991–7994
24. Berdys J, Anusiewicz I, Skurski P, Simons J (2004) J Am Chem Soc 126:6441–6447
25. Berdys J, Skurski P, Simons J (2004) J Phys Chem B 108:5800–5805
26. Berdys J, Anusiewicz I, Skurski P, Simons J (2004) J Phys Chem A 108:2999–3005
27. Gu J, Xie Y, Schaefer HF (2005) J Am Chem Soc 127:1053–1057
28. Zheng Y, Cloutier P, Hunting DJ, Sanche L, Wagner JR (2005) J Am Chem Soc 127: 16592–16598
29. Zheng Y, Cloutier P, Hunting DJ, Wagner JR, Sanche L (2006) J Chem Phys 124:064710
30. Simons J (2006) Acc Chem Res 39:772–779
31. Sanche L (2005) Eur Phys J D 35:367–390
32. Li X, Sanche L, Sevilla MD (2006) Radiat Res 165:721–729
33. LaVerne JA, Pimblott SM (1995) Radiat Res 141:208–215
34. Kumar A, Sevilla MD (2007) J Phys Chem B 111:5464–5474
35. Sanche L (2009) Nature 461:358–359
36. Wang C-R, Nguyen J, Lu Q-B (2009) J Am Chem Soc 131:11320–11322
37. Wang C-R, Lu Q-B (2010) J Am Chem Soc 132:14710–14713
38. Gu J, Wang J, Leszczynski J (2010) Chemphyschem 11:175–181
39. Gu J, Wang J, Leszczynski J (2010) Nucleic Acids Res 38:5280–5290
40. Schiedt J, Weinkauf R, Neumark DM, Schlag EW (1998) Chem Phys 239:511–524
41. Gu J, Xie Y, Schaefer HF (2006) J Am Chem Soc 128:1250–1252
42. Wesolowski SS, Leininger ML, Pentchev PN, Schaefer HF (2001) J Am Chem Soc 123: 4023–4028
43. Rienstra-Kiracofe JC, Tschumper GS, Schaefer HF, Nandi S, Ellison GB (2002) Chem Rev 102:231–282
44. Gu J, Xie Y, Schaefer HF (2005) J Phys Chem B 109:13067–13075
45. Stokes ST, Li X, Grubisic A, Ko YJ, Bowen KH (2007) J Chem Phys 127:084321–6
46. Li X, Sevilla MD (2007) Adv Quantum Chem 52:59–87
47. Cossi M, Barone V, Cammi R, Tomasi J (1996) Chem Phys Lett 255:327–335
48. Li Z, Zheng Y, Cloutier P, Sanche L, Wagner JR (2008) J Am Chem Soc 130:5612–5613
49. Gu J, Wang J, Leszczynski J (2011) J Phys Chem B 115:14831–14837
50. Schyman P, Laaksonen A (2008) J Am Chem Soc 130:12254–12255
51. von Sonntag C (2007) Adv Quantum Chem 52:5–20

Index